



# 6<sup>TH</sup> CONFERENCE ON ELEMENTARY PROCESSES IN ATOMIC SYSTEMS

Contributed Papers



**9. - 12. JULY 2014**  
**BRATISLAVA**

# **CEPAS 2014**

## **CONTRIBUTED PAPER**

**Editors**

**Štefan Matejčík Peter Papp Ondrej Bogár**

**Department of Experimental Physics, Comenius University  
Bratislava, Slovakia**

**Bratislava, 2014**

**CONTRIBUTED PAPERS**  
**of the**  
**6<sup>th</sup> CONFERENCE ON ELEMENTARY PROCESSES IN ATOMIC SYSTEMS**

**9<sup>th</sup> - 12<sup>th</sup> July 2014,**  
**Bratislava, Slovakia**

**Editors**

**Štefan Matejčík Peter Papp Ondrej Bogár**

**Publisher**

**Comenius University**  
**Faculty of mathematics physics and informatics**  
**Mlynská dolina**  
**842 48 Bratislava, Slovakia**

**ISBN 978-80-8147-021-9**

# EPJ.org



sponsored lecture

John Tanis

**TRANSMISSION OF ELECTRONS THROUGH MICROMETER GLASS CAPILLARIES  
AND DIFFERENCES WITH IONS**



# **Conference Topics**

1. photo-processes and laser collisions
2. electron(positron)/atom collisions
3. collisions with biomolecules
4. heavy particles (ion/atom) collisions
5. interactions with surfaces
6. processes with nanosized complex systems

## **Local Organizing Committee, (Comenius University, Bratislava, Slovakia)**

Štefan Matejčík (Chairman)

Peter Papp (Secretary)

Katarína Matejčíková

Ondrej Bogár

Michal Lacko

Anita Ribar

## International Scientific Committee

Bratislav P. Marinković	Serbia
Károly Tőkesi	Hungary
Zoran Lj. Petrović	Serbia
Mariusz Zubek	Poland
Jiří Horáček	Czech Republic
Gustavo Garcia Gomez-Tejedor	Spain
Joachim Burgdorfer	Austria
John A. Tanis	USA
Friedrich Aumayr	Austria
Robert DuBois	USA
Andrey Solov'yov	Germany
Ladislau Nagy	Romania
Viorica Stancalie	Romania
Nigel J. Mason	United Kingdom
Otto B. Shpenik	Ukraine

# Contents

DECORATION OF FULLERENE IONS WITH SIMPLE MOLECULES .....	5
SWIFT HEAVY ION IRRADIATION OF GRAPHENE .....	8
ELECTRON TRANSMISSION THROUGH MICROMETER GLASS CAPILLARIES AND DIFFERENCES WITH IONS.....	9
FULLY DIFFERENTIAL CROSS SECTIONS FOR IONIZATION OF H <sub>2</sub> BY PROTON IMPACT .....	13
INDIRECT DISSOCIATIVE RECOMBINATION OF SIMPLE IONS .....	15
ELASTIC SCATTERING FROM PLASMA MOLECULES AND RADICALS .....	18
MEASUREMENTS OF THE RADIATIVE ELECTRON CAPTURE TO CONTINUUM (RECC).....	24
COMPARISON OF EXPERIMENT AND THEORY FOR ELECTRON IMPACT IONIZATION OF LASER-ALIGNED MG ATOMS. ....	25
THEORETICAL AND EXPERIMENTAL INVESTIGATION OF (E,2E) FOR ALIGNED H <sub>2</sub> MOLECULES.....	29
ZERO ENERGY RESONANCES IN A FUSION PLASMA .....	32
VORTICES IN THE POSITRON-IMPACT IONIZATION OF ATOMS .....	34
ON HOW JOST CAN HELP BREIT AND WIGNER TO BETTER DESCRIBE A RESONANCE.....	37
ETHYNYL RADIATION PRODUCED BY DISSOCIATION EXCITATION OF ACETYLENE BY ELECTRON IMPACT .....	39
PROJECTILE CHARGE EFFECTS IN DIFFERENTIAL IONIZATION OF MOLECULAR NITROGEN BY POSITRONS AND ELECTRONS .....	43
ON ELECTRON EXCITATION OF SOME QUASIMETASTABLE STATES OF POTASSIUM ATOM .....	47
THEORETICAL INVESTIGATIONS ON THE PROJECTILE COHERENCE EFFECTS IN FULLY DIFFERENTIAL IONIZATION CROSS SECTIONS.....	50
THE LIGAND DISSOCIATIONS FROM MPS, DMPS AND TMPS MOLECULES BY ELECTRON IMPACT .....	53
SECOND-KIND COLLISION OF ELECTRONS WITH CADMIUM METASTABLE ATOMS .....	61

EJECTED ELECTRON SPECTRA FROM AUTOIONIZATION REGION IN NEON AT INCIDENT ELECTRON ENERGY OF 505 EV AND EJECTION ANGLES OF 40° AND 130.....	63
ELASTIC ELECTRON SCATTERING ON MOLECULE IN OPTICAL POTENTIAL APPROACH.....	65
APPEARANCE ENERGIES OF THE SF <sub>6</sub> MOLECULE IONIC FRAGMENTS STUDIED <i>AB INITIO</i> .....	67
ELASTIC ELECTRON SCATTERING BY PHOSPHOROUS ATOM IN OPTICAL POTENTIAL APPROACH.....	69
MASS SPECTROMETRIC STUDIES OF COAL THERMAL DESTRUCTION PRODUCTS .....	71
CLASSIFICATION OF LOW-ENERGY CORE EXCITED AUTOIONIZING STATES IN BARIUM.....	74
EXCITATION OF SELENIUM IN GAS-PHASE BY ELECTRON IMPACT.....	77
EXCITATION OF SULPHUR BY SLOW ELECTRONS .....	79
DISSOCIATIVE ELECTRON ATTACHMENT TO VOLATILE ANAESTHETICS AND CHLORINATED ETHANES .....	81
EXPERIMENTAL (E,2E) STUDY OF STATE-TO-STATE INTERFERENCE BETWEEN AUTOIONIZING STATES OF HE.....	84
DISSOCIATIVE EXCITATION OF FE(CO) <sub>5</sub> STUDIED USING ELECTRON INDUCED FLUORESCENCE APPARATUS.....	87
DISSOCIATIVE ELECTRON ATACHMENT TO NITROMETHANE STUDIED BY VELOCITY SLICE IMAGING .....	91
ELECTRON-IMPACT-INDUCED TRYPTOPHAN MOLECULE FRAGMENTATION....	97
ELECTRON IMPACT (E, 2E) IONIZATION OF NH <sub>3</sub> AND CH <sub>4</sub> .....	99
IONIZATION OF WATER BY ELECTRON IMPACT.....	101
DIELECTRONIC RECOMBINATION RATE COEFFICIENTS OF RUBIDIUMLIKE TUNGSTEN.....	104
ISOTOPE-SPECIFIC K .....	107
ELECTRON-SCATTERING CROSS SECTIONS FOR SELECTED ALKYNE MOLECULES .....	109
SPECTRAL LINES OF CAESIUM HYDRIDE IN HIGH VACUUM .....	112
NEAR-THRESHOLD EXCITATION OF THE RESONANCE $\lambda$ 182.2 NM LINE AT ELECTRON - PB <sup>+</sup> ION COLLISIONS .....	113

ELECTRON-IMPACT EXCITATION OF THE IN <sup>+</sup> ION: CASCADE CONTRIBUTION TO RESONANCE TRANSITIONS.....	116
PERIODIC VARIATIONS OF AUGER ENERGY MAXIMUM DISTRIBUTION FOLLOWING HE <sub>2</sub> <sup>+</sup> + H <sub>2</sub> COLLISIONS : A COMPLETE ANALOGY WITH PHOTON INTERFERENCES .....	120
ATOMIC AND MOLECULAR PROCESSES OF INTEREST FOR MODELING OF DISCHARGES IN LIQUIDS.....	121
SURFACE AND GAS PHASE PROCESSES IN AFTERGLOW PLASMAS AIMED FOR MEDICAL STERILIZATION .....	123
ACCURACY OF THEORETICAL CALCULATIONS FOR ELECTRON-IMPACT IONIZATION OF MOLECULES .....	126
ELECTRON PRODUCTION AND TRANSPORT IN BIOLOGIC MATERIAL INDUCED BY FAST IONS .....	127
DISSOCIATION OF PEPTIDES BY IONS AND PHOTONS.....	128
METASTABLE FRAGMENTATION OF BIOMOLECULES .....	129
ABSOLUTE CROSS SECTIONS FOR ELASTIC ELECTRON SCATTERING FROM FURAN AND THF MOLECULES .....	133
ELECTRON INDUCED DECOMPOSITION OF BIOMOLECULES PROBED IN POTASSIUM COLLISIONS .....	136
MOMENTUM TRANSFER TO A FREE FLOATING DOUBLE SLIT: REALIZATION OF A THOUGHT EXPERIMENT FROM THE EINSTEIN-BOHR DEBATES.....	137
LOW ENERGY REACTIVE COLLISIONS IN O <sup>+</sup> +H <sub>2</sub> .....	138
ELECTRONIC DYNAMICS IN LOW-ENERGY HEAVY-ION COLLISIONS .....	140
NEW DEVELOPMENTS OF THE PS <sup>-</sup> STUDIES .....	141
ELECTRON AND NUCLEAR DYNAMICS IN THE PHOTOIONIZATION OF MOLECULES .....	146
TRANSMISSION OF SLOW HIGHLY CHARGED IONS THROUGH 1 NM THICK CARBON NANOMEMBRANES .....	147
GUIDED TRANSMISSION OF IONS THROUGH NANOCAPILLARIES: VARIATIONS IN DISCHARGING DYNAMICS .....	150
PHOTOABSORPTION AND PHOTOIONIZATION WITH TWISTED LIGHT .....	153
PHOTOIONIZATION OF FULLERENES AND OTHER NANOCARBON SYSTEMS...	154
SPATIAL INTERFERENCE EFFECTS DURING THE IONIZATION OF ATOMS BY FEW-CYCLE LASER PULSES .....	156



TIME DEPENDENCE OF INTERATOMIC COULOMBIC DECAY .....	159
SUBCYCLE INTERFERENCE IN ATOMIC IONIZATION BY SCULPTED LASER PULSES .....	160
DYNAMICS OF BIMOLECULAR RECOMBINATION IN SYMMETRICAL CHANNELS .....	164
RELATIVISTIC CALCULATIONS OF IONIZATION AND PAIR CREATION PROBABILITIES IN LOW-ENERGY HEAVY-ION COLLISIONS.....	166
EMPIRICAL FORMULAE AND SCALINGS.....	168
FOR THE 1 <sup>ST</sup> AND 2 <sup>ND</sup> ORDER CONTRIBUTIONS TO DOUBLE IONIZATION OF HELIUM .....	168
AUGER PHOTOEMISSION SPECTROSCOPY FROM SURFACES OF FE-SI .....	173
VARIATION OF THE ELECTRONIC DENSITY ASSOCIATED TO THE EXCITATION OF PLASMONS DESCRIBED IN THE FRAME OF COHERENT STATES .....	175
PLASMON CHANGES FOR IN-OUT ASYMMETRY OF IONIC PROJECTILES TRAJECTORIES IN SOLID SURFACES .....	177
NATURAL WIDTHS AND BLACKBODY-RADIATION-INDUCED SHIFT AND BROADENING OF RYDBERG LEVELS IN MAGNESIUM IONS. ....	179
ELECTRON ATTACHMENT TO TETRAFLUOROQUINONE.....	190
ELASTICALLY AND INELASTICALLY TRANSMITTED ELECTRONS THROUGH INSULATING PET NANOCAPILLARIES .....	194
ONE-ELECTRON CAPTURE IN FAST ION-ATOMIC COLLISIONS.....	204
DISSOCIATIVE IONIZATION OF CH <sub>4</sub> MOLECULES INDUCED BY H <sup>+</sup> AND N <sup>+</sup> PROJECTILES.....	208
ELECTRON EXCITATION OF THE SORBITOL MOLECULE BY LOW-ENERGY ELECTRONS.....	211
ELECTRON IONIZATION MASS SPECTROMETRIC STUDY OF PYRIMIDINE MOLECULE .....	214
ELECTRON-IMPACT IONIZATION AND DISSOCIATIVE IONIZATION OF SORBITOL IN GAS PHASE .....	220
IONIZATION OF CYTOSINE MOLECULE BY ELECTRON IMPACT .....	223
POSITIVE AND NEGATIVE ION FORMATION IN THE GLYCEROL VAPOUR BY ELECTRON IMPACT .....	227
POSITIVE AND NEGATIVE ION FORMATION IN URACIL BY LOW-ENERGY ELECTRONS.....	230

MODIFICATION OF THIN FILMS INDUCED BY SLOW HEAVY IONS ANALYZED WITH PIXE AND SRIM .....	233
ELECTRON-IMPACT IONIZATION CROSS SECTIONS CALCULATIONS FOR PURINE AND PYRIMIDINE MOLECULES .....	236
MEASUREMENTS OF ABSOLUTE TOTAL CROSS SECTIONS FOR LOW- AND INTERMEDIATE-ENERGY ELECTRON SCATTERING FROM ANALOGUES OF BIOMOLECULES .....	239
SYNCHROTRON RADIATION INDUCED DEFECT FORMATION KINETICS IN RARE-GAS SOLIDS .....	242
IONIZATION OF ADENINE AND THYMINE MOLECULES BY ELECTRON IMPACT .....	245
TOWARDS COMPLEX RESONANCE ENERGIES FROM REAL CALCULATION .....	250
ON THE INFLUENCE OF LOW- AND HIGH-ENERGY IONIZING RADIATION ON THE AMINO ACID MOLECULE STRUCTURE: PROLINE.....	254
PHOTOIONIZATION DYNAMICS OF THE RYDBERG STATES OF C <sup>2+</sup> ION.....	257
EFFECT OF SMALL ADMIXTURE OF H <sub>2</sub> O ON THE ELECTRON DRIFT VELOCITY IN ARGON: EXPERIMENTAL MEASUREMENTS AND CALCULATIONS .....	261
COLLISIONAL FORMATION OF H <sup>-</sup> ANIONS AND PROTONS .....	266
FROM HYDROGEN-CONTAINING MOLECULAR SPECIES .....	266
VIA A BINARY-ENCOUNTER PROCESS.....	266
CLASSICAL AND QUASI-CLASSICAL MONTE CARLO CODE FOR THE ANALYSIS OF ION-ATOM COLLISIONS .....	269
ELASTIC AND INELASTIC GUIDING OF ELECTRONS THROUGH MICROMETER-SIZED FUNNEL-SHAPED GLASS CAPILLARIES.....	273

## DECORATION OF FULLERENE IONS WITH SIMPLE MOLECULES

A. Kaiser<sup>1</sup>, A. Mauracher<sup>1</sup>, M. Probst<sup>1</sup>, J. Postler<sup>1</sup>, M. Renzler<sup>1</sup>, M. Kuhn<sup>1</sup>, S. Ralser<sup>1</sup>, M. Harnisch<sup>1</sup>, S. Zöttl<sup>1</sup>, M. Daxner<sup>1</sup>, S. Denifl<sup>1</sup>, M.M. Goulart<sup>2</sup>, F. Zappa<sup>2</sup>, D.K. Bohme<sup>3</sup>, O. Echt<sup>4</sup> and P. Scheier<sup>1</sup>

<sup>1</sup> *Institut für Ionenphysik und Angewandte Physik, Universität Innsbruck, Austria*

<sup>2</sup> *Departamento de Física, ICE, Universidade Federal de Juiz de Fora, MG36036-330, Brazil*

<sup>3</sup> *Department of Chemistry, York University, Toronto, ON, Canada M3J 1P3*

<sup>4</sup> *Department of Physics, University of New Hampshire, Durham, NH 03824, United States*

E-mail: paul.scheier@uibk.ac.at

Experimental data obtained from mass spectra of He nanodroplets doped sequentially with fullerenes and various atoms or molecules reveal pronounced magic numbers that indicate particularly stable configurations. For clusters of fullerenes the pits between three fullerenes are often preferential binding sites, followed by the grooves between two fullerenes. Depending on the interaction between two adsorbate species and one adsorbate unit and the fullerene, commensurate decoration (formation of a monomolecular film) or agglutination (droplet formation) of the adsorbate is observed. Molecular dynamics and DFT studies are essential to develop models that explain the experimental results. Three examples (a dipolar, quadrupolar and apolar adsorbate) are discussed and compared with results for graphite, graphene and nanotubes found in the literature.

### 1. Introduction

Physisorption is a widely observed phenomenon and occurs in any solid/fluid or solid/gas system. In contrast to chemisorption it is a process in which the electronic structure of the atom or molecule is barely perturbed upon adsorption. Island growth has often been observed starting from initial adsorption at steps or defects. Besides single crystal metal and salt surfaces graphite is one of the most thoroughly investigated surfaces. The hexagonal arrangement of the atoms forms a weakly corrugated surface where the center of the hexagon represents the most favorable binding site for many atoms and molecules. The distance between two hexagonal rings is smaller than the van der Waals radius of even the smallest atom or molecule. Thus, ordered layers which are commensurate with the graphite lattice, such as the  $\sqrt{3} \times \sqrt{3}$  phase where every third hexagon is covered with an adsorbate have lower density than a theoretical  $1 \times 1$  phase.

The curvature of carbon nanotubes and fullerenes enhances the average distance between hexagonal (and pentagonal) faces and thus provides sufficiently more space than a flat graphene or graphite surface. Experiments and theoretical studies have been performed on the physisorption of atoms and molecules to films of fullerenes and nanotubes, deposited to surfaces [1]. Thereby grooves and pits form between two and three fullerenes, respectively. Rare gas atoms, for instance, prefer occupation of pit-sites between three fullerenes [2] and grooves between two fullerenes or nanotubes [3]. Decoration of single neutral fullerenes has been investigated via computational methods for various systems [4]–[6], however, only very few experimental studies have been published so far for charged species [7],[8]. Mass spectrometry provides a method to investigate the decoration of single isolated fullerenes. Shell closures represent structures with higher stability and for evaporative ensembles, such as excited clusters, and are reflected in intensity anomalies (magic numbers) in the mass spectra.

### 2. Results and discussion

In the present study weakly bound complexes, consisting of one or more fullerenes and various physisorbed atoms or low-mass molecules (e.g. He, H<sub>2</sub>, H<sub>2</sub>O, CO<sub>2</sub> and CH<sub>4</sub>) are formed upon sequential pickup into superfluid helium nanodroplets. Mono- and multilayer coverage can be realized

by controlled experimental settings. Decoration and the formation of molecular ad-layers around these chosen model surfaces are studied by means of high-resolution mass spectrometry and molecular dynamics calculations. Shell closures are often expressed by magic numbers in cluster size distributions. The effect of the polarizability and the dipole moment of the adsorbates are investigated and intra-cluster reactions driven by the ionization process compared to clusters that do not contain fullerenes.

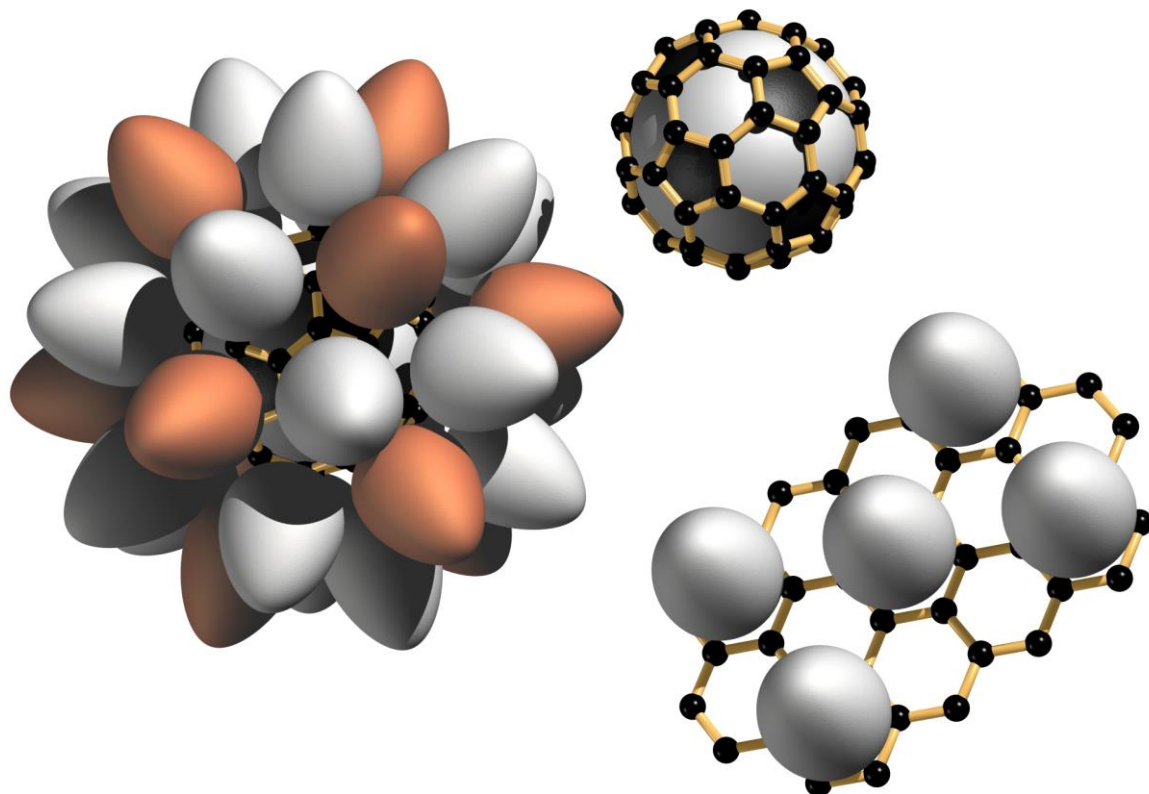


Fig. 1. Decoration of fullerenes and graphene by apolar molecules (here indicated as eggs). For the flat surface the commensurate layer with highest density is a  $\sqrt{3} \times \sqrt{3}$  phase. The curvature of the fullerene surface increases the distance between the adsorbates and a commensurate  $1 \times 1$  phase can be formed. The brown eggs are located on-top of the 12 pentagonal faces. For a curved egg box a similar increase in adsorption sites can be observed.

For apolar adsorbates a commensurate  $1 \times 1$  phase is observed where one atom or molecule occupies each hexagonal and pentagonal face. The van der Waals radius of He and H<sub>2</sub> is low enough that the first layer is not fully occupied by this commensurate phase and additional adsorbates can be accommodated by displacing the atoms/molecules on-top of the pentagonal faces [9],[10].

Polar molecules, in contrast, are not wetting the fullerene surface and form clusters that are weakly perturbed by the presence of the charged fullerene [11]. Magic numbers in the cluster size distribution of charged fullerene-water complexes agree very well with calculated stability maxima for neutral water clusters.

CO<sub>2</sub> interacts with the fullerene almost as strongly as with other CO<sub>2</sub> molecules. This leads to the growth of an incommensurate layer which contains 40 molecules for the neutral complex that preferentially lay flat on the fullerene surface. By positively charging the fullerene, the CO<sub>2</sub> molecules bend out of the surface. Thereby they occupy less area and about 20% more molecules fit into the first layer. To our knowledge this is the first time that such a charge induced effect on the adsorption density of molecular layers has been observed and in the case of the greenhouse gas CO<sub>2</sub> interesting possibilities for future applications concerning the storage of CO<sub>2</sub> can be expected.

This work was supported by the FWF, Wien (P23657, I978 and P26635)

### 3. References

- [1] S.M. Gatica, M.M. Calbi, R.D. Diehl, and M.W. Cole, 2008 *J. Low Temp. Phys.* **152** 89-107
- [2] S.M. Gatica, H.I. Li, R.A. Trasca, M.W. Cole, and R.D. Diehl, 2008 *Phys. Rev. B* **77** 045414
- [3] S.M. Gatica, M.J. Bojan, G. Stan, and M.W. Cole, 2001 *J. Chem. Phys.* **114** 3765-3769
- [4] S. Acosta-Gutiérrez, J. Bretón, J. M. Gomez Llorente, and J. Hernández-Rojas, 2012 *J. Chem. Phys.* **137** 074306.
- [5] R. Ludwig, and A. Appelhagen, 2005 *Angew. Chem. Int. Ed.* **44** 811-815
- [6] A. Martinez-Alonso, J.M.D. Tascon, and E.J. Bottani, 2001 *J. Phys. Chem. B* **105** 135-139
- [7] U. Zimmermann, N. Malinowski, U. Näher, S. Frank, and T.P. Martin, 1994 *Phys. Rev. Lett.* **72** 3542–3545
- [8] U. Zimmermann, N. Malinowski, A. Burkhardt, and T.P. Martin, 1995 *Carbon* **33** 995-1006
- [9] C. Leidlmair, Y. Wang, P. Bartl, H. Schöbel, S. Denifl, M. Probst, M. Alcamí, F. Martín, H. Zettergren, K. Hansen, O. Echt, and P. Scheier, 2012 *Phys. Rev. Lett.* **108** 076101
- [10] C. Leidlmair, P. Bartl, H. Schöbel, S. Denifl, M. Probst, P. Scheier, and O. Echt, 2011 *Astrophys. J.* **738** L4
- [11] S. Denifl, F. Zappa, I. Mähr, F. Ferreira da Silva, A. Aleem, A. Mauracher, M. Probst, J. Urban, P. Mach, A. Bacher, O. Echt, T. D. Märk, P. Scheier, 2009 *Angew. Chem. Int. Ed.* **48** 8940-8943



# SWIFT HEAVY ION IRRADIATION OF GRAPHENE

Oliver Ochedowski, Orkhan Osmani, Benedict Kleine-Bußman and Marika Schleberger

*Fakultät für Physik and CENIDE, Universität Duisburg-Essen, 47048 Duisburg, Germany*  
E-mail: oliver.ochedowski@uni-due.de

Graphene, the most prominent member of the emerging material class of two dimensional crystals, is imagined to play a key role many future applications such as sensors, ultrathin membranes or transparent electrodes. In most cases however, using pristine graphene is not ideal and modifications have to be introduced in order for graphene to play out its strengths.

In this presentation we show that single high energy ions can be used as a tool to locally modify the properties of graphene. For this, graphene samples are irradiated with swift heavy ions with typical kinetic energies in the range of 100 MeV. By combining analytical techniques like atomic force microscopy, transmission electron microscopy and Raman spectroscopy it is shown that depending on the irradiation parameters (ion energy, angle of incidence, choice of substrate for graphene) various modifications like local defective areas, pores in form of origami-like foldings and even doping can be introduced into the graphene sheet [1,2,3].

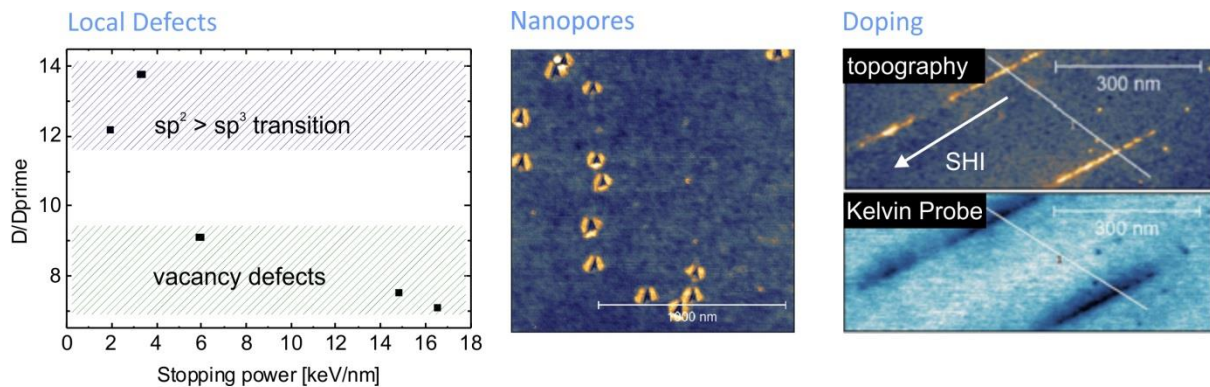


Fig. 1. Graphene modifications induced by swift heavy ions. **Left:** Local defects can be introduced. The energy of the ion changes the nature of the defects. **Middle:** Nanopores created by glancing incidence irradiation with swift heavy ions. **Right:** Doping of graphene on SiC by implantation of substrate material.

## References

- [1] Akcöltekin et al., Appl. Phys. Lett. 98, 103103 (2011)
- [2] Ochedowski et al., Appl. Phys. Lett. 102, 153103 (2013)
- [3] Ochedowski et al., Nat. Comm., accepted

# **ELECTRON TRANSMISSION THROUGH MICROMETER GLASS CAPILLARIES AND DIFFERENCES WITH IONS**

J. A. Tanis<sup>1</sup>, S. J. Wickramarchchi<sup>1</sup>, T. Ikeda<sup>2</sup>

<sup>1</sup>*Department of Physics, Western Michigan University, Kalamazoo, Michigan 49008 USA*

<sup>2</sup>*RIKEN Nishina Center for Accelerator Based Science, 2-1 Hirosawa Wako, Saitama*

*351-0198, Japan*

E-mail: john.tanis@wmich.edu

The transmission of 500 and 1000 eV electrons through micrometer-sized capillaries has been studied and the results are compared with those for slow (~30 keV) highly-charged ions through similar capillaries. For electrons it is found that elastic and inelastic contributions give rise to distinguishable peaks in the transmitted profile, while for ions only an elastic contribution is seen. For 500 eV electrons elastic transmission dominates the profile, while both elastic and inelastic contribute strongly for 1000 eV.

Electron transmission through a micrometer-sized capillary with inlet diameter ~800  $\mu\text{m}$  and outlet diameter ~100  $\mu\text{m}$  has been studied for incident 500 and 1000 eV electrons. Measurements of the transmitted angular profiles as a function of the capillary tilt angle with respect to the incident beam direction, the centroid energies of the outgoing electrons, and the full-width-half maxima, in both the angular and outgoing energy distributions, were made, with each showing properties of the electron transmission. The results of the electron work are contrasted with those obtained for slow (~30 keV) highly-charged ion beams on similar capillaries, but with outlet diameters of ~20  $\mu\text{m}$  [1]. For slow highly-charged ions, the transmission properties have been studied [2] and the capillaries have been found to be useful in various biological and technical applications [3].

For the present work with electrons incident on the capillary, measurements were made for a funnel-shaped (tapered) borosilicate glass capillary. These measurements were done at Western Michigan University using samples obtained from the RIKEN laboratory in Japan. For the slow ion studies, a funnel-shaped capillary obtained from the same source was also used, and in addition a nearly ideal conical-shaped glass capillary was studied that was obtained from the ETH laboratory in Zurich. The funnel-shaped and the conical-shaped capillaries had similar input and output dimensions in the ion work so the results could be compared directly.

In the electron work, some rather surprising properties were found. In particular, the transmitted angular profile showed three peaks for small tilt angles (within about  $1^\circ$  of true zero degrees) and furthermore, 500 eV electrons showed larger contributions from transmitted elastic electrons than for 1000 eV. For 1000 eV the transmitted electrons always had a significant inelastic component for capillary tilt angles that were outside the aspect ratio (~ $1^\circ$ ) of the capillary, but for 500 eV the transmission did not show inelasticity until the tilt angle reached ~ $5^\circ$ . This difference is attributed to the energy dependence of the transmission of electrons incident on the capillary, with 500 eV electrons able to form a larger negative charge patch that creates a sufficient potential to deflect the incoming electrons. This effect also shows up in the centroid energies of the transmitted electrons as well as for the FWHMs in both the angular and transmitted energy spread.

These anomalies do not appear for slow ions passing through the capillaries [1]. This is to be expected in view of the much lower velocity (about 30 times) for the ions than the electrons. However, for the ions a significant difference in the transmission was observed for the funnel-shaped and the conical capillaries. The funnel-shaped capillary suffered from complete blocking that occurred more quickly with increasing incident beam up to 10 pA. On the other hand, the conical capillary showed continuous transmission even as the beam was increased up to 10 pA incident current. For electrons incident on the capillary blocking effects were seen for beam currents of about 50 pA.

The various properties of electron and ion transmission will be discussed in this talk, with particular emphasis on electron transmission. The similarities and differences in transmission through the capillaries for electrons and ions will be pointed out. The reasons for the differences in the transmission will be discussed and attributed to what are believed to be the underlying causes.

### References

- [1] Zhou C L, Simon M, Ikeda T, Guillous S, Iskandar W, Méry A, Rangama J, Lebius H, Benyagoub A, Grygiel C, Müller A, Döbeli M, Tanis J A, Cassimi A 2013 *Phys. Rev. A* **88** 050901(R)
- [2] Ikeda T, Kanai Y, Kojima T M, Iwai Y, Kambara T, Yamazaki Y, Hoshino M, Nebiki T., Narusawa T, 2006 *Appl. Phys. Lett.* **89**, 163502.
- [3] Ikeda T, Kojima T M, Kobayashi T, Meissl W, Mäckel V, Kanai Y and Yamazaki Y 2012 *J. Phys. Conf. Ser.* **399**, 012007.

## GUIDING OF MEV ION BEAMS

G.U.L. Nagy<sup>1</sup>, I. Rajta<sup>1</sup>, R.J. Bereczky<sup>1</sup> and K. Tőkési<sup>1</sup>

<sup>1</sup>*Institute for Nuclear Research, Hungarian Academy of Sciences (Atomki), Debrecen, Hungary, EU*  
E-mail: tokesi.karoly@atomki.mta.hu

The ion guiding phenomenon was studied using 1 MeV proton microbeam. Single, straight micrometer sized capillaries made of PTFE and simple parallelly placed flat plates made of various insulator and conductor materials were used as targets. The time dependence of the intensity, the energy distribution and the deflection of the transmitted beam were investigated. Our results show that the ion guiding effect is possible when using MeV/amu energies.

### 1. Introduction and motivation

Charged particles are able to pass through insulator capillaries keeping their initial energy and charge state even if the capillary axis is tilted with respect to the incident beam axis larger than the geometrical limitation. The phenomenon is called the ion guiding effect and has been intensively studied since its discovery [1]. According to our recent knowledge the guiding effect is based on the creation of self-organized charge patches on the inner surface of the target capillaries, producing a guiding electric field. The guiding sets in when these charge patches reach a dynamical equilibrium, i.e. the arriving and leaving ions result in a constant amount of charge: arriving ions come from the incident beam, while the accumulated charge decreases by transport into the bulk or on the surface towards the capillary exit.

The first experimental and theoretical works used insulating foils (PET, Al<sub>2</sub>O<sub>3</sub> etc.) with randomly distributed nanocapillaries as targets combined with highly charged, slow heavy ions (HCIs) as projectile ions. These conditions showed up certain difficulties such as the imperfect parallelism of the capillaries or the collective effect of the neighbouring capillaries. Later, to avoid these difficulties, the single, micrometer-sized and cylindrical shaped capillaries came into focus [2]. The other advantage of using these type of targets is the many possible technical applications of them such as steering or focusing ion beams without any external power supplies. Although many researcher groups have joined to the investigation of the guiding phenomenon, there are still many open questions to be answered.

In our experiments we also used a single microcapillary made of PTFE (Teflon) and then to further simplify the experimental conditions we changed the cylindrical shaped targets to simple flat surfaces [3]. The flat plates were made of different insulator and conductor materials. In addition, we used single charged H<sup>+</sup> ions as projectiles. The energy of the proton microbeam was 1 MeV and we prove that it is possible to guide an ion beam with MeV/amu energy through an insulator capillary in its initial energy and charge state.

### 2. Experimental conditions

After the successful construction of our new experimental setup [4], we became able to measure both the intensity, the energy distribution and the deflection of the proton microbeam transmitted through either the capillary or between the flat plates. The intensity could be measured by a Faraday-cup placed at the capillary exit. Using a beam chopper in front of the samples we could continuously measure the incoming beam intensity, compare the transmission to that and express it in relative units (i.e. in %). The energy of the particles was analysed by a particle detector that was mounted on a rotatable disk along with the Faraday-cup. For the charge state determination an electrostatic deflector was mounted in the target chamber (Figure 1.). By switching high voltage on the deflector, the charged and neutral particles guided or transmitted through the samples were separated and displayed on a fluorescent screen behind.

The sample positioning was carried out using an optical microscope and Rutherford Backscattering (RBS) mapping technique. The 5-axis sample stage of the Atomki microbeam line ensured the accurate sample positioning.

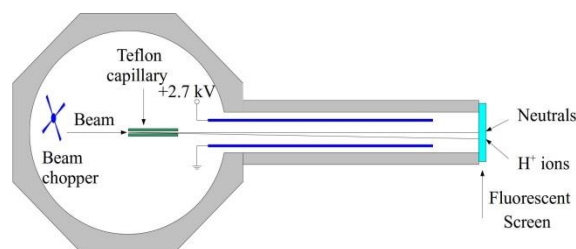


Fig. 1. Experimental set-up for charge state determination.

The PTFE microcapillary samples were  $L=44,5$  mm long and  $d=800$   $\mu\text{m}$  in diameter. The tilt angle of the capillary axis was  $1^\circ$  relative to the beam axis. Since the aspect ratio of our capillary samples is  $\sim 55$  and the divergence of the proton microbeam is less than  $0,3^\circ$  [5] this is enough to ensure the geometrical non-transparency. The beam was focused on the capillary entrance and the beam spot size was around  $2$   $\mu\text{m}$ .

The flat samples were made of two side by side placed flat plates with  $d=150$   $\mu\text{m}$  gap between them. Glass and Teflon as insulators and glass with gold layer on the top as conductor were used as target materials. The flat plates were positioned to be parallel to the beam axis. The beam entered to the center of the gap and the plate was moved towards the beam. When the plate was close enough to the beam axis, a fraction of the particles suffered close collision with the sample due to the beam divergence. The other fraction of the particles passed the plates without collision.

### 3. Results

Initially the PTFE microcapillaries had a transmission of around 20% with respect to the incident beam intensity due to forward scattering, but it immediately started to gradually increase. After the charge-up process it reached around 90% transmission rate and remained stable. During the measurements we identified three completely different stages of the transmission regarding the energy distribution of the transmitted particles. We showed that after the charge-up process the beam was guided through the capillary in its original energy. Moreover, the whole beam was deflected due to the high voltage which means that the protons kept their initial charge state. These are the direct proofs of the guiding effect.

In case of the flat surfaced samples we found major differences between the conductor and insulator targets. The proton microbeam suffered significant deflection due to the image acceleration when using conductor material. In the spectra of transmitted beam we found that it contained mainly forward scattered particles. In case of the glass and Teflon plates the beam was deflected into the opposite direction. In addition, the incident particles did not suffer significant energy loss, which also proves the guiding effect.

### 4. Acknowledgements

This work was supported by the Hungarian Scientific Research Fund OTKA No. NN 103279 and by the COST Action CM1204 (XLIC).

### 5. References

- [1] N. Stolterfoht, et al, *Phys. Rev. Lett.* (2002) **88** 133201.
- [2] R.J. Berezsky, et al, *NIM B* (2009) **267** 317-320.
- [3] K. Tőkési, et al, *NIM B* (2012) **279** 173-176.
- [4] G.U.L. Nagy, et al, *AIP Conf. Proc.* (2013) **1525** 40-42.
- [5] L.Z. Tóth and I. Rajta, *Atomki Annual Report* (2010) 84.



# FULLY DIFFERENTIAL CROSS SECTIONS FOR IONIZATION OF H<sub>2</sub> BY PROTON IMPACT

M. Schulz<sup>\*</sup>, S. Sharma<sup>\*</sup>, T.P. Arthanayaka<sup>\*</sup>, A. Hasan<sup>\*,†</sup>, B.R. Lamichhane<sup>\*</sup>, J. Remolina<sup>\*</sup>, A. Smith<sup>\*</sup>, S. Akula<sup>\*</sup>, D.H. Madison<sup>\*</sup>

<sup>\*</sup>Physics Department, Missouri University of Science & Technology, Rolla, MO 65409, USA

<sup>†</sup>Department of Physics, UAE University, Al Ain, Abu Dhabi, UAE

E-mail: schulz@mst.edu

Two-center molecular interference in collisions of charged particles with H<sub>2</sub> has been studied extensively over the last decade [e.g. 1-3]. However, it is not straight forward to extract the interference term  $I$  from experimental data. In principle,  $I$  is given by the ratio between the coherent and incoherent cross sections  $d\sigma_{\text{coh}}/d\sigma_{\text{inc}}$ . But  $d\sigma_{\text{inc}}$  is experimentally not easily accessible and in previous studies was usually approximated as twice the theoretical cross section for atomic hydrogen or the experimental cross section for He. About three years ago, we demonstrated that the coherence properties of the projectile beam can be varied through the geometry of a collimating slit placed in front of the target [4]. Thereby, we were able to extract the double differential cross section ratio, i.e. the interference term  $I$ , without using any approximation. Here, we report on the first measured fully differential interference term.

A 75 keV proton beam was collimated with a slit placed at two different distances from the target and intersected with a very cold H<sub>2</sub> beam from an ultra-cold jet. For the large slit distance the beam was coherent and incoherent for the small distance. The H<sub>2</sub><sup>+</sup> ions produced in the collision were momentum-analyzed using a COLTRIMS apparatus. The deflected projectiles were energy-analyzed using a parallel-plate analyzer and detected by a two-dimensional position-sensitive detector. From the position information the azimuthal and polar projectile angles were obtained so that the projectile momentum could be determined. The electron momentum was obtained from momentum conservation.

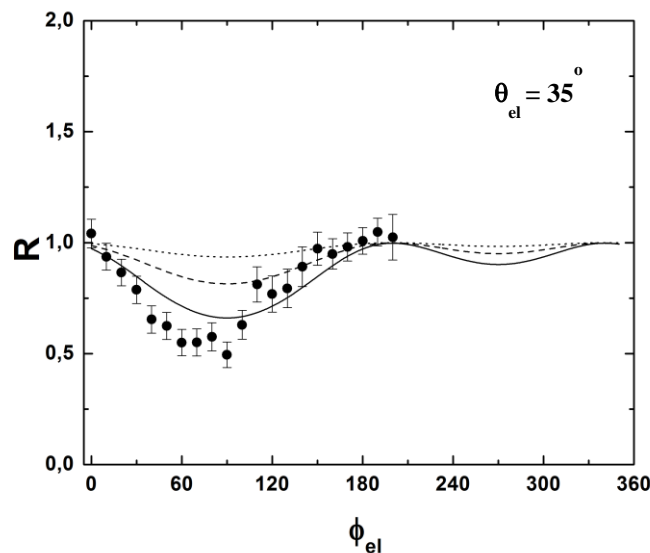


**Figure 1.** Fully differential interference term,  $\varepsilon = 30$  eV.

In Fig. 1 the fully differential cross section ratio is shown for fixed recoil momentum (0.2 a.u.), polar electron angle  $\theta_{\text{el}}$  (35°), and energy loss  $\varepsilon$  (30 eV) as a function of the azimuthal electron angle  $\phi_{\text{el}}$ . The curves show various model interference terms all assuming that the phase angle is determined by the transverse component of the momentum transfer  $q_{\text{tr}}$ . The good agreement of the data with the solid curve suggests that the phase angle is not primarily

determined by the recoil momentum, as assumed for molecular two-center interference, but by  $q_{tr}$ . This is an indication that the data are dominated by single-center interference. However, for  $\varepsilon = 57$  eV the data are consistent with two-center interference with the phase angle being determined by the recoil momentum.

This work was supported by the National Science Foundation.

## 6. References

- [1] N. Stolterfoht et al 2003 Phys. Rev. Lett. 87 23201
- [2] L. Schmidt et al 2008 Phys. Rev. Lett. 101 173202
- [3] J.S. Alexander et al 2008 Phys. Rev. A. 78 060701(R)
- [4] K.N. Egodapitiya et al 2011 Phys. Rev. Lett. 106 153202

# INDIRECT DISSOCIATIVE RECOMBINATION OF SIMPLE IONS

Roman Čurík

*J. Heyrovský Institute of Physical Chemistry, ASCR, Czech Republic*

E-mail: roman.curik@jh-inst.cas.cz

Molecular ions  $\text{LiH}^+$  and  $\text{LiHe}^+$  are prototypes of the indirect dissociative recombination (DR) process, in which a colliding electron destroys the molecule through Rydberg capture pathways. In the present study we develop a quantitative test of the Siegert state multichannel quantum-defect theory description of indirect DR for a diatomic molecular ion. We identify the doorways to fast indirect DR as complex resonance manifolds, which couple closed channels having both high and low principal quantum numbers. This sheds new light on the competition between direct and indirect DR pathways and suggests the reason previous theory underestimated the DR rate by an order of magnitude.

## 4. Introduction and quantum defects

It has long been suggested that chemical processes involving lithium atoms and ions could have played an important role in the chemistry of the early universe. Lithium atoms and ions were formed in reactions with other simple partners in the early universe environment such as  $\text{H}$ ,  $\text{H}^+$ ,  $\text{D}$ ,  $\text{D}^+$ , and  $\text{He}$  or  $\text{He}^+$ . Their significant role was assumed in driving cooling processes after the initial big bang event [1].

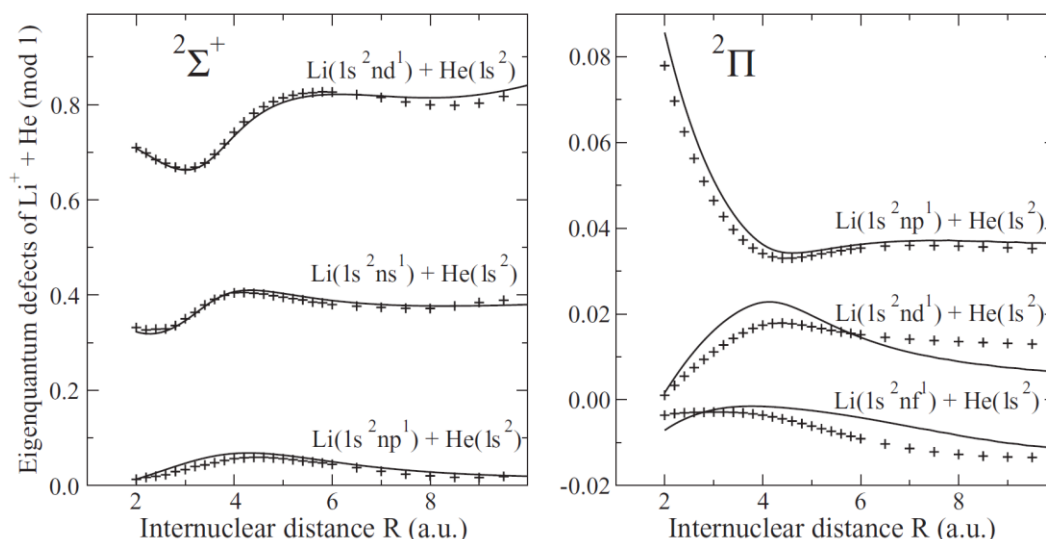


Fig. 1. Dependence of eigenquantum defects for the  $\text{LiHe}$  system, extracted via the use of Eq. (1) from the  $n = 4$  curves). Pluses denote the eigenquantum defects obtained by diagonalization of the scattering phase shifts.

The accurate evaluation of the quantum defects that describe the unpaired lithium electron now moving in the presence of  $1s^2$  closed shell of lithium atom while being perturbed by a neutral helium or hydrogen atoms, is the chief outcome of our electronic structure results. The quantum defects are sole electronic structure data necessary to enter the nuclear dynamics calculations that we shall describe in the following section. Eigenquantum defects  $\mu_\lambda(R)$ , are related to energy differences between potential energy curves of the cation  $U^+(R)$  and the neutral Rydberg states  $U_{n\lambda}(R)$  by Mulliken's equation

$$U_{n\gamma}(R) - U^+(R) = -\frac{1}{2[n - \mu_\gamma(R)]^2}. \quad (1)$$

The eigenquantum defects (1) may also be obtained by diagonalization of a quantum defects matrix  $\mu_{ll'}(R)$  that is obtained from scattering calculations via transformation of eigenphase shifts  $\eta_\gamma(R)$ . The connection is made by use of Seaton's theorem in which one finds that the quantum defects calculated just below the ionization threshold smoothly connect to short-range scattering phase shifts (divided by  $\pi$ ) determined just above the threshold. It follows from the above that, at a zero collision energy, the following equality is exactly satisfied:

$$\mu_{ll'}(R) = \frac{1}{\pi} \sum_{\gamma} U_{l\gamma}(R) \eta_{\gamma}(R) U_{l'\gamma}(R), \quad (2)$$

where the unitary matrix  $U_{l\gamma}(R)$  transforms the short range  $K$ -matrix (or phase shift matrix) into its diagonal form [2]. Figure 1 displays this practical demonstration of Seaton's theorem and it also helps to estimate the accuracy and reliability of the present calculations.

## 5. Nuclear dynamics and the dissociative recombination

While the internuclear distance  $R$  is a good quantum number for a compact electronic system (Born-Oppenheimer approximation holds) it becomes less useful for higher Rydberg states or for very low-energy scattering states where the electron “sees” a molecule in a vibrational state instead of having a fixed internuclear distance. The connection of these two quantization schemes is carried out by employing rovibrational frame transformation theory [3]. Furthermore, in the present study we have exploited a specific technique that uses Siegert pseudostates  $\chi_{jv}(R)$ , which obey the vibrational Schrödinger equation

$$\left[ -\frac{d^2}{dR^2} + 2MU^+(R) + \frac{j(j+1)}{R^2} - k_{jv}^2 \right] \chi_{jv}(R) = 0, \quad (3)$$

with Siegert boundary conditions at the origin and at  $R_0$ ,

$$\chi_{jv}(0) = 0, \quad \left[ \frac{d}{dR} - ik_{jv} \right] \chi_{jv}(R_0) = 0. \quad (4)$$

The boundary conditions above account not only the vibrational bound states but also the incoming- or outgoing-wave continuum states necessary to describe the dissociation. Fig. 2 demonstrates that the dissociative process is highly resonant for collision energies under the highest vibrational threshold.

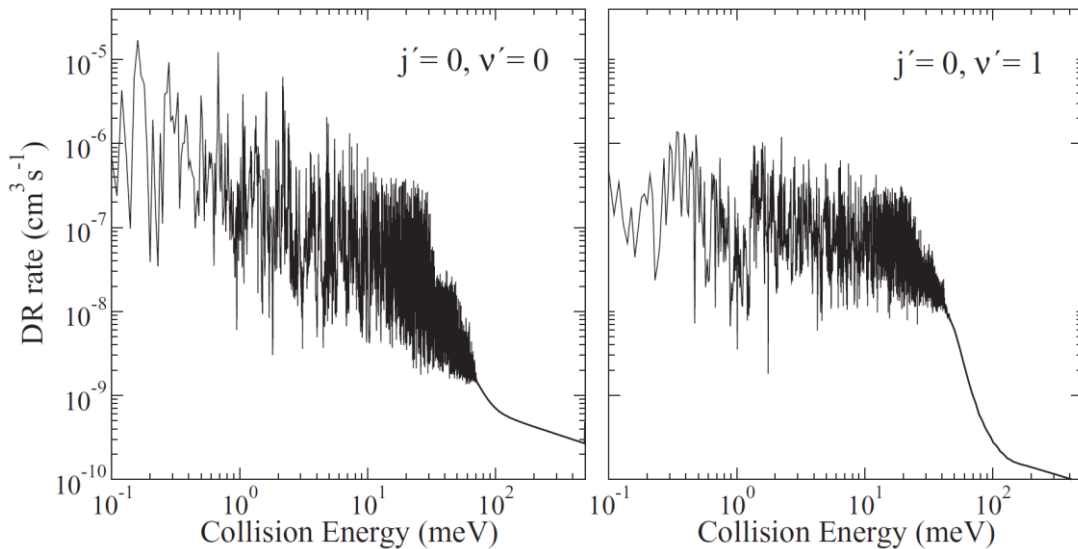


Fig. 2. Dissociative recombination rate as a function of collision energy. The left panel displays the data for the initial rovibrational target  $j'=0, v'=0$ , while the right panel is for vibrationally excited target cation with  $j'=0, v'=1$ .

## 6. References

- [1] Lepp S and Shull J M 1983 *Astrophys. J.* **270** 578
- [2] Čurík R and Greene C H 2007 *Phys. Rev. Lett.* **98** 173201
- [3] Cheng E S and Fano U 1972 *Phys. Rev. A* **6** 173



# ELASTIC SCATTERING FROM PLASMA MOLECULES AND RADICALS

M. Hoshino<sup>1</sup>, P. Limão-Vieira<sup>1,2</sup>, H. Kato<sup>1</sup>, H. Cho<sup>3</sup>, F. Ferreira da Silva<sup>2</sup>, D. Almeida<sup>2</sup>, F. Blanco<sup>3</sup>, G. García<sup>4</sup>, O. Ingólfsson<sup>5</sup>, and H. Tanaka<sup>1</sup>

<sup>1</sup> Department of Physics, Sophia University, Chiyoda-ku, Tokyo 102-8554, Japan

<sup>2</sup> Laboratório de Colisões Atômicas e Moleculares, CEFITEC, Departamento de Física, Faculdade de Ciências e Tecnologia, Universidade Nova de Lisboa, 2829-516, Caparica, Portugal

<sup>3</sup> Department of Physics, Chungnam National University, Daejeon 305-764, South Korea

<sup>4</sup> Departamento de Física Atómica, Molecular y Nuclear, Universidad Complutense de Madrid, Avenida Complutense, 28040 Madrid, Spain

<sup>5</sup> Instituto de Física Fundamental, Consejo Superior de Investigaciones Científicas (CSIC), Serrano 113-bis, 28006 Madrid, Spain

<sup>6</sup> Department of Chemistry, Science Institute, University of Iceland, 107 Reykjavik, Iceland

E-mail: masami-h@sophia.ac.jp

We report absolute elastic differential cross sections (DCSs) for electron interactions with the C<sub>4</sub>F<sub>6</sub> isomers, hexafluoro-1,3-butadiene (1,3-C<sub>4</sub>F<sub>6</sub>), hexafluoro-2-butyne (2-C<sub>4</sub>F<sub>6</sub>) and hexafluorocyclobutene (c-C<sub>4</sub>F<sub>6</sub>) in the impact energy region of 1.5 – 200 eV, and at the scattering angle of 15°–130°. Present DCSs for each molecule have been compared with the independent atom configuration including screening corrections (IAM-SCAR), and agreements between our data sets and the calculated results are generally very well above 30 eV, in terms of the magnitudes and angular distributions of DCSs. Elastic integral cross sections and momentum transfer cross sections of these molecules have been also obtained by extrapolating the measured DCSs and compared with the previous total cross sections.

## 1. Introduction

In the chemical etching processes, some radicals such as the CF<sub>2</sub>, CF<sub>3</sub>, and F produced from perfluorocarbons have been used to make the large-scale integrated circuit on the silicon wafer. Recently, C<sub>4</sub>F<sub>6</sub> molecule has been considered to be used in selective etching processes of silicon oxide on Si layers for fabricating sharp grooves in ultra large scale integrated circuits. It is well known that low-energy electrons play an important role in such low temperature plasma, because the electron temperature in weakly ionized plasma, is usually a couple of ten thousand K, that is the order of eV. Especially, in the non-equivalent plasma, whose degree of ionization is estimated to be about 10<sup>-3</sup> or 10<sup>-4</sup>, most of parent molecules still remain. Therefore, the cross section data of the elastic, vibrational, and electronic excitation of molecules and product radicals as well as ionization have been required in order to understand the fundamental processes in low temperature plasma.

In this study, we report a new and original experimental contribution for the measurement of elastic differential, integral and momentum transfer cross section data for C<sub>4</sub>F<sub>6</sub> isomers and their comparison with the independent atom configuration including screening corrections (IAM-SCAR)<sup>[1]</sup>.

## 2. Experiment

Two different crossed-beam electron spectrometers were used in the present work <sup>[2], [3]</sup>. One was used for low-impact energies and high resolution (EELS-1) and the other for energies above 50 eV and low resolution (EELS-2). In the both spectrometer, a monochromatic electron beam is generated with a hemispherical electron monochromator and crossed at right angles with an effusive molecular beam. After interactions with the target gas, the scattered electrons are energy analysed with a hemispherical electron analyser, which can be rotated around the gas nozzle, and detected with an electron multiplier. In the current experiments the energy resolution of the incident electron beam was 35-45 meV and 80-100 meV (FWHM), for EELS-1 and EELS-2, respectively. The absolute scale of the DCS was set using the relative flow technique with the well known elastic DCS of helium<sup>[4]</sup> as the reference species.

## 3. Results and Discussion

Figure 1 shows the experimental DCSs for the C<sub>4</sub>F<sub>6</sub> isomers at impact energies of 50, 100, and 200 eV together with the calculated DCSs from the IAM-SCAR. The calculated DCSs are well agreement

with the measured DCS of all isomers and it is found that the absence of any relevant molecular structural effect on the measured DCS at higher impact energy has been clearly observed, which means the scattering process might be only sensitive to the presence of the fluorine atoms surrounding the target molecules. In order to further investigate, the elastic DCSs for the  $C_4F_6$  isomers were compared with other fluorinated molecules, such as  $SF_6$  and  $C_nF_6$  ( $n = 2, 3$  and  $6$ )<sup>[1]</sup>. We note that for all the six-F containing molecules, the scattering process for electron energies above 30 eV is indistinguishable. Finally, the elastic ICS data for 1,3- $C_4F_6$  by extrapolating the measured DCSs is shown in Fig. 2. This ICS data is compared with the IAM-SCAR calculation as well as previous total cross section (TCS) measurements<sup>[5]</sup> and generally found to be in very good agreement with our calculated IAM-SCAR.

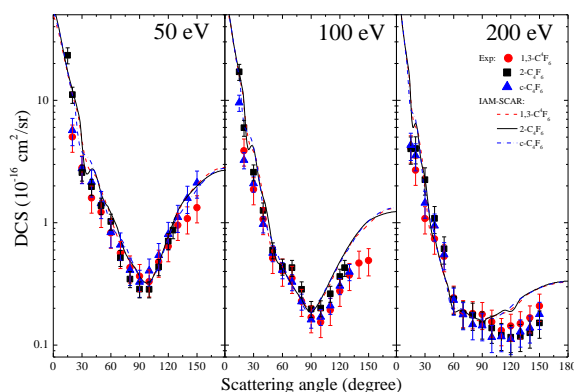


Fig. 1. The elastic DCSs for the  $C_4F_6$  isomers at impact energies of 50, 100, and 200 eV.

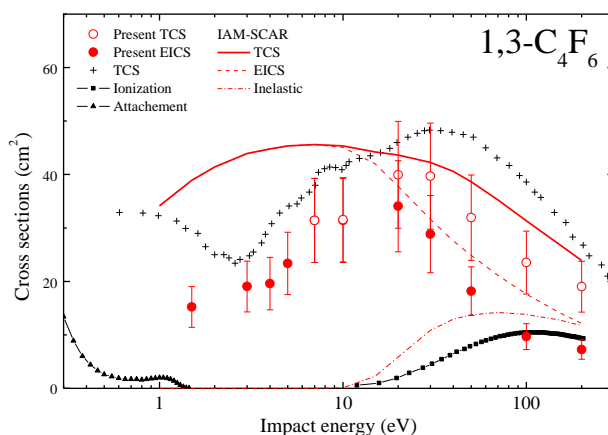


Fig. 2. The elastic ICSs for the 1,3- $C_4F_6$  (●) and ICS plus inelastic cross sections (○), compared against our elastic IAM-SCAR ICS (dashed line), our total IAM-SCAR cross sections (solid line) and our IAM-SCAR ICS for total inelastic processes (dashed-dot line)

#### 4. References

- [1] M. Hoshino et al., *J. Chem. Phys. Submitted*.
- [2] H. Tanaka et al., *Phys. Rev. A* **57**, 1798 (1998).
- [3] H. Kato et al., *J. Chem. Phys.* **132**, 074309 (2010).
- [4] L. Boesten and H. Tanaka, *At. Data Nucl. Data Tables* **52**, 25 (1992).
- [5] C. Szmytkowski and S. Kwitniewski, *J. Phys. B: At. Mol. Opt. Phys.* **36**, 2129 (2003).

# ELECTRON IONISATION AND ELECTRON ATTACHMENT OF METALORGANIC COMPOUNDS

Peter Papp<sup>1</sup>, Michal Lacko<sup>1</sup>, Karol Wnorowski<sup>2</sup>, Štefan Matejčík<sup>1</sup>

<sup>1</sup>*Department of Experimental Physics, Faculty of Mathematics, Physics and Informatics, Comenius University, Mlynska dolina, 84248 Bratislava, Slovakia*

<sup>2</sup>*Department of Physical Chemistry, Faculty of Science, Siedlce University of Natural Sciences and Humanities, 3 Maja 54, 08-110 Siedlce, Poland*

E-mail: papp@fmph.uniba.sk

The crossed electron/molecular beams technique was used to study the dissociative electron attachment (DEA) and electron ionization (EI) of gas phase iron pentacarbonyl molecule, Fe(CO)<sub>5</sub>. The sequential loss of carbonyl ligands (with 2 low energy and 3 core-excited resonances) is typical for the DEA, complete decomposition to Fe<sup>-</sup> atom can be seen. By the means of density functional theory the electron affinity of ~0.817 eV has been evaluated for Fe(CO)<sub>5</sub> for the first time. Contrary to that the EI mass spectrum of Fe(CO)<sub>5</sub> is rich of peaks produced by sequential CO ligand losses, C=O bond cleavages, multiply charged products and the products consisting of Fe isotopes. The experimental ionisation energy 8.45±0.25 eV agrees well with previous works.

## 1. Introduction

Electron induced processes in gas-phase metalorganic compounds are subject of this work. Our recent studies are important for understanding of processes for Focused Electron Beam Ion Deposition (FEBID) techniques. Chemical and physical processes between electrons, target molecules and their fragments and surfaces are very important to know for FEBID. In this sense the role of secondary electrons in FEBID is very important and already well known [1]. Broadening of the deposited structure width or contamination by ligands can be produced via low energy electron induced dissociation by electron attachment (DEA) or electron ionization (EI). One of the molecules interesting for FEBID is iron pentacarbonyl Fe(CO)<sub>5</sub>. There are several studies about electron ionisation [2-9] and electron attachment [10-12] to Fe(CO)<sub>5</sub> however with large amount of discrepancy of the resulting thresholds of ionic products and corresponding experimentally evaluated bond dissociation energies (BDE) of the ligands.

## 2. Experiment

The studies of electron induced processes on metalorganic compounds were performed at the Comenius University using the crossed electron/molecular beams techniques [13]. The experiment is equipped with a trochoidal electron monochromator [14] producing an almost monoenergetic electron beam. The resolution of the kinetic energy of electrons can be up to ~50 meV, however normally set to ~180 meV to achieve higher electron current in the beam. Calibration of the electron energy for positive ions is made by measuring the ionisation threshold of Ar gas and scaling to the well known value of 15.759±0.001 eV [15], for negative ions is made by calibrating to the resonance of SF<sub>6</sub><sup>-</sup> at ~0 eV. The measured sample can be introduced into a high vacuum via a heated inlet system terminated by a small capillary perpendicularly to the electron beam. The charged products are extracted by a weak electric field into a quadrupole mass spectrometer with extraction time ~10 µs and flight time through the spectrometer ~50 µs. The mass spectra are normally recorded at the incident electron energy of 70 eV, for evaluating of the appearance energies (AE) of positive ions, fitting procedure based on Wannier law [16]) or of the resonances (for negative ions) the ion efficiency curves as a function of electron energy are measured.

## 3. Theory

Density functional theory (DFT) has been used to interpret the experimental results. Among the large number of widely used DFT methods the PBE functional [17, 18] has been selected for evaluation of the total ground state energies, optimal geometries of neutral and ionic molecule and its fragments. Vibrational analysis has been included in the calculations to exclude any transition states. Substances including transient metallic atom(s) are known to lie in higher spin states to minimize the total energy of the system. Therefore for each molecular fragments its three lowest spin states have

been calculated and only the lowest energies were taken into account for deriving the BDEs in neutral, cationic as well as anionic  $\text{Fe}(\text{CO})_5$  target.

#### 4. Results and discussion

The mass spectrum of  $\text{Fe}(\text{CO})_5$  produced via electron ionisation consists of many peaks which can be assigned normally to singly charged fragments, some of them are doubly charged fragments and isotopic peaks. In this work we are mostly interested in the loss of CO ligands. The efficiency of corresponding  $(\text{CO})_n\text{Fe}^+ - \text{CO}$  bond break reactions rises with the number of ligands dissociated from the molecular ion ( $m/z$  196). The discussed fragments are having masses  $m/z$  168 for  $\text{Fe}(\text{CO})_4^+$ , then 140, 112, 84 and finally  $m/z$  56 for  $\text{Fe}^+$ . Other typical fragments of the spectrum of  $\text{Fe}(\text{CO})_5$  are produced via  $\text{C}=\text{O}$  bond breaks, visible only at  $m/z$  124, 96, 80, 72 and 68 for  $\text{FeC}(\text{CO})_2^+$ ,  $\text{FeC}(\text{CO})^+$ ,  $\text{FeC}_2^+$ ,  $\text{FeO}^+$  and  $\text{FeC}^+$  respectively. Products like  $\text{FeC}(\text{CO})_4^+$  and  $\text{FeC}(\text{CO})_3^+$  are missing in the mass spectrum, these reactions can be either inefficient or under the detection limit of our experiment as no peaks were detected at masses  $m/z$  180 and 152 respectively. The existence of these two products has been never shown in previous works also. In the mass spectrum of  $\text{Fe}(\text{CO})_5$  under  $m/z$  100 a strong contribution of double charged products can be visible, namely  $\text{Fe}(\text{CO})_3^{2+}$ ,  $\text{Fe}(\text{CO})_2^{2+}$ ,  $\text{FeCO}^{2+}$ ,  $\text{Fe}^{2+}$  and  $\text{FeC}(\text{CO})^{2+}$  as well. Many other peaks in the mass spectrum have very low intensities and we were not able to measure the efficiency curves for them as well as to evaluate the threshold energies of corresponding fragmentation reactions. Most of these peaks can be associated with the isotopic pattern of Fe atom with two significant isotopes 2 amu below and 1 amu over its major mass. The known and the recently measured and calculated bond dissociation energies of CO ligands are summarized in Fig. 1. The average BDE of first CO ligand is 0.82 eV from previous works [2-9], recent measurement underestimates this value by 0.27 eV while the DFT calculation results in 1.05 eV. The experimental BDEs have been calculated from the appearance energies (AE) of the corresponding products according to the following formula (1).

$$\text{BDE}[(\text{CO})_n\text{Fe}^+ - \text{CO}] = \text{AE}[\text{Fe}(\text{CO})_n^+] - \text{AE}[\text{Fe}(\text{CO})_{n+1}^+] \quad (1)$$

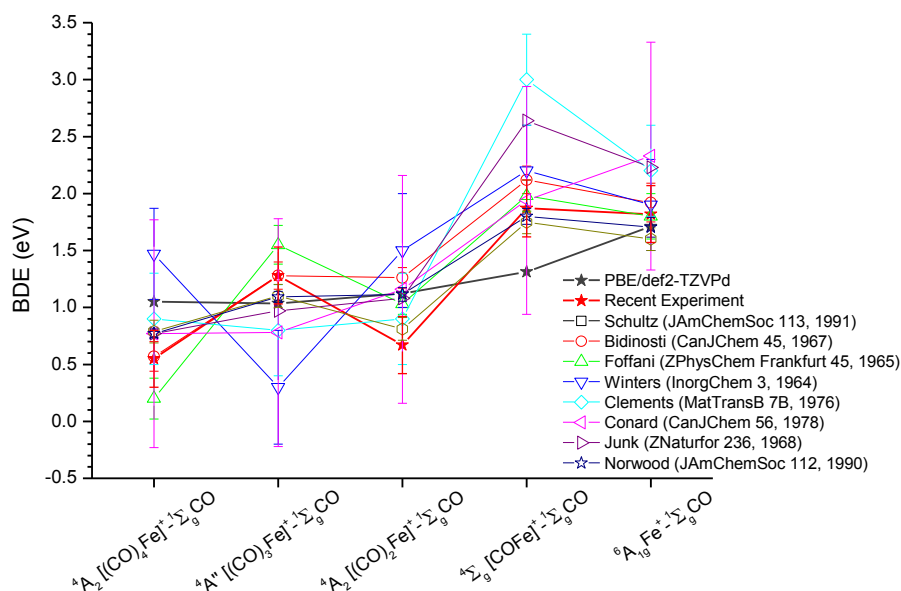
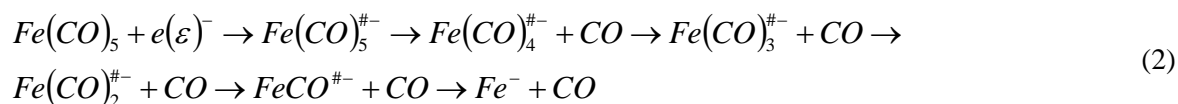


Fig. 1. Bond dissociation energies of  $(\text{CO})_n\text{Fe}^+ - \text{CO}$  ( $n = 4 - 0$ ) for positive ions, comparison of previous works with recent experimental (red stars) and DFT results (black stars).

If we take into account that the measured ionization energy of  $\text{Fe}(\text{CO})_5$  is  $8.45 \pm 0.25$  eV which agrees well with the average ionization energy of 8.36 eV from previous works [2-9], only the increase of the fitted  $\text{AE}[\text{Fe}(\text{CO})_4^+]$  can bring the  $(\text{CO})_4\text{Fe}^+ - \text{CO}$  BDE closer to the average value of 0.82 eV. Moreover this could help to improve the experimental BDE of second ligand ( $1.28 \pm 0.25$  eV) by decreasing to lower value and approaching the average from previous works (0.99 eV). Another interesting observation visible in Fig. 1 is that for dissociation of the first three CO ligands from

$\text{Fe}(\text{CO})_5^+$  we need only  $\sim 1$  eV for each bond break while for the dissociation of the last two CO ligands we need  $\sim 1.7$  eV for each. This is in good agreement with our DFT calculations with PBE/def2-TZVPd, where from the calculated molecular enthalpies the BDEs were evaluated. The ground state of the molecular ion is the doublet  $^2A_1$  state with  $C_{4v}$  symmetry, with every CO ligand loss the ground states of the corresponding fragment cations become quartet states according to our DFT results, with  $C_{2v}$ ,  $C_s$ ,  $C_{2v}$  and  $C_{\infty v}$  symmetries respectively. Only the  $\text{Fe}^+$  product has higher symmetry of the  $^6A_{1g}$  ground state.

The formation of negative ions from  $\text{Fe}(\text{CO})_5$  molecule by DEA proceeds via transient negative ion  $[\text{Fe}(\text{CO})_5]^\#$ . The measured ion efficiency curves confirmed the existence of 5 negative ions formed via CO ligand losses with final decomposition to atomic ion of  $\text{Fe}^-$ , as shown previously [10-12]. The  $[\text{Fe}(\text{CO})_5]^\#$  was not detected probably due its shorter lifetime than is the flight time through the quadrupole spectrometer onto the detector. Low energy resonances are typical for  $\text{Fe}(\text{CO})_4^-$  and  $\text{Fe}(\text{CO})_3^-$ . The first product has one resonance with a threshold at  $\sim 0$  eV and very sharp increase to its maximum while the second product has the threshold also at  $\sim 0$  eV leading to one intensive resonance centred at  $\sim 1.3$  eV and weaker resonance centred at  $\sim 3.45$  eV. It is also important to note that the intensities of resonances decrease by one order as listed in formula (2), with the number of dissociated CO ligands the efficiency decreases rapidly. Higher energy resonances, the so called core excited resonances, are typical for the remaining three products,  $\text{Fe}(\text{CO})_2^-$ ,  $\text{FeCO}^-$  and  $\text{Fe}^-$ . The threshold of  $\text{Fe}(\text{CO})_2^-$  resonance is around  $\sim 2.4$  eV and slowly rises to its maximum at  $\sim 4.2$  eV. The ion  $\text{FeCO}^-$  is the only one with two identically intensive resonances centred at  $\sim 5.8$  eV and  $\sim 8.6$  eV, the first resonance with its threshold at  $\sim 4$  eV. Finally the  $\text{Fe}^-$  resonance has its threshold at  $\sim 6$  eV and a peak maximum around  $\sim 8.7$  eV.



The BDEs of CO ligands in negative ions are contrary to the positive ions energetically more demanding, see Fig. 2. According to the DFT calculations there exist only a shallow minimum on the potential energy surface of  $\text{Fe}(\text{CO})_5^-$ , resulting in a positive electron affinity of this ion  $\sim 0.82$  eV and a BDE of the first axial CO ligand  $\sim 0.13$  eV. The second axial CO ligand dissociated from  $\text{Fe}(\text{CO})_4^-$  needs more than 1.9 eV. Both negative ions are doublet ground states contrary to the remaining three negative fragments being in higher quartet spin states. Around 2.17 eV is needed for dissociation of third CO that is the largest BDE from our calculations, the last two ligands can be dissociated with 1.5 and 1.17 eV respectively.

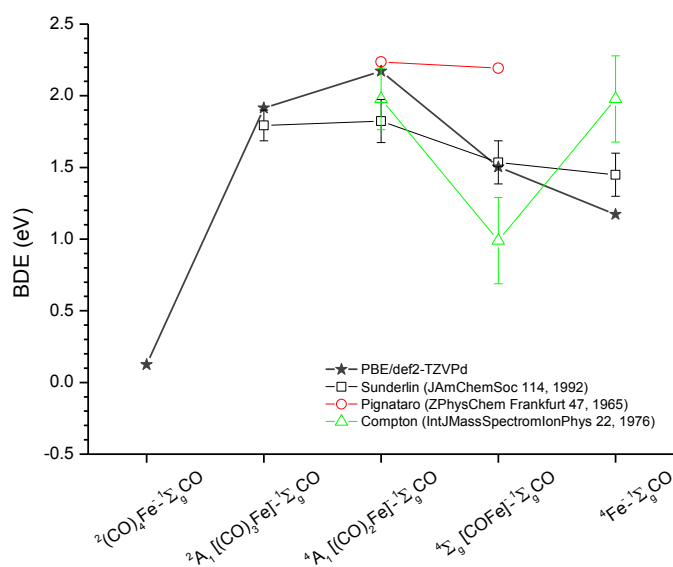


Fig. 2. Bond dissociation energies of  $(\text{CO})_n\text{Fe}^- - \text{CO}$  ( $n = 4 - 0$ ) for negative ions, comparison of previous works with recent DFT results (black stars).

## 5. Conclusions

The role of low energy electron induced process on metalorganic compounds for FEBID technologies has been shown by the means of crossed electron/molecular beams technique and theoretical calculations with DFT. The dissociation of the CO ligands was shown as a common process for both dissociative electron ionisation and dissociative electron attachment. It has been shown that beyond the ionisation energy of  $\text{Fe}(\text{CO})_5$  molecule ( $\sim 8.45$  eV) another  $\sim 6.2$  eV are enough to decompose to atomic  $\text{Fe}^+$ . The same is typical for DEA to  $\text{Fe}(\text{CO})_5$  as the  $\text{Fe}^-$  ion has its broad and weak resonance with a threshold from  $\sim 6$  eV.

## 6. Acknowledgments

This work was supported by the Slovak Research and Development Agency under Contract No. APVV-0733-11, the Comenius University student grant program no. UK/528/2014, the Slovak grant agency VEGA V/0514/12. This work was conducted within the framework of the COST Action CM1301 (CELINA).

## 7. References

- [1] S. Engmann, M. Stano, P. Papp, M.J. Brunger, Š. Matejčík, O. Ingólfsson, *Journal of Chemical Physics*, 138 (2013).
- [2] R.E.K. Winters, R. W., *Inorganic Chemistry*, 3 (1964) 4.
- [3] D.R.M. Bidinosti, N. S., *Canadian Journal of Chemistry*, 45 (1967).
- [4] P.J. Clements, F.R. Sale, *Metallurgical Transactions B*, 7 (1976) 171-176.
- [5] B.R.S. Conard, R., *Canadian Journal of Chemistry*, 56 (1978) 2.
- [6] K. Norwood, A. Ali, G.D. Flesch, C.Y. Ng, *Journal of the American Chemical Society*, 112 (1990) 7502-7508.
- [7] G.A.S. Junk, H.J., *Z. Naturforsch.*, 23b (1968).
- [8] A.P. Foffani, S.; Cantone, B.; Grasso, F., *Z. Physik. Chem. (Frankfurt)*, 45 (1965).
- [9] R.H. Schultz, K.C. Crellin, P.B. Armentrout, *Journal of the American Chemical Society*, 113 (1991) 8590-8601.
- [10] R.N. Compton, J.A.D. Stockdale, *International Journal of Mass Spectrometry and Ion Physics*, 22 (1976) 47-55.
- [11] L.S. Sunderlin, D. Wang, R.R. Squires, *Journal of the American Chemical Society*, 114 (1992) 2788-2796.
- [12] S. Pignataro, A. Foffani, F. Grasso, B. Cantone, *Zeitschrift für Physikalische Chemie*, 1965, pp. 106.
- [13] M. Stano, S. Matejčík, J.D. Skalny, T.D. Märk, *Journal of Physics B: Atomic, Molecular and Optical Physics*, 36 (2003) 261.
- [14] A. Stamatovic, G.J. Schulz, *Review of Scientific Instruments*, 39 (1968) 1752-1753.
- [15] S.G. Lias, Ion energetics data, in: NIST Chemistry WebBook, NIST Standard Reference Database Number 69. Available from: <http://webbook.nist.gov/chemistry/>, ([cited 2013 April]).
- [16] G.H. Wannier, *Physical Review*, 90 (1953) 817-825.
- [17] J.P. Perdew, K. Burke, M. Ernzerhof, *Physical Review Letters*, 77 (1996) 3865-3868.
- [18] J.P. Perdew, K. Burke, M. Ernzerhof, *Physical Review Letters*, 78 (1997) 1396-1396.

## MEASUREMENTS OF THE RADIATIVE ELECTRON CAPTURE TO CONTINUUM (RECC)

P.-M. Hillenbrand<sup>1,2</sup>, S. Hagmann<sup>1,3</sup>, D. Banas<sup>4</sup>, C. Brandau<sup>2,5</sup>, E. De Filippo<sup>6</sup>,  
A. Gumberidze<sup>5</sup>, D. L. Guo<sup>7</sup>, D. Jakubassa-Amundsen<sup>8</sup>, M. Lestinsky<sup>1</sup>,  
Yu. A. Litvinov<sup>1</sup>, A. Müller<sup>2</sup>, H. Rothard<sup>9</sup>, S. Schippers<sup>2</sup>, M. S. Schöffler<sup>3</sup>,  
U. Spillmann<sup>1</sup>, A. Surzhykov<sup>10</sup>, S. Trotsenko<sup>1,10</sup>, A. Voitkiv<sup>11</sup>, Th. Stöhlker<sup>1,10</sup>

<sup>1</sup>*GSI Helmholtzzentrum für Schwerionenforschung, 64291 Darmstadt, Germany*

<sup>2</sup>*Institut für Atom- und Molekülphysik, Justus-Liebig-Universität, 35392 Giessen, Germany*

<sup>3</sup>*Institut für Kernphysik, Goethe-Universität, 60438 Frankfurt am Main, Germany*

<sup>4</sup>*Institute of Physics, Jan Kochanowski University, 25406 Kielce, Poland*

<sup>5</sup>*ExtreMe Matter Institute, 64291 Darmstadt, Germany*

<sup>6</sup>*Istituto Nazionale di Fisica Nucleare Sezione di Catania, 95123 Catania, Italy*

<sup>7</sup>*Institute for Modern Physics, Lanzhou 730000, China*

<sup>8</sup>*Mathematisches Institut, Ludwig-Maximilians-Universität, 80333 München, Germany*

<sup>9</sup>*CIMAP-CIRIL-GANIL, 14070 Caen, France*

<sup>10</sup>*Helmholtz-Institut Jena, 07743 Jena, Germany*

<sup>11</sup>*Max-Planck-Institut für Kernphysik, 69117 Heidelberg, Germany*

E-mail: p.m.hillenbrand@gsi.de

The high-energy endpoint of electron-nucleus bremsstrahlung is of fundamental interest due to its close relation to photoionization (PI) and radiative electron capture (REC). It provides most stringent tests for understanding the coupling between a matter field and an electromagnetic field. In this process, the incoming electron scatters inelastically off an atomic nucleus and transfers almost all of its kinetic energy onto the emitted bremsstrahlung photon. Alternatively the electron can be understood as being radiatively captured into the continuum of the projectile (RECC). Experimentally this process is only accessible using inverse kinematics, where quasi-free target electrons scatter off fast highly charged heavy projectiles. For collisions  $U^{88+} + N_2$  @ 90 MeV/u new measurements of the electron energy distribution in coincidence with the emitted photon have been conducted at the Experimental Storage Ring ESR at GSI, using the upgraded magnetic electron spectrometer [1,2]. Furthermore, electron energy distributions for non-radiative electron capture to continuum (ECC) and the electron loss to continuum (ELC) could be determined. Comparison with various theoretical calculations will be presented.

### 1. References

- [1] P.-M. Hillenbrand, PhD-Thesis University Giessen (2013)
- [2] P.-M. Hillenbrand et. al., PRA, submitted (2014)

# COMPARISON OF EXPERIMENT AND THEORY FOR ELECTRON IMPACT IONIZATION OF LASER-ALIGNED Mg ATOMS.

Sadek Amami<sup>1</sup>, Don Madison<sup>1</sup>, Kate Nixon<sup>2</sup>, Andrew Murray<sup>2</sup>, Gregory Armstrong<sup>3</sup>, James Colgan<sup>3</sup>, Al Stauffer<sup>4</sup>

<sup>1</sup> *Physics Department, Missouri University of S&T, Rolla, Mo and 65409, USA.*

<sup>2</sup> *School of Physics and Astronomy, University of Manchester, Manchester M13 9PL, UK.*

<sup>3</sup> *Theoretical Division, Los Alamos National Laboratory, Los Alamos, New Mexico, USA.*

<sup>4</sup> *Department of Physics and Astronomy, York University, Toronto, Ontario, Canada*  
E-mail: samc5@mst.edu

We will present Low energy theoretical and experimental quadruple differential cross sections (QDCS) for electron impact ionization of magnesium atoms that have been aligned by lasers. The incident projectile electron has an energy of 43.31eV, the scattered and ejected electrons were detected with equal energies ( $E_1=E_2=20\text{eV}$ ), one of the final state electrons was detected at a fixed scattering angle of  $30^\circ$ , and the other final state electron is detected at angles ranging between  $35^\circ$  and  $120^\circ$ . The Mg atoms are excited to the 3p state using a linearly polarized laser which produces a standing wave aligned perpendicular to the laser beam direction. Theoretical results will be compared with the experimental data for several different alignment angles both in the scattering plane as well as in the plane perpendicular to the incident beam direction.

## 1. Introduction

One of the recent significant advances in the field of electron impact ionization, or (e,2e), has been the development of the capability to measure ionization of aligned molecules which provides a more sensitive test of theory than measurements which average over all molecular alignments. On the atomic level, the equivalent measurement would be ionization of atoms which have been excited into a laser aligned standing-wave state. Nixon and Murray [1] have performed such a measurement for laser aligned Mg and the purpose of this work is to see how well our theoretical calculations compare with the measurements.

The experiments were performed in the scattering plane, for asymmetric angles with equal outgoing electron energies ( $E_1=E_2=20\text{eV}$ ). Measurements were made for ionization of both the ground 3s state as well as the laser aligned 3p state. The incident projectile had an energy of 47.67 eV for ionization of the 3s state and 43.31 eV for ionization of the 3p state. One of the final state electrons was detected at a fixed angle of  $30^\circ$  and the other electron was detected at angles ranging between  $35^\circ - 120^\circ$ . The theoretical models used for the calculations were the DWBA (distorted wave Born) approximation, the 3DW (three body distorted wave model) [2], and the TDCC (time dependent close coupling) method [3].

## 2. Theory

We have used two different perturbation approximations and one time dependent close coupling method to describe the process of interest. Each of them has been described in detail previously [2, 3]. Here we will give a brief summarize of the two distorted wave methods. Details about the TDCC can be found in Armstrong *et al.* [3]. Since the DWBA is a special case of the more general 3DW approximation, we will discuss the 3DW. The 3DW  $T$ -matrix can be written as,

$$T_{fi}^{3DW} = \langle \Phi_f | W | \Phi_i \rangle \quad (1)$$



where  $\Phi_i$  and  $\Phi_f$  are the initial- and final-state wave functions respectively, and  $W$  is the perturbation. The initial-state wavefunction  $\Phi_i$  is approximated as a product of the initial bound state of the atom ( $\psi_A$ ) times a distorted wave function  $\chi_i$  for the incoming electron (the projectile)

$$\Phi_i = \psi_A \chi_i. \quad (2)$$

For atoms, we use the Hartree-Fock bound state wave function ( $\psi_{HF}$ ) for the target. For the laser excited 3p states, we have used the 3p(m=0) standing wave (z-axis parallel to the incident beam direction) rotated to the alignment direction. The perturbation  $W$  is given by

$$W = V - U_i \quad (3)$$

Here  $V$  is the exact initial state interaction between the incident electron and the atom, and  $U_i$  is the initial state spherically symmetric static approximation for  $V$ , which is asymptotically equal to zero.

The final-state wave function  $\Phi_f$  is approximated as a product of two final-state continuum electron distorted waves ( $\chi_{\text{scat}}$  and  $\chi_{\text{eject}}$ ), and the Coulomb interaction between the outgoing electrons ( $C_{\text{ele-ele}}$ ), which is normally called the post-collision interaction (PCI),

$$\Phi_f = \chi_{\text{scat}} \chi_{\text{eject}} C_{\text{ele-ele}}. \quad (4)$$

The post-collision Coulomb interaction between the two electrons ( $C_{\text{ele-ele}}$ ), depends on the relative distance between the two electrons  $\mathbf{r}_{12}$  and the relative momentum  $\mathbf{k}_{12}$ . With these approximations, the 3DW  $T$ -matrix becomes

$$T_{fi}^{3DW} = \langle \chi_{\text{scat}} \chi_{\text{eject}} C_{\text{ele-ele}} | V - U_i | \psi_A \chi_i \rangle \quad (5)$$

The only difference between the DWBA and 3DW is the final state Coulomb interaction  $C_{\text{ele-ele}}$  is ignored in the DWBA. Finally, the triple differential cross section (TDCS) for a given alignment can be written in atomic units as

$$\frac{d^3\sigma}{d\Omega_f d\Omega_e dE_e} = \frac{1}{(2\pi)^5} \frac{k_f k_e}{k_i} (|T|^2) \quad (6)$$

### 3. Results and Discussion

Triple Differential Cross Sections (TDCS) for ionization of the (3s) ground state and Quadruple differential Cross Sections (QDCS) for ionization of laser aligned 3p excited states are presented in Fig. 1. The 3DW, DWBA, and TDCC results are compared with experiment for ionization of the ground 3s state in the top panel of Fig 1. Since the experiments are not absolute, all the theories and the experimental data are normalized to unity at the binary peak. It is seen that the 3DW results are in excellent agreement with the 3s cross section. Both the DWBA and TDCC predict binary peaks shifted to smaller angles.

In the middle and lower panel of Fig. 1, 3DW and DWBA results are compared with experiment for atoms laser aligned in a plane perpendicular to the incident electron beam. We use a coordinate system for which the incident beam direction is the z-axis, the scattering plane is the xz plane and the xy plane is the plane perpendicular to the incident beam. The middle panel corresponds to an alignment parallel to the x-axis and the lower panel corresponds to an alignment at  $45^\circ$  between the x- and y-axes. We have normalized the experiment and 3DW to unity at the maximum cross section for the x-axes (middle panel). The experimental data are relatively absolute so the same normalization is

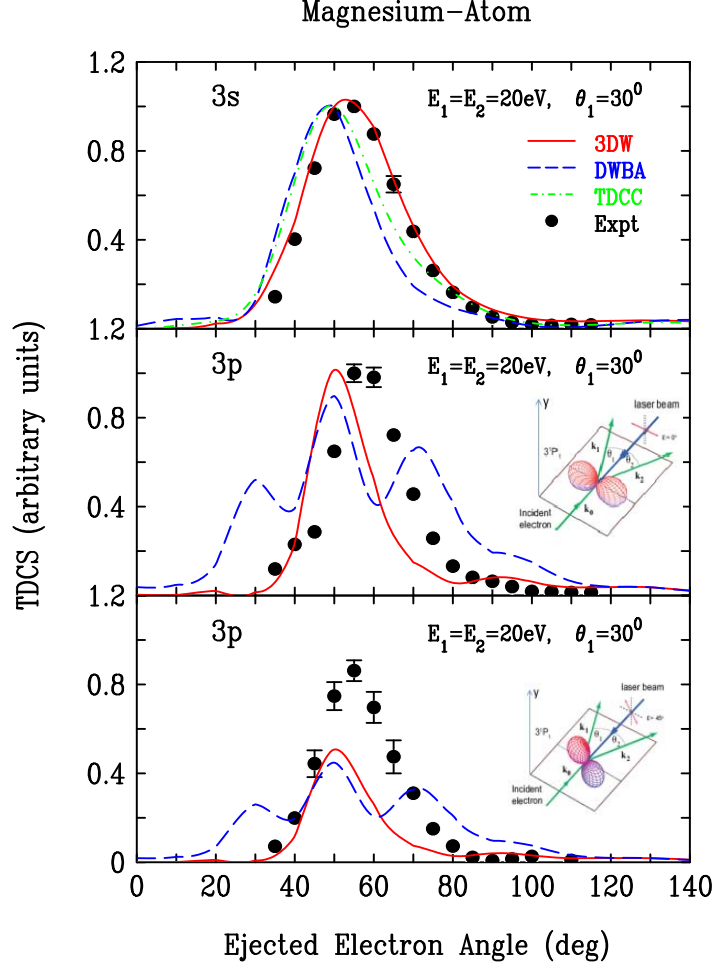


Figure.1. Experimental and theoretical TDCS for electron-impact ionization of Mg. The projectile scattering angle is  $30^\circ$  and both outgoing electrons have the same energy ( $E_1=E_2=20\text{eV}$ ). The top panel is for ionization of the 3s state, the middle panel is for ionization of the 3p state laser aligned parallel to the x-axis (see text) and the bottom panel is for ionization of the 3p state laser aligned at  $45^\circ$  between the x- and y-axes. The theoretical calculations are: 3DW solid Red; DWBA dashed blue; and TDCC dash-dot green. The experimental data are the solid circles. See text for normalization of theories and experiment.

used for the bottom panel and Fig. 2. In the middle panel, the 3DW predicts the proper shape of the cross section but the experimental peaks are shifted by about  $5^\circ$  to larger angles. The DWBA has the wrong shape with 3 peaks instead of one. The fact that the 3DW has the correct shape while the DWBA does not indicates that the Coulomb interaction between the two electrons (PCI) plays the major role in this collision. Looking at the bottom panel (alignment at  $45^\circ$  between the x- and y-axes), the DWBA and 3DW results are exactly half the results in the middle panel, which can also be predicted using the method of Al Stauffer [4,5] and the T-matrix symmetry for the z-axis along the beam direction i.e.  $T(m=+1) = -T(m=-1)$ . Obviously, the experimental data are not in accord with this symmetry condition.

Experiments were also performed for ionization of the 3p state that has been laser aligned parallel to the y-axis (perpendicular to incident beam and perpendicular to the scattering plane). For this case the 3DW and DWBA numerical results were exactly zero for all ejected electron angles and the Stauffer-method also predicts zero. Figure 2 compares experiment and theory for alignment along the y-axis. The top part of Fig. 2 shows non-convoluted theoretical results (i.e. the 3DW and DWBA results are zero) while the experiment finds significant non-zero results. The experimental acceptance angular

range is  $\pm 3^\circ$ . To see if this could explain the large difference between experiment and theory, the 3DW results convoluted over the experimental uncertainty angular range of  $\pm 3^\circ$  are shown in the bottom panel of Fig. 2 (solid red). Although this process yielded a small non-zero result for the cross section, it was still far from experiment. As an interesting exercise, we tried making the acceptance window wider and found that  $\pm 30^\circ$  yielded excellent agreement with experiment (dashed blue in bottom panel). Obviously this is nonsense but we show the results for academic interest only.

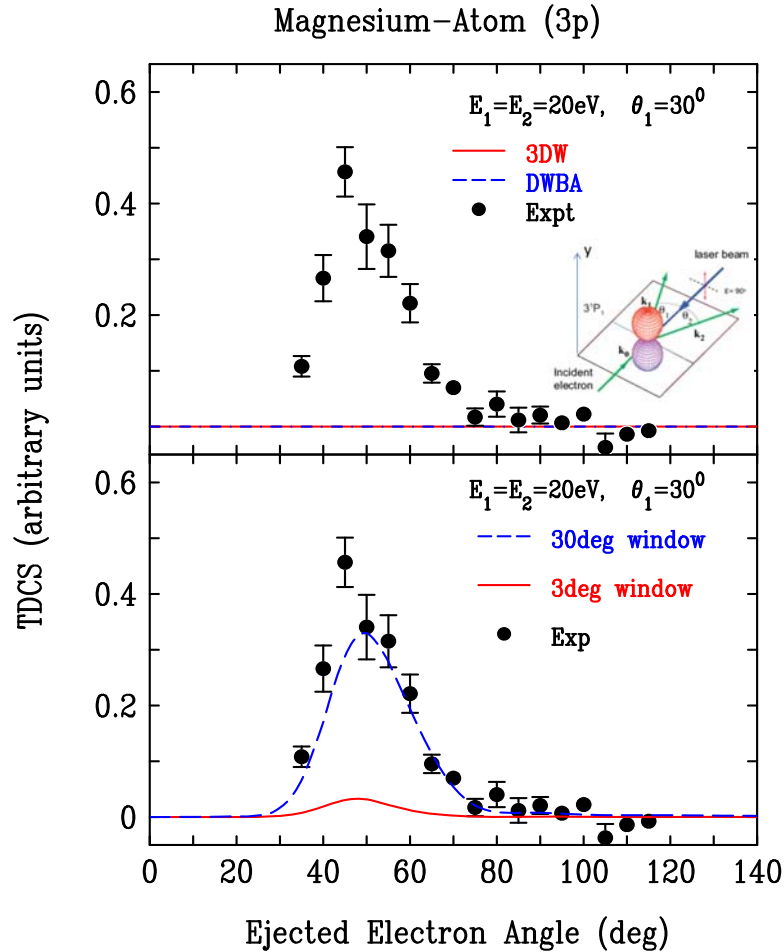


Figure 2. Differential cross sections for ionization of the 3p state laser aligned parallel to the y-axis. In the top panel, the 3DW and DWBA results are exactly zero. In the bottom panel, the 3DW results have been convoluted over an experimental uncertainty of  $\pm 3^\circ$  (solid red) and convoluted over an experimental uncertainty of  $\pm 30^\circ$  (dashed blue).

## 4. References

- [1] Nixon K. L. and Murray A. J. 2011 *Phys. Rev. Lett.* **106**, 123201.
- [2] Madison D H and Al-Hagan O 2010 *Journal of Atomic, Molecular, and Optical Physics* 367180.
- [3] Armstrong G. S. J. Colgan J. and Pindzola M. S. 2013 *Phys. Rev. A* **88** 042713.
- [4] Stauffer A. D. 2014 *Phys. Rev A* **89** 032710.
- [5] Stauffer A. D. 2014 *Phys. Rev A* **89** 049906.

# THEORETICAL AND EXPERIMENTAL INVESTIGATION OF (E,2E) FOR ALIGNED H<sub>2</sub> MOLECULES

Esam Ali<sup>1</sup>, Don Madison<sup>1</sup>, X. Ren<sup>2</sup>, A. Dorn<sup>2</sup>, C. Ning<sup>3</sup>

<sup>1</sup>Missouri University of Science & Technology, Rolla, MO 65409, USA

<sup>2</sup>Max-Planck-Institute for Nuclear Physics, 69117 Heidelberg, Germany

<sup>3</sup>Tsinghua University, Beijing 100084, People's Republic of China

E-mail: eaagx2@mst.edu

Experimental and theoretical Quadruple Differential Cross Sections (QDCS) are presented for electron impact ionization of H<sub>2</sub> with simultaneous excitation of the  $2s\sigma_g$  state in the perpendicular plane. Results are presented for three different alignments in the xy-plane (scattering plane is xz) - alignment along y-axis, x-axis, and 45° between the x- and y-axes for incident electron energies of 4 and 10 eV and a fixed projectile scattering angle of 30° in the perpendicular plane. Theoretical M4DW (molecular 4-body distorted wave) results are compared to experimental data, and overall we found reasonably good agreement between experiment and theory.

## 1. Introduction

Electron-impact-induced ionization and fragmentation of molecules is a rich field with important applications of biological, industrial, and theoretical relevance. Here we present experimental and theoretical M4DW results for ionization plus simultaneous excitation of H<sub>2</sub> to the  $2s\sigma_g$  excited state which immediately dissociates and the alignment of the molecule is determined by detecting one of the fragments. Results are presented for three different alignments as shown in Fig. 1. The scattering plane is xz and the orientations of interest are in the xy-plane which is perpendicular to the incident beam direction - alignment along y-axis, x-axis, and 45° between the x- and y-axes.

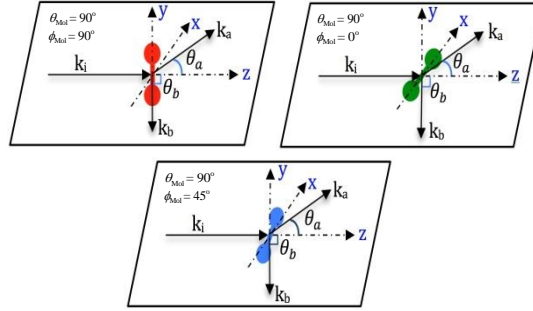


**Fig. 1.** Different molecular alignments. The incident electron momentum is  $k_i$  along the z- axis, the scattering and ejected electrons momentum are  $k_a, k_b$  respectively,  $k_a$  is in the scattering plane (xz) and the ejected electron momentum  $k_b$  is in the perpendicular plane (xy).

## 2. Theory

The M4DW (molecular 4-body distorted wave) method for treating the dissociative – ionization process to determine the alignment of H<sub>2</sub> molecules has been discussed before [1]. The T-matrix for excitation-ionization can be written as:

$$T_{fi} = \langle \psi_f | H - H_0 | \phi_i \rangle \quad (1)$$

Where  $H$  is the full Hamiltonian which contains three parts and is giving by

$$H = H_{\text{target}} + K_i + V_i \quad (2)$$

Where  $H_{\text{target}}$  is the Hamiltonian for a neutral target with eigenfunctions  $\psi_{\text{target}}$ , and  $K_i, V_i$  are the kinetic energy and initial-state interaction between the projectile and target. The approximate Hamiltonian  $H_0$  is given by

$$H_0 = H_{\text{target}} + K_i + U_i \quad (3)$$

Here  $U_i$  is the initial-state spherically symmetric approximation for the projectile-target interaction. The perturbation term is

$$H - H_0 = V_i - U_i \quad (4)$$

The initial-state wavefunction,  $\phi_i$  is given by

$$|\phi_i\rangle = |\chi_i(\mathbf{r}_0) \psi_{\text{target}}(\mathbf{r}_1, \mathbf{r}_2)\rangle \quad (5)$$

Here,  $\chi_i(\mathbf{r}_0)$  is a distorted wave for incident projectile electron and  $\psi_{\text{target}}(\mathbf{r}_1, \mathbf{r}_2)$  is the ground state wave function. We use the variational method wavefunction of Rosen [2,3].

The final-state wave function,  $\psi_f$  which contains four terms and is approximated by

$$|\psi_f\rangle = |\chi_a(\mathbf{r}_0) \chi_b(\mathbf{r}_1) \phi_{\text{ion}}(\mathbf{r}_2) C_{a-b}(\mathbf{r}_{01})\rangle \quad (6)$$

Where  $\chi_a(\mathbf{r}_0), \chi_b(\mathbf{r}_1)$  are distorted wave functions for the scattered and ejected electrons,  $\phi_{\text{ion}}(\mathbf{r}_2)$  is the excited state wave function for  $H_2^+$  ion, and  $C_{a-b}(\mathbf{r}_{01})$  is the coulomb distortion factor between the two scattered and ejected electrons.

$$T_{fi} = \langle \chi_a^-(\mathbf{k}_a, \mathbf{r}_0) \chi_b^-(\mathbf{k}_b, \mathbf{r}_1) \phi_{\text{ion}}(\mathbf{r}_2) C_{a-b}(\mathbf{r}_{01}) | V_i - U_i | \psi_{\text{target}}(\mathbf{r}_1, \mathbf{r}_2) \chi_i^+(\mathbf{k}_i, \mathbf{r}_0) \rangle \quad (7)$$

### 3. Results

Experimental and theoretical M4DW results for 126 eV incident electrons, a fixed projectile scattering angle of  $30^\circ$ , and electrons ejected into the perpendicular plane with energies of 4, and 10 eV are presented as a function of the electron emission angle in Fig. 2 for the  $H_2$  transition  $1s\sigma_g \rightarrow 2s\sigma_g$ . Results are presented for the three orientations shown in Fig. 1. The relative experimental data have been normalized for the best visual agreement with theory for y-orientation at 4 eV and  $30^\circ$ . We use the same normalization for all other cases, since the experimental data are relatively absolute. Similar to previous works [4, 5], both experiment and theory find a very strong alignment dependence in the QDCS.

As can be seen from the figure, overall there is very good agreement between theory and experiment. The experimental measurements are relatively absolute and although the shape of the theory is in very good to excellent agreement with experiment, for the 4 eV x-orientation case, the magnitude of the theory is about a factor of two smaller than experiment. For molecular alignment along the x- and y- axis, there is symmetry about the scattering plane (i.e. 0 to  $180^\circ$  is the mirror image of  $180^\circ$  to  $360^\circ$ ). However, this symmetry is not present for the  $45^\circ$  orientation case and again theory predicts nicely the same asymmetry as found in experiment. The plots show that the intensity and positions of the peaks depend strongly on the molecular alignment.

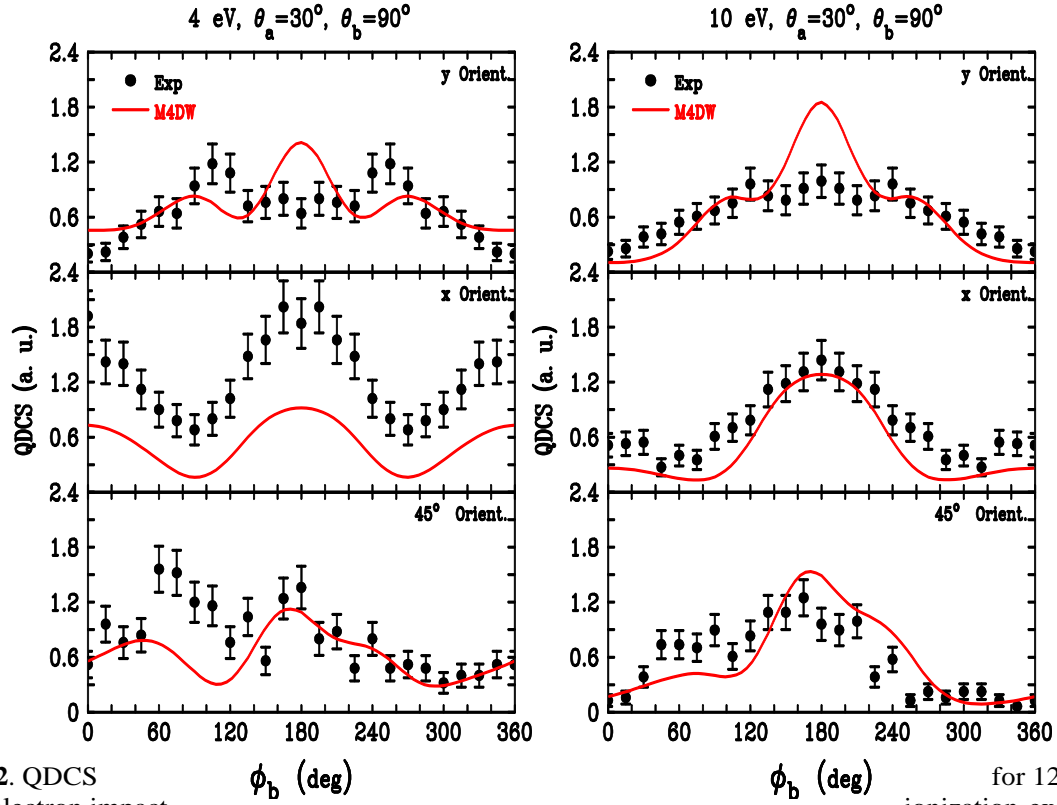


Fig 2. QDCS electron impact of H<sub>2</sub>. Experiment is normalized to theory for the best visual fit for the 4 eV and y-orientation, and the same normalization is used for all the other orientations since the experimental data are relatively absolute.

## 4. References

- [1] A. L. Harris, M. Foster, J. L. Peacher, and D. H. Madison 2008 *J. Phys. B* **41**, 135203.
- [2] E. Ali, A. L. Harris, J. Lower, E. Weigold, C. G. Ning, and D. H. Madison 2014 *Phys. Rev. A* (to be published).
- [3] N. Rosen, 1931 *Phys. Rev.* **38**, 2099.
- [4] M. Takahashi, N. Watanabe, Y. Khajuria, Y. Udagawa, and J. H. D. Eland 2005 *Phys. Rev. Lett.* **94**, 213202.
- [5] X. Ren, T. Pflüger, S. Xu, J. Colgan, M. S. Pindzola, A. Senftleben, J. Ullrich, and A. Dorn 2012 *Phys. Rev. Lett.* **109**, 123202

# ZERO ENERGY RESONANCES IN A FUSION PLASMA

C. F. Clauser<sup>1</sup>, R. O. Barrachina<sup>1</sup>

<sup>1</sup>*Centro Atómico Bariloche and Instituto Balseiro, Comisión Nacional de Energía Atómica and Universidad Nacional de Cuyo, Av. Bustillo 9500, 8400 Bariloche, Argentina*

E-mail: barra@cab.cnea.gov.ar

In this communication we investigate different atomic processes that might occur in the interior of fusion plasmas, including inertial and magnetic confinement, with special emphasis in photoionization and radiative recombination processes. In particular we apply the Final-State Interaction theory in order to study the behaviour of the corresponding cross sections when the relative energy of a pair of charged particles in the initial or final states vanishes. Through this analysis we uncover the presence of zero energy resonances for particular configurations of density and temperature, which might have an important impact on the working conditions and performance of fusion reactors.

## 1. Introduction

Let us consider an atomic transition taking place within a plasma [1]. Naturally, the corresponding transition matrix element depends on the parameters that characterize the atomic partners before or after the transition. Furthermore, it also depends on the given conditions of density and temperature of the plasma, since they can affect the corresponding interactions. A notorious example is given by the screening of the interaction between charged particles.

In many cases of interest, the situation where the relative momentum  $k$  of a pair of charged partners in the initial or final configuration vanishes can be relevant for the transition under study. When  $k\lambda \gg 1$ , where  $\lambda$  is the screening length the potential, the amplitudes converge to the Coulomb ones, but this condition should fail for small enough values of  $k$ . In this communication we discuss on very general grounds the kind of consequences that such a screening might have on the atomic transitions taking place within the plasma, and whether they might be observable or lead to sizeable effects.

## 2. Final State Interaction Theory

According to the final-state interaction theory [2], the  $k \rightarrow 0$  limit of transition matrix element is dominated by the inverse of the s-wave Jost function, which in atomic units reads,

$$f_0(k, \lambda) = 1 + \frac{2\mu}{k} \int_0^\infty e^{ik\lambda} V_\lambda(r) \phi_{0k}(r) dr \quad (1)$$

Here  $V_\lambda(r)$  is the screened Coulomb potential between the active particles of reduced mass  $\mu$ , relative momentum  $k$  and distance  $r$ , while  $\phi_{0k}(r)$  represents the  $\ell = 0$  regular solution of the radial equation. When factored out of the transition matrix element in the  $k \rightarrow 0$  limit, the Jost function would produce an enhancement factor  $F(k, \lambda) = 1/|f_0(k, \lambda)|^2$  with very different behaviours for screened and unscreened Coulomb potentials. Here we are considering only attractive potentials (i.e.  $V_\infty(r) = -Z/r$  with  $Z > 0$ ). Under very general conditions, it can be shown that for small values of  $k\lambda$  the enhancement factor would produce a Lorentzian-shape peak

$$F(k, \lambda) \propto \frac{a^2}{1 + k^2 a^2} \quad (2)$$

where  $a = a(\lambda)$  is the s-wave scattering length for the potential  $V_\lambda(r)$ . On the other hand, for a pure Coulomb potential (i.e.  $\lambda \rightarrow \infty$ )

$$F(k, \lambda) \approx \frac{2\pi\mu Z}{k} \quad (3)$$

Note that the two limits  $k \rightarrow 0$  and  $\lambda \rightarrow \infty$  do not commute. Furthermore, for screened potentials, the enhancement factor diverges like  $k^{-2}$  at these zero energy resonances (i.e. for  $a \rightarrow \infty$ ) [3], a behaviour that is very different from the  $k^{-1}$  divergence corresponding to a pure Coulomb potential.

### 3. Radiative Recombination Processes

We apply the previous results to the radiative recombination process, where an electron is captured by an ion or atom with emission of a photon. We model  $V_\lambda(r)$  by means of a Hulthén potential and evaluate the reduced cross section within a dipolar approximation. We relate the screening length  $\lambda$  to the density  $n$  and temperature  $T$  by means of a standard interpolation [4]

$$\lambda^2 \approx \frac{1}{4\pi n} \left( \frac{(3\pi^2 n)^{2/3}}{3} + T \right) \quad (4)$$

Further details of the calculation will be provided at the conference. We compare our results with recent numerical calculations of photoionization cross sections [5], finding an excellent agreement.

In Fig 1 we show the reaction frequency for the radiative recombination of  $H^+$  and  $He^{++}$  in the case of inertial confinement as a function of the temperature  $T$ . We clearly observe that it increases by as much as an order of magnitude whenever the temperature of the plasma matches a zero energy resonance condition.

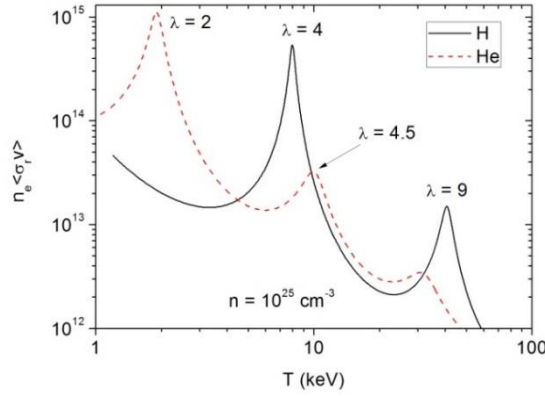


Fig. 1. Reaction frequency for the radiative recombination of  $H^+$  and  $He^{++}$  in inertial confinement (with  $n = 10^{25} \text{ cm}^{-3}$ ) as a function of the temperature  $T$ .

### 4. Conclusions

In this communication we have uncovered the presence of zero energy resonances in plasmas for particular configurations of density and temperature. We applied our model to the particular case of a radiative recombination process, but the same effects will be present in any atomic process whenever the relative momentum of a pair of charged partners in the initial or final configuration vanishes. The impact that these resonances might have on the working conditions and performance of a fusion reactor for both inertial and magnetic confinement is to be analysed and pondered.

### 5. References

- [1] Salzmänn D 1998 *Atomic Physics in Hot Plasmas* (Oxford University Press Inc., NY).
- [2] Gillespie J 1964 *Final State Interactions* (Holden-Day Inc., San Francisco).
- [3] Macri P A and Barrachina R O 2013 *J. Phys. B* **46** 065202.
- [4] Neufeld J and Ritchie R H 1955 *Phys. Rev.* **98** 1632.
- [5] Lin C Y and Ho Y K 2010 *Eur. Phys. J. D* **57**, 21.



# VORTICES IN THE POSITRON-IMPACT IONIZATION OF ATOMS

F. Navarrate<sup>1</sup>, M. Feole<sup>1</sup>, R. O. Barrachina<sup>1</sup>

<sup>1</sup>*Centro Atómico Bariloche and Instituto Balseiro, Comisión Nacional de Energía Atómica and Universidad Nacional de Cuyo, Av. Bustillo 9500, 8400 Bariloche, Argentina*

E-mail: barra@cab.cnea.gov.ar

By means of a systematic theoretical study of the positron-atom ionization collision in a collinear geometry, we uncover the presence of isolated zeroes in the triply differential cross section (TDCS) at intermediate impact energies. We analyse them in the framework of Madelung's Hydrodynamic and De Broglie-Bohm interpretations of Quantum Mechanics and demonstrate that they actually represent quantum vortices in the generalized velocity field associated to the transition matrix element. We investigate their main characteristics and show that they appear in pairs of opposite circulation, in accordance with one of the scenarios for their emergence.

## 1. Introduction

Vortices are very well-known features of many-body systems. They are routinely observed in gases, liquids and plasmas, and in connection with quantum effects as superfluidity, superconductivity, and Bose-Einstein condensation. The description of these many body systems customarily resorts to the inclusion of ad-hoc potentials or nonlinear terms. Here, on the other hand, we investigate their appearance in an extremely simple quantum system, consisting of an electron, a positron and a proton.

## 2. Vortices in Positron-Hydrogen Ionization Collisions

In this communication we present a systematic study of vortices in the  $e^+ + H$  ionization collision. When analysed in the framework of Madelung's Hydrodynamic [1] and De Broglie-Bohm [2] interpretations of Quantum Mechanics, the time evolution of the corresponding electron - positron - proton system is equivalent to the flow of a perfect fluid that is irrotational everywhere, except at vortices where the corresponding density vanishes. During the ionization process, vortices emerge as closed submanifolds or in pairs of opposite circulation [3]. They may collapse at later times, but some can survive up to macroscopic distances and, according to the imaging theorem [4], manifest themselves as zeroes of the ionization matrix element  $T$  [5].

We evaluate the transition matrix element  $T$  by employing a correlated approximation of the final three-body state [6]. In figure 1, we show the square modulus of  $T$  for the ionization of a Hydrogen atom by the impact of a positron of 275 eV. Instead of the “symmetric geometry” [7] customarily used in the study of  $(e,2e)$  collisions, we employ an “energy sharing” or collinear arrangement, where the electron and the positron move along the same direction in the final state. The presence of three zeroes are clearly observed in the figure. We demonstrate that they actually represent vortices, i.e. they are zeroes of the real and the imaginary parts of the transition matrix element with a circulation of the generalized velocity field  $\text{Im } \nabla_{\mathbf{k}} \ln T$  equal to  $2\pi$  around each of them. In this sense, they are akin to similar effects experimentally observed in the ionization of atoms by the impact of electrons [5] and ions [8], and theoretically analysed for electric pulses [9].

The zero in the middle of fig. 1 is related to a deep minimum observed more than two decades ago by Brauner and Briggs [10], even though at that time it was not recognized as a vortex itself. Furthermore it was observed at extremely high impact energies, where the TDCS was too small to be experimentally accessible. Here we demonstrate that it might still be present at much smaller impact energies, thus being amenable to be experimentally investigated. Furthermore, we show how this vortex is paired with a second one of opposite circulation at its left, in accordance with one of the scenarios for their emergence. The other vortex in the lower right corner might persists at impact energies as small as 30 eV [11]. It is also paired to another vortex of opposite circulation, but outside the figure.

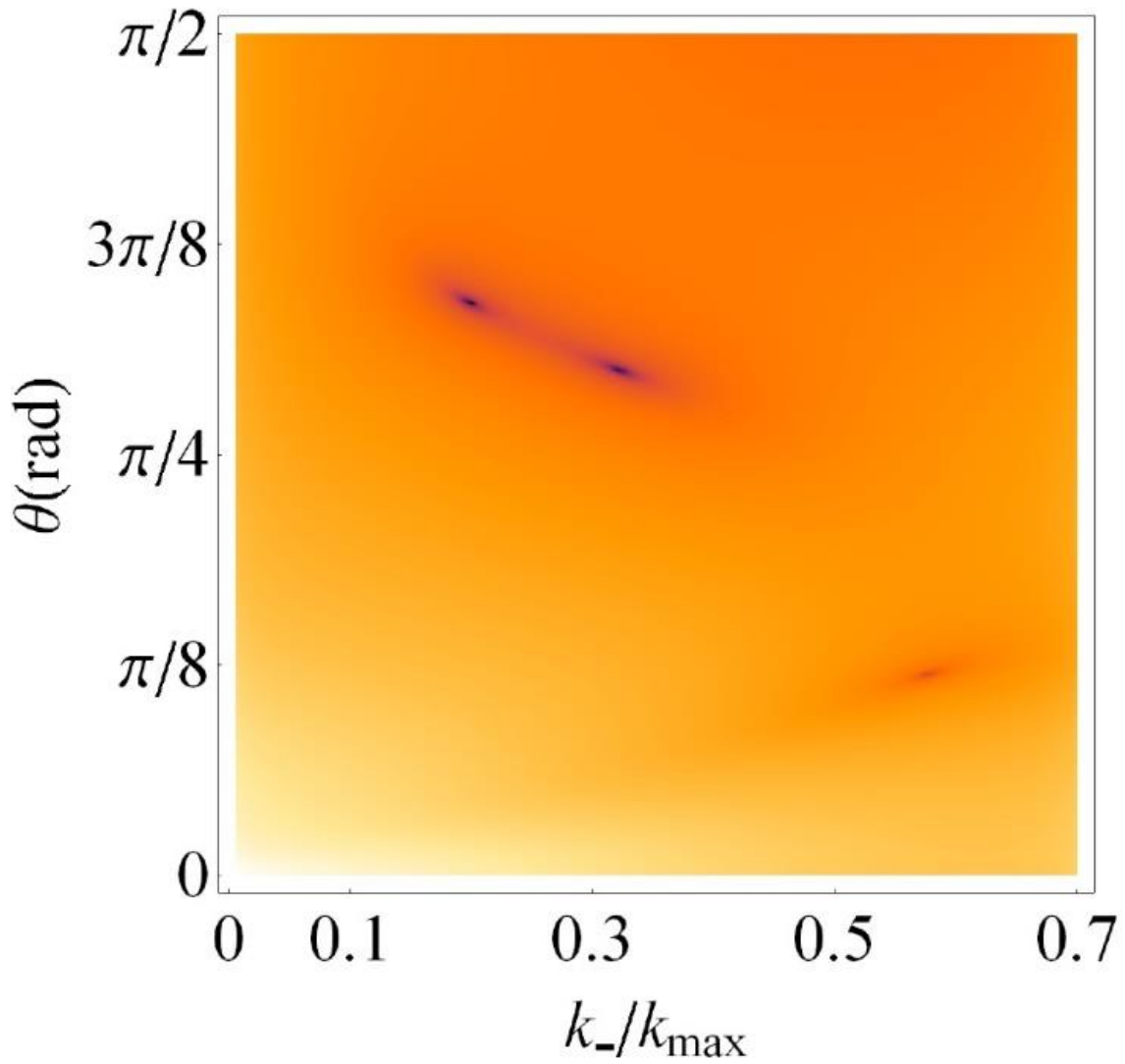


Fig. 1. Square modulus of the transition matrix element for the ionization of a Hydrogen atom by the impact of a positron of 275 eV. Conditions are set to a collinear geometry configuration (see text).  $k_-$  and  $\theta$  are the electron's momentum and emission angle (with respect to the direction of the initial velocity of the positron), respectively.  $k_{max}$  is the maximum value of the electron momentum allowed by energy conservation. The logarithmic scale in arbitrary units sets the lowest and highest values in dark red and light yellow, respectively.

Finally, let us mention that when studied over a long range of impact energies, these vortices seem to emerge from or move towards significant points related to particular collision mechanisms, as the direct ionization and capture to the continuum cusps, or the saddle-point and Thomas processes.

### 3. References

- [1] Ghosh S K and Deb B M 1982 *Phys. Rep.* **92** 1
- [2] Dürr D and Teufel S 2009 *Bohmian Mechanics: The Physics and Mathematics of Quantum Theory* (Berlin: Springer-Verlag)
- [3] Bialynicki-Birula I, Bialynicka-Birula Z and Sliwa C 2000 *Phys. Rev. A* **61** 032110
- [4] Dollard J D 1971 *Rocky Mountain J. Math.* **1** 5.
- [5] Macek J H, Sternberg J B, Ovchinnikov S Yu and Briggs J S 2010 *Phys. Rev. Lett.* **104** 033201
- [6] Berakdar J and Briggs J S 1994 *J. Phys. B* **27** 4271; *Phys. Rev. Lett.* **72** 3799
- [7] Gottschalk B, Shlaer W J and Wang K H 1965 *Phys. Lett.* **16** 294
- [8] Schmidt L Ph H, Gohl C, Metz D, Schmidt-Böcking H, Dörner R, Ovchinnikov S Yu, Macek J H and Schultz D R 2014 *Phys. Rev. Lett.* **112** 083201
- [9] Ovchinnikov S Yu, Sternberg J B, Macek J H, Lee T-G and Schultz D R 2010 *Phys. Rev. Lett.* **105** 203005
- [10] Brauner M and Briggs J S 1991 *J. Phys. B* **24** 2227
- [11] Navarrete F, Della Picca R, Fiol J and Barrachina R O 2013 *J. Phys. B* **46** 115203

# ON HOW JOST CAN HELP BREIT AND WIGNER TO BETTER DESCRIBE A RESONANCE

R. O. Barrachina<sup>1</sup>, P. A. Macri<sup>2</sup>

<sup>1</sup>*Centro Atómico Bariloche and Instituto Balseiro, R8402AGP, S. C. Bariloche, Río Negro, Argentina*

<sup>2</sup>*Instituto de Investigaciones Físicas de Mar del Plata – Departamento de Física, FCEyN, Universidad Nacional de mar del Plata, Argentina*

E-mail:

In this work we propose a parametrization of cross sections by means of the Jost function's zeros which represent bound, virtual and resonant states of the interaction. This formula overcomes all the shortcomings of well-known formulas as the ones provided by Breit-Wigner and Fano.

## 1. Theory

One of the main goals of Scattering Theory is to predict the behavior of cross sections as a function of the parameters which define the interaction. Frequently, full knowledge of these parameters is not accessible but instead some spectral information of the interaction is available as, for instance, the position of bound, virtual and resonant states. In fact, most of the striking phenomena observed in scattering experiments [1] can be described in terms of these spectral characteristics of the interaction. In particular, resonances which display a sudden increase of the cross section at an energy  $E_o$  are considered to be the manifestation of a transitorily bound state with energy  $E_o$  and half life  $1/\Gamma$ , and described by the celebrated Breit-Wigner formula [2]  $\sigma \propto (\Gamma^2/4)/((E - E_o)^2 + \Gamma^2/4)$ . This formula provided one of the first descriptions of a specific feature of a cross section in terms of the spectral properties of the interaction. In spite of its enormous success in nuclear, atomic and molecular physics, this formula presents severe shortcomings if (i) the energy  $E_o$  lies close to threshold, (ii) the half life  $1/\Gamma$  is not large enough, (iii) the interaction produces a noticeable background phase shift before the onset of the resonance or (iv) there is another proximate resonant state.

In this work, we propose a new spectral formula based on one or more  $L$ -wave Jost function's zeros on the complex momentum plane [4,5]. We demonstrate that it is possible to solve difficulty (i) by considering the correct low energy expansion of the Jost function. In this way, a momentum-dependent half life is introduced allowing to find a formula which satisfies the well-known partial-wave threshold law  $\sigma \propto E^{2L}$  [3] as can be seen in Fig. 1. Difficulty (ii) appears when the net repulsive part of the potential barrier is weaker than a centrifugal-like term as occurs in Fig. 2. It can show up even for  $s$ -waves in systems with "negative" dipole polarizabilities as observed in the  $5^2G$  partial photodetachment of  $K^-$  [7]. This difficulty can be solved by considering the contribution of the imaginary part of the Jost zero to the resonant position which is ignored in the Breit-Wigner formula. Difficulty (iii) can be solved by means of a non-spectral contribution to the background Jost function which plays the role of the well-known Fano's shape parameter  $q$  [6]. Finally, shortcoming (iv) can be overcome simply by considering the contribution of two or more relevant zeros as can be inferred from Fig. 2. We finally demonstrate that the obtained formula can be extended to inelastic processes.

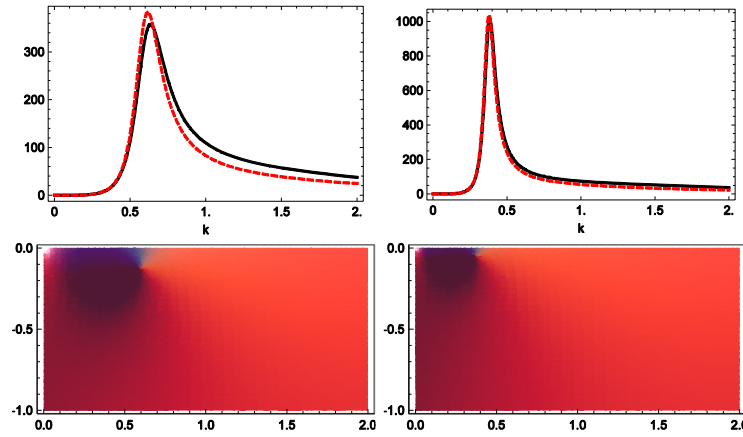


Fig. 1. The Breit-Wigner formula fails to describe the threshold law  $\sigma \propto E^{2L}$ . The single-zero Jost function approximation (red broken line), on the other hand, describes the exact results (black lines) for a spherical well potential. Upper panels:  $p$ -wave cross section in the proximity of a resonance. Lower panels: logarithm of the inverse modulus of the Jost function showing the presence of a resonant zero in the fourth quadrant of the complex  $k$ -plane. On left panels the potential intensity is slightly higher than in the right panels.

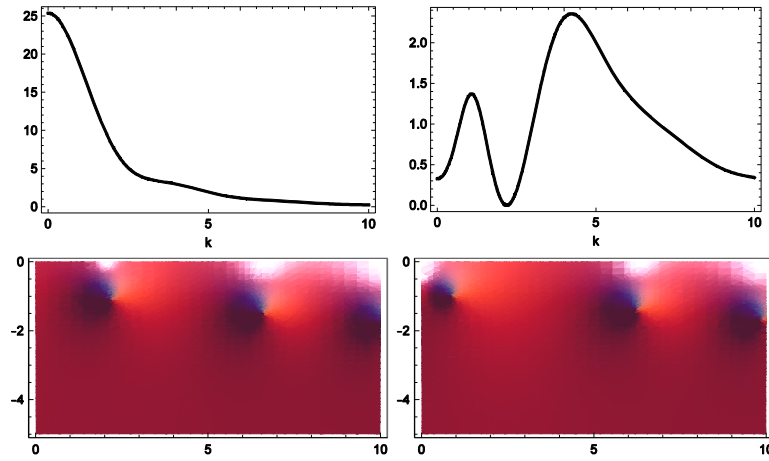


Fig. 2. Upper panels:  $s$ -wave cross section in the proximity of several zeros of the Jost function with small half lives for a spherical well potential. Lower panels: logarithm of the inverse modulus of the Jost function in the fourth quadrant of the complex  $k$ -plane. On left panels the potential intensity is slightly lower than in the right panels.

## 2. References

- [1] J. R. Taylor 1972 *Scattering Theory: The Quantum Theory on Nonrelativistic Collisions* (New York: John Wiley & Sons)
- [2] G. Breit and E. Wigner 1936 *Phys. Rev.* 49 519
- [3] E. P. Wigner 1948 *Phys. Rev.* 73 1002
- [4] R. Jost and A. Pais 1951 *Phys. Rev.* 82 840
- [5] P. A. Macri and R. O. Barrachina 2013 *J. Phys. B* 46 065202
- [6] U. Fano 1961 *Phys. Rev.* 124 1866
- [7] A. O. Lindahl, J. Rohlfen, H. Hultgren, I. Yu. Kiyan, D. J. Pegg, C. W. Walter and D. Hanstorp 2012 *Phys. Rev. Lett.* 108 033004

# ETHYNYL RADIATION PRODUCED BY DISSOCIATION EXCITATION OF ACETYLENE BY ELECTRON IMPACT

Marián Danko<sup>1</sup>, Juraj Országh<sup>1,2</sup>, Peter Čechvala<sup>1</sup>, Štefan Matejčík<sup>1</sup>

<sup>1</sup> Comenius University, Faculty of Mathematics, Physics and Informatics, Bratislava, Slovak Republic

<sup>2</sup> Empa - Swiss Federal Laboratories for Materials Science and Technology, Thun, Switzerland

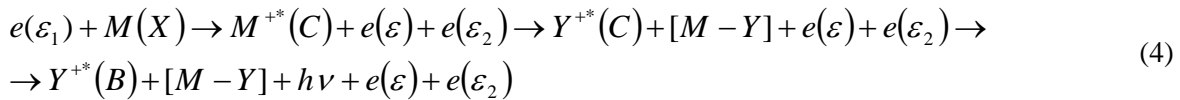
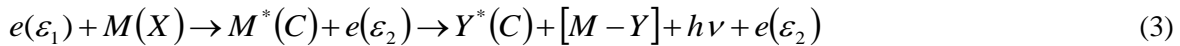
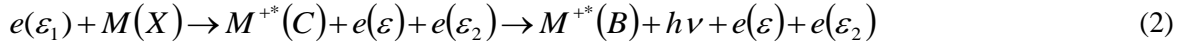
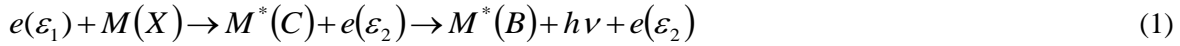
E-mail: stefan.matejcik@fmph.uniba.sk

Electron induced fluorescence of acetylene molecule was studied by a cross beam experimental apparatus. The impact of monoenergetic electrons with 5-100 eV energy led to dissociative excitation processes from which radiation of C<sub>2</sub>H, CH, CH<sup>+</sup>, C<sub>2</sub>, C, and H fragments originated. The focus of this paper was put on C<sub>2</sub>H( $\tilde{A}^2\Pi \rightarrow \tilde{X}^2\Sigma^+$ ) quasi-continuum radiation observed in the spectral region of 400-650 nm. Relative emission function was measured for this transition at 526 nm. Threshold energies were estimated and discussed.

## 1. Introduction

The importance of acetylene molecule C<sub>2</sub>H<sub>2</sub> is significant in a few scientific and technological areas. The knowledge of the molecule is applied in astrophysics, since it is abundant in comets and interstellar clouds [1], and takes part in chemical processes in the atmospheres of gas giants and some of their moons [2]. It is also applied in fusion technology in diagnostics of tokamak divertor erosion [3] and in the development of organic conjugated polymers applicable in the semiconductor technology [4]. Acetylene is a substitute for methane in the CH<sub>4</sub>-H<sub>2</sub> gas mixture used for artificial diamond growth [5].

Our present work deals with the fluorescence radiation of C<sub>2</sub>H, CH, CH<sup>+</sup>, C<sub>2</sub>, C, and H radicals induced by a monoenergetic electrons impact on the acetylene molecules in a cross beam apparatus. The investigated reaction channels are electron induced excitation (1), electron induced ionization and excitation (2), electron induced dissociative excitation (3), and electron induced dissociative ionization and excitation (4):



The interest of this paper is focused on the continuum radiation produced by ethynyl radical C<sub>2</sub>H. The ethynyl radical is an important agent in interstellar molecular clouds participating in chemical reactions leading to the formation of many different carbon-containing species, and also in chemical reactions of outer shells of carbonated stars [1] [6]. It also plays important role in combustion processes of carbohydrates [6]. Even though their importance, electron induced fluorescence processes on both acetylene and ethynyl radical were poorly studied. These can bring new understanding of the energetic structure of the molecules and the chemistry they are involved in.

## 2. Experiment

A cross-beam apparatus was used to perform measurements of spectra and emission functions of acetylene. High vacuum is required for the experiment. The vacuum chamber, where the beams are crossing and the reaction takes place, was pumped down to  $\sim 10^{-8}$  mbar. The ambient pressure in the chamber during the experiment was  $\sim 1.5 \times 10^{-4}$  mbar. Single collision conditions were confirmed according to the linearity of spectral line intensity to pressure dependence (7).

The source of electrons was a tungsten hairpin filament. The electron beam was formed by electron lenses of a trochoidal electron monochromator (TEM) (8). The formed electron beam was energetically analyzed in a dispersion region by applied perpendicular electric field (0-10 V) and

parallel magnetic field ( $5 \times 10^{-3}$  T), both perpendicular to each other. The beam of selected electrons of narrow energy distribution ( $\sim 500$  meV) was focused and accelerated to desired energy by electron lenses into the reaction chamber, where it collided with a beam of acetylene molecules, formed by effusive flow through a capillary ( $d = 0.3$  mm). The electron current (typically  $I \sim 10^2$  nA) was measured on a Faraday cup behind the reaction chamber, where the electron beam headed after passing the reaction region.

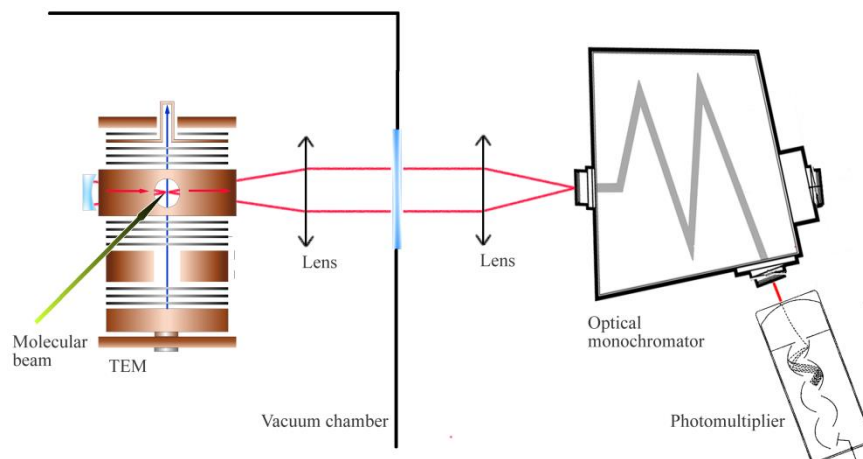


Fig. 1. Cross beam apparatus equipped with a trochoidal electron monochromator (TEM).

The electron induced fluorescence processes that take place in the reaction chamber allow us to study optically forbidden excitations, since an electron is unlike photon capable of exciting molecular states of a different multiplicity. The fluorescence photons emitted in the process of de-excitation of acetylene molecules were gathered by UV grade silica lens and guided through an  $\text{MgF}_2$  window and another UV grade silica lens to the entrance slit of a Czerny-Turner  $\frac{1}{4}$  m optical monochromator (Oriel Cornerstone 260). Some of the dispersed signal was returned to the gathering optics by a spherical mirror with UV enhanced aluminium coating placed opposite to the first lens (see Fig.1). After passing through the optical monochromator, the intensity of the signal at the set wavelength (usually in the order of  $10^0$ - $10^1$  photons per second) was detected by a low-noise (0.5-2 cps), Peltier-cooled R4220P Hamamatsu photomultiplier working in the range of 190-700 nm.

### 3. Results and discussion

To observe the radiation of the ethynyl radical  $\text{C}_2\text{H}$ , fluorescence spectrum was measured in the spectral range of 400-650 nm at the electron energy of 13 eV. At this electron energy only quasi-continuum of  $\text{C}_2\text{H}(\tilde{\text{A}}^2\Pi \rightarrow \tilde{\text{X}}^2\Sigma^+)$  transition has been detected. Boyé (1) and Saito (9) found this continuum to span from 400 nm to IR. Present spectrum is shown in the Figure 2. We compared it with the photolysis measurements of acetylene of Boyé (1), who obtained a few spectra in the photon energy range of 9.94 - 11 eV. The particular energies were selected in such a way that the acetylene molecule was excited into different Rydberg states. These states led to the predissociation of the molecule and to the creation of  $\text{C}_2\text{H}(\tilde{\text{A}}^2\Pi)$  fragment.

We have compared  $\text{C}_2\text{H}(\tilde{\text{A}}^2\Pi \rightarrow \tilde{\text{X}}^2\Sigma^+)$  spectrum induced by impact of electrons with the spectra of Boyé. The comparison shows, that our spectrum is a consequence of dissociation of acetylene from different Rydberg states which intensities are superimposed. The area of 400-460 nm of our spectrum is similar in the shape with the 11 eV spectrum of Boyé, which correspond to the dissociation from  $6d\pi^1\Sigma_u^+ + 6d\sigma^1\Pi_u$  states, close to the ionization threshold. This spectrum has a hump in the area of 430 nm, which can be observed also in our spectrum. From 500 nm to higher wavelengths the intensity starts to drop, which is at variance with present measurement. The area of 510-650 nm of present spectrum is more similar to the Boyé spectra rising from lower lying Rydberg

states  $\tilde{G}(4s\sigma)^1\Pi_u$  and  $\tilde{H}(3d\delta)^1\Pi_u$  (9.94 and 9.98 eV) which above 500 nm continue to rise. These spectra, however, do not contain hump at 430 nm. Thus we conclude that the present electron induced spectrum at 13 eV, is a superposition of radiation originating from acetylene dissociation from different Rydberg states.

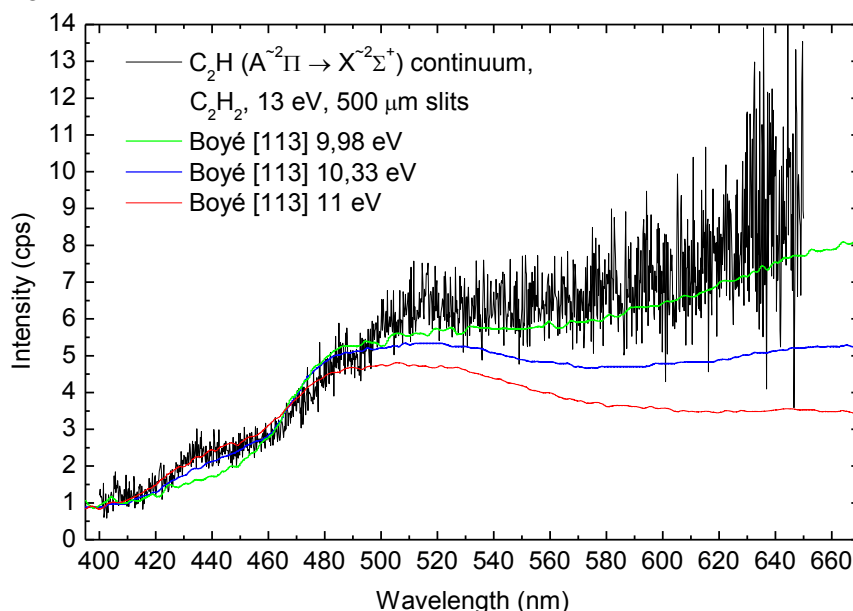


Fig. 2. Fluorescence spectrum in the range 400-650 nm measured at the electron energy 13 eV and optical monochromator slits 500  $\mu\text{m}$ . Only quasi-continuum of  $\text{C}_2\text{H}(\tilde{A}^2\Pi \rightarrow \tilde{X}^2\Sigma^+)$  transition is present. Comparison with Boyé spectra (1).

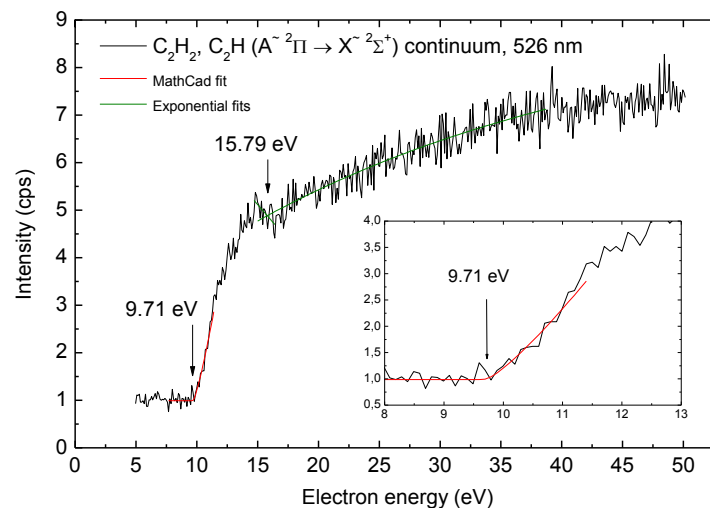


Fig. 3. Relative emission function of the quasi-continuum radiation of the transition  $\text{C}_2\text{H}(\tilde{A}^2\Pi \rightarrow \tilde{X}^2\Sigma^+)$ , measured at 526 nm. Threshold energies were estimated.

Theoretical value of the threshold energy of the dissociative excitation of acetylene molecule to the state  $\text{C}_2\text{H}(\tilde{A}^2\Pi)$  is 5.32 eV. It corresponds to the threshold of radiation of the  $\text{C}_2\text{H}(\tilde{A}^2\Pi \rightarrow \tilde{X}^2\Sigma^+)$  (0,0) vibronic transition at the wavelength 2.7  $\mu\text{m}$ . The dissociation channel  $[\text{e} + \text{C}_2\text{H}_2 = \text{C}_2\text{H} + \text{H} + \text{e}]$  requires 4.86 eV minimum energy and the excitation to  $\tilde{A}^2\Pi$  0.46 eV (10). The radiation of ethynyl radical from  $\tilde{A}^2\Pi$  state spreads far to the visible spectral region though, and its relative emission function which we measured (figure 3) shows its threshold energy to be 9.71 eV. This is caused by a high rotational and vibrational excitation of  $\text{C}_2\text{H}$  fragment, which is caused by  $\text{C}_2\text{H}$



keeping high energy from predissociation processes in Rydberg states of acetylene. Vibrational modes causing bending of the bonds of the ethynyl radical are linked to the wide maximum of the fluorescence radiation in the area of 500 nm, while stretching modes form quasi-continuum which spreads to the IR range. The continuum characteristic of the radiation is caused by a high concentration of rovibronic transitions from  $\tilde{A}^2\Pi$  state. (1)

The threshold energy of 15.79 eV corresponds to an unknown radiative transition, which is superimposed at 526 nm on the intensity of the quasi-continuum. It can be attributed to one of the C<sub>2</sub> systems, since these possess similar values of threshold energies.

#### 4. Acknowledgments

We would like to express gratitude for the support of our research to the following projects: VEGA 1/0514/12 and by the Slovak Research and Development Agency, project Nr. APVV-0733-11.

#### 5. References

- [1] Boyé S, Campos A, Douin S, Fellows C, Gauyacq D, Shafizadeh N, Halvick P and Boggio-Pasqua M 2002 *Journal of Chemical Physics* **116** 8843.
- [2] Pang K D, Ajello J M, Franklin B and Shemansky D E 1987 *Journal of Chemical Physics* **86** 2750.
- [3] Fantz U, Meir S, ASDEX Upgrade Team 2005 *Journal of Nuclear Materials* **337-339** 1087.
- [4] Lischka H, Karpfen A 1986 *Chemical Physics* **102** 77.
- [5] Smith J A, Cameron E, Ashfold M N R, Mankelevich Y A and Suetin N V 2001 *Diamond and Related Materials* **10** 358.
- [6] Somé E, Remy F, Macau-Hercot D, Dubois I, Breton J and Bredohl H 1995 *Journal of Molecular Spectroscopy* **173** 44.
- [7] Filippelli A R, Lin C C, Anderson L W and McConkey J W 1994 *Advances in Atomic, Molecular, and Optical Physics* **33** 1.
- [8] Matúška J, Kubala D and Matejčík Š 2009 *Meas. Sci. Technol.* **20** 015901.
- [9] Saito Y, Hikida T, Ichimura T and Mori Y 1984 *The Journal of Chemical Physics* **80** 31.
- [10] NIST Chemistry Webbook, NIST Standard Reference Database 69 (<http://webbook.nist.gov/chemistry/>).

# PROJECTILE CHARGE EFFECTS IN DIFFERENTIAL IONIZATION OF MOLECULAR NITROGEN BY POSITRONS AND ELECTRONS

O. G. de Lucio<sup>1</sup>, R. D. DuBois<sup>2</sup>

<sup>1</sup>*Instituto de Física, Universidad Nacional Autónoma de México,  
Apartado Postal 20-364, México DF, México*

<sup>2</sup>*Department of Physics, Missouri University of Science and Technology,  
Rolla, MO 65409, USA*

E-mail: dododrillo@yahoo.com

Differential information is presented for 250 eV positron and electron impact ionization of molecular nitrogen. By establishing coincidences between target ions and scattered projectiles (or ejected electrons), and coincidences between target ions, scattered projectiles and ejected electrons; singly, doubly or triply differential information can be generated in terms of projectile energy loss and scattering angles. A comparison between positron and electron impact will be presented in this work.

## 1. Introduction

Over the last decades ionization by electron impact has been exhaustively studied, with special attention on describing inelastic interactions. Most of these studies have focused on measurements of ionization probabilities or attempts to describe the kinematics involved during and after the collision process. More recently, ionization by anti-particle impact has been a trending subject for theoretical and experimental physicists. For positrons, experimental studies commonly use noble gas atoms as target [1], where individual interactions between the involved particles can be easily described. Main goals of such experiments are to provide accurate information on how similar or different are the particle-matter and antiparticle-matter interactions; isolating certain processes, in order to provide a sensitive test of theoretical models. Importance of such experiments arise from the fact that while earlier first-order perturbation theories employed to describe such interactions predicted identical total and differential cross sections for high-energy particle and antiparticle impact, recently more sophisticated approximations exhibit the existence of differences in the differential electron emission measured as a function of the momentum transfer [2,3,4]. Also, as a result of these approximations for binary electron emission (which are interactions where the other bound electrons and target nucleus act as spectators) is expected an enhancement (decrement) for positron (electron) impact; while for the recoil intensity (corresponding to interactions where the ejected electron also interacts with the target nucleus as it leaves) they anticipate opposite effects. As a result of such predictions it is also expected the existence of a dependence on the sign of the charge, and that directions of the binary and recoil lobes will shift with respect to the momentum transfer direction [5]. It is possible to even go further in describing ionization mechanisms and consider higher order ionization processes. Despite the fact that single ionization dominates, it has been possible to experimentally demonstrate that multiple ionization contribution can be of significance to the total ionization cross section, as well as to energy and momentum transferred in the collision [6,7,8]. For instance, if we consider the deposited energy, it is evident the importance of multiple ionization because of the increased binding energies associated with each electron removal. Therefore, accurate ionization theories must also account for multiple electron removal processes specially when heavier atoms or molecules are involved.

## 2. Experimental Method

A simple gas jet of molecular Nitrogen is ionized by a beam of positrons (electrons) in order to measure coincidences between the various ionization products. The beam and the target overlap at the center of two biased plates used to produce a weak electric field (1.2 V/cm) perpendicular to the beam

direction. Using a single apparatus for these studies and establishing as identical conditions as possible, allows for experimental uncertainties between the positron and electron impact data to be minimized.

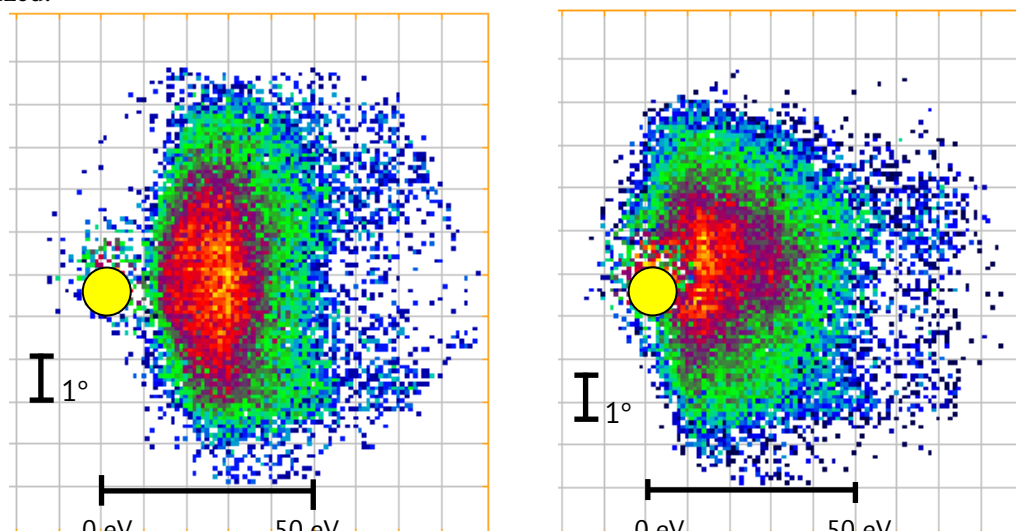


Fig. 1. DDCCS data for single ionization of molecular nitrogen by 250 eV positron (left) and electron (right) impact. Vertical and horizontal axes correspond to projectile scattering angle (degrees) and energy loss (eV). The yellow circle corresponds to the non-scattered beam position (0 degrees scattering angle and 0 eV energy loss)

The positron beam was produced using a  $^{22}\text{Na}$  source, a tungsten moderator, and an electrostatic transport system. Electron beam is generated by an electron gun inserted into the positron beamline, in such a way, that the electron beam entered the scattering chamber via the same input aperture and trajectory used for positron impact. Target ions were extracted by the weak electric field and recorded by a channeltron, which is placed below the interaction region. Time of flight techniques established their charge states and masses, providing also information on molecular fragmentation. Scattered projectiles were measured as a function of their scattering angle and energy loss by using an electrostatic energy analyzer and a position sensitive channelplate. Electrons ejected from the target were measured as a function of their detection angle using a second position sensitive channelplate positioned above to the interaction region and at  $90^\circ$  with respect to the beam direction. List mode data collection allowed correlations between the various particles, angles, and energies to be established. Coincidences between singly ionized target atoms (or molecules) and scattered projectiles provided doubly differential cross section (DDCS) information as a function of scattering angle and energy loss. While coincidences between target ions, scattered projectiles, and ejected electrons provided triply differential cross section (TDCS) information, which could be generated either for the scattered projectile or for the ejected electron. Examples of DDCCS data for 250 eV positron and electron impact on molecular nitrogen are shown in Fig. 1. Where the vertical axis is the projectile scattering angle, in degrees; and the horizontal axis is the energy loss in eV. Negative scattering angles imply that the projectile is scattered vertically downwards while positive angles imply upward scattering. Since the electron detector is located above the interaction region, only “upward” emitted electrons are detected. Thus, the TDCS intensities for negative scattering angles, e.g., correlated downward scattered projectiles and upward emitted target electrons, are a direct indication of binary events since the scattered projectile and ejected electron are detected in opposite hemispheres. Likewise the intensities for positive scattering angles indicate recoil events because both particles are detected in the same hemisphere. Forward scattered projectiles were limited to a horizontal scattering range of  $0^\circ \pm 2.4^\circ$  by a slit at the entrance to the energy analyzer and to vertical scattering angles less than  $\pm 6^\circ$  because of the projectile channelplate size and distance from the interaction region. The energy loss ranges could be set by adjusting the spectrometer voltages. The ejected electron channelplate was sensitive to geometric emission angles between  $30^\circ$  and  $150^\circ$  along and perpendicular to the beam direction. No energy analysis of the ejected electrons is performed by the apparatus. However, their energies can be

determined by using coincidences with projectiles that suffered a particular energy loss, which for single ionization unequivocally defines the ejected electron energy. Additional experimental details can be found in references [9-11].

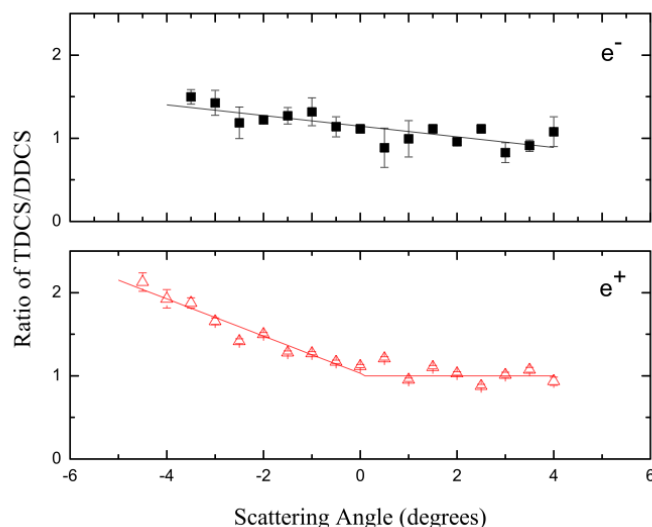


Fig. 2. Ratios of triply to doubly differential cross sections for electron (up) and positron (down) impact single ionization of molecular nitrogen. The solid lines are linear fits to the data.

### 3. Results

Doubly and triply differential information were generated from experimental data such as the shown in figure 1, for scattering angles between  $-5^\circ$  and  $+5^\circ$  and for an energy loss ranging from 18.1 eV to 29.9 eV; in order to reduce the statistical uncertainties, data within this range was added. Identical conditions were used for positron and electron impact. Ratios of triply to doubly differential cross sections were then calculated from the integrated intensities. Using ratios removes any problems or artifacts associated with electric field effects on the ejected electron trajectories as well as any contribution from solid angle effects, since the influence of such parameters is the same for both the doubly and triply differential data. It also removes any experimental asymmetries between positive and negative scattering angles since by definition the DDCS must be symmetric with respect to zero degrees. In Figure 2, we present an example of these ratios. The general trend for different energy losses (not presented here) is similar to the one shown in this figure. For positron impact, in all cases ratios are nearly isotropic for positive scattering angles and present a monotonic increase for increasing negative scattering angles. It is worth mentioning again that negative scattering angles indicate binary interactions while positive angles indicate recoil interactions. Thus, the data show that the relative number of binary to recoil interactions increases as a function of scattering angle, i.e., as a function of increasing momentum transfer. Previous studies indicate that this is independent of target species and also of impact energy [12]. For electron impact, ratios appear to form a simple straight line, increasing for increasing negative angles, but decreasing for positive scattering angles. The amplitude of these ratios is also minor than that of positron impact.

Since the experimental device allows us to distinguish both charge state and mass, it was also possible to study how the fragmentation processes take place. For this work we calculated the ratios of the recorded  $N^+$  to  $N_2^+$  as a function of the energy loss, which are presented in figure 3. Both projectiles exhibit a similar tendency, but electron impact information presents a larger amplitude and a faster growth for the smaller energy losses. This experimental data indicates that fragmentation of the  $N_2$  molecule is more probable for electron impact than for positron impact, while molecular ionization is more likely to occur for positrons.

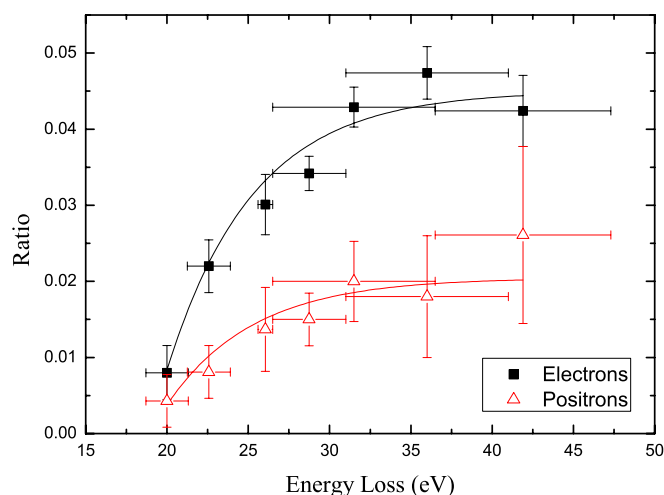


Fig. 2. Ratios of  $N^+$  to  $N_2^+$  for electron (black solid squares) and positron (red hollow triangles) impact and ionization of  $N_2$ . Solid curves are exponential fits of the data.

#### 4. Summary

Doubly and triply differential data for single ionization of molecular nitrogen have been measured for positron and electron impact. By comparing the data for each projectile it can be seen that differences associated with the sign of the charge appear; worth of mention is the enhancement of the binary interactions for positrons, which is consistent with theoretical predictions. Theory also predicts that the opposite effect should be observed for the recoil lobe intensities, experimental results show that the amplitude of such interactions decrease for positrons, but also indicates no angular dependence for such projectile, at least for the studied range. Information regarding the ionization/fragmentation of the  $N_2$  molecule was also presented, and shows differences for each projectile as well.

ACKNOWLEDGEMENTS: Work supported partially by UNAM-PAPIIT under contract No. TA100213, and by National Science Foundation.

#### 5. References

- [1] G. Laricchia et al., *J. Phys. Conf. Ser.* **194** (2009) 012 036.
- [2] S. Sharma and M. K. Srivastava, *Phys. Rev. A* **38** (1988) 1083.
- [3] M. Brauner and J. S. Briggs, *J. Phys. B* **26** (1993) 2451.
- [4] J. Berakdar, J. S. Briggs, and H. Klar, *J. Phys. B* **26** (1993) 285.
- [5] Á. Benedek and R. I. Campeanu, *Nucl. Instrum. Methods Phys. Res., Sect. B* **266** (2008) 458.
- [6] R.D. DuBois, L.H. Toburen, and M.E. Rudd, *Phys. Rev. A* **29** (1984) 70.
- [7] R.D. DuBois, *Phys. Rev. A* **39** (1989) 70.
- [8] F. Frémont, C. Leclercq, A. Hajaji, A. Naja, P. Lemennais, S. Boulbain, V. Broquin, and J.-Y. Chesnel, *Phys. Rev. A* **72** (2005) 042702.
- [9] O. G. de Lucio, S. Otranto, R. E. Olson, and R. D. DuBois, *Phys. Rev. Lett.* **104** (2010) 163201.
- [10] O. G. de Lucio, J. Gavin, and R. D. DuBois, *Phys. Rev. Lett.* **97** (2006) 243201.
- [11] R. D. DuBois, O. G. de Lucio, and A. C. F. Santos, *Radiation Physics Research Progress*, edited by A. N. Camilleri (Nova, New York, 2008).
- [12] R. D. DuBois, *J. Phys. Conf. Series* **288** (2011) 012011

# ON ELECTRON EXCITATION OF SOME QUASIMETASTABLE STATES OF POTASSIUM ATOM

Hennadiy Bohachov

*Institute of Electron Physics, Uzhgorod, Ukraine*

E-mail: bogach.gen@gmail.com

Thorough investigation of the excitation functions for the potassium spectral lines originating from the quasimetastable levels of the  $3p^5 4s 3d$  and  $3p^5 4s 4p$  configurations revealed new features in the near threshold region of electron energies. Analysis shows that these features have a resonance origin and can be attributed to the high-energy states of the potassium temporary negative ions.

Here we present on the results of new studies on the VUV spectrum in the 40–120 nm region excited in the electron-potassium atom collisions. This region includes a few spectral lines resulted from the radiative decay of the quasimetastable autoionizing states ( $KI^{**}$ ) to the common  $KI$  states [1]. Figure 1 demonstrates the spectra recorded at the electron energies 22, 27 and 200 eV. The data for all noticeable lines in the spectral region under study are generalized in Table 1. It is evident from the figure and the table that these lines related to the  $KI^{**}$  states dominate at low electron energies whereas at 200 eV they are almost imperceptible against a background of the  $K^+$  ion resonance lines. Except of the  $K^+$  ion resonance lines, excitation of the double-charged potassium ion resonance doublet at 76.6 and 77.8 nm is well noticeable in the spectrum at 200 eV. Note that an attempt to identify a group of lines above 90 nm was unsuccessful, while these lines below 60 nm belong to the KII spectrum as referred to the data [1].

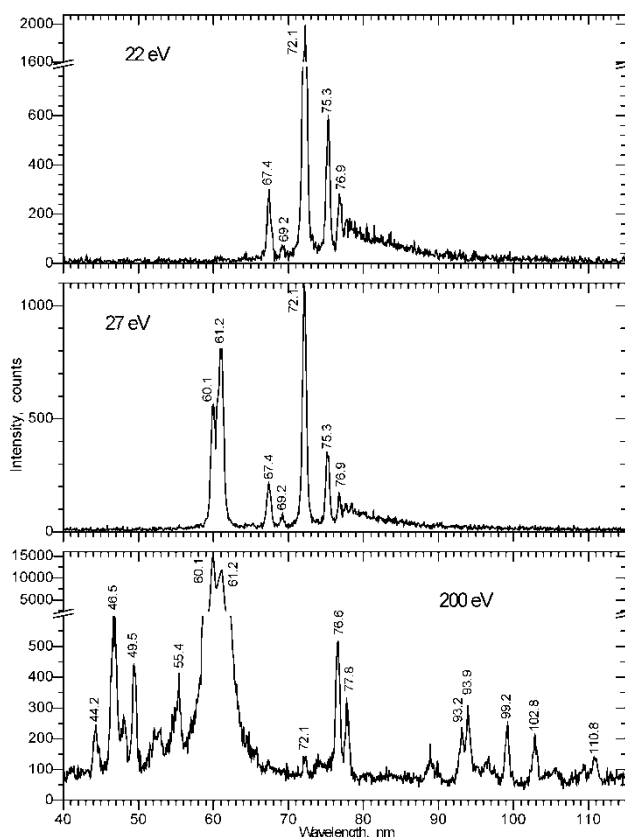


Fig. 1. VUV emission spectra of potassium

As is well known, a decrease of the incident electron energy spread results in revelation of the new features in the excitation function (EF) obtained. Therefore we have measured the EFs for the spectral lines originating from the quasimetastable levels when an electron gun was tuned to operate

with the least possible electron energy spread. But here one has to take into account that such electron gun tuning results in the decrease of its working current. As a result, a useful signal storage time increases.

Table 1. Spectroscopic data on the VUV potassium lines observed

$\lambda$ , nm	$E_{\text{exc.}}$ , eV	Transition	$I_{22}$ , arb. un.	$I_{200}$ , arb. un.
44.2	?	K II (?)	–	240
46.5	31.0	K II $3p^6\ ^1S_0 - 3p^5(^2P_{1/2}^o)5s$ $1/2[1/2]0$	–	610
49.5	29.38	K II $3p^6\ ^1S_0 - 3p^53d\ ^1P^o_1$	–	430
55.4	26.71	K II $3p^6\ ^1S_0 - 3p^53d\ ^3D^o_1$	–	410
60.1	24.98	K II $3p^6\ ^1S_0 - 3p^54s\ ^1P^o_1$	–	15200
61.2	24.58	K II $3p^6\ ^1S_0 - 3p^54s\ ^3P^o_1$	–	11600
67.4	20.01	K I** $3p^64p\ ^2P^o_{1/2, 3/2} - 3p^54s4p\ ^4S_{3/2}$	300	–
69.2	20.59	K I** $3p^63d\ ^2D - 3p^53d4s\ ^4F^o_{3/2}$	80	–
72.1	19.87	K I** $3p^63d\ ^2D - 3p^53d4s\ ^4P^o_{5/2}$	1990	140
75.3	19.87	K I** $3p^64d\ ^2D - 3p^53d4s\ ^4P^o_{5/2}$	600	–
76.9	19.87	K I** $3p^65d\ ^2D - 3p^53d4s\ ^4P^o_{5/2}$	280	–
76.6	51.16	$^2G$ K III $3s^23p^5\ ^2P^o_{3/2} - 3s3p^6$	–	510
77.8	51.16	$^2G$ K III $3s^23p^5\ ^2P^o_{1/2} - 3s3p^6$	–	330
93.2	??	K III (?)	–	240
93.9	??	K III (?)	–	310
99.2	??	K III (?)	–	250
102.8	??	K III (?)	–	220
110.8	??	K III (?)	–	140

We have measured thoroughly the EFs for the two strongest KI\*\* lines – 72.1 and 67.4 nm (see Fig. 2). The electron energy range in our measurements was varied from the threshold up to 25 eV, the energy step was 33 meV. The electron energy spread (FWHM) measured by a retarded-potential method appeared to be close to 0.4 eV.

In Fig. 2 showing also the data of the previous measurements of the Efs for these lines [2, 3], the result is clearly seen being obtained with an enhanced electron energy resolution. Note that the first EFs studies for the 72.1 nm line [2] (curve 3 in Fig. 2) revealed no specific features. It is natural because the above measurements have been carried out using a low energy resolution electron beam (FWHM~1.5 eV). Later on [3], the EFs for the 72.1 and 67.4 nm lines with an enhanced incident electron resolution (FWHM~1.2 eV) were obtained showing slight features in a form of bends and shoulders (curves 2, 5 in Fig. 2). New features have been revealed in our EFs for the both above lines (see curves 1, 4 in Fig. 2). For instance, the curve for 72.1 nm shows a sharp maximum just near the excitation threshold, while at higher energies at least three extra features were revealed – at 21.3, 21.7 and 22.9 eV. Obviously, these features correlate with the bends and shoulders found in the EF for this line in [3].

The near-threshold peak in the 67.4 nm line curve with a width of about 1 eV correlates also with that found in [3], however, the latter appeared to be significantly broader, i.e. up to 1.5 eV. In addition, several features have also been revealed at 21.8 and 23.9 eV.

The near-threshold maximum half-width in the 72.1 nm line EF is about 0.5 eV. Therefore, one may assume that the electron energy spread in the beam does not exceed this value. Furthermore, in some cases of the electron gun tuning for measuring this maximum only, we succeeded to record it with substantially less width, i.e. up to 0.3 eV. Thus, we may conclude that this maximum reflects unambiguously the electron beam energy spread and can serve as its measure.

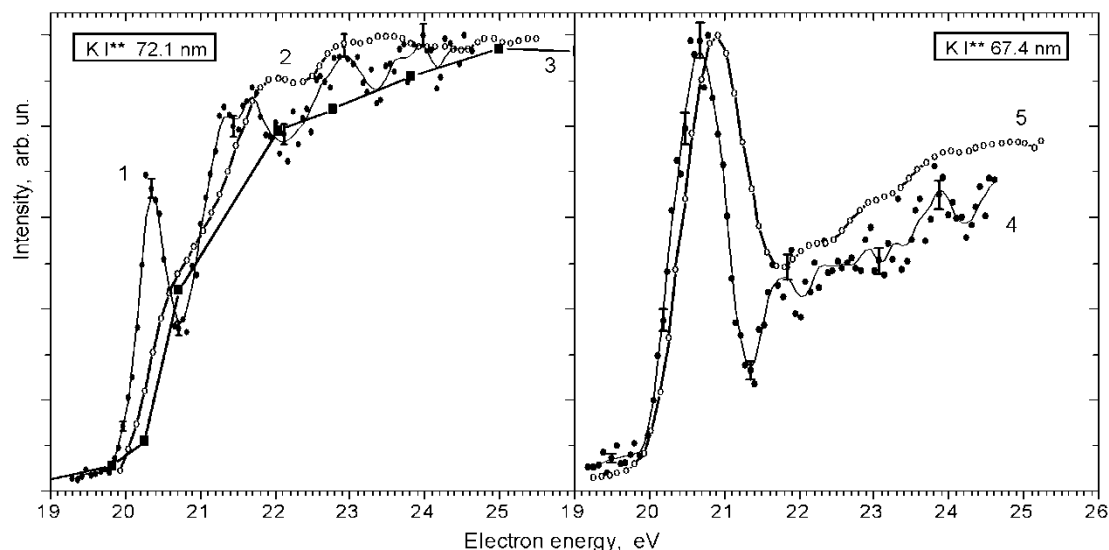


Fig. 2. Excitation functions for the KI\*\* spectral lines

1, 4 – present results, 2, 5 – data from [3], 3 – data from [2]

Since the near-threshold peak width for the 67.4 nm line is much larger than 0.5 eV, it seems that this peak may contain several closely located narrow maxima (resonances). This assumption is confirmed by the results of [4]. In this paper, using the electron spectroscopy method, the EF for the quasimetastable level initial for the 67.4 nm line was measured in the energy range 3 eV above the threshold with the energy resolution of 0.25 eV. It has been found that this EF is generally similar to that obtained by us, whereas the near-threshold peak is indeed a sum of several strong resonances. They are well described by the theoretical calculation performed using a complex R-matrix-based model. Note that this calculation also provides the branching value for the decay of the quasi-metastable  $3p^5 4s 4p^4 S_{3/2}$ -state in both the electron and optical channels being equal to 0.16:0.69.

## References

- [1] Sansonetti J E 2008 *J. Phys. Chem. Ref. Data* **37** 7.
- [2] Aleksakhin I S, Bogachev G G, Zapesochnyi I P, and Ugrin S Yu 1981 *Sov. Phys. JETP* **53** 1140.
- [3] Bogachev G G, Aleksakhin I S 1996 *Ukrainian Journal of Physics* **41** 530 (in Ukrainian).
- [4] Borovik A A, Jr., Borovik A A, Zatsarinny O, and Bartschat K 2006 *Phys. Rev. A* **73** 062701.



# THEORETICAL INVESTIGATIONS ON THE PROJECTILE COHERENCE EFFECTS IN FULLY DIFFERENTIAL IONIZATION CROSS SECTIONS

Ferenc J rai-Szab <sup>1</sup>, Ladislau Nagy<sup>1</sup>

<sup>1</sup>*Faculty of Physics, Babeş-Bolyai University, Kogalniceanu str. 1, 400084 - Cluj-Napoca, Romania*  
E-mail: ferenc.jarai@phys.ubbcluj.ro

Fully differential single ionization cross section calculations for helium produced by fast charged projectiles are performed in the framework of the semiclassical approximation. Projectile coherence effects are investigated through fully differential electron emission cross section ratios resulting from coherent and incoherent calculations based on the same ionization amplitudes. The obtained results are compared to the experimental data. By these calculations we confirm that projectile coherence effects may have important role in ionization processes.

## 1. Introduction

Fully differential ionization cross sections (FDCS) give us the most complete information about an ionization process. After the development of the reaction microscopes [1] a great interest has been focused on measuring and calculating this quantity for different ionization processes. Regarding this topic, one of the most discussed processes is the ionization of helium by fast charged projectiles [2-6]. Despite of the existence of many theoretical descriptions, significant discrepancies between measured and calculated FDCS values have been reported. It was thought that partly the projectile-target nucleus scattering [5] and partly the experimental uncertainties [7] are responsible for these discrepancies.

In the last few years, qualitative differences in case of ionization of helium by fast charged projectiles depending on the projectile beam coherence have been reported [8]. FDCS for ionization of He by 3 MeV proton impact have been measured, with projectile beam of a coherence length larger than typical atomic scales. Compared to the incoherent 100 MeV/u C<sup>6+</sup> projectile beam pronounced effects have been observed.

In the present work we investigate theoretically the effect of the projectile beam coherence on the single ionization process by calculating FDCS with a quantum mechanical and an impact parameter approximation. In both cases the calculations are based on the same ionization amplitudes obtained in the framework of the semiclassical approximation.

## 2. Theory

The semiclassical model for ionization of helium by fast charged projectiles [5] treats the projectile separately and only the electron system is described by a time-dependent Schr dinger equation. Then, the ionization probability amplitudes are calculated using first order time dependent perturbation theory. In these calculations the initial state of the two-electron system is described by a Hartree-Fock wavefunction. The final state is described by a symmetric combination of a hydrogen-type and a continuum radial wavefunction, which is calculated in the mean field of the final He<sup>+</sup> ion.

By the use of this semiclassical approximation the transition amplitude  $A(\vec{b})$  is calculated. Then, two possibilities arise to calculate FDCS.

On one hand, as used in case of the impact parameter approach [5], by classical scattering theory and transverse momentum balance [1] impact parameter values  $b$  to a certain momentum transfer  $q$  are assigned. Then, the FDCS are calculated at these impact parameter values. By this method each projectile particle is treated separately, no coherence exists between ionization processes caused by different projectiles.

On the other hand, using the quantum scattering theory, the scattering matrix element is calculated by the inverse Fourier transform

$$R(\vec{q}_\perp) = \frac{1}{2\pi} \int d\vec{b} e^{i\vec{b}\vec{q}_\perp} A(\vec{b}). \quad (1)$$

The FDCSs are then obtained as the square of modulo of the scattering matrix element

$$\frac{d^4\sigma}{dE_e d\Omega_e d\vec{q}_\perp} = k |R(\vec{q}_\perp)|^2, \quad (2)$$

where  $k$  is the projectile momentum. By these calculations the projectile beam coherence is taken into account. Consequently, interference may occur between the ionization by different projectiles.

By calculating coherent and incoherent projectile FDCS ratios for single ionization of He by fast charged projectile impact, the differences between the two approaches can be highlighted.

### 3. Results

In the top panel of the Figure 1 we present calculated FDCS values by both the coherent and incoherent theories in comparison with the experimental data obtained for the coherent 3 MeV p and the incoherent 100MeV/u C<sup>6+</sup> projectile beams [8]. Here only the results for the azimuthal plane will be considered. As it can be observed, there is a significant difference between the coherent and incoherent calculations. Here we have to note, that the results for the coherent beam may be improved by calculating the integral over the impact parameter in (1) more precisely by using larger integration domains.

The ratios of the coherent and incoherent FDCS, presented in the bottom panel of Figure 1 represent the interference effects due to projectile coherence. Here, in qualitative agreement with the experimental data, an oscillation pattern is observed which supports the explanation that FDCS for the coherent calculations are affected significantly by interference effects [8].

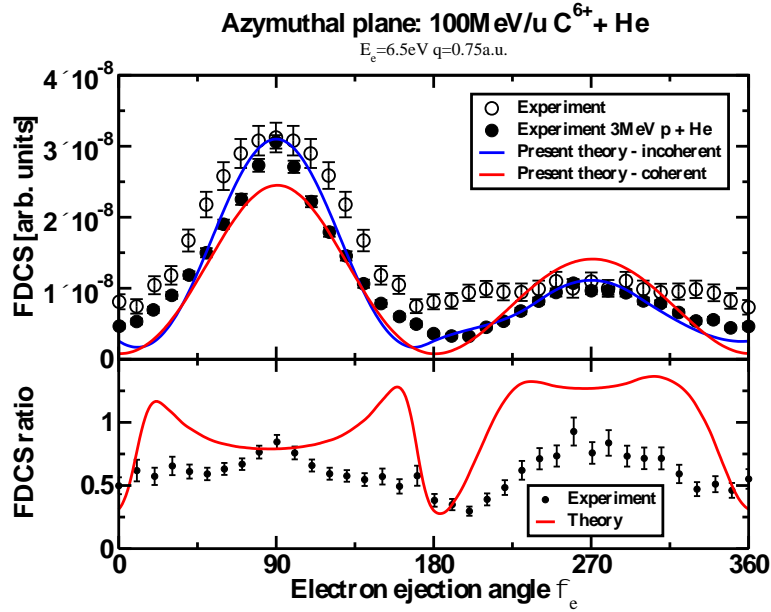


Fig. 1. Calculated coherent and incoherent FDCS values compared to experimental data (top) and the comparison of the coherent and incoherent FDCS ratios (bottom).

### 4. Conclusions

In conclusion, we investigated theoretically the effect of the projectile beam coherence on the single ionization process by calculating coherent and incoherent ionization FDCSs in the framework of the same semiclassical approximation. According to the presented results, the experimentally funded assumption, that interference effects significantly influence FDCS for coherent projectile beams, are qualitatively supported by our semiclassical theory.

### 5. Acknowledgement

This work was supported by a grant of the Romanian CNCS UEFISCDI, project number PN-II-ID-PCE-2011-3-0192

## 6. References

- [1] Ullrich J et al. 1997 *J. Phys. B: At. Mol. Opt. Phys.* **30** 2917.
- [2] Schulz M et al. 2003 *Nature* **422** 48.
- [3] Dürre M et al. 2008 *Phys. Rev. A* **77** 032717.
- [4] Madison D H et al 2003 *Phys. Rev. Lett.* **91** 253201.
- [5] Járαι-Szabó F and Nagy L 2007 *J. Phys. B: At. Mol. Opt. Phys.* **40** 4259.
- [6] Dey R and Roy A C 2009 *Nucl. Instr. Methods B* **267**, 2357.
- [7] Fiol J, Otrantoand S, Olson R E 2006 *J. Phys. B: At. Mol. Opt. Phys.* **39** L285.
- [8] Wang X et al. 2012 *J. Phys. B: At. Mol. Opt. Phys.* **45** 211001.

# THE LIGAND DISSOCIATIONS FROM MPS, DMPS AND TMPS MOLECULES BY ELECTRON IMPACT

Michal Lacko<sup>1</sup>, Amer Al Mahmoud Alsheikh<sup>2</sup>, Peter Papp<sup>1</sup>, Štefan Matejčík<sup>1</sup>

<sup>1</sup>Comenius University, Faculty of Mathematics, Physics and Informatics, Bratislava, Slovakia

<sup>2</sup>Brno University of Technology, Faculty of Chemistry, Brno, Czech Republic

E-mail: lacko16@uniba.sk

Methylphenyl Silane (MPS) and Trimethylphenyl Silane (TMPS) molecules were studied using a crossed electron/molecular beams experiment. The ionization energies as well as the appearance energies with a focus on a dissociation of methyl and phenyl ligands were estimated. Considering the previous results of Dimethylphenyl Silane (DMPS) electron induced dissociation; the effect of substitution of methyl and hydrogen ligands will be discussed.

## 1. Introduction

The description of electron – molecular interaction in the gas phase gives insight in the structure and thermochemistry of molecules. The fragmentation patterns are important in description of some chemical reactions in plasma applications, as well as for development of new precursors. Organo - silicon molecules are in present time used in Plasma Enhanced Chemical Vapour Deposition (PECVD) application [1,2] as precursors for preparation of thin films. In future these molecules could be used also in nanotechnological application such as Focused Electron Beam Induced Deposition (FEBID).

In present work Methylphenyl silane (MPS) and Trimethylphenyl silane (TMPS) molecules were studied. Experimental investigation of electron ionization and dissociative ionization of these molecules were carried out with main focus on ligand - lost reaction. The comparison of electron ionization (EI) and dissociative ionization (DI) reactions of MPS and TMPS with Dimethylphenyl silane (DMPS) [3] can help to determine the effects of methyl group on dissociation patterns in MPS and TMPS.

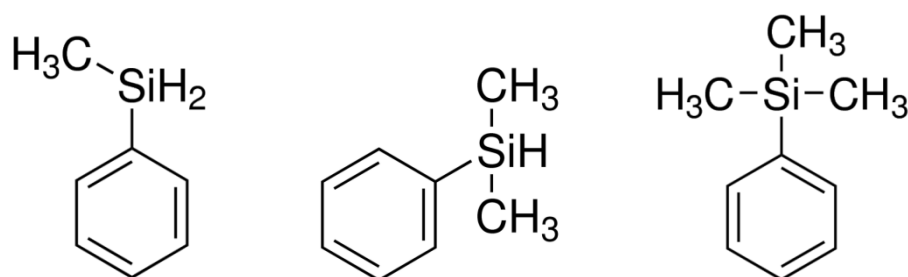


Fig. 1. The schematic representation of MPS (left), DMPS (centre) and TMPS (right) molecules.[4]

## 2. Experiment

The experimental study of the electron induced processes on MPS and TMPS was performed using crossed electron and molecular beam apparatus, located at Department of Experimental Physics of Comenius University in Bratislava [5]. The molecular beam is created by effusion of the vapours of the liquid MPS/TMPS sample via a small capillary into the reaction region. There it collides with the electron beam, which has perpendicular orientation to the molecular beam. The electron beam is formed using a trochoidal electron monochromator, with the resolution of electron energy used in this study of around 300 meV. The calibration of the electron energy scale was made for EI using Ar<sup>+</sup>/Ar reaction with threshold at 15.76 eV [6]. A weak electric field extracts the produced ions from the reaction region into the ion optics of the quadrupole mass analyzer. The mass separated ions (according to m/z) are detected with the electron multiplier.

Two different modes of operation of the experiment were applied, the first one, the mass spectrum was recorded at constant electron energy ~70 eV. In the second mode, we have measured the ion efficiency curves for particular ions (for given m/z) as function of the incident electron energy.

The experimental thresholds for EI and DI processes have been evaluated, which is an important information about the energetics of reaction. The thresholds were evaluated using a fitting procedure based on generalized Wannier law [7] with the following function:

$$S(\varepsilon) = b ; \varepsilon < AE$$

$$S(\varepsilon) = b + a(\varepsilon - AE)^d ; \varepsilon > AE$$

where  $\varepsilon$  represents electron energy and  $b, a, d$  are variable fitting parameters.

### 3. Results and discussion

The ionization energies (IE) of MPS and TMPS were estimated as 9.33 eV and 8.97 eV. From the comparison of these values and the ionization energy of DMPS molecule (9.04 eV [3]) a decrease of IE is observed with increasing number of methyl ligands. However, according to the known data the IE of phenyl silane (PS) (9.09 eV [8]; 9.25 eV [9]; 9.1 eV[10]) does not fit in this tendency. The appearance energies (AE) of measured ions for both molecules are collected in table 1.

Tab. 1. The AE of MPS (left) and TMPS (right) products.

m/z	ion	AE (eV)
122	MPS <sup>+</sup>	9.33 ± 0.25
121	(MPS-H) <sup>+</sup>	10.56 ± 0.25
120	(MPS-2H) <sup>+</sup>	10.65 ± 0.25
107	(MPS-CH <sub>3</sub> ) <sup>+</sup>	11.34 ± 0.25
105	C <sub>6</sub> H <sub>5</sub> Si <sup>+</sup>	12.27 ± 0.50
78	C <sub>6</sub> H <sub>6</sub> <sup>+</sup>	9.46 ± 0.25
69	SiC <sub>3</sub> H <sub>5</sub> <sup>+</sup>	18 ± 0.50
59	SiC <sub>2</sub> H <sub>7</sub> <sup>+</sup>	11.31 ± 0.50
45	SiH <sub>2</sub> CH <sub>3</sub> <sup>+</sup>	11.76 ± 0.50
44	SiHCH <sub>3</sub> <sup>+</sup>	11.28 ± 0.25
43	SiCH <sub>3</sub> <sup>+</sup>	11.7 ± 0.50

m/z	ion	AE (eV)
150	TMPS <sup>+</sup>	8.97 ± 0.25
135	(TMPS-CH <sub>3</sub> ) <sup>+</sup>	9.76 ± 0.25
121	C <sub>6</sub> H <sub>5</sub> SiHCH <sub>3</sub> <sup>+</sup>	14 ± 1
119	C <sub>6</sub> H <sub>5</sub> SiCH <sub>2</sub> <sup>+</sup>	15.94 ± 0.5
107	C <sub>6</sub> H <sub>5</sub> SiH <sub>2</sub> <sup>+</sup>	14.54 ± 0.25
105	C <sub>6</sub> H <sub>5</sub> Si <sup>+</sup>	16.93 ± 0.5
93	SiC <sub>3</sub> H <sub>5</sub> <sup>+</sup>	17.27 ± 0.5
91	SiC <sub>3</sub> H <sub>3</sub> <sup>+</sup>	15.44 ± 0.5
77	C <sub>6</sub> H <sub>5</sub> <sup>+</sup>	12.5 ± 0.5
74	HSi(CH <sub>3</sub> ) <sub>3</sub> <sup>+</sup>	10.69 ± 0.5
73	Si(CH <sub>3</sub> ) <sub>3</sub> <sup>+</sup>	11.29 ± 0.5
67.5	(TMPS-CH <sub>3</sub> ) <sup>2+</sup>	23.79 ± 0.5
59	SiC <sub>2</sub> H <sub>7</sub> <sup>+</sup>	11.13 ± 0.5
53	SiC <sub>2</sub> H <sup>+</sup>	20.09 ± 1
43	SiCH <sub>3</sub> <sup>+</sup>	11.5 ± 0.5

The mass spectrum of MPS (fig. 2) shows typical patterns with dissociation of H and 2H atoms or H<sub>2</sub> from MPS<sup>+</sup>, represented by two peaks at  $m/z = 121$  and  $m/z = 120$ . Moreover, the formation of (MPS – H)<sup>+</sup> ion is more efficient than that of the parent ion. The TMPS molecule does not show dehydrogenation reaction, we were not able to detect (TMPS – H)<sup>+</sup> or (TMPS – 2H)<sup>+</sup>. The bond dissociation energies of Si – H in MPS<sup>+</sup> can be calculated as  $AE(MPS^+ - H) - AE(MPS^+) = 1.23$  eV, similarly 1.32 eV for the dissociation of second H atom from MPS<sup>+</sup>. In DMPS molecule the  $BDE(DMPS^+ - H)$  of 1.38 eV [3] was determined. These values are significantly lower than the Si – H BDE calculated for similar molecules but without the phenyl ligand (H<sub>3</sub>Si-H, MeSiH<sub>2</sub>-H, Me<sub>2</sub>SiH-H, Me<sub>3</sub>Si-H, BDE are around 3.8 eV) [11].

The CH<sub>3</sub> dissociation energy from MPS/DMPS/TMPS is decreasing with the number of methyl ligands on the molecule (  $BDE(MPS - CH_3) = 2.01$  eV;  $BDE(DMPS - CH_3) = 1.47$  eV [A];  $BDE(TMPS - CH_3) = 0.79$  eV). (TMPS-CH<sub>3</sub>)<sup>+</sup> is the most intensive ion in TMPS spectrum at  $m/z$  135. In the mass spectrum of MPS molecule the demethylation is followed by the loss of both 2H/H<sub>2</sub> from Si. Similar products were observed for DMPS molecule, the reported ions are (DMPS – 2CH<sub>3</sub>)<sup>+</sup> and (DMPS – H – 2CH<sub>3</sub>)<sup>+</sup>. TMPS molecule, however, has no intensive dissociation channel resulting into (TMPS – 2CH<sub>3</sub>)<sup>+</sup> ion. Here, the dissociation channel result into creation C<sub>6</sub>H<sub>5</sub>SiHCH<sub>3</sub><sup>+</sup> and C<sub>6</sub>H<sub>5</sub>SiCH<sub>2</sub><sup>+</sup> and C<sub>6</sub>H<sub>5</sub>SiH<sub>2</sub><sup>+</sup> molecules. Finally, the dissociation of all three methyl groups from TMPS ion can be detected. From AE of this ion the bond energy of methyl group can be estimated as 2.65 eV.

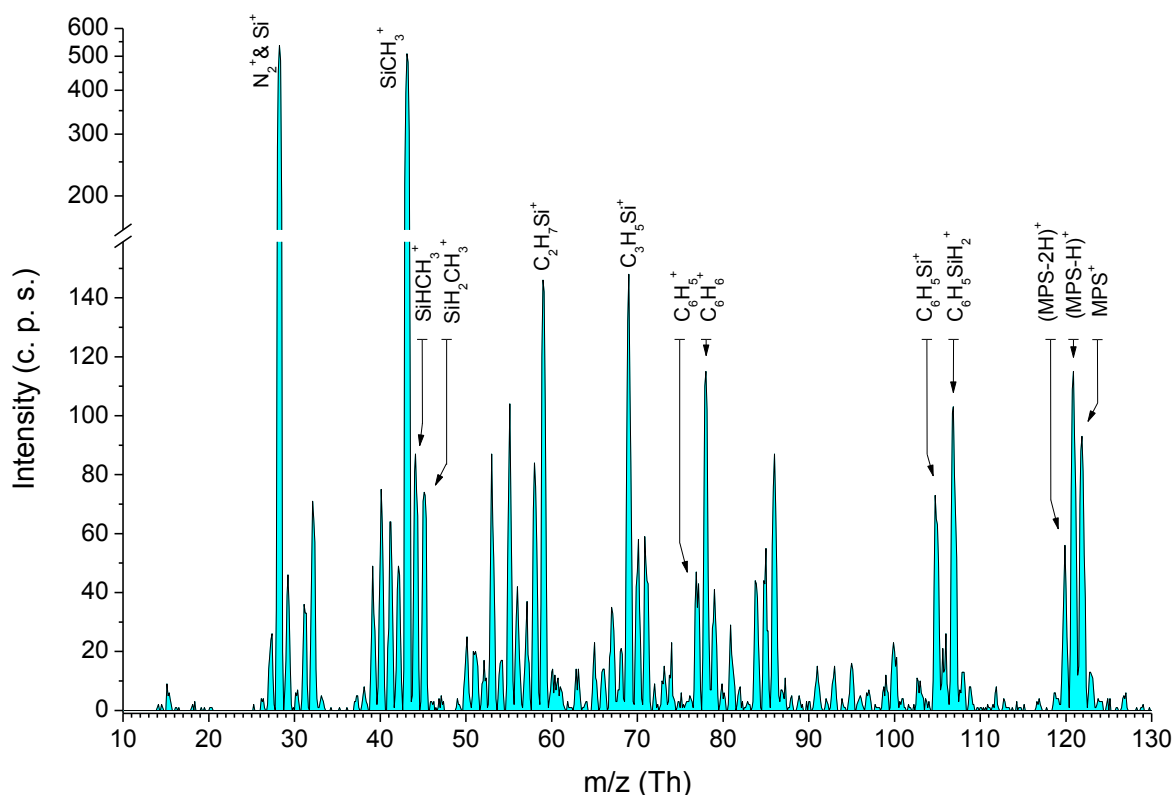


Fig. 2. The mass spectrum of MPS molecule.

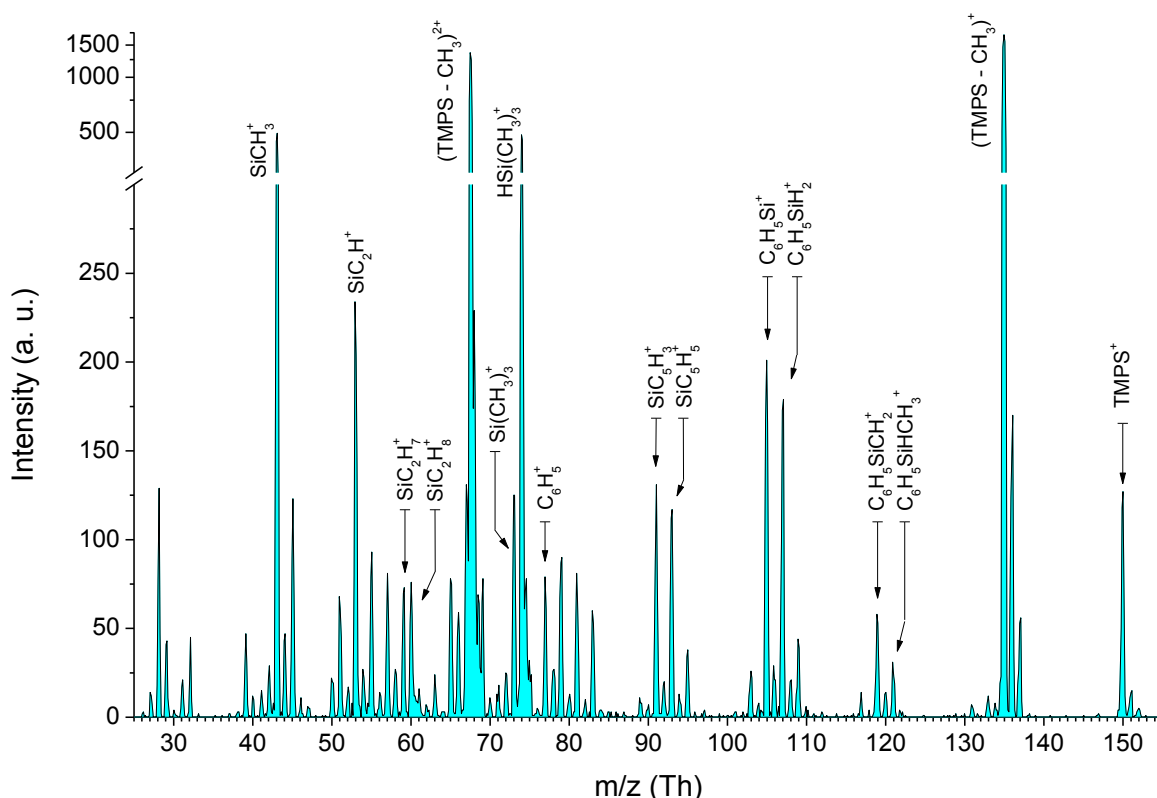


Fig. 3. The mass spectrum of TMPS molecule.

On the other side the dissociation of phenyl group from MPS/DMPS/TMPS is dependent of hydrogenation of the central silicon atom. In the case of MPS/DMPS, the dissociation results in creation of  $(\text{MPS/DMPS} - \text{C}_6\text{H}_5)^+$ ,  $(\text{MPS/DMPS} - \text{C}_6\text{H}_6)^+$  and in parallel to creation of a  $\text{C}_6\text{H}_6^+$  ion. Formation of  $(\text{MPS/DMPS} - \text{C}_6\text{H}_6)^+$  ion is in both cases more effective and energetically more efficient than of  $(\text{MPS/DMPS} - \text{C}_6\text{H}_5)^+$  ion. Only for MPS the  $\text{C}_6\text{H}_5^+$  ion can be also visible. The loss of phenyl can be also visible in TMPS molecule. However, the dissociation of  $\text{C}_6\text{H}_6$  was not recorded probably due to a missing hydrogen – silicon bond. Also the inversion process results in formation of  $\text{C}_6\text{H}_5^+$  ion exclusively. Moreover, fragmentation of  $\text{TMPS}^+$  results in intensive ions like  $\text{HSi}(\text{CH}_3)_3^+$  (instead of the expected dissociation of phenyl and one methyl group), as well as  $\text{SiC}_2\text{H}_7^+$  and  $\text{SiC}_2\text{H}_8^+$ . Finally, the intensive ion of  $\text{SiCH}_3^+$  was detected for all molecules.

The pure silicon ion was uniquely detected only for MPS molecule. However, the AE of this ion wasn't evaluated due to the presence of atmospheric nitrogen at the same mass with  $\text{IE}(\text{N}_2) = 15.58 \text{ eV}$  [6] being lower than the threshold of  $\text{Si}^+$  at the same mass.

#### 4. Conclusions

The ionization energies and the appearance energies of some products of MPS and TMPS molecules were estimated. The DI of MPS molecule is mainly resulting in formation of  $\text{SiCH}_3^+$  ion. The DI of TMPS molecule has intensive channels for  $(\text{TMPS}-\text{CH}_3)^+$ ,  $(\text{TMPS}-\text{CH}_3)^{2+}$ ,  $\text{HSi}(\text{CH}_3)_3^+$  and  $\text{SiCH}_3^+$  ions. We have shown that dissociation of single  $\text{CH}_3$  ligand from all three target molecules is less favourable for MPS molecule, probably due to a lower spatial repulsion between the ligands. The increase of  $\text{CH}_3$  ligands on the Si atom causes the decrease of the Si- $\text{CH}_3$  BDE. Contrary, to this the loss of hydrogen atom is visible only for MPS and DMPS with comparable energetical demand.

#### 5. Acknowledgements

This work was supported by the Slovak Research and Development Agency under Contract No. APVV-0733-11, the Comenius University student grant program no. UK/528/2014, the Slovak grant

agency VEGA V/0514/12. This work was conducted within the framework of the COST Action CM1301 (CELINA).

## 6. References

- [1] Kuritka I. Broza P et al 2007 *Plasma Process. Polym.* **4** 53-61.
- [2] Schauer F. Kuritka I et al 2002 *Phys E* **14** 272.
- [3] Kočíšek J. Stružinský O et al 2012 *Plasma Process. Polym.* **9** 298-303.
- [4] Pictures taken from: <http://www.sigmaaldrich.com>
- [5] Stano M. Matejčík Š et al 2003 *J. Phys. B: At. Mol. Opt. Phys.* **36** 261.
- [6] Lias S G Ion energetic data. in: NIST Chemistry WebBook. NIST Standard Reference Database Number 69. <http://webbook.nist.gov/chemistry/> [cited 2014 June].
- [7] Wanier G H 1953 *Phys. Rev.* **90** 817.
- [8] McLean R A N 1973 *Can. J. Chem.* **51** 2089.
- [9] Pitt C G 1973 *J. Organomet. Chem.* **61** 49.
- [10] Fujii T. Ishii H and Tokiwa H 1990 *J. Organomet. Chem.* **391** 147-153.
- [11] Walsh R 1981 *Acc. Chem. Res.* **14** 246-252.



# ON HELIUM ANIONS IN HELIUM DROPLETS

Andreas Mauracher, Stefan E. Huber

*Institut für Ionenphysik und Angewandte Physik, Leopold-Franzens-Universität Innsbruck  
Technikerstraße 25/3, A-6020 Innsbruck, Austria*

E-mail: andreas.mauracher@uibk.ac.at / s.huber@uibk.ac.at

Helium droplets provide an ideal environment to study elementary processes in atomic systems at very low temperatures. Here, we discuss properties of charged and neutral, atomic and molecular helium species formed in helium droplets upon electron impact. By studying their interaction with atomic ground state helium we find that  $\text{He}$ ,  $\text{He}_2^*$  and excited (metastable)  $\text{He}^{*-}$  are well bound within the helium droplet. In comparison,  $\text{He}^*$ ,  $\text{He}_2^*$  and  $\text{He}_2^{*-}$  are found to be squeezed out due to energetic reasons. We also present the formation pathways of atomic and molecular helium anions in helium droplets. Transition barriers in the energetic lowest  $\text{He}^{*-}$ – $\text{He}$  interaction potentials prevent molecule formation at the extremely low temperatures in helium droplets. In contrast, some excited states allow a barrier-free formation of molecular helium (anions).

## 1. Introduction

Helium droplets have opened a pathway to study atoms and molecules at very low temperatures and have thus received substantial attention over the last decade [1-5]. To employ mass spectrometric techniques for the investigation of cold atoms or molecules, the dopants have to be ionised. A possibility to achieve ionisation of embedded molecules is to cross the doped beam of helium droplets with a beam of free electrons which can lead to either positive [6] or negative ions [7]. Of particular interest here is the process of charge transportation inside the helium droplet. For positive charges this proceeds via a resonant charge-hopping process [8] which is terminated either by irreversibly forming a molecular helium cation [9] or by ionisation of the dopant [10]. The situation is different for negative charge transportation. Electrons solvated in liquid helium and in helium droplets form bubbles [11] with a radius in a range of 11 – 15 Å [12]. The formation of anions of molecules embedded in helium droplets is expected to happen via direct interaction with electrons in the low energy range (< 20 eV) [7] and via intermediated excitation of a helium atom and then again direct electron interaction for higher electron energies (> 20 eV) [13].

## 2. Methodology

Our method is quantum mechanical calculations of the CCSD(T) type [14]. All calculations employed a specialized multiply-augmented basis set based on the d-aug-cc-pVXZ, X = T, Q of Woon and Dunning [15], but using a global scaling with a factor of 1/3 for the exponents of the diffuse functions (beyond the second least diffuse one) instead of angular momentum dependent scaling factors. Excited states were calculated using the EOM-CCSD approach [16]. All calculations were carried out with the Gaussian 09 suite of programmes [17] and have been corrected for basis set superposition errors (if applicable) [18].

## 3. Results and Discussion

In order to investigate the interaction of the atomic  $\text{He}^+$ ,  $\text{He}$ ,  $\text{He}^*$  and  $\text{He}^{*-}$  species with ground state helium, we performed scans of the potential energy surface (PES) by varying the interatomic distance. In Figure 1 we show the interaction curves for these systems. It can be seen that for the systems  $\text{He}^* - \text{He}$  and  $\text{He}^{*-} - \text{He}$  transition barriers prevent the molecule formation at the extremely low temperatures present in helium droplets. A detailed discussion was recently presented in [19]. In addition we investigated the potential energy landscape of the molecular species  $\text{He}_2$ ,  $\text{He}_2^*$  and  $\text{He}_2^{*-}$  experienced by an additional ground state helium. From these data the energy gain and energy cost can be calculated for each species [19]. It is found that  $\text{He}^{*-}$  remains inside the droplet and can thus polarise a present dopant species in the HND and can interact with it, for example by transferring its loosely bound electron resulting in dopant anions. In contrast,  $\text{He}_2^{*-}$  is pushed to the surface of the

droplet, and will reside at the surface in a “head-on” position, i.e. where the molecular axis is perpendicular to the surface.

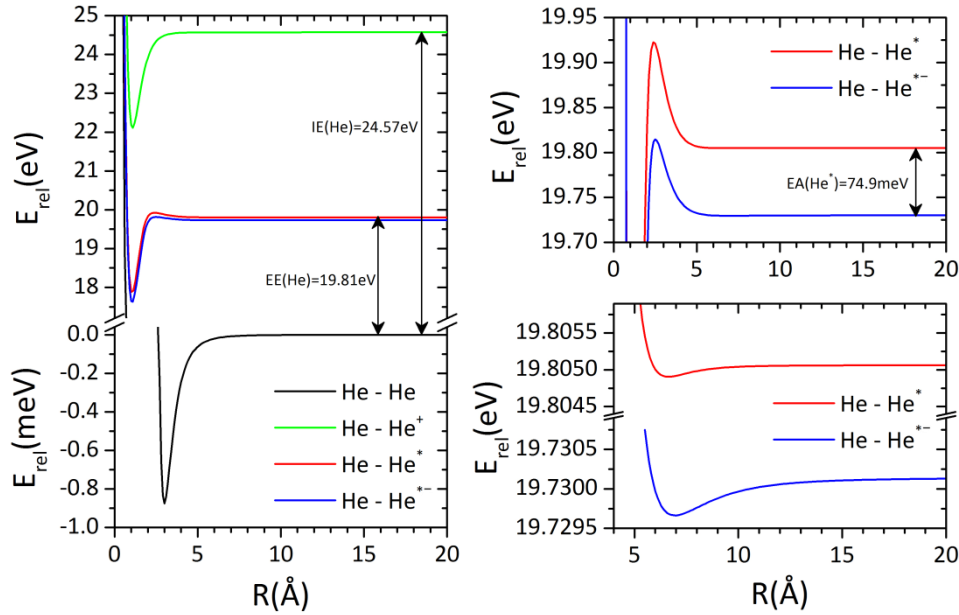


Fig. 1. Potential energy scans for He ( $^1S$ ) – He ( $^1S$ ) (black curve), He ( $^1S$ ) – He $^+$  ( $^2S$ ) (green curve), He ( $^1S$ ) – He $^*$  ( $^3S$ ) (red curve) and He ( $^1S$ ) – He $^{*-}$  ( $^4P$ ) (blue curve) at CCSD(T)/q-aug-cc-pVQZ level of theory and basis set. Right upper panel: magnification of the barrier for He ( $^1S$ ) – He $^*$  ( $^3S$ ) and He ( $^1S$ ) – He $^{*-}$  ( $^4P$ ). Right lower panel: magnification of the local minima for He ( $^1S$ ) – He $^*$  ( $^3S$ ) and He ( $^1S$ ) – He $^{*-}$  ( $^4P$ )

Furthermore, we calculated interaction potentials between helium atoms excited to the lowest lying triplet states and ground state helium [20]. As mentioned before, helium molecule formation is hindered by a barrier for the lowest of these excited configurations, i.e. excitation of an electron into the 2s-orbital (and concurrent spin-flip). In Figure 2 the interaction potentials are depicted. Further investigations show that barriers vanish if one electron is excited into a p-orbital perpendicular to the diatomic axis instead.

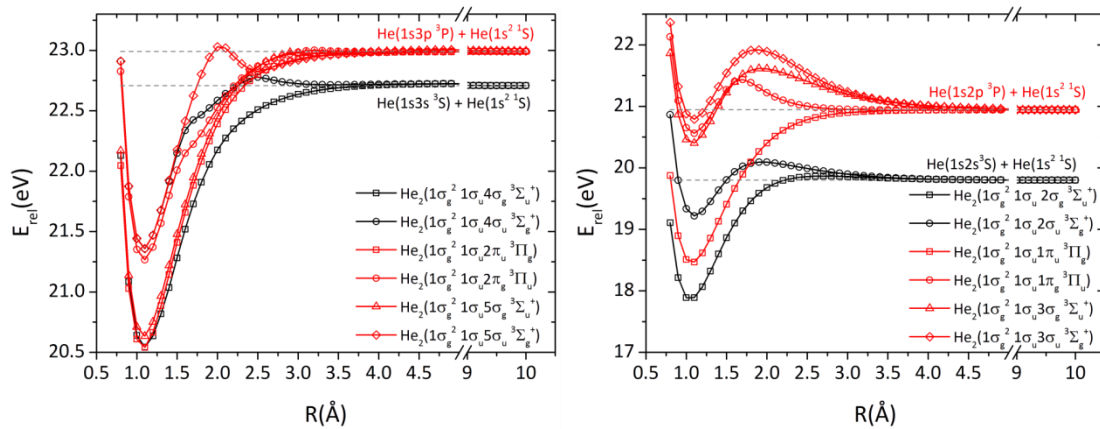


Fig. 2. He–He interaction potentials for various excited triplet states. The respective dissociation energies are indicated by gray dashed lines as well as the respective, atomic dissociation configurations.

## 4. Acknowledgement

This work was partly supported by the Austrian Fund Agency, FWF, via project I 978-N20 and the Austrian Ministry of Science BMWF as part of the Konjunkturpaket II and as part of the UniInfrastrukturprogramm of the Focal Point Scientific Computing at the University of Innsbruck. The computational results presented have been achieved in part using the Vienna Scientific Cluster (VSC). SEH gratefully acknowledges funding from the Austrian Science Fund (FWF) DK+ project Computational Interdisciplinary Modelling, W1227-N16. AM gratefully acknowledges a grant from the Nachwuchsförderung of the University of Innsbruck.

## 5. References

- [1] Townsend J S and Tiyard H T 1912 *Proc. of the Royal Society of London. Series A* **87** 357.
- [1] Toennies J P and Vilesov A F 2004 *Angew. Chem. Int. Ed.* **43** 2622.
- [2] Stienkemeier F and Lehmann K K 2006 *J. Phys. B: At. Mol. Opt. Phys.* **39** R127.
- [3] Barranco M, Guardiola R, Hernández S, Mayol R, Navarro J and Pi M 2006 *J. Low Temp. Phys.* **142** 1.
- [4] Choi M Y, Doublerly G E, Falconer T M, Lewis W K, Lindsay C M, Merritt J M, Stiles P L and Miller R E 2006 *Int. Rev. Phys. Chem.* **25** 15.
- [5] Yang S and Ellis A M 2013 *Chem. Soc. Rev.* **42** 472.
- [6] Zappa F, Denifl S, Mähr I, Lecointre J, Rondino F, Echt O, Märk T D and Scheier P 2007 *Eur. Phys. J. D* **1-3/43** 117.
- [7] Denifl S, Zappa F, Mähr I, Lecointre J, Probst M, Märk T D and Scheier P 2006 *Phys. Rev. Lett.* **97** 043201.
- [8] Scheidemann A, Schilling B and Toennies J P 1993 *J. Chem. Phys.* **97** 2128.
- [9] Callicoatt B E, Förde K, Ruchti T, Jung L and Kenneth C J 1998 *J. Chem. Phys.* **108** 9371.
- [10] Ellis A M and Yang S 2007 *Phys. Rev. A* **76** 032714.
- [11] Kupfer C G 1961 *Phys. Rev.* **122** 1007.
- [12] Poitrenaud J and Williams F I B 1972 *Phys. Rev. Lett.* **29** 1230.
- [13] Schöbel H, Bartl P, Leidlmair C, Daxner M, Zöttl S, Denifl S, Märk T D, Scheier P, Spångberg D, Mauracher A, *et al.* 2010 *Phys. Rev. Lett.* **105** 243402.
- [14] Pople J A, Head-Gordon M and Raghavachari K 1987 *J. Chem. Phys.* **87** 5968.
- [15] Woon D E and Dunning Jr, T H 1997 *J. Chem. Phys.* **100** 2975.
- [16] Stanton J F and Bartlett R J 1993 *J. Chem. Phys.* **98** 7029.
- [17] Gaussian 09, Revision D.01, Frisch M J, Trucks G W, Schlegel H B, Scuseria G E, Robb M A, Cheeseman J R, Scalmani G, Barone V, Mennucci B, Petersson G A, *et al.* Gaussian, Inc., Wallingford CT, 2009.
- [18] Boys S F and Bernardi F 1970 *Mol. Phys.* **19** 553.
- [19] Huber S E and Mauracher A 2014 *Mol. Phys.* **112** 794.
- [20] Huber S E and Mauracher A 2014 *J. Phys. Chem. A*. accepted.

## SECOND-KIND COLLISION OF ELECTRONS WITH CADMIUM METASTABLE ATOMS

Mykola Margitych, Yuriy Svyda, Viktor Marushka, Roman Fedorko, Marianna Solontay, Ivan Shafranyosh

*Uzhgorod National University*

E-mail: margitych@gmail.com

Under the conditions of electron and atom beams crossing in the energy interval of 0.3–5 eV, there are performed the experimental investigations of processes of electrons' second-kind collisions with cadmium metastable atoms. There is obtained the collisions' cross-section energetic dependence, which reproduces both potential diffusion and resonance processes. The occurrence of resonances is classified as the manifestation of the formation and decay of cadmium negative ions' energetic states.

### 1. Experiment Methods and Technology

The inelastic second-kind collisions take place between the electron and atom being in the excited state. In case of these collisions, the electron acquires additional energy at the expense of the atom's internal energy. For this reason, such collisions are often called super-elastic, and the diffusion of electrons on the atom – super-elastic diffusion. Since in the low-temperature plasma a significant amount of atoms are in the excited state, it is obligatory to take into consideration the contribution of the super-elastic collision processes. The collisions between electrons and metastable atoms are the important cases of this type.

Experimental investigations of the electrons' super-elastic diffusion on the cadmium metastable atoms were performed under the conditions of atom and electron beams crossing at right angle, in the energy interval of 0.3–5 eV. The beam of cadmium metastable atoms was obtained by means of discharge [1]. Discharge parameters: current – 200 mA, voltage – 90 V. The degree of the atoms' converting into metastable states was ~10%. The five-electrode electron gun with a tungsten cathode was used as the source of the electron beam (the electron beam current  $\sim 5 \cdot 10^{-6}$  A, energy inhomogeneity  $\Delta E_{1/2} \sim 0.3$  eV). The experiment scheme is shown in Fig. 1.

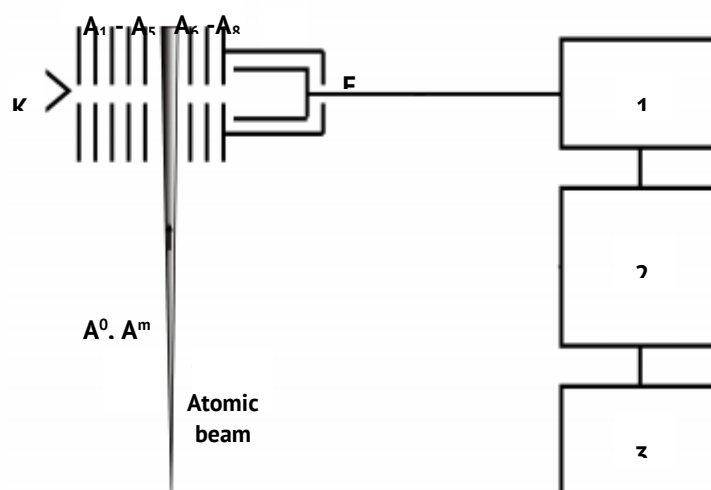


Fig. 1. The experimental equipment scheme:

K – cathode; A1-A5 – electron gun electrodes; A6-A8 – the electrodes of the electron energy analyzer; F – Faraday cylinder;  $A^0$ ,  $A^m$  – atoms in the ground and metastable states respectively; 1 – digital-to-analog converter; 2 – voltage amplifier; 3 – automatized system of diffused electrons' registration.

The calibration of the electrons' energy scale was performed in accordance with the energetic position of the resonance of negative ions  $SF_6^-$  formation; the position of this resonance determined the scale zero. For this purpose, the collision chamber was filled with the gas  $SF_6$ .

The diffused electrons' energies were analyzed by the brake-type energy analyzer, which was a system of three plane electrodes with round diaphragms and Faraday cylinder. The deep Faraday cylinder served as an electron detector and was located inside the cylinder-shape decelerating electrode. The potentials of the analyzer edge electrodes were set to be identical and they were equal to the accelerating potential  $V_e$ , and the decelerating negative-value potential  $V_r$  was supplied to the middle electrode. At the energy of 2 eV the analyzer's resolution reached the value  $5 \cdot 10^{-2}$ .

The system of registering the electrons, which passed the analyzer, worked in the analog regime and consisted of the electrometer B7-30, the double-coordinate ("X-Y") recorder, the system of the primary electrons' energy scan, and the system of processing the experiment data.

The sources of electron and atom beams and the analyzer of electrons' energy were fixed on the removable assembled flange, which was located inside the collision chamber made of stainless steel. The preparation for the measurements included long-time heating and purification of the surfaces of the gun electrodes and electron analyzer under the high vacuum conditions. The necessary vacuum was provided by the vacuum pumping system consisting of the forevacuum, oil and magnetic-discharge pumps. The investigations were made at the vacuum of  $6.5 \cdot 10^{-6}$  Pa.

## 2. Results and Discussions

Cadmium is the transition metal of the 12th group. The electron configuration of the atom ground state is  $4d^{10} 5s^2$ , the term  $^1S_1$  corresponds to it. The deepest excited states are the triplet metastable states  $5s5p\ ^3P_{0,2}$  (energies 3.73 eV and 3.94 eV respectively). Note that cadmium appeared to be a very complicated element for obtaining an atom beam.

During the experiments, there was obtained the energy dependence of the cross-section of the electrons' super-elastic diffusion on the cadmium atoms in the interval of the electrons' energy from the process threshold to 5 eV. On the obtained experimental curve, there is found the structure manifesting in the form of resonances in the intervals of the electrons' energy  $0.3 \div 1.4$  eV.

Such behavior of the super-elastic diffusion cross-section testifies to the complicated mechanisms of the process of the electrons' interaction with the metastable atoms. In our opinion, a significant probability in this range of the electron energies is intrinsic in the processes of formation and decay of the cadmium negative ion, which, in turn, leads to the formation of the structure in the near-threshold part of the energy dependence. The details of the obtained experimental data and the possible mechanisms of the electrons' interaction with metastable atoms are discussed.

## 3. References

- [1] Shafranyosh I I and Margitich M O 2000 J.Phys.B: At.Mol.Opt.Phys **33** 905.

# EJECTED ELECTRON SPECTRA FROM AUTOIONIZATION REGION IN NEON AT INCIDENT ELECTRON ENERGY OF 505 eV AND EJECTION ANGLES OF 40° AND 130°

Bratislav P. Marinković, Jozo J. Jureta, Aleksandar R. Milosavljević

*Laboratory for Atomic Collision Processes, Institute of Physics, University of Belgrade,  
Pregrevica 118, 11080 Belgrade, Serbia  
E-mail: bratislav.marinkovic@ipb.ac.rs*

In the present work we have studied autoionizing states and resonances in neon atom, in the energy region of ejected electrons from 21 to 30 eV (42.56 to 51.56 eV of excitation energy), at the constant incident electron energy of 505 eV and two ejection angles of 40° and 130° with respect to the incident beam direction. The measurements have been carried out on a high-resolution crossed electron-atom beam apparatus, allowing to resolve both singlet and triplet states. Furthermore, we found that the shape of spectral features close to the resonances strongly depend on the ejection angle.

## 1. Introduction

Autoionization states and resonances in neon have been studied in the past by electrons, photons and ions but with lack of theoretical calculations comparing to calculations in helium. Especially, the energy region from 43 to 51 eV of excitation energies has been studied by low energy electrons [1] as well as by high energy electron using energy-loss spectroscopy at zero scattering angle [2,3]. Also, the resonances in this energy region have been studied in the past using low energy electrons as projectiles [4]. Here we present measurements of autoionizing states and resonances in neon at constant incident electron energy of 505 eV and two ejection angles of 40° and 130° with respect to the incident beam direction in order to show the angular behavior of excited states.

## 2. Experimental Set-up

The measurements have been carried out on a crossed electron-atom beam apparatus OHRHA [5] which involves an electron gun that can be rotated around analyzer axis, electrostatic lenses, a hemispherical analyzer with 7 channeltrons as detectors and an interaction region with a gas needle as an atomic source. The energy resolution of the ejected electron spectra was measured as full width at half maximum (FWHM) of the narrowest feature in the spectrum and was typically between 60 and 80 meV.

## 3. Results

The results of measurements are shown in figure 1. We present the ejected electron spectra with subtracted background without any normalization of the obtained data measured at two different ejection angles of 40° and 130°. The high energy resolution is demonstrated in the separation between triplet and singlet states of 0.1 eV. The difference in form of the measured spectral features for the two ejection angles is clearly visible from the figure. Two series of triplet and singlet  $2s2p^6ns,np$  excited states could be assigned. There are also several dominant resonances. The calibration point was taken from the mixture of helium and neon at 505 eV identifying the well known  $(2s2p)^1P$  state in autoionization region of helium at 35.54 eV (60.13 eV of excitation energy) [6]. The autoionizing states have been assigned according to the reference [7]. The positions of resonances from literature [4] are shown at the bottom of the figure. Most of the resonances measured at low incident electron energy are not seen in our ejection spectra except two of them at 22 eV (R1), and 27.54 eV (R2) indicating that they belong to the class of non-valence resonances already seen in helium [8,9].

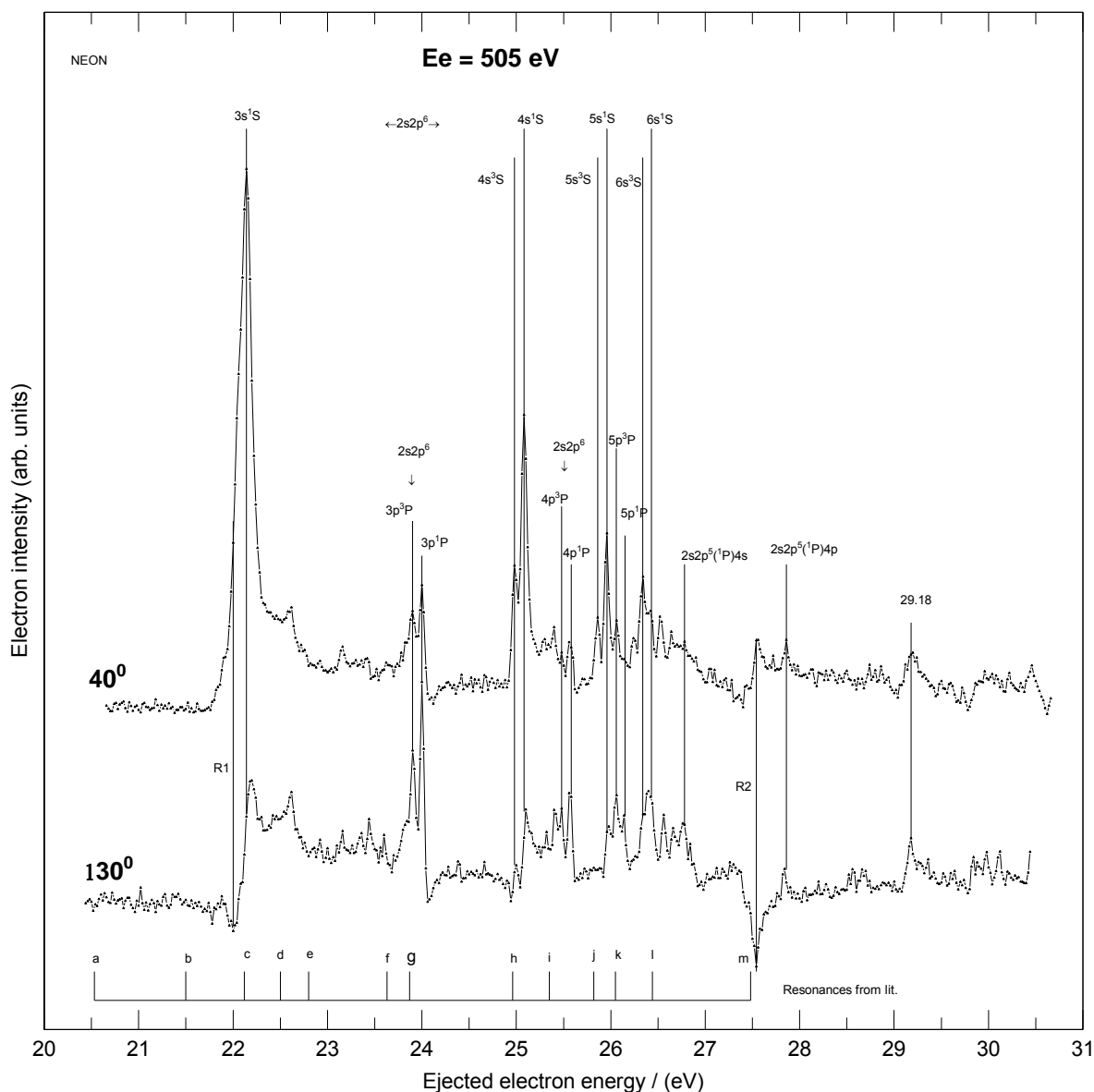


Fig. 1. Ejected electron spectra of autoionizing states of neon obtained at the excitation electron energy of 505 eV and the ejection angles of 40° and 130° labeled on the left hand side of the figure. The energy region of ejected electrons is from 20.5 to 30.5 eV or 42.06 to 52.06 eV of excitation energy with energy width per channel of 0.020 eV. Long vertical lines show energy positions of the features, while short vertical lines at the bottom of the figure mark positions of resonances from literature [4].

#### 4. References

- [1] Sharp J M, Comer J and Hicks P J, 1975 *J. Phys. B : Atom. Molec. Phys.* **8** 2512.
- [2] Chan W F, Cooper G, Guo X and Brion C E 1992 *Phys. Rev. A* **45** 1420.
- [3] Zhong Z P *et al* 1997 *Phys. Rev. A* **55** 3388.
- [4] Buckman S J and Clark C W, 1994 *Rev. Mod. Phys.* **66** 539.
- [5] Jureta J J, Milosavljević A R and Marinković B P 2014 *Int. J. Mass Spectrom.* DOI: [10.1016/j.ijms.2014.03.002](https://doi.org/10.1016/j.ijms.2014.03.002)
- [6] Madden R P and Codling K 1963 *Phys. Rev. Lett.* **10** 516.
- [7] Edwards A K and Rudd M E 1968 *Phys Rev* **170**, 140.
- [8] Nesbet R K 1978 *J. Phys. B : At. Mol. Phys.* **11** L21.
- [9] van der Burgt P J M and Heideman H G M 1985 *J. Phys. B : At. Mol. Phys.* **18** L755.

# ELASTIC ELECTRON SCATTERING ON MOLECULE IN OPTICAL POTENTIAL APPROACH

Shandor Demesh, Eugene Remeta, Vladimir Kelemen

*Institute of Electron Physics, National Academy of Sciences of Ukraine,  
Uzhgorod, Ukraine*

E-mail: demesh.shandor@gmail.com

Relativistic optical potential method has been proposed for the potential electron scattering by molecules in framework of independent atom model. For the consistent study of electron scattering process on the atoms from the molecule, potentials and atomic characteristics are determined in the local approach of the stationary (with the self-interaction energy correction) and time-dependent density functional theory with the account of some relativistic effects.

## 1. Optical Potential Method

The scattering partial phase shifts  $\delta_\ell^\pm(E) = \varepsilon_\ell^\pm(E) + i\xi_\ell^\pm(E)$  (for  $\ell < \ell_{\min}$ ) for the potential electron scattering on the atom of the molecule could be find by solving the phase equations with complex optical potential (OP) in the variable phase method [1,2]

$$V_{opt}^\pm(r, E) = V^\pm(r, E) + iV_A(r, E), \quad (1)$$

and the parameter-free real OP

$$V^\pm(r, E) = V_S(r) + V_e^R(r, E) + V_p(r) + V_R(r, E) + V_{so}^\pm(r, E). \quad (2)$$

Sign "+" corresponds to the total angular momentum of incident electron  $j = \ell \pm 1/2$ ,  $\ell$  – its orbital momentum. The potential components of OP –  $V_S$ ,  $V_e^R$ ,  $V_p$ ,  $V_A$  in (2) and (1) – are the following potentials: static; exchange; polarization and absorption. Scalar relativistic

$$V_R(r, E) = -\alpha^2 V_S^2 / 2 + \chi / 4 \cdot d^2 V_S / dr^2 + 3\chi^2 / 8 \cdot (dV_S / dr)^2 \quad (3)$$

and spin-orbit interaction

$$V_{so}^\pm(r, E) = \zeta^\pm(j, \ell) \cdot \chi / r \cdot dV_S / dr \quad (4)$$

potentials are describe the relativistic effects in scattering,  $\chi = \alpha^2 / [2 + \alpha^2(E - V_S)]$ ;  $\zeta^+(j, \ell) = \ell / 2$ ,  $j = \ell + 1/2$ ;  $\zeta^-(j, \ell) = -(\ell + 1) / 2$ ,  $j = \ell - 1/2$ ;  $\alpha = 1/137.036$  (in atomic units).

Nonrelativistic exchange potential in the free electron-gas approximation is

$$V_e^{NR}(r, E) = -\frac{k_F(r)}{\pi} \left( 1 + \frac{1 - \kappa^2}{2\kappa} \ln \left| \frac{1 + \kappa}{1 - \kappa} \right| \right), \quad (5)$$

$k_F(r) = [3\pi^2 \rho_n(r)]^{1/3}$  is the Fermi-momentum for the  $n$ -th atom of the target molecule expressed via the total electron density  $\rho_n(r)$ ,  $\kappa(r, E) = k_s(r, E) / k_F(r)$ ,  $[k_s(r, E)]^2 = k^2 + V(r, k^2 / 2)$ , wave number of incident electron with the energy  $E$  is  $k = \sqrt{2E}$ . Function  $V(r, k^2 / 2)$  is connected with the interaction potentials. Some simple model expression is  $V(r, k^2 / 2) = [k_F(r)]^2 + 2I / [1 + (kr)^2 / 2]$ ,  $I$  is the ionization potential of the atom. Relativistic exchange potential ( $r_s(r) = [3 / 4\pi \rho_n(r)]^{1/3}$ )

$$V_e^R(r, E) = V_e^{NR}(r, E) + \bar{\Psi}_R(r_s) V_e^{NR}(r, E), \quad \bar{\Psi}_R(r_s) = \frac{3}{2} \left[ \frac{\ln \xi}{\beta \eta} - 1 \right], \quad \bar{\Psi}_R = \Psi_R - 1. \quad (6)$$

$\beta(r_s) = [3\pi^2 \rho_n(r)]^{1/3} / c$ ,  $\eta(r_s) = [1 + \beta(r_s)^2]^{1/2}$ ,  $\xi(r_s) = \beta(r_s) + \eta(r_s)$ ,  $c = 137.036$  (light velocity).

For the polarization potential the parameter-free expression for local potential of correlation-polarization interaction of electrons in the inhomogeneous electron gas is used. Potential consists of two parts, which describe interactions in small (SR)  $V_p^{SR}(r)$  and in large (LR) distances

$V_p^{LR}(r) = -\alpha_d(0) / 2r^4$ ,  $\alpha_d(0)$  – dipole static polarizability of the  $n$ -th atom. Potentials  $V_p^{SR}$  and  $V_p^{LR}$



cross each other in the point  $r_c$ . Polarizability of the atoms  $\alpha_d(0)$  was calculated in local approximation of time-dependent density functional theory.

The absorption effects (at the  $E > \Delta_n$  – energy of the first inelastic threshold of  $n$ -th atom) described with two absorption potentials: for small energies empirical McCarthy-type potential  $V_{aMc}(r, E) = -W(E) r^2 \rho_{H,n}(r) / [T_{loc}(r, E)]^2$ ,  $T_{loc} = E - V_s - V_e^R - V_p$  is the local kinetic energy,  $\rho_{H,n}$  is the electron density of the  $n$ -th atom valence subshell. For greater energies non-empirical Staszewska-type potential  $V_{af}(r, E) = -v_{loc}(r, E) \rho_n(r) \bar{\sigma}_b(r, E) / 2$  in quasi-free scattering model is used, where  $v_{loc} = [2T_{loc}]^{1/2}$  is the local incident electron velocity. The averaged binary collision cross section  $\bar{\sigma}_b(r, E)$  connected with the  $\alpha(r, E)$  and  $\beta(r, E)$  functions. We use the version 2 of the potential  $V_{af}$ :  $\alpha = k_F^2 + \Delta - 2(V_s + V_e^R)$  and  $\beta = \alpha$ . Parameters of  $W(E)$  could be determine with comparison of absorption cross sections, achieved with these absorption potentials. The parametric analytical expressions for the densities  $\rho_n(r)$ ,  $\rho_{H,n}$  and static potential  $V_s(r)$  are used.

## 2. Differential and Integral Cross Sections

The differential elastic cross section for the potential electron scattering by  $N$ -atomic molecule in the independent atom model framework is [3-5]

$$\frac{d\sigma_{el}}{d\Omega} = \sum_{m=1}^N \sum_{n=1}^N [f_m(\theta, k) f_n^*(\theta, k) + g_m(\theta, k) g_n^*(\theta, k)] \frac{\sin(sr_{nm})}{sr_{nm}}.$$

Here  $\theta$  is the scattering angle,  $f_m(\theta, k)$  and  $g_m(\theta, k)$  are the complex direct and spin-flip scattering amplitude due to the  $m$ -th atom of the molecule

$$f_m = \frac{1}{2ik} \sum_{\ell=0}^{\infty} \{(\ell+1) [\frac{\exp(2i\varepsilon_{\ell}^+)}{\exp(2\xi_{\ell}^+)} - 1] + \ell [\frac{\exp(2i\varepsilon_{\ell}^-)}{\exp(2\xi_{\ell}^-)} - 1]\} P_{\ell}(\theta), \quad g_m = \frac{1}{2ik} \sum_{\ell=1}^{\infty} [\frac{\exp(2i\varepsilon_{\ell}^-)}{\exp(2\xi_{\ell}^-)} - \frac{\exp(2i\varepsilon_{\ell}^+)}{\exp(2\xi_{\ell}^+)}] P_{\ell}^1(\theta),$$

$P_{\ell}(\theta)$  and  $P_{\ell}^1(\theta)$  are the Legendre polynomials,  $s = 2k \sin(\theta/2)$  is the magnitude of the momentum transfer during collision,  $r_{nm}$  is the distance between the  $n$ -th and  $m$ -th atoms.

The integral cross sections are found from the equations: elastic –  $\sigma_{el}(E) = \sum_n \sigma_{el,n}(E) + \sum_{n,m} \sigma_{el(nm)}(E)$ ; absorption –  $\sigma_{abs}(E) = \sum_n \sigma_{abs,n}(E) + \sum_{n,m} \sigma_{abs(nm)}(E)$ ; total (from the optical theorem)  $\sigma(E) = \frac{4\pi}{k} \sum_n \text{Im} f_n(\theta=0, k) = \sum_n \sigma_n(E)$  or  $\sigma(E) = \sigma_{el}(E) + \sigma_{abs}(E)$ ;  $\sigma_{el,n}$ ,  $\sigma_{abs,n}$ ,  $\sigma_n$  are the elastic, absorption and total cross sections of the  $n$ -th atom; momentum transfer and viscosity

$$\sigma_{mom}(E) = 2\pi \int_0^{\pi} d\theta \sin \theta (1 - \cos \theta) d\sigma_{el}(E, \theta) / d\Omega, \quad \sigma_{vis}(E) = 2\pi \int_0^{\pi} d\theta \sin^3 \theta d\sigma_{el}(E, \theta) / d\Omega.$$

Asymptotic values (for  $\ell_{\max} > \ell > \ell_{\min}$ ) of the phase shifts are calculated from the expression  $tg \delta_{\ell}^{as} = \pi \alpha_d(0) k^2 / [(2\ell+3)(2\ell+1)(2\ell-1)]$ .

The scattering characteristics may be calculated in the such approaches: spin-unpolarized [1]; spin-polarized [2]; full relativistic (with  $V_R$  and  $V_{so}^{\pm}$ ); semirelativistic (only with  $V_R$  or with  $V_{so}^{\pm}$ ).

## 3. References

- [1] Kelemen V I and Remeta E Yu 2012 *J. Phys. B: At. Mol. Phys.* **45** 185202.
- [2] Remeta E Yu and Kelemen V I 2010 *J. Phys. B: At. Mol. Phys.* **43** 045202.
- [3] Mott N F and Massey H S W 1965 *The theory of atomic collisions*.
- [4] Raj D 1991 *Phys. Lett. A* **169** 571.
- [5] Mozejko P, Zywicka-Mozejko B and Szmytkowski Cz 2000 *Uzhhorod Univ. Sci. Herald, Ser. Phys.* **8** Part 1 108.

# APPEARANCE ENERGIES OF THE SF<sub>6</sub> MOLECULE IONIC FRAGMENTS STUDIED *AB INITIO*

Shandor Demesh, Eugene Remeta

*Institute of Electron Physics, National Academy of Sciences of Ukraine,  
Uzhgorod, Ukraine*

E-mail: demesh.shandor@gmail.com

The theoretical analyses of appearance energies that corresponds to formation of  $SF_k^+$  ion fragments in electron impact dissociative ionization processes of the  $SF_6$  molecule is presented. In order to calculate the total energies of neutral and ionic fragments we used of the GAMESS computer code. There were made conclusion about the importance of different excitation paths of  $SF_k^+$  fragments and  $F_2$  molecules, which besides the processes of dissociative ionization through the electronic autoionizing repulsive terms of  $SF_6$  molecule, could result in exceeding of the observed appearance energies over the theoretical values.

## 1. Method

The best way to achieve a good agreement between the calculations and experiments is to use the first principle computational methods. Calculations of the energy characteristics for the  $SF_6$  molecule and its fragments  $F$ ,  $F_2$ ,  $F_2^\pm$ ,  $SF_k$ ,  $(SF_k)^\pm$  ( $k=0-6$ ) were performed by a density functional theory (B3LYP and B3PW91 methods) using the GAMESS computer code [1]. The vibrational energy  $G_v$  at 0°K (zero point energy) is taking into account.

Appearance (AP) energy of the ionic fragment  $SF_k^+$  from the  $SF_6$  ( $n=6-k$ ) is

$$E_{AP}[(SF_k^+ - nF)/SF_6] = E_t(SF_k^+) + nE_t(F) - E_t(SF_6) = D[(SF_k - nF)/SF_6] + I(SF_k) .$$

Here  $E_t$  total energies of the suitable molecular or atomic particles. In case of formation of  $F_2$  molecule the AP energy decreasing by the binding energy of fluorine atoms. During the formation of  $F_2^-$  and  $F^-$  ions the AP energy also decreasing by their electron affinity value, while the excitation of the final products leads on its increasing.

## 2. Results

The adiabatic values for atomic and molecular characteristics – ionization potential  $I$ , electron affinity  $E_a$ , vibrational energy  $G_v$ , dissociation energy  $D$ , appearance energy  $E_{AP}$  – in a quiet good agreement with different data in general. They were used in order to calculate the AP energies  $E_{AP}^{th}$  of the  $SF_k^+$  ions for some channels (see Tab.1,  $\Delta G_v = G_v(SF_6) - G_v(SF_k^+)$ ). The qualitative behavior of the calculated and measured AP energies of  $SF_k^+$  ionic fragments in comparison with the number of remained fluorine atoms is similar. There was observed exceeding of experimental values  $E_{AP}^{exp}$  [2] above theoretical  $E_{AP}^{th}$  – greater for small  $k$  and smaller for large  $k$  (see fig.1). This exceeding is interpreted with effective excitation of high-energy regions of repulsion autoionization electronic terms in case of  $SF_6$  molecule, excited by electrons. Such kind of mechanism in the dissociative ionization process induce a chance to find the final atomic and molecular products in excited states and they may have a significant kinetic energy.

A more exact interpretation of the mentioned appearance energies for ionic fragments and the determination of the repulsion autoionization electronic terms in case of initial molecule requires the measuring of characteristics of final products, like a kinetic energy, excited and charged states which corresponds to different dissociative ionization channels.

Tab.1. Appearance energies of  $SF_k^+$  fragments (1 – B3LYP; 2 – B3PW91)

$SF_k^+$ -fragments	$\Delta G_v$ , eV	$E_{AP}^{exp}$ , eV [2]	$E_{AP}^{th}$ , eV		
			Channel	1	2
$SF_6^+$	0.114	15.7	—	14.78	14.84
$SF_5^+$	0.084	15.50±0.5	$F$	14.10	14.16
			$F^-$	10.75	10.84
$SF_4^+$	0.232	18.44±0.5	$2F$	17.02	17.27
			$F_2^*$	17.51	17.75
			$F_2$	15.51	15.75
$SF_3^+$	0.300	18.70±0.5	$3F$	17.47	17.80
			$F-F_2^*$	17.96	18.28
			$F-F_2$	15.96	16.28
$SF_2^+$	0.411	27.00±0.5	$4F$	21.11	21.55
			$2F_2^*$	22.09	22.51
			$2F-F_2^*$	21.60	22.03
$SF^+$	0.495	30.44±0.5	$5F$	24.74	25.26
			$F-2F_2^*$	25.72	26.22
			$3F-F_2^*$	25.23	25.74
$S^+$	0.558	36.40±0.5	$6F$	28.49	29.00
			$3F_2^*$	29.96	30.44
			$2F-2F_2^*$	29.47	29.96
			$4F-F_2^*$	28.98	29.48

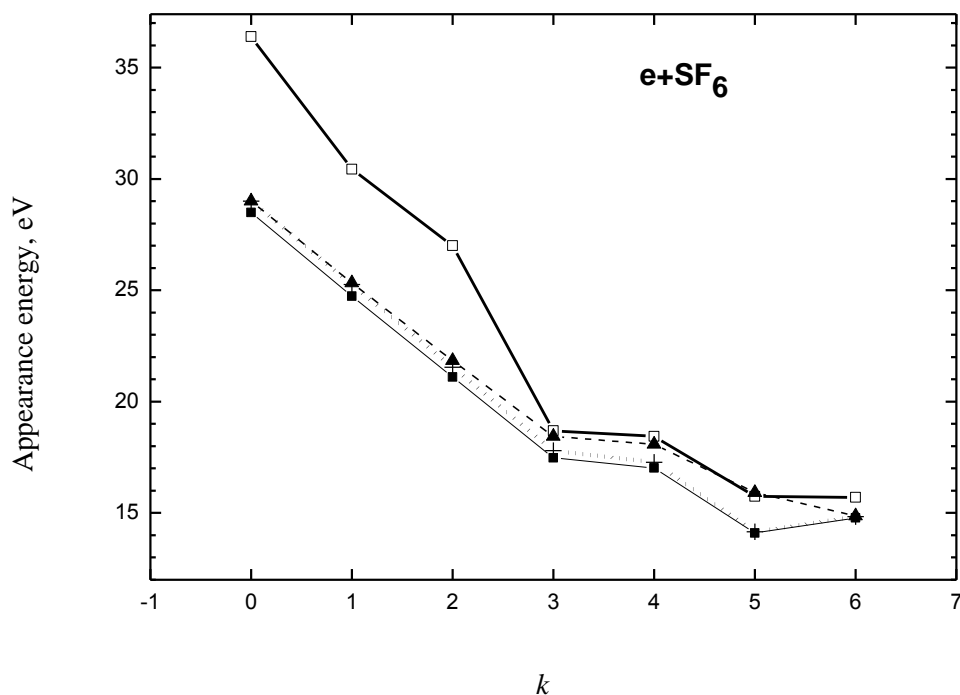


Fig. 1. Appearance energy  $E_{AP}$  of the ionic fragments  $SF_k^+$  as a function of the number  $k$ . Experimental values  $E_{AP}^{exp}$  [2] (□). Adiabatic values  $E_{AP}^{th}$ : B3LYP (■); B3PW91: (+) and (▲, vertical). At  $k=6$  experimental and calculated  $I(SF_6)$ .

### 3. References

- [1] Schmidt M W et al. 1993 *J. Comput. Chem.* **14** 1347.  
 [2] Zaviropulo A N et al 2005 *Pis'ma ZhTF.* **31** 44. (in Russian)

# ELASTIC ELECTRON SCATTERING BY PHOSPHOROUS ATOM IN OPTICAL POTENTIAL APPROACH

Eugene Remeta, Vladimir Kelemen

*Institute of Electron Physics, National Academy of Sciences of Ukraine,  
Uzhgorod, Ukraine*

E-mail: remetov@inbox.ru

Elastic electron scattering on the phosphorous atoms in collision energy range 0.01-200 eV is investigated theoretically for the first time. Integral, differential cross sections and spin exchange asymmetry are calculated in the spin-polarized approximation for the relativistic parameter-free real optical potential. Total and spin electron densities, electrostatic and spin exchange and correlation-polarization potentials for the  $P(3p^3)$  atom are found in the local spin density approximation of density functional theory. Our data compared with data for the neighboring atoms of  $S(3p^4)$ ,  $Cl(3p^5)$  and  $Ar(3p^6)$ .

## 1. Method

Using the optical potential (OP) method we calculate the total and differential cross sections for the elastic electron scattering of the phosphorous –  $P(3p^3\ ^4S)$  atom. Cross sections were compared with similar data for the electron scattering on neighbor atoms, like  $S(3p^4\ ^3P)$ ,  $Cl(3p^5\ ^2P)$ ,  $Ar(3p^6\ ^1S)$ .

The electron's spin on the semi-occupied  $3p^3$ -orbital have the same directions. The electron-shells of this atom could be divided into two occupied spin-orbital – 9 electrons with spin up ( $sp=\uparrow$ ) with density  $\rho_\uparrow(r)$  and 6 electrons with spin down ( $sp=\downarrow$ ) –  $\rho_\downarrow(r)$ . In the spin-polarized approximation (SPA) we have two cases for electron scattering: 1. The directions of spin of the projectile electron and the atom are the same – the scattering with parallel spins ( $\uparrow\uparrow$ , the total spin of the system is 2); 2. The spins have an opposite direction – scattering with antiparallel spins ( $\downarrow\uparrow$ , the total spin is 1). The electron scattering could be describe with the real spin OPs ( $\lambda=\uparrow\uparrow, \downarrow\uparrow$ ), which defined with spin densities  $\rho_\uparrow(r)$  and  $\rho_\downarrow(r)$  from the local spin density approximation [1,2]

$$V_{opt}^\lambda(r, E) = V_S(r) + V_{ex}^\lambda(r, E) + V_{pol}^\lambda(r) + V_R(r, E) + V_{so}^\pm(r) . \quad (1)$$

These OP (1) is the sum of such kind of potentials, like: static  $V_S$ , spin exchange  $V_{ex}^\lambda$  and polarization  $V_{pol}^\lambda$ , relativistic  $V_R$  and spin-orbit interaction  $V_{so}^\pm$ . In the spin-unpolarized approximation (LA) OP determined with total density  $\rho(r)$  from the local density approximation [1,2].

## 2. Results

In various approximations – with (full relativistic) and without (spin-orbit interaction only)  $V_R(r, E)$  potential – thoroughly studied the low-energy features, up to 10 eV, in the integral cross sections. Integral elastic cross sections  $\sigma_{el}(E) = (\sigma_{el}^{\downarrow\uparrow} + \sigma_{el}^{\uparrow\uparrow})/2$  for the  $e+P$  and  $e+Ar$  scattering are compared in fig.1. The behavior of the calculated cross sections for phosphorous – deep Ramsauer–Townsend minima ( $E_{RT}=0.24$  eV,  $\sigma_{RT}=1.3715 \cdot 10^{-20} m^2$ , in full relativistic SPA approach) and maxima ( $E_{max}=8.2$  eV,  $\sigma_{max}=36.976 \cdot 10^{-20} m^2$ ) – agreement qualitatively with the experimental results for argon cross sections. Excluding in (1) the potential  $V_R(r, E)$  leads to the shift of minima to the smaller energies and to smaller values of cross sections for threshold energies.

The energy dependence of the spin exchange asymmetry  $A_{el}(E) = (\sigma_{el}^{\downarrow\uparrow} - \sigma_{el}^{\uparrow\uparrow})/2\sigma_{el}$  is presented in fig.2. There is a significant influence of the relativistic effects to this characteristic at small energies. Near the Ramsauer–Townsend minimum the asymmetry is the greatest –  $\approx 70\%$ .

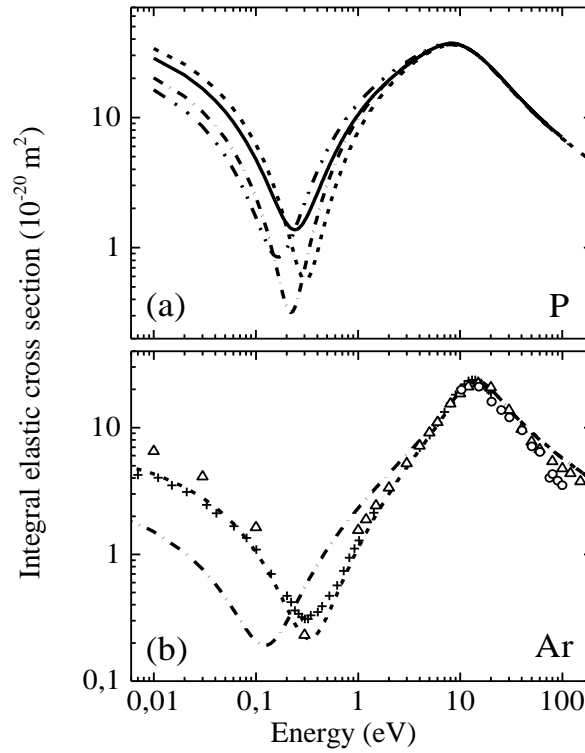


Fig. 1. Integral elastic cross sections for  $e+P$  (a) and  $e+Ar$  (b) scattering. Full relativistic approach: SPA (solid); LA (dashed). Spin-orbit interaction only approach: SPA (dash-dot-dot); LA (dash-dot). Experiment: [3] (+); [4] ( $\Delta$ ); [5] (o).

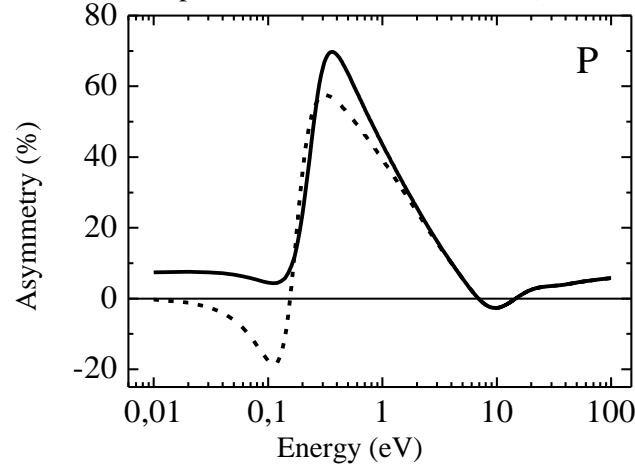


Fig. 2. Spin-exchange asymmetry in elastic  $e+P$  scattering. Full relativistic (solid) and spin-orbit interaction only (dashed) approaches.

### 3. References

- [1] Remeta E Yu and Kelemen V I 2010 *J. Phys. B: At. Mol. Phys.* **43** 045202.
- [2] Kelemen V I and Remeta E Yu 2012 *J. Phys. B: At. Mol. Phys.* **45** 185202.
- [3] Kurokawa M et al. 2011 *Phys. Rev. A* **84** 062717.
- [4] Shimamura I 1989 *Scient. Papers of the Institute of Phys. and Chem. Research* **82** 1.
- [5] Panajotović R. et al. 1997 *J. Phys. B: At. Mol. Opt. Phys.* **30** 5877.

# MASS SPECTROMETRIC STUDIES OF COAL THERMAL DESTRUCTION PRODUCTS

Mykhailo Mykyta, Olha Pylypchynets, Anatoly Zavilopulo

*Institute of Electron Physics, National Academy of Sciences of Ukraine, 88017, Uzhgorod, Ukraine*

E-mail: gzavil@gmail.com

The methods and results of mass-spectrometric studies of gas products of coals thermal destruction by electron impact mass spectrometry are described. Experiment is carried out using a monopole mass spectrometer. The mass spectra of different coal samples over a wide temperature range have been obtained, on the basis of which the temperature dependencies of the ion yields of thermal destruction products of coals have been made.

## 1. Introduction

In recent years there has been an increasing interest towards the fundamental studies of bituminous coal and its conversion processes [1]. Such interest is caused by the better understanding of coal structure and fundamental processes, which occur during its conversion. It is important for the development of new ecologically and economically effective technologies for coal utilization.

The mass spectrometry method is successfully used in studies of different types of complex compound [2], mixtures [3], products of polymerization [4], and polycondensation [5]. It makes possible to obtain extensive information about both qualitative and quantitative composition of different organic compounds.

There are different modifications of mass spectrometric method for high-molecular compounds investigation. One of them refers to the study of thermal decomposition products, as it can be suggested, that thermal destruction products in the high vacuum don't undergo any changes and they preserve the structure, which corresponds to the original molecule.

In this work mass spectrometric studies of coal samples from Donets Basin with various degrees of coalification are represented. The essence of this experimental procedure consists of the following steps: the small quantities of coal samples were being heated in vacuum in a wide range of temperatures, than the gas products of thermal decomposition were being analyzed by an electron impact ionization mass spectrometric setup. Plotting the ion yield intensity depending on the temperature of sample heating was the next stage of our studies. On the one hand, such studies are useful because any processes of coal conversion include the stage of thermal transformations [6]. On the other hand, the products distribution of thermal destruction as a function of temperature gives fundamental information about constituent parts of the coal macromolecule.

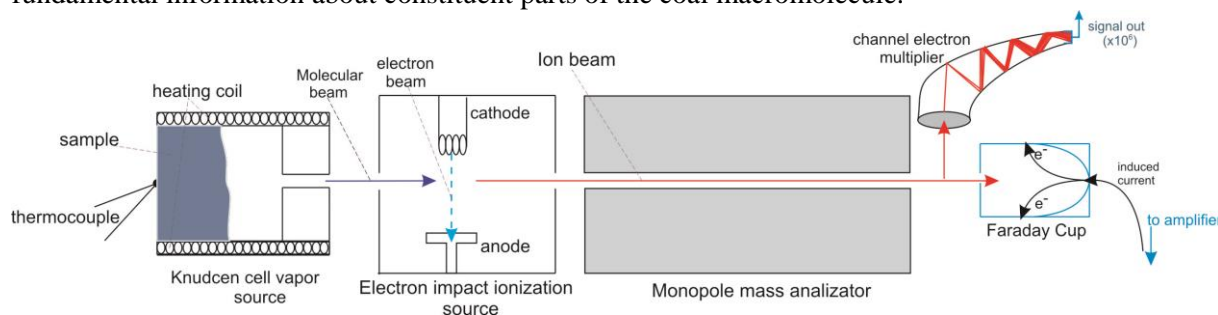


Fig. 1. Схема експериментальної установки.

## 2. Results and Discussion

The experiment was carried out using a setup (fig. 1), which described in detail in the work [7]. The molecular beam of test sample from the effusion source at right angle was sent to the ion source. The heating temperature of effusion source was being fixed by the platinum-rhodium thermocouple. The concentration of investigated molecules in the interaction region with the electron beam was  $10^{10}$

–  $10^{11} \text{ cm}^{-3}$ . Ion source worked in the stabilization regime of ion current and this allowed to get electron beams at a current of  $5.0 \mu\text{A}$  and energy spread  $\Delta E = 200 \text{ meV}$ . Produced ions are sent to the mass analyzer, which was the double-pole mass filter. The ions, whose frequency did not correspond to the frequency of the field that created by the analyzer, were neutralized by rods, but others reached to detector. A secondary-electron multiplier was used to detect ions. The parameters and experiment condition were being controlled by the computer. Calibration of the masses scale was being conducted with the aid of the mass lines of Ar and Xe atoms.

Four coal samples were chosen for the experiment, characteristics of which were given in table 1. Samples were powdered to the size of particles less than  $100 \mu\text{m}$ . The sample placed in the heating camera did not exceed more than 1 gram.

Tab. 1. Characterization of the coal samples.

Sample	Volatile matter (d, %)	Carbon content (d, %)	Combustion heat, (Q, kcal/kg)	Huminite reflectance ( $R_m$ , %)
D (1)	39	76	7500-8000	0,50-064
G (2)	36	83	7900-8600	0,65-0,84
Zh (3)	30	86	8300-8700	0,85-1,14
K (4)	20	88	8400-8700	1,15-1,84

The mass spectra of different coal samples at different temperatures are shown in fig. 2. At the initial stage of heating (Fig. 2a) under the temperature of 300 K the most intense peaks for all coal samples are peaks with mass numbers 14, 16, 18, 28, 32, which correspond to molecules of oxygen, nitrogen and water. The release of the adsorbed gases and adsorbed water from the surface layers of samples occurs at this heating stage. The groups of peaks with different mass numbers are observed for all coal samples with an increase to temperature of 550 K (Fig. 2b). It is explained by the intensive yield of water, CO, CO<sub>2</sub> molecules and nitrogen. The breakup of the organic structure of coal occurs, as evidenced by the peaks, which correspond to such compound as pyrrole ( $m/z$  68), benzene ( $m/z$  78), toluene ( $m/z$  91-92), xylene ( $m/z$  105 - 106), indole ( $m/z$  117), methylnaphthalene ( $m/z$  141 - 142). In the spectra which were obtained at temperature 750 K a complete absence of peaks belonging to aromatic and aliphatic compounds is observed. The peaks of water, carbon dioxide and nitrogen remain intensive. The maximum intensity for these temperatures is the peak which corresponds to the molecular ion of methane which indicates its intensive evolution of this range.

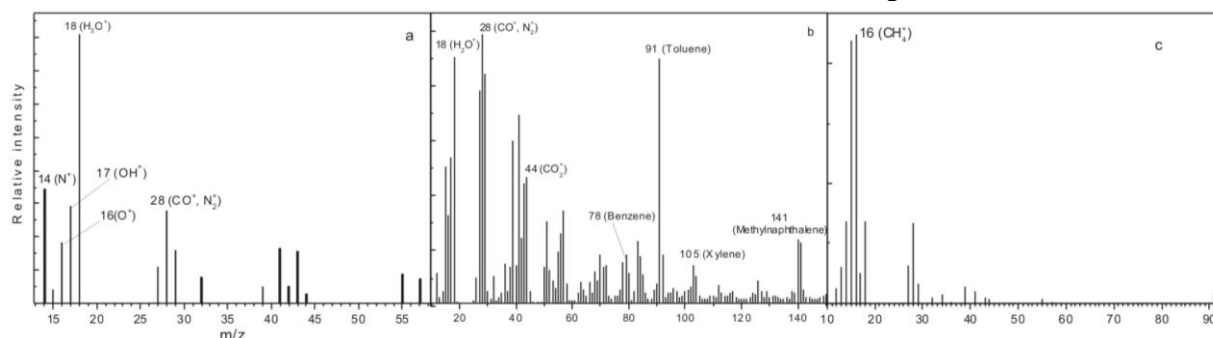


Fig. 2. Electron impact ionization mass spectrum of coal samples: a) sample (1),  $T = 300 \text{ K}$ ; b) sample (4),  $T = 550 \text{ K}$ ; c) sample (3),  $T = 750 \text{ K}$ . Ionization energy  $E_i = 70 \text{ eV}$ .

The collection of mass spectra obtained by us with a temperature step of  $10 \text{ K/min}$  made it possible to construct the temperature dependences of the characteristic ion yields. The temperature dependences of the molecular ion yields of such compound as  $\text{CH}_4^+$ ,  $\text{NO}^+$  and  $\text{HCN}^+$  are shown in Fig. 3. These compounds are the main pollutants of environment during the combustion of coal and are the major components of greenhouse gases [8]. As can be seen in Fig. 3., the ion yields methane ( $\text{CH}_4$ ) and nitrogen oxide (NO) initiated at temperature of about  $550 \text{ K}$ , which is common to all samples involved in the test. The peak of ion yield of methane is wider and reaches a maximum at  $T = 700 - 750 \text{ K}$  in contrast to the nitrogen oxide, which peaks at  $T = 650 - 700 \text{ K}$ . The temperature kinetics of

hydrogen cyanide (HCN) ions are little different from those of previous compounds. Specifically, the temperature range of this compound yield is wide and within the limits from 450 to 900 K peaked at 650 – 750 K.

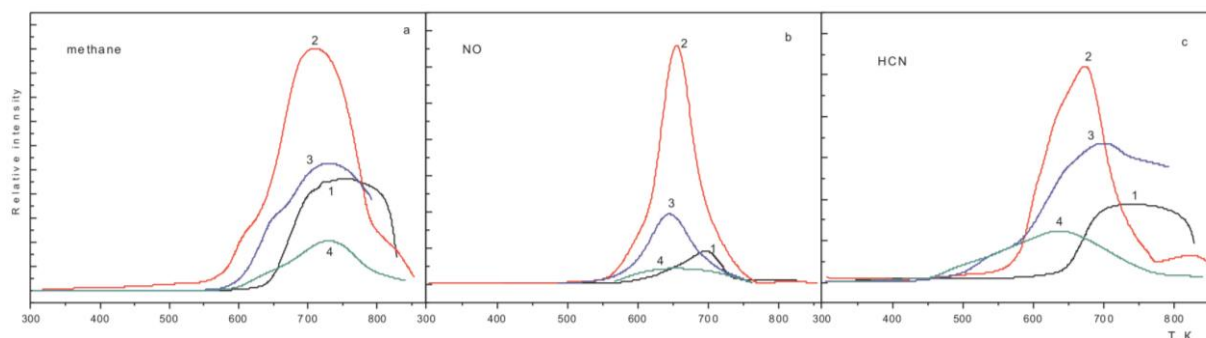


Fig. 3. Temperature dependent of ions intensity for different coal samples: a) methane ( $\text{CH}_4$ ); b) nitrogen oxide NO; c) hydrogen cyanide HCN.

Hence the inspection of mass spectra of the coal thermal decomposition shows that the use of an electron impact mass spectrometry to study such processes. Such studies are informative and make it possible to investigate both the qualitative and quantitative composition of the products of coal thermal destruction. With their aid it is possible to determine the temperature range which the yields of main components of the greenhouse gasses are most intense.

### 3. References

- [1] James G. Speight, *The chemistry and technology of coal*, CRC Press, Boca Raton, 2013, p. 835.
- [2] Shigeo Hayakawa, [Fundamentals of Mass Spectrometry](#), Springer, New York, 2013, p. 239.
- [3] [Fanyu Meng](#) et al., 2007 *Journal of the American Society for Mass Spectrometry*, **18**, 2, 226.
- [4] Soeriyadi, A. H., R. Whittaker, M., Boyer, C. and Davis, T. P. 2013 *J. Polym. Sci. A Polym. Chem.*, **51**: 1475–1505.
- [5] Biasone A, Cianci G, Di Tommaso D, Piaggese A, Tagliavini E, Galletti P, Moretti F., 2013 *J Chromatogr A*. 1282:142-52.
- [6] Guo Z. 1992 *Chemistry of Coal*, Chemical Industry Press, Beijing, p. 149.
- [7] A. N. Zaviropulo, M. I. Mykyta, A. N. Mylymko, and O. B. Shpenik 2013, *Technical Physics*, Vol. 58, No. 9, pp. 1251.
- [8] Whitaker, M., Heath, G. A., O'Donoghue, P. and Vorum, M. 2012 *Journal of Industrial Ecology*, **16**: S53–S72.



# CLASSIFICATION OF LOW-ENERGY CORE EXCITED AUTOIONIZING STATES IN BARIUM

Vasil Hrytsko<sup>1</sup>, Pavlo Markush<sup>1</sup>, Alicija Kupliauskiene<sup>2</sup>, Alexander Borovik<sup>1</sup>

<sup>1</sup>*Institute of Electron Physics, Uzhhorod 88017, Ukraine*

<sup>2</sup>*Institute of Theoretical Physics and Astronomy, Vilnius University, Vilnius, LT-01108, Lithuania*

E-mail: shargov11@gmail.com

Ejected-electron spectra of barium atoms were measured at incident electron energies from 18 to 42 eV, an observation angle of 54.7° and ejected-electron energy resolution of 0.12 eV. Using the results of theoretical calculation, 12 lines were identified with multichannel electron decay of the lowest states in  $5p^56s^25d$  configuration.

## 1. Ejected-electron spectra

Spectroscopic classification of core-excited autoionizing states (AIS) in barium is complicated by overlapping of ejected-electron lines arising from the decay of atomic  $5p^5n_1l_1n_2l_2n_3l_3$  and ionic  $5p^5n_1l_1n_2l_2$  states [1, 2]. In the present work, we attempted to solve this problem by studying the excitation dynamics of ejected-electron spectra at low impact energies and by performing the calculations of energies and decay probabilities for atomic and ionic AIS.

The ejected-electron spectra of barium atoms were measured by using an electron spectrometer consisted of monochromator of the incident electron beam, an ejected-electron analyser (both of 127° electrostatic type) and resistively heated atomic beam source. The measurements were performed with an incident electron energy resolution of 0.2 eV and ejected-electron energy resolution of 0.12 eV [3]. The ejected-electron spectra were measured at an observation angle of 54.7° for impact energy values between 18 and 42 eV.

Figure 1 shows the ejected-electron spectrum obtained in the electron energy range of 9.8-13.7 eV at impact energy value of 19.5 eV. The latter is below of the lowest excitation threshold for the  $5p^5n_1l_1n_2l_2$  ionic AIS at ~21 eV [2]. In total, 42 lines were observed in spectra. The uncertainty of the ejected-electron energy scale was determined at  $\pm 0.05$  eV.

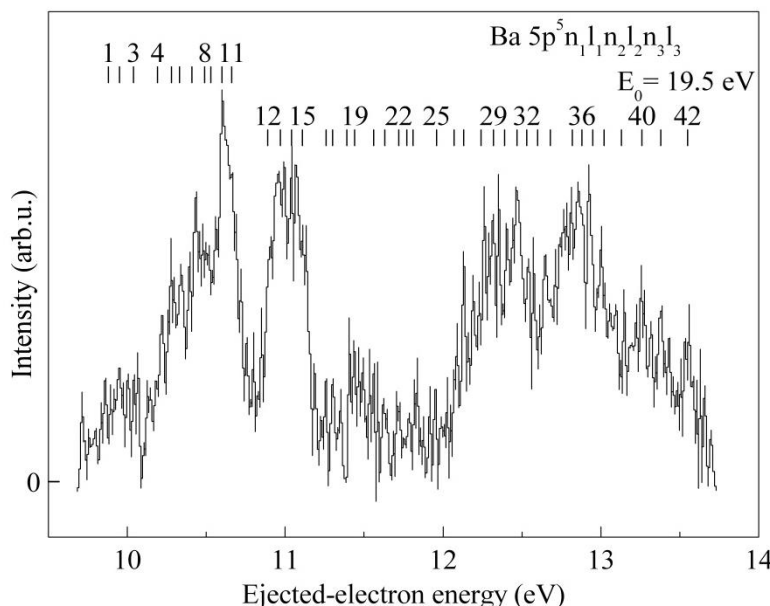


Fig. 1. Ejected-electron spectrum of barium atoms at impact energy of 19.5 eV. The spectrum has been flattened by subtracting a nonlinear background function.

## 2. Classification of lines

The excitation energies, electron-impact excitation cross sections and autoionization probabilities for Ba and Ba<sup>+</sup> levels were calculated in configuration interaction approximation by using numerical solutions of Dirac-Fock-Slater equations [4]. In the case of Ba<sup>+</sup>, the singly excited 5p<sup>6</sup>nl (n = 6,..., 12; l = 0, 1, 2; nl = 4f, 5f) and core-excited 5p<sup>5</sup>nln'l' (n = 6,...,7; l = 0, 1, 2, 3; n' = 6,...,11; l' = 0, 1, 2, 3) configurations were used to take into account the correlation effects. The total number of levels was 12485. The calculations of the spectroscopic parameters for 5p-core excited Ba was more complicated due to the existence of the autoionizing states 5p<sup>6</sup>nln'l' lying below 5p<sup>5</sup>nln'l'n''l'' states. For the correlation effects arising from the singly excited and autoionizing states the configurations 5p<sup>6</sup>nln'l' (n = 6, 7; l = 0, 1, 2; nl = 4f; n' = 6,...,9; l' = 0, 1, 2; n'l' = 5f, 6f, 7f, 5g) were used. The basis of core-excited states consisted of the configurations 5p<sup>5</sup>nln'l'n''l'' (nl = 6s, 6p, 5d, 6d, 5f; n'l' = 6s, 7s, 6p, 7p, 5d, 6d, 4f, 5f; n''l'' = 6s, 7s, 8s, 6p, 7p, 8p, 5d, 6d, 5f, 6f, 5g). The total number of states was 40937.

By using the calculated data on energies and decay probabilities, 12 lines were identified with multichannel electron decay of the 5p<sup>5</sup>6s<sup>2</sup>5d states. Table 1 presents these data. Comparing the data in table 1 and figure 1 shows that the <sup>3</sup>P<sub>0</sub>, <sup>3</sup>P<sub>1</sub>, <sup>3</sup>P<sub>2</sub>, <sup>3</sup>F<sub>3</sub>, <sup>3</sup>D<sub>2</sub>, <sup>1</sup>D<sub>2</sub> states possess the largest excitation efficiency in the whole impact energy region studied. The preferable decay channels are the transitions into 5p<sup>6</sup>6s and 5p<sup>6</sup>5d Ba<sup>+</sup> states.

The rest of the observed lines (30) could be preliminary assigned with multichannel decay of the states from 5p<sup>5</sup>5d<sup>2</sup>6s configuration which is located in the same energy region. To establish more accurately the excitation thresholds of these states, the further measurements will be performed at electron impact energies below 18 eV.

Table 1. Experimental and calculated excitation energies  $E_{ex}$ , spectroscopic classification, decay channels and autoionization probabilities  $A^a$  for (5p<sup>5</sup>6s<sup>2</sup>5d) *LSJ* autoionizing states in barium atoms.

Line	$E_{ej}$ , eV	$E_{ex}$ , eV		State	Decay channel	$A^a$ , s <sup>-1</sup>
		Experiment	Theory			
7	10.41	15.62	15.77	<sup>3</sup> P <sub>0</sub>	5p <sup>6</sup> 6s <sup>2</sup> S <sub>1/2</sub>	2.90+13 <sup>a</sup>
10	10.60	15.81	16.00	<sup>3</sup> P <sub>1</sub>	5p <sup>6</sup> 6s <sup>2</sup> S <sub>1/2</sub>	2.60+13
12	10.89	16.10	16.41	<sup>3</sup> P <sub>2</sub>	5p <sup>6</sup> 6s <sup>2</sup> S <sub>1/2</sub>	2.01+13
6	10.33			---	5p <sup>6</sup> 5d <sup>2</sup> D <sub>3/2</sub>	9.92+11
14	11.04	16.25	16.43	<sup>3</sup> F <sub>4</sub>	5p <sup>6</sup> 6s <sup>2</sup> S <sub>1/2</sub>	4.23+13
6	10.33			---	5p <sup>6</sup> 5d <sup>2</sup> D <sub>5/2</sub>	4.07+12
15	11.11	16.32	16.56	<sup>3</sup> F <sub>3</sub>	5p <sup>6</sup> 6s <sup>2</sup> S <sub>1/2</sub>	3.02+13
9	10.53			---	5p <sup>6</sup> 5d <sup>2</sup> D <sub>3/2</sub>	3.72+12
7	10.41			---	5p <sup>6</sup> 5d <sup>2</sup> D <sub>5/2</sub>	9.59+10
16	11.26	16.47	16.89	<sup>3</sup> F <sub>2</sub>	5p <sup>6</sup> 6s <sup>2</sup> S <sub>1/2</sub>	1.54+13
38	13.13	18.34	18.19	<sup>3</sup> D <sub>1</sub>	5p <sup>6</sup> 6s <sup>2</sup> S <sub>1/2</sub>	3.67+13
42	13.55	18.76	18.84	<sup>3</sup> D <sub>2</sub>	5p <sup>6</sup> 6s <sup>2</sup> S <sub>1/2</sub>	1.61+13
36	12.94			---	5p <sup>6</sup> 5d <sup>2</sup> D <sub>3/2</sub>	4.97+11
41	13.38	19.19	18.98	<sup>1</sup> D <sub>2</sub>	5p <sup>6</sup> 5d <sup>2</sup> D <sub>3/2</sub>	3.26+10
42	13.55	19.36	19.11	<sup>1</sup> F <sub>3</sub>	5p <sup>6</sup> 5d <sup>2</sup> D <sub>3/2</sub>	4.38+10

<sup>a</sup> 2.90+13 implies 2.90×10<sup>13</sup>

### 3. References

- [1] D Rassi and K J Ross 1980 *J. Phys. B* **13** 4683.
- [2] A A Borovik et.al. 1985 *Opt. Spektrosc.* **58** 988.
- [3] A Borovik et.al 2005 *J. Phys. B* **38** 1081.
- [4] M F Gu 2008 *Can. J. Phys.* **86** 675.

# EXCITATION OF SELENIUM IN GAS-PHASE BY ELECTRON IMPACT

Mykola Erdevdy, Pavlo Markush, Otto Shpenik, Vitalij Zvenihorodsky

*Institute of Electron Physics, Ukrainian National Academy of Sciences,  
21 Universitetska str. Uzhgorod 88017, Ukraine*

E-mail: 1988.markus@gmail.com

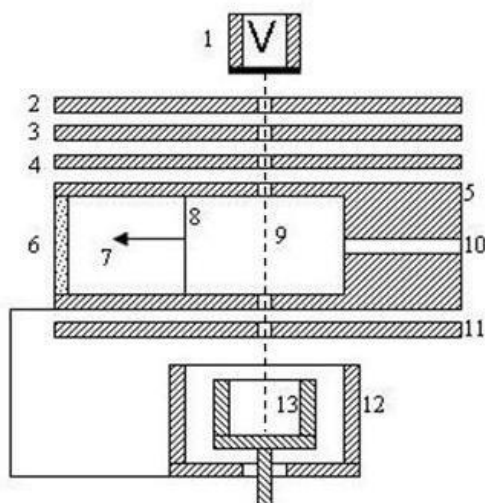
Using an optical spectroscopy method, slow electron excitation of selenium in the gas-phase has been studied. Experiment was carried out applying a gas-filled cell at the incident electron current of 25  $\mu\text{A}$  (the energy spread being 0.4 eV) provided by a four-electrode gun with an oxide cathode. The emission spectrum of selenium was recorded in the wavelength range between 200-600 nm at the incident electron energy of 50 eV. The optical excitation functions for the most intense spectral band  $\lambda_{\text{max}}=383$  nm and line  $\lambda_{\text{max}}=473$  nm have also been measured.

## 1. Introduction

Selenium is a non metallic chemical element, which has good photovoltaic and photoconductive properties, extensively used in electronics, such as photocells, light meters and solar cells. Selenium is well known to tend to form molecules  $\text{Se}_n$  ( $n=1-8$ ) during its evaporation, in addition the concentration of different species heavily depends on the temperature [1]. There have been few works carried out studying the emission spectrum of selenium in gas phase. The aim of this work is to investigate the electron-impact excitation of the gas-phase selenium.

## 2. Experiment

Experiment was carried out using a gas-filled cell at the incident electron current of 25  $\mu\text{A}$  provided by a four-electrode gun with an oxide cathode (Fig. 1) [2]. A container with the crystalline selenium was placed in a close proximity to the cell provided with direct heating. In all our measurements, the container temperature was maintained within the 160-180  $^{\circ}\text{C}$  range. To prevent selenium condensation on the electron gun and collision cell elements their temperature was kept 20-30  $^{\circ}\text{C}$  above that of the selenium container. The residual gas pressure in the vacuum chamber under operating conditions did not exceed  $10^{-6}$  Torr. A collimated electron beam (2 mm in diameter, within the energy range 1-50 eV) passed the vapor-filled cell and was detected by a deep Faraday cup. The instability of the electron current having passed the collision chamber did not exceed 3%. The electron beam energy spread in vacuum was 0.4 eV (full width at half-maximum of the differentiated current-voltage characteristic). When measuring the optical excitation functions the electron energy was varied with 200 meV step. Radiation selected by a diffraction monochromator MDR-2 was detected by a



1-oxide cathode, 2-first anode, 3-second anode, 4-third anode, 5-fourth anode, 6-quartz window for transmitting radiation, 7-direction of radiation to the spectral device, 8-area of the collision of molecules with electrons, 9-electrons trajectory, 10-intake of the vapour of investigated molecules, 11-hold back anode, 12, 13-external and internal (Faraday cup) cylinders.

Fig. 1. The layout of a four-electrode gun.

FEU-106 photomultiplier. The single photo-electron pulses from photomultiplier were amplified, shaped by a wideband amplifier-discriminator and entered the pulse counter via the PC interface card. In order to maintain the accuracy of measurements, when the statistical scatter of the pulses did not exceed 5-10%, the accumulation of signal at each point was carried out with an exposure of 10 to 40 s. The emission spectrum in the 200-600 nm spectral region was measured with an 1 mm wide monochromator slit (i.e.  $\Delta\lambda=2$  nm) at fixed electron energy of 50 eV. The spectrum was measured with a modulated electron beam, i.e. the cathode radiation was subtracted from the total signal with no taking into account the spectral sensitivity of the photomultiplier and the spectral transmission characteristics of the monochromator. For better visibility, the emission spectrum and the optical excitation functions (OEFs) in figures 2 and 3 are represented by solid lines connecting discrete experimental points. For correct interpretation of the results of measurements, calibration of the energy scale of the incident electron beam is an essential problem. Calibration was carried out with respect to the shift of the voltage dependence of electron current onto the collector.

### 3. Results and discussion

Fig. 2 shows the emission spectrum of selenium measured in the wavelength range between 200-600 nm at the incident electron energy of 50 eV. The spectrum appears to be continuous in the 300-600 nm region in addition a number of spectral lines can be observed. The continuous emission is caused by the excitation of selenium molecules ( $\text{Se}_2\text{-Se}_8$ ) produced during evaporation. Narrow spectral lines with the maxima at 432.8, 473.0/473.9, 536.5/537.8 nm were identified as spectral lines of the atomic selenium as well as those in the ultraviolet region of spectrum at 207.4, 216.4 and 226 nm.

Fig. 3 shows the optical excitation functions (OEFs) for the band  $\lambda_{\text{max}}=383$  nm and line  $\lambda_{\text{max}}=473$  nm. The 383 nm band excitation threshold energy was determined to be  $3\pm0.3$  eV, furthermore three features were revealed at 4, 9.5 and 15 eV. The 473 nm spectral line excitation threshold energy was determined to be  $4\pm0.3$  eV and some features were found at 12.6, 18 and 26 eV.

This work has been supported by the Collegium Talentum grant.

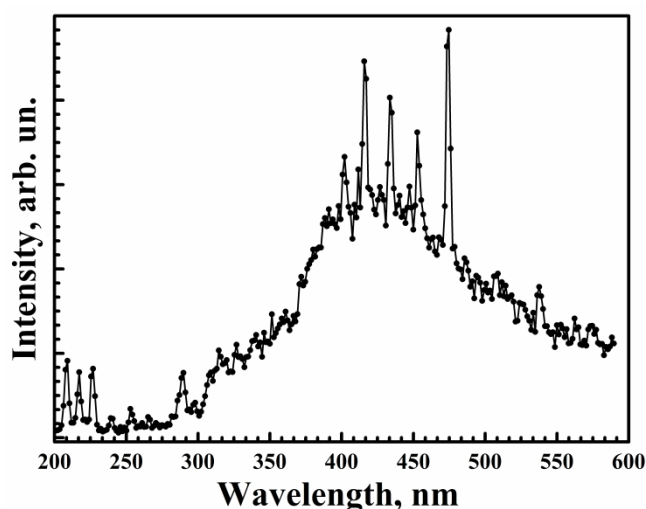
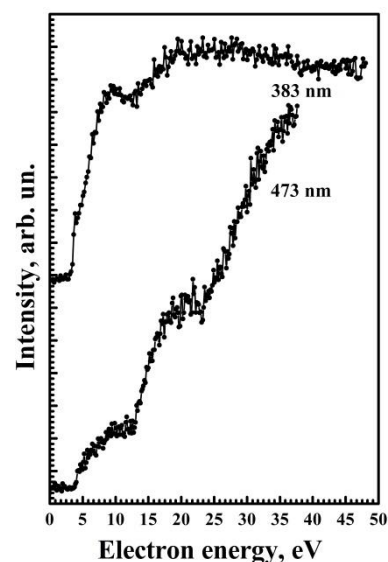


Fig. 2. Selenium emission spectrum.

Fig. 3. OEFs of the spectral band  $\lambda_{\text{max}}=383$  nm and line  $\lambda_{\text{max}}=473$  nm.

### 4. References

- [1] Berkowitz J and Chupka W A 1968 *J. CHEM. PHYS.* **48** 5743.
- [2] Shpenik O B, Erdevdy N M, Zvenigorodsky V V and Romanova L G 2013 *Journal of Applied Spectroscopy.* **80** 46.

# EXCITATION OF SULPHUR BY SLOW ELECTRONS

Mykola Erdevdy, Otto Shpenik, Pavlo Markush, Vitalij Zvenihorodsky

*Institute of Electron Physics, Ukrainian National Academy of Sciences,  
21 Universitetska str. Uzhgorod 88017, Ukraine*

E-mail: 1988.markus@gmail.com

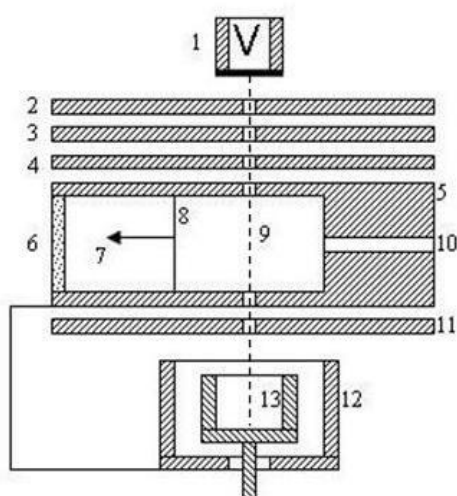
Using an optical spectroscopy method, slow electron excitation of sulphur in the gas-phase has been studied. Experiment was carried out applying a gas-filled cell at the incident electron current of 25  $\mu\text{A}$  (the energy spread being 0.4 eV) provided by a four-electrode gun with an oxide cathode. The emission spectrum of sulphur was recorded in the wavelength range between 270-550 nm at the incident electron energy of 50 eV. The optical excitation functions for the most intense spectral band  $\lambda_{\text{max}}=376$  nm and line  $\lambda_{\text{max}}=528$  nm have also been measured.

## 1. Introduction

Sulphur is an important element both scientifically and industrially. In astrophysics, neutral sulphur emissions have been observed from comets and its absorption lines occur in the interstellar medium toward  $\zeta$  Oph [1]. Sulphur is well known to tend to form molecules  $\text{S}_n$  ( $n=1-8$ ) during its evaporation, in addition the concentration of different species heavily depends on the temperature [2]. Perhaps it is the reason why there are so few works carried out studying its emission spectrum. The aim of this work is to investigate the electron impact excitation of sulphur in the gas phase.

## 2. Experiment

Experiment was carried out using a gas-filled cell at the incident electron current of 25  $\mu\text{A}$  provided by a four-electrode gun with an oxide cathode (Fig. 1) [3]. A container with the crystalline sulphur was placed in a close proximity to the cell provided with direct heating. In all our measurements, the container temperature was maintained within the 50-60  $^{\circ}\text{C}$  range. To prevent sulphur condensation on the electron gun and collision cell elements their temperature was kept 20-30  $^{\circ}\text{C}$  above that of the sulphur container. The residual gas pressure in the vacuum chamber under operating conditions did not exceed  $10^{-6}$  Torr. A collimated electron beam (2 mm in diameter, within the energy range 0-30 eV) passed the gas-filled cell and was detected by a deep Faraday cup. The instability of the electron current having passed the collision chamber did not exceed 3%. The electron beam energy spread in vacuum was 0.4 eV (full width at half-maximum of the differentiated current-voltage characteristic). When measuring the optical excitation functions the electron energy was varied with 200 meV step. Radiation selected by a diffraction monochromator MDR-2 was detected by a



1-oxide cathode, 2-first anode, 3-second anode, 4-third anode, 5-fourth anode, 6-quartz window for transmitting radiation, 7-direction of radiation to the spectral device, 8-area of the collision of molecules with electrons, 9-electrons trajectory, 10-intake of the vapour of investigated molecules, 11-hold back anode, 12, 13-external and internal (Faraday cup) cylinders.

Fig. 1. The layout of a four-electrode gun.

FEU-106 photomultiplier. The single photo-electron pulses from photomultiplier were amplified, shaped by a wideband amplifier-discriminator and entered the pulse counter via the PC interface card. In order to maintain the accuracy of measurements, when the statistical scatter of the pulses did not exceed 5-10%, the accumulation of signal at each point was carried out with an exposure of 10 to 40 s. The emission spectrum in the 270-550 nm spectral region was measured with an 1 mm wide monochromator slit (i.e.  $\Delta\lambda=2$  nm) and at fixed electron energy of 50 eV. The spectrum was measured with a modulated electron beam, i.e. the cathode radiation was subtracted from the total signal with no taking into account the spectral sensitivity of the photomultiplier and the spectral transmission characteristics of monochromator. For better visibility, the spectrum and optical excitation functions (OEFs) in figures 2 and 3 are represented by solid lines connecting discrete experimental points. For correct interpretation of the results of measurements, calibration of the energy scale of the incident electron beam is an essential problem. Calibration was carried out with respect to the shift of the voltage dependence of electron current onto the collector.

### 3. Results and discussion

The emission spectrum of sulphur was measured in the wavelength range between 270-550 nm at the incident electron energy of 50 eV (Fig. 2). The spectrum appears to be continuous being caused by the excitation of the vibrational and electronic energy levels of the sulphur molecules  $S_n$  ( $n=2-8$ ). However, the spectral lines as well as the bands can also be observed in the spectrum. The spectral lines are probably formed due to the decay of the excited levels of both sulphur atoms and ions.

Fig. 3 shows the optical excitation functions for the band  $\lambda_{\max}=376$  nm and line  $\lambda_{\max}=528$  nm. The 376 nm band excitation threshold energy was determined to be  $4\pm0.3$  eV, three features were revealed at 5, 10 and 19.5 eV. The 528 nm spectral line excitation threshold energy was determined to be  $15\pm0.3$  eV with further smooth curve rise. One may conclude that the experimental approach used in this study made it possible to obtain the new data on the electron impact excitation of sulphur.

This work has been supported by the Collegium Talentum grant.

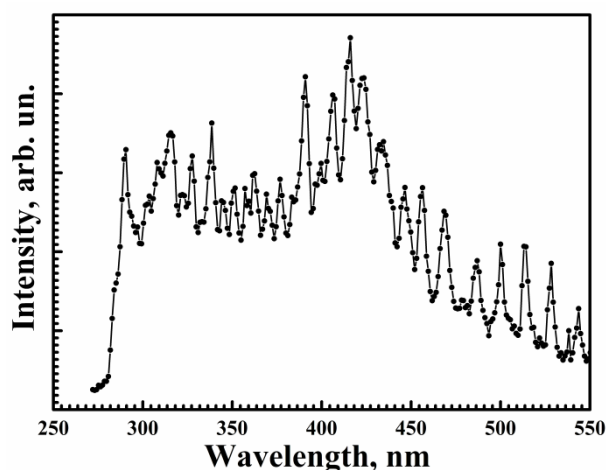


Fig. 2. Sulphur emission spectrum.

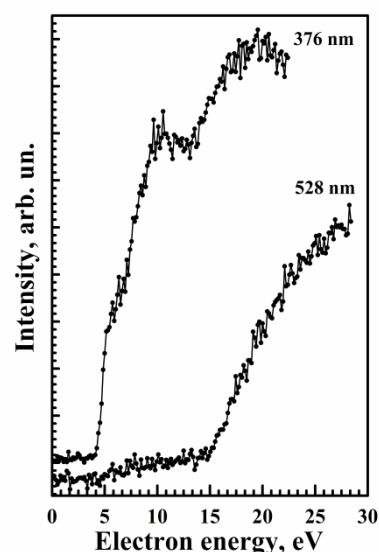


Fig. 3. OEFs of the spectral band  $\lambda_{\max}=376$  nm and line  $\lambda_{\max}=528$  nm.

### 4. References

- [1] Federman S R and Cardelli J A 1995 *Astrophys J.* **452** 269.
- [2] Meyer B 1976 *Chem. Rev.* **76**(3) 367.
- [3] Shpenik O B, Erdevdy N M, Zvenihorodsky V V and Romanova L G 2013 *Journal of Applied Spectroscopy.* **80** 46.

# DISSOCIATIVE ELECTRON ATTACHMENT TO VOLATILE ANAESTHETICS AND CHLORINATED ETHANES

C. Matias<sup>1</sup>, A. Mauracher<sup>1</sup>, S. E. Huber<sup>1</sup>, S. Denifl<sup>1</sup>, P. Limão-Vieira<sup>1,2</sup>, R. González-Méndez<sup>3</sup>, P. Watts<sup>3</sup>, C. A. Mayhew<sup>3</sup>

<sup>1</sup> *Institut für Ionenphysik und Angewandte Physik, Universität Innsbruck, Technikerstraße 25, A-6020 Innsbruck, Austria*

<sup>2</sup> *School of Physics and Astronomy, University of Birmingham, Edgbaston, Birmingham B15 2TT, UK*

<sup>3</sup> *Laboratório de Colisões Atômicas e Moleculares, CEFITEC, Departamento de Física, Faculdade de Ciências e Tecnologia, Universidade Nova de Lisboa, 2829-516 Caparica, Portugal*

E-mail: Carolina.Matias@uibk.ac.at

Negative ion formation upon dissociative electron attachment (DEA) to gas-phase volatile anaesthetics, enflurane and isoflurane ( $\text{C}_3\text{H}_2\text{ClF}_5\text{O}$ ), and chlorinated ethanes, pentachloroethane ( $\text{C}_2\text{HCl}_5$ ) and hexachloroethane ( $\text{C}_2\text{Cl}_6$ ), was studied using a crossed electron-molecular beam experiment. Anion efficiency curves for several negatively charged fragments were measured in the electron energy region from about 0–17 eV with an energy resolution of  $\sim 1$  eV. Regarding the volatile anaesthetics, product anions were observed mainly in the 2–3 eV and 9 eV energy regions with the exception of  $\text{Cl}^-$  showing a feature at approximately 0.9 eV. For the chlorinated ethanes, resonance features are generally found at  $\sim 0$  eV and at 7.5 eV

## 1. Introduction

The present work represents a study of negative ion formation upon dissociative electron attachment (DEA) to gas-phase volatile anaesthetics, enflurane ( $\text{CHFCl}-\text{CF}_2-\text{O}-\text{CF}_2$ ) and its isomer isoflurane ( $\text{CF}_3-\text{CHCl}-\text{O}-\text{CHF}_2$ ) and chlorinated ethanes, pentachloroethane ( $\text{C}_2\text{HCl}_5$ ) and hexachloroethane ( $\text{C}_2\text{Cl}_6$ ). These studies were performed using a crossed electron-molecular beam setup equipped with a double focusing two-sector field mass spectrometer with a standard Nier-type ion source.

Although isoflurane and enflurane are known to belong to the halogenated ether compounds which had extended use in medical applications, in particular inhalational anaesthesia, in this work the study of such compounds lies on the interest of knowing their potential use as dopants in ion mobility spectrometry (IMS). The same motive is behind the study of the chlorinated ethanes.

Dopants are commonly used in IMS, to enhance sensitivity and/or selectivity. The dopant is typically a molecule with a high electron detachment energy, which is the case for halogens and it will preferentially ionise the compound in study, blocking possible interferences. To understand the role dopants play in the ion-molecule chemistry occurring in IMS systems it is important to have a knowledge of the electron attachment properties. In particular, an understanding of the electron attachment processes will provide information as to whether a molecule will be a good candidate as a dopant.

## 2. Results and discussion

Figure 1 shows the negative ion mass spectra of isoflurane and enflurane measured at 0.9 eV electron energy. Although isoflurane and enflurane are isomers, they exhibit different DEA patterns. The formation of  $\text{Cl}^-$  upon DEA is the most abundant fragment anion for both molecules, however when DEA is performed at electron energies of 0.9 eV, fragments such as  $\text{C}_3\text{HClF}_4\text{O}^-$ ,  $\text{C}_2\text{H}_2\text{F}_3^-$  and  $\text{ClFH}^-$ , observed for enflurane, are not present in the case of isoflurane.

Figure 2 shows the negative ion formation of pentachloroethane and hexachloroethane at  $\sim 0$  eV, where  $\text{Cl}^-$  shows the highest anionic signal. The second most intense signal is assigned to  $\text{Cl}_2^-$ . Other reactions like the loss of several other neutral units with an onset of the resonant ionic yields at zero energy are observed as well.



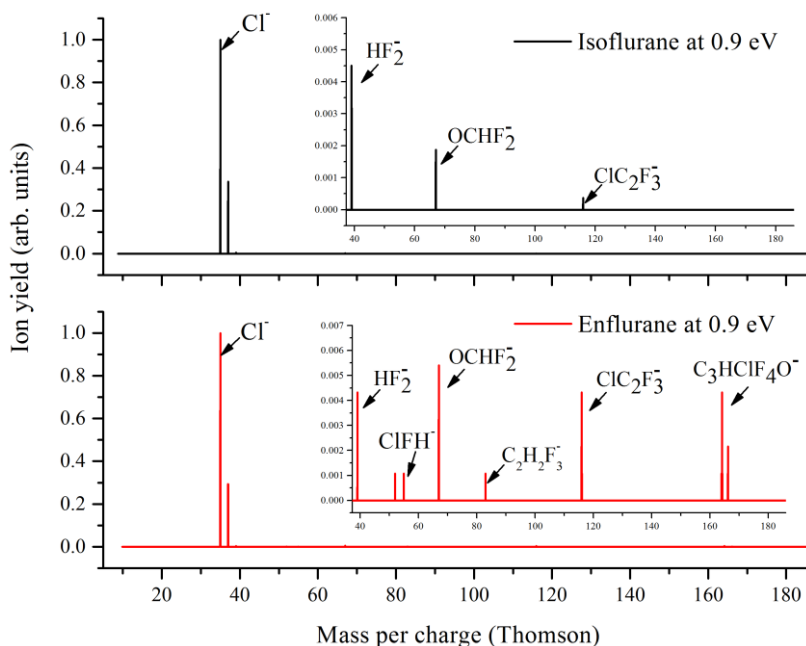


Fig. 1. mass Negative ion spectrum of isoflurane (upper panel) and enflurane (lower panel) measured at 0.9 eV electron energy. For a better comparison both graphs were normalised to the highest signal ( $\text{Cl}^-$ ).

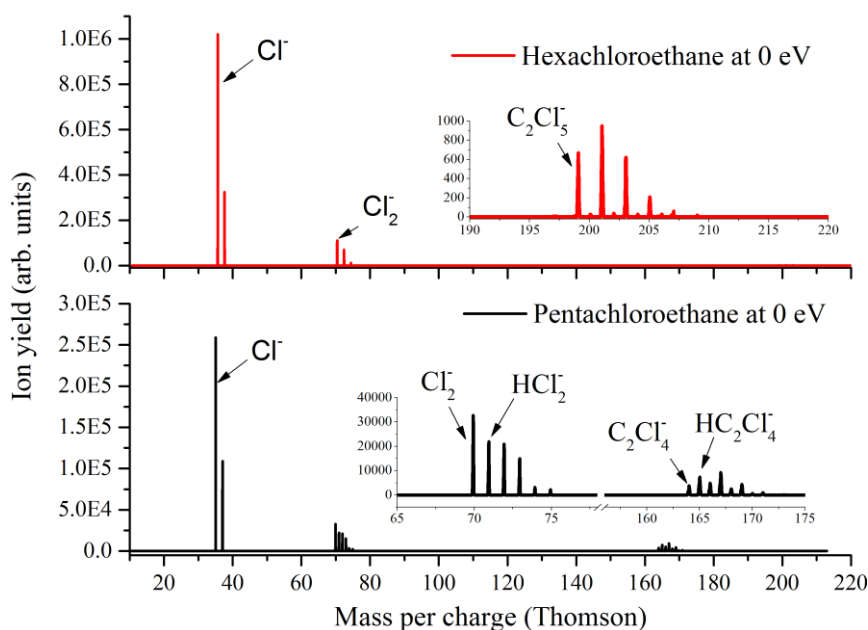


Fig. 2. Negative ion mass spectrum of pentachloroethane (upper panel) and hexachloroethane (lower panel) measured at ~0 eV electron energy.

Anion efficiency curves for the negatively charged fragments have also been measured in the electron energy region 0–17 eV with an energy resolution of ~1 eV. Regarding the volatile anaesthetics, the product anions are mainly observed in the 2–3 eV and 9 eV energy regions with the exception of  $\text{Cl}^-$ , which shows a strong feature at around 0.8 eV. Only in the case of isoflurane it is possible to detect a dehydrogenated parent anion. For the chlorinated ethanes, the product anions are mainly formed around 0 eV and 7.5 eV.

From these DEA studies it seems reasonable to say that some of the compounds under consideration can be used as dopants in ion mobility spectrometry (IMS). In order to probe the role of such chemical compounds, we have started experimental work on IMS.

### **3. Acknowledgments**

This work has been supported by the Austrian Science Fund (FWF Project No. 22665). The funding of the Early Stage Researcher (RGM) was supported through the PIMMS Initial Training Network which in turn is supported by the European Commission's 7th Framework Programme under Grant Agreement Number 287382. This work was supported by the Austrian Ministry of Science BMWF as part of the UniInfrastrukturprogramm of the Focal Point Scientific Computing at the University of Innsbruck. AM acknowledges a grant from the Nachwuchsförderung of the University of Innsbruck. SEH gratefully acknowledges funding from the Austrian Science Fund (FWF) DK+ project Computational Interdisciplinary Modeling, W1227-N16. PLV acknowledges the Portuguese Foundation for Science and Technology (FCT-MEC) for partial funding from the research grant PTDC/FIS-ATO/1832/2012.

# EXPERIMENTAL (e,2e) STUDY OF STATE-TO-STATE INTERFERENCE BETWEEN AUTOIONIZING STATES OF He

Béla Paripás, Béla Palásthy, Gábor Pszota

*Inst. of Physics, University of Miskolc, 3515 Miskolc-Egyetemváros, Hungary*  
E-mail: fizpari@uni-miskolc.hu

We have studied the interference of two autoionizing resonances decaying to a common final ionic state. Our method is based on the selective detection of electron pairs related to the selected final state. We have performed a constant ionic state (e,2e) experiment (CIS), isolating the final state by keeping the sum of transmission energies of two independent electron spectrometers constant. In the focus of this work are the exchange interference effects of  $2s^2(^1S)$  and  $2p^2(^1D)$  autoionizing states of helium decaying to the  $\text{He}^+1s^{-1}$  final ionic state with energy  $E_F = 24.6$  eV. Around the critical energy, a few tenths of eV modification in primary energy causes a significant change in the CIS spectra, which indicates the presence of exchange interference effects.

## 1. Method

Two autoionizing resonances ( $R'$  and  $R''$ ) with a common final ionic state ( $F$ ) can be made to interfere at a given electron impact energy. The atomic ground state  $G$  is excited by electron impact:

$$\begin{aligned} G(0) + e(E_0) &\rightarrow R'(E_{R'}) + e_{s'} \rightarrow F(E_F) + e_{s'} + e_{a'} \\ &\rightarrow R''(E_{R''}) + e_{s''} \rightarrow F(E_F) + e_{s''} + e_{a''} \end{aligned}$$

Electron pairs are observed in coincidence by two electron spectrometers, and the interference condition requires that the energy of the scattered electron from one reaction path equals the energy of the ejected electron released along the other reaction path: in that case electron pairs  $(e_{s'}, e_{a'})$  and  $(e_{s''}, e_{a''})$  are indistinguishable. Such state-to-state (exchange) interference essentially differs from the interference of direct and indirect processes (Fano interference), and it occurs at a unique (critical) electron impact energy:  $E_0 = E_{R'} + E_{R''} - E_F$ .

In our previous work [1], we made an effort to experimentally address a possible existence of this exchange interference: we studied the resonant Auger peaks of  $[2p_{1/2}]4p$  and  $[2p_{3/2}]4p$  resonances decaying into the same  $[3p^2](^1D_2)4p$  ( $^2P$ ,  $^2D$ ) final ionic state of argon. Our experimental approach is based on a comparison of CIS (constant ionic state) spectra for the selected final state recorded in the coincidence mode, by scanning simultaneously the transmission energies of the two spectrometers in the opposite direction, so as to keep the sum of transmission energies constant. Our “box” type cylindrical mirror analysers (CMA) have similar structure [2], but slightly different energy resolutions (A: 0,55%; B: 0,78% (FWHM)) and accepted scattering angular ranges (A:  $43^\circ$ - $137^\circ$ ; B:  $65^\circ$ - $115^\circ$ ). Although we found a systematic difference between the spectra around the „critical“ energy, the difference was not significant enough to state unambiguously the existence of interference effects. We concluded that the main complication arises from the fact that there are several final states in the measuring window, having different total angular momenta. They interfere independently, dispersing the interference effects.

In this work we chose the possible simplest target, the helium, in which autoionizing states decay to the same simple  $\text{He}^+1s^{-1}$  final state with  $E_F = 24.6$  eV. These autoionizing states are:  $2s^2(^1S)$ ,  $2s2p(^3P)$ ,  $2p^2(^1D)$  and  $2s2p(^1P)$  at energies 57.8 eV, 58,3 eV, 59.9 eV and 60.1 eV, respectively. Their CIS spectrum at 96.9 eV primary energy (above the critical energy) is shown in Fig. 1. The peaks of the ejected and scattered electrons can be easily identified even in the total (non-coincident) spectra, they are well separated (low energy side: ejected (autoionizing) electrons, high energy side: scattered electrons). The energy scales of the spectrometers are reversed, since in the (e,2e) CIS measurements the sum of the electron energies is kept constant. The corresponding scattered-ejected electron peak-pairs are just opposite in the two spectra and are connected by a dashed line. The coincidence spectrum belongs equally to both scales, of course. Its high background shows the determinant role of the direct process in the formation of  $\text{He}^+$  ions.

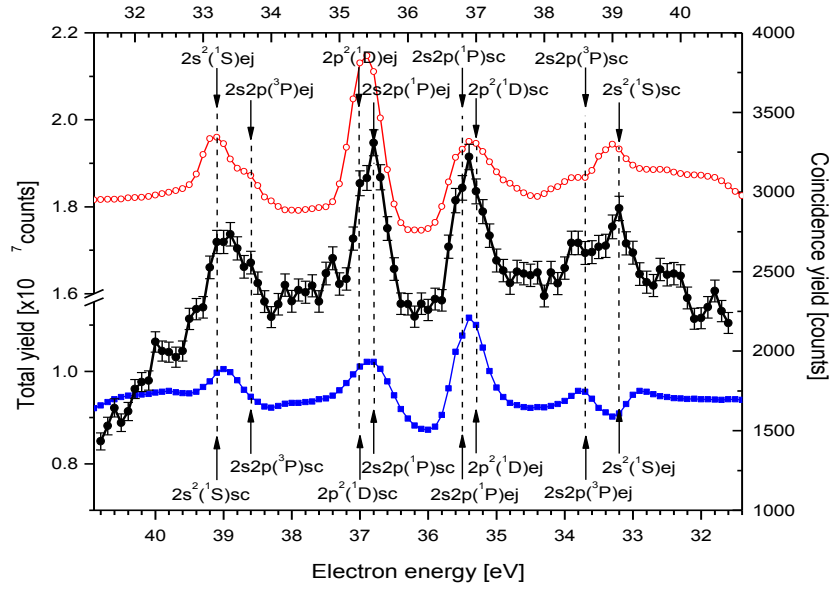


Fig. 1: The CIS spectrum measured at 96.9 eV primary energy with  $E_0 - E_F = E_A + E_B = 72.3$  eV. The energy spectrum measured by the A (open red circles, upper energy scale) and by the B (full blue squares, lower energy scale) spectrometers are also shown (see also the text). The random coincidences ( $\approx 20\%$ ) were subtracted from the coincidence signals, the error bars contain the statistical error of this background removal, too.

## 2. Results around the critical primary energy

The state-to-state interference of the  $2s^2(^1S)$  and  $2p^2(^1D)$  autoionizing states of He have been studied previously by others [3,4], applying quite different methods. We chose the same resonance pair, the corresponding resonance energies are  $E_R = 57.8$  eV,  $E_{R'} = 59.9$  eV, and the state-to-state interference is expected to occur at  $E_0 = 93.1$  eV. When the final state is populated, the sum of the outgoing electron energies is given by  $E_0 - E_F = 68.5$  eV. To ease the understanding, these energy levels and transitions are shown in a bar diagram of Fig. 2.

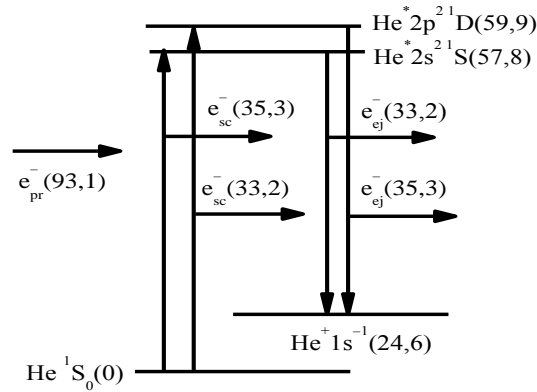


Fig. 2. The bar diagram of the energy levels and transitions of the considered inter-channel exchange interference.

A lot of spectra have been measured around the critical energy, two of them are shown in Fig. 3. On the upper spectrum the primary energy equals the critical energy, at least within the error of our energy calibration. On the lower spectrum the primary energy is 0.2 eV higher ( $E_0 = 93.3$  eV). In both cases, of course, we kept the sum of scattered and ejected electron energies constant, 24.6 eV below the primary energy, according to the energy of the final ionic state.

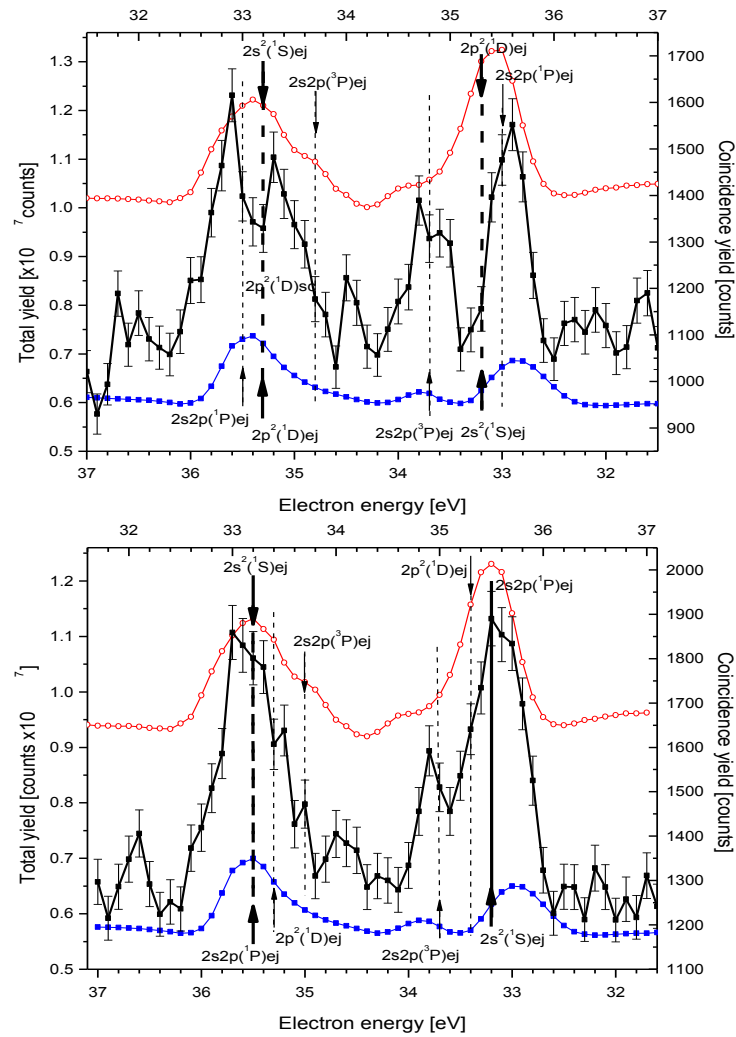


Fig. 3. The same as in Fig. 2, but measured at the critical energy  $E_0 = 93.1$  eV (upper figure) and just above it, at  $E_0 = 93.3$  eV (lower figure).  $E_F = 24.6$  eV in both cases.

The total (non-coincident) spectra measured at the two primary energies in the case of A and B spectrometers are practically the same, but the CIS (coincident) spectra are significantly different. This indicates the presence of exchange interference effects, since the interference with the direct process cannot change this much for a few tenths of eV modification.

### 3. Acknowledgments

This research was (partially) carried out in the framework of the Centre of Excellence of Mechatronics and Logistics at the University of Miskolc.

### 4. References

- [1] Paripás B, Palásthy B and Žitník 2013 *J. Electr. Spectr.* **189** 65.
- [2] Paripás B, Palásthy B, Štuhec M and Žitník M 2010 *Phys. Rev. A* **82** 032508-1–032508-1066.
- [3] den Brink J P V, Nienhuis G, van Eck J and Heideman H M 1989 *J. Phys. B* **22** 3501.
- [4] den Brink J P V, van Eck J and Heideman H G M 1988 *Phys. Rev. Lett.* **61** 2106.

# DISSOCIATIVE EXCITATION OF $\text{Fe}(\text{CO})_5$ STUDIED USING ELECTRON INDUCED FLUORESCENCE APPARATUS

Anita Ribar, Marian Danko, Juraj Országh and Štefan Matejčík

*Department of Experimental Physics, Comenius University Bratislava, Šafárikovo nám. 6, 818 06 Bratislava, Slovakia*

E-mail: anita.ribar@gmail.com

Organo-metalic molecule, Iron pentacarbonyl ( $\text{Fe}(\text{CO})_5$ ), has been studied using a cross-beam experimental setup, the electron induced fluorescence apparatus (EIFA). This experiment allows electron induced fluorescence (EIF) and dissociative excitation (DE) studies to molecules. Using the EIFA we were able to measure emission spectra of the molecules as well as the excitation-emission cross sections initiated by electron impact. In this work the emission spectrum of  $\text{Fe}(\text{CO})_5$  obtained with 50 eV electrons in the wavelength range between 220 nm and 450 nm will be presented. Further, we present excitation-emission cross sections for several DE channels of this molecule and determined thresholds for these reactions.

## 1. Introduction

In FEBID technologies (Focused Electron Beam Induced Deposition), low energy electrons come as products of collisions between the high energy electron beam and the surface [1]. Chemistry above and on the treated surface is severely influenced by the secondary electrons. Their kinetic energy is in the energy range of dissociation and dissociative excitation reactions. Iron pentacarbonyl is a molecule widely used in these technologies, [2] and there is a great interest for detailed investigation on the interaction between  $\text{Fe}(\text{CO})_5$  and low energy electrons.

$\text{Fe}(\text{CO})_5$  has been extensively studied in the past, mostly its ionization energy and appearance energies,[3] electron affinity,[4] ionization efficiency curves,[5] electronic structure [6], absorption [7] and emission spectra, both in theory and experiment [8]. Metal carbonyls and simple organometalics are claimed to not fluoresce in general, [9] however emission spectra have been reported in UV, VIS and NIR region [8, 10] .

Interaction between low energy electrons and molecules can lead to (i) electron induced fluorescence (EIF) (ii) and dissociative excitation (DE) among others. As a product of these processes, one can detect photons emitted from excited particles and obtain emission spectra and/or emission cross sections for EIF or DE as function of electron energy.

Our group studies EIF and DE processes by means of electron induced fluorescence apparatus (EIFA) [11]. Using the electron/molecular cross-beam apparatus, we are able to observe EIF and DE reactions by detecting of radiation in the UV-VIS range of spectra. The gas molecules in the vacuum chamber collide with monoenergetic electrons and photons resulting from EFI or DE reactions are detected. At normal conditions,  $\text{Fe}(\text{CO})_5$  is in liquid state. The high vapour pressure makes this molecule suitable for examination by EIFA. In contrast to photon sources, with electron beam instrument one can excite optically forbidden states, so the rich emission spectrum is expected. Using the EIFA apparatus we are able to measure electron energy resolved emission spectra of molecules, emission cross sections for EIF and DE processes and the thresholds for these reactions, which represent a valuable information for the understanding of the molecule's behaviour in presence of low energy electrons.

## 2. Results and discussion

Iron pentacarbonyl investigation by EIFA consists of two types of measurements: (i) emission spectrum measurement (Fig.1) and (ii) emission cross-section measurement with determination of the thresholds (Fig. 2-3). The spectral resolution of the emission spectra may be adjusted by monochromator slits (Fig. 1). The emission spectrum of  $\text{Fe}(\text{CO})_5$  was measured in the range of 220-450 nm and we have identified several CO and  $\text{CO}^+$  bands in this region, as well as Fe I and Fe II atomic lines. The most intense radiation comes from quintet and septet states of Fe I, which has been reported by previous authors [10]. The spectrum is very rich, as it can be seen in Fig. 1. Bands of CO and  $\text{CO}^+$  are overlapping and due to the limited resolution of the optical spectrometer (0.8 nm), we were not able

resolve vibrational transitions overlapping each or iron atom lines. There were detected several Fe I and Fe II lines that were relatively isolated, so we could perform analysis of the emission cross-sections (Fig. 2-3) recorded at wavelengths corresponding to the maximum of the lines.

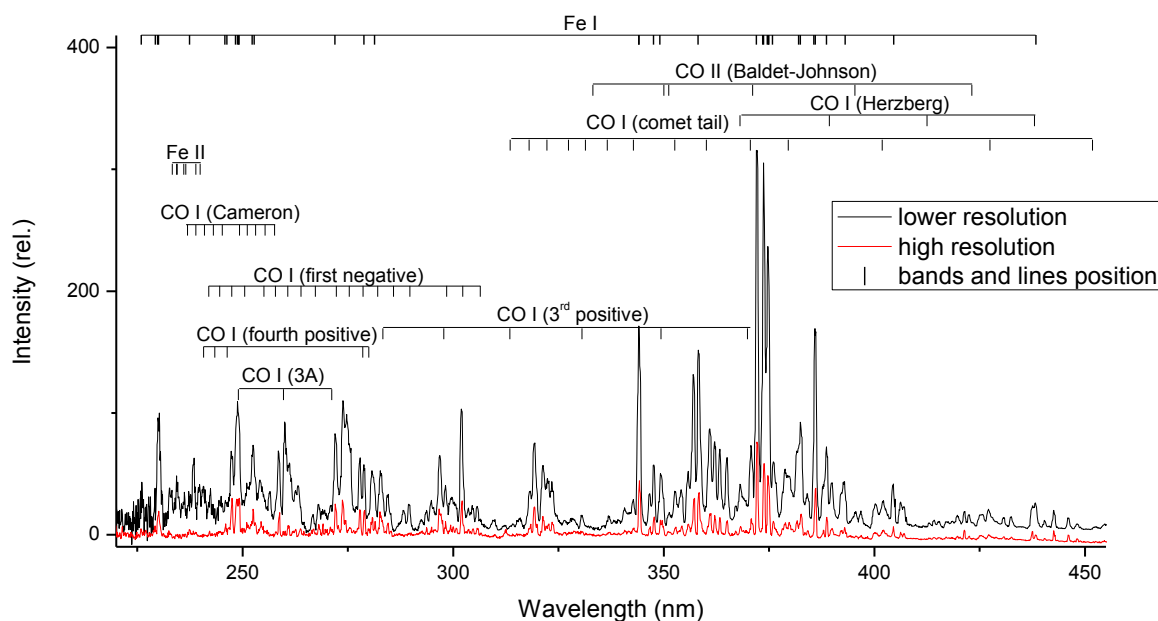


Fig. 1 Spectrum of  $\text{Fe}(\text{CO})_5$  at 50 eV energy of impact electrons with slits opened at 100  $\mu\text{m}$  (high resolution-red line) and 200  $\mu\text{m}$  (lower resolution-black line).

DE emission cross-section for Fe I and Fe II were recorded at corresponding wavelengths. At 372 nm (Fig. 2), based on the NIST atomic database, the following radiative transitions of Fe I have the highest probability:  $a^5D(4) \leftarrow z^5F^o(5)$  at 371.99 nm;  $a^5P(3) \leftarrow w^5F^o(4)$  at 372.13 nm;  $a^5D(2) \leftarrow z^5F^o(2)$  at 372.26 nm. With optical resolution of our spectrometer we are not able to distinguish between these transitions. For the mixture of these Fe I states we have estimated experimental threshold of  $11.4 \pm 0.5$  eV, which is within the error bars in accordance with theoretical values 9.5 eV, 11.7 eV and 9.6 eV respectively.

The second emission cross-section was recorded at 373.7 nm wavelength (Fig. 2). According to the NIST database, the most intense lines in this range are 373.49 nm ( $a^5F(5) \leftarrow y^5F^o(5)$ ); 373.53 nm ( $z^7P^o(4) \leftarrow e^7P(4)$ ); 373.71 nm ( $a^5D(3) \leftarrow z^5F^o(4)$ ); and 373.83 nm ( $b^3H(5) \leftarrow ^1I^o(6)$ ) with theoretical thresholds at 10.39 eV; 12.47 eV; 9.58 eV; 12.79 eV respectively. The experimentally determined threshold has a value of  $11.3 \pm 0.5$  eV.

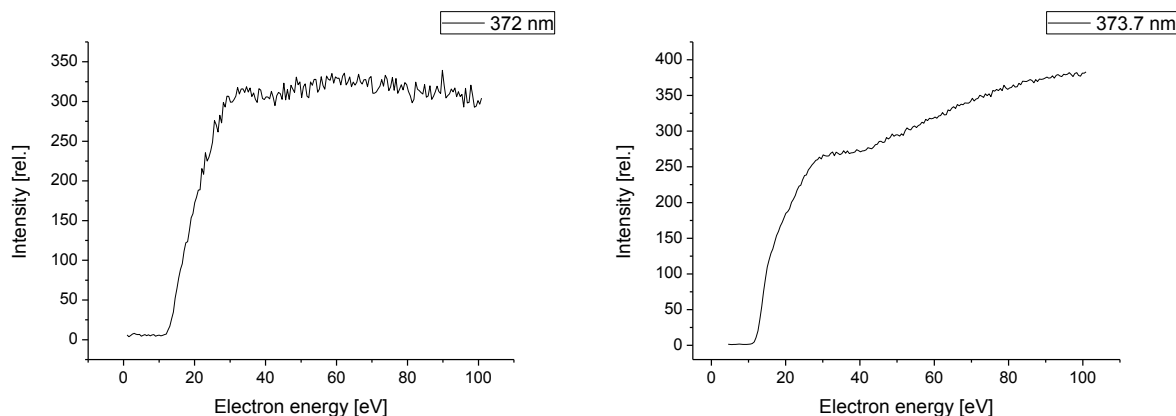


Fig. 2 Emission cross-sections recorded at 372 nm (left) and 373.7 nm (right)

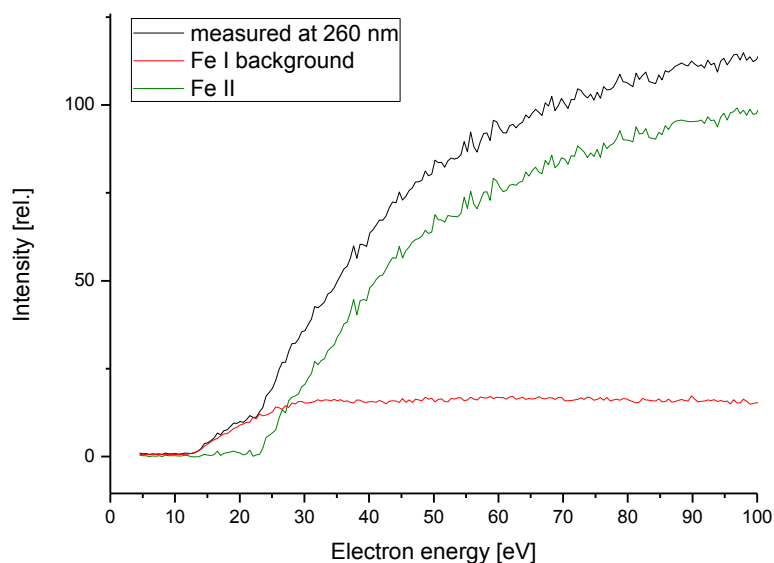


Fig. 3 Emission cross-section recorded at 260 nm (black) compared with 372 nm emission cross-section (red) subsequently subtracted from the 260 nm measurement

Further investigation involved Fe II transition analysis. Based on the NIST atomic database, Fe II lines in region around 260 nm are more intense than Fe I lines. We recorded the emission cross-section measurement at 260 nm (Fig.3) and observed several structures in the curve which indicates mixing of the Fe I and Fe II lines. First threshold was detected at  $12.8 \pm 0.5$  eV and it corresponds to Fe I transition at 259.96 nm  $a^5F(4) \leftarrow x^5G^\circ(4)$  (theoretical threshold of 11.89 eV electron energy needed for observation of this line originating from  $Fe(CO)_5$ ). The second threshold is at  $23 \pm 0.5$  eV and is obtained by subtracting the Fe I cross-section. The most intense Fe II transition in this range of wavelengths is  $a^6D(9/2) \leftarrow z^6D^\circ(9/2)$  at 259.94 nm, whose upper state is at 4.77 eV above the ground state of the iron positive ion, which gives a theoretical threshold of 18.87 eV electron energy needed for observation of this transition from  $Fe(CO)_5$ . Similarly as in case of 372 nm and 373.7 nm cross-sections, there are several more transitions with lower intensity than 259.94 nm line, and cannot be distinguished from it. The energy needed to cause excitation to the upper level of corresponding transitions is in range between 18.86 – 29 eV.

### 3. Conclusions

Investigation of the fluorescence induced by electron impact to iron pentacarbonyl was done using the EIFA apparatus in two modes: emission spectrum measurement in UV-VIS region and emissive cross-section with electron energies in the range between 0-100eV. Rich emission spectrum was obtained and main lines and bands were identified as Fe I, Fe II, CO and  $CO^+$ . Emissive cross-sections at three different wavelengths were measured and thresholds have been determined. We have recorded emission cross sections for Fe I lines at 372 nm and 373.7 nm. Similarly, at 260 nm wavelength, we observe recorded emission cross section for mixture Fe II and Fe I lines which we were able to separate and determine the threshold for both of the fragments.

### 4. Acknowledgement

This work was partially supported by the Slovak Research Agency, project Nr. APVV-0733-11, DO7RP-0025-11 and Grant UK Nr. UK/140/2014. This work was conducted within the framework of the COST Action CM1301 (CELINA).

### 5. References

[1] Huth M, Porrati F, Schwalb C, Winhold M, Sachser R, Dukic M, Adams J, Fantner G, 2012 *Beilstein J. Nanotechnol.* **3** 597



- [2] Lukaszczuk T, Schirmer M, Steinrück H P, Marbach H 2009 *Langmuir* **25** 11930
- [3] Norwood K, Ali A, Flesch G D, Ng C Y, 1990 *J. Am. Chem. Soc.* **112** 7502
- [4] Engelking P C, Lineberger W C, 1979 *J. Am. Chem. Soc.* **101** 5569
- [5] Distefano G, 1970 *J. Res. Nat. Bur. Stand.* **74A** 233
- [6] Daniel C, Bénard M, Dedieu A, Wiest R, Veillard A, 1984 *J. Phys. Chem.* **88** 4805.
- [7] Marquez A, Daniel C, Sanz J F, 1992 *J. Phys. Chem.* **96** 121
- [8] Horák D V, Winn J S, 1983 *J. Phys. Chem.* **87** 265
- [9] Whetten R L, Fu K J, Grant E R, 1983 *J. Chem. Phys.* **79** 4899
- [10] Hale B C, 1983 *California Univ., Berkeley. Lawrence Berkeley Lab*
- [11] Danko M, Orszagh J, Durian M, Kocisek J, Daxner M, Zottl S, Maljkovic J B, Fedor J, Scheier P, Denifl S, Matejcik S, 2013 *J. Phys. B: At. Mol. Opt. Phys.* **46** 045203

# DISSOCIATIVE ELECTRON ATTACHMENT TO NITROMETHANE STUDIED BY VELOCITY SLICE IMAGING

Anita Ribar<sup>1</sup>, Ewelina Szymańska-Skolimowska<sup>2</sup>, Nigel Mason<sup>2</sup>, Štefan Matejčík<sup>1</sup>

<sup>1</sup> Department of Experimental Physics, Comenius University Bratislava, Šafárikovo nám. 6, 818 06 Bratislava, Slovakia

<sup>2</sup> Department of Physical Sciences, The Open University, Walton Hall, MK7 6AA Milton Keynes, United Kingdom

E-mail: anita.ribar@gmail.com

A detailed experimental investigation of dissociative electron attachment (DEA) to nitromethane, CH<sub>3</sub>NO<sub>2</sub> is presented. To investigate this process a Time of Flight (TOF) mass spectrometer operating with Velocity Slice Imaging (VSI) technique was used. DEA in CH<sub>3</sub>NO<sub>2</sub> is found to lead to the formation of O<sup>-</sup> and NO<sub>2</sub><sup>-</sup> anionic products produced through scattering resonances in the electron energy range of 5 - 12 eV. The VSI was used for obtaining the information about the angular distributions and kinetic energy distributions of the anionic fragments. The results for O<sup>-</sup> and NO<sub>2</sub><sup>-</sup> anions are further discussed in the paper.

## 1. Introduction

Nitromethane is a simple nitro compound whose electronic states spectroscopy and reaction dynamics with low energy electrons has been studied extensively in the past. [1-5] The major motivation of these studies has been due to the abundance of this compound in the Earth's atmosphere, where it may influence local chemistry. [6] It can also act as a human carcinogenic agent [7], and it has typical characteristics of explosives and propellants [8].

Interaction of the nitromethane and low energy electrons can lead to dissociation and ionization of the molecule. Di Domenico and Franklin [1] studied ion formation in pressure range 10<sup>-2</sup> - 10<sup>-4</sup> mbar and improved the understanding of reaction kinetics of nitromethane. Resonant energies for the formation of anions as well as the rate constants for ion-molecule interactions were determined. In recent past Modellia and Venuti [2] have studied the gas-phase empty level structures by means of DEA and electron transmission spectroscopy (ETS) as well as the *ab initio* calculations in the 0-6 eV electron energy range. Resonances were studied and vertical electron affinities were calculated for few nitro derivatives. Walker and Fluendy [3] have also obtained DEA spectra, as well as electron energy – loss spectra and re-measured the photoabsorption spectrum by using a synchrotron radiation source. Most recently, two publications [4,5] were devoted to high-resolution mass spectrum of anions produced by DEA on nitromethane. Efficiency curves for the 16 anionic fragments have been obtained. The most dominant products (NO<sub>2</sub><sup>-</sup>, O<sup>-</sup>, OH<sup>-</sup>, CN<sup>-</sup>, CNO<sup>-</sup>) have high-energy resonances in range between 5 eV and 10 eV. [5]

The electronic configuration of nitromethane allows it to form valence anions and dipole bound anions such that the interaction of low energy electrons with neutral molecule can lead to DEA, the process of capturing an incident electron by the neutral molecule (AB) at resonant energy and subsequent stabilization by forming the anionic A<sup>-</sup> and neutral B fragments:



When AB<sup>\*-</sup>, the transient negative ion (TNI) decays, fragments fly with equal momentum but in opposite directions. If this event repeats many times, a spherical distribution in velocity space builds up (a 'Newton sphere' is formed). Using a TOF spectrometer allows a time resolved spectra of ions emerging on the detector to be recorded where the recorded arrival time depends on the mass to charge ratio of the anions. Recording the Newton sphere in the 2D plane within a narrow time window (order of nanoseconds) by VSI technique provides information about the kinetic energy of the anions, since

the kinetic energy is proportional to the square root of the radius of the Newton's sphere. The internal energies of the fragment anions can be determined from the kinetic energy measurement, as well as dissociation limits of the parent negative ion resonant states responsible for the DEA process. VSI measurements also allow us to obtain the angular distributions of anions. In contrast with the conventional turn table techniques that can measure the range between 20 – 160°, with VSI we can obtain a complete angular distribution from 0 – 180°. The symmetry of the TNI can then be deduced from such angular distributions.

Formation of O<sup>-</sup> anion from nitromethane might defer this molecule from its isomer, methyl nitrite. Investigating the resonances of nitromethane's fragments by DEA coupled with VSI is way proposed for getting the answer to this hypothesis.

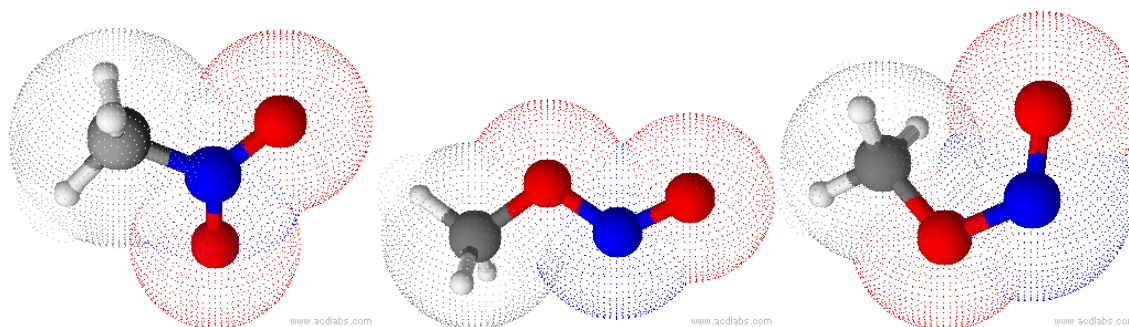


Fig. 1. Chemical structures of: nitromethane (left), trans-methyl nitrite (middle) and cis-methyl nitrite (right). The white atoms represent hydrogen, dark gray are the carbon atoms, blue are nitrogen atoms and red represent oxygen. All three structures were drawn in ACD/ChemSketch

## 2. Experimental setup

DEA to nitromethane was investigated using an experimental apparatus - GASIC (Fig. 2) in the Molecular Physics laboratory at the Open University in Milton Keynes, UK. The apparatus uses a TOF spectrometer operating with VSI technique to study an electron induced anion formation process in the gas phase; and has been described in more detail in previous publications [9].

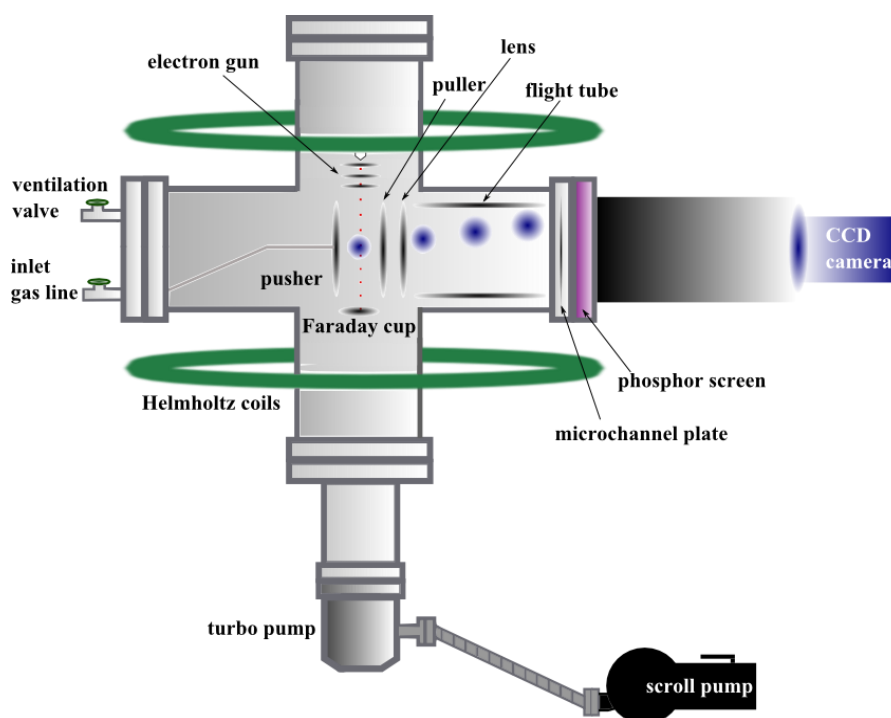


Fig. 2. Schematic diagram of gas phase experimental apparatus – GASIC [10]

Briefly, it consists of an ultra-high vacuum chamber ( $1 \times 10^{-9}$  mbar,) where the low energy pulsing electron gun (pulse width is 200 ns) is placed, followed by the interaction region where the magnetically collimated electron beam crosses the molecular beam. A pair of Helmholtz coils generates a uniform magnetic field to allow collimation of the electron beam. The target molecules enter the interaction region through the effusive capillary electrically isolated from the pusher plate (Fig. 2). Anions formed in the interaction region are extracted into the flight tube using a pulsed electric field applied 200 ns after the electron pulse. A position sensitive detector is placed (PSD) at the end of the flight tube. It consists of three micro-channel plates (MCP), a phosphor screen and a CCD camera. The PSD operates in two modes: (i) a pulse counting mode, when the mass spectra and electron energy dependence of the anion yield are measured, and (ii) VSI mode, used for detection of the anion fragment distribution images. During the second mode, a high voltage (2 kV) Bhelke switch is used for fast (100 ns) pulsing in order to slice the Newton sphere in its centre and record the incident anions.

The electron energy resolution of the electron gun used in GASIC apparatus is calculated to be about 1 eV and the mass resolution of TOF spectrometer is 1.6. Liquid samples of nitromethane ( $\text{CH}_3\text{NO}_2$ ) used for this study were purchased from Sigma-Aldrich with a stated purity of >99%. The liquid sample was placed in a small glass bulb and connected to the vacuum chamber via a gas line with a precision leak valve. The sample was degassed by freeze out procedure. The inlet pressure of nitromethane was about  $2 \times 10^{-6}$  mbar during the measurements. The anion mass scale was calibrated using two reference gases:  $\text{O}_2$  and  $\text{CF}_4$ . The absolute electron energy scale was calibrated using the well-known resonance energy (at 6.5 eV) of the DEA reaction  $\text{e}^- + \text{O}_2 \rightarrow \text{O}_2^* \rightarrow \text{O}^- + \text{O}$ . [9]

### 3. Results and discussion

The formation of anionic products formed by the interaction of low energy electrons and nitromethane molecules was observed by measuring the mass spectra of anions between 3 eV and 20 eV. In all of the obtained spectra two peaks were dominant. They are ascribed to  $\text{O}^-$  and  $\text{NO}_2^-$  fragments. Due to low mass resolution of the TOF spectrometer we weren't able to distinguish as many ions as authors of previously published papers were [5]. Ion yields of  $\text{O}^-$  and  $\text{NO}_2^-$  were measured. Resonances at 6 eV and 10 eV were observed for both fragments. Velocity images were obtained and are presented in Figure 3 and 4. The narrow 'spot' of  $\text{NO}_2^-$  ion distributions indicate that the initial kinetic energy of the anion is relatively low. This could mean that either the excess energy of the TNI was distributed into internal excitation energy of the neutral fragment, or the dissociation was occurring through more than one bond breakage. In contrast the  $\text{O}^-$  ion distribution occurs as big 'spot' without any anisotropic structure. The large radius of the 'spot' suggests high kinetic energy of the anions. The lack of any distinct momentum distribution in the  $\text{O}^-$  ions is rather unusual for a two-body fragmentation process, unless any 'memory' of the attachment process is wiped out by structural changes in the TNI or even by rotation of the TNI, before the dissociation takes place.

Table 1. Kinetics of DEA channels leading to the formation of  $\text{O}^-$  and  $\text{NO}_2^-$  based on thermochemical data. The bond energies ( $D_{\text{AB-C}}$ ) and electron affinities ( $\text{EA}_{\text{C}}$ ) were taken from Sailer *et al.* [4] The incident electron energy ( $E_{\text{e}}$ ) was taken from our results. All values given are in eV.

Negative ion channel	$\text{EA}_{\text{C}}$	$D_{\text{AB-C}}$	$E_{\text{threshold}}$	$E_{\text{e}}(\text{max peak})$	$E_{\text{KER}}$	$m_{\text{AB}}/m_{\text{ABC}}$	$E_{\text{max}}$
$\text{O}^- + \text{CH}_3\text{NO}$	1.46	4.76	3.3	6	2.7	0.7377	1.9918
				10	6.7		4.9426
$\text{NO}_2^- + \text{CH}$	2.27	2.64	0.37	6	5.63	0.2459	1.3844
				10	9.63		2.368

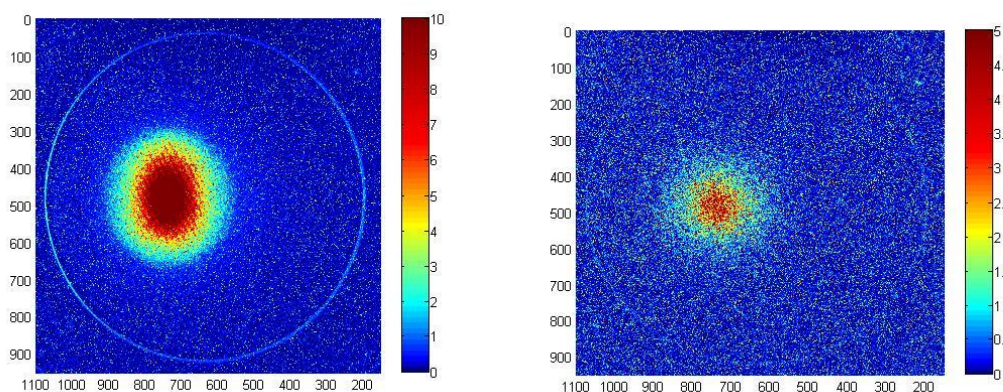


Fig. 3. The VSI of  $\text{O}^-$  from  $\text{CH}_3\text{NO}_2$  obtained at 6 eV (left) and 10 eV (right).

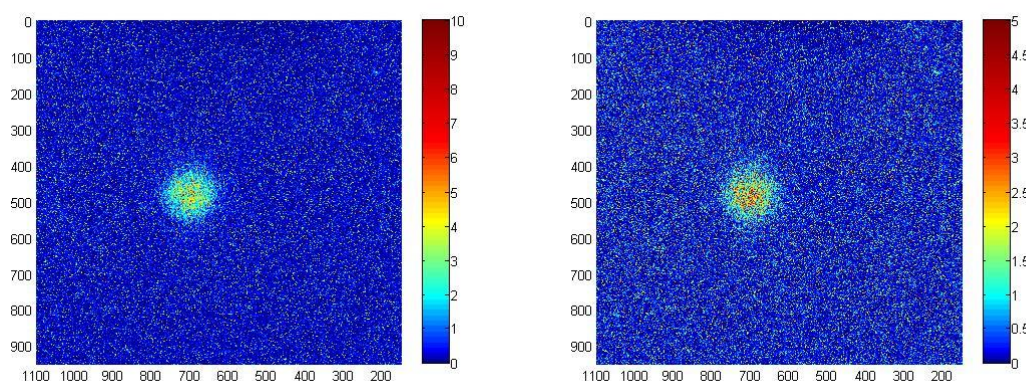


Fig. 4. The VSI of  $\text{NO}_2^-$  from  $\text{CH}_3\text{NO}_2$  obtained at 6 eV (left) and 10 eV (right).

## 4. Conclusions

Investigation of anions formed by dissociative electron attachment to nitromethane has been performed using a TOF mass spectrometer operating with VSI technique. We observed the formation of two dominant anions,  $\text{O}^-$  and  $\text{NO}_2^-$ . VSI images do not show any anisotropic structure. The lack of anisotropy in angular distribution preserves us from clear information about the TNI symmetry. For better quality images the collection time has to be extended. For further investigation also lower base pressure (below  $10^{-8}$  mbar) is needed to make further conclusions.

## 5. Acknowledgement

This work was partially supported by EU FP7 projects Lassie (ITN) and SUP@VAMDC and ARGENT (ITN)

## 6. References

- [1] Di Domenico A, Franklin J L, 1972 *Int. J. Mass Spectrom. Ion Phys.* **9** 171.
- [2] Modelli A, Venuti M, 2001 *Int. J. Mass Spectrom.* **205** 7
- [3] Walker I C, Fluendy M A D, 2001 *Int. J. Mass Spectrom.* **205** 171.
- [4] Sailer W, Pelc A, Matejcik S, Illenberger E, Scheier P, Märk T D, 2002 *J. Chem. Phys.* **117** 7989.
- [5] Alizadeh E, Ferreira da Silva F, Zappa F, Mauracher A, Probst M, Denifl S, Bacher A, Märk T D, Limao-Vieira P, Scheier P 2008 *Int. Jour. of Mass Spec.* **271** 15.
- [6] Taylor W D, Allston T D, Moscato M J, Fazekas G B, Kozlowski R, Takacz G A 1980 *International Journal of Chemical Kinetics* **12** 231.
- [7] Takeuchi A, Nishimura Y, Kaifuku Y, Imanaka T, Natsumeda S, Ota H, Yamada S, Kurotani I, Sumino K, Kanno S, 2010 *J. Occup. Health* **52** 194.
- [8] Klezenberg S, Eisenreich N, Eckl W, Weiser V, 1999 *Propellants, Explosives, Pyrotechnics* **24** 189.
- [9] Nandi D, Prabhudesai V S, Krishnakumar E, Chatterjee A, 2005 *Rev. Sci. Instrum.* **76** 053107.
- [10] Szymańska-Skolimowska E, PhD thesis, *The Open University*, Milton Keynes, UK, 2014

# L-X-RAY PRODUCTION CROSS SECTIONS BY POSITRONS

Takeshi Mukoyama<sup>1</sup>, Károly Tőkési<sup>1</sup>, Yasuyuki Nagashima<sup>2</sup>

<sup>1</sup>*Institute of Nuclear Research of the Hungarian Academy of Sciences (ATOMKI), Debrecen, Hungary*

<sup>2</sup>*Department of Physics, Tokyo University of Science, 1-3 Kagurazaka, Shinjuku, Tokyo, Japan*

E-mail: mukoyama@atomki.mta.hu

The L-shell x-ray production cross sections for Ag, In and Sn by positron impact have been calculated with two methods based on classical mechanics, the binary-encounter approximation and the classical trajectory Monte Carlo method. The results are compared with the experimental data and quantum mechanical calculations. Both classical treatments are found to well describe the inner-shell ionization processes by positrons.

## 1. Introduction

Inner-shell ionization process by positron impact is of fundamental importance to understand the collision dynamics between anti-particle and atom. Extensive experimental and theoretical investigations have been reported. At high energies the inner-shell ionization cross sections by positrons are almost same as those by electrons. On the other hand, in the case of low-energy region large difference in cross sections between electrons and positrons is expected because of the Coulomb defection of the projectile due to the target nucleus and the exchange effect.

Recent advance in experimental techniques makes it possible to measure inner-shell ionization cross sections by positrons in the low-energy region near to the threshold [1]. Theoretically quantum mechanical methods, such as the plane-wave Born approximation (PWBA), have been applied to calculate ionization cross sections. However, it is useful if the inner-shell ionization process by positron impact in low-energy region can be treated classically and the ionization cross sections are obtained in a simple manner.

We have already shown [2] that for K-shell ionization by positron impact the binary-encounter approximation (BEA) and the classical trajectory Monte Carlo (CTMC) method can yield ionization cross sections in agreement with the experimental results and the PWBA calculations. It is the purpose of the present work to extend the classical methods used for K shell to the case of L-shell ionization cross sections by positrons.

## 2. Theory

We use two classical methods, the BEA and the CTMC. Details of the BEA are described in our paper on K-shell ionization [2]. We follow the formalism proposed by Gryziński and Kowalski [3] for K-shell ionization cross sections by positron impact. However, we modified their model at one point. Gryziński and Kowalski used the free-fall model to obtain the velocity distribution. In the present work, we calculate velocity distributions for additional three different atomic models, i.e. the nonrelativistic hydrogenic model, the relativistic hydrogenic (Dirac) model and the Hartree-Fock-Roothaan (HFR) model.

The CTMC calculation is principally similar to the method of Olson and Salop [4]. Only three particles, i.e. the incident positron, one of the L-shell electrons and the target nucleus, are considered. They are assumed to interact with each other through the pure Coulomb force. Then classical equations of motions for three-body system are solved numerically for large number of trajectories with given initial conditions. The initial conditions correspond to the impact parameter of the incident positron, the position and velocity of the target electron. These parameters are randomly selected by the use of pseudo-random numbers. The ionization cross section is determined from the actual values of impact parameter, which leads to the ionization event, and the total number of trajectories.

## 3. Results and discussion

The L-shell x-ray production cross sections for Ag, In and Sn by positron impact were calculated with two different classical methods. First, L-subshell ionization cross sections are obtained with the BEA and the CTMC for three different L subshells ( $L_1$ ,  $L_2$  and  $L_3$ ). Then these three cross sections are converted into the x-ray production cross section by the use of fluorescence yield for each subshell

and the Conster-Kronig coefficients between subshells. The BEA cross sections are obtained for four different atomic models, i.e. the free-fall model, the nonrelativistic and relativistic hydrogenic models, and the HFR model.

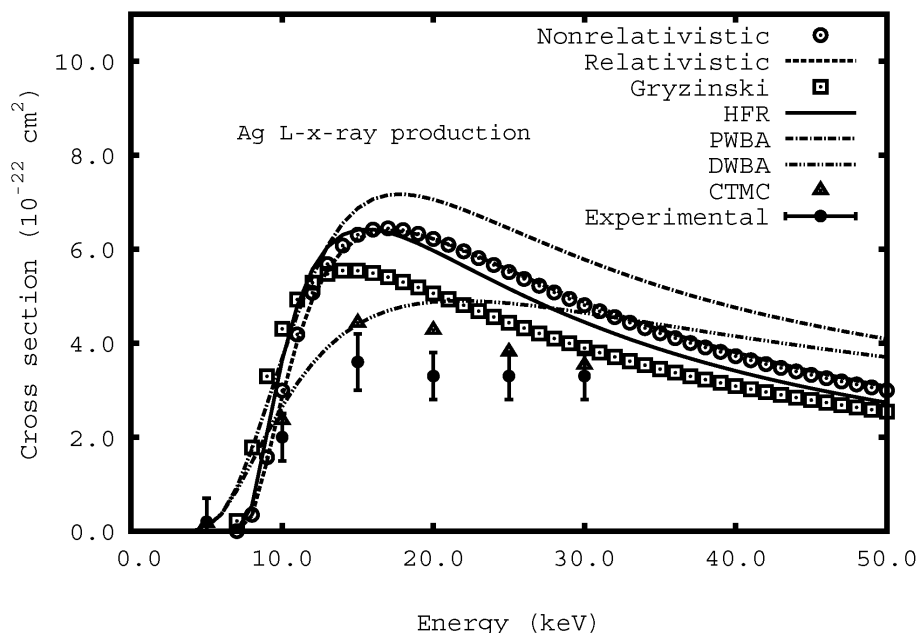


Fig. 1. L-x-ray production cross section for positrons on Ag.

Figure 1 shows the L-x-ray production cross sections of Ag as a function of the incident positron energy. The BEA cross sections with the relativistic hydrogenic model is almost same as those with the nonrelativistic one. This indicates that the electronic relativistic effect is small for L-shell ionization cross sections. In the free-fall model, indicated as Gryzinski, the cross section rises quickly near to the threshold and decreases rapidly at high energy. This behaviour can be expected from the fact that in the free-fall model the velocity distribution is concentrated at low velocities [2]. The HFR method gives larger cross sections in low-energy region, but smaller values at high energies. However, this wave-function effect is small and ascribed to the screening effect of the atomic electrons. These BEA results suggest the validity of the three-body system used in the CTMC calculations.

The BEA cross sections and the CTMC results are compared with the measured values [1]. The CTMC calculations are in good agreement with the experimental data. On the other hand, the BEA values with different velocity distributions are generally larger than the experimental results in the energy region higher than 15 keV, except for the case of the free-fall model at 30 keV.

For comparison, two quantum mechanical calculations, the PWBA [5] and the distorted-wave Born approximation (DWBA) [6], are also shown in the figure. It is interesting to note that the CTMC results agree well with the DWBA calculations. The PWBA gives larger results than other theoretical models. However, in general it can be said that the BEA and the CTMC are roughly in agreement with the quantum mechanical models and the classical models can well describe the inner-shell ionization process by positron impact. For In and Sn, the situation is quite similar.

## 4. References

- [1] Nagashima Y, Shigeta W, Hyodo T and Iwaki M 2007 *Rad. Phys. Chem.* **76** 465.
- [2] Mukoyama T, Tőkési K, Nagashima Y 2014 *Eur. Phys. J. D* **68** 64
- [3] Gryziński M and Kowalski M 1993 *Phys. Lett. A* **183** 196.
- [4] Olson R E and Salop A 1977 *Phys. Rev. A* **16** 531
- [5] Khare S P and Wadehara J M 1996 *Can. J. Phys.* **75** 376
- [6] Bote D, Salvat F, Jablonski A and Powell C J 2009 *At. Data Nucl. Data Tables* **95** 871.



# ELECTRON-IMPACT-INDUCED TRYPTOPHAN MOLECULE FRAGMENTATION

Jelena Tamuliene<sup>1</sup>, Liudmila G. Romanova<sup>2</sup>, Vasily S. Vukstich<sup>2</sup>, Alexander V. Papp<sup>2</sup>, Alexander V. Snegursky<sup>2</sup>

*1Vilnius University, Institute of Theoretical Physics and Astronomy, 12A. Goštauto str., 01108, Vilnius, Lithuania*

*2Institute of Electron Physics, Ukr. Nat. Acad. Sci., 21 Universitetska str., 88017 Uzhgorod, Ukraine*  
E-mail: Jelena.Tamuliene@tfai.vu.lt

Fragmentation of the gas-phase tryptophan molecule by a low-energy (<70 eV) electron impact has been studied both experimentally and theoretically. Various positively charged fragments have been observed and analyzed. A special attention has been paid to the energy characteristics of the ionic fragment yield. The geometrical parameters of the initial molecule rearrangement have also been analyzed. The fragmentation observed is due to either simple bond cleavage or more complex reactions involving atomic rearrangement in molecules.

## 1. Methods of investigations

Electron-molecule interaction is a fundamental and very important process involved in various fields, such as radiation biology. In this area, electrons with low energies represent the most predominant species formed at a very short time following the deposition of high energy ionizing quanta into a biological medium [1]. Once produced, they are able to degrade the environing biological molecules such as DNA and proteins, inducing chromosome aberrations, such as cancer, mutations, genetic transformation etc. [2]. Thus, it is worth to investigate in detail the underlying mechanisms of the above processes by studying the degradation of the biosystem sub-units by low energy electrons. We have studied interactions of low-energy (<100 eV) electrons with tryptophan molecule belonging to the essential amino acids in order to probe the intrinsic properties of the molecule and trace its change(s) under electron impact.

The experimental technique used in this work was described in detail in a number of our previous papers (see, e.g. [3–4]). The crossed-beam method with mass separation of the collision products by means of a magnetic mass-spectrometer was applied. Note that our apparatus is capable of studying ionic fragments with respect to their mass-to-charge ratio within the 1–720 a.m.u. mass range with high sensitivity (about  $10^{-16}$  A) and relative mass resolution ( $m/\Delta m=1100$ ). The tryptophan molecule beam was produced by a heated effusion source providing the molecule concentrations of about  $10^{10}$  cm<sup>-3</sup>. The electron energy scale calibration was carried out against known ionization thresholds for the Ar atom and N<sub>2</sub> molecule allowing the accuracy of not worse than  $\pm 0.1$  eV to be reached [3]. The tryptophan molecule mass-spectrum was measured at the 70 eV electron energy, which is typical for mass-spectrometric studies, the appearance energies for the positively charged fragment ions were determined within the 5–30 eV energy range using technique described in [3–4]. The several structures of the tryptophan molecule and their fragments has been studied by the Becke's three-parameter hybrid functional, applying the non-local correlation provided by Lee, Yang, and Parr (B3LYP) [5], – a representative standard DFT method with the cc-pVTZ basis [6]. The structures of the molecule conformers and their fragments under study have been optimized without any symmetry constraint. The most stable conformer was chosen for the further investigation. In order to model the fragmentation processes, the fragment anions, cations and fragments with a zero charge both with and without geometry optimization have been evaluated to predict the influence of dissociation energy on the fragmentation processes. The appearance energies have been calculated as the difference between the total energy of the investigated conformer of the molecule and the sum of the energies of the fragments predicted.

## 2. Results

The tryptophan molecule mass-spectrum measured in our experiment at the 70 eV electron energy is generally close to that published in the NIST database [7]. This spectrum is characterized by a high



selectivity since, besides the main channel of the molecular ion dissociation with subsequent production of the fragment with the  $m=130$  a.m.u. mass, the intensities of the most clear peaks corresponding to the ions with the  $m=28$ , 77, and 103 a.m.u masses do not exceed 7% of the main peak intensity. Referring to the results obtained we determined the above mention fragments, their appearance energy and probable scheme of ion formation. The results obtained are listed in Table 1.

Tab. 1. Chemical composition of fragments obtained in mass spectra, appearance energy calculated and ion formation pathways.

Fragment mass, a.m.u.	Chemical composition	Appearance energy, eV	Ion formation pathways
130	$C_9H_8N$	8.07	$C_{11}H_{12}N_2O_2 + e \rightarrow C_9H_8N^+ + C_2H_4NO_2^0 + 2e$
103	$C_8H_7$	8.65	$C_{11}H_{12}N_2O_2 + e \rightarrow (C_8H_6 + H)^+ + (CH_2N + C_2H_3NO_2)^- + e$ $\rightarrow C_8H_7^+ + (CH_2N + C_2H_3NO_2)^- + e$
103	$C_7H_5N$	12.02	$C_{11}H_{12}N_2O_2 + e \rightarrow C_7H_5N^+ + C_4H_7NO_2^0 + 2e$
77	$C_5H_3N$	20.04	$C_{11}H_{12}N_2O_2 + e \rightarrow C_5H_3N^+ + (C_4H_4 + H + C_2H_4NO_2)^0 + 2e$
77	$C_6H_5$	14.07	$C_{11}H_{12}N_2O_2 + e \rightarrow C_6H_5^+ + C_5H_7N_2O_2^- + e$
28	$CH_2N$	9.64	$C_{11}H_{12}N_2O_2 + e \rightarrow CH_2N^+ + (COOH + C_9H_8N)^- + e$
		12.82	$C_{11}H_{12}N_2O_2 + e \rightarrow CH_2N^+ + (C_{10}H_{10}NO_2)^- + e$

It should be noted here that under the electron impact a number of fragments are produced having the peak intensity in the mass-spectrum not exceeding 3%. The main fragment at the tryptophan electron collision dissociation is formed at a simple cleavage of the  $C_\alpha$ – $C_\beta$  bond of the initial molecule. This bond dissociation is the most probable at the electron energies slightly exceeding the tryptophan molecule ionization potential. When the electron energy is sufficient to ionize the deeper molecular orbitals, first of all, the nitrogen and oxygen lone pair orbitals, it will result in a dissociation of the neighboring bonds, producing, in general, more fragmentation channels. These dissociation channels are minor, because the aromatic group stabilizes the positive charge and reduces fragmentation.

We seem to be the first who have observed the low-intensity peaks with the  $m=57.5$ , 64.5 and 65.5 a.m.u. masses corresponding to the doubly charged  $C_8H_5N^{2+}$ ,  $C_9H_7N^{2+}$  and  $C_9H_9N^{2+}$  ions, respectively, in the tryptophan mass spectrum. The indole ring demonstrates its ability to keep stability at detaching the different number of the hydrogen atoms with simultaneous elimination of two electrons. We also observed the diffuse peak at about 81.5 a.m.u. that corresponds to the decay of the ion with the  $m=130$  a.m.u. mass and production of that with the  $m=103$  a.m.u. mass. So the peak with the  $m=103$  mass with significant intensity could be not only due to the initial molecule dissociation but may result from the secondary fragmentation of the 3-methyleneindole part of the parent molecule.

### 3. References

- [1] Abdoul-Carime H, Gohlke S, Illenberger E 2005 *Chem. Phys. Lett.* **402** 497.
- [2] Fuciarelli A F, Zimbrick J D 1995 *Radiation Damage in DNA: Structure/Function Relationship at Early Times*, Battelle Press, Columbus OH.
- [3] Vukstich V S, Imre A I, Snegursky A V 2009 *Tech. Phys. Lett.* **15** 1071.
- [4] Vukstich V S, Imre A I, Romanova L G, Snegursky A V 2010 *J. Phys. B* **43** 185208.
- [6] Becke A D 1993 *J. Chem. Phys.* **98** 5648.
- [7] Kendall R A, Dunning Jr. T H, Harrison R J 1992 *J. Chem. Phys.* **96** 6796.
- [8] *National Institute of Standards (NIST), Standard Reference Database: Chemistry Webbook.* <http://webbook.nist.gov>.

# ELECTRON IMPACT (e, 2e) IONIZATION OF NH<sub>3</sub> AND CH<sub>4</sub>

István Tóth<sup>1</sup>, Ladislau Nagy<sup>1</sup>, Radu I Campeanu<sup>2</sup>

<sup>1</sup>*Faculty of Physics, Babeş-Bolyai University, 400084 Cluj-Napoca, Romania*

<sup>2</sup>*Department of Physics and Astronomy, York University, Toronto, Canada M3J 1P3*

E-mail: istvan.toth@phys.ubbcluj.ro

Triple-differential cross sections for the ionization of NH<sub>3</sub> and CH<sub>4</sub> by electron impact were determined for coplanar and non-coplanar geometries and for different energy configurations of the emitted electrons. Good agreement with the experimental data were obtained.

## 1. Introduction

Kinematically complete studies provide the most complete set of information about the ionization process of atoms and molecules by electron impact. The physical quantity, which characterizes such processes is the TDCS (triple or fully differential cross section). The complete description of (e, 2e) processes is still incomplete, especially in case of molecular targets. On the experimental side one of the main difficulties is the separation of molecular orbitals, which may be very closely spaced in energy. The theoretical description of such complex processes faces difficulties mainly in the description of the multi-center nature of the target or the correct simulation of the interaction between the different particles involved in the ionization process.

In the present study we present calculated TDCSs for the ionization of NH<sub>3</sub> and CH<sub>4</sub> by electron impact. These targets are iso-electronic, therefore a comparison of the p-like and s-like orbitals of the two molecules may provide useful insight related to the influence of the molecular structure on the TDCS. In the case of the NH<sub>3</sub> we have considered the 3a<sub>1</sub> and 1e<sub>1</sub> orbitals, while in case of the CH<sub>4</sub> molecule the 1t<sub>2</sub> orbital was studied. All these orbitals are of p-character. The corresponding orbitals of s-character are the 2a<sub>1</sub> orbitals for both targets.

The TDCSs were calculated in the scattering and the perpendicular planes, for equal energy-sharing of the outgoing electrons. Since the electrons considered in this study have energies lower or equal than 20 eV, it is expected a significant influence of the PCI (post collision effects) on the cross section. In our study these effects are taken into account through the Gamow or the Coulomb distortion factors of [1]. The obtained results are compared with the experimental data presented in [2].

## 2. Theoretical aspects and results

In the framework of the DWBA (distorted-wave Born approximation) method the TDCS may be given as

$$\frac{d^3\sigma}{d\hat{\mathbf{k}}_f d\hat{\mathbf{k}}_e dE_e} = 2(2\pi)^4 \frac{k_f k_e}{k_i} |t|^2. \quad (1)$$

Here,  $t$  is the transition matrix

$$|t|^2 = |t_d|^2 + |t_{ex}|^2 - |t_d||t_{ex}|. \quad (2)$$

The transition matrix is given in terms of the direct and exchange matrix elements

$$t_d = \langle \phi_f(\mathbf{r}_1) \phi_e(\mathbf{r}_2) | V(r_{12}) | \phi_b(\mathbf{r}_2) \phi_i(\mathbf{r}_1) \rangle \quad (3)$$

and

$$t_{ex} = \langle \phi_e(\mathbf{r}_1) \phi_f(\mathbf{r}_2) | V(r_{12}) | \phi_b(\mathbf{r}_2) \phi_i(\mathbf{r}_1) \rangle, \quad (4)$$

where,  $\phi_x$  ( $x = f, e, i$  or  $b$ ) stands for the wave function of the scattered, ejected, incident or bound electrons, respectively. In order to describe the initial state of the bound electron, we have employed Gaussian-type functions. Thus, the molecular orbitals are a linear combination of atomic wave functions, which are constructed in terms of Gaussian contractions.

The TDCSs are calculated by two methods, the TS (total screening) and TS\*. Both methods employ distorted waves in order to describe the incident, scattered and ejected electrons. In the TS\* model we assume that the scattered and ejected electrons move in the same, spherically averaged

potential of the residual ion, while in the TS model only the slower electron experiences the effect of this field, the faster electron moves in the field of the neutral molecule. TDCSs will also be presented for an enhanced nuclei-electron interaction, by reducing the distances of the constituent nuclei of the target from the molecular center.

Here, we present some preliminary results obtained for the  $3a_1$  orbital of the  $\text{NH}_3$  molecule. The scattered and ejected electron energies are  $E = E_f = E_e = 20$  eV. We consider a symmetric emission of the outgoing electrons. PCI effects are taken into account only through the Gamow factor. As Fig. 1 shows the TDCS calculated with the TS\* method are in better agreement with the experimental data.

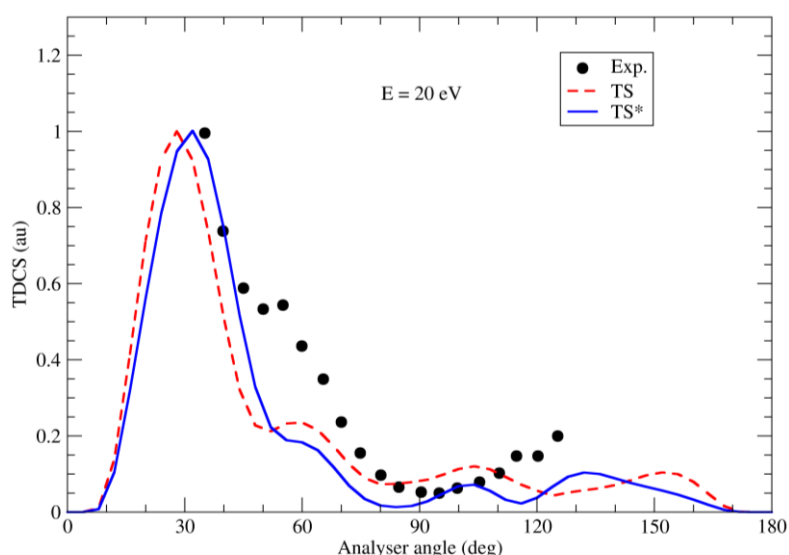


Fig. 1. TDCSs for the ionization of the  $3a_1$  orbital of the  $\text{NH}_3$  molecule in the scattering plane as a function of the analyser angle. Experimental data are from [2].

### 3. Conclusions

We have determined TDCSs for the ionization of  $\text{NH}_3$  and  $\text{CH}_4$  molecules by electron impact. The obtained preliminary results show promising agreement with the experimental data. Detailed results for coplanar and perpendicular geometries and for the considered molecular orbitals, will be presented at the CEPAS 2014 conference.

### Acknowledgements

This work was supported by a grant of the Romanian National Authority for Scientific Research, CNCS-UEFISCDI, project number PN-II-ID-PCE-2011-3-0192 and by a grant of the Babeş-Bolyai University, project number GTC\_34032/2013.

### 4. References

- [1] Ward S J and Macek J H 1994 *Phys. Rev. A* **49** 1049
- [2] Nixon K L et al 2013 *J. Chem. Phys.* **138** 174304

# IONIZATION OF WATER BY ELECTRON IMPACT

Ladislau Nagy<sup>1</sup>, István Tóth<sup>1</sup>, Radu I Campeanu<sup>2</sup>

<sup>1</sup>*Faculty of Physics, Babeş-Bolyai University, 400084 Cluj-Napoca, Romania*

<sup>2</sup>*Department of Physics and Astronomy, York University, Toronto, Canada M3J 1P3*

E-mail: lnagy@phys.ubbcluj.ro

Triple-differential cross sections for the ionization of water by electron impact were determined for coplanar and non-coplanar geometries and for different energy configurations of the emitted electrons. Reasonably good agreement with the experimental data were obtained in case of both geometrical arrangements.

## 1. Introduction

The interaction of charged particles with matter is of interest for several research fields, like astrophysics, radiobiology, atmospheric sciences and even medical sciences. Water is one of the most abundant molecules on earth. It is largely present in biological tissues, therefore it is regarded as a test case for the interaction of charged particles with living tissues.

The ionization of water by electron impact has attracted much interest lately. In the last years, both experimental and theoretical studies were performed [1-5]. TDCSs (triple-differential cross sections) were determined mainly for coplanar symmetric and asymmetric configurations, but also non-coplanar studies were performed for intermediate and low-energy electrons.

In our present work we have calculated TDCSs for the single ionization of water by electron impact. In a previous study [5] we have calculated TDCSs for a coplanar asymmetric configuration with intermediate impact energies. Now, we refine these calculations by taking into account the PCI (post-collision interaction) effects through the Gamow and the full Coulomb-distortion factor presented in [6]. TDCSs were calculated and will be presented also for low-energy coplanar and non-coplanar geometries and for equal and non-equal energy sharing.

## 2. Theory

The TDCS for the ionization the water molecule by electron impact in the distorted-wave formalism is written as follows

$$\frac{d^3\sigma}{d\mathbf{k}_f d\mathbf{k}_e dE_e} = 2(2\pi)^4 \frac{k_f k_e}{k_i} |t|^2 \quad (1)$$

The TDCS is differential with respect to the angles of the scattered and ejected electrons and the energy of the emitted electron. Here,  $t$  is the transition matrix

$$|t|^2 = |t_d|^2 + |t_{ex}|^2 - |t_d||t_{ex}|. \quad (2)$$

The transition matrix is given in terms of the direct and exchange matrix elements

$$t_d = \langle \phi_f(\mathbf{r}_1) \phi_e(\mathbf{r}_2) | V(r_{12}) | \phi_b(\mathbf{r}_2) \phi_i(\mathbf{r}_1) \rangle \quad (3)$$

and

$$t_{ex} = \langle \phi_e(\mathbf{r}_1) \phi_f(\mathbf{r}_2) | V(r_{12}) | \phi_b(\mathbf{r}_2) \phi_i(\mathbf{r}_1) \rangle, \quad (4)$$

where,  $\phi_x$  ( $x = f, e, i$  or  $b$ ) stands for the wave function of the scattered, ejected, incident or bound electrons, respectively. In order to describe the initial state of the bound electron, we have employed Gaussian-type functions. Thus, the molecular orbitals are a linear combination of atomic wave functions, which are constructed in terms of Gaussian contractions.

The TDCSs are calculated by two methods, the TS (total screening) and TS\*. Both methods employ distorted waves in order to describe the incident, scattered and ejected electrons. In the TS\* model we assume that the scattered and ejected electrons move in the same, spherically averaged potential of the residual ion, while in the TS model only the slower electron experiences the effect of this field, the faster electron moves in the field of the neutral molecule. TDCSs were calculated also for an enhanced nuclei-electron interaction, by reducing the distances of the constituent nuclei of the target from the molecular center.

### 3. Results and discussions

Here, we present only a few results for the ionization of water by electron impact. We show results in case of the  $3a_1$  orbital of the molecule for coplanar (all particles are in the same plane) and perpendicular (the electrons are emitted perpendicular to the incident direction) geometries, respectively. The results presented below were obtained for equal-energy sharing of the scattered and ejected electrons ( $E_f = E_e = 10$  eV) and for a symmetric emission of the outgoing electrons. PCI effects were taken into account only through the Gamow factor. The numbers in the figure legends represent the fraction of the original distance between the constituent nuclei of the target and the molecular center. The obtained cross sections are compared with the experimental data and the theoretical predictions of the MDW (molecular distorted-wave Born approximation) model [1].

As both Fig. 1 and Fig. 2 show the results are in relatively good agreement with experimental measurements for both geometries. Fig. 1 shows that by increasing the nuclei-electron interaction, does not increase the intensity of the recoil peak. In the perpendicular plane, we obtain better agreement in case of a stronger nuclei-electron interaction at these energies.

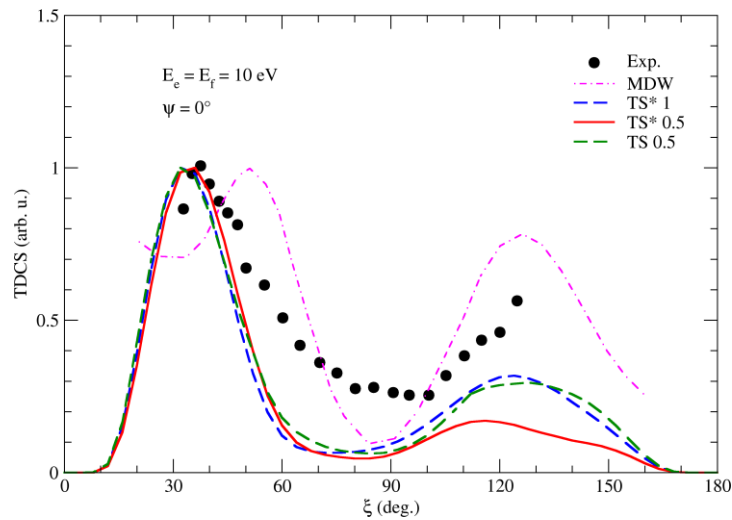


Fig. 1. TDCSs for the ionization of the  $3a_1$  orbital of the water molecule in the scattering plane as a function of the analyser angle. Experimental and the MDW results are from [1].

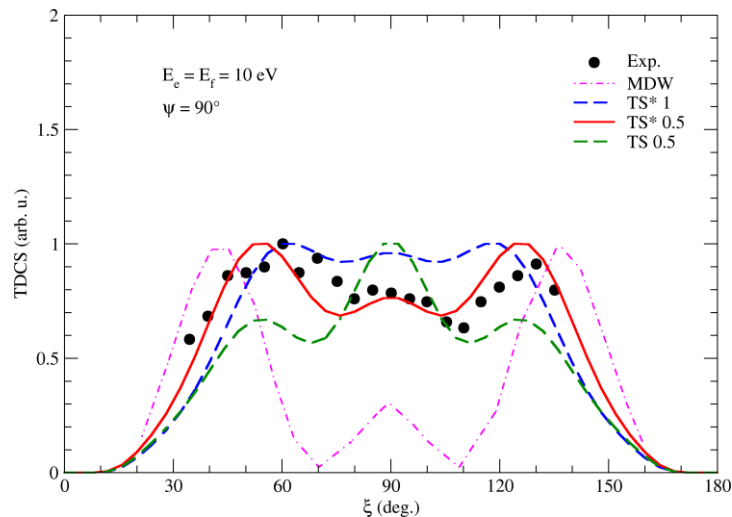


Fig. 2. TDCSs for the ionization of the  $3a_1$  orbital of the water molecule in the perpendicular plane as a function of the analyser angle. Experimental and the MDW results are from [1].

## 4. Conclusions

We have calculated TDCSs for the ionization of the water molecule by electron impact. The obtained results for the  $3a_1$  orbital show a good agreement with experimental measurements for both geometrical arrangements presented here. In the scattering plane the enhanced nuclei-electron interaction does not increase the recoil peak, while for a perpendicular geometry we obtained better agreement with the experimental data by taking into account this enhancement. The results for other orbitals of the water molecule and for other energies of the ejected and scattered electrons will be presented in detail at the CEPAS 2014 conference.

## Acknowledgements

This work was supported by a grant of the Romanian National Authority for Scientific Research, CNCS-UEFISCDI, project number PN-II-ID-PCE-2011-3-0192 and by a grant of the Babeş-Bolyai University, project number GTC\_34032/2013.

## 5. References

- [1] Nixon K L et al 2010 *J. Phys. B: At. Mol. Opt. Phys.* **43** 035201
- [2] Champion C et al 2006 *Phys. Rev. A* **73** 012717
- [3] Milne-Brownlie D S et al 2004 *Phys. Rev. A* **69** 032701
- [4] Sahlaoui M et al 2013 *J. Phys. B: At. Mol. Opt. Phys.* **46** 115206
- [5] Tóth I et al 2012 *Eur. Phys. J. D* **66** 21
- [6] Ward S J and Macek J H 1994 *Phys. Rev. A* **49** 1049

# DIELECTRONIC RECOMBINATION RATE COEFFICIENTS OF RUBIDIUMLIKE TUNGSTEN

Zhongwen Wu<sup>1,2</sup>, Chenzhong Dong<sup>1</sup>, Yizhao Zhang<sup>3</sup>, Yanbiao Fu<sup>1</sup>,  
Andrey Surzhykov<sup>2</sup>, Stephan Fritzsche<sup>2,4</sup>

<sup>1</sup>Key Laboratory of Atomic and Molecular Physics & Functional Materials of Gansu Province, College of Physics and Electronic Engineering, Northwest Normal University, Lanzhou 730070, China

<sup>2</sup>Helmholtz-Institut Jena, D-07743 Jena, Germany

<sup>3</sup>Lanzhou University Second Hospital, Lanzhou 730030, China

<sup>4</sup>Theoretisch-Physikalisches Institut, Friedrich-Schiller-Universität Jena, D-07743 Jena, Germany  
E-mail: wuzhongwen05@126.com

Dielectronic recombination (DR) rate coefficients from the ground state of rubidiumlike W<sup>37+</sup> ion through doubly excited states  $(3s^23p^63d^{10}4s^24p^64d)^{-1}nl'n'l'$  have been calculated in the temperature range from 1 to  $5 \times 10^4$  eV using fully relativistic configuration interaction method. Comparison of these rate coefficients from different subshell excitations shows that the 4p excitation dominates total DR rate coefficients in the whole energy region, followed by the 4s and 4d excitations, while the 3d, 3p, and 3s excitations become important with increasing electron energy. Moreover, it also shows that DR rate coefficients are much larger than the radiative recombination and three-body recombination ones, and thus the DR process can strongly influence the ionization balance.

## 1. Introduction

Dielectronic recombination (DR) is a basic atomic process in electron-ion collisions. Accurate DR rate coefficients are crucial for studying the ionization balance of highly ionized ions in hot plasmas [1]. The knowledge on DR rate coefficients is also very important for the research of x-ray lasers, and especially for determinations of populating and depopulating lasing levels [2]. Moreover, DR process is one of the best strategies to investigate the structure and radiative decay dynamics of atomic doubly excited states. On the other hand, tungsten will be used for a certain plasma-facing components in the divertor region of the International Thermonuclear Experimental Reactor (ITER), and also used for the diagnostics of erosion of heavy species into reaction plasmas [3]. Also, with regard to studies of the divertor plasma modelling and radiative cooling, accurate atomic data of highly ionized tungsten ions are essential, especially the data on DR process, since which is a major source of radiation losses. Because of this, DR rate coefficients for various ionized tungsten ions, such as Ne-, Co-, Ni-, Cu-, Y-, and Er-like ions [4], have been calculated in full detail recently. Since Rb-like tungsten is one of the most abundant charge states of tungsten plasma under the operating condition of ITER, it is of great interest to study the DR process of Rb-like tungsten.

## 2. Theoretical background

In the isolated resonance approximation, the DR rate coefficients from initial state  $i$  of dielectronic capture into a final state  $f$  through an intermediate doubly excite state  $j$ . Assuming a Maxwellian velocity distribution of the thermal plasma electrons, ignoring the detailed structure of the resonance profiles and using the detailed balance principle, the DR rate coefficient can be expressed as

$$\alpha_{ijf}^{DR}(kT_e) = \left( \frac{2\pi\hbar^2}{m_e kT_e} \right)^{3/2} \frac{g_j}{2g_i} A_{ji}^a \frac{A_{jf}^r}{\sum_k A_{jk}^a + \sum_{f'} A_{jf'}^r} \exp\left(-\frac{E_{ij}}{kT_e}\right), \quad (1)$$

where  $m_e$  is the mass of electron,  $kT_e$  is the electron temperature,  $g_i$  and  $g_j$  denote the statistical weights of states  $i$  and  $j$ , and  $E_{ij}$  is the resonant energy. Moreover,  $A^a$  and  $A^r$  represent the Auger and radiative decay rates, respectively, which can be given as follows

$$A_{ji}^a = \frac{2\pi}{\hbar} \left| \left\langle \Psi_{i\varepsilon_j} \left| \sum_{p < q} \frac{1}{r_{pq}} \right| \Psi_j \right\rangle \right|^2 \quad (2)$$

$$A_{if}^r = \frac{4e^2\omega}{3c^3g_j\hbar} \left| \langle \Psi_f | T^{(1)} | \Psi_i \rangle \right|^2. \quad (3)$$

where  $\Psi_{ij}$  is the state consisting of the initial atomic state and a free electron,  $\Psi_j$  and  $\Psi_f$  represent the intermediate and final states, respectively, and  $T^{(1)}$  denotes the electric dipole transition operator.

### 3. Results and discussions

In this work, the Flexible Atomic Code (FAC) based on fully relativistic configuration-interaction method was employed to calculate DR rate coefficients. We here considered the DR processes of Rb-like  $W^{37+}$  ion in the ground state  $[Ne]3s^23p^63d^{10}4s^24p^64d$  through the following doubly excited states,  $3s3p^63d^{10}4s^24p^64d\ nln'l'$ ,  $3s^23p^53d^{10}4s^24p^64d\ nln'l'$ , and  $3s^23p^63d^94s^24p^64d\ nln'l'$  with  $n' \leq 16$  and  $l' \leq 9$ ,  $3s^23p^63d^{10}4s4p^64d\ nln'l'$ ,  $3s^23p^63d^{10}4s^24p^54d\ nln'l'$ , and  $3s^23p^63d^{10}4s^24p^6\ nln'l'$  with  $n' \leq 18$  and  $l' \leq 12$ . Equation (1) can be used in order to calculate DR rate coefficients from different subshell excitations. For example, Fig. 1 displays total DR rate coefficients and partial contributions corresponding to the 3s, 3p, 3d, 4s, 4p and 4d subshell excitations from the ground state of Rb-like  $W^{37+}$  ion. As shown clearly, the 4p subshell excitation dominates total DR rate coefficients in the whole region of electron energy, followed by the 4s and 4d subshell excitations with much less contribution to the total DR rate coefficients. Furthermore, the 3d, 3p, and 3s excitations start playing roles in sequence at high energies and become more and more important with increasing electron energy.

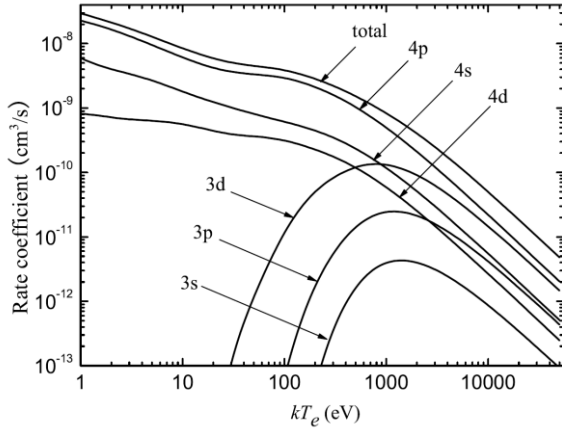


Fig. 1. Total DR rate coefficients for the ground state of Rb-like  $W^{37+}$  ion as well as the partial contributions from 3s, 3p, 3d, 4s, 4p, and 4d excitations as functions of electron temperature.

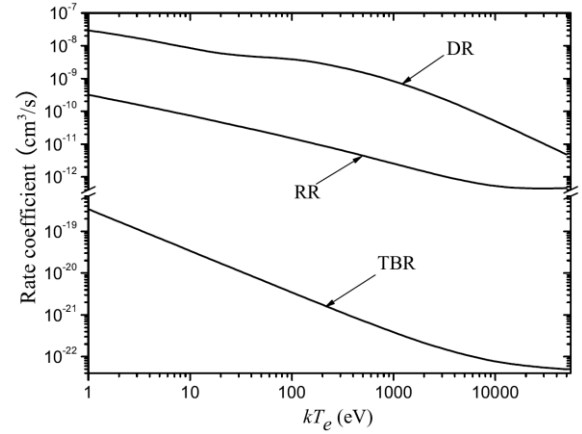


Fig. 2. Total DR, RR, and TBR rate coefficients for the ground state of Rb-like  $W^{37+}$  ion as functions of electron temperature.



Apart from the DR process, the radiative recombination (RR) and three-body recombination (TBR) are also two basic recombination processes in plasmas. For this reason, we estimated here the total RR and TBR rate coefficients for Rb-like  $W^{37+}$  ion semiempirically in which the density of free electron was assumed to be  $10^{14} \text{ cm}^{-3}$ . As shown in Fig. 2, the total DR rate coefficients are larger than the RR and TBR ones by nearly 2 and 11 orders of magnitude, respectively, in the whole region of electron temperature. Therefore, the DR process can strongly influence the ionization balance in plasmas.

#### 4. References

- [1] Dubau J and Volante S 1980 *Rep. Prog. Phys.* **43** 199.
- [2] Burgess A 1964 *Astrophys. J.* **139** 766.
- [3] Skinner C H 2008 *Can. J. Phys.* **86** 285.
- [4] Safronova U I and Safronova A S 2012 *Phys. Rev. A* **85** 032507.

# ISOTOPE-SPECIFIC $K\alpha_1$ EMISSION OF HELIUMLIKE IONS DUE TO HYPERFINE INTERACTION EFFECTS

Zhongwen Wu<sup>1</sup>, Andrey Surzhykov<sup>1</sup>, Stephan Fritzsche<sup>1,2</sup>

<sup>1</sup>*Helmholtz-Institut Jena, D-07743 Jena, Germany*

<sup>2</sup>*Theoretisch-Physikalisches Institut, Friedrich-Schiller-Universität Jena, D-07743 Jena, Germany*

E-mail: wuzhongwen05@126.com

The anisotropy of the  $K\alpha_1$  emission following the radiative electron capture into finally heliumlike ions with nonzero nuclear spin has been studied. Special attention was placed upon the question of how the hyperfine interaction affects the  $K\alpha_1$  emission. Detailed calculations were performed for selected heliumlike  $\text{Sn}^{48+}$ ,  $\text{Xe}^{52+}$  and  $\text{Tl}^{79+}$  isotopes. It was shown that the hyperfine interaction could significantly affect the  $K\alpha_1$  angular properties for realistic values of the magnetic dipole moment  $\mu_I$  and especially for the nuclear spin  $I = 1/2$ , while its effect was suppressed for isotopes with spin  $I > 1/2$ . We therefore suggest that accurate measurements of the  $K\alpha_1$  anisotropy can be utilized as an independent tool for determining the nuclear parameters of isotopes with  $I \neq 0$ .

## 1. Introduction

The angular anisotropy of the characteristic x-ray emissions of highly charged ions has been studied extensively during the last decades. When compared to measurements of the total decay rates of these ions, such angle-resolved studies were often found to be much more sensitive with regard to various interactions and effects. Until now, however, most studies on the x-ray emission have been performed for atomic ions with zero nuclear spin,  $I = 0$ , while much less attention was paid so far to isotopes with  $I \neq 0$ . Recently, we [1] have studied the  $K\alpha_1$  emission following the radiative electron capture into the  $1s2p_{3/2}^{1,3}P_{1,2}$  levels of finally heliumlike ions with nonzero nuclear spin within the framework of the density matrix theory and the multiconfiguration Dirac-Fock method. Emphasis was especially placed upon the hyperfine interaction and how this interaction of the magnetic moment of the nucleus with those of the electrons affects the angular properties of the  $K\alpha_1$  radiation.

## 2. Theoretical background

The angular anisotropy of the overall  $K\alpha_1$  emission can be described in terms of effective anisotropy parameter  $\beta_2^{\text{eff}}$  by taking the average over the corresponding hyperfine- and fine-structure parameters. For the isotopes with nuclear spin  $I = 1/2$ , for example, this effective anisotropy parameter can be expressed as [1]

$$\beta_2^{\text{eff}}(K\alpha_1; I = 1/2) = \frac{1}{3\sqrt{2}} N_{J=1} A_{20}({}^1P_1) + \frac{2}{5} \sqrt{\frac{7}{5}} N_{J=2} A_{20}({}^3P_2) \left( \frac{\sqrt{6}}{2} \frac{a_{E1}}{a_{M2}} - \frac{\sqrt{2}}{4} - \frac{3\sqrt{2}}{7} \right) \quad (1)$$

where  $N_i$  is the statistical weights and  $A_{20}$  the alignment parameters of fine-structure levels involved. Moreover, the  $a_{pL}$  there denotes the reduced radiative transition amplitudes for the leading M2 and hyperfine-induced E1 channels of the  $1s2p_{3/2} {}^3P_2$ ,  $F_i = 3/2 \rightarrow 1s^2 {}^1S_0$ ,  $F_f = 1/2$  hyperfine-resolved transition, which depend on the nuclear magnetic dipole moment  $\mu_I$  of the isotopes. For spin  $I = 0$ , this effective anisotropy parameter can be simplified as follows [1]

$$\beta_2^{\text{eff}}(K\alpha_1; I = 0) = \frac{1}{\sqrt{2}} N_{J=1} A_{20}({}^1P_1) - \sqrt{\frac{5}{14}} N_{J=2} A_{20}({}^3P_2) \quad (2)$$

which purely depends on the weight factors and the alignment parameters of the excited  $1s2p_{3/2} {}^{1,3}P_{1,2}$  levels, independent of any nuclear parameters or the amplitudes of the associated transitions.

### 3. Results and discussions

Equations (1) and (2) can be utilized in order to analyze the anisotropy of the characteristic  $K\alpha_1$  line and to understand the changes in the overall observed  $K\alpha_1$  angular emission of ions with nonzero nuclear spin owing to the hyperfine interaction. For example, Fig. 1 displays the effective anisotropy parameter  $\beta_2^{\text{eff}}$  of the  $K\alpha_1$  radiation as functions as nuclear magnetic dipole moment  $\mu_I$ , following the radiative electron capture into initially hydrogenlike projectiles. In this figure, all calculations were carried out for a projectile energy  $T_p = 50$  MeV/u. Results are shown for isotopes with zero nuclear spin  $I = 0$  (shadowed area) as well as for selected spin-1/2 tin isotopes  $^A\text{Sn}^{48+}$  ( $A = 119, 113, 121$ ; black points), xenon isotopes  $^A\text{Xe}^{52+}$  ( $A = 129, 127, 125, 123$ ; red squares), and thallium isotopes  $^A\text{Tl}^{79+}$  ( $A=187, 205, 207$ ; blue triangles) [2]. As seen from this figure, the effective anisotropy  $\beta_2^{\text{eff}}$  ( $I = 0$ ) is nearly the same for all mid- and high- $Z$  elements, while the parameters  $\beta_2^{\text{eff}}$  ( $I = 1/2$ ) decrease roughly linear with the magnetic dipole moment  $\mu_I$  of the isotopes. Take the isotope  $^{119}\text{Sn}^{48+}$  for example, the  $\beta_2^{\text{eff}}$  increases from 0.04 to 0.104, when compared to its zero-spin counterpart. Such a change in the  $\beta_2^{\text{eff}}$  parameter can be easily detected by using present-day detectors [3]. Furthermore, for the isotopes with larger nuclear spin  $I > 1/2$ , these effects of the hyperfine interaction are typically washed out, which can be understood as the mutual cancelation of averaging over the fine- and more complex hyperfine-structure components of the  $K\alpha_1$  emission.

From our theoretical analysis, we therefore suggest that accurate measurements of the  $K\alpha_1$  angular emission at ion storage rings can be utilized as an independent approach for determining the nuclear parameters, such as the nuclear spin and magnetic moment of rare stable or radioactive isotopes with nonzero nuclear spin.

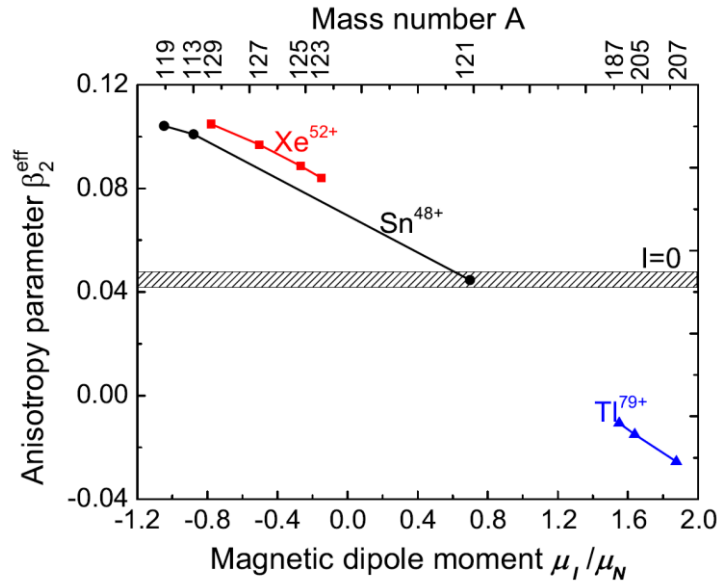


Fig. 1. Effective anisotropy parameter  $\beta_2^{\text{eff}}$  of the  $K\alpha_1$  emission as functions of the magnetic dipole moment  $\mu_I$  following the radiative electron capture into  $1s2p_{3/2} \ ^{1,3}\text{P}_{1,2}$  levels of initially hydrogenlike projectiles with energy  $T_p = 50$  MeV/u. results are shown for selected spin-1/2 isotopes as well as their zero-spin counterparts (shadowed area).

### 4. References

- [1] Wu Z W, Surzhykov A and Fritzsche S 2014 *Phys. Rev. A* **89** 022513.
- [2] Stone N J 2005 *At. Data Nucl. Data Tables* **90** 75.
- [3] Weber G and Bräuning H *et al.* 2010 *Phys. Rev. Lett.* **105** 243002.

# ELECTRON-SCATTERING CROSS SECTIONS FOR SELECTED ALKYNE MOLECULES

Mateusz Zawadzki, Paweł Możejko, Elżbieta Ptasińska-Denga,  
Czesław Szmytkowski

*Atomic Physics Division, Department of Atomic, Molecular and Optical Physics,  
Faculty of Applied Physics and Mathematics, Gdańsk University of Technology,  
ul. G. Narutowicza 11/12, 80-233 Gdańsk, Poland*

E-mail: m.zawadzki@mif.pg.gda.pl

We report comparative studies based on cross-section results from experimental studies on electron collisions with 1-butyne ( $\text{HC}\equiv\text{C}-\text{CH}_2\text{CH}_3$ ), acetylene ( $\text{HC}\equiv\text{CH}$ ) and 1,2-butadiene molecules. The experimental TCS curves, for a series of acetylenic compounds: acetylene ( $\text{HC}\equiv\text{CH}$ ), propyne ( $\text{HC}\equiv\text{C}-\text{CH}_3$ ), and 1-butyne ( $\text{HC}\equiv\text{C}-\text{CH}_2\text{CH}_3$ ), are compared to study the substitutional effect. Finally, the influence of the structural differences on the electron-scattering TCS for isomers of the  $\text{C}_4\text{H}_6$  molecule (1-butyne, 2-butyne, and 1,3-butadiene) is depicted.

## 1. Introduction

Understanding physical, among others, phenomena accompanying the interaction of charged particles with matter requires comprehensive information about the total cross sections for electron collisions with polyatomic molecules. In addition, information about the collisions of electrons with the particles is essential in modeling and controlling the physico-chemical reactions.

The total cross section (TCS), containing complex information from all scattering channels, is a quantity, which can be determined with good accuracy without any normalization procedures. Due to its reliable absolute value, the experimental TCS can be used as a calibration standard or upper limit reference for the normalization of cross sections for particular processes, as well as for the estimation of scattering quantities, which are difficult to obtain. The TCS data also may test the reliability of theoretical models and computational procedures used in the electron-scattering calculations. However, in spite of unceasing interest in the electron-driven processes for media containing hydrocarbons, there is still a need to gather the data for more complex compounds.

In our work we focus on comparison of TCSs for electron scattering from structurally related alkynes: acetylene ( $\text{H}-\text{C}\equiv\text{C}-\text{H}$ ), propyne, ( $\text{H}-\text{C}\equiv\text{C}-\text{CH}_3$ ), and 1-butyne ( $\text{H}-\text{C}\equiv\text{C}-\text{CH}_2\text{CH}_3$ ). Fig. 1 depicts the geometry of the studied compounds.

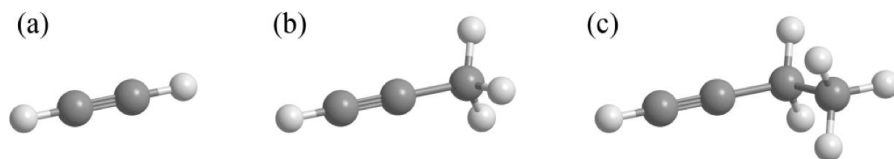


Fig. 1. Schematic geometry of molecules: (a) acetylene ( $\text{C}_2\text{H}_2$ ),  
(b) propyne ( $\text{C}_3\text{H}_4$ ) and (c) 1-butyne ( $\text{C}_4\text{H}_6$ )

Additionally we compare the electron scattering TCSs for isomers of the  $\text{C}_4\text{H}_6$  molecule: 1-butyne, 2-butyne, and 1,3-butadiene. Fig. 2 presents the schematic geometries of considered hydrocarbon isomers.

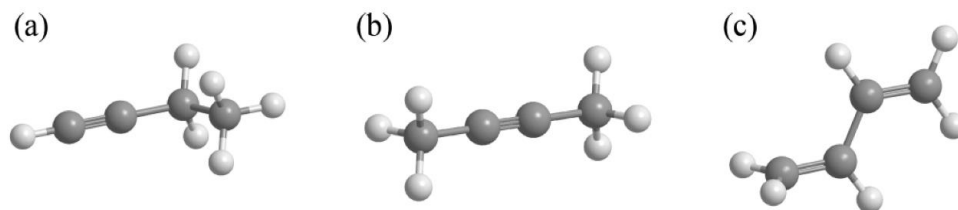


Fig. 2. Schematic geometry of C<sub>4</sub>H<sub>6</sub> isomers: (a) 1-butyne, (b) 2-butyne and (c) 1,3-butadiene

## 2. Substitutional and isomeric effects

At first, one hydrogen atom in the acetylene molecule was replaced with the methyl group (CH<sub>3</sub>) to form a propyne molecule (H–C≡C–CH<sub>3</sub>) or with the ethyl group (CH<sub>2</sub>CH<sub>3</sub>) to form 1-butyne (H–C≡C–CH<sub>2</sub>CH<sub>3</sub>). The substitution of one hydrogen atom in the acetylene molecule with a functional unit of increasing length enlarges the size of the resulting compound and, as a consequence, should lead to the increase of the respective electron-scattering TCS values. The observed relation between data for different functional groups substituted in the acetylene molecule is shown in Fig 3.

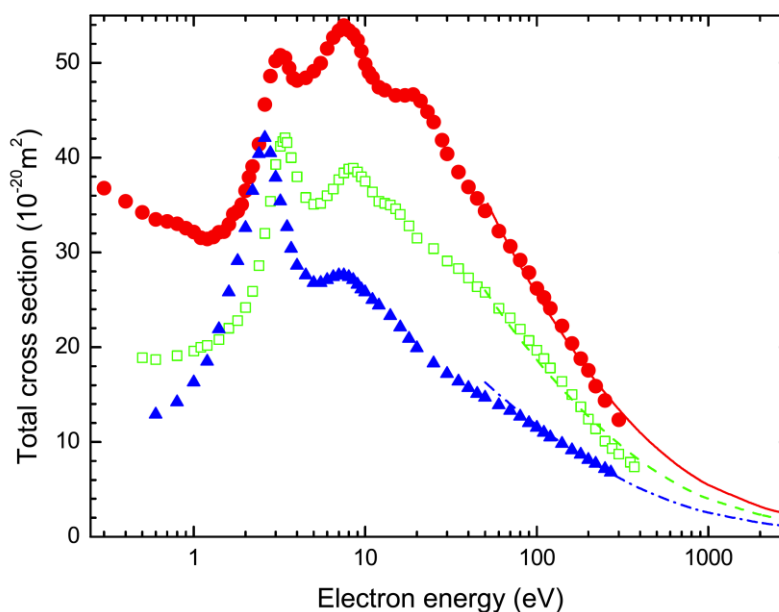


Fig. 3. Comparison of total absolute cross sections for electron scattering from the acetylene molecule and its derivatives. H–C≡C–H: full (blue) triangles; H–C≡C–CH<sub>3</sub>: open (green) squares; H–C≡C–CH<sub>2</sub>CH<sub>3</sub>: full (red) circles; the lines correspond to the theoretical calculations [1].

Making use of the experimental absolute TCS data for selected C<sub>4</sub>H<sub>6</sub> compounds, we could examine how a different arrangement of atomic components of molecule affects the electron-scattering cross sections. While geometry of the considered compounds are shown in Fig. 2, the figure below (Fig. 4) gives insight into total absolute cross sections measured in our laboratory for electron scattering from C<sub>4</sub>H<sub>6</sub> isomers.

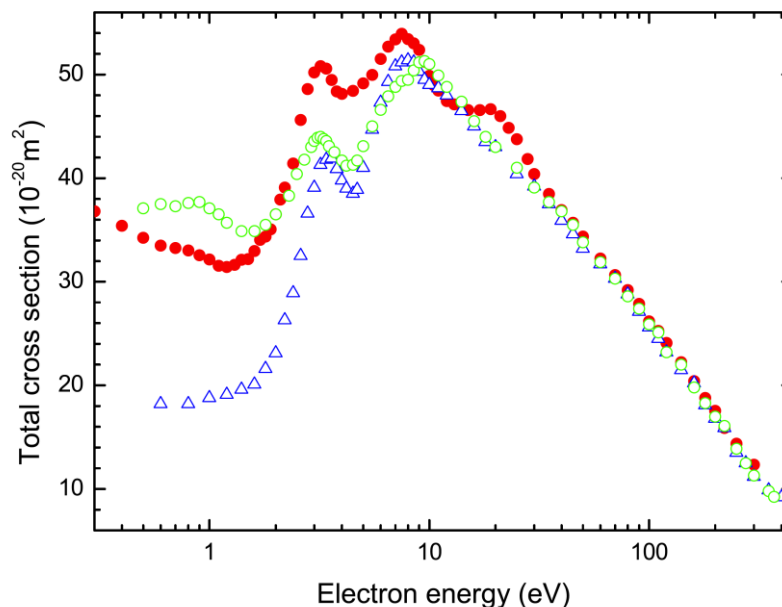


Fig. 4. Comparison of total absolute cross sections from  $C_4H_6$  isomers:  $H-C\equiv C-CH_2CH_3$ , full (red) circles;  $H_3C-C\equiv C-CH_3$ , open (blue) triangles;  $H_2C=CHCH=CH_2$ , open (green) circles, [2].

Recently we have extended our studies on the other  $C_4H_6$  isomers, including 1,2-butadiene, which is a hydrocarbon that contains two carbon double bonds. The main objective of that study is to compare its TCS data with 1,3-butadiene – a compound with conjugated double carbon-carbon bonds from  $C_4H_6$  isomeric group (Fig. 5).

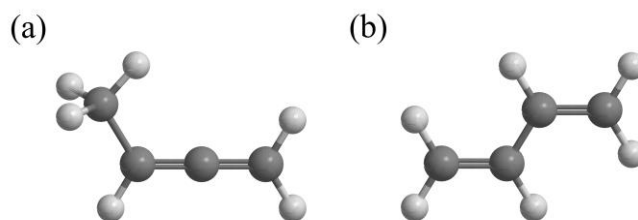


Fig. 5. Schematic geometry of  $C_4H_6$  isomers: (a) 1,2-butadiene; (b) 1,3-butadiene

### 3. References

- [1] Szmytkowski Cz, Możejko P, Zawadzki M, Maciąg K and Ptasńska-Denga E 2014 *Phys. Rev. A* **89** 052702
- [2] Szmytkowski Cz and Kwitniewski S 2003 *J. Phys. B* **36** 2129

## SPECTRAL LINES OF CAESIUM HYDRIDE IN HIGH VACUUM

Ján Škoviera<sup>1</sup>, Ivan Černušák<sup>1</sup>, Florent Louis<sup>2</sup>

<sup>1</sup>*A Department of Physical and Theoretical Chemistry, Comenius University Bratislava*

<sup>2</sup>*Laboratoire de PhysicoChimie des Processus de Combustion et de  
l'Atmosphère (PC2A) Université Lille1 Sciences et Technologies, Villeneuve d'Ascq, France*

E-mail: skoviera@fns.uniba.sk

Experiments BATMAN and ELISE in Max Planck Institute for plasma physics are designed to produce negative hydrogen ion beam by converting hydrogen cations on cesium-covered cathode. Since the diagnostics system carries a visual spectrometer, to identify the spectral lines the Einstein coefficients for visible spectroscopy and energy differences of the electronic states are the most valuable. We calculated spectroscopic properties of Cesium Hydride and its ions along with the Einstein coefficients. We used CASPT2 to calculate the manifold of singlet and triplet states. We used the state interaction method to calculate the spin-free and spin-orbital energies along with the spin-orbital coupling.

# NEAR-THRESHOLD EXCITATION OF THE RESONANCE $\lambda$ 182.2 NM LINE AT ELECTRON - $\text{Pb}^+$ ION COLLISIONS

Anna Gomonai, Yuriy Hutykh, Aleksandr Gomonai

*Institute of Electron Physics, Ukrainian National Academy of Sciences,  
21 Universitetska str., 88017 Uzhgorod, Ukraine*

E-mail: annagomonai@gmail.com

Near-threshold electron-impact excitation of the resonance  $6s^2 6d^2 D_{5/2} \rightarrow 6s^2 6p^2 P^o_{3/2}$  ( $\lambda = 182.2$  nm) line of the  $\text{Pb}^+$  ion is studied using a spectroscopic method and a crossed electron and ion beams technique. Distinct features observed in the energy dependence of the effective excitation cross-section for this line are due to the cascade decay of the ordinary  $5d^{10} 6s^2 nl$  states as well as resonance excitation due to the electron decay of the  $5d^{10} 6s^2 nl n_1 l_1$ ,  $5d^9 6s^2 6p^3$ , and  $5d^9 6s^2 6p^2 np, nf$  autoionizing states. Our experimental studies confirm not only the crucial role played by electron-electron correlations, but also suggest that correlation phenomena can be a new tool for investigation of the collision process details.

## 1. Introduction

Precise experimental measurements of electron-impact excitation of heavy ions are needed for many different applications including diagnostics of the temperature and density of an emitting plasma, and the abundances of the elements within the plasma, development of optical atomic clocks, testing theories, etc. In addition, lead has been identified in different astrophysical objects. Pb II was detected in several stars with the Goddard high resolution spectrograph (GHRS) aboard the Hubble Space Telescope [1]. The resonance lines of Pb II are accessible in the GHRS spectral range (1150–3100 Å) as well as in the interstellar medium [2].

The  $\text{Pb}^+$  ion is in the same line of the Periodic Table as the  $\text{Ti}^+$  ion which showed a significant contribution of resonance processes to electron-impact excitation cross-sections [3]. In addition, a full understanding of scattering phenomena related to both structure and dynamics of the  $\text{Pb}^+$  ion is an important step in modeling complex multi-electron ions. With a filled  $5d^{10}$  and  $6s^2$  subshells and outer  $6p$  shell, the  $\text{Pb}^+$  ion is an important example of both complexity of electron correlation and importance of relativistic effects.

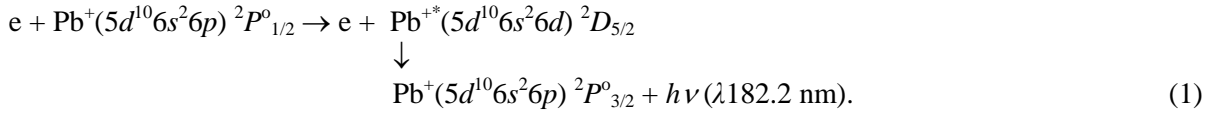
## 2. Experimental apparatus

The idea of our experiment was to bombard a target of  $\text{Pb}^+$  ions in the ground state by variable-energy electrons and to detect photons originating due to the radiative decay of the  $5d^{10} 6s^2 7s^2 S_{1/2}$  level to the  $5d^{10} 6s^2 6p^2 P_{1/2}$   $\text{Pb}^+$  ion ground state. The crossed-charged-beams apparatus and technique applied were described in detail in [4]. The design of the ion source intended to produce single charged lead ions in the ground state was described in detail elsewhere [5]. The typical ion-beam current in the collision region was  $(0.5\text{--}1.0) \times 10^{-6}$  A at 800 eV. The ion beam was reproducible and stable with the relative uncertainty better than 0.5% for the operating period of about 3000 hours. The electron beam current in the energy region of  $E_e = (6 \div 20)$  eV was  $(5 \div 10) \times 10^{-5}$  A and the energy spread (FWHM) of the electron beam was 0.6 eV. The electron energy scale was calibrated with an accuracy of  $\pm 0.1$  eV. The photon detection system comprised a 70° VUV monochromator, a photomultiplier, and an electronic detection system. The monochromator is based on the Seya-Namioka scheme with a concave toroidal grating ( $50 \times 40$  mm<sup>2</sup> working area with 1200 grooves/mm) and has an inverse linear dispersion  $\partial\lambda/\partial l = 1.7$  nm/mm. The radiation was detected by a cooled solar-blind FEU-142 photomultiplier. The dark count of the photomultiplier was typically 0.2 counts/s.



### 3. Results and discussion

We investigated the emission cross-section for the electron-impact excitation of the  $6s^2 6d^2 D_{5/2} \rightarrow 6s^2 6p^2 P^o_{3/2}$  resonance transition in  $Pb^+$ :



The result is shown in Fig.1 as the function of the electron energy with 68% confidence level statistical error bars. The excitation function for the resonance line below and above the ion ionization potential reveals the distinct features. The analysis of the data on electron configurations and energy positions of  $Pb^+$  ion levels [6] and Pb atom autoionizing states (AIS) [7] has shown that the features are mainly due to the cascade decay of ordinary  $5d^{10} 6s^2 nl$  states as well as  $5d^{10} 6s^2 nl n_1 l_1$ ,  $5d^9 6s^2 6p^3$ , and  $5d^9 6s^2 6p^2 np, nf$  AIS at the resonance excitation process to the  $5d^{10} 6s^2 6d$  level. Our experimental studies confirm not only the crucial role played by electron-electron correlations but also suggest that correlation phenomena can be a new tool for investigation of the collision process details.

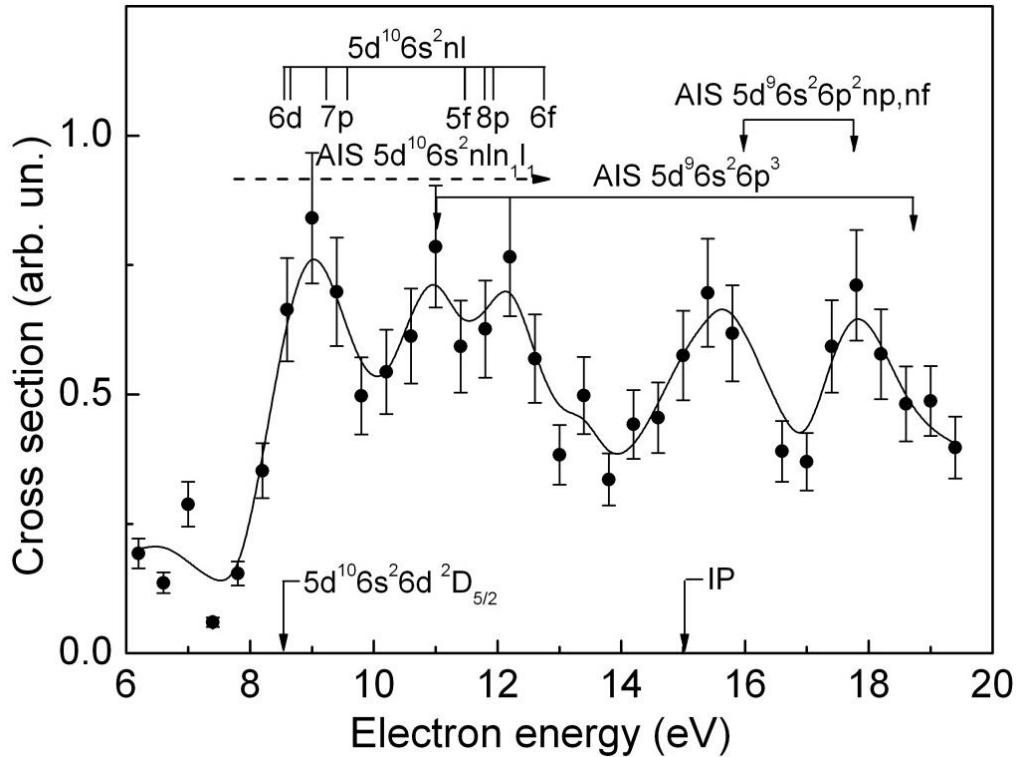


Fig. 1. Electron-impact excitation effective cross-sections of the  $Pb^+$  ion  $\lambda 182.2$  nm spectral line.

Unfortunately, up to date there are no theoretical calculations capable of adequate description of the electron-impact excitation mechanism for the  $Pb^+$  ion. Therefore, to provide further progress in studying the AIS revelation in the effective excitation cross-sections for such complex many-electron ions as  $Pb^+$ , one requires quantum-mechanical calculations. Especially this is related to the near-threshold energy region where the resonance contribution of AIS dominates.

## 4. References

- [1] Cardelli J A, Federman S R, Lambert D L, and Theodosiou C E 1993 *Astrophys. J.* **41** L416.
- [2] Welty D E., Hobbs L M, Lauroesch J T, Morton D C, and York D G 1995 *ApJ* **449** L1.
- [3] Imre A and Gomonai A 2007 *Radiation Physics and Chemistry* **76** 533.
- [4] Ovcharenko E V, Imre A I, Gomonai A N, and Hutysh Yu I 2010 *J. Phys. B* **43** 175206.
- [5] Gomonai A, Ovcharenko E, Imre A, and Hutysh Yu I 2005 *Nucl. Instr. Meth. Phys. Res. B* **233** 250.
- [6] Sansonetti J E and Martin W C 2005 *J. Phys. Chem. Ref. Data* **34** 1559.
- [7] Connerade J P, Garton W R S, Mansfield M W D, and Martin M A P 1977 *Proc. R. Soc. Lond. A* **357** 499.

# ELECTRON-IMPACT EXCITATION OF THE IN<sup>+</sup> ION: CASCADE CONTRIBUTION TO RESONANCE TRANSITIONS

Anna Gomonai, Yuriy Hutyh, Aleksandr Gomonai

*Institute of Electron Physics, Ukrainian National Academy of Sciences,  
21 Universitetska str., 88017 Uzhgorod, Ukraine*

E-mail: annagomonai@gmail.com

Electron-impact excitation cross-sections for the cascade  $5s6s \rightarrow 5s5p$ ,  $5s5d \rightarrow 5s5p$ , and  $5p^2 \rightarrow 5s5p$  transitions were measured by using a crossed electron and In<sup>+</sup> ion beam technique and photon-counting method. The emission cross-sections of these transitions equal  $\sim 10^{-16}$  cm<sup>2</sup> and are of the same order of magnitude as those for the resonance  $5s5p \ ^3P^o_1 \rightarrow 5s^2 \ ^1S_0$  and  $5s5p \ ^1P^o_1 \rightarrow 5s^2 \ ^1S_0$  transitions. Radiative cascade transitions in the In<sup>+</sup> ion are an important factor of the excited levels population and as a consequence the intensity value of the appropriate spectral lines, especially resonance ones.

## 1. Introduction

High-precision measurements of the energy dependences of effective electron excitation cross-sections of the In<sup>+</sup> ion resonance  $\lambda$  158.6 nm [1, 2] and intercombination  $\lambda$  230.6 nm [3] lines revealed a considerable resonance contribution to the excitation cross-sections related to the formation of autoionizing states (AIS) followed by their decay directly or via cascade transitions. It is seen from Fig.1 that transitions from the In<sup>+</sup> ion ordinary  $5s6s$  and  $5s5d$  as well as displaced  $5p^2$  levels [4] can make the greatest contribution to the population of the  $5s5p \ ^3P^o_1$  as well as the  $5s5p \ ^1P^o_1$  level. Note that the levels of the  $4d^9 5s^2 5p$  configuration formed due to the excitation of an electron from the  $4d^{10}$  shell are high-lying (practically they lie in the vicinity of the In<sup>+</sup> ion ionization potential IP = 18,86 eV) [5, 6] and do not play a considerable role in the near-threshold excitation of resonance lines.

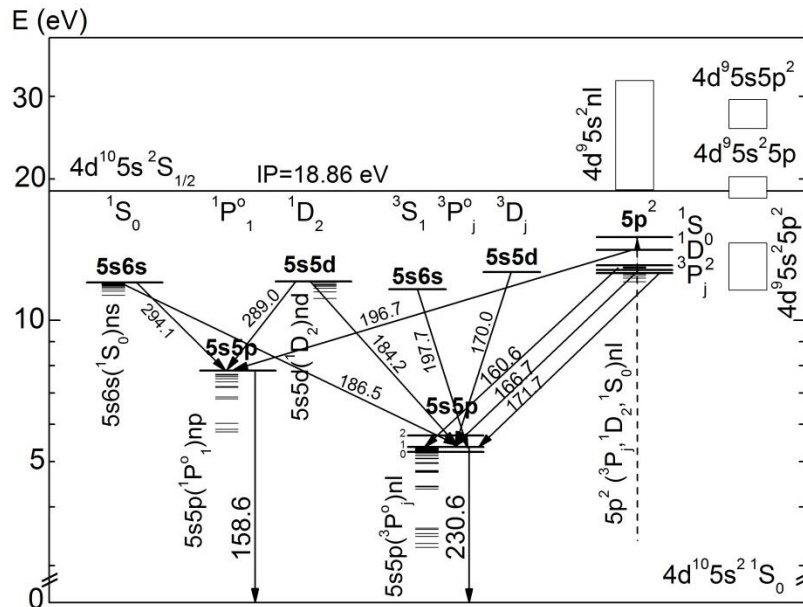


Fig. 1. Energy levels of the In<sup>+</sup> ion.

## 2. Experimental apparatus and procedure

The experimental procedure included bombardment of target  $\text{In}^+$  ions by electrons with controlled energy and detection of photons emitted by excited  $\text{In}^+$  ions. The crossed-charged-beams apparatus and technique applied were described in detail in [1,7].

Note that measurement of the electron-impact excitation functions of the spectral lines emitted from the  $\text{In}^+$  ion  $5s6s$  and  $5s5d$  as well as  $5p^2$  levels was a rather complex task. Since most of these lines slightly differ in wavelength (see Fig.1), their excitation functions, taking into account the monochromator spectral resolution ( $d\lambda/dl \approx 1,7$  nm/mm), were measured simultaneously. In particular, this concerns the cascade transitions  $5s5d\ ^3D \rightarrow 5s5p\ ^3P^o_1$  ( $\lambda 170.3$  nm) and  $5p^2\ ^3P_0 \rightarrow 5s5p\ ^3P^o_1$  ( $\lambda 171.7$  nm),  $5s5d\ ^1D_2 \rightarrow 5s5p\ ^3P^o_1$  ( $\lambda 184.2$  nm) and  $5s6s\ ^1S_0 \rightarrow 5s5p\ ^3P^o_1$  ( $\lambda 186.5$  nm),  $5p^2\ ^1D_2 \rightarrow 5s5p\ ^1P^o_1$  ( $\lambda 196,7$  nm) and  $5s6s\ ^3S_1 \rightarrow 5s5p\ ^3P^o_1$  ( $\lambda 197.7$  nm). In the experiment the electron-impact excitation functions were measured at the wavelengths of more intense lines [4]. In our opinion, the wavelength overlap of the lines under consideration could slightly affect the form and position of the electron-impact excitation functions structure. However, it did not considerably affect the cross-section value.

## 3. Results and discussion

The results of investigation of the electron-impact excitation functions for the cascade transitions to the  $5s5p\ ^3P^o_1$  and  $5s5p\ ^1P^o_1$  levels are shown in Fig.2 and Fig.3, respectively. As it was noted in [3], the transitions from the  $\text{In}^+$  ion  $5p^2$  levels play an essential role at the electron-impact excitation of the spin-forbidden  $5s5p\ ^3P^o_1 \rightarrow 5s^2\ ^1S_0$  transition. It is seen from Fig.2 that the features of the structure of the excitation functions (including those related to the resonance contribution of the AIS) of the  $\lambda 171.7$  nm line correlate well with those of the intercombination line. The excitation effective cross-section of this line is the largest among the investigated ones. This testifies that the transitions from the  $5p^2$  levels are one of the most effective channels of the population of the  $\text{In}^+$  ion  $5s5p\ ^3P^o_1$  level. At the  $5p^2$  levels excitation thresholds the radiative decay of the  $4d^{10}5p^2(^3P_{0,1,2})nl$  AIS due to dielectronic recombination can result in a decrease of the resonance excitation efficiency [8]. Therefore, such competitive channel of the AIS decay, which can considerably affect the effective cross-sections value, should be taken into account.

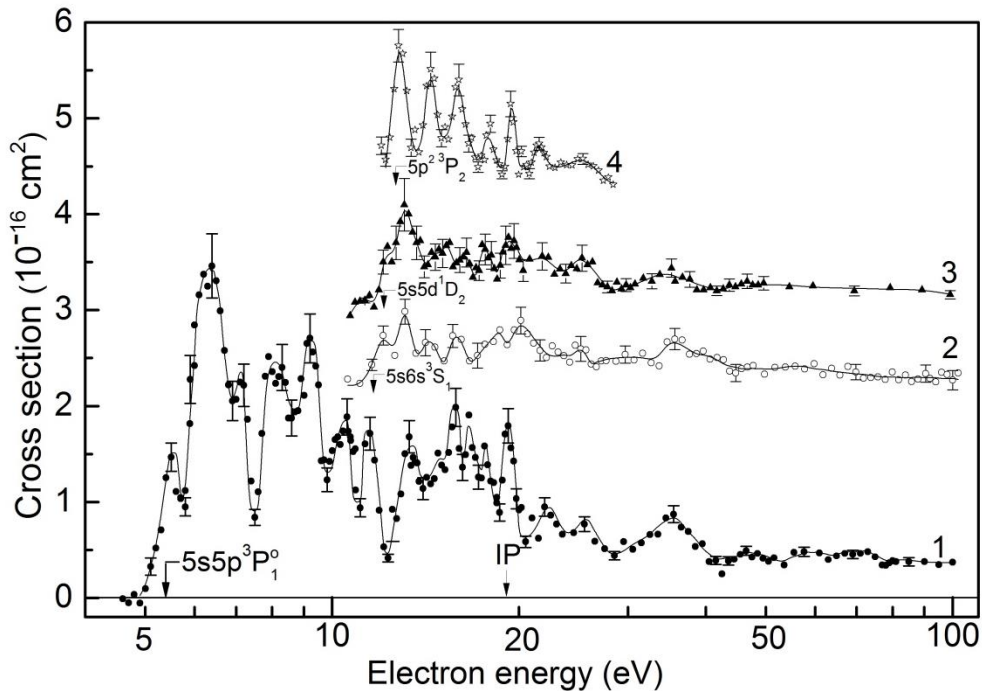


Fig. 2. Electron-impact excitation effective cross-sections of the  $\text{In}^+$  ion  $\lambda 230.6$  nm (1),  $\lambda 193,6$  nm (2),  $\lambda \lambda 184,2 + 186,5$  nm (3),  $\lambda \lambda 171,7 + 170,3$  (4) nm spectral lines.

As for the cascade transitions to the  $\text{In}^+$  ion  $5s5p\ ^1P^o_1$  level, though the transitions  $5s6s\ ^1S_0 \rightarrow 5s5p\ ^1P^o_1$  ( $\lambda 294.1$  nm) and  $5s5d\ ^1D_2 \rightarrow 5s5p\ ^1P^o_1$  ( $\lambda 289.0$  nm) also slightly differ in wavelength, they are already spectrally resolved in the experiment. In addition, there is a strong configuration interaction of the  $5s5d\ ^1D_2$  and  $5p^2\ ^1D_2$  levels [9]. Therefore, the electron-impact excitation functions of the  $5p^2\ ^1D_2 \rightarrow 5s5p\ ^1P^o_1$  ( $\lambda 196.7$  nm) and  $5s5d\ ^1D_2 \rightarrow 5s5p\ ^1P^o_1$  ( $\lambda 289.0$  nm) transitions should be similar. This is what we observed in the experiment (see curves 2 and 4 in Fig.3). However, the decrease of the  $\lambda 196.7$  nm spectral line excitation function was found to be more sharp. This is probably due to the fact that in the experiment we investigated the integrated excitation function of the  $\lambda \lambda (196.7 + 197.7)$  nm lines where  $\lambda 197.7$  nm line is related to the transition between the triplet states ( $5s6s\ ^3S_1 \rightarrow 5s5p\ ^3P^o_1$ ).

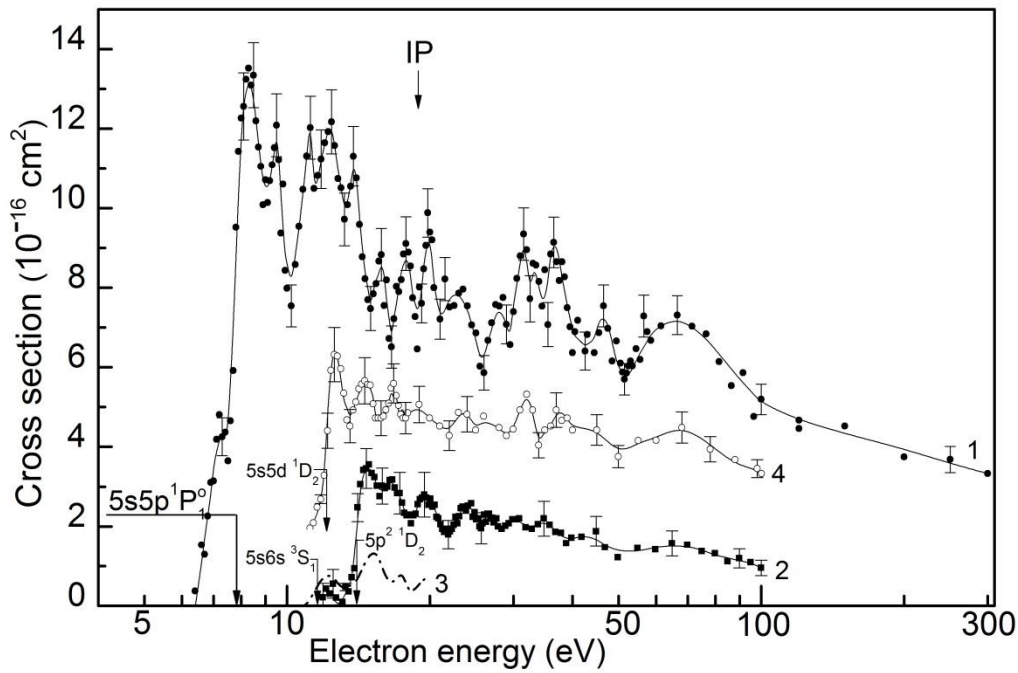


Fig. 3. Electron-impact excitation effective cross-sections of the  $\text{In}^+$  ion  $\lambda 158.6$  nm (1),  $\lambda \lambda 196.7 + 197.7$  nm (2),  $\lambda 197.7$  nm (3),  $\lambda 289.0$  nm (4) spectral lines.

It follows from the obtained data analysis that in addition to the resonance transitions both allowed and intercombination transitions from  $5s6s$ ,  $5s5d$ , and  $5p^2$  levels are effectively excited at slow electron-ion collisions. Therefore, radiative cascade transitions in ions are an important factor of the excited levels population and, as a consequence, the intensity value of the appropriate spectral lines, especially the resonance ones.

#### 4. References

- [1] Gomonai A, Ovcharenko E, Imre A, Hutysh Yu I 2005 *Nucl. Instr. Meth. Phys. Res. B* **233** 250.
- [2] Gomonai A N, Imre A I, Ovcharenko E V, Hutysh Yu I 2009 *Journal of Physical Studies* **13** 230X.
- [3] Ovcharenko E V, Imre A I, Gomonai G M, Hutysh Yu I 2005 *Ukr. J. Phys* **50** 1111.
- [4] Kramida A 2013 *Journal of Research of NIST* **118** 52.
- [5] Duffy G and Dunne P 2001 *J. Phys. B* **34** L173.
- [6] Kilbane D, Mosnier J-P, Kennedy E T, Costello J T and Van Kampen P 2006 *J. Phys. B* **39** 773.
- [7] Ovcharenko E V, Imre A I, Gomonai A N, Hutysh Yu I 2010 *J. Phys. B* **43** 175206.
- [8] Gomonai G M, Imre A I, Ovcharenko E V, Hutysh Yu I 2009 *Ukr. J. Phys* **54** 957.
- [9] Martinez B, Blanco F and Campos J 1996 *J. Phys. B* **29** 2997.

# PERIODIC VARIATIONS OF AUGER ENERGY MAXIMUM DISTRIBUTION FOLLOWING $\text{He}^{2+} + \text{H}_2$ COLLISIONS : A COMPLETE ANALOGY WITH PHOTON INTERFERENCES

M. Cholet<sup>1</sup>, F. Minerbe<sup>1</sup>, G. Oliviero<sup>1</sup>, V. Pestell<sup>1</sup> and F. Frémont<sup>2</sup>

<sup>1</sup>Université de Caen, 6 bd du Mal Juin 14050 Caen Cedex France

<sup>2</sup>Centre de Recherche sur les Ions, les Matériaux et la Photonique, Unité Mixte Université de Caen-CEA-CNRS-EnsiCaen, 6 bd du Mal Juin, 14050 Caen Cedex 4, France

We present experimental evidence of a particular electron-interference phenomenon. The electrons are provided by autoionization of  $2\ell 2\ell'$  doubly excited He atoms following the capture of  $\text{H}_2$  electrons by a slow  $\text{He}^{2+}$  incoming ion. Each spectrum consists of three structures labeled  $2s^2\ ^1\text{S}$ ,  $2p^2\ ^1\text{D}$  and  $2s2p\ ^1\text{P}$ . To separate each structure, Gaussian curves are distorted by a function of the type  $\exp\{a_0 \arctan[b_0/(E - E_0^L)]\}$  (The quantity  $E_0^L$  is the energy at the maximum of the structure, while  $a_0$  and  $b_0$  are fitting parameters).

To get evidence for oscillations in the angular distribution of the energy maximum of the  $2s^2\ ^1\text{S}$  configuration, the difference between the  $2p^2\ ^1\text{D} - 2s2p\ ^1\text{P}$  energy is extracted from experiment and compared with the calculated difference. Figure 1 shows the difference  $\delta E_d^{\text{exp}}$  between the experiment and the polynomial function used to cancel the main dependency, as a function of  $\theta_d$ . It is clearly seen that  $\delta E_d^{\text{exp}}$  oscillates in the range from  $130^\circ$  to  $160^\circ$ , with a period of  $\sim 15^\circ$ . The period is very close to those found for the total intensity and the Auger width. In addition, the observed oscillations are in very good agreement with calculations based on a simple model [1].

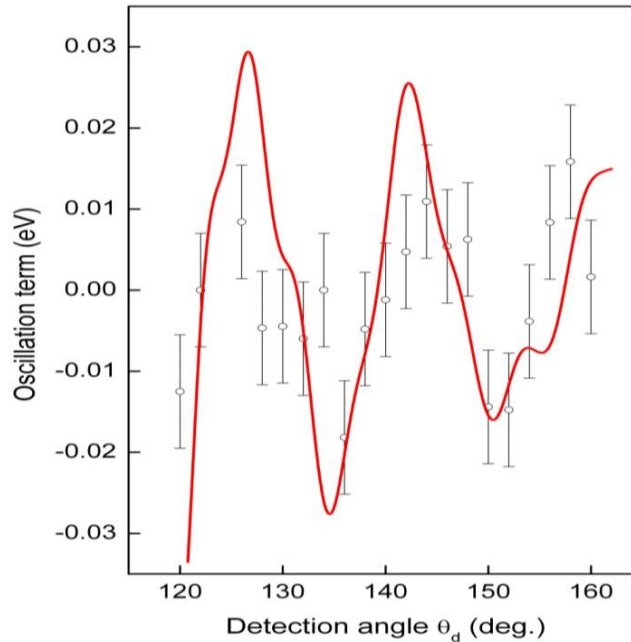


Figure 1

[1] M. Cholet et al., Journal of Electron Spectroscopy and Related Phenomena, in press.

## ATOMIC AND MOLECULAR PROCESSES OF INTEREST FOR MODELING OF DISCHARGES IN LIQUIDS

Dragana Marić, Jelena Sivoš, Nikola Škoro, Vladimir Stojanović, Srđan  
Marjanović, Ana Banković, Saša Dujko, Gordana Malović and Zoran Petrović

*Institute of Physics, University of Belgrade, Serbia*

E-mail: dragana.maric@ipb.ac.rs

We will present the most recent advances in knowledge and understanding of atomic and molecular processes relevant for modelling of discharges in vapours, liquids and their interface. A detailed review of current issues in the field will be given, with possible directions for resolving them.

Discharges in liquids and in contact with liquids are lately attracting considerable interest within plasma community due to the growing field of possible applications. Regardless of a great number of developing applications and, in some cases, well advanced tests of devices, elementary processes in gas phase, liquid phase and their interface still suffer from a number of inconsistencies and lack of data. Even understanding of main mechanisms of breakdown in liquids is still open for debate in the community. In return, the lack of complete understanding of basic processes impedes further improvement of the existing applications and development of the new ones.

Transport of charged particles in liquids is a challenging problem. In liquids, rates of momentum and energy transfer are not the same, momentum balance is structure dependent making extrapolation from gas phase results difficult. Due to a coherent elastic scattering, interference effects arise, leading to lower momentum transfer cross section, as compared to the gas phase. Only at energies higher than 4-5 eV, one could expect transport of charged particles to be the same in liquids and gases [1], unless some new effects become important. Transport in polar liquids is another challenging problem, as charged particles stick to the polar molecules, which creates slow species (hydrated electrons, clusters). Number of charged particles varies and there is still no universal description of such effects, at least not at a quantitative level.

An obvious starting point in resolving issues of discharges in liquids is in data on elementary processes, cross sections and transport in gas phase – vapours of liquids. However, there are many issues to be resolved even in vapours [2]. Do we even have a complete set of cross sections for scattering of electrons on H<sub>2</sub>O molecule? There is a number of compilations of cross sections available, e.g. LxCat data base [3] and [4]. However, not all the compilations are verified by swarm analysis. Several earlier swarm analyses are assumed to give good results [5-8]. Still, with new measurements of cross sections [9] and new measurements transport coefficients [10], a complete revision of cross section sets by swarm analysis is required. Special care has to be given to the range of electron energies where transport coefficients can be pressure-dependent [7,8,11].

Further needs in data on elementary processes are in cross sections for ion and fast neutral collisions with water molecule. So far, we have completed sets of cross sections for positive ions H<sup>+</sup>, OH<sup>+</sup>, H<sub>2</sub><sup>+</sup>, H<sub>3</sub><sup>+</sup>, H<sub>2</sub>O<sup>+</sup>, H<sub>3</sub>O<sup>+</sup> [12]. This work will be extended to important negative ions (OH<sup>-</sup>, O<sup>-</sup>, H<sub>2</sub>O<sub>2</sub><sup>-</sup>). Experimental measurements of breakdown and emission profiles [13] have shown that contribution of fast H atoms should be taken into account too. Data on electron collisions with radicals (OH, HO<sub>2</sub>) are also being analyzed. Here, complete sets of cross sections are needed only in channels that significantly influence the energy balance while specific channels are required for dominant reactions.

Studies of breakdown in vapours and liquids have commenced with a goal of providing information on related processes at surfaces. Breakdown studies in vapours provide us with data on ionization coefficients at medium and higher E/N [14], which we use in normalization of cross sections at high energies (~10 eV); and secondary electron yields with metallic electrodes [15,16]. Breakdown in liquids is a more complex issue, where the discharge can be initiated through formation of the bubble of vapour [17,18], or directly in liquid phase. In the latter case, possibilities of different mechanisms of breakdown are being discussed – shock waves, microexplosions, electrostrictive mechanism [18-21], that could



explain local density reduction induced by high field, which in turn leads to an increase of  $E/N$  and facilitates breakdown in liquid.

## References

- [1] White R D, Dujko S, Robson R E, Petrović Z Lj and McEachran R P 2010 *Plasma Sources Sci. Technol.* **19** 034001.
- [2] Graham B, Bruggeman P, Kushner M, Petrović Z Lj 2013 66th Annual Gaseous Electronics Conference ( Princeton, New Jersey, USA, September 30<sup>th</sup> – October 4<sup>th</sup> 2013) *Bulletin of the American Physical Society* **58** (no. 8) HW1 5
- [3] <http://www.lxcat.net>
- [4] Itikawa Y and Mason N 2005 *J. Phys. Chem Ref Data.* **34** 1.
- [5] Phelps A V and Cohen R S (unpublished).
- [6] Hayashi M, in: L.C. Pitchford, B.V. McKoy, A. Chutjian, S. Trajmar (Eds.) *Swarm Studies and Inelastic Electron-Molecule Collisions*, Springer-Verlag, New York, 1987, p. 167.
- [7] Ness K F and Robson R E 1988 *Phys. Rev. A* **38** 1446.
- [8] Yousfi M and Benabdessadok M D 1996 *J. Appl. Phys.* **80** 15.
- [9] Thorn P, Campbell L and Brunger M 2009 *PMC Phys. B* **2** 1.
- [10] Ruiz-Vargas G, Yousfi M and Urquijo J 2010 *J. Phys. D* **43** 455201.
- [11] Petrović Z Lj 1985 (unpublished).
- [12] Stojanović et al (unpublished).
- [13] Sivoš J, Škoro N, Marić D, Malović G and Petrović Z Lj 2012 *ESCAMPIG XXI* (Viana do Castelo, Portugal, July 10-14. 2012 ) 9 (2pp).
- [14] V. Stojanović, J. Sivoš, D. Marć, N. Škoro, Z. Lj. Petrović 2012 26<sup>th</sup> *SPIG* (Zrenjanin, Serbia, August 27-31. 2012) 35-38.
- [15] Škoro N, Sivoš J, Marić D, Malović G and Petrović Z Lj (unpublished).
- [16] Klas M, Matejčik S, Radmilović-Radjenović M and Radjenović B 2012 *EPL* **99** 57001.
- [17] Sommers B S, Foster J E 2014 *Plasma Sources Sci. Technol.* **23** 015020.
- [18] Bruggeman P, Leys C 2009 *J. Phys. D: Appl. Phys.* **42** (no. 5) 053001.
- [19] Dobrynin D, Seepersad Y, Pekker M, Shneider M N, Friedman G and Fridman A 2013 *J. Phys. D: Appl. Phys.* **46** 105201.
- [20] Starikovskiy A 2013 *Plasma Sources Sci. Technol.* **22** 012001.
- [21] Kolb J F, Joshi R P, Xiao S and Schoenbach K H 2008 *J. Phys. D: Appl. Phys.* **41** 234007.

# **SURFACE AND GAS PHASE PROCESSES IN AFTERGLOW PLASMAS AIMED FOR MEDICAL STERILIZATION**

Kinga Kutasi

*Wigner Research Centre for Physics of the Hungarian Academy of Sciences, Institute for Solid State Physics and Optics, Konkoly Thege M. út 29-33, H-1121 Budapest, Hungary*  
E-mail: kutasi.kinga@wigner.mta.hu

The sterilization process and the related molecular kinetics are studied in the afterglow of a surface-wave microwave discharge, which is an atomic and molecular kinetics dominated region. The density of species which play role in the application are controlled by the gas phase and surface processes. In the presentation the role of different collisional processes, and the difficulties in determining their rates will be discussed for the afterglow of an N<sub>2</sub>-O<sub>2</sub> and Ar-O<sub>2</sub> surface-wave microwave discharge, respectively. The role of afterglow plasma modelling in revealing the uncertainties of reaction rates, and the need for collisional data will be addressed.

## **1. Introduction**

Low temperature, i.e. non-equilibrium plasmas favour enormous number of technological applications thanks to the radiating species, active radicals and energetic ions present in the plasma environment. Among the applications we find two very important and prosperous areas, such as biomedicine and nanotechnology.

In the case of non-equilibrium (non-thermal) plasmas the power – electric or electromagnetic – communicated to the neutral gas is aimed to be consumed for electron acceleration – rather than for gas heating – which gives the possibility for the electrons to ionize, excite or dissociate the gas atoms and molecules, resulting in a media rich in active radicals, energetic charges and radiating species. When the discharge is generated in flowing gas the species created in the active region can be transported into a field free region – which can have larger dimensions than the active plasma – dominated by atomic and molecular collisions. This afterglow region favours the treatment of sensitive – for heat and sputtering – samples, since it is free of charged species, which can induce the damage, and it is characterized by low – close to room – gas temperature. Due to these characteristics the afterglow has been found a potential environment for the sterilization of heat sensitive medical tools. The sterilization occurs due to the interaction of chemically active atomic species with the bacteria surface and the proteins, and due to the damaging effect of the UV radiation [1,2]. The UV radiation in this system, which is based usually on an O<sub>2</sub> and N<sub>2</sub> content plasma can be due to the excited NO molecules, which are created in the afterglow through molecular collisions [1,3]. In order to optimize these systems for applications the production of useful species should be optimized, which implies the understanding of the atomic and molecular collisions occurring in the gas phase and on the surfaces.

## **2. The afterglow of a surface-wave microwave discharge**

The sterilization process and the related molecular kinetics have been studied in the afterglow of a surface wave microwave discharge, which has been proven to be a good candidate for real applications [1]. The advantage of the system is, that the composition of the afterglow can be easily tuned [4], which makes it optimal for surface process studies [2,5].

The afterglow system is composed of a surface-wave microwave discharge generated in flowing gas (typically under 1000 sccm gas flow conditions) in a 5 mm inner diameter quartz tube, with 2.45 GHz frequency microwave. The pressure in the discharge tube is typically 100-700 Pa. The discharge tube is further connected to an afterglow tube or chamber, which can have different dimensions depending on the application purpose, see Fig. 1. In the case of large afterglow chambers a connecting tube can be also

used, which makes possible an easier tuning of the afterglow composition. The composition of the afterglow in the studied region can be tuned by varying the distance between the discharge region and the give position, since the different species under different pressure and gas composition conditions have different relaxation or recombination time. The exact composition of the plasma in the different part of the system can be easily determined by means of modelling, which also implies the knowledge of the rates of different atomic and molecular collisions.

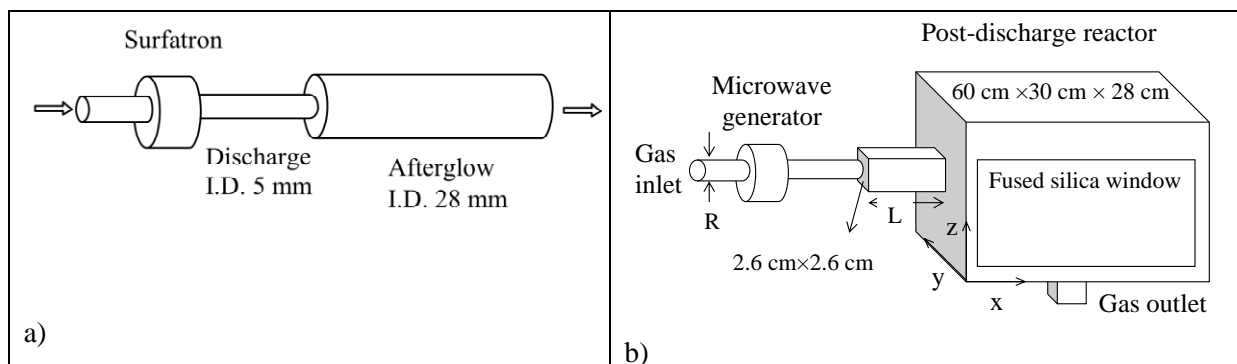


Fig. 1. Afterglow systems based on a surface-wave microwave discharge.

### 3. Modelling the atomic and molecular kinetics dominated afterglow

The post-discharge system can be described with two different models valid for the discharge and the afterglow region, respectively. The species densities in the discharge region are calculated with a 1-D kinetic model, which solves the homogeneous electron Boltzmann equation coupled together with the rate balance equations describing the creation and destruction of different species [6]. The evolution of the species densities in the afterglow are followed with a 3-D hydrodynamic model composed of: (i) total mass conservation equation (ii) momentum conservation equation, (iii) energy conservation equation and (iv) species continuity equations [7]. In  $N_2$ - $O_2$  systems the species taken into account in the model are:  $N_2(X,v)$  and  $O_2(X,v')$  molecules (with  $0 \leq v \leq 45$  and  $0 \leq v' \leq 15$ ), ground state  $N(^4S)$  and  $O(^3P)$  atoms; electronic states of molecular and atomic nitrogen and oxygen  $N_2(A,B, B', C, a', a, w)$ ,  $O_2(a,b)$  and  $N(^2D, ^2P)$ ; the formed species  $NO(X,A,B)$ ,  $NO_2(X,A)$  and  $O_3$ ; the main positive ions  $N_2^+(X, B)$ ,  $N_4^+$ ,  $O_2^+$ ,  $O^+$  and  $NO^+$ ; and negative ions  $O^-$ ; while in  $Ar$ - $O_2$ :  $Ar(^1S_0, ^3P_2, ^3P_1, ^3P_0, ^1P_1)$ ,  $O_2(X \ ^3\Sigma_g^-, v)$ ,  $O_2(a \ ^1\Delta_g, b \ ^1\Sigma_g^+)$ ,  $O(^3P)$ ,  $O_3$ ,  $Ar^+$ ,  $O_2^+$ ,  $O^+$ ,  $O^-$ . In the afterglow we neglect some of the excited species and all the ions, since due to deactivation and recombination their densities become negligible.

The molecular kinetic scheme includes all the possible two and three body gas phase reactions, radiative quenching [3,6,8] and surface processes [7]. The comparison of measured and calculated densities gives the possibility to revisit the molecular kinetics and find new collision pathways, as well as to point out the uncertainty of cross sections/reaction rates of certain processes. As an example, here we show the evolution of  $O_2(b)$  molecules in the afterglow, which is shown to be controlled by the gas phase reactions. The experimental measurements conducted by Mafra *et al.* [5] have shown that the total emission intensity of the atmospheric band of  $O_2$ , that is a transition from the  $O_2(b)$  state to the  $O_2(X)$  state, at 4 mbar decreases 20% along 35 cm in the afterglow, while at 10 mbar this decrease is 60%. Fig. 2 shows the  $O_2(b)$  density (summed in depth) distribution along the middle axis of the reactor. Previously the  $O_2(b)$  density profile has been fitted with using a low surface recombination probability  $10^{-3}$ , however our calculation have shown that the  $O_2(b)$  density is controlled by the quenching with  $O$ -atoms. To obtain the experimentally measured decay the rate of the quenching reaction needed to be decreased more than one order of magnitude comparing to the one found in the literature, while the variation of the surface recombination did not give a significant change in the distribution.

In what concerns the surface processes – that are mostly the recombination of atoms on the surfaces –, their rates are system dependent. The state of the surface varies with applications and also due to

continuous running of the system. Therefore it is very difficult to define the recombination probability of species on surfaces for „real systems“ based on surface kinetic models using ideal surfaces, as well as experiments conducted under „clean“ conditions [9,10]. One of the most widespread method is fitting the surface recombination probability through fitting the measured densities [11], which allows the definition of an effective recombination probability characteristic for the given system. Similarly the creation of molecules in surface mediated collisional processes can be estimated [7].

In the presentation the role of the different collisional processes, and the difficulties in the determination of their rates will be discussed for the afterglow of an N<sub>2</sub>-O<sub>2</sub> and Ar-O<sub>2</sub> surface-wave microwave discharge, respectively. The need for collisional data will be addressed.

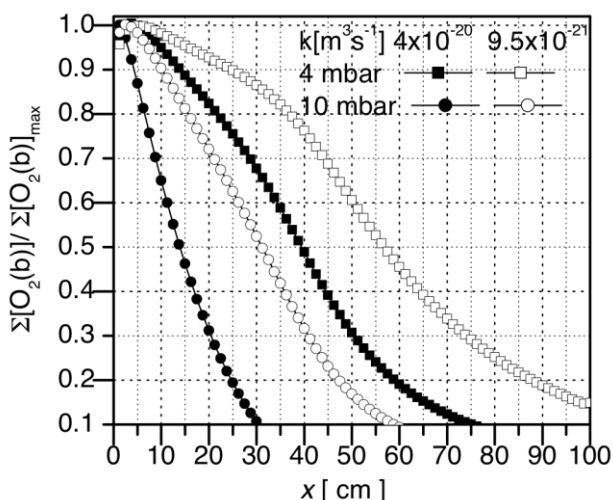


Fig. 2. Normalized O<sub>2</sub>(b) density distribution along the middle axis of a 28 mm inner diameter afterglow tube (set-up shown in Fig.1. a.).

The work has been supported by the Hungarian Science Foundation OTKA, through project K-104531.

#### 4. References

- [1] Moisan M *et al.* 2013 *Eur. Phys. J. Appl. Phys.* **63** 10001-p1-p46.
- [2] Duday D *et al.* 2013 *Plasma Process. Polym.* **10** 864-879.
- [3] Kutasi K *et al.* 2008 *Plasma Process. Polym* **5** 840.
- [4] Kutasi K *et al.* 2011 *Plasma Sources Sci. Technol.* **20** 035006.
- [5] Mafra M *et al.* 2009 *Plasma Process. Polym.* **6** S198.
- [6] Pintassilgo C D *et al.* 2005 *J. Phys. D: Appl. Phys.* **38** 417.
- [7] Kutasi K and Loureiro J 2007 *J. Phys. D: Appl. Phys.* **40** 5612.
- [8] Kutasi K *et al.* 2010 *J. Phys. D: Appl. Phys.* **43** 175201.
- [9] Kim Y C and Boudart M 1991 *Langmuir* **7** 2999.
- [10] Guerra V 2006 *Jpn. J. Appl. Phys.* **45** 8200.
- [11] Adams S F and Miller T A 2000 *Plasma Sources Sci. Technol.* **9** 1.

## **ACCURACY OF THEORETICAL CALCULATIONS FOR ELECTRON-IMPACT IONIZATION OF MOLECULES**

Don Madison

*Missouri University of Science and Technology, Rolla, MO, USA 65409*

E-mail: Martin.Cizek@mff.cuni.cz

Recent experimental advances have allowed measurements of unprecedented accuracy for electron-impact ionization of molecules for low to intermediate energy incident electrons. Most of the measurements do not determine the orientation of the molecule so theory has to average over all orientations. However, more recently, measurements are being performed which determine the orientation of the molecule by looking at a state which will dissociate and then detecting one of the fragments. In this talk we will show the current status of agreement between experiment and theory for low and intermediate energy single ionization of small, medium, and large molecules for experiments both averaging over all orientations and for molecules with known orientations.

## **ELECTRON PRODUCTION AND TRANSPORT IN BIOLOGIC MATERIAL INDUCED BY FAST IONS**

J. L. Shinpaugh<sup>1</sup>, R. A. McLawhorn<sup>1</sup>, S. L. McLawhorn<sup>1</sup>, K. D. Carnes<sup>2</sup>,  
M. Dingfelder<sup>1</sup>, and L. H. Toburen<sup>1</sup>

<sup>1</sup>*Department of Physics, East Carolina University, Greenville, North Carolina, USA*

<sup>2</sup>*Department of Physics, Kansas State University, Manhattan, Kansas, USA*

E-mail: shinpaughj@ecu.edu

The severity of damage in biological systems from charged particle radiation generally depends on the density of energy deposition in the material. Clustered damage can challenge repair systems and lead to genomic instability and cell mutations. Descriptions of the spatial patterns of radiation damage are typically obtained from track structure simulations of secondary electron transport. To test the accuracy of electron transport in track structure simulations, we have measured electron emission yields from thin films of biologically relevant material induced by fast ion impact. The experimental results are compared to calculations from the PARTRAC Monte Carlo track structure simulation code for electron transport in liquid water.

## **DISSOCIATION OF PEPTIDES BY IONS AND PHOTONS**

Sadia Bari<sup>1</sup>

<sup>1</sup>*European XFEL GmbH, Hamburg, Germany*

E-mail: [sadia.bari@xfel.eu](mailto:sadia.bari@xfel.eu)

Little is known about biological radiation action on the molecular level. Experiments with small biomolecules in the gas phase have the advantage of studying ionization and fragmentation dynamics in finite systems but are less realistic radiation damage models. To be able to investigate more complex biomolecular systems, such as peptides and proteins, we have developed a new apparatus in which a home built electrospray source can be interfaced with a low energy (keV) ion beamline or different photon beamlines (e.g. of synchrotron or free electron laser). First spectra of peptides obtained with this set-up will be presented. Dependencies on projectile energies as well as peptide length and structure will be thereby discussed.

# METASTABLE FRAGMENTATION OF BIOMOLECULES

O. Ingólfsson

*Science Institute and University of Iceland, Dunhaga 3, 107 Reykjavik, Iceland*

E-mail: odduring@hi.is

Metastable fragmentation of deprotonated, negatively charged DNA and RNA components and their compositions is studied by means of matrix-assisted laser desorption/ionization (MALDI) mass spectrometry. The systems studied are the individual nucleobases, ribose, ribose-monophosphates, the individual nucleosides and nucleoside 5'-monophosphates and selected oligonucleotides. Chemical modifications along with isotopic labelling and classical dynamics simulations are used to unambiguously identify fragments and to better understand the underlying mechanisms.

## 1. Introduction

Until the turn of the century, fragmentation of genomic DNA through high-energy radiation was mainly attributed to radical species and reactive oxygen species (ROS) formed along the radiation track [1-3]. However, in the year 2000, low energy electrons (LEEs) were shown to resonantly cause single and double strand breaks in condensed DNA [4]. Such LEEs are abundant along the radiation track ( $5 \cdot 10^5 \text{ MeV}^{-1}$ ) [5] and, correspondingly, this work triggered great interest in the role of dissociative electron attachment (DEA) in damage caused by high-energy radiation. In this context, a number of detailed DEA studies on various, isolated nucleic acid components, in the gas phase, have been carried out (see for example references [6-12]). In these studies the focus has been on the negative ion formation and the primary dissociation mechanisms, and it has been shown that one of the dominating channels is hydrogen abstraction forming the anion  $[M - H]^-$ . This channel may in some cases be an intermediate step before further metastable dissociation of the vibrationally-activated  $[M - H]^-$  [13, 14].

In the current contribution we give a short summary of our studies on the secondary fragmentation of  $[M - H]^-$  ions of DNA components [15-20]. We use matrix-assisted laser desorption/ionisation (MALDI) to generate deprotonated molecules and to study their metastable decay [15]. By using MALDI, intact  $[M - H]^-$  ions of large molecules can be generated in the gas phase. We take advantage of this, to study the fragmentation of larger molecules than have been studied in gas phase DEA experiments. In this context we have studied metastable decay of the deprotonated nucleobases [14-16], sugars [15, 17, 18], nucleosides [15, 19], sugarphosphates [15, 17] and nucleoside monophosphates [15], as well as short, single stranded oligonucleotides [15, 20]. We have also systematically blocked deprotonation sites by chemical modification in the nucleobase thymine [14-16] and the nucleosides uridine and guanosine [19] to provide correlation between site of deprotonation and further fragmentation, and for unambiguous identification of fragmentation sites from the deprotonated sugars,  $^{13}\text{C}$ - and D- isotope labelling was used [18]. Finally, classical dynamics simulations of the fragmentation of deprotonated thymine, the nucleosides and d-fructose were conducted to gain insight into the dynamics and the fragmentation mechanisms [15, 18, 19].

## 2. Methods

### 2.1. Metastable decay measurements

Figure 1 shows a schematic presentation of the MALDI instrument. Sample molecules are co-crystallized, on a metallic substrate, with an excess amount of matrix molecules (small aromatic molecules with acidic and/or basic functional groups). The substrate is placed into the MALDI-ToF instrument, such that it serves as the repeller in a typical Wiley-McLaren double focusing setup. For data acquisition the sample is irradiated with a focused, pulsed  $\text{N}_2$ -laser

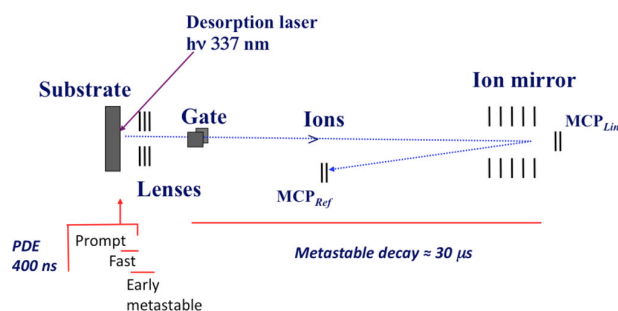


Fig. 1. Schematic representation of the MALDI instrument. Adapted from [ 15 ]



(337 nm, 7-10 Hz). This causes an explosive evaporation of the crystallized mixture of the sample and matrix molecules, which are ionized through proton exchange in the process. The laser power was kept about 20% above the detection threshold of the respective parent ions. After a 200 ns delay, the deprotonated, negatively charged ions are extracted with a high-voltage pulse into the field-free flight tube of the ToF, where a single  $m/z$  ratio is selected by a, *normally closed*, deflector placed about 75 cm down stream. After the flight through the linear section of the ToF MS (125 cm), which takes about 6-36  $\mu$ s depending on  $m/z$  ratio of the selected ion, the fragmentation is analysed with a griddles reflectron (ion mirror). Further detail on data acquisition and sample preparation can be found in reference [ 15 ] and references therein.

## 2.2. Classical dynamics simulations

For the simulations, density functional theory (DFT) was used with a plane wave basis set (energy cut-off at 395.994 eV) and the PW91 functional as implemented in the VASP code [21, 22]. Periodic boundary conditions of 18 Å were used to ensure that interactions between periodic images could be neglected. Further, to ensure zero total charge within the system, despite the extra charge brought in by the deprotonated anions, an uniform background charge was introduced. The molecular geometries of the neutral molecules were first optimized using damped molecular dynamics and, when the force became smaller than 0.3 Å/eV, the conjugate gradient algorithm was used. The same procedure was carried out for the deprotonated anions to assure for their stability. The atomic velocities of the neutral geometry were then scaled to an internal energy corresponding to 298 K, and the vibrational modes were allowed to equilibrate over 1000 fs with microcanonical classical dynamics using a Verlet algorithm to integrate Newton's equation of motion. The simulations were allowed to continue for a further 1000 fs in order to create a set of 10 configurations of 100 fs intervals. These were used as starting geometries for further simulations. To account for the excitation energy acquired in the MALDI process, an internal energy of 8 eV was added to each configuration by scaling the atomic velocities. Then a hydrogen was removed from the respective deprotonation site and an additional charge was defined within the system. A constant energy (microcanonical) simulation of the vibrationally-excited, deprotonated anions in their electronic ground state were carried out for 500 fs using the Verlet algorithm to integrate Newton's equations of motion. The dissociations which occurred during this simulation period were documented and the charge of each fragment was determined by Bader's method. [23, 24]

## 3. Results and discussion

In the current contribution we give a short summary of the fragmentation pattern of the pyrimidine bases and the ribose unit to compare these with the fragmentation pattern of the combined ribose monophosphate and the combined ribose and nucleobases; i.e., the nucleosides. We then compare these compositions with the respective nucleoside monophosphates and finally with short single-stranded oligonucleotides. For further detail on these studies see reference [15] and references therein. Figure 2 shows mass spectra of the deprotonated pyrimidine bases cytosine, uracil and thymine. The most prominent fragment from these nucleobases appears at the  $m/z$  ratio 42, which corresponds to  $\text{NCO}^-$ . Furthermore, by blocking selected deprotonation sites through methylation we could shown that in metastable decay of deprotonated thymine in MALDI this fragment is only formed after deprotonation of 3N. This is also reflected in our classical dynamics simulations, where four out of 10 trajectories of thymine deprotonated at N3 result in  $\text{NCO}^-$  formation while this is only the case

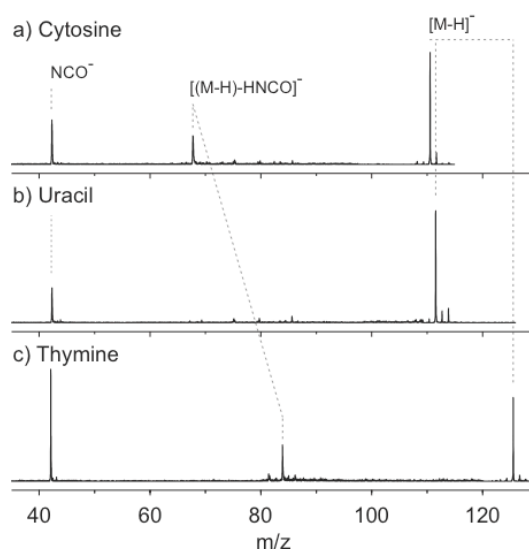


Fig. 2. Metastable decay spectra of the pyrimidine nucleobases; cytosine (a), uracil (b) and thymine (c). Adapted from [15]

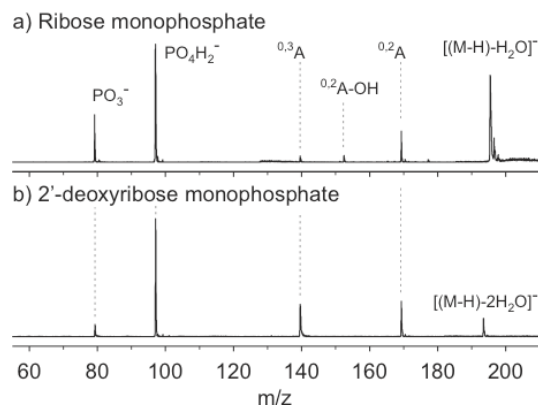


Fig. 3. Metastable decay spectra of deprotonated ribose monophosphate (a) and 2'- deoxyribose monophosphate (b). Adapted from [15].

we could show that this channel proceeds through both  $^{0.2}\text{A}$  and  $^{0.3}\text{X}$  cross ring cleavage [15, 17, 18]. Figure 4 and 5 show mass spectra of the metastable decay of ribose monophosphate and of the nucleosides cytidine and uridine. Interestingly, the main fragmentation channel observed for the pyrimidine nucleosides is the formation of  $\text{NCO}^-$  as is the case for the isolated bases [19]. However,  $^{0.2}\text{X}$  cross ring cleavage of the sugar moiety is also observed. This channel is complementary to the  $^{2.0}\text{A}$  channel observed as one of the main channels in the sugar fragmentation [17, 18]. In addition to the channels we have observed from the isolated bases and the isolated ribose unit, the cleavage of the glycosidic bond is also an efficient channel in the nucleosides. In our classical dynamics simulations we found that the base fragmentation only takes place if the initial deprotonation is at the base and that the glycosidic bond rupture and sugar cross ring cleavage is only initiated through deprotonation at the 2'- or 3'-OH. These predictions were confirmed by selectively blocking the respective deprotonation sites of the nucleoside in the MALDI experiments [15, 19]. From ribose monophosphate we also observe  $^{2.0}\text{A}$  cross ring cleavage, but here phosphoester bond cleavage leading to the formation of  $\text{PO}_3^-$  or  $\text{H}_2\text{PO}_4^-$  is dominating [17]. Finally, when the bases, the ribose and the phosphate unit are combined to form the individual nucleoside monophosphates, the phosphoester and glycosidic bond ruptures dominate the spectra [15]. This is also the case for the single stranded oligonucleotides we have studied [15, 20], where phosphodiester and glycosidic bond ruptures dominate the metastable fragmentation. In these cases, however, the sequence of the nucleosides (nucleobases) determines which phosphodiester and glycosidic bonds are ruptured.

#### 4. Conclusions

Here we have given a short summary of our studies on metastable decay of the deprotonated nucleobases, ribose, ribose-monophosphate, the nucleosides and nucleoside 5'-monophosphates and selected oligonucleotides. The fragmentation of the pyrimidine bases is dominated by loss of  $\text{NCO}^-$

for one trajectory when thymine is deprotonated at N1 [14-16]. Interestingly, in metastable decay of the dehydrogenated thymine ions formed in DEA, this ion is also formed after hydrogen loss from N1 as well as N3 [16]. We note in this context that both the fragmentation in MALDI and in our simulations proceed from the electronic ground state, while this is not necessarily the case in DEA [16]. In addition to  $\text{NCO}^-$ , we also observed the fragment  $[(\text{M} - \text{H}) - \text{HNCO}]^-$  from cytosine and thymine, which is complementary to  $\text{NCO}^-$  with respect to the retention of the hydrogen. No other fragments are observed from the pyrimidine bases. Ribose, on the other hand, shows a fairly rich fragmentation pattern characterized by the loss of water and formaldehyde units [17]. The most efficient of these channels is the loss of two  $\text{CH}_2\text{O}$  units (or  $\text{C}_2\text{H}_4\text{O}_2$ ) ( $m/z = 89$ ), and through isotope labeling

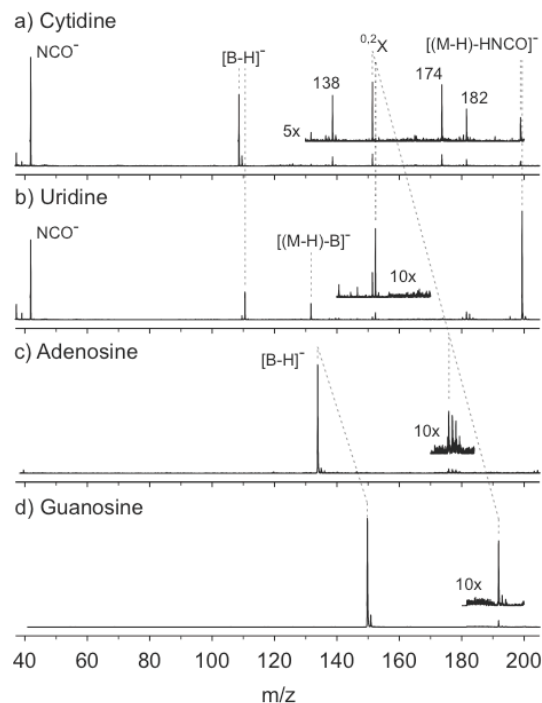


Fig. 4. Metastable decay mass spectra from deprotonated 2'-deoxynucleosides; 2'-deoxy cytidine (a), thymidine (b), 2'-deoxy adenosine (c) and 2'-deoxy guanosine (d). Adapted from [15]

for the single stranded oligonucleotides we have studied [15, 20], where phosphodiester and glycosidic bond ruptures dominate the metastable fragmentation. In these cases, however, the sequence of the nucleosides (nucleobases) determines which phosphodiester and glycosidic bonds are ruptured.

and that of ribose by the loss of one or more CH<sub>2</sub>O units and one or more H<sub>2</sub>O units. When ribose and the bases are combined to form the respective nucleosides, the dominating fragmentation channels observed for isolated ribose and the isolated bases prevail. However, a new channel, the glycosidic bond rupture, also becomes prominent. On the other hand, when ribose is combined with a phosphate group to form the ribose monophosphate, phosphoester bond ruptures become the predominant channels. Finally, in the nucleoside monophosphates and in single stranded oligonucleotides, phosphoester and glycosidic bond ruptures are the dominating channels and base fragmentation and sugar cross-ring cleavage do not play significant roles. In the case of the oligonucleotides, however, the fragmentation pattern still depends strongly on the nature of the bases, i.e., the base sequence largely determines the fragmentation.

### Acknowledgements

This work was supported by the Icelandic Centre for Research (RANNIS) and by the University of Iceland Research Fund. Financial support from COST action P9 (Radiation Damage in Biomolecular Systems, RADAM) and by the European Science Foundation (ESF) program: Electron induced processes at the molecular level (EIPAM) is also acknowledged. This work was conducted within the framework of the cost action MP1002 (Nano-IBCT).

## 5. References

- [1] A.P. Breen, J.A. Murphy, *Free Radic. Biol. Med.*, 1995, **18**, (6) 110.
- [2] K.J.A. Davies, *J. Biol. Chem.*, 1987, **262**, 20.
- [3] B. Epe, *Chem. Biol. Interact.*, 1991, **80** (3), 112.
- [4] B. Boudaiffa, P. Cloutier, D. Hunting, M.A. Huels, L. Sanche, *Science*, 2000, **287** (5458) 114.
- [5] ICRU, International Commission on Radiation Units and Measurements, 1979.
- [6] H. Abdoul-Carime, J. Langer, M.A. Huels, E. Illenberger, *Eur. Phys. J. D*, 2005, **35**, 2.
- [7] S. Denifl, P. Sulzer, F. Zappa, S. Moser, B. Krautler, O. Echt, D.K. Bohme, T.D. Märk, P. Scheier, *Int. J. Mass Spectrom.*, 2008, **277**, 1.
- [8] S. Ptasinska, S. Denifl, V. Grill, T.D. Märk, E. Illenberger, P. Scheier, *Phys. Rev. Lett.*, 2005, **95**, 9.
- [9] S. Ptasinska, S. Denifl, M. Mróz, M. Probst, V. Grill, E. Illenberger, P. Scheier, T.D. Märk, *J. Chem. Phys.*, 2005, **123**, 12.
- [10] H. Abdoul-Carime, S. Gohlke, E. Fischbach, J. Scheike, E. Illenberger, *Chem. Phys. Lett.*, 2004, **387**, 4.
- [11] S. Denifl, S. Ptasinska, M. Probst, J. Hrusak, P. Scheier, T.D. Märk, *J. Phys. Chem. A*, 2004, **108**, 31.
- [12] S. Ptasinska, S. Denifl, V. Grill, T.D. Märk, P. Scheier, S. Gohlke, M.A. Huels, E. Illenberger, *Angew. Chem. Int. Ed.*, 2005, **44**, 11.
- [13] S. Denifl, F. Zappa, A. Mauracher, da F.F. Silva, A. Bacher, O. Echt, T.D. Märk, D.K. Bohme, P. Scheier, *Chem. Phys. Chem.*, 2008, **9**, 10.
- [14] F.F. da Silva, C. Matias, D. Almeida, G. García, O. Ingólfsson, H.D. Flosadóttir, B. Ómarsson, S. Ptasinska, B. Puschnigg, P. Scheier, P. Lima-Vieira, S. Denifl, *J. Am. Soc. Mass Spectrom.*, 2013, **24** (11), 1787-1797.
- [15] H.D. Flosadóttir, B. Ómarsson, I. Bald, and O. Ingólfsson, *Eur. Phys. J. D*, 2012, **66**, 13.
- [16] I. Bald, H.D. Flosadóttir, B. Ómarsson, O. Ingólfsson, *Int. J. Mass Spectrom.*, 2012, **313**, 15-20.
- [17] I. Bald, H.D. Flosadóttir, J. Kopyra, E. Illenberger, O. Ingólfsson, *Int. J. Mass Spectrom.*, 2009, **280**, 1.
- [18] H.D. Flosadóttir, I. Bald, O. Ingólfsson, *Int. J. Mass Spectrom.*, 2011, **305**, 50.
- [19] H.D. Flosadóttir, H. Jónsson, S. Th. Sigurdsson, O. Ingólfsson, *Phys. Chem. Chem. Phys.*, 2011, **13**, 33.
- [20] M. Stano, H.D. Flosadóttir, O. Ingólfsson, *Rapid Commun. Mass Spectrom.*, 2006, **20**, 23.
- [21] G. Kresse, J. Furthmüller, *Phys. Rev. B*, 1996, **54**, 16.
- [22] G. Kresse, J. Hafner, *Phys. Rev. B*, 1994, **49**, 20.
- [23] G. Henkelman, A. Arnaldsson, H. Jónsson, *Comput. Mater. Sci.*, 2006, **36** (3), 74.
- [24] E. Sanville, S.D. Kenny, R. Smith, G. Henkelman, *J. Comput. Chem.*, 2007, **28** (5), 76.

# ABSOLUTE CROSS SECTIONS FOR ELASTIC ELECTRON SCATTERING FROM FURAN AND THF MOLECULES

J. B. Maljković<sup>1</sup>, F. Blanco<sup>2</sup>, G. García<sup>3,4</sup>, B. P. Marinković<sup>1</sup> and  
A. R. Milosavljević<sup>1</sup>

<sup>1</sup>*Laboratory for Atomic Collision Processes, Institute of Physics Belgrade, University of Belgrade, Pregrevica 118, 11080 Belgrade, Serbia*

<sup>2</sup>*Departamento de Física Atómica Molecular y Nuclear, Facultad de Ciencias Físicas, Universidad Complutense, Avda. Complutense s/n, E-28040 Madrid, Spain*

<sup>3</sup>*Instituto de Matemáticas y Física Fundamental, Consejo Superior de Investigaciones Científicas, Serrano 121, 28006 Madrid, Spain*

<sup>4</sup>*Centre for Medical Radiation Physics, University of Wollongong, NSW 2522, Australia*  
E-mail: jelenam@ipb.ac.rs

The results of experimental and theoretical investigation of electron interaction with molecules that are analogue to deoxyribose in DNA are reported for 50 eV and 100 eV incident electron energie. Molecules used as targets are furan, tetrahydrofuran (THF) and 3-hidroksytetrahydrofuran (3hthf). The measurements were performed using a crossed beam technique, for scattering angles from 20° to 110°. The calculations of electron interaction cross sections are based on a corrected form of the independent-atom method, known as the SCAR (Screen Corrected Additivity Rule) procedure, using an improved quasifree absorption model. Calculated results agree very well with the experiment.

## 1. Introduction

The investigation of electron interaction with the molecules that are analogue to some parts of DNA has been motivated in recent years by research of radiation damage in biomaterial. Recently, group of Leon Sanche [1] has established that low energy electrons induce damage of single and double strand breaks in DNA. Molecules presented in this paper are furan (C<sub>4</sub>H<sub>4</sub>O), tetrahydrofuran (THF, C<sub>4</sub>H<sub>8</sub>O) and 3-hydroxytetrahydrofuran (3hthf, C<sub>4</sub>H<sub>8</sub>O<sub>2</sub>), that may be considered as analogue to deoxyribose sugar in DNA. Experimental and theoretical results for these molecules [2-4] are compared on the absolute scale. Furan is a five-member unsaturated hydrocarbon ring, belonging to C<sub>2v</sub> point symetry group. It different in only four H atoms from THF and in H<sub>4</sub>O from 3hthf. Therefore, according to the independent atom model (IAM) approximation [5,6] (see below) at high incident electron energies, the elastic differential cross sections for these molecules should be very similar on the absolute scale. on the other hand, although furan, THF and 3hthf are similar from the structual standpoint, furan posseses a signficaly different dipol moment (0.71 D for furan, 1.75 D for THF and 1.67 D for 3hthf). Since for the molecule with high permanent dipol moment rotational excitations become more significant [5,6], this could influence the experimentaly and theoretically obtained absolute DCSs.

## 2. Experimental set up and theory

The measurements of relative and absolute differential cross sections were performed using cross beam experimental setup, described previously [7]. Briefly, an electron gun produces a well collimated electron beam, which is crossed perpendicularly with molecular beam produced from a stainless steel needle. Electrons, formed in the interaction volume, are retard and focused by a four element electrostatic lens into a double mirror analyzer. Electrons are further guided by a three-element lens into the single channel electron multiplier. All these components are enclosed in a double  $\mu$ -metal shielded vacuum chamber. The base pressure was about  $4 \times 10^{-7}$  mbar, obtained by a turbo molecular pump. Working pressure was about  $2 \times 10^{-6}$ . Angular resolution was better than  $\pm 2^\circ$ . Experimental results were compared with previous once at the incident electron energy where a referent gas (here Ar) has deep minima [8]. The energy resolution

was about 0,4 eV, limited by a thermal spread of primary electrons. Experimental procedure included measurements of both relative and absolute differential cross sections (DCSs). Relative differential cross sections are normalized to the absolute scale according to the points obtained by the relative flow method [9,10]. Present calculations of molecular cross sections are based on a corrected form of the independent atom method, known as the screen corrected additivity rule (SCAR) procedure [5,6], with an improved quasifree absorption model potential, which includes relativistic and many body effects, as well as inelastic processes. The standard IAM approximation is based on reducing the problem of electron – molecule collisions to collisions with individual atoms by assuming that each atom of the molecule scatters independently. The role of SCAR correction to the standard IAM procedure is reducing the values obtained from the standard additivity rule to account for geometrical overlapping of atomic cross sections.

### 3. Results

Results of experimental and theoretical absolute differential cross sections for elastic electron scattering from furan, THF and 3hthf molecules, which are analogue to deoxyribose in DNA, has been shown in the Fig 1. In the present contribution, the results for furan, THF and 3hthf are compared and discussed for 50eV and 100eV. As expected, absolute DCSs show similar redistribution of scattered electrons from target molecules and cross sections are very close on the absolute scale for both energies. The agreement depends on both the incident energy and the scattering angle. At 100 eV DCSs for THF and 3hthf are slightly higher than the absolute points for furan and this difference is even more pronounced at 50eV at small scattering angles. This effect could be due to very different dipole moment of furan compared to THF and 3hthf. Absolute calibration for all three molecules was different. Relative flow method with Ar as the referent gas was used for furan [2], N<sub>2</sub> for THF and Kr for 3hthf [4]. The absolute DCSs for 3hthf should be the biggest on the absolute scale, considering the size of molecule. However, a precise comparison is difficult to perform with the present experimental accuracy. Also, 3hthf molecule has a low vapour pressure, so the heating was needed, which can include presence of isomers, so DCSs can be different from the expected ones.

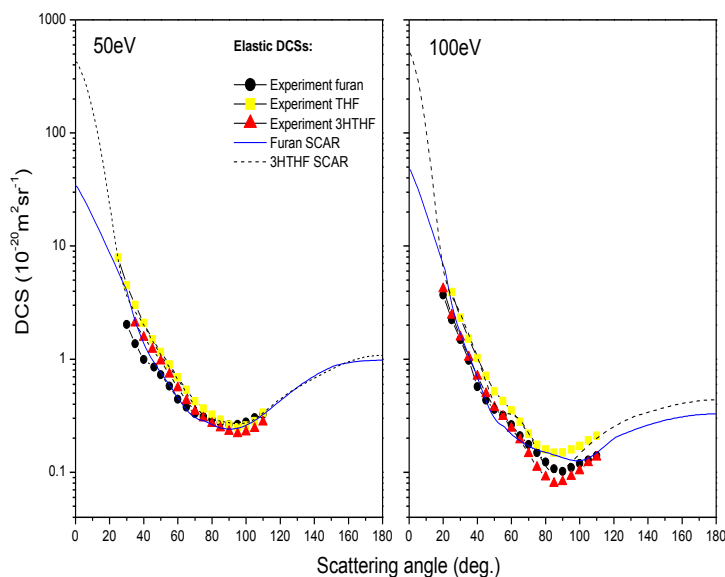


Fig. 1. Comparison of differential cross sections for furan [2], THF [3] and 3Hthf [4] molecule.

## 4. Acknowledgments

The work was supported by the Ministry of Education, Science and Technological Development of Republic of Serbia (Project No. 171020) and Spanish Ministerio de Ciencia e Innovación Project No. FIS2012-31230, and motivated by the COST Action MP 1002 (Nano-IBCT).

## 5. References

- [1] Boudaiffa B., Cloutier P., Hunting D., Huels M. A., and Sanche L., 2000 *Science* **287**, 1658
- [2] Maljković J. B, Blanco F., Čurik R., García G., Marinković B. P. and Milosavljević A. R. 2012, *J. Phys. Chem.* **137** 064312.
- [3] Milosavljević A. R., Giuliani A., Šević D., Hubin-Franskin M. J. and Marinković B. P 2005, *Eur. Phys. J. D.* **35**, 411.
- [4] Milosavljević A. R., Blanco F., Maljković J. B., Šević D., García G. and Marinković B. P. 2008, *New J. Phys.* **10**, 103005.
- [5] Blanco F. and García G., 2003 *Phys. Lett. A* **317**, 458 .
- [6] Blanco F. and García G., 2004 *Phys. Lett. A* **330**, 230.
- [7] Milosavljević A. R., Blanco F., Šević D., García G., and Marinković B. P., 2006 *Eur. Phys. J. D.* **40**, 107.
- [8] Williams J.W. and Willis B. A., 1975 *J. Phys. B.* **8**, 1670.
- [9] Nickel J. C., Mott C., Kanik I., and McCollum D.C., 1988 *J. Phys. B* **21**, 1867.
- [10] Nickel J. C., Zetner P.V., Shen G., and Trajmar S., 1989 *J. Phys. E* **22**, 730.

## **ELECTRON INDUCED DECOMPOSITION OF BIOMOLECULES PROBED IN POTASSIUM COLLISIONS**

F. Ferreira da Silva<sup>1</sup>, G. Meneses<sup>1</sup>, T. Cunha<sup>1</sup>, D. Almeida<sup>1</sup>, G. García<sup>2</sup> and P. Limão-Vieira<sup>1</sup>

<sup>1</sup> *Laboratório de Colisões Atômicas e Moleculares, CEFITEC, Departamento de Física, Faculdade de Ciências e Tecnologia, Universidade Nova de Lisboa, Campus de Caparica, 2829-516 Caparica, Portugal*

<sup>2</sup> *Instituto de Física Fundamental, Consejo Superior de Investigaciones Científicas (CSIC), Serrano 113-bis, 28006 Madrid, Spain*

f.ferreiradasilva@fct.unl.pt

Electron driven reactions are of interest in many areas of science and technology, including low-temperature plasmas, the interstellar and planetary atmospheres and dense interstellar clouds as well as biological processes and medicine. Within the biological environment, the structure and functionality of proteins can be described by the specific sequence in the chain of amino acids joined by the peptide bonds. This specific sequence gives to polypeptides the compact shape that contains coils, zigzags, turns or loops. These arrangements lead to a specific conformation that will contribute for the protein functionality. However, such can be disturbed within the physiological environment upon electron capture as a result of radiation induced processes. Understanding low-energy electrons induced decomposition, allows a proper description of the underlying molecular mechanisms. Electron transfer through the chain of amino acids can induce fragmentation leading to the loss of integrity of a protein.

Electron transfer studies in potassium collisions with amino acids and simple carboxylic acids have been performed in order to understand how low energy electrons induced fragmentation via negative ion formation. [1, 2] In this communication single amino acids as tyrosine and acetic acid decomposition upon collisions with potassium atoms will be presented in order to elucidate their fragmentation pathways.

### **References**

- [1] F. Ferreira da Silva, M. Lanca, D. Almeida, G. Garcia, P. Limao-Vieira, *European Physical Journal D*, 66 (2012) 78.
- [2] F. Ferreira da Silva, J. Rafael, T. Cunha, D. Almeida, P. Limao-Vieira, *International Journal of Mass Spectrometry*, 365-366 (2014) 238-242.

# **MOMENTUM TRANSFER TO A FREE FLOATING DOUBLE SLIT: REALIZATION OF A THOUGHT EXPERIMENT FROM THE EINSTEIN-BOHR DEBATES**

Lothar Ph. H. Schmidt

*Goethe-Universität, Max-von-Laue-Str.1, 60438 Frankfurt am Main, Germany*

E-mail: Lothar.Schmidt@atom.uni-frankfurt.de

In 1927 in one of the most famous physics debates Einstein challenged Bohr with a thought experiment. He proposed that measuring the momentum transfer to a double slit would unveil through which of the two slits the quantum particle had passed. We translate this experiment to experimental reality using an isotope labeled free floating diatomic molecular ion as the double pinhole. The reaction  $\text{HD}^+ + \text{He} \rightarrow \text{H} + \text{D} + \text{He}^+$  was measured in a kinematically complete experiment [1,2] by using COLTRIMS. We find that the Helium does not only travel delocalized through both slits, but even more counter intuitive and completely opposite to Einstein's assumption, it transfers momentum to both slits simultaneously [3].

## **References**

- [1] Schmidt L Ph H et al. 2008 *Phys Rev. Lett.* **101**, 173202
- [2] Schmidt L Ph H et al. 2012 *Phys Rev. Lett.* **108**, 073202
- [3] Schmidt L Ph H et al. 2013 *Phys Rev. Lett.* **111**, 103201



# LOW ENERGY REACTIVE COLLISIONS IN O<sup>-</sup>+H<sub>2</sub>

Martin Čížek, Karel Houfek

*Faculty of Mathematics and Physics, Institute of Theoretical physics, Charles University in Prague,  
V Holešovičkách 2, Praha 8, Czech Republic*

E-mail: Martin.Cizek@mff.cuni.cz

In this contribution we present preliminary results for reactive scattering of O<sup>-</sup> anion with hydrogen molecule. The three lowest potential energy surfaces for the anion are calculated for large number of geometries. The conical intersections of these three states are located together with the intersections with the potential energy surface for the neutral molecule. Classical trajectory calculations of the dynamics are also presented. Finally we will discuss the plans to include the effects beyond the Born-Oppenheimer approximation and the spin-orbit coupling.

## 6. Introduction

The reactive collisions of negative ions with neutral molecules represent the important class of processes in physics of planetary atmospheres and interstellar medium. The prototype of these reactions is the associative detachment of the negative hydrogen ion  $H+H \rightarrow H_2+e$ , which has been characterised in detail recently both theoretically and experimentally [1]. The numerical procedure to calculate such processes in diatomic systems is now well developed and has also been applied to other systems [2]. In triatomic systems the theoretical treatment of similar reaction is still a challenge. Here we want to show preliminary results in path to complete description of low-energy collision  $O^-+H_2$ .

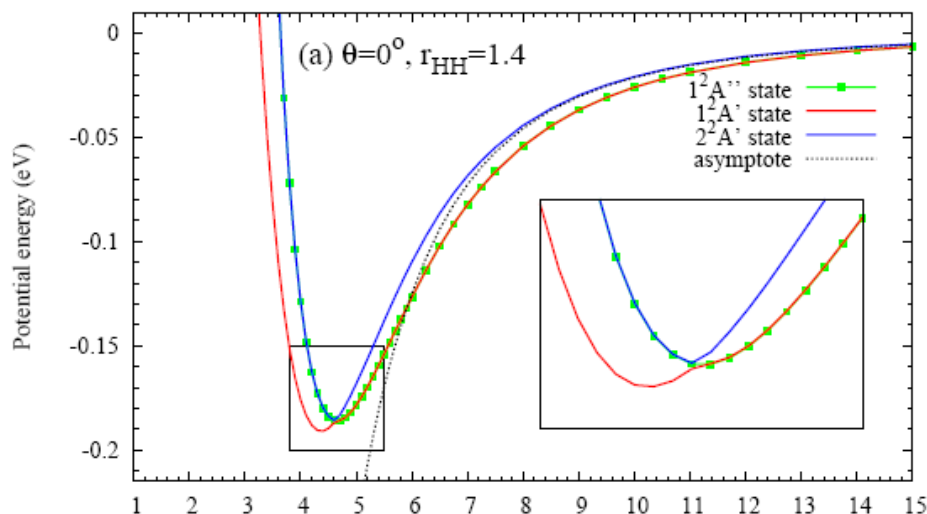


Fig. 1. Potential energy surfaces for the lowest three states of  $O^-+H_2$  plotted along Jacobi coordinate in linear geometry. The conical intersection region is enlarged. Only the lowest state leads to the autodetachment region for low collision energies.

## 7. Preliminary results for electronic structure and nuclear dynamics.

The first step in the description of the dynamics of the system is the ab initio calculation of the Born-Oppenheimer potential energy surfaces. There are three electronic states of hydrogen molecular anion important for  $O^-+H_2$  collisions [3]. We did an extensive calculation of these states with the multireference CI method for many geometries. We also calculated the lowest potential energy surface of the neutral molecule to locate the  $H_2O+e$  autodetachment region. The three anion states are interconnected through a conical intersection at collinear geometry (see Fig. 1). In the talk I will discuss the three dimensional

structure of these potential energy surfaces, conical intersections and the location of autodetachment region in detail.

To perform the nuclear dynamics on the calculated surfaces is highly nontrivial task. The full quantum mechanical treatment of the three body reactive scattering has been performed for neutral systems in past [4], but we are not aware of any calculation for the negative ions. The situation is complicated here by the presence of the conical intersections and the electron autodetachment continuum. As a first step in gaining the better grasp of the system, we performed the calculation of the classical trajectories along each potential energy surface separately. An example of such trajectory is shown in Fig. 2.

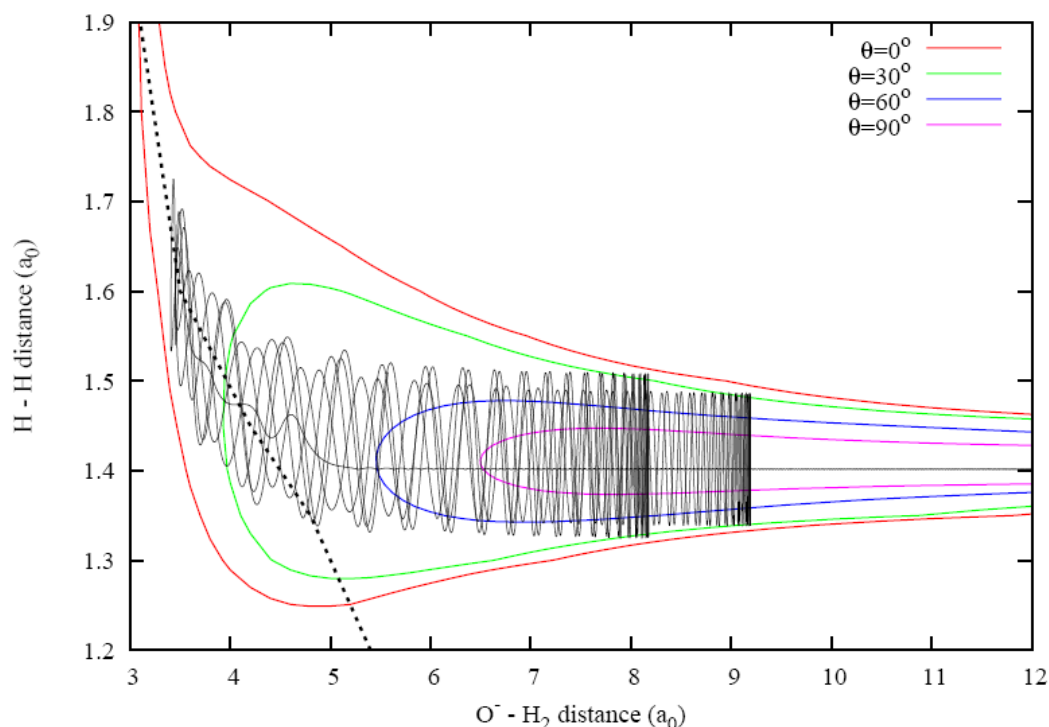


Fig. 2. Representative example of the projection of the classical trajectory for the  $O^- + H_2$  dynamics (black line) in the plane defined by two Jacobi coordinates. The CMS energy of the collision is 15 meV. The equipotential lines for the lowest electronic state are also plotted for this energy and for different angle  $\theta$  between the two Jacobi vectors. The position of the conical intersection with the other two states at  $\theta=0$  is shown with dashed black line.

At the end of the talk I will finally summarize the additional steps that we have to implement to achieve the full quantum mechanical description of the system and to calculate the state specific cross sections for the final channels  $H_2O + e$  and  $H + OH$ .

## 8. References

- [1] Kreckel H, Bruhns H, Čížek, M, Glover SCO, Miller KA, Urbain X and Savin DW 2010 *Science* **328**, 69.
- [2] Živanov S, Čížek M, Horáček J and Allan M 2003 *J. Phys. B* **36**, 3513.
- [3] Werner HJ, Manz U and Rosmus P 1987 *J. Chem. Phys.* **87**, 2913.
- [4] Brouard M and Vallance C (editors): *Tutorials in Molecular Reaction Dynamics*, RSC Publishing, Cambridge 2010.

# ELECTRONIC DYNAMICS IN LOW-ENERGY HEAVY-ION COLLISIONS

Yury S. Kozhedub<sup>1</sup>, Ilya I. Tupitsyn<sup>1</sup>, Vladimir M. Shabaev<sup>1</sup>

Thomas Stöhlker<sup>2</sup>

<sup>1</sup>*Department of Physics, St. Petersburg State University,  
Uljanovskaya 1, Petrodvorets, St. Petersburg 198504, Russia*

<sup>2</sup>*Gesellschaft für Schwerionenforschung, Planckstrasse 1, D-64291 Darmstadt, Germany*  
E-mail: kozhedub@pcqnt1.phys.spbu.ru

We present results of non-perturbative relativistic calculations of electronic quantum dynamics in low-energy ion-atom collisions. Method of calculations employs an independent particle model with effective single-electron Dirac-Kohn-Sham operator. Solving of the single-electron equations is based on coupled-channel approach with atomic-like Dirac-Sturm-Fock orbitals, localized at the ions (atoms) [1]. Many-particle probabilities are calculated in terms of single-particle amplitudes employing the formalism of inclusive probabilities [2]. Calculations are performed for low-energy ion-atom collisions, which is already studied experimentally and theoretically, as well as for systems, which experimental research is planed at GSI and FAIR in the nearest future [3].

[1] I.I. Tupitsyn, Y.S. Kozhedub, V.M. Shabaev, A.I. Bondarev, G.B. Deyneka, I.A. Maltsev, S. Hagmann, G.Plunien, and Th. Stöhlker, *Phys. Rev. A* **82**, 042701 (2010); **85**, 032712 (2012).

[2] H. J. Lüdde and R. M. Dreizler, *J. Phys. B* **18**, 107 (1985).

[3] S. Hagmann *et al.*, *Electron Emission following 1s Adiabatic Ionization and Quasi-resonant 1s-1s Charge Transfer in Symmetric Ion-Atom Collisions*, GSI proposal (unpublished).

## NEW DEVELOPMENTS OF THE $\text{Ps}^-$ STUDIES

Yasuyuki Nagashima

*Department of Physics, Tokyo University of Science*  
*1-3 Kagurazaka, Shinjuku, Tokyo 162-8601, Japan*  
E-mail: ynaga@rs.kagu.tus.ac.jp

The positron, an anti-particle of the electron, can bind with an electron to form positronium. Another electron can also bind to a positronium atom weakly to form a positronium negative ion. The development of intense sources of the ions using alkali-metal coated surfaces has opened the door to a new era of the experimental studies of this ion. Its photodetachment and development of an energy-tunable positronium beam using the photodetachment technique have been accomplished successfully. In this presentation, recent progresses in the experimental studies on this ions will be reported.

Since the prediction and the first observation of the positron, it has been widely used for elementary particle physics, atomic physics, fermiology of metals, defect studies and crystallography from their unique interactions with materials. Positrons are also used for medical applications such as positron emission tomography for the studies of brains and detection of cancer in human bodies.

A positron can bind with an electron to form a hydrogen-like two body system, positronium ( $\text{Ps}$ ). After the experimental confirmation of the existence of  $\text{Ps}$ , a large number of investigations on  $\text{Ps}$  atoms have been performed from the view point of basic physics and material science.

Another electron can also bind to  $\text{Ps}$  to form a weakly bound state, positronium negative ion ( $\text{Ps}^-$ ).  $\text{Ps}^-$  is a bound state of three particles via Coulomb interaction. It is similar to  $\text{H}^-$  or  $\text{H}_2^+$  although theoretical approaches for these ions are not adequate for  $\text{Ps}^-$  because all three components have the same mass. Thus  $\text{Ps}^-$  must be investigated as a genuine three-body system and many theoretical studies have been performed since the prediction by Wheeler in 1946 [1]. However, after the experimental confirmation of the existence of  $\text{Ps}^-$  by Mills in 1981 [2], only a few experimental studies have been performed for more than 25 years because of the low production efficiency.

In 2008, we succeeded in the efficient production of  $\text{Ps}^-$  using alkali-metal coated tungsten surfaces [3]. We have also succeeded in the first observation of the photodetachment of  $\text{Ps}^-$  [4] and production of an energy-tunable  $\text{Ps}$  beam using the  $\text{Ps}^-$  photodetachment technique [5]. In this presentation, I will review recent progresses of the experimental studies on this ions including: (i) efficient emission of  $\text{Ps}^-$  from alkali-metal coated surfaces [3, 6], (ii)  $\text{Ps}$  emission from alkali-metal coated surfaces [7], (iii)  $\text{Ps}^-$  photodetachment experiment [4] and (iv) development of an energy-tunable beam of  $\text{Ps}$  using the  $\text{Ps}^-$  photodetachment technique and a linac-based pulsed slow positron beam [5]. I will also discuss about our new project, development of an energy-tunable  $\text{Ps}$  beam using buffer-gas positron trap (Surko trap) and its applications.

### References

- [1] Wheeler J A 1946 *Ann. New York Acad. Sci.* **48** 219.
- [2] Mills A P jr 1981 *Phys. Rev. Lett.* **46** 717.
- [3] Nagashima Y, Hakodate T, Miyamoto A and Michishio K 2008 *New J. Phys.* **10** 123029.
- [4] Michishio K, Tachibana T, Terabe H, Igarashi A, Wada K, Kuga T, Yagishita A, Hyodo T and Nagashima Y 2011 *Phys. Rev. Lett.* **106** 153401.
- [5] Michishio K, Tachibana T, Suzuki R H, Wada K, Yagishita A, Hyodo T and Nagashima Y 2012 *Appl. Phys. Lett.* **100** 254102.
- [6] Terabe H, Michishio K, Tachibana T and Nagashima Y 2012 *New J. Phys.* **14** 015003.
- [7] Terabe H, Iida S, Wada K, Hyodo T, Yagishita A and Nagashima Y 2013 *J. Phys. Conf. Ser.* **443** 012075.

# INTERACTION OF ANTIPROTONS AND PROTONS WITH ATOMS: A DENSITY-FUNCTIONAL THEORY PERSPECTIVE

Matthew Baxter and Tom Kirchner

*Department of Physics and Astronomy, York University, Toronto, Ontario, Canada M3J 1P3*

E-mail: tomk@yorku.ca

We study antiproton- and proton-induced ionization of helium atoms from the viewpoint of time-dependent density-functional theory. A frozen-correlation approximation to the correlation potential and an adiabatic model for the correlation integral are used to calculate one- and two-electron removal cross sections in the 5-2000 keV impact energy range. Significant improvement upon results obtained in an independent-electron model description is obtained for both projectiles.

## 1. Introduction

Comparing antiproton and proton impact ionization yields has been popular with the atomic physics community for many years and for good reasons. The first Born approximation demands these yields to be the same. Measurements have shown that they are not, except for single ionization at high impact energies. Studying lower energies and/or multiple ionization processes thus holds the promise to provide interesting insights into collision-induced electron dynamics. A substantial body of published works – reviewed in Refs. [1-3] – is testament to the fact that rich physics is indeed at play.

As theorists, we can turn the argument around and ask what the comparison of antiproton and proton impact collisions teaches us about the methods we use to describe them. We take this viewpoint to look at one of the simplest problems in this context, namely, the one- and two-electron removal from helium atoms. A great deal is known about this problem – thanks to accurate experimental data and sophisticated calculations [1-3]. We will take advantage of this and look at these collisions from the viewpoint of time-dependent density-functional theory (TDDFT) [4] with the goal to shed some light on TDDFT's usefulness and (current) limitations.

TDDFT is centred around the not-at-all obvious fact that the intricacies of a many-body system are encoded in its density and that, in principle, knowledge of that density alone suffices to describe the system completely. This is ensured by the Runge-Gross theorem [5], which goes on to say that the exact density can be obtained from the solution of a set of single-particle equations – the so-called time-dependent Kohn-Sham (TDKS) equations. In applications of the theory this poses two fundamental (and also a few computational) challenges: (i) to find a suitable approximation for the potential that drives the TDKS equations, (ii) to find suitable models for extracting the observables of interest from the density. The words *approximation* and *model* signal the downside of TDDFT: the Runge-Gross theorem does not come with prescriptions of how to calculate these quantities. To paraphrase a sentence from a recent review article on ground-state DFT where the situation is similar: we are assured of the existence of those density functionals, but no explicit expressions are known [6].

Recent work [7] suggests that the observable problem (ii) is the more important one when it comes to calculating accurate single and double ionization cross sections in antiproton-helium collisions, and that a relatively simple model appropriated from the world of laser-induced ionization [8] provides a decent solution to it. In this work we use the same model to address proton-helium collisions. Given that the physics of antiproton- and proton-impact collisions is not the same this is a nontrivial extension that sheds some light on the generality of the model.

## 2. Theory

We solve the TDKS equations using our basis generator method and the frozen correlation approximation to the potential as described in Ref. [7]. This provides us with the density  $n$  of the two-electron system. We use it to calculate a single-particle probability for electron removal

$$p = 1 - \frac{1}{2} \int_T n(\vec{r}, t_f) d^3r, \quad (1)$$

where  $t_f$  is the final time of the propagation and  $T$  some volume that contains all target bound-state contributions to  $n$ . Introducing the correlation integral

$$I_c = \int_T d^3r_1 \int_T d^3r_2 \left[ \frac{\rho(\vec{r}_1, \vec{r}_2, t_f)}{n(\vec{r}_1, t_f)n(\vec{r}_2, t_f)} - \frac{1}{2} \right] n(\vec{r}_1, t_f)n(\vec{r}_2, t_f), \quad (2)$$

which in addition to the one-electron density  $n$  contains the two-electron density  $\rho$ , the exact probabilities for  $j$ -fold ( $j=0,1,2$ ) electron removal can be written as [7,8]

$$\begin{aligned} p_0 &= (1-p)^2 + \frac{1}{2} I_c \\ p_1 &= 2p(1-p) - I_c \\ p_2 &= p^2 + \frac{1}{2} I_c. \end{aligned} \quad (3)$$

Clearly, assuming  $I_c=0$  produces the standard independent-electron model (IEM) expressions for zero-, one-, and two-fold ionization. In lieu of the exact two-electron density  $\rho$ , which is unknown unless one performs a fully correlated time-dependent two-electron calculation, Wilken and Bauer (WB) proposed an adiabatic model for  $I_c$ , which only contains ground-state one- and two-electron densities and a factor that is related to the single-particle probability  $p$  [8]. We have adapted this model with success in our recent study of antiproton-helium collisions [7], and we use it here for proton-helium collisions as well. The question of how to extend the WB model in order to separate capture and ionization for the latter system will be addressed in a future work.

## 3. Results and Discussion

In Figure 1 we present total cross sections for one-electron removal. We only compare our results with experimental data to avoid overburdening of the figures and to keep the discussion simple. For the antiproton case the comparison with other theoretical results was carried out in Ref. [7], while we will provide a thorough discussion of our proton results together with cross sections obtained from other theoretical methods in a future publication.

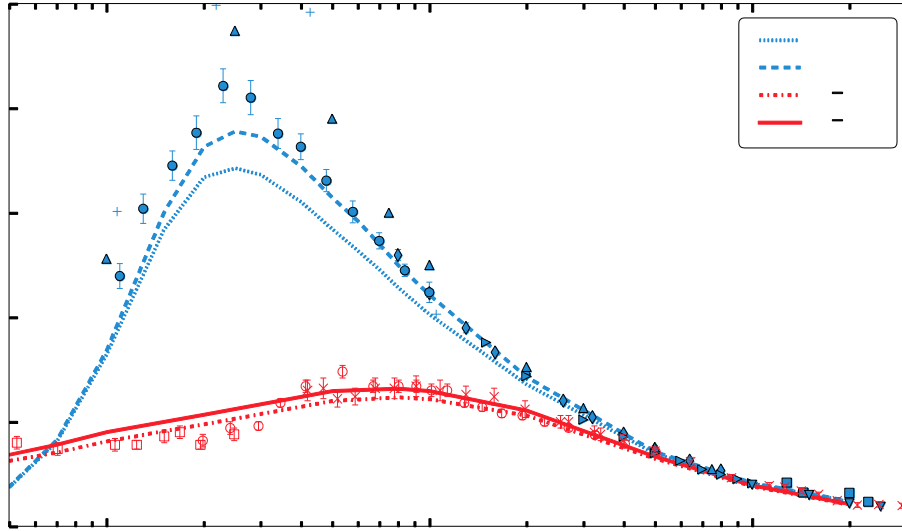


Fig. 1. Total cross section for one-electron removal from helium atoms as a function of impact energy. Red lines and symbols: antiproton impact; blue lines and symbols: proton impact. Experimental data - protons:  $\blacktriangle$  [9],  $+$  [10],  $\bullet$  [11],  $\blacklozenge$  [12],  $\blacktriangleright$  [13],  $\blacktriangledown$  [14],  $\blacksquare$  [15]; antiprotons:  $\square$  [16],  $\circ$  [17],  $\times$  [18].

The WB model for  $I_c$  enhances the IEM<sup>2</sup> cross section visibly for both antiproton and proton impact except at the highest impact energies. For antiproton impact the experimental cross sections do not help us with assessing the correctness of this tendency. In contrast, a clear improvement of the agreement with the data is observed for proton projectiles.

For two-electron removal (not shown) we find that the WB model represents a clear improvement over the IEM for both projectiles. However, significant discrepancies with the experimental data persist for proton-helium collisions in the regime in which electron capture becomes increasingly strong.

## 4. References

- [1] Schultz D R, Olson R E and Reinhold C O 1991 *J. Phys. B* **24** 521.
- [2] Knudsen H and Reading J F 1992 *Phys. Rep.* **212** 107.
- [3] Kirchner T and Knudsen H 2011 *J. Phys. B* **44** 122001.
- [4] Ullrich C A 2012 *Time-Dependent Density-Functional Theory* (Oxford University Press, Oxford, UK).
- [5] Runge E and Gross E K U 1984 *Phys. Rev. Lett.* **52** 997.
- [6] Becke A D 2014 *J. Chem. Phys.* **140** 18A301.
- [7] Baxter M and Kirchner T 2013 *Phys. Rev. A* **87** 062507.
- [8] Wilken F and Bauer D 2006 *Phys. Rev. Lett.* **97** 203001.
- [9] DuBois R D, Toburen L H and Rudd M E 1984 *Phys. Rev. A* **29** 70.
- [10] Solov'ev E S, Il'in R N, Oparin V A, Federenko N V 1962 *Sov. Phys. JETP* **15** 459.
- [11] Shah M B, McCallion P and Gilbody H B 1989 *J. Phys. B* **22** 3037.
- [12] Shah M B and Gilbody H B 1985 *J. Phys. B* **18** 899.
- [13] Puckett L J and Martin D W 1970 *Phys. Rev. A* **1** 1432.
- [14] Wexler S 1964 *J. Phys. Chem.* **41** 1714.
- [15] Knudsen H et al 1984 *J. Phys. B* **17** 3545.
- [16] Knudsen H et al 2008 *Phys. Rev. Lett.* **101** 043201.
- [17] Hvelplund P et al 1994 *J. Phys. B* **27** 925.

<sup>2</sup> We use the tag IEM for our results obtained from  $I_c=0$ , even though they are not strictly on the independent-electron level because of the inclusion of a (frozen) correlation potential.

[18] Andersen L H et al 1990 *Phys. Rev. A* **41** 6536.



## **ELECTRON AND NUCLEAR DYNAMICS IN THE PHOTOIONIZATION OF MOLECULES**

Fernando Martín<sup>1,2</sup>

<sup>1</sup> *Departamento de Química, Facultad de Ciencias, Módulo 13, Universidad Autónoma de Madrid, 28049 Madrid, Spain*

<sup>2</sup> *Instituto Madrileño de Estudios Avanzados, IMDEA-Nanociencia, Cantoblanco, 28049 Madrid, Spain*

E-mail: Fernando.martin@uam.es

The development of attosecond laser pulses allows one to probe the inner working of atoms, molecules and surfaces on the timescale of the electronic response. In molecules, attosecond pump-probe spectroscopy enables investigations of the prompt charge redistribution and localization that accompany photo-excitation processes, where a molecule is lifted from the ground Born-Oppenheimer potential energy surface to one or more excited surfaces, and where subsequent photochemistry evolves on femto- and attosecond timescales. In this talk I will present a few theoretical examples of realistic molecular attosecond pump-probe experiments in which simple molecules are ionized with a single attosecond pulse (or a train of attosecond pulses) and are subsequently probed by one or several infrared or xuv few-cycle pulses. The evolution of the electronic and nuclear densities in the photo-excited molecule or remaining molecular ions is calculated with attosecond time-resolution and is visualized by varying the delay between the pump and probe pulses. The results of these calculations [1-4] allow one to explain several experimental observations as well as to guide future experimental efforts to uncover ultrafast electron and nuclear dynamics in molecules.

### **References**

- [1] G. Sansone et al, Nature 465, 763 (2010).
- [2] S. E. Canton et al, Proc. Natl. Acad. Sci. 108, 7302 (2011)
- [3] A. González-Castrillo et al, Phys. Rev. Lett. 108, 063009 (2012)
- [4] A. Palacios, A. González-Castrillo and F. Martín, Proc. Natl. Acad. Sci. 111, 3973 (2014).

# TRANSMISSION OF SLOW HIGHLY CHARGED IONS THROUGH 1 NM THICK CARBON NANOMEMBRANES

Elisabeth Gruber<sup>1</sup>, Richard A. Wilhelm<sup>2,3</sup>, René Heller<sup>2</sup>, Robert Ritter<sup>1</sup>,  
Stefan Facsko<sup>2</sup>, and Friedrich Aumayr<sup>1</sup>

<sup>1</sup>*TU Wien - Vienna University of Technology, Institute of Applied Physics, 1040 Vienna, Austria*

<sup>2</sup>*Helmholtz-Zentrum Dresden-Rossendorf, Institute of Ion Beam Physics and Materials Research, 01328 Dresden, Germany, EU*

<sup>3</sup>*Technische Universität Dresden, 01069 Dresden, Germany, EU*

E-mail: egruber@iap.tuwien.ac.at

We irradiate ultrathin carbon nanomembranes (CNMs) with slow highly charged Xe ions and measure charge state and energy loss for the transmitted ions as well as analyse the irradiated nanomembranes using high resolution imaging techniques. Surprisingly, we observe for all incident charge states two distinct exit charge state distributions accompanied by charge exchange dependent energy losses. In addition, above a charge state of about 25+ circular nanopores are created in the CNM by single ion impacts. The size of the nanopores depends on the kinetic and potential energy of the impinging ion.

## 1. Introduction

The production of nanostructures by slow highly charged ions (HCIs) on surfaces has been a hot topic in the last years [1]. We have recently discovered that the impact of individual HCIs is able to create permanent nano-sized hillocks on the surface of a CaF<sub>2</sub> single crystal [2]. The experimentally observed threshold of the projectile's potential energy necessary for hillock formation could be successfully linked to a solid-liquid phase transition (nano-melting) [1 - 3]. Meanwhile a variety of materials has been found, which is susceptible to nano-structuring by the impact of slow HCI [1]. The nature, appearance and stability of the created structures, however, depend heavily on the properties of the target material and the involved interaction processes (determined by the potential and kinetic energy of the projectiles) [3]. Not in all cases nano-hillocks are formed on the surface but also nano-craters or -holes have been found, e.g. on KBr [4] or PMMA [5].

Starting from a different point as compared to a solid bulk material, in this contribution we present investigations in which freestanding 1nm thick carbon nanomembranes (CNMs) are irradiated with individual slow highly charged ions. CNMs are engineered two-dimensional carbon nanolayers, which are produced by cross-linking of an aromatic self-assembled monolayer of biphenyl units with low-energy electrons as described in [6]. The substrate is then subsequently removed and the resulting nanomembrane is transferred onto a TEM grid.

We analyse the charge state and energy loss of projectiles transmitted through the CNMs [7] as well as present transmission electron microscope (TEM) and helium ion microscope (HIM) images of nano-pores produced by impact of individual HCIs [8].

## 2. Nanopores milled into CNMs using slow HCI

CNMs are irradiated with slow highly charged Xe<sup>q+</sup> ions of various charge states ( $20 \leq q \leq 40$ ) and kinetic energies ( $4 \text{ keV} \leq E \leq 180 \text{ keV}$ ) at the two source facility of HZDR. After irradiation the CNMs are inspected by high resolution imaging techniques, e.g. transmission electron microscopy (TEM), secondary electron microscopy (SEM), atomic force microscopy (AFM) and He-ion microscopy (HIM) [8]. Above a charge state of 25+ we find nanopores at positions, where the membrane suspends over holes in the TEM grid (fig. 1) [8]. Slow HCI are able to produce nanosized pores from 30 nm down to only 3 nm, without creating further visible damage, because of their very localized energy deposition.

The number density corresponds well with the incident ion fluence, indicating that every pore is produced by a single ion impact. For a fixed impact energy, the pore diameter increases with the potential energy of

the HCI, indicating that bond breaking due to electron exchange and emission processes is the main mechanism for nanopore formation.

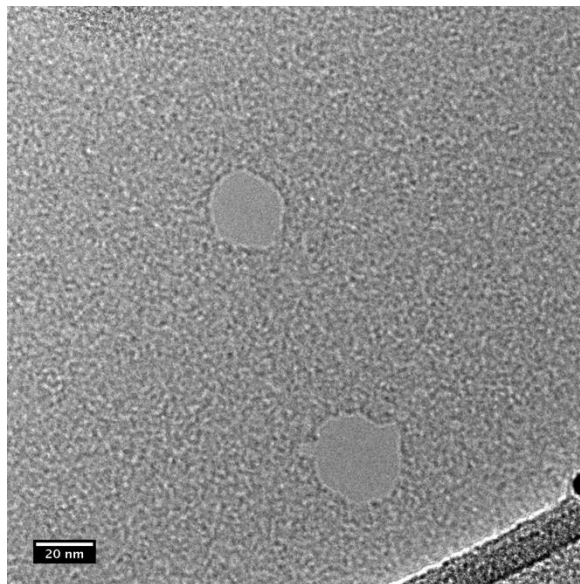


Fig. 1. TEM image of 2 nanopores in a carbon nanomembrane induced by impact of two  $\text{Xe}^{40+}$  ions ( $E_{\text{kin}} = 40 \text{ keV}$ ,  $E_{\text{pot}} = 38.5 \text{ keV}$ ).

### 3. Charge state and energy loss of HCI transmitted through CNMs

The extremely small thickness of this special target offers us a second opportunity - the observation of the projectile right after the interaction process in terms of its energy loss and charge exchange. For this purpose we designed an electrostatic analyser that allows us to determine both quantities experimentally.

The measurements show the unexpected result of two distinct exit charge distributions: on the one hand (a) ions with very high charge states (close to the initial one) that loose nearly no kinetic energy and on the other hand (b) very low charged ions that loose a significant amount of kinetic energy (see fig. 2). The energy loss for ions exhibiting large charge loss shows a quadratic dependency on the incident charge state indicating that equilibrium stopping force values do not apply in this case [7].

In addition angle resolved transmission measurements point to a significant contribution of elastic energy loss.

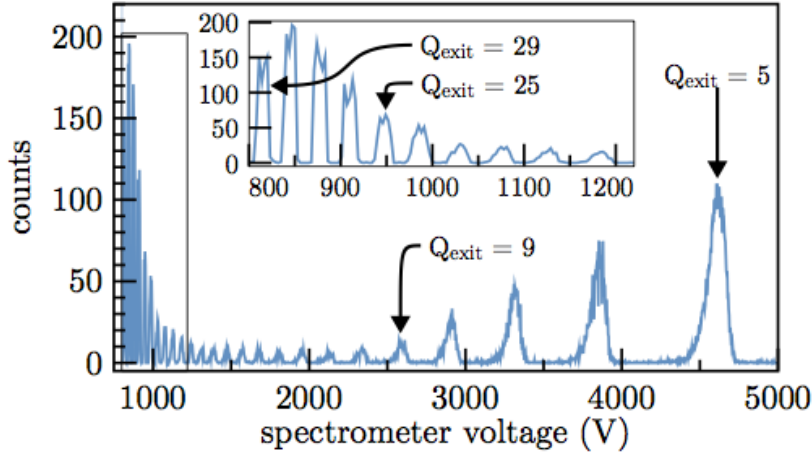


Fig. 2. Charge state and energy loss spectrum of 1050 eV/amu  $\text{Xe}^{30+}$  ions after passing a 1 nm thick carbon nanomembrane. All charge states below  $Q = 30$  (but larger than  $Q = 4$ ) are visible, whereas two distinct distributions can be observed. The high exit charge state distribution is magnified in the inset.

The measurements show that the different impact parameter regimes can be separated and thus a particle's energy deposition in an ultrathin solid target may not be described in terms of an averaged energy loss per unit length (for more details see [7]).

#### 4. Acknowledgements

Financial support from the Deutsche Forschungsgemeinschaft (DFG) (Project No. HE 6174/1-1) and from the Austrian FWF (Project No. I 1114-N20) is acknowledged.

#### 5. References

- [1] Aumayr F, et al. 2011, *J.Phys.: Cond.Mat.* **23**, 393001.
- [2] El-Said A S, et al. 2008, *Phys. Rev.Lett.* **100**, 237601.  
El-Said A S, et al. 2012 *Phys. Rev.Lett.* **109**, 117602.
- [3] Lemell C, et al. 2007, *Solid-State Electron.* **51**, 1398.
- [4] Heller R, et al. 2008, *Phys. Rev.Lett.* **101**, 096102.
- [5] Ritter R, et al. 2012, *EPL* **97**, 13001.
- [6] Turchanin A and Götzhäuser A 2012, *Prog. Surf. Sci.* **87**, 108.
- [7] Wilhelm R A, et al. 2014, *Phys. Rev.Lett.* **112**, 153201.
- [8] Ritter R, et al. 2013, *Appl. Phys. Lett.* **102**, 063112.

# GUIDED TRANSMISSION OF IONS THROUGH NANOCAPILLARIES: VARIATIONS IN DISCHARGING DYNAMICS

P. Herczku<sup>1</sup>, B. Sulik<sup>1</sup>, Z. Juhász<sup>1</sup>, S. T. S. Kovács<sup>1,2</sup>, R. Rácz<sup>1</sup>, S. Biri<sup>1</sup> and N. Stolterfoht<sup>3</sup>

<sup>1</sup>*Institute for Nuclear Research (ATOMKI), Bem tér, 18/c, H-4026 Debrecen, Hungary*

<sup>2</sup>*Dept. of Experimental Physics, University of Debrecen, Egyetem tér 1, H-4032 Debrecen, Hungary*

<sup>3</sup>*Helmholtzzentrum für Materialien und Energie, 14109 Berlin, Germany*

E-mail: juhasz.zoltan@atomki.mta.hu

We measured the transmission of 3-keV  $^{22}\text{Ne}^{7+}$  ions through nanocapillaries with diameter of 200 nm in polyethylene terephthalate foils of 12  $\mu\text{m}$  thickness. After charging up of the capillaries and developing stable transmission the ion beam was switched off and on for short periods for time to time in order to probe the depletion of charges from the capillaries. The transmission decreased following a non-exponential decay curve, indicating a nonlinear conductivity. The experiment was repeated later. Surprisingly, different non-exponential decay curves were measured. After, we tested whether contamination of water vapour is the cause for the differences. We did not find such an effect but we observed that the changes are due to the effects of previous ion irradiations.

## 1. Introduction

Guiding of keV-energy ions through tilted arrays of nanometer sized capillaries attracted significant interest since 2002 [1-4]. This phenomenon is governed by a self-organizing deposition of charges developing an electrostatic field inside the capillaries, which deflects later coming ions to the exit.

Most of the experiment showed that after some time a stable transmission of ions develops. Though the basic principle is well understood, there are many open questions concerning the details of the phenomenon. The mechanism of the charge migration at the inner surface of capillary is one of the most important details, which determines the dynamics of the ion-transmission. It can be effectively studied by measuring the decrease of the transmission as a function of the discharging time, i.e., the time without ion beam. This can be measured by short beam pulses, which are strong enough to accurately sample the transmission, but practically do not charge up the capillary walls.

The first experiments showed that the discharging dynamics are much slower than the charging up dynamics, while in case of linear conductivity one can expect similar characteristic times [1,2]. Therefore a non-linear conductivity model for charge migration was proposed [3]. Alternatively, these observations were attributed to different characteristic times for charge migration on the surface and in the bulk [4]. In these models the decrease of the transmission follows a non-exponential decay curve, which is revealed only in a long time scale of several hours. Our experimental apparatus allowed us to measure long time discharge dynamics without significant re-charge effect of the probing beam pulses.

## 2. Experimental details

The experiments were carried out at the beamline of Electron Cyclotron Resonance Ion Source (ECRIS) of Atomki, Debrecen. The 3-keV  $^{22}\text{Ne}^{7+}$  beam was collimated to 0.5 mm in diameter before entering to the vacuum chamber. The background pressure was less than  $1 \times 10^{-6}$  mbar. The target sample was a polyethylene terephthalate (PET) foil with straight capillaries of 200 nm diameter and 12  $\mu\text{m}$  length. The areal capillary density was about  $1.2 \times 10^8/\text{cm}^2$ . The front and back side of the foil were covered by golden layers, which were grounded in order to ensure evacuation of charges.

We collected two-dimensional profiles of the transmitted particles with a position sensitive detector. In front of the detector an electric field was applied in order to separate the different charge states in the transmitted beam. In the charging up experiments, frames were collected for 9 s which were followed by 1 s breaks until the transmission reached nearly an equilibrium state. Right after this, the

charging down experiments were performed. Ideally one should apply infinitely short pulses in order to avoid the charging up of the inner capillary wall again. Therefore finite pulses of the ion beam as short as possible were directed to the sample and the transmission yield was measured in order to test the status of accumulated charges in the capillaries. Three of the pulses of 2 s duration followed closely each other with breaks of 1 s in order to test re-charging effects. Breaks between the groups of three short pulses were increasing in time. In order to minimize the re-charging of the capillary walls we synchronized the beam with the measuring periods. The beam was introduced to the sample during the 2-s measuring periods only. The obtained transmission values in the three consecutive frames were checked and it was found that they are matching within the experimental uncertainties. Thus we could establish that during the charging down experiments the walls of the capillaries were not significantly charged up again.

### 3. Results and conclusions

We measured and compared the percentage of ions transmitted through the capillaries as function of deposited charge on the sample. After charging up, the discharging dynamics was measured for each tilt angle and sample position. The first set of measurements was performed in May 2012. A strong nonlinearity of the discharging process was observed i.e. the transmission versus discharge time did not follow an exponential decay law. This indicates a nonlinear conductivity governs the evacuation of charges. The sample was relatively fresh. Earlier it was used before 2005 only and the results are found in ref. [2]. In the subsequent time the sample was stored in air. Presumably, this period was sufficiently long for the sample material to relax from the effects of previously impinging charges.

Next, in January 2014, the experiment was repeated in order to check the reproducibility. The sample was placed in the setup from air, again, just before the experiment. This time, we observed also non-exponential discharge curves but, surprisingly, they were less steep. It was proposed that the reason for this might be an adsorbed water layer on the surface of capillaries, which changes surface conductivity. This layer may get thinner with time since the sample spends more and more time in vacuum. The vacuum level in the chamber was  $8\text{--}10 \times 10^{-7}$  mbar slowly decreasing with time. So the experiment was performed again in May 2014. Before we mounted a little water reservoir on the chamber through a needle valve. After reproducing the measurement with the same conditions, the chamber was flushed with water vapour for few minutes with the sample in. Then we repeated the measurement again in order to see the effects of the presumably deposited water layer.

The comparison of the results from the different sets of measurements is shown in Fig. 1 for charging up and in Fig. 2 for discharging dynamics for tilt angle of  $3.3^\circ$ . From the second set of measurement, we used the same position on the sample. We expected that the discharge curves would decay rapidly after introducing the water vapour but no such effect occurred. Instead the steepness of the curves decreased at each run regardless of the water vapour flushes. This indicates that the previous charging by the ion beam changes the conductivity of the material. The insulating capability increases with each charging. This effect is permanent with a time scale of several years. Note that the measured spot on the sample in set II was already used in the set I two years before. Supporting the idea of the effects previous irradiation, we measured a steep decay in set III when using a fresh place.

With higher resistance, the capillaries can accumulate more charge. This explains the increasing transmission ratio at equilibrium of charging up dynamics in each subsequent set (see Fig. 1). But there are no other significant differences in the curves. Their shapes are quite similar. In the shape of discharge curves, however, there are significant differences. This shows that measuring of the discharging process is a sensitive tool to study the insulating properties of the samples and their changes due to ion irradiation. More analysis will be given at the conference.

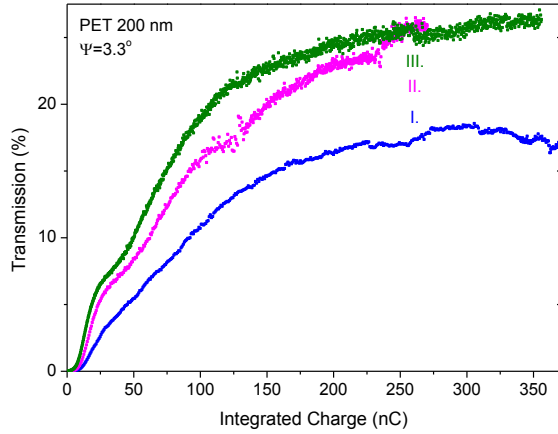


Fig. 1. The transmitted fraction of ions during charge up process as function of deposited charge on the sample. The different sets of measurements : I. May 2012, II. January 2014, III. May 2014 are indicated on the figure. Only the first charging up dynamics at each set is shown, so the samples are uncharged at the beginning.

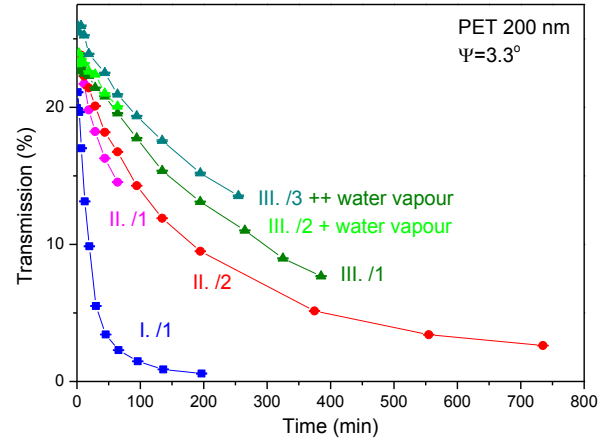


Fig. 2. The transmitted fraction of ions during discharging process as function of time. The different sets (roman numerals) of measurements and the different runs (arabic numerals) at each sets are indicated in the figure. Before the second run of set III water vapour was introduced in the chamber with pressure of  $10^{-5}$  mbar for 5 minutes and  $10^{-6}$  mbar for 10 minutes. Before the run III/3 water vapour of  $10^{-4}$  mbar was introduced for 1 hour.

#### 4. Acknowledgement

This work was supported by the Hungarian OTKA Grant no. K83886, as well as by the TÁMOP-4.2.2/B-10/1-2010-0024 and the TÁMOP 4.2.2.A-11/1/KONV-2012-0036 projects, co-financed by the EU and the European Social Fund.

#### 5. References

- [1] Stolterfoht N, et al 2002 *Phys. Rev. Lett.* **88** 133201.
- [2] Stolterfoht N, et al 2005 *Surface & Coatings Technology* **196** 389.
- [3] Stolterfoht N 2013 *Phys. Rev. A* **87** 012902.
- [4] Schiessl K, et al 2005 *Phys. Rev. A* **72** 062902.

## PHOTOABSORPTION AND PHOTOIONIZATION WITH TWISTED LIGHT

S. Fritzsche<sup>1,2</sup>, O. Matula<sup>3</sup>, A. G. Hayrapetyan<sup>3</sup>, A. Surzhykov<sup>1</sup>

<sup>1</sup>*Helmholtz-Institut Jena, D-07743 Jena, Germany*

<sup>2</sup>*Theoretisch-Physikalisches Institut, Friedrich-Schiller-Universität Jena, D-07743 Jena, Germany*

<sup>3</sup>*Physikalisches Institut, Ruprechts-Karls-Universität Heidelberg, D-69126 Heidelberg, Germany*  
E-mail: s.fritzsche@gsi.de

For many decades, atomic photoabsorption and photoionization processes have been studied with plane-wave light from lasers or synchrotron radiation. These investigations revealed much information about the electron-photon interaction if each photon just carries a spin-angular momentum. However, beams of light (as well as electrons) may possess also a well-defined orbital angular momentum along its propagation direction and, hence, some spiral wave front. It is shown in this talk that the angular momentum provides not only an additional degree of freedom for the photons but also affect the photoabsorption, photoionization as well photon scattering of atoms. Sizeable effects were found especially for the alignment parameters of residual ions as well as for the angular distribution of the emitted photons and electrons, even if the results are averaged over the spatial intensity distribution of the beams.

In this talk, details of these theoretical investigations are presented and discussed. Calculations were performed especially for atomic hydrogen und selected hydrogenic ions [1-2].

[1] Matula O, Hayrapetyan A G, Serbo V G, Surzhykov A and Fritzsche S 2013 *J. Phys. B* **46** 205002.

[2] Matula O, Hayrapetyan A G, Serbo V G, Surzhykov A and Fritzsche S 2014 *New J. Phys.* *in print*.



# PHOTOIONIZATION OF FULLERENES AND OTHER NANOCARBON SYSTEMS

Alexey Verkhovtsev<sup>1,2</sup>, Andrei Korol<sup>2,3</sup>, Andrey Solov'yov<sup>2,3</sup>

<sup>1</sup>Frankfurt Institute for Advanced Studies, Frankfurt am Main, Germany

<sup>2</sup>MBN Research Center, Frankfurt am Main, Germany

<sup>3</sup>Physics Department, Goethe University, Frankfurt am Main, Germany

E-mail: verkhovtsev@fias.uni-frankfurt.de

We present the results of investigation of electron excitations in various carbon nanosystems (highly-symmetric fullerenes, carbon buckyonions, and PAHs) in the process of photoionization. The calculations are performed within the *ab initio* TDDFT framework and the model approach based on the plasmon resonance approximation. By comparing the results of the *ab initio*- and model-based calculations, we elucidate the contributions of classical and quantum phenomena appearing in the ionization process of the carbon nanosystems. In particular, we map the well-resolved features of the photoionization spectrum of  $C_{60}$  to different types of single-particle and collective electron excitations having the different physical nature.

Photoionization of fullerenes as well as other atomic clusters and nanoscale systems involves a number of prominent phenomena, which have been studied by means of various theoretical methods. Being by its nature a quantum phenomenon, the photoionization process can be described within the *ab initio* framework based on the time-dependent density functional theory (TDDFT) [1, 2]. However, it is well established that photoionization of nanoscale carbon systems, fullerenes in particular, as well as various metallic clusters and nanoparticles, takes place through collective excitations of delocalized valence electrons, called plasmons, induced by an external electric field. The plasmon excitations correspond to oscillations of the electron density with respect to the positively charged ions. Such collective excitations, appearing in many-electron systems, are well known in classical electrodynamics and are described in classical physics terms (Refs. [3, 4] and references therein).

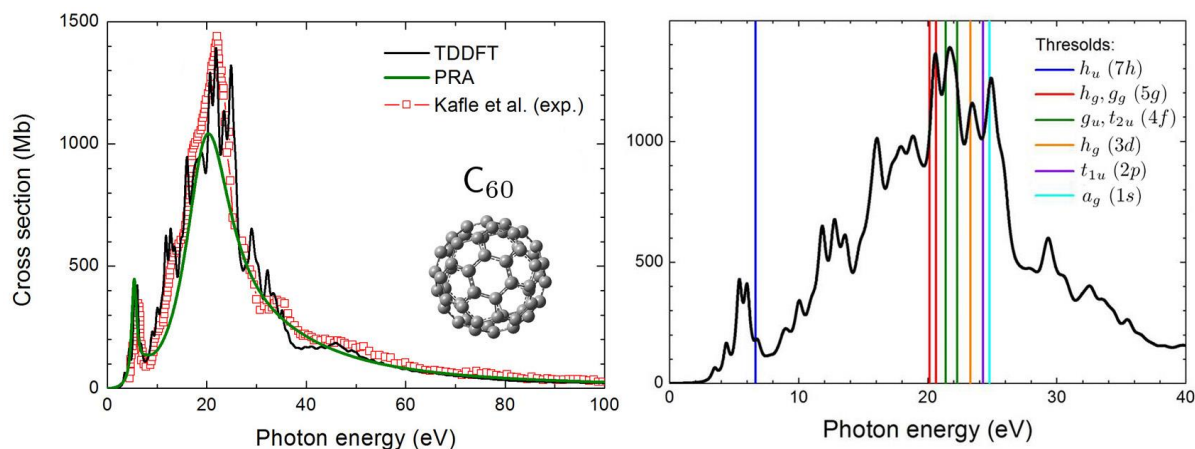


Figure 1. Left panel: The photoabsorption cross section of  $C_{60}$  calculated within the TDDFT method (thin solid curve) and the plasmon resonance approximation (thick solid curve). Theoretical curves are compared to the experimental data compiled by Kafle et al. [6]; Right panel: Ionization thresholds of the HOMO ( $h_u$ ) as well as of a number of innermost valence orbitals of  $C_{60}$ .

Considering photoionization of the  $C_{60}$  fullerene as a case study, we elucidate the contributions of various classical and quantum physics phenomena appearing in this process. Comparing the TDDFT

results with those based on the plasmon resonance approximation (Refs. [3-5] and references therein), we map the well-resolved features of the photoabsorption spectrum of  $C_{60}$  to single-particle and collective excitations which have a different physical nature [7]. It is demonstrated that the peculiarities arising in the photoionization spectrum of  $C_{60}$  atop the dominating plasmon excitations have the quantum origin. In particular, we demonstrate that a series of individual peaks can be assigned either to the optically allowed discrete transitions or to the ionization of particular molecular orbitals of the system (see Figure 1).

A similar method, based on the comparative analysis of the *ab initio* and model-based approaches, is utilized to study the photoionization spectra of other carbon-based nanoscale systems, such as polycyclic aromatic hydrocarbons (PAHs) [8] and carbon buckyonions (see Figure 2). In particular, the TDDFT-based calculations of the photoionization spectrum of the  $C_{60}@C_{240}$  system revealed the absence of strong plasmonic couplings between individual fullerenes which were proposed earlier [9].

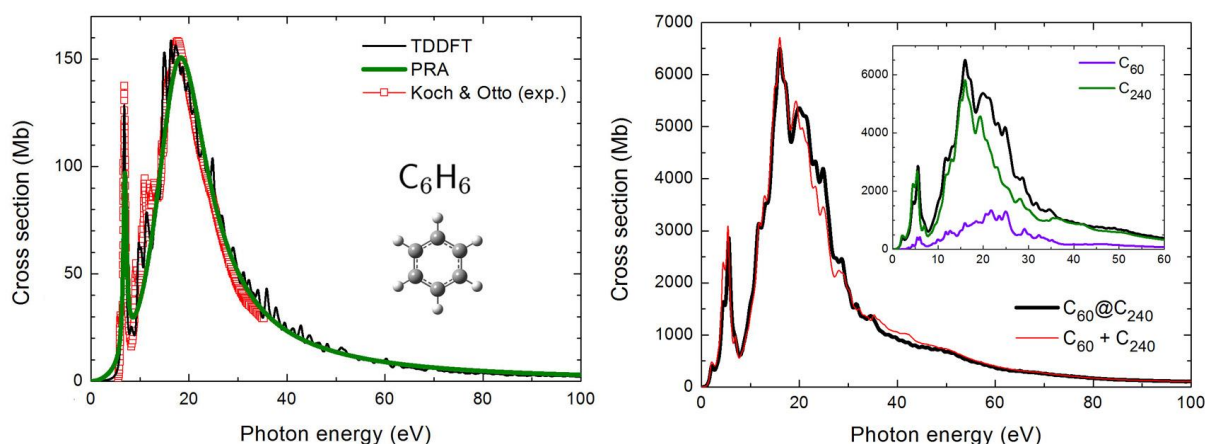


Figure 2. Left panel: The photoabsorption cross section of the benzene molecule calculated within the TDDFT method (thin solid curve) and the plasmon resonance approximation (thick solid curve). Theoretical curves are compared to the experimental data [10]; Right panel: The photoabsorption cross section of the  $C_{60}@C_{240}$  buckyonion (thick solid curve) and the sum (thin curve) of the spectra of isolated  $C_{60}$  and  $C_{240}$  (shown in the inset) calculated within the TDDFT method.

The results of the *ab initio* and model-based calculations are found to be in close mutual agreement and correspond well to the available experimental results on photoionization of fullerenes and PAHs (Figures 1 and 2). The developed methodology is proved to be an efficient and reliable tool for the calculation and analysis of ionization spectra of complex molecular systems.

## References

- [1] Runge E and Gross E K U 1984 *Phys. Rev. Lett.* **52** 997
- [2] Malcioglu O B, Gebauer R, Rocca D and Baroni S 2011 *Comp. Phys. Commun.* **182** 1744
- [3] Connerade J-P and Solov'yov A V 2002 *Phys. Rev. A* **66** 013207
- [4] Solov'yov A V 2005 *Int. J. Mod. Phys. B* **19** 4143
- [5] Verkhovtsev A V, Korol A V and Solov'yov A V 2012 *Eur. Phys. J. D* **66** 253
- [6] Kafle B P *et al* 2008 *J. Phys. Soc. Jpn.* **77** 014302
- [7] Verkhovtsev A V, Korol A V and Solov'yov A V 2013 *Phys. Rev. A* **88** 043201
- [8] Verkhovtsev A V, Korol A V and Solov'yov A V 2014 *J. Phys.: Conf. Ser.* **490** 012159
- [9] McCune M A, De R, Madjet M E, Chakraborty H S and Manson S T 2011 *J. Phys. B: At. Mol. Opt. Phys.* **44** 241002
- [10] Koch E E and Otto A 1972 *Chem. Phys. Lett.* **12** 476

# SPATIAL INTERFERENCE EFFECTS DURING THE IONIZATION OF ATOMS BY FEW-CYCLE LASER PULSES

Borbély Sándor<sup>1</sup>, Tóth Attila<sup>1</sup>, Tőkési Károly<sup>2</sup>, Nagy Ladislau<sup>1</sup>

<sup>1</sup> Faculty of Physics, Babes-Bolyai University, Kogalniceanu Street No. 1, 400084 Cluj, Romania

<sup>2</sup> Institute for Nuclear Research of the Hungarian Academy of Sciences (ATOMKI), P.O. BOX 51, H-4001 Debrecen, Hungary

E-mail: sandor.borbely@phys.ubbcluj.ro

During the ionization of atoms by few-cycle laser pulses beside the dominant ionization secondary processes with significant impact on the final momentum distribution also occur. These are the result of interference between electronic wave packets following different spatial and temporal paths. In the present work we focus our attention on the interference between electronic wave packets emitted at the same time, but following different spatial paths (**spatial interference**). By using *ab initio* quantum mechanical and classical trajectory Monte Carlo (CTMC) calculations we have investigated how the shape of the spatial interference pattern is influenced by the laser pulse parameters, and by the structure of the target atom.

## 1. Introduction and Theory

With the development of laser generation techniques, few-cycle laser pulses with various photon frequencies are available [1]. At high field intensities, when such a laser pulse interacts with atomic systems, the dominant process is the ionization (above-threshold, tunnelling, or over-the-barrier ionization, depending on the Keldysh parameter [2]). Beside the dominant ionization, secondary processes also occur, which have a significant impact on the final momentum distribution of the electrons. As discussed in detail by Bian et al. [3], these are the result of interference between electronic wave packets following different paths. From the numerous possible scenarios [3], only two have a significant impact (measurable in experiments) on the final momentum distribution of the free electrons. In the first scenario, electronic wave packets emitted at different parts of the laser pulse (i.e., at different time moments) interfere, leading to a fringe structure in the electron energy spectrum [4], consisting of circular interference maxima and minima, which are perpendicular to the laser polarization. In the second scenario, electronic wave packets emitted at the same time (i.e., during the same quarter-pulse cycle) follow different paths, accumulating different final phases, leading to a radial fringe structure in the electron spectra [3,5]. In a simplistic picture [5], the radial fringe structure is a result of the interference between the direct (i.e., unscattered) and the scattered wave packets, where the direct wave packet can be considered as a reference while the scattered wave packet as a signal wave. In this picture, the interference fringe structure can be interpreted as the holographic mapping (HM) of the target atom's or molecule's state [5]. Since in the HM pattern the interference extrema are strongly influenced by the short-range potential encoding the structure of the target atom or molecule, the HM is a potentially powerful tool to investigate the internal structure of atoms and molecules. In our recent works [6,7] we have investigated theoretically the influence of the laser pulse parameters on the shape of the HM interference pattern. In agreement with the experimental findings of Huismans et. al [8] we found that for a fixed atomic target the density of HM interference pattern is mainly determined by the  $z_0$  parameter. This  $z_0$  parameter measures the maximum distance from the core reached by the electronic wave packet before it is redirected toward the parent ion by the oscillating laser field. The value of  $z_0$  is directly influenced by the parameters of the laser field:  $z_0$  can be increased by increasing the intensity, or the period of the laser field [6].

The above presented investigations were performed for the ionization of H targets by using *ab initio* quantum mechanical calculations. These calculations are based on the numerical solution of the time-dependent Schrödinger equation in the framework of the time-dependent close-coupling (TDCC) model [9]. In the TDCC approach, during the spatial discretization first the time-dependent wave function is expanded into terms of spherical harmonics

$$\Psi(\vec{r}, t) = \sum_{l,m} \frac{R_{lm}(r)}{r} Y_{lm}(\Omega_r), \quad (1)$$

while the remaining radial wave function is represented on a finite-element discrete variable representation (FEDVR) grid [10]. The time-dependent radial wave functions were propagated in time using the short iterative Lanczos [11] method according to the TDCC equations (for details see [6]). In the present work we have extended our TDCC model from H atom to noble gas atoms, where only a single active electron was considered, and the screening of all the other electrons was included in the effective Coulomb potential [12] acting on the active electron.

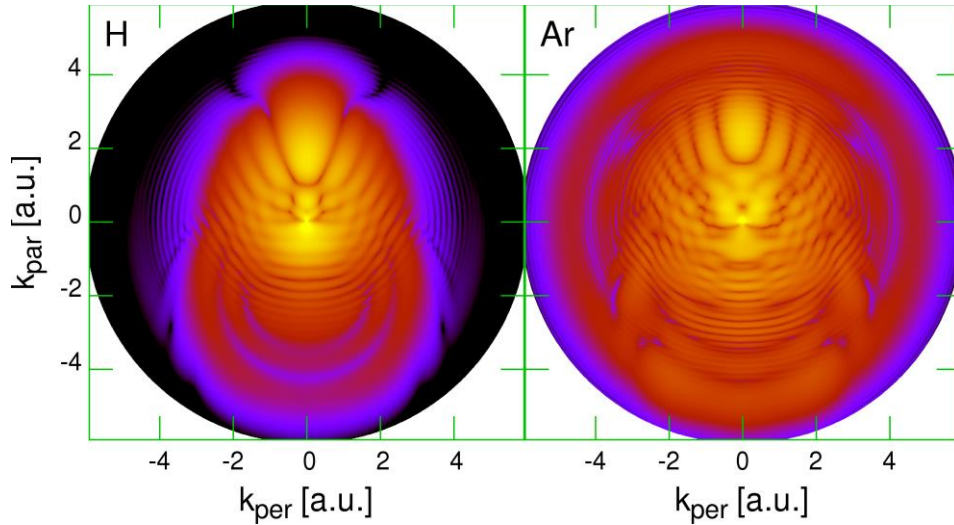


Fig. 1. The distribution of continuum electrons as a function of momentum components perpendicular and parallel to the laser field polarization for the ionization of H and Ar atom. The field intensity was set to  $E_0=1$  a.u. On both figures the HM interference pattern is clearly visible as radial maxima and minima.

## 2. Results and Conclusions

Using our extended TDCC model we have performed calculations for the ionization of H, He, Ne, Ar atoms by two-cycle laser pulse with photon energy  $\omega_0=0.4445$  a.u. at various field intensities. On Figure 1. we show a typical set of results for the ionization of H and Ar atoms where the interference pattern is clearly visible in the form of radial maxima and minima. Since the values of the ionization potentials of the H and Ar (0.5 a.u. and 0.579 a.u.) targets are close, the structures of the nascent free electronic wave packet for both targets are very similar. However, in the recollision phase, the returning electronic wave packet in the case of the Ar target meets a much deeper Coulomb potential well. This translates to the accumulation of a more rapidly varying phase for the scattered quantum path, and inherently to the formation of a denser HM pattern for Ar atoms observable on Figure 1.

Due to the recent theoretical and experimental works [5,6,7,8] we found how the laser field influences the formation of the HM pattern, and we also know that the shape of the HM pattern is significantly influenced by the atomic species of the target. This illustrates the potential of the HM technique to become a useful tool for atomic structure investigation.

This work was supported by a grant of the Romanian National Authority for Scientific Research, CNCS UEFISCDI Project No. PN-II-ID-PCE-2011-3-0192, and partially the Hungarian Scientific Research Fund OTKA No. NN 103279 and K103917, and by the COST Action CM1204 (XLIC)

### 3. References

- [1] A. Baltuska, T. Udem, M. Uiberacker, M. Hentschel, E. Goulielmakis, C. Gohle, R. Holzwarth, V. S. Yakovlev, A. Scrinzi, T. W. Hansch, and F. Krausz 2003 *Nature (London)* 421, 611.
- [2] L. V. Keldysh 1965 *Sov. Phys. JETP* 20, 1307.
- [3] X.-B. Bian, Y. Huismans, O. Smirnova, K.-J. Yuan, M. J. J. Vrakking, and A. D. Bandrauk 2011 *Phys. Rev. A* 84, 043420.
- [4] F. Lindner, M. G. Schatzel, H. Walther, A. Baltuska, E. Goulielmakis, F. Krausz, D. B. Milosevic, D. Bauer, W. Becker, and G. G. Paulus 2005 *Phys. Rev. Lett.* 95, 040401.
- [5] Y. Huismans, A. Rouzee, A. Gijsbertsen, J. H. Jungmann, A. S. Smolkowska, P. S. W. M. Logman, F. Lépine, S. Z. C. Cauchy, T. Marchenko, J. M. Bakker, G. Berden, B. Redlich, A. F. G. Van der Meer, H. G. Muller, W. Vermin, K. J. Schafer, M. Spanner, M. Y. Ivanov, O. Smirnova, D. Bauer, S. V. Popruzhenko, and M. J. J. Vrakking 2011 *Science* 331, 61.
- [6] S. Borbély, A. Tóth, K. Tökési, L. Nagy 2013 *Phys. Rev. A* 87, 013405.
- [7] S. Borbély, A. Tóth, K. Tökési, L. Nagy 2013 *PHYSICA SCRIPTA* T156, 014066
- [8] Y. Huismans, A. Gijsbertsen, A. S. Smolkowska, J. H. Jungmann, A. Rouzee, P.S.W.M. Logman, F. Lépine, C. Cauchy, S. Zamith, T. Marchenko, J.M. Bakker, G. Berden, B. Redlich, A.F.G. van der Meer, M. Ivanov, T.M. Yu. and Yan, D. Bauer, O. Smirnova, M.J.J. Vrakking 2012 *Phys. Rev. Lett.* 109, 013002.
- [9] J. Colgan and M. S. Pindzola 2002 *Phys. Rev. Lett.* 88, 173002.
- [10] B. I. Schneider and L. A. Collins 2005 *J. Non-Cryst. Solids* 351, 1551.
- [11] Lanczos C 1950 *Journal of Research of the National Bureau of Standards* 45 255
- [12] X. M. Tong and C. D. Lin 2005 *J. Phys. B: At. Mol. Opt. Phys.* 38 2593

## TIME DEPENDENCE OF INTERATOMIC COULOMBIC DECAY

F. Trinter

*Goethe-Universität, Max-von-Laue-Str. 1, 60438 Frankfurt am Main, Germany*

E-mail: trinter@atom.uni-frankfurt.de

We will discuss experimental studies of Interatomic Coulombic Decay (ICD) in van der Waals dimers of rare gas atoms and small molecules using the Cold Target Recoil Ion Momentum Spectroscopy (COLTRIMS) technique. The talk will cover ICD after resonant Auger excitation [1] and two studies unveiling the time dependence of ICD in the energy [2] and in the time domain [3]. A new technique to make ultrafast movies without the use of short pulses will be discussed.

### References

- [1] Trinter F et al. 2014 *Nature* **505**, 664.
- [2] Trinter F et al. 2013 *Phys. Rev. Lett.* **111**, 233004.
- [3] Trinter F et al. 2013 *Phys. Rev. Lett.* **111**, 093401.

# SUBCYCLE INTERFERENCE IN ATOMIC IONIZATION BY SCULPTED LASER PULSES

Diego G. Arbó<sup>1</sup>, Stefan Nagele<sup>2</sup>, Xinhua Xie<sup>3</sup>, Markus Kitzler<sup>3</sup>, and Joachim Burgdörfer<sup>2</sup>

<sup>1</sup>*Institute for Astronomy and Space Physics, IAFE (Conicet-UBA), Buenos Aires, Argentina*

<sup>2</sup>*Institute of Theoretical Physics, Vienna University of Technology, Vienna, Austria, EU*

<sup>3</sup>*Photonic Institute, Vienna University of Technology, Vienna, Austria, EU*

E-mail: diego@iafe.uba.ar

We present a study about interference effects resulting from the interaction of an isolated atom with intense two-color laser pulses, where the second frequency doubles the fundamental. With the help of a semiclassical model, we identify the interplay between the *intra*- and *intercycle* interferences of electron trajectories in multicycle two-color laser photoionization. We explore the effect of the Coulomb potential of the remaining core on the electron yield, especially on the resulting interference pattern. Our theory facilitates the understanding of attosecond strong-field electron-wavepacket interferometry experiments with sub-10-attosecond precision [1].

## 1. Introduction

Photoionization in the tunnelling regime is a highly nonlinear quantum-mechanical phenomenon which predominantly occurs around the maxima of the absolute value of the electric field within each optical cycle. Photoelectrons can be classified as *direct* or *rescattered* electrons according to the three-step model [2]. In few-cycle pulses, temporal double-slit interference patterns were experimentally measured [3,4] and theoretically studied [5]. Direct electron emission in multi-cycle photoelectron spectra can be identified as a diffraction pattern at a time grating composed of *intracycle* or *subcycle* and *intercycle* interferences [6,7].

Two-color pulses with commensurate frequencies, usually consisting of a fundamental component and one of its low harmonics, have been used to sculpt the laser field shape and to control interference fringes in the electron momentum spectra [1,8]. Coherent phase control allows to investigate the physical processes involved in atomic ionization as a function of the relative phase  $\varphi$  of the two frequency components of the field [9]. Many advances in theory have been attained by neglecting the potential of the ionic core, which results in the strong field approximation. However, accurate results should include the effect of the atomic potential on the emitted electron yield.

We analyze the validity of the factorization of the electron emission distribution in terms of a time grating in the presence of long-range Coulomb forces for the case of atomic ionization by two-color lasers emphasizing the role of  $\varphi$  in the visibility of the *intracycle* interference pattern. We inspect how the Coulomb potential affects both the *intra*- and *intercycle* interference stemming from the superposition of wavepackets released at different emission times.

## 2. Theory

The evolution of the electronic quantum state of an atom in the single-active electron approximation subject to a linearly polarized strong laser pulse is governed by the time-dependent Schrödinger equation for the Hamiltonian

$$H = \frac{\mathbf{p}^2}{2} + V(r) + zF(t), \quad (1)$$

where  $V(r)$  is the atomic potential,  $\mathbf{p}$  is the electron momentum, and  $r$  the distance from the core to the electron. As the result of the interaction, an electron initially bound to the core with energy  $-I_p$ , where  $I_p$  is the ionization potential, is emitted with final momentum  $\mathbf{k}$  and energy  $E = k^2 / 2$ .

From the transition matrix, the electron momentum distribution can be calculated as

$$\frac{dP}{dk} = |T_{if}|^2, \quad (2)$$

where  $T_{if}$  is the T-matrix element of the transition.

Using a semiclassical theory along the lines of the so-called “simple man’s model” (SMM), leads to a transition amplitude to the continuum state of the form [7,10]

$$T_{if}^{\mathbf{r}}(k) = -\sum_{i=1}^M G(t_r^{(i)}, \mathbf{r}, k) \exp[iS(t_r^{(i)})], \quad (3)$$

where  $M$  is the number of electron trajectories born at ionization times  $t_r^{(i)}$  which reach a given final momentum  $\mathbf{r}$ , and  $G(t_r^{(i)}, \mathbf{r}, k)$  is the ionization amplitude. In Eq. (3),  $S$  is given by the Volkov action [11], where the time dependence of the initial state is included. The release times  $t_r^{(i)}$  can be approximated within the SMM as  $k_z + A(t_r^{(i)}) = 0$ .

We use a two-color linearly polarized electric field, where one frequency doubles the other

$$F(t) = f(t) [\cos(\omega t) + \cos(2\omega t + \varphi)]. \quad (4)$$

In Eq. (4)  $\omega$  is the fundamental laser frequency,  $\varphi$  is the relative phase between the two frequency components, and  $f(t)$  is the envelope function of the sculpted laser pulse. In general, two solutions per optical cycle contribute: the early and late release times. Within the SMM, we consider a flat top pulse, i.e.,  $f(t) = F_0$  in the main region of the pulse consisting of  $N$  optical cycles and neglect the ionization probability during the adiabatic switch on and off.

The sum over interfering trajectories [Eq. (3)] can be decomposed into those associated with two release times within the same cycle and those associated with release times at different cycles [7,8]. Accordingly, the transition probability of Eq. (2) can be written as

$$\frac{dP}{dk} = 4\Gamma(k) F(k) B(k), \quad (5)$$

where

$$\begin{aligned} \Gamma(k) &= \left[ \left( G(t_r^{(1)}, \mathbf{r}, k) + G(t_r^{(2)}, \mathbf{r}, k) \right) / 2 \right]^2, \\ F(k) &= \cos^2\left(\frac{\Delta S}{2}\right) + \left( \frac{G(t_r^{(1)}, \mathbf{r}, k) - G(t_r^{(2)}, \mathbf{r}, k)}{G(t_r^{(1)}, \mathbf{r}, k) + G(t_r^{(2)}, \mathbf{r}, k)} \right)^2 \sin^2\left(\frac{\Delta S}{2}\right), \\ B(k) &= \left[ \frac{\sin(N\varphi/2)}{\sin(\varphi/2)} \right]^2, \end{aligned} \quad (6)$$

which indicates that the interference can be factorized in two contributions: *Intracycle* interference stemming from a pair of trajectories within the same optical cycle governed by  $F(k)$ , and *intercycle* interference stemming from trajectories at different optical cycles resulting in the well-known ATI peaks given by  $B(k)$ . For the case of a laser pulse with  $\varphi = \pi/2$ ,  $G(t_r^{(1)}, \mathbf{r}, k) = G(t_r^{(2)}, \mathbf{r}, k)$ , and the *intracycle* interference factor reads  $F(k) = \cos^2(\Delta S/2)$ , in coincidence with the one-color case [7].

### 3. Results

Calculations for a hydrogen atom initially in its ground state within the SMM [Eq. (3)] are compared to the strong field approximation (SFA) [12], the Coulomb-Volkov approximation [13], and the numerical results of the essentially exact time-dependent Schrödinger equation (TDSE) [14]. In order to calculate the electron yield within the SFA, CVA, and TDSE, we consider a finite pulse which includes an envelope  $f(t)$  with a two-cycle square-sine ramp-on and ramp-off to ensure that the ionization times in the flat top region are the same as for the pulse with adiabatic switch-on and -off.



By comparing the SFA and CVA, we can directly probe the effect of the Coulomb potential on the interference pattern. When the nuclear charge  $Z_T$  of the final channel is varied, the Coulomb phase can be arbitrarily adjusted between zero (corresponding to the SFA) and its full value (corresponding to the CVA). We calculate the photoelectron spectrum into a cone of  $10^\circ$  in the backward direction for a laser field with an intensity of  $10^{14}$  W/cm<sup>2</sup> 800 nm, and for  $\varphi = \pi/2$ . In Fig. 1 we observe a monotonic shift of the intracycle envelope  $F(k)$  as the strength of the Coulomb potential parameterized by  $Z_T$  increases, clearly illustrating the effect of the Coulomb tail on the form factor  $F(k)$ . On the other hand, no significant changes of the multiphoton positions described by  $B(k)$  are observed.

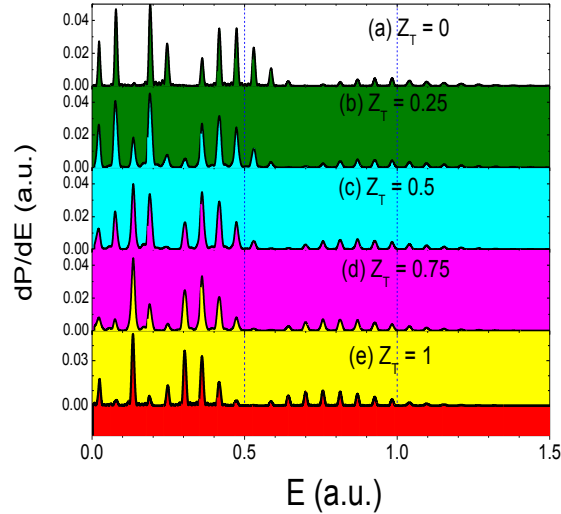


Fig. 1. CVA photoelectron spectra in a cone of  $10^\circ$  in the backward direction for  $Z_T=0, 0.25, 0.5, 0.75$ , and 1 for an eight-cycle pulse with an intensity of  $10^{14}$  W/cm<sup>2</sup>, a wavelength of 800 nm, and  $\varphi = \pi/2$ .

We also calculate the doubly differential momentum distributions as a function of the longitudinal  $k_z$  and transversal  $k_\perp$  momenta. Fig. 2 shows the distributions for the two-color field with same parameters as Fig. 1 for  $\varphi = \pi/2$ . The lower halves of Fig. 2a shows the SMM results corresponding to a four-cycle pulse, whereas the upper halves exhibit the *intracycle* pattern obtained by setting  $B(k) = 1$  in Eq. (5). The *intracycle* pattern in the upper half of Fig. 2a for  $\varphi = \pi/2$  clearly modulates the *intercycle* rings shown in the lower panel of Fig. 2a. The SMM longitudinal momentum is symmetrical for  $\varphi = 0$  (not shown), in contrast to Fig. 2a for  $\varphi = \pi/2$  which shows asymmetric longitudinal momenta, constrained to the classical limits of  $k_z$ . Quantum calculations (SFA, CVA, and TDSE) result in more elongated momentum distributions beyond the classical boundaries for the momenta. CVA distribution in Figs. 4d are slightly narrower in transversal direction than the SFA distributions in Figs. 4b due to Coulomb focusing. When we compare the CVA and SFA distributions for  $\varphi = \pi/2$ , we observe that the CVA *intracycle* fringes in Fig. 2d are a slightly shifted towards the origin with respect to the SFA ones in Fig. 2b. The TDSE distribution in Fig. 2d displays similar interference patterns as CVA, SFA, and SMM. Furthermore, the TDSE results for hydrogen in Fig. 5 (d) are very similar to Fig. 2 (f) in Ref. [1].

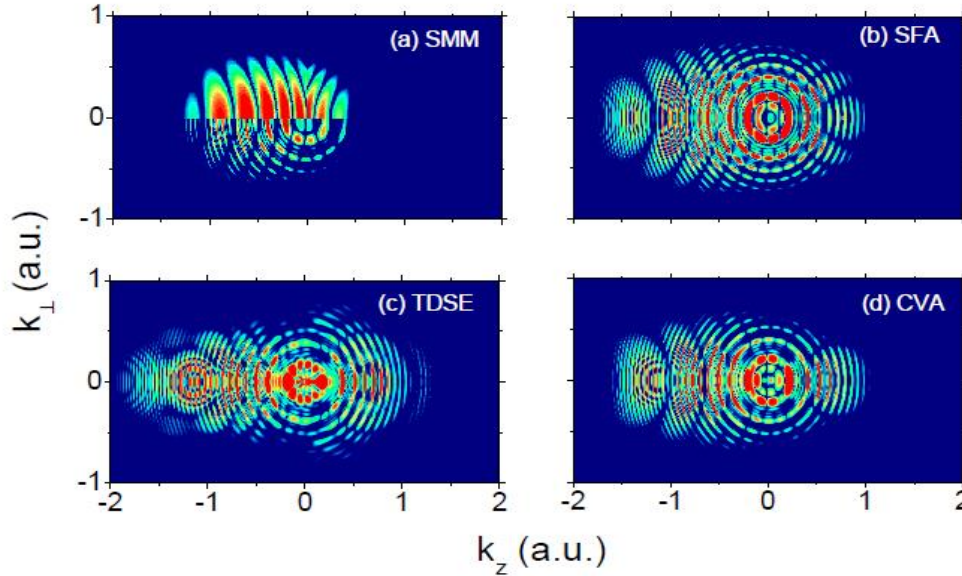


Fig. 2. Doubly differential momentum distribution. The laser parameters are the same of Fig. 1.

#### 4. Conclusions

We have demonstrated that the semiclassical analysis performed for two-color fields in terms of a time grating [8] remains valid when the Coulomb potential of the atomic core is considered. Approximating SFA and CVA calculations for ionization of an isolated atom by intense two-color laser pulses were tested against the solutions of the essentially exact TDSE. Coherent superposition of electron wave packets released within the same sculpted optical cycle are most clearly observed in TDSE calculations involving laser pulses with relative phase  $\varphi = \pi/2$ . The theory facilitates the understanding of attosecond strong-field electron interferometry experiments with sub-10-attosecond precision [1]. The dependence of the *intracycle* modulations on the long-range atomic Coulomb potential opens the possibility of imaging the core potential in the experimentally easily obtained direct electron yield.

#### 5. References

- [1] X. Xie *et al.*, Phys. Rev. Lett. **108**, 193004 (2012).
- [2] P.B. Corkum *et al.*, Opt. Lett. **19**, 1870 (2012).
- [3] R. Gopal *et al.*, Phys. Rev. Lett. **103**, 053001 (2009).
- [4] F. Lindner *et al.*, Phys. Rev. Lett. **95**, 040401 (2005).
- [5] D.G. Arbó *et al.*, Phys. Rev. A **74**, 063407 (2006).
- [6] S. Bivona *et al.*, Phys. Rev. A **75**, 063415 (2007); *ibid* **79**, 035403 (2009).
- [7] D.G. Arbó *et al.*, Phys. Rev. A **82**, 043426 (2010).
- [8] D.G. Arbó *et al.*, Phys. Rev. A **89**, 043414 (2014).
- [9] F. Ehlotzky, Phys. Rep. **345**, 175 (2001).
- [10] M Lewenstein *et al.*, Phys. Rev. A **51**, 1495 (1995); *ibid* **49**, 2117 (1994).
- [11] D.M. Volkov, Z. Phys. **94**, 250 (1935).
- [12] V. Keldysh, Zh. Eksp. Theo. Fiz. **47**, 1945 (1964) [Sov. Phys. JETP **20**, 1307 (1965)].
- [13] A. Basile *et al.*, Phys. Rev. A **37**, 1050 (1988).
- [14] X-M. Tong and S.I. Chu, Chem. Phys. **217**, 119 (1997).

## DYNAMICS OF BIMOLECULAR RECOMBINATION IN SYMMETRICAL CHANNELS

Vladimir M. Azriel, Lev Yu. Rusin

*Institute of Energy Problems of Chemical Physics, the Russian Academy of Sciences,*

*Leninski prospect 38, Bldg.2, Moscow 119334, Russia*

E-mail: Azriel\_Vladimir@mail.ru

Dynamics of a bimolecular recombination at simultaneous interaction of two singly-charged positive and two negative heavy ions is investigated by a method of quasiclassical trajectories on a potential energy surface which quantitatively describes the return process of collision-induced dissociation. Dependences of recombination probability on total collision energy of ions for two various sets of being formed molecules are received.

Quasiclassical trajectory simulation of dynamics of the collision-induced dissociation in symmetric systems CsCl + RbJ and CsJ + RbCl, which differ by mass ratio of colliding molecules, showed that excitation functions of channels of formation of four independent ions for both systems are described by qualitatively similar curves, however in all range of the counted collision energies the cross sections of dissociation for system CsJ + RbCl is slightly higher [1].

Similar calculations on the same potential energy surface of the return processes of a bimolecular recombination of four ions with the formation respectively two sets of stable molecules according to the following scheme



also show similar dependences of recombination probability on total kinetic energy of colliding ions (see figure 1). Thus the recombination probability for the channel of formation of molecules CsJ and RbCl for all values of collision energy appears a little less than probability of formation of the pair CsCl + RbJ.

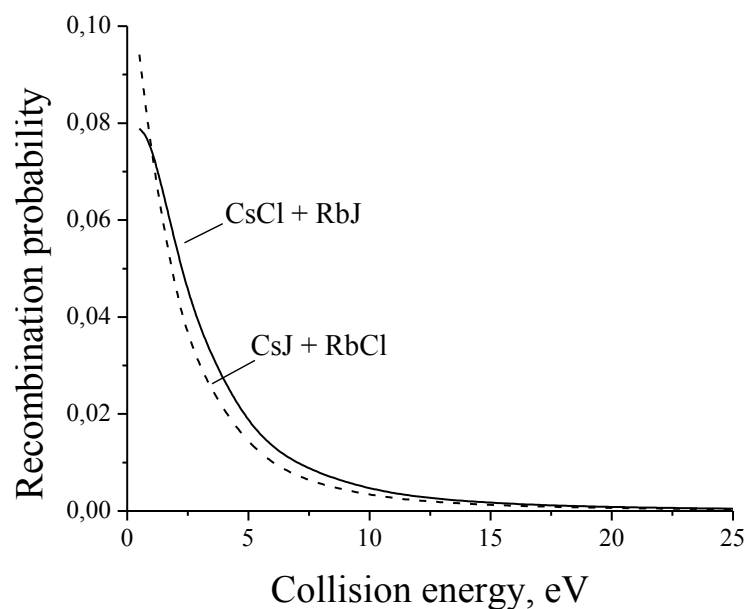


Fig. 1. Dependence of probability of a bimolecular recombination of four ions on their total kinetic energy in symmetric channels of formation of molecular pairs CsCl + RbJ and CsJ + RbCl.

#### References

- [1]. V.M. Akimov, V.M. Azriel, D.B. Kabanov, L.Yu. Rusin. *Dynamics of collision-induced dissociation in the symmetric systems CsCl + RbJ and CsJ + RbCl*. // In: *16-th European Conference on Dynamics of Molecular Systems (MOLEC XVI 2006), Levico Terme (Trento), Italy, 2006*, p.127.

# RELATIVISTIC CALCULATIONS OF IONIZATION AND PAIR CREATION PROBABILITIES IN LOW-ENERGY HEAVY-ION COLLISIONS

Andrey Bondarev<sup>1</sup>, Ilya Tupitsyn<sup>1</sup>, Günter Plunien<sup>2</sup>

<sup>1</sup>*Department of Physics, St. Petersburg State University, Ulianovskaya 1,  
Petrodvorets, St. Petersburg 198504, Russia*

<sup>2</sup>*Institut für Theoretische Physik, Technische Universität Dresden,  
Mommensenstrasse 13, D-01062 Dresden, Germany*

E-mail: bondarev@pcqnt1.phys.spbu.ru

Collisions of highly charged ions allow to study relativistic and quantum electrodynamic effects. If the total charge of the colliding nuclei is larger than  $Z_c = 173$ , the ground state of the combined quasimolecular system should dive into the negative-energy Dirac continuum. Investigation of the processes accompanying such collisions can gain insight into the detection of the diving phenomenon. Relativistic calculations of the differential ionization and electron-positron pair creation probabilities in the  $U^{91+}(1s) - U^{92+}$  collision at 6 MeV/u are performed. Two methods of differential probability evaluation are compared. One of them uses an exact wave function of continuum, while another one uses a wave function of discretized continuum in a finite basis.

## 1. Introduction

Collisions of highly charged ions allow to study the dynamics of relativistic and quantum electrodynamic effects in atomic processes. Of particular interest is the collision of two heavy ions provided that the total charge of the colliding nuclei exceeds the critical value  $Z_c = 173$  [1]. The investigation of processes accompanying such a collision gives a unique opportunity of testing quantum electrodynamics in the supercritical Coulomb field. At small internuclear distances when nuclei are close to each other the ground state of the combined quasimolecular system should dive into the negative-energy Dirac continuum. If this state is not fully occupied by electrons, such a diving should lead to the spontaneous creation of electron-positron pairs. However, direct experimental observation of this effect is extremely challenging. Nevertheless, it is expected that the diving phenomenon can be detected indirectly by observing other processes occurring during the collision.

## 2. Method

Herein the probabilities of ionization and pair creation processes in the low-energy collision of a hydrogen-like ion with a bare nucleus are studied. At first the two-center time-dependent Dirac equation which governs the electron motion is solved in the monopole approximation. The former means that the Coulomb potential of the projectile is approximated by its spherically symmetric part with regard to the target. To solve the time-dependent Dirac equation we use the dual kinetically balanced B-spline basis-set method [2]. This method provides complete basis set which includes bound states, positive- as well as negative-energy discretized continuum states. The time-propagation is carried out using the Crank-Nicolson scheme [3]. Once the time-dependent Dirac equation is solved, one can calculate probabilities of electron transitions. The transition probabilities to the states of the discretized Dirac positive-energy continuum give the ionization probabilities while those to the negative-energy states correspond to pair creation probabilities. Also a more accurate method of ionization and pair creation probabilities calculation is compared with this naive one. The first one implies the separate calculation of the hydrogenic wave function belonging to the continuum. Projecting the solution of the time-dependent Dirac equation on such a wave function results in evaluation of the differential probabilities of ionization and pair creation processes.

Moreover, the total ionization probability is calculated beyond the monopole approximation. For this calculation one need reexpand the projectile potential to the origin where the target is located. Then one could examine the influence of accounting for the higher multipole potential terms on the probabilities of desired processes.

### 3. References

- [1] Greiner W, Müller B and Rafelski J, *Quantum Electrodynamics of Strong Fields* (Springer, Berlin, Heidelberg, 1985).
- [2] Shabaev V M , Tupitsyn I I, Yerokhin V A, Plunien G and Soff G 2004 *Phys. Rev. Lett.* **93** 130405.
- [3] Crank J and Nicolson P 1947 *Proc. Camb. Philos. Soc.* **43**, 50.

# EMPIRICAL FORMULAE AND SCALINGS FOR THE 1<sup>ST</sup> AND 2<sup>ND</sup> ORDER CONTRIBUTIONS TO DOUBLE IONIZATION OF HELIUM

R.D. DuBois<sup>1</sup>, A.C.F. Santos<sup>2</sup>, S.T. Manson<sup>3</sup>

<sup>1</sup>*Missouri University of Science and Technology, Rolla, MO 65409 USA*

<sup>2</sup>*Instituto de Fisica, Universidade Federal do Rio de Janeiro,  
PO 68528, 21941-972 Rio de Janeiro, RJ, Brazil*

<sup>3</sup>*Department of Physics and Astronomy, Georgia State University, Atlanta, GA 30303 USA  
E-mail: dubois@mst.edu*

Published ionization cross sections and cross section ratios for direct single and double electron removal from helium by antiprotons and fully stripped positive ions were analysed within the framework of the first- and second-order mechanism model originally proposed by McGuire. After subtracting the constant high velocity value, the double to single ionization ratios for positive ions ranging from He<sup>2+</sup> to U<sup>90+</sup> were found to scale by dividing the ratios by  $Z^{6/5}$  and the impact velocities by  $Z^{2/5}$ . This scaling, plus empirical fits to the cross sections, provide quantitative values for the 1<sup>st</sup> and 2<sup>nd</sup>-order contributions plus for the interference term for antiprotons and any positive ion for scaled impact velocities from  $\sim 0.1$  to 100 a.u.

## 1. Introduction

Although single electron transitions dominate in fast ion-atom collisions, experimental studies have shown that multi-electron transitions involving two or more outer shell electrons are important contributors to the total target ionization cross section. This is particularly true for lower impact energies and highly charged ion impact. Therefore, the inclusion of multi-electron processes is essential for any theoretical treatment attempting to accurately describe energy deposition and radiation damage associated with charged particles traversing and slowing down in various media. However, while perturbation techniques such as the first Born approximation can accurately describe single ionization, more complicated methods are required to model multiple ionization.

For these reasons numerous experimental and theoretical studies of double ionization of helium were performed during the 1980's and 90's. Often, ratios of double to single ionization,  $R_2$ , were studied in order to improve the sensitivity and to avoid experimental problems associated with measuring absolute cross sections. At high velocities the ratios were found to approach an asymptotic constant that was the same for all fully stripped projectiles [1]. But with decreasing velocity,  $v$ , the ratios were found to increase roughly as  $v^{-2}$  [see for example 1,2]. In addition, for low and intermediate velocities the ratios for antiproton impact were found to be larger than for proton impact [3 and references therein]. McGuire showed that these features are consistent with two channels contributing to double ionization of the outer shell [4]. These channels, often referred to as the TS-1 (two-step, one interaction) and TS-2 (two-step, two interactions) channels, involve one, and two, projectile-target interactions respectively.

For the TS-1 channel, the projectile interacts with and ejects one of the target electrons. As this electron leaves it can interact with and eject a second electron, or a second electron can be ionized after the first electron has departed. The latter case is typically called shakeoff (SO). For the TS-2 channel the projectile interacts independently with each electron. This process is sometimes referred to as the independent particle (IPM) or independent event (IEV) channel. The amplitudes for the TS-1 and TS-2 channels scale as  $Ze/v$  and  $(Ze/v)^2$  respectively where  $Z$  and  $e$  are the projectile and bound electron charges. Thus the double ionization cross sections will scale as the sum of these amplitudes squared and will have an interference term that scales as  $(Ze/v)^3$ . Since single ionization cross sections scale as  $(Ze/v)^2$  the one interaction term will dominate the cross section ratios at high velocities while the two interaction term will dominate at lower velocities thus yielding the observed velocity dependences. In addition, the interference term explained the larger ratios observed for antiproton impact. Using a similar expansion

within a forced impulse method (FIM) [4,5], cross sections were calculated for proton and antiproton impact and found to agree well with experimental data at higher velocities. The differences between antiproton and proton impact have also been attributed to electron-electron correlations of the initial state where one of the target electrons is attracted to/repelled from the incoming projectile depending on the sign of the projectile charge [6].

Although many comparisons between experiment and theory have been performed, generally only the squared sum of the first- and second-order amplitudes has been used and often the comparisons have been hampered at lower energies where transfer ionization influences the experimental data. A few comparisons have been made for low  $Z$  projectiles, typically  $Z \leq 3$ , but the vast majority are for proton and antiproton impact on helium. Thus, little is known about the relative importance of the individual double ionization channels described above or how they scale for various targets. Therefore we have recently analysed available data for direct single and double ionization of helium, neon, and argon by fully stripped ions ranging from  $Z = -1$  to  $+92$  and have extracted empirical formulae for the TS-1, TS-2 and the interference channels. A sample of the results is presented in the next section.

## 2. Results

The first step of our analysis was assembling a large database of experimental single and double ionization cross sections and cross section ratios from the literature. For multicharged ion impact on helium it was found that by subtracting the asymptotic high velocity value of 0.00259 the double to single ionization ratios,  $R_2$ , could be scaled by dividing the measured ratios by  $Z^{6/5}$  and the impact velocities by  $Z^{2/5}$ . Results of this scaling are shown in Fig. 1. Note that this subtraction essentially removes the TS-1 contribution and that the high velocity dependence is approximately  $v^{-2}$ , as shown by the dashed lines in the figure. As will be shown below, for multicharged ion impact the interference contribution generally does not play a significant role which is why the scaling we obtain is consistent with the  $(Z/v)^2$  scaling as predicted by McGuire for the TS-2 contribution. However, as seen the proton and antiproton data fall below and above the scaled multicharged ion data and demonstrate different velocity dependences. These features we attribute to a significant contribution from the interference term. As will be shown below, these features are consistent with the 1<sup>st</sup>- and 2<sup>nd</sup>-order constitution model while the failure for the proton data to scale in the same manner as other positive ions seems to discount the model proposed in ref. 6.

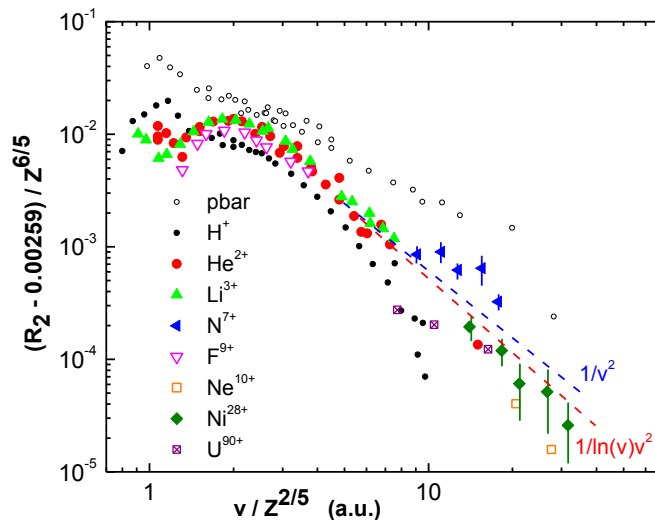


Fig. 1. TS-2 plus interference contributions to double to single ionization ratios of helium. Data are from refs. 1-3 and 7-15.

In order to extract information about the various terms which contribute to double ionization, empirical fits were made to the single ionization cross sections and to the TS-2 portion of the double ionization cross section using simple functions of the form  $C_{lo} v_{sc}^m$  below the cross section maxima and  $C_{hi}$



$\ln(v_{sc})/v_{sc}^n$  above the maximum. Here  $C_{lo}$ ,  $C_{hi}$ ,  $m$  and  $n$  are fitting parameters and  $v_{sc} = v/Z^{2/5}$ . The overall fit was the combination of these functions in the following manner;

$$\sigma_q = (Z^{6/5})^q [1/C_{lo} v_{sc}^m + 1/C_{hi} \ln(v_{sc}) v_{sc}^{-n}]^{-1} \quad (1)$$

where  $q = 1, 2$  for single and double ionization respectively. To extend the “hi” function to velocities less than 1, a constant, 0.4, was added in the  $\ln$  term to avoid any negative  $\ln$  values in the low velocity region. Good fits to the single ionization data were achieved using the following parameters.

Single ionization	$C_{lo}$	$m$	$C_{hi}$	$n$
$Z = +/- 1$	0.375	4	4.75	2
$Z > 1$	0.35	6	4.75	2

For the TS-2 component of double ionization, both the McGuire model and the FIM model assume that three terms contribute, namely  $\sigma_2 = \sigma_{TS1} + \sigma_{TS2} + \sigma_{Int}$  with the interference term being positive for antiproton impact and negative for positive ion impact.  $\sigma_{TS1}$  was obtained by multiplying  $\sigma_1$  by  $R_2(\infty)$ , i.e., 0.00259, which should be valid since  $\sigma_{TS1}$  is proportional to  $\sigma_1$  and only plays an important role at high velocities. For multiply charged ions, Fig. 1 implies  $\sigma_{Int}$  is relatively unimportant so  $\sigma_{TS2}$  was obtained by subtracting  $\sigma_{TS1}$  from the measured double ionization cross sections. For proton and antiproton impact, Fig. 1 indicates that the interference term is quite important. But, here the following equations apply.

$$\sigma_2(\text{proton}) = \sigma_{TS1} + \sigma_{TS2} - \sigma_{Int} \quad (2)$$

$$\sigma_2(\text{antiproton}) = \sigma_{TS1} + \sigma_{TS2} + \sigma_{Int} \quad (3).$$

$$\text{Therefore} \quad \sigma_{TS2}(Z=+/- 1) = [\sigma_2(\text{proton}) + \sigma_2(\text{antiproton})] - \sigma_{TS1} \quad (4).$$

Empirical fits to  $\sigma_{TS2}$  obtained in this manner yielded

$\sigma_{TS2}$	$C_{lo}$	$m$	$C_{hi}$	$n$
$Z = +/- 1$	0.008	2	0.5	4
$Z > 1$	0.0035	4	0.5	4

Finally,  $\sigma_{Int}$  is obtained for  $Z=+/- 1$  by subtracting equations (2) and (3) and for  $Z>1$  from

$$\sigma_{Int} = 2\cos(\varphi)[\sigma_{TS1}\sigma_{TS2}] \quad (5)$$

where  $\cos(\varphi)$  is obtained using equations (2), (3) and (5) and plotted versus impact velocity. A fit to the  $\cos(\varphi)$  versus  $v$  yielded

$$\cos(\varphi) = 0.35 + 0.4v^{-2} \quad \text{with the maximum value being 1} \quad (6)$$

which was assumed to be the same for all projectiles.

Using this method, cross sections for  $\sigma_{TS1}$ ,  $\sigma_{TS2}$  and  $\sigma_{Int}$  were determined. Fig. 2 shows a few examples the TS-2 and interference contributions compared to experimental data. As predicted, for multicharged ion impact  $\sigma_{TS2}$  generally is large compared to  $\sigma_{Int}$  with their sum in reasonable agreement with experimental data where the  $\sigma_{TS1}$  contribution has been subtracted.

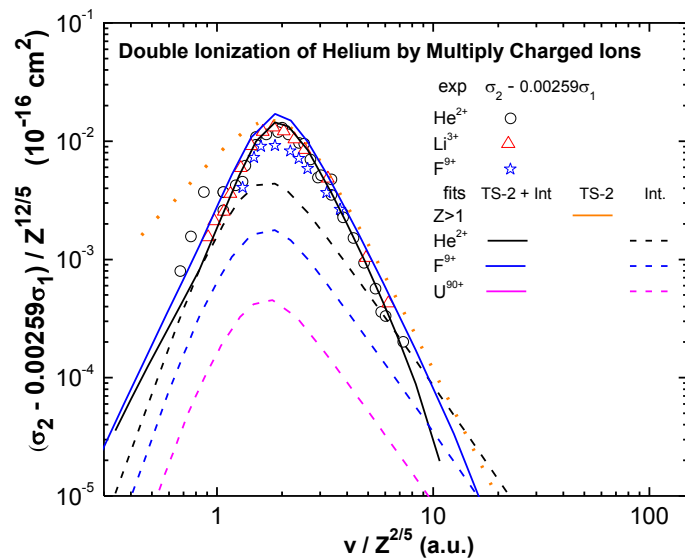


Fig. 2. TS-2 and interference contributions to double ionization of helium by multicharged ions. Data are from refs. 2,10,12,14. The fits are obtained using the formulae described in the text.

Acknowledgments: This work was supported by the National Science Foundation, the Department of Energy, Office of Chemical Sciences, CNPq and the Brazil-U.S. Physics Professorship/Lectureship Program.

### 3. References

- [1] Ullrich J, Moshhammer R, Berg H, Mann R, Tawara H, Dorner R, Euler J, Schmidt-Bocking H, Hagmann S, Cocke C L, Unverzagt M, Lencinas S, and Mergel V, 1993 *Phys. Rev. Lett.* **71**, 1697.
- [2] Knudsen H, Andersen L H, Hvelplund P, Astner G, Cederquist H, Danared H, Liljeby L and Rensfelt K-G, 1984 *J. Phys. B: At. Mol. Phys.* **17**, 3545-3564.
- [3] Knudsen H, 1997 *Hyperfine Interactions* **109**, 133–143.
- [4] Reading J F and Ford A L, 1987 *Phys. Rev. Lett.* **58**, 544.
- [5] Ford A L and Reading J F, 1990 *J. Phys. B: At. Mol. Phys.* **29**, 5831-42.
- [6] Végh L, 1988, *Phys. Rev. A* **37**, 992.
- [7] Andersen L H, Hvelplund P, Knudsen H, Manlier S P, Pedersen J O P, Tang-Petersen S, Uggerhøj E, Elsener K and Morenzoni E, 1990 *Phys. Rev. A* **41**, 6536.
- [8] K. Paludan K, H. Bluhme H, H. Knudsen H, 1997 *J. Phys. B: At. Mol. Opt. Phys.* **30**, 3951.
- [9] Knudsen H, Kristiansen H-P E, Thomsen H D, Uggerhøj U I, Ichioka T, Møller S P, Hunniford C A, McCullough R W, Charlton M, Kuroda N, Nagata Y, Torii H A, Yamazaki Y, Imao H, Andersen H H, and Tökési K, 2008 *Phys. Rev. Lett.* **101**, 043201 and 2009 *Nucl. Instr. and Meth. in Phys. Res. B* **267**, 244.
- [10] Shah M B and Gilbody H B, 1985 *J. Phys. B: At. Mol. Phys.* **18**, 899.
- [11] DuBois R D, 1986 *Phys. Rev. A* **33**, 1595.
- [12] Woitke O, Závodszky P A, Ferguson S M, Houck J H, and Tanis J A, 1998 *Phys. Rev. A* **57**, 2692 (1998).
- [13] Heber O, Bandong B B, Sampoll G, and Watson R L, 1990 *Phys. Rev. Lett.* **64**, 851.
- [14] Shinpaugh J L, Sanders J M, Hall J M, Lee D H, Schmidt-Bocking H, Tipping T N, Zouros T J M and Richard P, 1992 *Phys. Rev. A* **45**, 2922 (1992).
- [15] Berg H, Jagutzki O, Dörner R, DuBois R D, Kelbch C, Schmidt-Bocking H, Ullrich J, Tanis J A, Schlachter A S, Blumenfeld L, d'Etat B, Hagmann S, Gonzales A and Quinteros T, 1992 *Phys. Rev. A* **46**, 5539.

# AUGER PHOTOEMISSION SPECTROSCOPY FROM SURFACES OF Fe-Si

J. L. Gervasoni<sup>1</sup>, M. Jenko<sup>2</sup>, B. Poniku<sup>2</sup> and I. Belič<sup>2</sup>

<sup>1</sup> *Centro Atómico Bariloche and Instituto Balseiro, Comisión Nacional de Energía Atómica Universidad Nacional de Cuyo R8402AGP S. C. de Bariloche, Rio Negro, Argentina. Member of the Consejo Nacional de Investigaciones Científicas y Técnicas (CONICET), Argentina*

<sup>2</sup> *Institute of Metals and Technology, Lepi pot 11, 1000 Ljubljana, Slovenia*  
E-mail: gervason@cab.cnea.gov.ar

In this presentation we investigate in detail the effects due to the interaction between an electron and a stationary positive ion (or atomic hole) in the neighbourhood of a surface of Fe-Si, having a strong plasmon peak in their electron energy loss spectra, when it is excited with synchrotron.

## 1. Introduction

Using a semi classical dielectric formulation [1], we carefully estimated the parameter  $r_s$ , which is critical in order to define the density of the alloy. With the cited formulation, we have obtained a detailed behaviour of the different contributions of the collective surface excitations [2]. We analyse the induced surface potential, taken into account the begrenzung effect of the surface.

It provides a simple way to calculate the density of states of the alloy in first approximation. For this result, we find some novel structures that are under discussion.

The method described here is useful for studying multiple plasmon excitations and in understanding the electron spectra excited from these alloy structures.

The plasmons leave a mark in the Auger spectrum which poses a challenge to the automatic spectra analysis. The results of the study are directly used to properly instruct the software to interpret the information correctly.

## 2. Description and Results

In order to investigate the energy loss of a Auger photoelectron due to plasmon excitation we use a semiclassical model developed in previous works [1], as well as the dielectric response model used by Yubero and Tougaard []. The excitations are taking place either due to the sudden creation of the photohole and as a consequence of the electron transport through the solid (extrinsic processes). For a specular and planar surface the hole and the electron are created at a distance  $z_0$  from the interface between the metal and the vacuum. We assume that the hole is fixed at  $\mathbf{r}_0 = (0, z_0)$  while the emitted electron with velocity  $\mathbf{u}$  follows a uniform trajectory  $\mathbf{r}_e = \mathbf{r}_0 + \mathbf{u}t$ , perpendicular to the surface, which remains undisturbed by the plasmon excitation events. This approximation holds for sufficiently large kinetic energies,  $\mu^2/2 \gg \hbar\omega_p$  []. Within our formalism this approach is fully justified: X-ray excited Auger electron spectroscopy (AES) the energy of the emitted electron is in the several hundred eV or in the keV range, while  $\hbar\omega_p$  is lower, than 20-25 eV.

We use the so called specular reflection model [] to describe the system and the involved field. In this frame, the behaviour of the material is given by the local dielectric function []:

$$\varepsilon(\mathbf{k}, \omega) = \varepsilon(\omega) = 1 - \omega_p^2 / \omega(\omega + i\gamma),$$

with the corresponding values for the plasma frequency  $\omega_p$  and the damping constant  $\gamma$ . Throughout the paper we use atomic units.

Following the same formalism developed in ref [1], the total energy dissipation rate due to the fields acting on the emitted electron is given by the induced potentials  $\phi^{ind}$  in the medium and in the vacuum. From the  $\phi^{ind}$  via Poisson and Laplace Equations Eq. (1), we obtain the bulk and surface electronic density  $\rho$ , respectively.

In the so-called jellium model the metal is replaced by a homogeneous electron gas and a background of positive charges with the same average density in order to maintain the system neutrality. The fundamental parameter of the model is  $r_s$  (u.a.), which is defined as the radius of the sphere occupied by one electron in the solid. And this quantity is related with the electronic density and this with the dielectric function.

As the electronic density is dependent of the parameter  $r_s$ , it is critical to determine from the alloy as a whole. We obtain it from jellium model approximation [2].

In Figure 1 we show the results for bulk and surface density for the Fe-Si alloy. It is interesting observe that the importance of the hole is neglectable with respect to the elements Fe and Si separately.

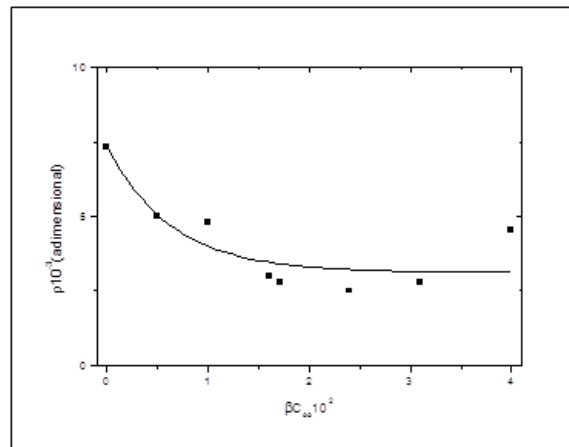


Fig. 1. Adimensional density of bulk (points) and surface (continued line) plasmons excited due to AES processes vs. adimensional characteristic distance from the surface of Fe-Si alloy, inside it. The emitted electron has a velocity  $v = 4$  a.u.  $C_\infty$  is the concentration of the solute at infinite dilution and  $\beta = r_s^{\text{Fe}} / r_s^{\text{Si}}$  is the rate of the parameter  $r_s$  of each element of the alloy.

We determined the characteristic parameter of the alloy using a model based on the density functional theory (DFT). The great importance and advantage of this method is that the treatment of a great number of electrons can be treating of a unique variable (tri-dimensional) in replace of the complete wave function. We demonstrate with this approximation that each atom is sensible only to its immediate environment.

The application of this formalism to cases of experimental interest in AES and XPS is currently under way.

### 3. References

- [1] C. Denton, J. L. Gervasoni, R. O. Barrachina and N. R. Arista, *Physical Review A* 57, 4498 (1998)
- [2] R. Raether, *Excitations of Plasmons and Interband Transitions by Electrons*, Springer Tracts in Modern Physics, Vol. 88, Springer, Berlin, (1980).
- [3] K.D. Sevier, *Low Energy Electron Spectrometry*, Wiley-Interscience, New York, (1972).
- [4] F. Yubero and S. Tougaard, *Phys. Rev. B* 71, 045414 (2005).
- [5] J. L. Gervasoni and F. Yubero, *Nuclear Instruments and Methods B* 182 (2001) pp.96-101.

# VARIATION OF THE ELECTRONIC DENSITY ASSOCIATED TO THE EXCITATION OF PLASMONS DESCRIBED IN THE FRAME OF COHERENT STATES

Juana Gervasoni<sup>1</sup>, Silvina Seguí<sup>2</sup>

<sup>1</sup> Centro Atómico Bariloche, (CNEA). Av. Bustillo 9500 (8400) Bariloche; Rio Negro, Argentina.  
Consejo Nacional de Investigaciones Científicas y Tecnológicas (CONICET), Argentina.  
Instituto Balseiro, Universidad Nac. de Cuyo, Argentina.

<sup>2</sup> Centro Atómico Bariloche, (CNEA). Av. Bustillo 9500 (8400) Bariloche; Rio Negro, Argentina.  
Consejo Nacional de Investigaciones Científicas y Tecnológicas (CONICET), Argentina.

E-mail: gervason@cab.cnea.gov.ar

We study the fluctuation of the electronic density of a given material associated with the wake potential generated by an external charged particle.

We analyze the variation of the electronic density related to these wave packets of plasmons excited by the particle for several cases of interest, as are the different trajectories of the external charged particle.

## 1. Theoretical description

Fluctuation of the electronic collective modes in a given material associated with the wake potential generated by an external particle of charge  $Ze$ . This perturbation is described as coherent states of plasmons spatially localized in an average distance of the order of the velocity of the particle divided by the plasmon frequency of the material [1, 2]. It is adequate to treat the state of plasmons as a coherent packet, not only because these states are the best approximation to a classic electromagnetic wave, but also because the collective mode generates coherent excitations in each mode [3, 4]

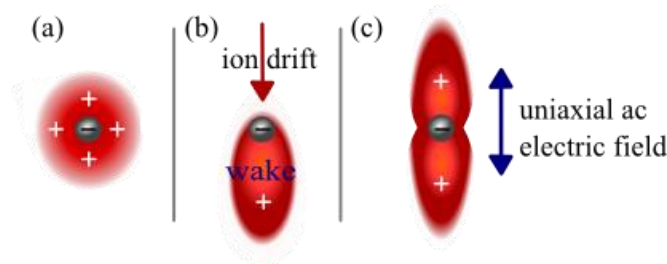


Fig. 1. Scheme of the system.

## 2. Results

Within this framework, plasmon modes are considered as a set of harmonic oscillators with given characteristic frequencies  $\omega_p$  determined by the composition and geometry of the studied system. The unperturbed plasmon field is described by its corresponding Hamiltonian, which yields a set of eigenstates of the system. With them, the temporal evolution of the plasmon field interacting with the external particles can be obtained in an exact quantum mechanical way as coherent states. We analyse the fluctuation of the electronic density that is related to the average number of excited plasmons (see detail in ref. 3 and 4).

In Figures 2 and 3, we show the collective fluctuation of both bulk and surface electronic density (plasmons), for different trajectories of the external charged particle, for Aluminum in its structure of planar surfaces and tubes.

One of the most remarkable features is that in all the cases, and within the employed approximation, the fluctuations are not negligible.

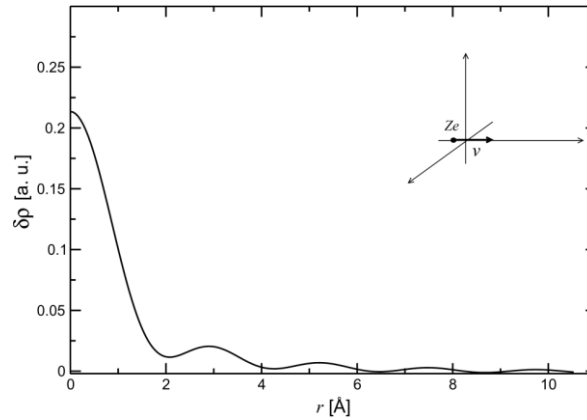


Fig. 2. Fluctuation of the electronic density due to a swift external particle of charge  $Ze$  and trajectory perpendicular to the surface of the planar Al surface.

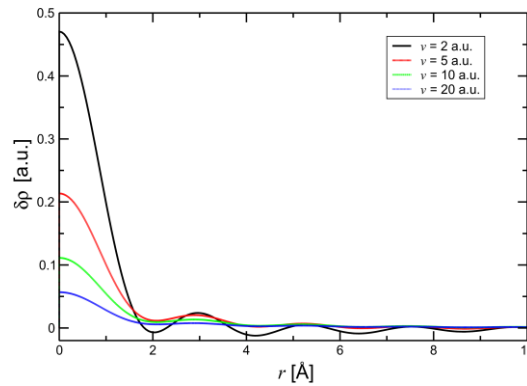


Fig. 3. Surface density variation as a function of the radial distance to the origin of a nanocylinder of Al for perpendicular trajectory of the external particle, for several velocities of it.

### 3. Summary

In summary, we can assume that it is adequate to treat the state of plasmons as a coherent packet, not only because these states are the best approximation to a classic electromagnetic wave, but also because the collective mode generates coherent excitations in each mode.

We show the fluctuation of both bulk and surface electronic density, for different trajectories of the external charged particle, for Aluminum in its structure of planar surfaces and tubes.

One of the most remarkable features is that in all the cases, and within the employed approximation, the fluctuations are not negligible.

Also we study the coupling for the dispersion relation between two displaced particles (molecule), in order to discuss the interference behavior, fact that must have taken into account for the Nano devices designs.

### 4. References

- [1] Gervasoni J L and Arista N R, 2003 Phys.Rev.B 68 235302.
- [2] Gervasoni JL, Segui S and Arista NR, 2007 Radiation Effects and Defects in Solids 162 267-275.
- [3] Segui S, Gervasoni JL and Arista NR, 2007 Surf. Sci. 601 4169-4174.
- [4] Mowbray DJ, Segui S, Gervasoni JL, Miskovic ZL and Arista NR, 2010 Phys. Rev. B 82, 035405.

# PLASMON CHANGES FOR IN-OUT ASYMMETRY OF IONIC PROJECTILES TRAJECTORIES IN SOLID SURFACES

Juana L. Gervasoni<sup>1,2</sup>, Silvina Segui<sup>1</sup>, Raul O. Barrachina<sup>1,2</sup>, W. Werner<sup>3</sup>

<sup>1</sup> *Centro Atómico Bariloche, Comisión Nacional de Energía Atómica, R8402AGP S. C. de Bariloche, Rio Negro, Argentina. Also member of the Consejo Nacional de Investigaciones Científicas y Técnicas (CONICET), Argentina.*

<sup>2</sup> *Balseiro Institute, Comisión Nacional de Energía Atómica and Universidad Nacional de Cuyo, R8402AGP S. C. de Bariloche, Rio Negro, Argentina.*

<sup>3</sup> *Institut fuer Angewandte Physik, TU Vienna, Wiedner Hauptstr 8-10, Austria.*

E-mail corresponding author: gervason@cab.cnea.gov.ar

We use both quantum mechanical and semiclassical dielectric formulations to study how an external charged particle, moving in the vicinity or traversing a solid surface, couples with the bulk and surface excitations. We pay special attention to the differences and similarities between incoming and outgoing trajectories, finding some novel oscillatory structures that can be ascribed to interference effects between direct and reflected plasmon excitations.

## 1. Theoretical framework

The purpose of this paper is to investigate in detail the interaction of charged particles with solid interfaces for incoming and outgoing trajectories, in terms of the dielectric formalism and the semiclassical approach, using the so-called surface reflexion [1-3]. This model has been quite useful for applications in studies of particles-surfaces interaction processes, as well as in the field of the electromagnetism [4].

Although in general, the surfaces are well defined to a macroscopic level, they usually present roughness at atomic scale that do very difficult their treatment, in the following we will constrained to smooth surfaces. This limitation must be taken into account when comparing with experimental results.

Turning to the problem established by the non-invariance translational of the dielectric function that characterizes the solid, we consider that the external particle follows a well-defined classical trajectory, exciting collective oscillations in the bulk and on the surface, called plasmons [1]. In this mechanism of excitation it losses energy, which depend of the material that it travel as well as of its initial energy (or velocity).

## 2. Results and discussions

Figure 1 illustrates in detail how different trajectories (perpendicular to the surface, one incoming and the other outcoming) contribute to the stopping power or, equivalently, to the excitation of bulk and surface plasmons.

Although the surface contribution is the same for both incoming and outgoing trajectories, we clearly see that there is an in-out asymmetry behaviour given by an oscillatory term of bulk plasmons that only appears when the projectile enters into the solid.

Figure 2 shows how different trajectories (perpendicular to the surface, one going inside, and the other outside the medium) of the particle participate on the excitation of bulk plasmons.

We find some novel oscillatory structures that can be ascribed to an interference effects between direct and reflected plasmon excitations (see details in ref. [6]).



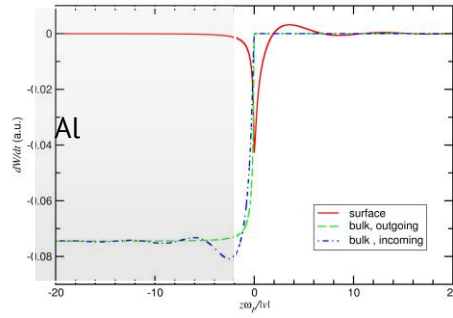


Fig. 1. Energy loss rate due to surface and bulk plasmon excitations for a charged projectile traveling with velocity  $v$  through an Aluminum interface vs. characteristic distance  $zwp/v$ , where  $w_p$  is the plasma frequency, and  $z$  is the distance to the surface [6].

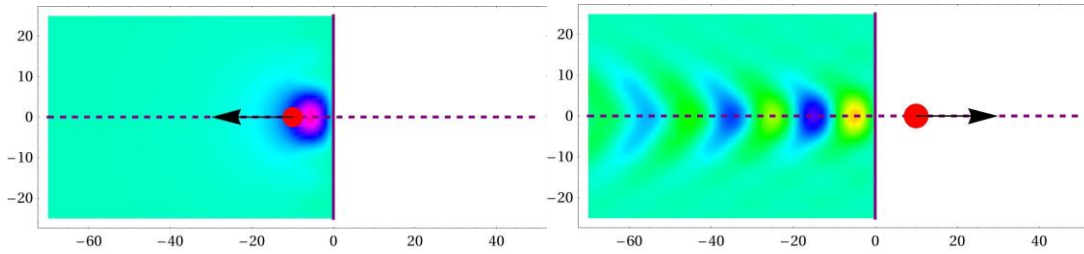


Fig. 2. Induced potential for a charged projectile with velocity  $v = 2$  a.u. traveling through an Aluminum interface for incoming (left) and outgoing (right) trajectories [6]. Lengths are given in atomic units.

In summary, we discuss the interaction of moving charged particles with bulk and surface plasmons. For planar surfaces, and using a semi classical dielectric formulation [1], we analyse the differences and similarities that arise when we compare incoming and outgoing trajectories. With the cited formulation, we have obtained a detailed behaviour of the induced potential, incorporating reasonably well the effects due to the local environment of the impurity. It provides a great simplicity in the analysis, and a way to calculate the corrections necessary for this approach.

Comparisons with experimental results using reflection electron energy loss and analysis in nanoscopic scale are under way.

### 3. References

- [1] R. H. Ritchie and A. L. Marusak, *Surf. Sci.* 4, (1966) 234.
- [2] F. Flores and F. Garcia-Moliner, *J. Phys. C: Solid State Phys.* 12, (1979) 907.
- [3] J. L. Gervasoni and N. R. Arista, *Surf. Sci.* 260, (1992) 329 C. D. Denton, J. L. Gervasoni, R. O. Barrachina and N. R. Arista, *Phys. Rev. A* 57 (1998) 4498
- [4] R. Raether, *Excitations of Plasmons and Interband Transitions by Electrons*, Springer Tracts in Modern Physics, Vol. 88, Springer, Berlin, (1980).
- [5] J. L. Gervasoni, S. Seguí, R. O. Barrachina, W. Werner, *Surface and Interface Analysis* (2013) 45, 1849–1853.

# NATURAL WIDTHS AND BLACKBODY-RADIATION-INDUCED SHIFT AND BROADENING OF RYDBERG LEVELS IN MAGNESIUM IONS.

Igor Glukhov<sup>1</sup>, Sergey Mokhnenko<sup>1</sup>, Elizaveta Nikitina<sup>1</sup>, Vitaly Ovsiannikov<sup>1</sup>

<sup>1</sup>*Voronezh State University, 394006 Voronezh, Russia*

E-mail: glukhovofficial@mail.ru

Theoretical analysis is presented of the natural lifetimes and blackbody-radiation-induced shifts and widths of Rydberg states with small and large angular momenta  $l$ . Asymptotic presentations in elementary functions are derived for matrix elements of bound-bound, bound-free and threshold radiative transitions from hydrogenic-type states with large angular momenta, applicable to many-electron atoms. For states with small angular momenta the data of two numerical methods based on the quantum defects is used are compared with one another and with the most reliable data of the literature. Asymptotic approximations are derived for the natural lifetimes, thermal shifts and broadening of Rydberg states with small and high  $l$  and high principal quantum numbers  $n$ .

## 1. Introduction

Intensive researches on the possibilities of the use of Rydberg states in practical applications stimulated arising interest to detailed studies of different optical properties of highly excited atoms and ions. The most important quantities determining optical properties of Rydberg atoms and ions are the natural lifetimes  $\tau_{nl}$  and electromagnetic susceptibilities, first of all, the static  $\alpha_{nl}(0)$  and dynamic (frequency-dependent)  $\alpha_{nl}(\omega)$  dipole polarizabilities, which represent the principal quantitative characteristics of interaction between atom in its bound state  $|nl\rangle$  and external field. Numerical values of static and dynamic polarizabilities determine the black-body-radiation(BBR)-induced shifts of energy levels in the low-temperature ( $kT \ll |E_{nl} - E_{n'l'}|$ ) and high-temperature ( $kT \gg |E_{nl} - E_{n'l'}|$ ) environment, correspondingly (here  $k$  is the Boltzmann constant,  $T$  is the absolute temperature,  $E_{nl} - E_{n'l'}$  is the energy of transition between nearest energy levels). It is important to note that  $\alpha_{nl}(0)$  and  $\alpha_{nl}(\omega)$  exhibit quite different behaviour as functions of the Rydberg-state principal quantum number  $n$ . The static polarizabilities are rapidly growing functions of  $n$ ,  $\alpha_{nl}(0) \propto n^7$  (see e.g. [1,2]), whereas the dynamic polarizability in the optical range of frequencies is approximately one and the same value for all Rydberg states, excluding only very narrow regions of resonances with lower-energy states.

In what follows, the atomic system of units is used, unless otherwise specified explicitly. The unit atomic speed is  $v_a = c/137.036$ , where  $c$  is the speed of light. For convenience, the temperature is described in Kelvin, the Boltzmann constant  $k = 1/T_a = 3.1668 \cdot 10^{-6}$  a.u./K, where  $T_a = 315776$  K is the atomic unit of temperature.

## 2. High-frequency polarizabilities of Rydberg states

The Rydberg-state dynamic polarizabilities determine energy shifts in a monochromatic electromagnetic wave. With the growth of principal quantum numbers these shifts gradually approach to their asymptotic values, corresponding to the energy of free-electron oscillations. At frequencies, well exceeding the ionization potential of a Rydberg state  $\omega/|E_{nl}| \equiv \Omega \gg 1$  and essentially smaller than the energy of two-electron excitations, the real part of scalar dynamic polarizability scales according to the law of inverse frequency squared, one and the same for all states, independently of quantum numbers [3-5]:

$$\text{Re}\{\alpha_{nl}^s(\omega)\} \approx -\frac{1}{\omega^2}. \quad (1)$$

The imaginary part is determined by the photoionization cross section:

$$\text{Im}\{\alpha_{nl}^s(\omega)\} \approx \frac{c}{4\pi\omega} \sigma_{nl}(\omega), \quad (2)$$

which is a rapidly vanishing function of the frequency  $\omega$  and the principal quantum number  $n$ ;  $c=137.036$  a.u. is the speed of light. For Rydberg states with  $l < 5$  ( $nS$ -,  $nP$ -,  $nD$ -,  $nF$ -,  $nG$ -states) the quasiclassical estimates [6] give  $\sigma_{nl}(\omega) \approx \sigma_{nl}^{thr} / \Omega^{7/3}$  where  $\sigma_{nl}^{thr} = \sigma_{nl}(\omega = |E_{nl}|)$  is the threshold cross section, for which also the WKB-approximation may be used [6,7]. The indicated dependencies demonstrate a rapid decrease of the imaginary part (2) with the increase of both the frequency and the principal quantum number,

$$\text{Im}\{\alpha_{nl}^s(\omega)\} \propto Z^{14/3} n^{-3} \omega^{-10/3}, \quad (3)$$

where  $Z$  is the charge of residual ion. Therefore, in the region of frequencies  $\omega \gg |E_{nl}|$ , the imaginary part of the Rydberg-state dynamic polarizability may be neglected in comparison with the real part (1). With the use of (1) and taking into account the rate of all the stimulated by the blackbody radiation (BBR) transitions, an asymptotic expression for the shift  $\varepsilon_{nl}^{BBR}(T)$  and broadening  $\Gamma_{nl}^{BBR}(T)$  of Rydberg energy levels by the BBR of the temperature  $kT \gg |E_{nl}|$  may be derived [8,9]:

$$\Delta E_{nl}^{BBR}(T) = \varepsilon_{nl}^{BBR}(T) - i \frac{\Gamma_{nl}^{BBR}(T)}{2} \approx \frac{\pi}{3c^3} (kT)^2 - i \frac{2kT}{3c^2 n^2}. \quad (4)$$

Rigorously speaking, the free-electron approximation (1) is applicable to states with sufficiently high angular momenta ( $l > 5$ ) and does not describe precisely polarizabilities of atomic states with low momenta, since it does not account for possible resonances with lower states of angular momenta  $l' = l \pm 1$ , the energy of transitions to which may be on the order of  $\omega$ . Moreover, equation (1) is valid in the single-electron approximation without account for modifications of the Rydberg-electron wave function due to the interaction with the core electrons of the residual ion. The modifications may be neglected only for the states repelled from the core by sufficiently strong centrifugal potential

$$U_c(r) = \frac{l(l+1)}{2r^2}. \quad (5)$$

The wave functions of low-angular-momentum states penetrate deeply inside the core and may be modified significantly, unlike the hydrogenic-type functions of high-angular-momentum states. That is why the asymptotic values of the frequency-dependent polarizability of states with  $l < 5$  may differ from those of equation (1).

The asymptotic equations for the Rydberg-state dynamic polarizability and higher-order in  $1/\omega^2$  corrections to the principal term (1) may be determined by reducing the infinite summations to the sum rules of oscillator strengths and their moments (see for example [4,5]), represented in terms of simple closed expressions [10,11]. In these sums the contribution of continuum is strongly dependent on the orbital momentum of the Rydberg state. This contribution may be significant for states with small momentum, whereas for large  $l$  (usually, for  $l > 5$ ) it vanishes exponentially with the increase of the principal quantum number  $n$ .

### 3. Asymptotic features of natural widths, photoionization cross sections and BBR-induced shifts and broadening of states with high angular momenta.

Detailed calculations of the shift and broadening of Rydberg-state energy levels in hydrogen, helium and alkali-metal atoms revealed noticeable departures from the asymptotic data, specifically for low-angular-momenta states, which in many-electron atoms have the largest quantum defects and therefore exhibit most clearly evident departures of optical properties from those of the hydrogenic states [12]. These departures were explained by contributions from the lower-energy states  $|n'l'\rangle$ , for which a relation holds  $E_{nl} - E_{n'l'} > kT$ , in contrast to the high-temperature asymptotic requirement  $|E_{nl} - E_{n'l'}| \ll kT$ . The separation of contributions from the lower- and upper-energy states (decays and excitations) into broadening of a low-momentum Rydberg state  $|nl\rangle$  in hydrogen, helium and alkali atoms has demonstrated significant dependencies of these contributions on individual structures of the energy spectra in S-, P-, D-, F-series of states [13, 14]. In addition, considerable contributions into shift and broadening come from continuum, which account for the BBR-induced ionization and the upward shifts of Rydberg levels. For the low- $l$  states these contributions are overestimated in the asymptotic equations since the threshold ionization cross section  $\sigma_{nl}^{thr}$  increases with  $n$  approximately as  $\sigma_{nl}^{thr} \propto n^{5/3}$ , while the above-threshold cross section rather smoothly decreases as a function of the BBR-photon frequency, approximately as [13, 14]:

$$\sigma_{nl}(\omega) \approx \sigma_{nl}^{thr} / \Omega^{7/3}. \quad (6)$$

For the low-momentum series of states, the use of asymptotic approximation (1), assumed to spread over all frequency range of the Planck's distribution from zero up to infinity, may either overestimate or underestimate the positive (upward) shift of the Rydberg-state energy by high-frequency thermal photons and the negative (downward) shift by low-frequency photons. In particular, the contributions of continuum are overestimated both in the level broadening [14], corresponding to the probability of BBR-induced ionization, and in the upward shift of energy.

The situation for high- $l$  hydrogenic-type orbits ( $10 < l \leq n-1$ ) is quite different. Here only a small number of states  $|n'l'\rangle$  with  $l'=l\pm 1$  and  $n'$  from  $n'=l'+1$  to  $n'=n-1$  remain below the state  $|nl\rangle$ . Evidently, the asymptotic condition  $|E_{nl} - E_{n'l'}| \ll kT$  may hold for them automatically if the binding energy is significantly smaller than the thermal,  $|E_{nl}| \ll kT$ . In addition, the radial matrix elements of dipole transitions decrease with the increase of difference between principal quantum numbers  $|n'-n|$  as  $n^{-|n'-n|}$ . Therefore the principal contribution to the spontaneous-decay rate  $P_{nl}^{sp}$  of high- $l$  states comes from two closest states with  $n'=n\pm 1$ . The general behaviour of the natural lifetime  $\tau_{nl}^{sp}$  of a state with high quantum numbers  $l$  and  $n$  may be presented as

$$\tau_{nl}^{sp} \approx t_0 n^3 l^2 f(n, l), \quad (7)$$

where  $f(n, l) \xrightarrow{n \rightarrow \infty} 1$  is a dimensionless function, which adjusts the right-hand-side expression with exact values of  $\tau_{nl}^{sp}$  for arbitrary  $l$  and  $n$ ,  $t_0 \approx 0.09$  nanoseconds is a constant value, independent of the Rydberg-state quantum numbers. Evidently, if the orbital quantum number is proportional to  $n$ , the rate of spontaneous decay vanishes following the law  $P_{nl}^{sp} \propto 1/n^5$ , which is reduced by the factor  $n^{-2}$  in comparison with the rate  $P_{nl}^{sp} \propto 1/n^3$  for fixed- $l$  states, for which the principal contribution to  $P_{nl}^{sp}$  comes from the lowest dipole-connected states.

The ionization cross section for high- $l$  states falls down exponentially with  $n \gg 1$ . For example, the cross section of the threshold ionization of a circular state,  $l=n-1$ , may be presented as:

$$\sigma_{n,l=n-1}^{thr} = \frac{16\pi^{3/2}n^{5/2}}{3Z^2c} \left(\frac{2}{e}\right)^{2n} \left(1 + \frac{1}{2n} + \frac{1}{2n^2} + o\left(\frac{1}{n^3}\right)\right). \quad (8)$$

The plot of the  $n$ -dependence of this function is given in figure 1, where the logarithmic scale for the cross section is used in the vertical axis. Above the threshold, the frequency-dependent cross section  $\sigma_{n,l=n-1}(\omega) = \sigma_{n,l=n-1}^{thr} f_n(\omega)$  is also a decreasing function of frequency, as is seen from the rapidly vanishing factor,

$$f_n(\omega) = \frac{\sigma_{nl}(\omega)}{\sigma_{nl}^{thr}} = \frac{1}{\Omega^{5/2}} \left( \frac{\exp\left(1 - \arctan\left(\sqrt{\Omega-1}\right)/\sqrt{\Omega-1}\right)}{\sqrt{\Omega}} \right)^{2n}. \quad (9)$$

Corresponding functions of the fractional frequency  $\Omega = \omega / |E_{nl}|$  are presented in figure 2 for circular states with  $n=10, 30, 50$ .

So, the principal contribution to the BBR-induced depopulation rate for high- $l$  Rydberg states comes from transitions to the closest upper and lower states with  $n'=n\pm 1$ . Besides that, the high- $l$  states in all atoms are hydrogen-like, without any quantum defects. Therefore, the single-electron sum rules for them hold with high precision, together with asymptotic equations for the frequency-dependent polarizability (there are no resonant states in the lower region of energy) and for the BBR-induced shift and broadening, where the contribution of continuum is negligibly small.

Figure 1. The threshold ionization cross section (8) of circular states with  $l=n-1$  as a function of the principal quantum number  $n$ . The logarithmic scale  $\log(\sigma_{n,l=n-1}^{thr})$  is presented in the vertical axis.

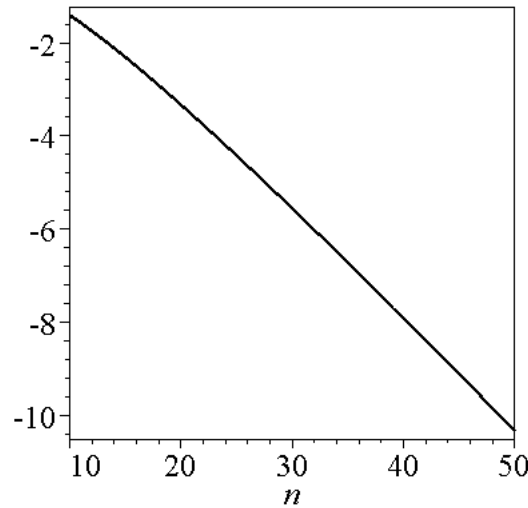
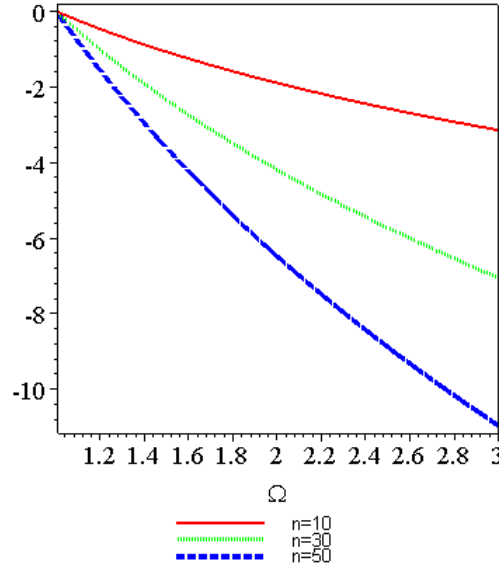


Figure 2. Dependences on the normalized frequency  $\Omega = \omega / |E_{nl}|$  of the fractional photoionization cross sections (9) for circular Rydberg states. The logarithmic scale,  $\log(f_n(\omega))$ , is given in the vertical axis.



#### 4. Asymptotic features of natural widths, photoionization cross sections and BBR-induced shifts and broadening of states with low angular momenta.

The basic optical characteristics for the low- $l$  states in many-electron atoms may differ significantly from those described above. In particular, due to a more rapid spontaneous decay, the natural lifetimes and corresponding line widths exceed those of the high- $l$  states. In addition, the cross sections of photoionization from the low- $l$  states do not vanish exponentially. Moreover, the threshold ionization cross section grows up together with the principal quantum number as  $\sigma_{n,l}^{thr} \propto n^{5/3}$  [6] and in the above-threshold region it does not decrease exponentially with frequency, but follows the power law (6). The dynamic polarizabilities of the low- $l$  states for the bulk of the BBR frequencies experience significant departures from the asymptotic law (1). In addition, the Rydberg states with  $l < 5$  in many-electron atoms have significant quantum defects which can modify the oscillator-strength sum rules. Therefore, the results of calculations based on different approximations to the radial wave functions of the low-angular-momentum states may differ significantly.

We consider two methods which use quantum defects for modifications of the Coulomb (hydrogenic) radial wave functions for describing the single-electron wave function in a many-electron atom, the Quantum Defect Method (QDM) [15] and the Fues' Model Potential (FMP) approximation [16]. The both approaches deal with one and the same object and modify the Coulomb wave function so as to take into account the exact single-electron spectrum of energies. To this end, the non-integer effective principal quantum number (PQN)  $\nu_{nl}$  is introduced instead of the integer PQN  $n$  at the cost of singularity of the wave function in the origin in the QDM approach and at the cost of introduction of the non-integer angular momentum  $l \rightarrow \lambda = \sqrt{(l+1/2)^2 + 2B_l} - 1/2 \neq l$  in the FMP approximation, where the model potential

$$\hat{V}_F(\mathbf{r}) = -\frac{Z}{r} + \sum_{l=0}^{\infty} \frac{B_l}{r^2} \sum_{m=-l}^l \hat{P}_{lm}(\theta, \varphi) \quad (10)$$

may import significant deviations to the centrifugal potential (5) and to the corresponding radial wave functions of the external-electron states.

Additional restrictions appear in the use of the QDM which becomes inapplicable to describing wave functions of low-energy states with high angular momentum  $l > \nu_{nl}$  (np<sup>6</sup> ground states of inert atoms, nd-states in alkaline-earth atoms and ions, etc.). Similar difficulties, caused by significant departures of the model potential (10) from the really existing centrifugal potential (5) inside the atomic core, may appear in the FMP approach for states with  $|\lambda - l| > 1$ . The most spectacular manifestation of these difficulties is the departure of the dipole-transition oscillator strengths  $2\omega_{n'l',nl} |\langle n'l' | z | nl \rangle|^2$ , determined by the FMP wave functions of such states, from the most reliable data of the literature ( $z$  is the component of the valence-electron position vector). These departures cause corresponding deviations from the Thomas-Reiche-Kuhn sum rules. This effect is due to the second term of the potential (10) with the sum of projection operators  $\hat{P}_{lm}(\theta, \varphi) = |Y_{lm}(\theta, \varphi)\rangle \langle Y_{lm}^*(\theta, \varphi)|$ , where the integration is implied over the angular variables  $\theta, \varphi$  of the position vector  $\mathbf{r}$ . This non-local term does not commute with the operator of dipole moment and introduces corresponding corrections to the sum rules:

$$S_{nl}(q) = \sum_{n'l'} 2\omega_{n'l',nl}^{1+q} |\langle n'l' | z | nl \rangle|^2 \quad (11)$$

So, for the basic sum rule,  $q=0$ , which in the single-electron approximation should equal unity, the wave-functions of the FMP approach give

$$S_{nl}(0) = 1 + \frac{2}{3(2l+1)} [lB_{l-1} + (l+1)B_{l+1} - (2l+1)B_l]. \quad (12)$$

This sum appears in the asymptotic value of the BBR-induced shift (the real part of equation (4)). The asymptotic value of BBR-induced broadening (the imaginary part of equation (4)) involves the sum  $q=l$ , which also includes the corrections appearing from the non-local part of the FMP (10):

$$S_{nl}(1) = \frac{Z^2}{3\nu_{nl}^2} \left[ 1 + \frac{l(B_l - B_{l-1})^2 + (l+1)(B_l - B_{l+1})^2}{(2l+1)(\lambda_l + 1/2)\nu_{nl}} \right], \quad (13)$$

However, the correction, determined in (13) by the fraction in the brackets, gradually decreases with the increase of the effective quantum number of the Rydberg state  $\nu_{nl}$  and becomes negligibly small for sufficiently high energy levels.

## 5. Natural widths and BBR-induced shifts and broadening of Rydberg states in Mg<sup>+</sup> ions.

So, in calculating BBR-induced shifts of Rydberg levels of small angular momenta with the use of the FMP approach, the results may differ considerably from the asymptotic values of equation (4). Nevertheless, for imaginary parts of (4), describing the broadening of high-energy Rydberg states ( $\nu_{nl} \gg 1$ ), the corrections disappear as is seen from (13) and the data for the coefficients  $B_l$  of the FMP (10) presented in table 1. Therefore the data for the natural widths and BBR-induced broadening may be determined in the FMP approximation.

Tab. 1. Numerical values of parameters  $B_l$  of the potential (10) and corresponding effective orbital momenta  $\lambda_l$  for S-, P-, D- and F-series of Rydberg states in Mg<sup>+</sup> ions

series	S <sub>1/2</sub>	P <sub>1/2</sub>	P <sub>3/2</sub>	D <sub>3/2</sub>	D <sub>5/2</sub>	F <sub>5/2,7/2</sub>
$B_l$	−0.031945	0.496937	0.499249	−0.111258	−0.111341	−0.0116302
$\lambda_l$	−0.068595	1.30108	1.30236	1.95509	1.95506	2.99668

From the FMP-data for spontaneous radiation-decay rates of the  $nS$  Rydberg states  $\Gamma_{nS}^{sp}$ , the asymptotic equation was derived for the natural lifetimes which is well consistent with the data of the literature and reproduces with a good precision the results of calculations in the QDM:

$$\tau_{nS}^{sp} = \frac{1}{\Gamma_{nS}^{sp}} = 0.063914n^3 \left( 1 - \frac{3.22}{n} + \frac{6.46}{n^2} - \frac{0.367}{n^3} \right) \text{ ns} \quad (14)$$

The asymptotic approximation for the lifetime of  $nP$ -states may be written as

$$\tau_{nP}^{sp} = 1.59894n^3 \left( 1 - \frac{2.394}{n} - \frac{56.42}{n^2} + \frac{342.5}{n^3} \right) \text{ ns} \quad (15)$$

Evidently, the  $nP$ -states are about 20-30 times longer living than the states of  $nS$ -series.

The BBR-induced broadening of the  $nl$ -states includes three separate kinds of transitions. One of them corresponds to the rate of BBR-stimulated downward transitions (decays)  $\Gamma_{nl}^d(T)$ , which is temperature-dependent and conveniently described by the fractional rate of decays  $R_{nl}^d = \Gamma_{nl}^d / \Gamma_{nl}^{sp}$ . The two remaining are the upward BBR-supported transitions: excitations of the upper bound levels determined by the fractional rate of excitations  $R_{nl}^{exc} = \Gamma_{nl}^{exc} / \Gamma_{nl}^{sp}$ , and BBR-induced transitions into continuum – photoionization, which is also determined by the fractional rate of ionization  $R_{nl}^{ion} = \Gamma_{nl}^{ion} / \Gamma_{nl}^{sp}$ . Thus, the  $nS$ -level broadening may be determined as

$$\Gamma_{nl}^{BBR}(T) = \Gamma_{nl}^{sp} (R_{nl}^d + R_{nl}^{exc} + R_{nl}^{ion}). \quad (16)$$

The separate terms in parenthesis are temperature dependent and in asymptotic region  $|E_{nl}| \ll kT$  are linear proportional to  $T$ . However, the dependence on the principal quantum number of  $R_{nl}^{ion}(T)$  differs from those of  $R_{nl}^{d(exc)}(T)$ , at least for the low- $l$  states [14]. This effect comes from different energy separation between states providing principal contributions to the three processes. Therefore, the rates of decays and excitations may be described by one and the same asymptotic interpolation equation:

$$R_{nl}^{d(exc)}(t) = \frac{a_0^{d(exc)}(T) + a_1^{d(exc)}(T)x + a_2^{d(exc)}(T)x^2}{n^2 \left[ \exp\left(\frac{Z^2 T_a}{n^3 T}\right) - 1 \right]}, \quad x = \frac{100}{nT^{1/3}}, \quad (17)$$

whereas the fractional rate of ionization is approximated by the equation

$$R_{nl}^{ion}(t) = \frac{a_0^{ion}(T) + a_1^{ion}(T)y + a_2^{ion}(T)y^2}{n^q \left[ \exp\left(\frac{Z^2 T_a}{2n^2 T}\right) - 1 \right]}, \quad y = \frac{100}{nT^{1/2}}, \quad (18)$$

where the exponent  $q=4/3$  for states  $l \neq 0$ . For  $nS$ -states the fitting procedures fix different values of  $q$  starting from  $1/4$  to  $3/4$  in different regions of  $n$ . The smooth dependence on the temperature of the coefficients  $a_i^{d(exc,ion)}(T)$  may also be polynomial-approximated, as follows:



$$a_i^{d(exc)} = \sum_{k=0}^2 b_{ik}^{d(exc)} t^k, \quad t = \left( \frac{100}{T} \right)^{1/3}; \quad a_i^{ion} = \sum_{k=0}^2 b_{ik}^{ion} \tau^k, \quad \tau = \left( \frac{100}{T} \right)^{1/2}. \quad (19)$$

The coefficients  $b_{ik}$  are constants, independent of  $n$  and  $T$ , determined by fitting the calculated data for the fractional rates for rather high Rydberg states of the series  $nl$ . Numerical values of the coefficient for  $nP$ -series of states in  $Mg^+$  ions are presented in table 2.

Tab.2. Numerical values of coefficients  $b_{ik}$  in the temperature-dependent polynomials (19) determining the coefficients of the asymptotic presentations (17), (18) for the rates of the BBR-induced radiation transitions from Rydberg  $nP$ -states of  $Mg^+$  ions.

$i$	$b_{i0}^d$	$b_{i1}^d$	$b_{i2}^d$	$b_{i0}^{exc}$	$b_{i1}^{exc}$	$b_{i2}^{exc}$	$b_{i0}^{ion}$	$b_{i1}^{ion}$	$b_{i2}^{ion}$
0	129.96	-20.83	21.32	391.24	-56.77	63.42	157.6	-66.62	5.372
1	-46.62	125.27	-133.8	-645.2	1108.8	-744.8	-2529	3450	-1532
2	-150.5	263.5	-28.36	307.0	-873.5	682.9	12612	-25180	13580

The real part of the shift (4) may also be approximated asymptotically as

$$\varepsilon_{nl}^{BBR} = 2416.6 \left( \frac{T}{300 \text{ K}} \right)^2 \left( a_0^\varepsilon(T) + a_1^\varepsilon(T)z + a_2^\varepsilon(T)z^2 \right) \text{ Hz}, \quad z = \left| \frac{E_{nl}}{kT} \right|^{1/2}$$

with coefficients smoothly dependent on the temperature, similar to (19):

$$a_i^\varepsilon = \sum_{k=0}^2 b_{ik}^\varepsilon \tau^k, \quad \tau = \left( \frac{100 \text{ K}}{T} \right)^{1/2}.$$

The coefficients  $b_{ik}^\varepsilon$  are constant values for each  $nl$ -series of states.

## Acknowledgments

This work was supported in part by the Russian Foundation for Basic Research (RFBR) grant No.14-02-00516-a.

## 6. References

- [1] Zong-Chao Yan 2000 *Phys. Rev. A* **62** 052502.
- [2] Il'inova E Yu, Kamenski A A and Ovsiannikov V D 2009 *J. Phys. B* **42** 145004.
- [3] Manakov N L, Ovsiannikov V D and Rapoport L P 1986 *Phys. Rep.* **141** 319.
- [4] Davydkin V A, Ovsiannikov V D and Zon B A 1993 *Laser Phys.* **3** 449.
- [5] Krylovetsky A A, Manakov N L and Marmo S I 2005 *J. Phys. B* **38** 311.
- [6] Delone N B, Goreslavsky S P and Krainov V P 1994 *J. Phys. B* **27** 4403.
- [7] Ovsiannikov V D, Glukhov I L and Nekipelov E A 2012 *J. Phys. B* **45** 095003.
- [8] Gallagher T F and Cooke W E 1979 *Phys. Rev. Lett.* **42** 835.
- [9] Cooke W E and Gallagher T F, 1980 *Phys. Rev. A* **21** 588.
- [10] Bethe H S and Salpeter E E 1957 *Quantum Mechanics of One- and Two-Electron Atoms* (New-York: Springer).
- [11] Fano U and Cooper J W 1968 *Rev. Mod. Phys.* **40** 441.
- [12] Farley J W and Wing W H 1981 *Phys. Rev. A* **23** 2397.
- [13] Glukhov I L, Nekipelov E A and Ovsiannikov V D 2010 *J. Phys. B* **43** 125002.
- [14] Ovsiannikov V D, Glukhov I L and Nekipelov E A 2011 *J. Phys. B* **44** 195010.
- [15] Bates D R and Damgaard A 1949 *Phil. Trans. A* **242** 101.
- [16] Simons G 1971 *J. Chem. Phys.* **55** 756; *ibid* **60** 645; *ibid* **62** 4799.
- [17] Derevianko A et al 1999 *JETP* **88** 272.

# TRANSVERSE ELECTRON MOMENTUM DISTRIBUTION FOR ARBITRARY POLARIZATION STATE OF THE IONIZING LASER PULSE

Igor Ivanov, Anatoli Kheifets

*Research School of Physical Sciences,  
The Australian National University  
E-mail: igor.ivanov@anu.edu.au*

We study evolution of the distribution of electron momenta in the direction perpendicular to the polarization plane with the change of the ellipticity parameter of the driving laser pulse. We show, that the distribution gradually changes from the singular cusp-like distribution for the close to linear polarization to the smooth gaussian-like structure for the close to circular polarization states. In the latter case, when the ellipticity parameter is close to 1, the strong field approximation formula for the transverse momentum distribution become quantitatively correct.

## 1. Introduction

Tunneling theories of photo-ionization are of great importance in understanding atomic or molecular ionization by strong infrared (IR) laser field. By tunneling theories we mean here a broad class of theories developing the pioneering work on the strong field approximation (SFA) by Keldysh [1]. The SFA in its original form did not include any interaction of ejected electron and parental ion. The importance of the effect of the Coulomb field of the parental ion on the ionization process has long been realized. Coulomb field of the residual ion was found responsible for such effects as low energy structures in electron spectra, Coulomb focusing, asymmetry in the spectra of above threshold ionization spectra, formation of a cusp in the transverse (i.e. in the direction perpendicular to the polarization plane) electron momentum distribution.

It is known, that for the case of the linearly polarized laser pulse, the transverse electron momentum distribution exhibits a sharp cusp-like peak at zero transverse momentum [2]. For the case of the circularly polarized light, on the contrary, this distribution was found not to deviate considerably from the gaussian-like structure predicted by the SFA [3]. We see, thus, two different forms (cusp-like and gaussian-like) of the transverse electron momentum distribution for two limiting polarization states of the driving pulse. The aim of the present work is to study transition between these two forms in detail. We shall consider below atom in the field of an elliptically polarized laser pulse, and consider evolution of the transverse electron momentum distribution with varying ellipticity. We use hydrogen atom as a model, atomic units are used below.

## 2. Theory

We solve the time-dependent Schrödinger equation (TDSE) for a hydrogen atom in the field of a circularly polarized laser pulse:

$$i \frac{\partial \Psi}{\partial t} = \hat{H}(t) \Psi \quad (1)$$

We follow the strategy we described in papers [4,5]. The wave function is represented as a series:

$$\Psi(t) = \sum_{lm} f_{lm}(r, t) Y_{lm}(\theta, \varphi) \quad (2)$$

Substitution of the expansion (2) into the TDSE gives us a system of coupled equations for the radial functions, describing evolution of the system in time. To solve this system we use the matrix iteration method [6]. Ionization amplitudes and electron momentum distributions are obtained by projecting solution of the TDSE at the end of the laser pulse on the set of the ingoing scattering states of hydrogen atom. We are interested in the transverse (i.e. in the direction perpendicular to the polarization plane) momentum distribution. For this distribution SFA predicts a smooth Gaussian form (here  $I$  is the ionization potential,  $E$ - the field strength, and  $\varepsilon$ - the ellipticity parameter of the laser pulse):

$$W(p_{\perp}) \propto \exp\left\{-\frac{(2I)^{1/2}\sqrt{1+\varepsilon^2}}{E}p_{\perp}^2\right\} \quad (3)$$

This smooth distribution is in striking contrast to the cusp-like structure observed in the experiment [2] for the ionization of noble gases by linearly polarized laser field. This cusp-like structure has been attributed to the Coulomb effects, which are, of course, neglected in the SFA. In the next section we shall present results of a systematic study of the perpendicular momentum distributions for various polarization states of the driving laser pulse. We shall see, that when state of polarization varies between linear and circular polarizations, spectra evolve from the cusp-like spectra observed in [2] to the gaussian form predicted by the SFA and observed in [3].

### 3. Results

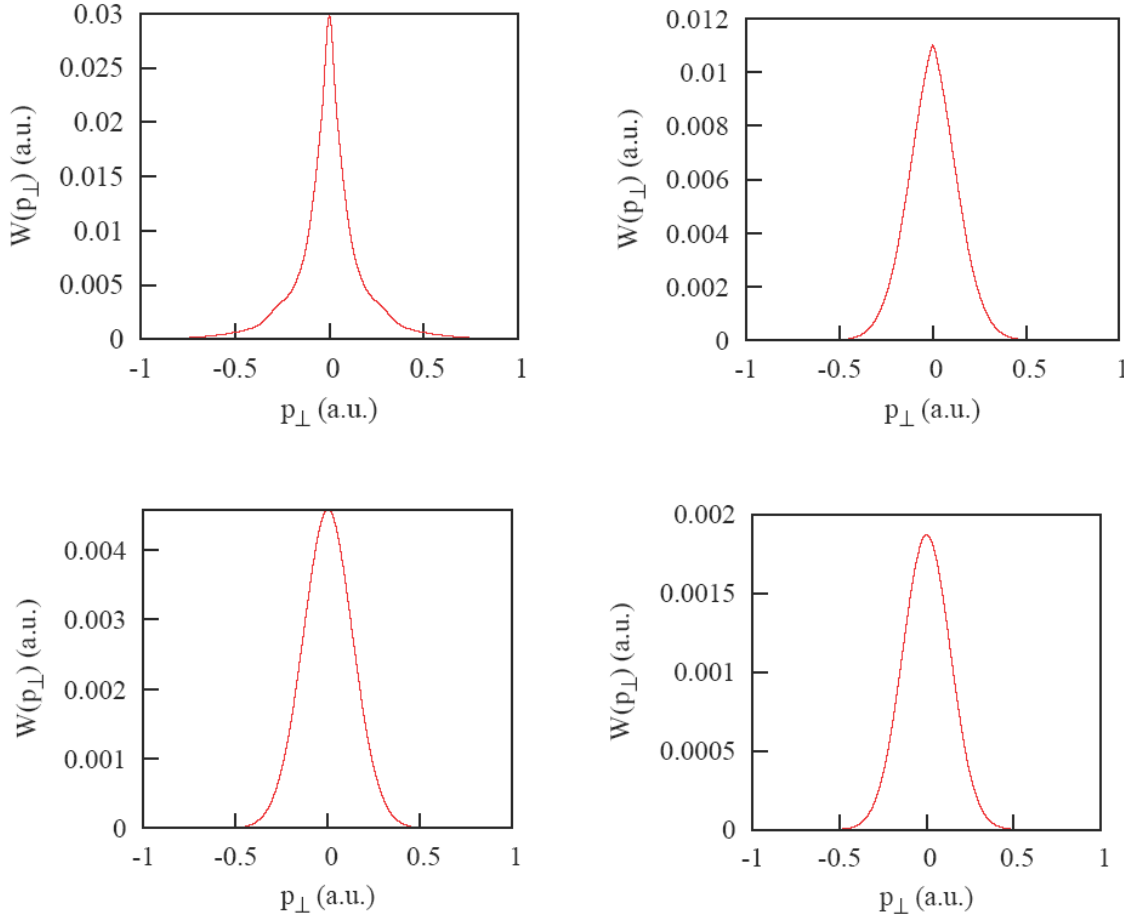


Fig. 1. Transverse electron momentum distribution for the following values of the ellipticity parameter: 0,0.5,0.7,1 (left to right, top to bottom). Pulse parameters: field strength 0.0534 a.u., frequency 0.057 a.u., pulse duration- four optical cycles.

Fig. 1 shows evolution of the transverse electron momentum distribution with varying ellipticity parameter. A feature clearly seen in the figure is the gradual transition from the cusp-like structure in the spectra to the smooth gaussian form predicted by the SFA.

## 4. References

- [1] Keldysh L. V. 1965 *Sov. Phys. -JETP* **20** 1307.
- [2] Rudenko A., Zrost K., Ergler T., Voitkiv A. B., Najjari B., de Jesus V. L. B., Feuerstein B., Schröter C. D., Moshhammer R., and Ullrich J., 2005 *Journal of Physics B* **38** L191.
- [3] Arissian L., Smeenck C., Turner F., Trallero C., Sokolov A. V., Villeneuve D. M., Staudte A., and Corkum P. B., 2010 *Physical Review Letters* **105** 133002.
- [4] Ivanov I. A. 2011 *Physical Review A* **83** 023421.
- [5] Ivanov I. A. and Kheifets A. S., 2013 *Physical Review A* **87** 033407.
- [6] Nurhuda M. and Faisal F. H. M., 1999 *Physical Review A* **60** 3125.

# ELECTRON ATTACHMENT TO TETRAFLUOROQUINONE

B. Ómarsson and O. Ingólfsson

*Science Institute and University of Iceland, Dunhaga 3, 107 Reykjavik, Iceland*

E-mail: odduring@hi.is

Electron attachment to tetrafluoro-*para*-benzoquinone (TFQ) is studied within the energy range 0–15 eV. The molecular anion is observed with high intensity close to 0 eV, and also near 0.5 eV. Extensive fragmentation is also observed through dissociative electron attachment (DEA), leading to the formation of  $[\text{TFQ} - \text{CO} - n\text{F}]^-$  ( $n = 0-3$ ) and  $[\text{TFQ} - 2\text{CO} - n\text{F}]^-$  ( $n = 0-4$ ). The most striking channel in DEA to TFQ is the formation of  $\text{C}_4^-$ , with a threshold at approximately 2.7 eV. This channel requires the formation of two neutral  $\text{F}_2\text{CO}$  molecules and recombination of the C-C units to form the anionic 4-carbon chain. The results are discussed in conjunction with quantum mechanical calculations carried out to determine the thermochemical thresholds for the processes.

## 1. Introduction

Quinones and quinone derivatives are a class of organic compounds that play an essential role in electron transfer processes in nature. Among these are the charge-transfer processes behind the production of ATP [1], where a paraquinone derivative, coenzyme Q, plays a vital role. Another example is the role of plastoquinones (simple para-benzoquinone (p-BQ) derivatives), in photosynthesis [2,3]. Hence, quinone derivatives are crucial in some of the most important processes in living organisms and probably present in some form in every living cell. Correspondingly, the simplest para-quinone, p-benzoquinone ( $\text{C}_6\text{H}_4\text{O}_2$ ), has been studied quite extensively with regards to the formation and decay of its molecular anion. These studies include electron swarm experiments [4, 5], a electron transfer and  $\text{SF}_6$  scavenger study [6] and a recent crossed beam electron attachment study [7].

Here, we summarize results from electron attachment to tetrafluoro-*para*-benzoquinone (TFQ), which we have discussed in detail elsewhere [8]. While the metastable molecular anion is observed at incident electron energies well above 0 eV dissociative electron attachment (DEA) leads to a distinct fragmentation patterns which we discuss here in relation to our calculations of the respective thermochemical thresholds. The observed fragmentation reactions can largely be described through two dissociation series: the formation of  $[\text{TFQ} - \text{CO} - n\text{F}]^-$  ( $n = 0-3$ ) and the formation of  $[\text{TFQ} - 2\text{CO} - n\text{F}]^-$  ( $n = 0-4$ ). The most striking fragment in DEA to TFQ, observed at incident electron energy as low as  $\sim 2.7$  eV, is the formation of  $\text{C}_4^-$ , which requires the formation of two neutral  $\text{F}_2\text{CO}$  molecules and recombination of the remaining moiety to form an anionic 4-carbon chain to be thermochemically possible at this low incident electron energy.

In addition to the complex dissociation channels, TFQ forms a long-lived metastable molecular anion at unusually high incident electron energy in electron attachment under single collision conditions. This rare ability, which is common to quite a few quinone derivatives [9-11], is also observed in electron attachment to para-benzoquinone [4-7, 12].

## 2. Methods

### 2.1 Experimental setup

The electron attachment measurements were conducted using a high vacuum (HV) crossed electron-molecule beam apparatus located at the Science Institute, University of Iceland. The experimental setup has been described in detail elsewhere [13] and we thus only give a brief description here. A fairly monochromatic electron beam is generated with a trochoidal electron monochromator (TEM) and crossed with an effusive gas beam entering the chamber through a stainless-steel inlet system. In the present study, the inlet system was kept at a constant temperature of approximately 80 °C and the monochromator was kept at 120 °C. The ions generated are analyzed with a Hiden Epic 1000 quadrupole mass spectrometer and detected with a channeltron. The electron energy scale was calibrated to the

formation of  $\text{SF}_6^-$  from  $\text{SF}_6$  at 0 eV and the electron energy resolution ( $\sim 120\text{--}140$  meV) was estimated from the full-width at half-maximum (FWHM) of the  $\text{SF}_6^-$  signal. The base pressure in the HV chamber is on the order of  $10^{-8}$  mbar and the working pressure was kept constant at around  $5 \times 10^{-7}$  mbar.

## 2.2 Calculations

Geometry optimizations and single point energy calculations were performed using the computational chemistry software Orca 2.9 [14]. The geometry of all molecules and fragments was optimized at the B3LYP/ma-TZVP level of theory [15] and single point energy calculations were performed at the B2PLYP/ma-TZVP level of theory [16]. Zero-point vibrational energy from harmonic vibrational frequency calculations was added to the total energy for each calculated species. The reaction enthalpy ( $\Delta H$ ) at 0 K was then obtained by subtracting the total energy of all fragments for a given dissociation channel from the total energy of the parent molecule. The thermal energy of the parent molecule at 80 °C was further subtracted from the reaction threshold to account for the experimental temperature. From the harmonic vibrational frequency calculations this factor has been determined to be 382 meV.

## 3. Results and discussion

Figure 1 shows the ion yield curve for the parent molecular anion ( $m/z$  180). The main contribution is observed close to 0 eV, but a distinct maxima is also observed close to 0.5 eV. We have discussed these contributions in detail earlier [8] where we tentatively attribute the 0 eV contribution to a single electron occupation of the  $A_1$  symmetry LUMO and the 0.5 eV contribution to the lower energy side of a  ${}^2B_u$  shape resonance, associated with single electron occupation of the LUMO+1. Figures 2 and 3 show the ion yield curves from DEA to TFQ in the energy range from 0-15 eV. The fragmentation can largely be described by the loss of one (fig. 2) and two (fig. 3) CO molecules and 0-3 and 0-4 fluorines, respectively. Hence, the formation of the anionic fragments  $[\text{M} - \text{CO} - n\text{F}]^-$  ( $n = 0\text{--}3$ ) and that of  $[\text{M} - 2\text{CO} - n\text{F}]^-$  ( $n = 0\text{--}4$ ).

The dominating DEA reaction observed from TFQ is the loss of a single neutral CO molecule (fig. 2a), observed through a resonance close to 1 eV. We find the thermochemical threshold for this dissociation channel to be  $-1.32$  eV if we assume the  $[\text{M} - \text{CO}]^-$  fragment to rearrange to form a five-membered ring. In electron attachment to TFQ, the parent anion is predominately observed through a

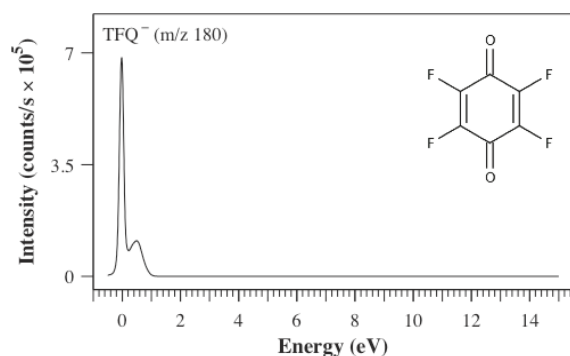


Fig. 1. The parent molecular anion observed in electron attachment to TFQ.

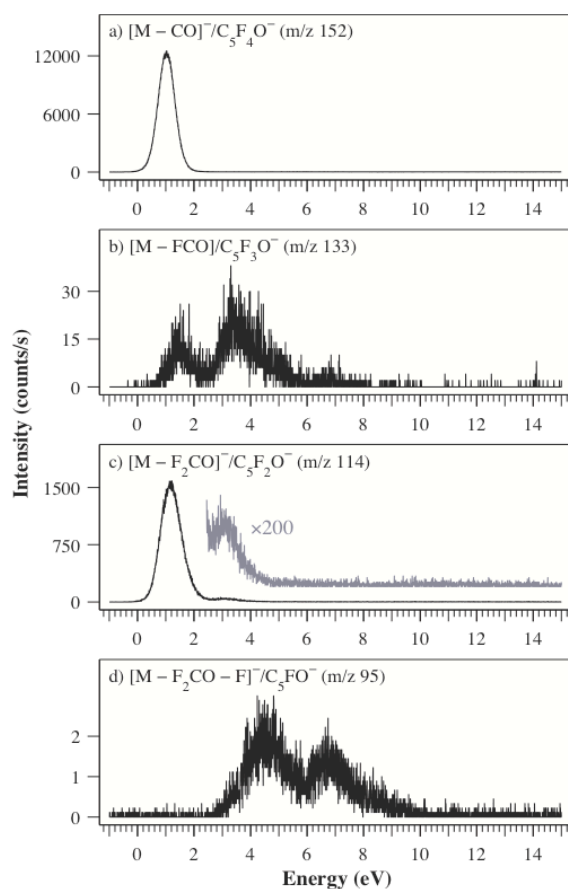


Fig. 2. Ion yield curves from DEA to TFQ showing the loss of one CO unit (a) and that of one CO unit and 1-3 fluorines (b-d).

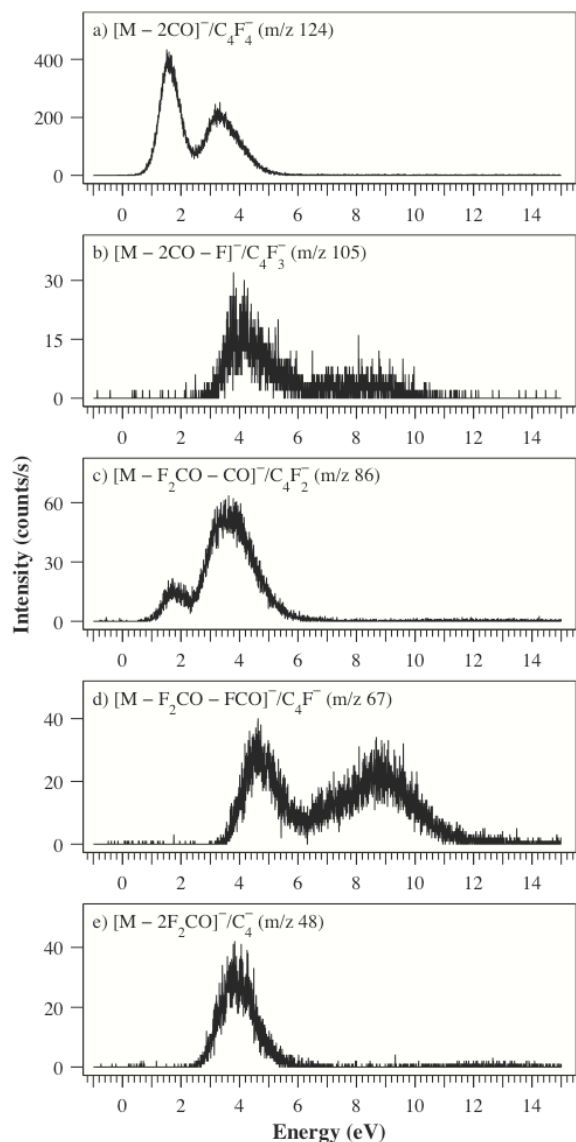


Fig. 3. Ion yield curves from DEA to TFQ showing the loss of two CO units (a) and that of two CO unit and 1-4 fluorines (b-e). Note that panel e) shows the ion yield curve for the formation of  $C_4^-$ .

e in fig. 2. This fragment, a linear carbon chain, is observed through a single resonant contribution with an onset close to 2.7 eV and a maximum close to 4 eV. The thermochemical threshold we calculate for this channel is 2.33 eV, assuming the formation of two neutral  $F_2CO$  molecules and a linear 4-carbon anion.

## 4. Conclusions

Low energy electron attachment to TFQ leads predominantly to the formation of the metastable molecular anion close to 0 eV. However, within the timeframe of our experiment (about 50  $\mu$ s) the molecular anion is also observed through a higher-lying resonance, with the ion yield peaking close to 0.5 eV. Though the molecular anion is the dominating ion observed, a number of complex fragmentation channels are also observed. These can largely be described through two dissociation series: the formation of  $[TFQ - CO - nF]^-$  ( $n = 0, 1, 2$  or  $3$ ) and that of  $[TFQ - 2 CO - nF]^-$  ( $n = 0, 1, 2, 3$  or  $4$ ). The most striking fragment is clearly  $C_4^-$ , which is formed at an incident electron energy as

resonance close to 0 eV (fig. 1). However, though CO loss from the molecular anion is an exothermic reaction, this channel is not observed at 0 eV. This is due to a high reaction barrier on the reaction path for the loss of CO from TFQ, as is discussed in detail in reference [8]. Somewhat surprisingly, the second most efficient channel from TFQ is the loss of CO and two fluorines, and not the loss of CO and one fluorine (see panels b and c in fig. 2). This is, however, readily understandable from thermochemical considerations alone, if we presume that these channels proceed through the formation of  $F_2CO$  and  $FCO$ , respectively. In this case, the thermochemical threshold for the formation of  $[M - F_2CO]^-$  is -0.46 eV and that for the formation of  $[M - FCO]^-$  is 1.06 eV. Finally, the formation of  $[M - F_2CO - F]^-$  is only observed through higher lying resonances and with limited ion yield. For this channel we find the lowest threshold to be 1.55 eV.

From the  $[M - 2CO - nF]^-$  ( $n = 0-4$ ) fragmentation channels shown in figure 3, the dominating ion is  $[M - 2CO]^-$ , i.e., the loss of two neutral CO molecules from TFQ. From thermochemical calculations we find a reaction threshold of 0.64 eV for this channel, assuming rearrangement that leads to a quasi-linear  $F_2CCCCF_2^-$  anion. The loss of two COs and one fluorine, shown in figure 3b, and the loss of two CO and three fluorines, shown in figure 3d, are only observed at fairly high energies through two resonances close to 4 and 8 eV. This is in good agreement with our thermochemical calculations, which place the threshold for these channels at 2.43 and 3.19 eV, respectively. The loss of two COs and two fluorines is thermochemically more favourable and is already observed at about 1 eV (fig 3c). This is in good agreement with the threshold of 1.22 eV that we calculate by assuming  $F_2CO$  formation and a rearrangement of the anionic fragment to form  $F_2CCCC^-$ , a linear carbon chain with two terminal fluorines. The most remarkable channel observed in DEA to TFQ is the formation of  $C_4^-$ , shown in panel

low as ~2.7 eV. This fragment can only be formed through the loss of both CO units and all fluorines, along with recombination of the two C-C units to form an anionic 4-carbon chain. From thermochemical considerations, this fragment also requires the formation of two neutral F<sub>2</sub>CO molecules in the process.

## Acknowledgements

The authors acknowledge financial support from the Icelandic Centre for Research (RANNIS) and the University of Iceland Research Fund. Special thanks goes to Dr. Ragnar Björnsson for technical assistance concerning calculations. This work was conducted within the framework of the COST action MP1002 on Nanoscale Insights into Ion Beam Cancer Therapy.

## 5. References

- [1] F. L. Crane, *J. Am. Coll. Nutr.*, 2001, **20**, 591–598.
- [2] A. Trebst, *Phil. Trans. R. Soc. B*, 1978, **284**, 591–599.
- [3] J.-D. Rochaix, *BBA - Bioenergetics*, 2011, **1807**, 375–383.
- [4] L. G. Christophorou, J. G. Carter, and A. A. Christodoulides, *Chem. Phys. Lett.*, 1969, **3**, 237–240.
- [5] P. M. Collins, L. G. Christophorou, E. L. Chaney, and J. G. Carter, *Chem. Phys. Lett.*, 1970, **4**, 646–650.
- [6] C. D. Cooper, W. T. Naff, and R. N. Compton, *J. Chem. Phys.*, 1975, **63**, 2752.
- [7] O. G. Khvostenko, P. V. Shchukin, G. M. Tuimedov, M. V. Muftakhov, E. E. Tseplin, S. N. Tseplina, and V. A. Mazunov, *Int. J. Mass. Spectrom.*, 2008, **273**, 69–77.
- [8] B. Ómarsson, O. Ingólfsson, *Phys. Chem. Chem. Phys.*, 2013, **15** (39), 16758–16767
- [9] P. M. Collins, L. G. Christophorou, E. L. Chaney, and J. G. Carter, *Chem. Phys. Lett.*, 1970, **4**, 646–650.
- [10] S. A. Pshenichnyuk, A. S. Vorob'ev, N. L. Asfandiarov, and A. Modelli, *J. Chem. Phys.*, 2010, **132**, 244313.
- [11] O. G. Khvostenko, V. G. Lukin, and E. E. Tseplin, *Rapid Commun. Mass Spectrom.*, 2012, **26**, 2535–2547.
- [12] M. Allan, *Chem. Phys.*, 1983, **81**, 235–241.
- [13] E. H. Bjarnason, B. Ómarsson, S. Engmann, F. H. Ómarsson and O. Ingoólfsson, *Eur. Phys. J. D*, 2014, **68**, 121.
- [14] F. Neese, *WIREs Comput. Mol. Sci.* 2012, **2**, 73
- [15] J. Zheng, X. Xu, and D. G. Truhlar, *Theor. Chem. Acc.*, 2010, **128**, 295–305.
- [16] S. Grimme, *J. Chem. Phys.*, 2006, **124**, 034108.



## ELASTICALLY AND INELASTICALLY TRANSMITTED ELECTRONS THROUGH INSULATING PET NANOCAPILLARIES

D. Keerthisinghe<sup>1</sup>, B. S. Dassanayake<sup>2</sup>, S. J. Wickramarachchi<sup>1</sup>, N. Stolterfoht<sup>3</sup> and  
J. A. Tanis<sup>1</sup>

<sup>1</sup>Department of Physics, Western Michigan University, Kalamazoo, Michigan, 49008, USA <sup>2</sup>Department of  
Physics, University of Peradeniya, Peradeniya, Sri Lanka

<sup>3</sup>Helmholtz-Zentrum Berlin für Materialien und Energie, D-14109, Berlin, Germany  
mail: [darshika.keerthisinghe@wmich.edu](mailto:darshika.keerthisinghe@wmich.edu)

E-

Transmission of electrons through PET nanocapillaries at incident energies of 300, 500 and 800 eV was studied for two samples with different capillary dimensions. Direct and indirect transmission with elastic and inelastic components was observed for both samples and the results are compared showing similar behaviors despite the different diameters and pore densities.

Transmission of electrons through insulating polyethylene terephthalate (PET) was measured for two samples with 100 and 200 nm diameters and  $5 \times 10^8/\text{cm}^2$  and  $5 \times 10^7/\text{cm}^2$  pore densities, respectively. The angular dependence study was performed for incident energies of 300, 500 and 800 eV for sample 1 and incident energies 500 and 800 eV for sample 2. The divergence of the beam for this work was  $\sim 0.4^\circ$  and  $\sim 0.6^\circ$  for samples 1 and 2, respectively. The angular dependence of electrons through PET has been studied previously by Das et al. for incident energies 500 and 1000 eV [1]. In the present work, both angular dependence and charge evolution studies were carried out. This work was done at Western Michigan University. The samples were mounted on a goniometer which was rotated around a vertical axis to give different tilt angles  $\psi$ . The observation angle  $\theta$  (the spectrometer had an inherent angular resolution  $\sim 0.3^\circ$ ) and the tilt angle  $\psi$  were measured with respect to the incident beam direction. The experimental set up can be found in a previous publication [2]. Energy spectra for the desired sample tilt angle and corresponding spectrometer angle were collected and normalized with respect to the incident beam.

**The variation of the normalized integrated transmitted intensity was studied for different tilt and spectrometer angles.** The sample was tilted in small steps near zero degrees where two peaks were observed as shown in Figure 1 for the tilt angles  $-1.5^\circ$  and  $-0.8^\circ$  (panels (c) and (d)) for samples 1 and 2, respectively. The intensity of the angular distribution decreases as the absolute value of the tilt angle increases and the two peaks become one peak when the sample reaches larger tilt angles (panels (e) and (f)). Preliminary findings for sample 1 have been published in Ref. 2. In the present work the relation of peak position, angular widths and the energy of outgoing electrons to tilt angle were studied. **The** angular profiles for each position were fit with Gaussian functions over the observation angles giving good fits.

Three regions were observed and are referred to as *direct*, *guiding* and the *transition* region between the two. The peak positions (observation angle) were found to be independent of tilt angle in the vicinity of zero degrees, and the peak positions are linearly related to the tilt angle in the guiding region. Both direct and guiding behavior is observed in the transition region. The angular widths (FWHM) are nearly independent of tilt angle in the direct and guiding regions having values  $\sim 0.7^\circ$  and  $\sim 1.5^\circ$ , respectively. The FWHM (deg.) in the direct region is a little more than twice the spectrometer resolution ( $\sim 0.3^\circ$ ) and half that of the guiding region value. The centroid energies (found from the energy spectra that correspond to peak positions of the angular profiles) are largest ( $\sim 304.5$ ,  $\sim 504.5$  and  $\sim 810.0$  eV) for the three incident energies 300, 500 and 800 eV in the direct region showing that there is little or no energy loss as electrons are transmitted on a straight line path

through the capillaries. Outgoing electrons that are guided can have smaller centroid energies due to deflection of electrons from the negative charge patch and due to close collisions of electrons with surface atoms. Similar behavior was observed for both samples despite the differences in the capillary diameters and the pore densities.

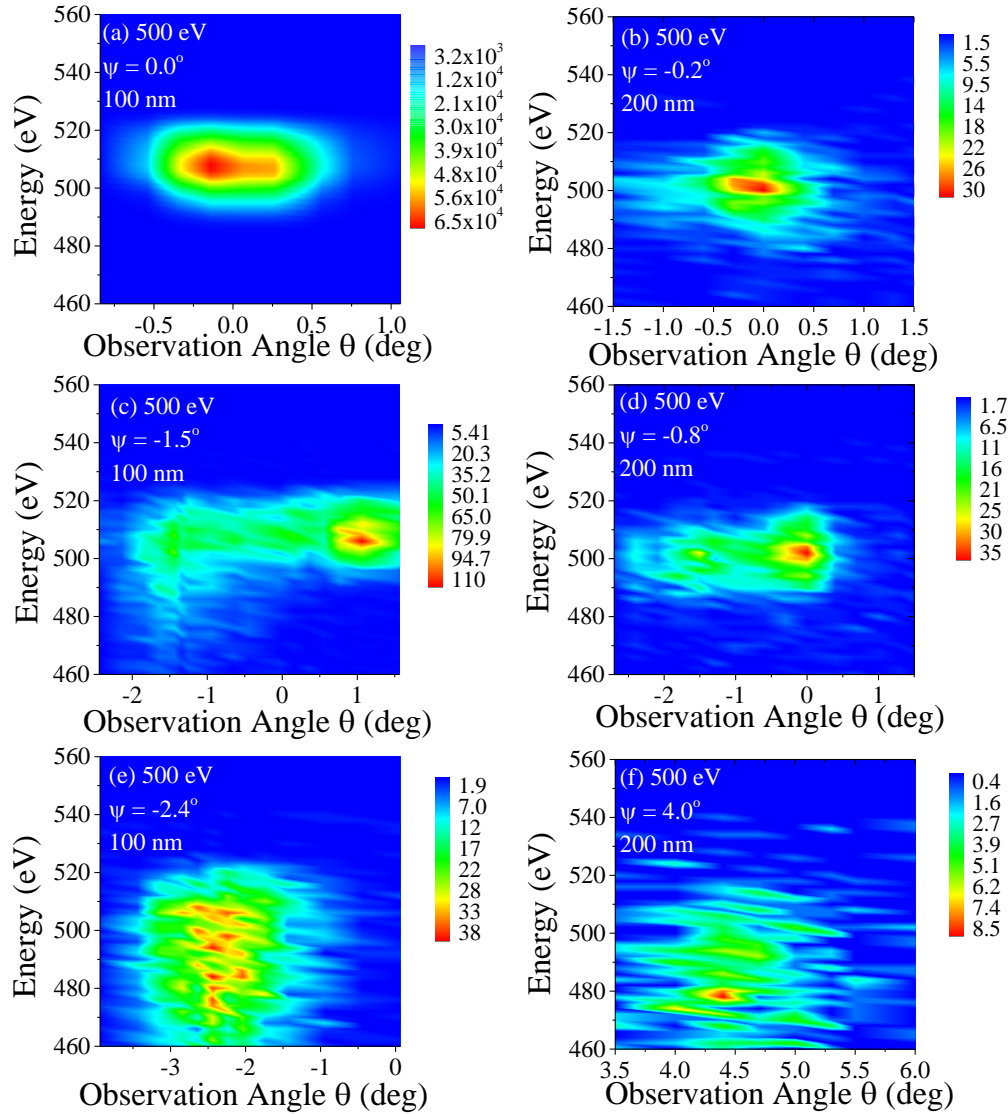


Fig.1 Contour plots for 500 eV incident electrons showing the angular distributions for selected tilt angles with the transmitted energy plotted against the observation angle  $\theta$  and the color representing the intensity at each point. Panels (a), (c) and (e) are for tilt angles  $\psi = 0.0^\circ$ ,  $-1.5^\circ$  and  $-2.4^\circ$  for sample 1 (100 nm) and panels (b), (d) and (f) are for tilt angles  $\psi = -0.2^\circ$ ,  $-0.8^\circ$  and  $4.0^\circ$  for sample 2 (200 nm).

## References

- [1] S. Das, B. S. Dassanayake, M. Winkworth, J. L. Baran, N. Stolterfoht, and J. A. Tanis, Phys. Rev. A **76**, 042716 (2007).

- [2] D. Keerthisinghe, B.S. Dassanayake, S. J. Wickramarachchi, A. Ayyad , N. Stolterfoht and J. A. Tanis, AIP Conf. Proc. **1525**, 36 (2013).

# LONG-RANGE TWO-ELECTRON EXCHANGE INTERACTION BETWEEN ATOMIC IONS AND POLAR MOLECULES

O.M. Karbovanets, M.I. Karbovanets, V.Yu. Lazur, M.V. Khoma

*Department of Theoretical Physics, Uzhhorod National University, Uzhhorod 88000, Ukraine*  
E-mail: m.khoma@gmail.com

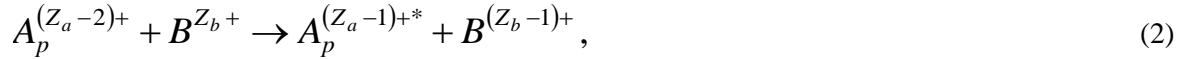
Processes of two-electron transfer in slow collisions of atomic ion with polar molecule has been considered. The closed analytic expression (in terms of full elliptic integrals) for matrix element of two-electron exchange interaction between atomic ion and polar target has been obtained. The wave functions of the initial and final states and corresponding exchange interaction potential has been constructed as the leading term of the semiclassical calculation in the framework of a surface integral method. The dynamical treatment of the collision process carried out using the impact parameter method with straight-line trajectories.

## 1. Introduction

The non-resonant two-electron transfer in slow collision between multicharged atomic ion  $B^{Z_b+}$  and polar molecule  $A_p^{(Z_a-2)+}$  attract continuous attention both from the theoretical and experimental groups [1,2]. The main elementary processes which occurs during the collision process are the non-dissociative one-electron capture



transfer excitation



and two-electron capture



We shall use the asymptotic version of the semiclassical approach for calculation of the exchange interaction potential and tunneling probability through the potential barrier between colliding particles.

The similar approach for studying the one-electron reaction of the type (1) have been considered in [1], we shall consider here elementary reactions of the type (2) and (3). In order to calculate asymptotically correct exchange matrix element  $H_{ab}$  responsible for reactions (2) and (3) it is necessary to use asymptotically correct two-electron wave function of the colliding system

$$[A_p B]^{(Z_a+Z_b-2)+} \quad (4)$$

which, at large projectile-target separation  $R$ , tend to unperturbed electronic wave functions of the isolated particles  $A_p^{(Z_a-2)+}$  and  $B^{(Z_b-2)+}$ . We shall assume that molecular  $A_p^{Z_a+}$  and ionic  $B^{Z_b+}$  cores remains unchanged during the collisional process. Atomic units will be used throughout the paper.

## 2. Calculation of the wave functions

In the two-electron approximation the electronic Hamiltonian of the system reads

$$H_{el} = -\frac{\Delta_1}{2} - \frac{\Delta_2}{2} + V_a(\vec{r}_{1a}) + V_a(\vec{r}_{2a}) + V_b(\vec{r}_{1b}) + V_b(\vec{r}_{2b}) + \frac{1}{r_{12}}, \quad (5)$$

here  $\vec{r}_{ia}$  ( $\vec{r}_{ib}$ ) are the radius-vector of the  $i$ -th electron with respect to the geometric center of particle  $A_p^{Z_a+}$  ( $B^{Z_b+}$ ) ( $i=1,2$ );  $V_a(\vec{r}_{ia})$  and  $V_b(\vec{r}_{ib})$  are the potentials of electronic interaction with atomic (molecular) cores has the following asymptotics

$$V_{a,b}(\vec{r}) \xrightarrow{r \rightarrow \infty} -\frac{Z_{a,b}}{r}. \quad (6)$$

The matrix element of two-electronic exchange interaction  $H_{ab}$  is given by

$$H_{ab} = \langle \Psi_b | H_{el} | \Psi_a \rangle - \langle \Psi_b | \Psi_a \rangle \langle \Psi_a | H_{el} | \Psi_a \rangle, \quad (7)$$

where  $\Psi_a$  and  $\Psi_b$  are the perturbed two-electronic wave functions (centered on the molecular and ionic cores  $A_p^{Z_a+}$  and  $B^{Z_b+}$  respectively) of the quasimolecular system. At infinite separation  $R \rightarrow \infty$  the wave functions  $\Psi_a$  and  $\Psi_b$  reduces to the wave functions of the initial

$$A_p^{(Z_a-2)+} + B^{Z_b+} \quad (8)$$

and the final

$$A_p^{Z_a+} + B^{(Z_b-2)+} \quad (9)$$

configurations respectively. The symmetrized two-electron wave function  $\Psi_a$  reads

$$\Psi_a = \frac{1}{2^{1/2}} \left[ \Phi_{1a}(\vec{r}_1, \vec{r}_2) + (-1)^{S_a} \Phi_{2a}(\vec{r}_1, \vec{r}_2) \right] \chi_{S_a M_{S_a}}, \quad (10)$$

where  $\chi_{S_a M_{S_a}}$  is the spin function,  $\Phi_{1a}$  and

$$\Phi_{2a}(\vec{r}_1, \vec{r}_2) \equiv \Phi_{1a}(\vec{r}_1 \leftrightarrow \vec{r}_2) \quad (11)$$

are the two-electron coordinate wave functions. The wave function of the final state  $\Psi_b$  reads

$$\Psi_b = \frac{1}{2^{1/2}} \sum_{m_{1b}, m_{2b}} C_{\ell_{1b} m_{1b}, \ell_{2b} m_{2b}}^{L_b M_{L_b}} \left[ \Phi_{1b}(\vec{r}_1, \vec{r}_2) + (-1)^{S_b} \Phi_{2b}(\vec{r}_1, \vec{r}_2) \right] \chi_{S_b M_{S_b}}, \quad (12)$$

where  $C_{\ell_1 m_1, \ell_2 m_2}^{LM}$  are the Clebsch-Gordan coefficients, and  $\ell_{1b} m_{1b}$ ,  $\ell_{2b} m_{2b}$  are the orbital momentums and its projections on the internuclear axis  $R$ . Substituting given above wave functions into the expression for matrix element (7) we come to the following expressions

$$H_{ab} = \frac{1}{2} \sum_{m_{1b}, m_{2b}} C_{\ell_{1b} m_{1b}, \ell_{2b} m_{2b}}^{L_b M_{L_b}} \left( (-1)^{S_b} H_{ab}^{(1)} + H_{ab}^{(2)} \right), \quad (13)$$

where

$$H_{ab}^{(1)} = \langle \Phi_{2b} | H_{el} | \Phi_{1a} \rangle + \langle \Phi_{1b} | H_{el} | \Phi_{2a} \rangle - \langle \Psi_a | H_{el} | \Psi_a \rangle (S_{1b,2a} + S_{2b,1a}), \quad (14)$$

$$H_{ab}^{(2)} = \langle \Phi_{1b} | H_{el} | \Phi_{1a} \rangle + \langle \Phi_{2b} | H_{el} | \Phi_{2a} \rangle - \langle \Psi_a | H_{el} | \Psi_a \rangle (S_{1b,1a} + S_{2b,2a}), \quad (15)$$

$$S_{k\lambda, k'\lambda'} = \langle \Psi_{k\lambda} | \Psi_{k'\lambda'} \rangle, \quad k, k' = 1, 2; \lambda, \lambda' = a, b. \quad (16)$$

In the following we need correct asymptotic expressions for the coordinate wave functions  $\Phi_{k\lambda}$  ( $k=1,2$ ,  $\lambda=a,b$ ). Obviously, that at large separations  $R$  functions  $\Phi_{ka}$  and  $\Phi_{kb}$  only slightly differ from the nonperturbed molecular  $\Phi_{ka}^{(0)}$  and atomic  $\Phi_{kb}^{(0)}$  wave functions. However this small difference responsible for the nature of exchange interaction between colliding particles. In the following

we shall represent the two-electron wave function as a product of one-electron orbitals in the following manner

$$\Phi_{1a}^{(0)}(\vec{r}_{1a}, \vec{r}_{2a}) = \varphi_a(\vec{r}_{1a})\varphi_a^{(0)}(\vec{r}_{2a}), \quad (17)$$

where the one-electronic orbitals are given by

$$\varphi_a(\vec{r}_{1a}) \xrightarrow{r_{1a} \gg 1} A_1 r_{1a}^{(Z_a-1)n_{1a}-1} \exp(-r_{1a}/n_{1a}) \Theta_1(\theta_{1a}, \phi_{1a}), \quad (18)$$

$$\varphi_a^{(0)}(\vec{r}_{2a}) \xrightarrow{r_{2a} \gg 1} A_2 r_{2a}^{Z_a n_{2a}-1} \exp(-r_{2a}/n_{2a}) \Theta_2(\theta_{2a}, \phi_{2a}). \quad (19)$$

Here  $1/2n_{1a}^2$  and  $1/2n_{2a}^2$  are the first and the second ionization potential of the molecule  $A_p^{(Z_a-2)+}$ ;

$\varphi_a$  and  $\varphi_a^{(0)}$  are the wave function of the valent electrons related to  $A_p^{(Z_a-2)+}$  and molecular ion  $A_p^{(Z_a-1)+}$  in the ground electronic and vibration state;  $A_{1,2}$  are the normalization constants of the

functions  $\varphi_a$  and  $\varphi_a^{(0)}$ ;  $\theta_{ia}$  is the angle between vector  $\vec{r}_{ia}$  and direction of the dipole momentum vector  $\vec{d}_i$  of the ion  $A_p^{(Z_a-1)+}$  ( $i=1$ ) or  $A_p^{Z_a+}$  ( $i=2$ );  $\Theta_i(\theta_{ia}, \phi_{ia})$  are the angular wave functions. The similar relations exist for other wave functions  $\Phi_{k\lambda}$ . Since the main contribution into the exchange matrix element makes the configuration when active electrons are localized near separate particles we can define the two-electron functions  $\Phi_{1a}$  and  $\Phi_{2b}$  for such configuration in the following manner

$$\Phi_{1a}(\vec{r}_1, \vec{r}_2) = \varphi_a^{(0)}(\vec{r}_2)\varphi_{ab}(\vec{r}_1), \quad \Phi_{2b}(\vec{r}_1, \vec{r}_2) = \varphi_b^{(0)}(\vec{r}_1)\varphi_{ba}(\vec{r}_2), \quad (20)$$

where  $\varphi_{ab}$  is the wave function of the 1-st electron of molecule  $A_p^{(Z_a-2)+}$  (the second index «b» of this function means that one consider it in the vicinity of particle  $B^{Z_b+}$ ),  $\varphi_a^{(0)}$  is the ground electronic wave function of the molecular ion  $A_p^{(Z_a-1)+}$ , and  $\varphi_{ba}$  is the wave function of the outer electron of atomic particle in the vicinity of molecular core, finally  $\varphi_b^{(0)}$  is the ground electronic wave function of the ion  $B^{(Z_b-1)+}$ . The similar relations are true for the functions  $\Phi_{2a}$  and  $\Phi_{1b}$ . The wave function  $\varphi_{ab}$  satisfy the two-center Schroedinger equation

$$\left( -\frac{\Delta}{2} + U_a(r_a) + V_b(r_b) - E_{1a} \right) \varphi_{ab}(\vec{r}_a) = 0, \quad (21)$$

where  $\vec{r}_b = \vec{r}_a - \vec{R}$ ,  $U_a(r_a)$  and  $V_b(r_b)$  are the interaction potentials of the electron with ions  $A_p^{(Z_a-1)+}$  and  $B^{Z_b+}$  respectively. In the following we accept the so-called point-dipole approximation for electronic interaction with permanent dipole moment  $d_1$ , hence  $U_a(r_a)$  reads

$$U_a(r_a) = -\frac{Z_a-1}{r_a} - \frac{\vec{d}_1 \cdot \vec{r}_a}{r_a^3}. \quad (22)$$

In the region between target and projectile potentials  $U_a(r_a)$  and  $V_b(r_b)$  can be replaced by its Coulomb asymptotics. Solution of the equation (21) in this region has been obtained in [2] and reads

$$\varphi_a(\vec{r}_a) \approx_{r_a \sim R/2} \frac{1}{n_{1a} \pi^{1/2} \Gamma^{1/2}(2n_{1a}(Z_a-1)+1)} \left( \frac{n_{1a}(Z_a-1)}{e} \right)^{n_{1a}(Z_a-1)} \frac{1}{z_a |p_a(z_a)|^{1/2}} \times$$

$$\exp\left(-\int_{z_{1a}}^{z_a} |p_a(z)| dz\right) \exp\left(-\frac{\rho^2 p_a(z_a)}{2z_a}\right) \times$$

$$\sum_{\ell \geq |m_{1a}|} \sum_{k=-\ell}^{\ell} a_{L\ell}^{m_{1a}}(d_1) D_{km_{1a}}^{\ell}(0, \beta, 0) \frac{1}{2^{|k|} |k|!} \left[ \frac{(2\ell+1)(\ell+|k|)!}{2(\ell-|k|)!} \right]^{1/2} \left(\frac{\rho}{z_a}\right)^{|k|} e^{ik\phi_a}, \quad (23)$$

Where  $D_{km_{1a}}^{\ell}$  are the Wigner functions,

$$p_a^2(z_a) = 2 \left( -|E_{1a}| + \frac{Z_a - 1}{z_a} + \frac{Z_b}{R - z_a} \right), \quad (24)$$

and the positions of a turning points are given by expression

$$z_{1a,2a} = \frac{1}{2} \left( R - \frac{Z_b - (Z_a - 1)}{|E_{1a}|} \right) \pm \frac{1}{2} \left[ \left( R - \frac{Z_b - (Z_a - 1)}{|E_{1a}|} \right)^2 - \frac{4(Z_a - 1)R}{|E_{1a}|} \right]^{1/2}. \quad (25)$$

The wave function  $\varphi_{ab}$  in the vicinity of ion  $B^{Z_b+}$  can be given in terms of a surface integral

$$\varphi_{ab}(\vec{r}_b) = -\frac{1}{2} \int_S [\varphi_{ab}(\vec{r}_b') \vec{\nabla} G_b(\vec{r}_b, \vec{r}_b'; E_{1a}) - G_b(\vec{r}_b, \vec{r}_b'; E_{1a}) \vec{\nabla} \varphi_{ab}(\vec{r}_b')] dS. \quad (26)$$

Here  $G_b(\vec{r}_b, \vec{r}_b'; E_{1a})$  is the one-electronic two-center Green's function of the quasimolecular system  $A_p^{(Z_a-1)+} + B^{Z_b+}$ , the S-plane divides the electronic location in the initial and final channels of the reaction. The Green's function  $G_b(\vec{r}_b, \vec{r}_b'; E_{1a})$  can be represented as the following expansion over partial waves

$$G_b(\vec{r}_b, \vec{r}_b'; E_{1a}) = -\frac{2}{r_b r_b'} \sum_{\ell'=0}^{\infty} \sum_{m'=-\ell'}^{+\ell'} g_{\ell'}(r_b, r_b'; E_{1a}) Y_{\ell'}^{m'}(\theta_b, \phi_b) Y_{\ell'}^{m'*}(\theta_b', \phi_b'), \quad (27)$$

where the radial Green's function  $g_{\ell'}(r_b, r_b'; E_{1a})$  reads

$$g_{\ell}(r_b, r_b'; E_{1a}) = \frac{-n_{1a}}{2} f_{1\ell}(r_<) f_{2\ell}(r_>), \quad r_< = \min(r_b, r_b'), \quad r_> = \max(r_b, r_b'), \quad (28)$$

where  $f_{1\ell,2\ell}(r)$  are linearly independent solutions of the radial equation

$$\frac{d^2 f_{i\ell}(r)}{dr^2} + 2 \left[ E_{1a} - U_a(|\vec{R} - \vec{r}|) - V_b(r) - \frac{\ell(\ell+1)}{2r^2} \right] f_{i\ell}(r) = 0, \quad i = 1, 2. \quad (29)$$

$$f_{1\ell}(r) \underset{r \rightarrow \infty}{=} r^{-n_{1a} Z_b} e^{r/n_{1a}}, \quad f_{2\ell}(r) \underset{r \rightarrow \infty}{=} r^{n_{1a} Z_b} e^{-r/n_{1a}}. \quad (30)$$

The leading contribution to the surface integral (26) comes from configuration where  $r_b' \sim R \gg 1$ , and  $r_b \sim 1$ . Hence, in our case  $r_< = r_b$  and  $r_> = r_b'$ . The function  $f_{1\ell}(r)$  in this region can be replaced by approximate solution  $f_{1\ell}^{(0)}(r)$  which satisfy the following equation

$$\frac{d^2 f_{1\ell}^{(0)}(r)}{dr^2} + 2 \left( E_{1a} - V_b(r) - \frac{\ell(\ell+1)}{2r^2} \right) f_{1\ell}^{(0)}(r) = 0. \quad (31)$$

Using the semiclassical solution of the equation (29) we can construct the semiclassical expression for Green's function  $G_b(\vec{r}_b, \vec{r}'_b; E_{1a})$  under the condition  $r'_b \sim R \gg 1$  and  $r_b \sim 1$ :

$$G_b(\vec{r}_b, \vec{r}'_b; E_{1a}) \approx \frac{n_{1a}}{4\pi} \left( \frac{n_{1a}^2 Z_b}{2e} \right)^{n_{1a} Z_b} \exp \left( - \int_{z'_a}^{z_{2a}} |p_a(z)| dz \right) \exp \left( - \frac{\rho^2 p(z'_b)}{2z'_b} \right) \frac{1}{z'_b} \times$$

$$\sum_{\ell'=0}^{\infty} \sum_{m'=-\ell'}^{+\ell'} \frac{(-1)^{|m'|} (2\ell'+1)}{2^{|m'|} |m'|} \frac{f_{1\ell'}^{(0)}(r_b)}{r_b} P_{\ell'}^{|m'|}(\theta_b) \left( \frac{\rho}{z'_b} \right)^{|m'|} e^{im'(\phi_b - \phi'_b)}. \quad (32)$$

Substituting obtained results into the surface integral (26) we come to the following expression for function  $\varphi_{ab}$  in vicinity of atomic ion

$$\varphi_{ab}(\vec{r}_{1b}) \approx D_a(R) \sum_{\ell \geq |m_{1a}|} (2\ell+1)^{1/2} a_{L\ell}^{m_{1a}}(d_1) \sum_{k=-\ell}^{+\ell} \frac{(-1)^{|k|}}{|k|!} D_{km_{1a}}^{\ell}(0; \beta; 0) \left[ \frac{(\ell+|k|)!}{(\ell-|k|)!} \right]^{1/2} \times$$

$$(n_{1a}/2)^{|k|+1/2} R^{-|k|-1} \sum_{\ell' \geq |k|} (2\ell'+1) \frac{f_{1\ell'}^{(0)}(r_{1b})}{r_{1b}} P_{\ell'}^{|k|}(\theta_{1b}) e^{ik\phi_{1b}}, \quad (33)$$

where

$$D_a(R) = \frac{-1}{2\pi^{1/2} \Gamma^{1/2}(2n_{1a}(Z_a-1)+1)} \left( \frac{n_{1a}^2 Z_b}{2e} \right)^{n_{1a} Z_b} \left( \frac{n_{1a}(Z_a-1)}{e} \right)^{n_{1a}(Z_a-1)} e^{-I_a(R)}, \quad (34)$$

And expression for barrier integral  $I_a(R)$  given through the elliptic integrals

$$I_a(R) = \frac{n_{1a}^{-1}}{\sqrt{(R-z_{1a})z_{2a}}} \left\{ \left[ -R^2 + (z_{1a} + z_{2a})R - z_{1a}z_{2a} \right] K(k_a) + (R-z_{1a})z_{2a} E(k_a) + \right.$$

$$\left. \left[ R^2 - (z_{1a} + 2z_{2a})R + z_{1a}z_{2a} + z_{2a}^2 \right] \Pi(\nu_a, k_a) \right\}, \quad (35)$$

where  $K(k)$ ,  $E(k)$  and  $\Pi(\eta, k)$  are the full elliptic integrals of the first, second and third kinds, and

$$\nu_a = \frac{z_{2a} - z_{1a}}{R - z_{1a}}, \quad k_a = \left( \frac{\nu_a R}{z_{2a}} \right)^{1/2}. \quad (36)$$

In the same manner one can construct the wave function  $\varphi_{ba}$  of the ion  $B^{(Z_b-2)+}$  in the vicinity of polar molecule core  $A_p^{Z_a+}$  with permanent dipole moment  $d_2$  [4].

### 3. Potential of the two-electron exchange interaction

Using obtained results for the two-electron wave functions we are able now to calculate the exchange matrix element responsible for direct two-electron capture process (3)

$$H_{ab} \approx (-1)^S \sum_{m_{1b}, m_{2b}} C_{\ell_{1b} m_{1b}, \ell_{2b} m_{2b}}^{L_b M_{L_b}} \langle \varphi_b^{(0)}(\vec{r}_{1b}) \varphi_{ba}(\vec{r}_{2a}) | H_{el} | \varphi_b^{(i)}(\vec{r}_{1b}) \varphi_a^{(0)}(\vec{r}_{2a}) \rangle. \quad (37)$$

It is also necessary to know the functions  $f_{1\ell}^{(0)}(r_{1b})$  and  $f_{1\ell m}^{(0)}(r_{2a})$  (see [4])



$$f_{1\ell}^{(0)}(r_{1b}) = \left(\frac{2}{n_{1a}}\right)^{n_{1a}Z_b} \frac{\Gamma(1+s_\ell - n_{1a}Z_b)}{\Gamma(2s_\ell + 2)} M_{n_{1a}Z_b; s_\ell + 1/2} \left(\frac{2r_{1b}}{n_{1a}}\right), \quad (38)$$

$$s_\ell = \sqrt{(\ell + 1/2)^2 + 2C} - 1/2, \quad (39)$$

and

$$f_{1\ell m}^{(0)}(r_{2a}) = \left(\frac{2}{n_{1b}}\right)^{n_{1b}Z_a} \frac{\Gamma(1+s_{\ell m} - n_{1b}Z_a)}{\Gamma(2s_{\ell m} + 2)} M_{n_{1b}Z_a; s_{\ell m} + 1/2} \left(\frac{2r_{2a}}{n_{1b}}\right). \quad (40)$$

Using obtained results for the wave functions we are ready now to calculate the matrix element responsible for direct two-electron transfer (3) which, in dipole approximation for electron-electron interaction  $r_{12}^{-1}$ , reads

$$H_{ab} = \frac{8\pi(-1)^{S+1}}{3R^3} \sum_{m_{1b}, m_{2b}} C_{\ell_{1b}m_{1b}, \ell_{2b}m_{2b}}^{L_b M_{L_b}} \sum_{q=-1}^{+1} \sum_{j=-1}^{+1} \frac{1}{(1+q)!(1-q)!} H_{1b} H_{2a}, \quad (41)$$

$$H_{1b} = \int \varphi_{ab}(\vec{r}_{1b}) \varphi_b^{(0)*}(\vec{r}_{1b}) r_{1b} Y_1^{-q}(\theta_{1b}, \phi_{1b}) d\vec{r}_{1b}, \quad (42)$$

$$H_{2a} = \int \varphi_{ba}^*(\vec{r}_{2a}) \varphi_a^{(0)}(\vec{r}_{2a}) r_{2a} Y_1^j(\tilde{\theta}_{2a}, \tilde{\phi}_{2a}) D_{qj}^1(0, \beta, 0) d\vec{r}_{2a}, \quad (43)$$

where

$$H_{1b} = \sqrt{3} B_2 D_a(R) (2\ell_{2b} + 1)^{1/2} \sum_{\ell \geq |m_{1a}|} a_{\ell}^{m_{1a}}(d_1) \sum_{k=-\ell}^{+\ell} \frac{1}{|k|!} \left(\frac{n_{1a}}{2}\right)^{|k|+1/2} \left[ \frac{(2\ell+1)(\ell+|k|)!}{(\ell-|k|)!} \right]^{1/2} \times \\ \times D_{k m_{1a}}^\ell(0, \beta, 0) \sum_{\ell' \geq |k|} (-1)^{-\ell'} (2\ell' + 1) \left[ \frac{(\ell' + |k|)!}{(\ell' - |k|)!} \right]^{1/2} T_{000}^{\ell' \ell_{2b} 1} T_{k m_{2b} - q}^{\ell' \ell_{2b} 1} \frac{J_b(n_{2b})}{R^{|k|+1}}, \quad (44)$$

and

$$J_b(n_{2b}, s_{\ell'}) = \left(\frac{2}{n_{1a}}\right)^{n_{1a}Z_b + s_{\ell'} + 1} \frac{\Gamma(1+s_{\ell'} - n_{1a}Z_b) \Gamma(s_{\ell_{2b}} + s_{\ell'} + 4)}{\Gamma(2s_{\ell'} + 2)} \left(\frac{n_{1a}n_{2b}}{n_{1a} + n_{2b}}\right)^{s_{\ell_{2b}} + s_{\ell'} + 4} \times \\ {}_2F_1\left(-n_{1a}Z_b + s_{\ell'} + 1, s_{\ell_{2b}} + s_{\ell'} + 4; 2s_{\ell'} + 2; \frac{2n_{2b}}{n_{1a} + n_{2b}}\right), \quad (45)$$

where  $T$  is the 3-j Wigner's symbols,  ${}_2F_1$  is the Hypergeometric function. By the same manner one can calculate matrix element  $H_{2a}$

$$H_{2a} = \sqrt{3} A_2 D_b(R) D_{qj}^1(0, \beta, 0) \sum_{\tilde{\ell}=0}^{\infty} \sum_{\tilde{m}=-\tilde{\ell}}^{+\tilde{\ell}} \sum_{\lambda \geq |\tilde{m}|} \sum_{\mu \geq |\tilde{m}|} a_{\tilde{\ell}\lambda}^{\tilde{m}}(d_2) a_{\tilde{\ell}\mu}^{\tilde{m}}(d_2) \left[ \frac{(2\mu+1)(\mu+|m_{1b}|)!}{(\mu-|m_{1b}|)!} \right]^{1/2} \times \\ \times D_{m_{1b}\tilde{m}}^\mu(0, \beta, 0) \sum_{n \geq |m_{2a}|} b_n^{m_{2a}}(d_2) (2n+1)^{1/2} (2\lambda+1)^{1/2} T_{000}^{\lambda n 1} T_{\tilde{m} m_{2a} j}^{\lambda n 1} J_a(n_{2a}, s_{\tilde{\ell}\tilde{m}}), \quad (46)$$

where

$$J_a(n_{2a}, s_{\tilde{\ell}\tilde{m}}) = \left(\frac{2}{n_{1b}}\right)^{n_{1b}Z_a + s_{\tilde{\ell}\tilde{m}} + 1} \frac{\Gamma(1 + s_{\tilde{\ell}\tilde{m}} - n_{1b}Z_a) \Gamma(n_{2a}Z_a + s_{\tilde{\ell}\tilde{m}} + 3)}{\Gamma(2s_{\tilde{\ell}\tilde{m}} + 2)} \left(\frac{n_{2a}n_{1b}}{n_{2a} + n_{1b}}\right)^{n_{2a}Z_a + s_{\tilde{\ell}\tilde{m}} + 3} \times$$

$${}_2F_1\left(-n_{1b}Z_a + s_{\tilde{\ell}\tilde{m}} + 1, n_{2a}Z_a + s_{\tilde{\ell}\tilde{m}} + 3; 2s_{\tilde{\ell}\tilde{m}} + 2; \frac{2n_{2a}}{n_{2a} + n_{1b}}\right). \quad (47)$$

#### 4. Conclusion

Equations (41)-(47) defines the leading term of the expansion for exponentially small long-range two-electron exchange interaction between multiply charged atomic ion and polar molecule in semiclassical version of the asymptotic theory. Calculation of the needed wave functions has been done in the framework of surface integral metod. If instead the exact calculations for barrier integrals (see equation (35)) one use its asymptotic representations, obtained results will reduce to the known two-center results for the exchange interaction obtained in [5]. Obtained results will be used for calculations of the total charge transfer cross sections of elementary reactions of the type (3) in slow collisions of atomic ions and polar targets.

#### 5. References

- [1] Otranto S and Olson R E 2008 *Phys. Rev.* **A77** 022709.
- [2] Khoma M V *et al* 2008 *Chemical Physics* **352** 142.
- [3] Lendyel V I, Lazur V Yu, Karbovanets M I and Janev R K *Introduction to the Theory of Atomic Collisions*. Lviv 1989.
- [4] Karbovanets O M *et al* 2013 Book of Abstr.15-th Small Triangle Meeting, Slovakia (*in print*).
- [5] Karbovanets M I, Lazur V Yu and Chibisov M I 1984 *Zh. Eksp. Theor. Phys.* **86** 84.

# ONE-ELECTRON CAPTURE IN FAST ION-ATOMIC COLLISIONS

Mykhaylo Khoma<sup>1</sup>, Volodymyr Lazur<sup>1</sup>, Dzevad Belkic<sup>2</sup>

<sup>1</sup>*Department of Theoretical Physics, Uzhgorod National University, Uzhgorod, Ukraine*

<sup>2</sup>*Nobel Medical Institute, Karolinska Institute, Stockholm, Sweden*

E-mail: m.khoma@gmail.com

We study one-electron capture in fast collision of a hydrogen-like atom and positively charged atomic ion. The distorted wave formalism based on usage of modified three-body Dodd-Greider equations has been used. The reaction amplitude is constructed as a first iteration of the Dodd-Greider integral equations and reduced to a simple one-dimensional integral representation convenient for numerical integration. The proposed approach allows to account a Coulomb re-scattering effects in the collision processes. The method is applied for study of a charge transfer processes in  $H + H^+$  collision at intermediate and high collision energies.

## 1. Introduction

Much attention has been recently called to the processes with particles rearrangement in energetic collisions of atomic particles. The increase of experimental and theoretical work in this field is motivated by new applications in medical physics (hadron therapy), astrophysics, biophysics [1]. In the present work we concentrate on investigation of the one-electron capture process



at intermediate and high collision velocities. Reaction of this type attract steady attention from many research groups for many decades. At intermediate and high energies there are wide variety of possible reaction channels even for simplest case of  $H + H^+$  collision. A high probability of target excitation initiate several two-step mechanisms of electron transfer that are main subject of the present investigation. It is commonly accepted that in the range of intermediate and high collision velocities, the dominant processes are a direct one-electron transfer (1) and a two-step Thomas mechanism of electron capture through the intermediate discrete or continuum states. The latter becomes especially important with increasing collision energy. Charge transfer reaction at high collision energies is usually treated by analytical perturbative approaches, since *ab-initio* approaches (like close-coupling method, etc.) in this case pose significant computational challenges. From the other hand, analytical perturbative approaches allows to obtain for reaction amplitude closed symbolic form or, at least, rather simple low-dimensional integral representations. The latter include different variation of the Distorted Waves Method [2] which are used for symmetrical collisions and Strong Potential Born (SPB) approximation [3], (used for non-symmetrical collisions) that takes into account strong pair interaction in all orders of perturbation theory and weak interaction in the first order of perturbation theory. The main drawback of mentioned approaches is a usage of some assumptions about the short range character of considered interaction potential. It was pointed out, however, (see [4]) that such assumptions are not 'safe' for applications. As an illustration we refer the publication [4] where it was demonstrated that initial version of the SPB-approximation [3] can not serve as a basis for construction of the approximate charge exchange theories, since scattering amplitude include contribution from the divergent terms. The reason of this drawback is non-accurate account for the Coulomb effects in the initial and final states. This circumstances confirms the general result of [5-7], where has been demonstrated the way of modification of the theories elaborated for the short-range potentials on the case of long-range potentials. In the present work on the basis of modified three-body Dodd-Greider integral equations [5,6] the method of one-electron capture cross section calculation is presented. The amplitude of reaction (1) is obtained as the first term of the iteration expansion of the solution of the correspondent Dodd-Greider equations for the three-body scattering operator with account of Coulomb effects in the final reaction channels. In the approximation of the

“single-step” mechanism of electron transition the method reduces to the version of the known Coulomb-Born approximation.

## 2. Basic kinematics and dynamics

For studied here ion-atomic reaction (1) we shall use the following designation:  $\alpha$  is a projectile particle,  $\beta$  is the target and  $\gamma$  is the active electron with masses  $m_\alpha$ ,  $m_\beta$  and  $m_\gamma$  respectively. The center of mass motion is assumed to be separated. The full Hamiltonian reads

$$H = H_0 + V, \quad (2)$$

and the arrangement channel Hamiltonians are

$$H_j = H_0 + V_j, \quad j = \alpha, \beta, \gamma \quad (3)$$

where  $H_0$  is the three-body kinetic energy operator in the center of mass system of coordinates,

$$V = \sum_{\alpha, \beta, \gamma} V_j, \quad (4)$$

is the full interaction. The subscript index  $j$  in  $V_j$  defines the missing particle in this interaction potential,

i.e. the  $V_\alpha$  is the operator for  $\beta$  and  $\gamma$  interaction. Finally

$$v_j = V - V_j, \quad (5)$$

Is the arrangement channel interaction. In Jacobi-type coordinates

$$\vec{s} = (a/m_\gamma)\vec{x} - \vec{r}_\alpha, \quad \vec{x} = (b/m_\gamma)\vec{s} - \vec{r}_\beta, \quad \vec{R} = \vec{x} - \vec{s}, \quad (6)$$

where

$$a = m_\gamma m_\beta / (m_\gamma + m_\beta), \quad b = m_\gamma m_\alpha / (m_\gamma + m_\alpha) \quad (7)$$

Are the reduced masses. In terms of this coordinates, the operator  $H_0$  can be represented in two equivalent forms

$$H_0 = -\frac{1}{2\mu_\alpha} \Delta_{r_\alpha} - \frac{1}{2a} \Delta_{r_x} = -\frac{1}{2\mu_\beta} \Delta_{r_\beta} - \frac{1}{2b} \Delta_{r_s}, \quad (8)$$

where the standard definition for Laplace operator is used and

$$\mu_\alpha = \frac{m_\alpha(m_\beta + m_\gamma)}{m_\alpha + m_\beta + m_\gamma}, \quad \mu_\beta = \frac{m_\beta(m_\alpha + m_\gamma)}{m_\alpha + m_\beta + m_\gamma}. \quad (9)$$

We split the potential  $v_j$  into two parts

$$v_j = V - V_j = U_j + W_j. \quad (10)$$

Here  $W_j$  defines the so-called “disturbing” potential which represents the weak long-range Coulomb interaction and  $U_j$  is the short-range perturbation responsible for electron transitions. From the definition

of the Hamiltonians  $H_\alpha$ ,  $H_\beta$  follows its eigenfunctions  $|\Phi_i^\alpha\rangle$ ,  $|\Phi_f^\beta\rangle$

$$|\Phi_i^\alpha\rangle = \varphi_i(\vec{x}) \exp(i\vec{k}_\alpha \cdot \vec{r}_\alpha), \quad (11)$$

$$|\Phi_f^\beta\rangle = \varphi_f(\vec{s}) \exp(i\vec{k}_\beta \cdot \vec{r}_\beta), \quad (12)$$

where  $\varphi_i, \varphi_j$  are the wave functions of the bound state of the pair  $(\beta, \gamma), (\alpha, \gamma)$  respectively, and the plain wave describes the relative motion of the free particles in initial and final reaction channels with momentum  $\vec{k}_\alpha$  and  $\vec{k}_\beta$  respectively. We shall introduce the arrangement Hamiltonians

$$H_{\alpha d} = H_\alpha + W_{\alpha d}, \quad H_{\beta d} = H_\beta + W_{\beta d}. \quad (13)$$

where  $W_{\alpha d}, W_{\beta d}$  are the auxiliary potentials which are described in [8]. Following [2], we introduce modified arrangement channel asymptotic states  $|\Phi_i^{\alpha+}\rangle, |\Phi_f^{\beta-}\rangle$  which correctly describes effects of the long-range Coulomb fields

$$|\Phi_i^{\alpha+}\rangle = \varphi_i(\vec{x}) \exp(i\vec{k}_\alpha \cdot \vec{r}_\alpha + i\sigma_\alpha), \quad (14)$$

$$|\Phi_f^{\beta-}\rangle = \varphi_f(\vec{s}) \exp(i\vec{k}_\beta \cdot \vec{r}_\beta - i\sigma_\beta), \quad (15)$$

where  $\sigma_\alpha$  and  $\sigma_\beta$  are the standard Coulomb phases.

### 3. Calculation of the transition amplitudes

Let us define by  $G_{\alpha d}^+$  and  $G_{\beta d}^-$  as the Green's functions of the model arrangement channel Hamiltonian  $H_{\alpha d}$  and  $H_{\beta d}$ , respectively

$$G_{\alpha d}^+ = (E - H_{\alpha d} + i\varepsilon)^{-1}, \quad G_{\beta d}^- = (E - H_{\beta d} - i\varepsilon)^{-1}, \quad (16)$$

and the Moeller wave operators  $\omega_\alpha^+, \omega_\beta^-$

$$\omega_\alpha^+ = 1 + g_{\alpha d}^+ \omega_\alpha \equiv 1 + (E - H_{\alpha d} - \omega_\alpha + i\varepsilon)^{-1} \omega_\alpha, \quad (17)$$

$$\omega_\beta^- = 1 + g_{\beta d}^- \omega_\beta \equiv 1 + (E - H_{\beta d} - \omega_\beta - i\varepsilon)^{-1} \omega_\beta. \quad (18)$$

We shall define now operators  $U_{\alpha\beta}^\pm$  as in [5,6]

$$U_{\alpha\beta}^+ = \omega_\beta^{-*} (\nu_\beta - W_\beta^*) [1 + G^+ (\nu_\alpha - W_\alpha)] \omega_\alpha^+, \quad (19)$$

$$U_{\alpha\beta}^- = \omega_\beta^{-*} [1 + (\nu_\beta - W_\beta^*) G^+] (\nu_\alpha - W_\alpha) \omega_\alpha^+, \quad (20)$$

where symbol  $*$  means the Hermitian conjugation. The matrix elements of the operators  $U_{\alpha\beta}^\pm$  between the Coulomb asymptotic states  $|\Phi_i^{\alpha+}\rangle$  and  $|\Phi_f^{\beta-}\rangle$  are the transition amplitudes  $T_{\alpha\beta}^\pm$  from channel  $\alpha$  to the channel  $\beta$  correspondingly in the *post* and *prior* formalism

$$T_{\alpha\beta}^\pm = \langle \Phi_f^{\beta-} | U_{\alpha\beta}^\pm | \Phi_i^{\alpha+} \rangle. \quad (21)$$

We omit the details of transition amplitude calculations and represent here only the final results for simplest case of  $H+H^+$  collision

$$T_{\alpha\beta}^- = N_1 N_2^- Z_\alpha \int_0^1 dt \frac{\partial}{\partial Z_\beta} \left( -\frac{1}{\Delta_-} \frac{\partial}{\partial \Delta_-} + \frac{\partial}{\partial Z_\alpha} \frac{1}{\Delta_-} \right) \Xi^-(\Delta_-), \quad (22)$$

$$\Xi^-(\Delta_-) = \frac{4\pi}{\omega_-^2} \left[ 1 - \frac{2\mu_\alpha \nu \sigma_+}{\omega_-^2} \right]^{i\nu_\alpha} \left[ 1 - \frac{2\mu_\beta \nu \sigma_-}{\omega_-^2} \right]^{i\nu_\beta} F(-i\nu_\beta, -i\nu_\alpha, 1, \tau_-), \quad (23)$$

where

$$N_2^- = (2/b^2) (Z_\alpha Z_\beta)^{3/2}, \quad \omega_-^2 = p^2 + \Delta_-^2, \quad N_1 = 1, \quad (24)$$

$$\tau_- = \frac{4\mu_\alpha \mu_\beta p_\perp \nu^2}{(\omega_-^2 - 2\mu_\alpha \nu \sigma_+)(\omega_-^2 - 2\mu_\beta \nu \sigma_-)}, \quad \sigma_\pm = i\Delta_-^2 \pm p_z. \quad (25)$$

Here vector  $\vec{p} = \vec{\beta} - \vec{Q}$  decomposes into the parallel  $p_z$  and perpendicular  $p_\perp$  components relative to the velocity vector  $\vec{v}$ . The following definitions has been used

$$\vec{Q} = (t-1)\vec{v}, \quad \Delta_-^2 = \nu^2 t(1-t) + tZ_\beta^2 + (1-t)(Z_\beta / \beta)^2. \quad (26)$$

In order to compute the integral (22) one should first to differentiate over the  $Z_\alpha$ ,  $Z_\beta$  and  $\Delta_-$  variables and then to make the following substitutions

$$\nu_\alpha \rightarrow Z_\alpha (Z_\beta - 1)/\nu, \quad \nu_\beta \rightarrow Z_\beta (Z_\alpha - 1)/\nu. \quad (27)$$

The transition amplitude  $T_{\alpha\beta}^+$  corresponding to the description of the electron transfer in the *post* formalism. The final result is

$$T_{\alpha\beta}^+ = N_1 N_2^+ Z_\beta \int_0^1 dt \frac{\partial}{\partial Z_\alpha} \left( -\frac{1}{\Delta_+} \frac{\partial}{\partial \Delta_+} + \frac{\partial}{\partial Z_\beta} \frac{1}{\Delta_+} \right) \Xi^+(\Delta_+), \quad (28)$$

$$\Xi^+(\Delta_+) = \frac{4\pi}{\omega_+^2} \left[ 1 - \frac{2\mu_\alpha \nu \sigma_-}{\omega_+^2} \right]^{i\nu_\alpha} \left[ 1 - \frac{2\mu_\beta \nu \sigma_+}{\omega_+^2} \right]^{i\nu_\beta} F(-i\nu_\beta, -i\nu_\alpha, 1, \tau_+), \quad (29)$$

$$N_2^+ = (2/a^2) (Z_\alpha Z_\beta)^{3/2}, \quad \omega_+^2 = p^2 + \Delta_+^2, \quad (30)$$

$$\tau_+ = \frac{4\mu_\alpha \mu_\beta q_\perp \nu^2}{(\omega_+^2 - 2\mu_\alpha \nu \sigma_-)(\omega_+^2 - 2\mu_\beta \nu \sigma_+)}. \quad (31)$$

Here the following designations have been used

$$\vec{q} = (q_z, \vec{q}_\perp), \quad (\vec{v}, \vec{q}_\perp) = 0, \quad q_z = (t-1/2)\nu + \Delta E \nu^{-1}, \quad \vec{q}_\perp = -\vec{\eta}. \quad (32)$$

## 4. References

- [1] Champion C, Hanssen J and Rivarola R D 2013 *Advances in Quantum Chemistry* **65** 269.
- [2] Belkic DZ, Gayet R and Salin A 1979 *Phys. Rept.* **56** 279.
- [3] Macek J and Alston S 1982 *Phys. Rev. A* **26** 250.
- [4] Dewangan D P and Eichler J 1985 *J. Phys. B* **18** L65.
- [5] Greider K R and Dodd L R 1966 *Phys. Rev.* **146** 671.
- [6] Dodd L R and Greider K R 1966 *Phys. Rev.* **146** 675.
- [7] Faddeev L D and Merkuriev S P 1993 *Quantum scattering theory for several particle systems*. Doderecht: Kluwer Academic Publishers.
- [8] Lazur V Yu and Khoma M V 2013 *Advances in Quantum Chemistry* **65** 363.

# DISSOCIATIVE IONIZATION OF CH<sub>4</sub> MOLECULES INDUCED BY H<sup>+</sup> AND N<sup>+</sup> PROJECTILES

S. T. S. Kovács<sup>1,2</sup>, P. Herczku<sup>1,2</sup>, L. Gulyás<sup>1</sup>, Z. Juhász<sup>1</sup>, B. Sulik<sup>1</sup>

<sup>1</sup>*Institute for Nuclear Research (Atomki), Bem tér 18/c, H-4026 Debrecen, Hungary*

<sup>2</sup>*University of Debrecen, Egyetem tér 1., H-4032 Debrecen, Hungary*

E-mail: kovacs.sandor@atomki.mta.hu

Ion induced fragmentation of gas phase CH<sub>4</sub> molecules was investigated experimentally by the impact of 650 keV N<sup>+</sup> and 1 MeV H<sup>+</sup> projectiles at the 5 MV Van de Graaff accelerator in Atomki. The energy and angular distribution of the charged fragments and emergent electrons were measured by an energy dispersive electrostatic spectrometer. Absolute fragmentation and multiple ionization cross sections of the target molecules were determined. For H<sup>+</sup> the obtained absolute electron emission cross sections are in good agreement with those of D. J. Lynch et al. (J. Chem. Phys. 64, 2616 (1976)) and with our CDW-EIS calculations. The fragment ion spectra show that the N<sup>+</sup> ions are far more effective in producing multiple ionization of CH<sub>4</sub> than protons.

## 1. Introduction

Dissociation of small molecules has been extensively studied in the past few decades on various collision systems [1-3]. A full understanding of the dynamics of fragmentation processes would be important in astrophysics, atomic and molecular physics, chemistry and in some applied field such as radiotherapy. When studying the biological effects of ionising radiation, methane is often used as tissue equivalent material. For both fundamental physics and applications the most important projectile energy region belongs to the Bragg-peak and its close surrounding, where the Linear Energy Transfer (LET) is maximal. However, the correlation between the LET and the fragmentation yield is not very strong [4].

Molecular dissociations are complex processes even for simple, few-atomic targets. In the collision the target molecule can be ionized and excited into several possible states. The created transient molecular ion may be stable against dissociation or it may dissociate. The emergent fragments can be charged or neutral, excited or ground state products. Following multiple ionization, the energy spectra of the fragments are mostly determined by the Coulomb-repulsion between charged fragments (Coulomb explosion), influenced by the initial and final excited states of the partners [5], and by the collision and dissociation conditions. There exist also two- or more-step fragmentation processes [3] i.e. sequential dissociations.

The aim of this work is to explore the low energy region of the Bragg-peak by the impact of singly charged, dressed or bare projectiles on CH<sub>4</sub> target. Since the majority of the fragmentation channels for methane are well known, we focus on the degree of ionization of the precursor molecular ion and the differences between the effects of dressed and bare projectile.

## 2. Experiment

In the last few years a new experimental setup was installed at a beamline of the VdG-5 accelerator in Atomki. The setup was designed specifically for molecule fragmentation experiments [6]. The methane gas is supplied by an effusive molecular gas-jet target system. The projectile ions are provided by the VdG-5 accelerator in Atomki. The fragment ions or electrons emerging from the reaction volume are energy and charge analysed by an energy dispersive electrostatic spectrometer designed specifically for molecule fragmentation experiments. The spectrometer is fixed on a rotatable ring which allows us to take the energy spectra at observation angles between 15 and 165 degrees. In the present experiment we studied the fragmentation of CH<sub>4</sub> molecules induced by 650 keV N<sup>+</sup> and 1 MeV H<sup>+</sup> projectiles. Energy distribution of the charged fragments and electrons

were measured in the energy range of 0.4 – 200 eV and 3 – 2000 eV respectively, at the observation angles of 45°, 90° and 135°. The chamber pressure was typically some 10<sup>-6</sup> mbar without the target gas and less than 1\*10<sup>-5</sup> mbar with the target gas injection.

### 3. Results and conclusions

The measured energy spectra for both ions and electrons were converted into absolute double differential cross sections DDCS. For the collision of H<sup>+</sup>+CH<sub>4</sub> the evaluated absolute ionization cross sections are in good agreement with those obtained by D. J. Lynch et al [7] for the same collision system (see figure 1.). Also a convincing agreement has been found with our CDW-EIS calculations [8].

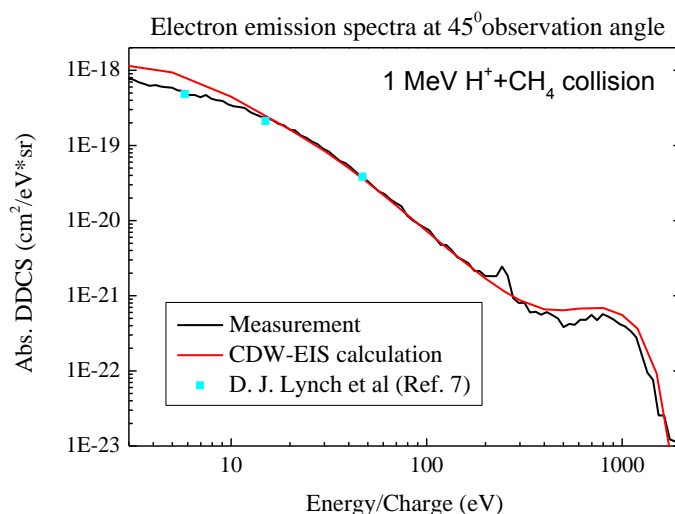


Fig. 1. DDCS for electron emission at 45° observation angle. The black line is our present measurement; the red line is the result of our CDW-EIS calculation; the blue squares are data from Ref 7. The present experiment is in good agreement with previous measurements, and also with theory.

The fragment ion spectra display three main structures as it is visible in figure 2. The peak below 2.5 eV contains most of the heavy fragments from all dissociation channels. Some of the proton fragments following single ionisation also contribute to it. The peak between 2.5- 3.7 eV is identified as due to H<sub>2</sub><sup>+</sup> fragments, also with some single ionization contribution. The broad, complex structure above 3.7 eV contains mostly protons, originating from the different fragmentation channels of the CH<sub>4</sub> molecules. The H<sup>+</sup> fragment energy reveals the ionization degree of its parent transient molecular ion. The fragment energy due to Coulomb repulsion increases with the increasing charge state of the precursor molecular ion and, in turn, with the charge state of the emerging fragments. Above 4 eV, e.g., one can find only protons originating from at least doubly ionized precursor states. Above 8 eV, higher degrees of ionization dominate. Thus from the energy dependence of the measured yields we can deduce the absolute double and multiple ionization cross sections belonging to the specific fragmentation channels.

We found that the obtained fragment ion spectra are completely different for the two projectiles as it is shown in figure 2. The most conspicuous deviation appears above 8 eV where multiple ionization channels dominate. The spectrum of H<sup>+</sup> projectile is dominated by single and double ionization events with a cut-off at 20 eV. For N<sup>+</sup> projectiles there is a broad structure which contains H<sup>+</sup> fragments from the multiply (mostly 3- and 4-fold) ionizations of the target molecule, and has a remarkable yield up to 50 eV. Another important difference is the relative strength of the three different peaks below 8 eV, which suggests that the relative strength of the different fragmentation channels are different for the two projectiles even at lower energies, in the single and double ionization region. According to the measured



fragments for  $H^+$  projectiles, the maximal ionization degree was  $q=2$  while in the case of  $N^+$  projectiles this maximum was found to be  $q=4$ . Theoretical approaches for the multiple ionization channels are under progress.

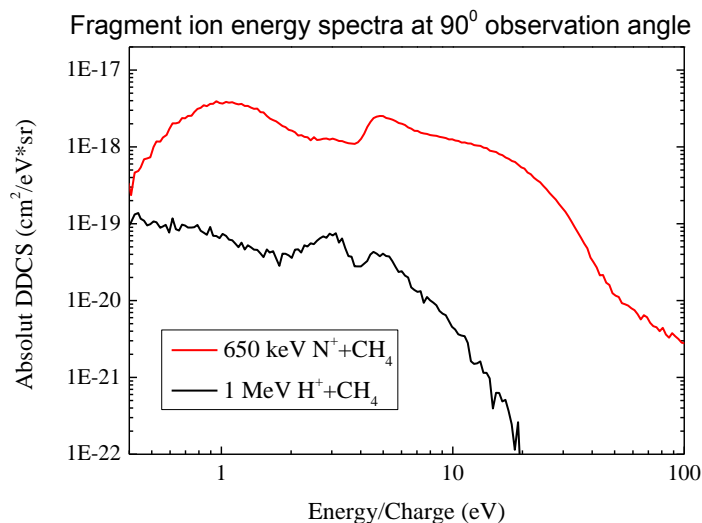


Fig. 2. The fragment ion-energy spectra at 90° observation angle for  $N^+$  and  $H^+$  projectiles.

This work was supported by the Hungarian OTKA Grant nos. K73703 and K109440, and by the TAMOP-4.2.2/B-10/1-2010-0024 and the TAMOP 4.2.2.A-11/1/KONV-2012-0036 projects, which are co-financed by the EU and the European Social Fund.

#### 4. References

- [1] H Luna, et al 2003 J. Phys. B **36** 4717.
- [2] G Dujardin, et al 1985 Phys. Rev. A **31** 3027.
- [3] I. Ben-Itzhak, et al 1993 Phys. Rev. A **47** 3748.
- [4] E C Montenegro, et al 2007 Phys. Rev. Lett. **99** 213201.
- [5] H B Pedersen, et al 2013 Phys. Rev. A **87** 013402.
- [6] S T S Kovacs, et al 2012 Act. Phys. Deb. **XLVI** 65.
- [7] D J Lynch, et al 1976 J. Chem. Phys. **64** 2616.
- [8] L Gulyás, et al (2013) J. Phys. B **46** 075201.

# ELECTRON EXCITATION OF THE SORBITOL MOLECULE BY LOW-ENERGY ELECTRONS

Irina V. Chernyshova, Pavlo P. Markush, Jeno E. Kontros, Otto B. Shpenik

Institute of electron Physics, Ukrainian National Academy of Sciences, 21 Universitetska str.,  
88017 Uzhgorod, Ukraine

E-mail: irinav.chernyshova @ gmail.com

The excitation of the lowest electronic states of the sorbitol molecule in the gas phase has been studied by electron energy loss spectroscopy. Along with excitation of the lowest singlet states at 9.7 eV, excitation of the three lowest triplet states at 3.15, 4.5 and 6.3 eV and vibrational excitation of the molecule in the energy range from 1.2 to 2.5 eV have been observed.

## 1. Introduction

Sorbitol ( $C_6H_{14}O_6$ ) is a hexahydric alcohol. It is applied extensively in the pharmaceutical, cosmetic and food industries, since it has a sweet taste and approximately 50-60% of the sucrose sweetness. Sorbitol can be used instead of sugar for people suffering from diabetes as well as in diabetic food and drinks. Along with methanol, ethanol and methyl glycerol it is treated as a potential environmentally friendly fuel to replace the traditional fossil one. The sorbitol molecule plays an essential role in living activity of live organisms, therefore, the comprehensive studies of the properties of this molecule at electron collisions are of great importance.

Here we report on the results of our studies concerning electron excitation of the sorbitol molecule by low-energy electrons.

## 2. Experiment

The excitation of the lowest electronic states of the sorbitol molecule was studied using a hypocycloidal electron spectrometer (HES) [1] (see Fig. 1). This instrument consists of two identical successive hypocycloidal electron monochromators (HEMs) (see detailed description in [2]): one of them operates like a monochromator, while the other is a scattered-electron analyzer. They are separated by a gas-filled cell, which serves as a collision chamber. We chose a HEM to form an elect-

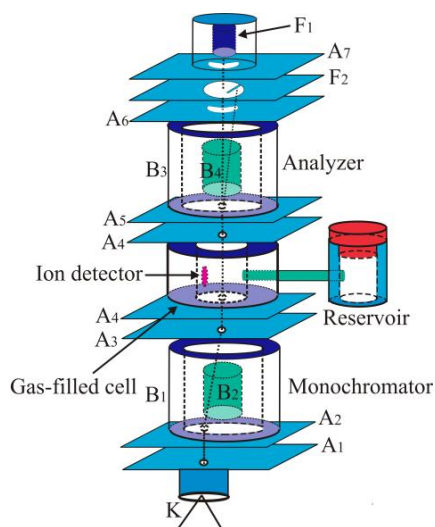


Fig. 1. Schematic view of the experimental setup.

ron beam because it provides beams of rather high density and small electron-energy spread and makes it possible to operate at very low (close to zero) energies. The best HEM energy resolution in these measurements was  $\Delta E_{1/2}=80$  meV (full width at half maximum of the electron-energy distribution) at an electron current of 10-20 nA.

The target in the gas phase was formed in a reservoir. It is a hollow stainless-steel cylinder heated resistively to desired temperature ( $\sim 52^\circ\text{C}$ ), at which there are no structural changes in the sorbitol molecule ( $T_m=112^\circ\text{C}$ ). The heating temperature was controlled by a calibrated chromel-alumel thermocouple fixed at the reservoir bottom. The preparation was placed in a quartz ampoule in the molecular source reservoir.

The excitation of the lowest electronic states of the sorbitol molecule was studied by electron energy loss (EEL) spectroscopy, which was successfully applied in our experiments on uracil and thymine molecules [3, 4]. The electron energy loss spectra were recorded in the constant residual electron energy mode [5]. In this mode, the analyzer was adjusted to detect inelastically scattered electrons with a fixed residual energy ( $E_r$ ), whereas the incident-electron energy ( $E_{in}$ ) was gradually changed from 0 to 9.5 eV. Under these conditions, the maximum aperture ratio ( $\sim 100\%$ ) of the analyzer is achieved near the process threshold; therefore, the peak amplitudes in a spectrum observed are proportional to the integral excitation cross sections of the levels near their thresholds (the threshold mode). The changes in the residual energy  $E_r$  and the solid angle of scattered electrons capture allow one to differentiate between the dipole-allowed transitions to the singlet states and those to the triplet states.

### 3. Results and discussion

The threshold spectra were measured using a hypocycloidal spectrometer with a resolution not worse than 0.15 eV. The spectra were detected at an angle close to  $0^\circ$  with respect to the incident electron beam. The target was formed in a gas cell ( $P \approx 10^{-3}$  Torr).

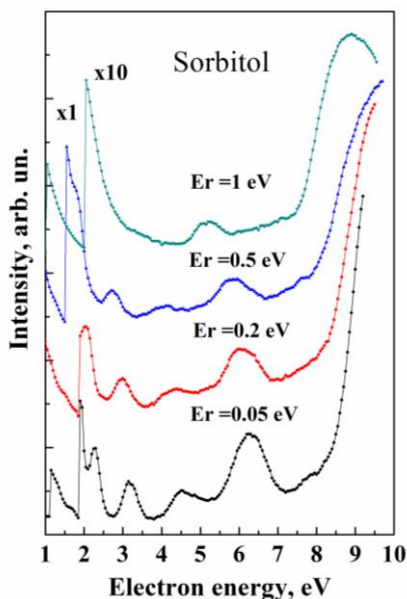


Fig. 2. Electron excitation of the sorbitol molecule. EEL spectra recorded at scattering angle  $5^\circ$ , and at residual energies  $E_r$  ranging from 0.05 to 1 eV.

Figure 1 shows the threshold spectra of the sorbitol molecule for the residual energies 0.05, 0.2, 0.5 and 1 eV. As seen, four bands are observed in the 2.0–7.0 eV energy range. The band in the 5.0–7.0 eV region is the most intensive and observed in all spectra. Its relative intensity in EEL spectrum decreases by a factor of about 4 with increasing  $E_r$  from 0.05 to 1 eV. This behavior and the observation of these processes at low residual energies indicates the transitions to the triplet states.

The bands at 3.15 and 4.5 eV are not observed in the spectrum for the  $E_r=1$  eV. It is characteristic for the transitions to the triplet states. The features with maxima at 2.3 eV and 1.7 eV are most probably caused by the vibrational excitation of the sorbitol molecule. This pattern is supported by the sorbitol absorption spectra recorded earlier [6].

In addition, we observed two extra bands in the EEL spectrum at higher energies. The first band (the low-intensity one) is revealed in the 7.5–8.1 eV region in a form of a shoulder of the second ( $E>8.2$  eV) band. It is not observed in the  $E_r=1$  eV spectrum, hence, it could be assigned to the transition into the triplet state. It should be noted that the similar pattern (i.e. the intense band shoulder) was observed earlier in the EEL for the monohydric alcohols [7]. The authors of [7] assigned this feature to the  $\sigma\rightarrow\sigma^*$  transition of the C–C bond electron.

The second band ( $E>8.2$  eV) has a high intensity and is observed in any spectra testifying to the assignment to the allowed transition into the singlet state. In [7], the similar band was assigned to the  $\sigma\rightarrow\sigma^*$  electron transition of the C–H bond.

The presence of the three optically forbidden transitions could explain the fact they were not observed earlier in the UV-absorption spectra.

#### 4. References

- [1] Kontros J E, Szoter L, Chernyshova I V, Shpenik O B 2002 *J. Phys. B.* **35** 2195.
- [2] Romanyuk N I, Shpenik O B, Mandi I A et al. 1993 *Zh. Tekh. Fiz.* **63** 138.
- [3] Chernyshova I V, Kontros J E, Markus P P, Shpenik O B 2012 *Opt. Spectr.(rus)* **113** 7.
- [4] Chernyshova I V, Kontros J E, Markus P P, Shpenik O B 2013 *Opt. Spectr.(rus)* **151** 730.
- [5] Cloutier P, Sanche L 1989 *Rev. Sci. Instrum.* **60** 1054.
- [6] Choi Eui-Sung, Lee Eun-Hae, Phee Sang-Ki 1995 *FEMS Microbiology Letters* **125** 45.
- [7] Hegde M S, Jayaram V, Kamath P Vishnu, Rao C N R 1985 *Pramana* **24** 293.

# ELECTRON IONIZATION MASS SPECTROMETRIC STUDY OF PYRIMIDINE MOLECULE

Muhailo Mykyta, Anatoly Zaviropulo, Anatoly Mylymko,

Olga Pulupchinec, Pavlo Markush

*Institute of Electron Physics, Ukrainian National Academy of Sciences,  
21 Universitetska str. Uzhgorod 88017, Ukraine*

E-mail: gzavil@gmail.com

In this work the experimental method and the results of mass spectrometric investigation of the positive ion formation of pyrimidine molecule by electron impact are presented. The experiments were carried out using a monopole mass spectrometer, the method of crossing electron and molecular beams being employed. The sorbitol molecule mass spectra have been measured at different ionizing electron energies. The most significant feature of the mass spectrum measured at the ionizing electron energy of 70 eV is the  $C_4H_4N_2^+$  ion peak. It has been found that its fragmentation taking place due to the loss of HCN molecule followed by the formation of fragment ion with  $m/z=53$ .

## 1. Introduction

The amino group has stronger electron-donating properties than hydroxyl group. It is also known, that the positive mesomeric effect of nitrogen atoms is more and the negative inductive effect is less than that of oxygen atoms. Therefore, fragmentation processes initiated by the radical center are characteristic for amines. Pyrimidine ( $C_4H_4N_2$ ) being a six-membered heterocyclics with two nitrogen atoms in the ring belongs to the amino group, it can be regarded as an analogue of the benzene, in which the two CH groups are replaced by nitrogen atoms. Nitrogen heterocycles have two different types of electron of the same energy: an electron which is not bound to the nitrogen atom and an other electron located in the aromatic ring  $\pi$ -orbital. This kind of electron location can affect the magnitude of the potential energy of pyrimidine. Pyrimidine can be found for instance in nucleic acids, three types of nucleobases are pyrimidine derivatives: cytosine, thymine and uracil. The aim of this work is to investigate the ionization processes of the pyrimidine molecule by electron impact.

## 2. Experiment

The experiment was carried out using a monopole mass spectrometer, the method of crossing electron and molecular beams being employed [1]. The molecular beam was formed by evaporating the investigated substance using an effusive multichannel source of neutral particles. The concentration of molecules in the area of interaction with the electron beam was not lower than  $10^{11}$ - $10^{12}$  cm<sup>-3</sup> at the residual gas pressure of  $10^{-6}$  Torr in the vacuum chamber. In order to avoid condensation of the substance under investigation on the vacuum chamber walls and the mass spectrometer electrodes, the mass analyzer chamber was heated to the temperature 400 K. Molecules were ionized in an ion source with electron bombardment. This source enables the electron beams of controlled energy to be obtained in the electron current stabilization mode at the current values 0.03-0.3 mA and with the energy spread not worse than  $\Delta E=250$  meV. The ions, extracted from the source, were focused into a beam, moved to the analyzer (mass filter) electrode area, separated according to their mass and detected by a secondary electron multiplier or an ion collector in the form of a Faraday cup. Our experimental setup makes it possible to measure, besides the mass spectra, the energy dependence of dissociative ionization cross sections in the energy range from the threshold to 90 eV. The mass scale was calibrated using the mass lines of N<sub>2</sub>, Ar and Kr

## 3. Results

The pyrimidine molecule mass spectra have been measured at the ionizing electron energy of 15, 20, 30, 70 eV and in the range of 10-90 a.u. (Fig. 1). The most significant feature of the mass spectrum



Fig. 2. Fragmentation scheme of pyrimidine.

There is one more possible mechanism of fragmentation shown on the right side of Fig. 2. It occurs with the detachment of H which results in the formation of fragment ion ( $m/z=79$ ), then the loss of HCN molecule from this fragment leads to the formation of  $C_4H_3N_2^+$  ion. It has been observed that the  $C_4H_4N_2^+$  parent ion ( $m/z=80$ ) had the largest intensity in all spectra measured and its intensity unlike the other fragment ions' ( $C_3H_3N^+$  with  $m/z=53$  and  $C_2H_2^+$  with  $m/z=26$ ) did not decrease significantly.

#### 4. References

- [1] A.N. Zaviropulo, O.B. Shpenik, P.P. Markush, M.I. Mykyta. 2014. Technical *Physics Letters* Vol. **40**. (No. 1) 13.
- [2] Jerry M. Rice, Gerald O. Dudek, Michael Barber. 1965. *Journal of the American Chemical Society* **87** 4569.
- [3] Townsend J S and Tiyard H T 1912 *Proc. of the Royal Society of London. Series A* **87** 357.

# **ELECTRON-IMPACT EXCITATION OF THE GAS-PHASE SORBITOL MOLECULE**

Mykola Erdevdy, Otto Shpenik, Vitalij Zvenihorodsky, Pavlo Markush

*Institute of Electron Physics, Ukrainian National Academy of Sciences,  
21 Universitetska str. Uzhgorod 88017, Ukraine*

E-mail: 1988.markus@gmail.com

Using an optical spectroscopy method, slow electron excitation of sorbitol in the gas-phase has been studied. Experiment was carried out applying a gas-filled cell at the incident electron current of 25  $\mu\text{A}$  (the energy spread being 0.4 eV) provided by a four-electrode gun with an oxide cathode. The emission spectra of sorbitol were recorded in the wavelength range between 270-500 nm at the incident electron energies of 17, 30 and 50 eV. The optical excitation functions for the most intense spectral bands  $\lambda_{\text{max}}=309$  nm and  $\lambda_{\text{max}}=340$  nm have also been measured.

## **1. Introduction**

Sorbitol is a sugar alcohol, which can be obtained by glucose reduction, changing the aldehyde group to a hydroxyl group. Sugars and sugar alcohols have been considered as biobased feedstocks to produce many of the chemicals in common use, which are derived from petroleum feedstocks [1]. Utilization of biobased materials will help to overcome energy shortage and prevent serious environmental pollution. This work has been devoted to the investigation of electron impact excitation of sorbitol in a gas phase.

## **2. Experiment**

Experiment was carried out using a gas-filled cell at the incident electron current of 25  $\mu\text{A}$  provided by a four-electrode gun with an oxide cathode (Fig. 1) [2]. A container with the powder sorbitol was placed in a close proximity to the cell provided with direct heating. In all our measurements, the container temperature was maintained within the 60-80  $^{\circ}\text{C}$  range. To prevent sorbitol condensation on the electron gun and collision cell elements their temperature was kept 20-30  $^{\circ}\text{C}$  above that of the sorbitol container. The residual gas pressure in the vacuum chamber under operating conditions did not exceed  $10^{-6}$  Torr. A collimated electron beam (2 mm in diameter, within the energy range 0-50 eV) passed the gas-filled cell and was detected by a deep Faraday cup. The instability of the electron current having passed the collision chamber did not exceed 3%. The electron beam energy spread in vacuum was 0.4 eV (full width at half-maximum of the differentiated current-voltage characteristic). When measuring the optical excitation functions the electron energy was varied with 200 meV step. Radiation selected by a diffraction monochromator MDR-2 was detected by a



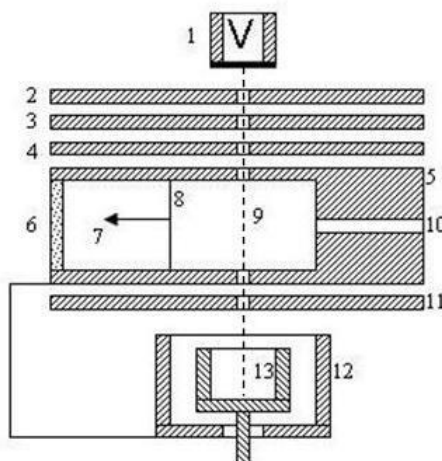


Fig 1. The layout of a four-electrode gun.

1-oxide cathode, 2-first anode, 3-second anode, 4-third anode, 5-fourth anode, 6-quartz window for transmitting radiation, 7-direction of radiation to the spectral device, 8-area of the collision of molecules with electrons, 9- electrons trajectory, 10-intake of the vapour of investigated molecules, 11-hold back anode, 12, 13-external and internal (Faraday cup) cylinders.

FEU-106 photomultiplier. The single photo-electron pulses from photomultiplier were amplified, shaped by a wideband amplifier-discriminator and entered the pulse counter via the PC interface card. In order to maintain the accuracy of measurements, when the statistical scatter of the pulses did not exceed 5-10%, the accumulation of signal at each point was carried out with an exposure of 10 to 40 s. The emission spectra in the 270-500 nm spectral region were measured with an 1 mm wide monochromator slit (i.e.  $\Delta\lambda=2$  nm) and at fixed electron energies of 17, 30 and 50 eV. The spectra were measured with a modulated electron beam, i.e. the cathode radiation was subtracted from the total signal with no taking into account the spectral sensitivity of the photomultiplier and the spectral transmission characteristics of the monochromator. For better visibility, the emission spectra and the optical excitation functions (OEFs) in figures 2 and 3 are represented by solid lines connecting discrete experimental points. For correct interpretation of the results of measurements, calibration of the energy scale of the incident electron beam is an essential problem. Calibration was carried out with respect to the shift of the voltage dependence of electron current onto the collector.

### 3. Results and discussion

Fig. 2 shows the emission spectra of sorbitol measured in the wavelengths range between 270-500 nm at the incident electron energies of 17, 30 and 50 eV. As seen, the spectra are relatively poor. A number of low-intensity emission bands are observed in the 350-500 nm region with the maxima at 290, 340, 392, 422-440 and 488 nm, as well as one extremely intense band with the maximum at 308-324 nm. This band could result from the excited OH radical (transition:  $X^2\Pi-A^2\Sigma^+$ ) [3].

Fig. 3 shows the optical excitation functions for the bands  $\lambda_{\max}=309$  nm and  $\lambda_{\max}=340$  nm. The 309 nm band excitation threshold energy was determined to be  $9.4\pm0.3$  eV, a sharp rise up to 18 eV following with an almost horizontal area could be observed. The 340 nm spectral band excitation threshold energy was determined to be  $11.7\pm0.3$  eV and a sharp feature was revealed at  $13.9\pm0.3$  eV.

This work has been supported by the Collegium Talentum grant.

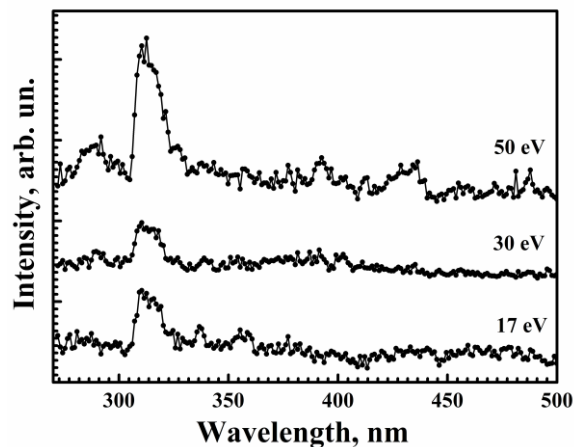


Fig. 2. Sorbitol emission spectrum.

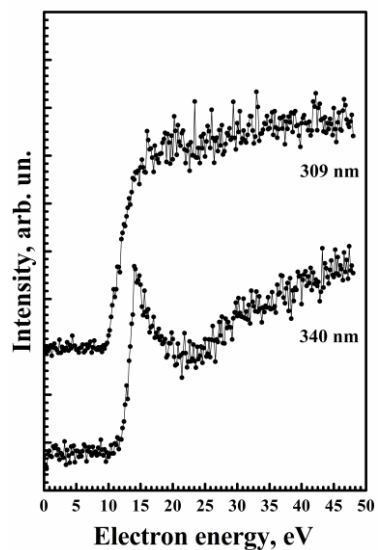


Fig. 3. OEFs of the spectral bands  $\lambda_{\text{max}}=309$  nm and  $\lambda_{\text{max}}=340$  nm.

#### 4. References

- [1] Yan W and J Suppes G 2008 *J. Chem. Eng. Data.* **53** 2033.
- [2] Shpenik O B, Erdevdy N M, Zvenigorodsky V V and Romanova L G 2013 *Journal of Applied Spectroscopy.* **80** 46.
- [3] Soskyda M T I 2004 *Uzhhorod University Scientific Herald. Series Physics.* **30** 54.

# ELECTRON-IMPACT IONIZATION AND DISSOCIATIVE IONIZATION OF SORBITOL IN GAS PHASE

Pavlo Markush, Anatoly Zavilopulo, Otto Shpenik, Irina Chernyshova

*Institute of Electron Physics, Ukrainian National Academy of Sciences,  
21 Universitetska str. Uzhgorod 88017, Ukraine*

E-mail: gzavil@gmail.com

The experiments were carried out by using two different experimental methods by means of a monopole mass spectrometer and a hypocycloidal electron spectrometer (HES) with a gas-filled cell. The sorbitol molecule mass spectrum has been measured at the ionizing electron energy of 70 eV. The most intense peaks in the mass spectrum correspond to the  $\text{CH}_3^+$ ,  $\text{H}_2\text{O}^+$ ,  $\text{C}_2\text{H}_5^+$ ,  $\text{C}_2\text{H}_5\text{O}^+$  and  $\text{C}_4\text{H}_9\text{O}^+$  fragment ions with  $m/z=15, 18, 29, 61, 73$ , respectively. The total ionization cross section for the sorbitol molecule within the energy range from the threshold up to 28 eV has been measured by means of the HES. The first ionization potential was determined to be 10.5 eV.

## 1. Introduction

Sorbitol is a sugar alcohol which, can be obtained by reduction of glucose changing the aldehyde group to a hydroxyl group. Sugars and sugar alcohols are considered as bio-based feedstocks to produce many of the chemicals in common use, which are derived from the petroleum feedstocks [1]. Utilization of bio-based materials will help to overcome energy shortage and prevent serious environmental pollution.

Electron impact studying of organic compounds is essential for the better understanding the processes taking place in the biological systems as a result of radiation. This work is devoted to the investigation of the sorbitol molecule by electron impact concentrating on the determination of the first ionization potential of sorbitol and the appearance energies of the fragment ions being formed due to dissociative ionization.

## 2. Experiment

The experiment was carried out using a monopole mass spectrometer, the method of crossing electron and molecular beams being employed [2]. The molecular beam was formed by evaporating the investigated substance using an effusive multichannel source of neutral particles. The concentration of molecules in the region of interaction with the electron beam was not lower than  $10^{11}$ - $10^{12}$  cm<sup>-3</sup> at the residual gas pressure of  $10^{-6}$  Torr in the vacuum chamber. In order to avoid condensation of the substance under investigation on the vacuum chamber walls and the mass spectrometer electrodes, the mass analyzer chamber was heated to the temperature  $\sim 150$ - $200^\circ\text{C}$ . Molecules were ionized in an ion source with electron bombardment. This source enables the electron beams of controlled energy to be obtained in the electron current stabilization mode at the current values 0.03-0.3 mA and with the energy spread not worse than  $\Delta E=250$  meV. The ions, extracted from the source were focused into a beam, moved to the analyzer (mass filter) electrode area, separated according to their mass and detected by a secondary electron multiplier or an ion collector in the form of a Faraday cup. Our experimental setup makes it possible to measure, besides the mass spectra, the energy dependence of dissociative ionization cross sections in the energy range from the threshold to 90 eV. The mass scale was calibrated using the mass lines of  $\text{N}_2$ , Ar and Kr.

Additional experiments were carried out applying a hypocycloidal electron spectrometer with a gas-filled cell to investigate more accurately the ionization processes of sorbitol by electron impact [3]. Powder sorbitol placed in a reservoir was heated resistively to  $60^\circ\text{C}$  to be obtained in the gas phase. The temperature of the spectrometer was maintained  $50^\circ\text{C}$  higher than that of the reservoir to avoid condensation of sorbitol on the HES elements. The residual gas pressure in the vacuum chamber under operating conditions did not exceed  $2 \cdot 10^{-6}$  Torr. The complete collection of electrons was ensured by an electron collector in a form of a deep Faraday cup. The energy spread of electrons in the beam did not

exceed  $\Delta E = 0.1$  eV. Positive ions formed in the collision region as a result of interaction with electrons were extracted to the ion detector, to which a positive potential of  $\sim 18$  V was applied. The current to the ion detector was measured by means of a digital picoammeter. The zero point of the energy scale was determined from the current-voltage characteristic.

### 3. Results

The sorbitol molecule mass spectrum was obtained at the ionizing electron energy of 70 eV and the temperature of 117 °C (Fig. 1). The spectrum is similar to those of polyalcohols. The presence of the hydrocarbon molecule in the organic compounds leads to lowering their ionization energies as well as to decrease of the initial molecular ion rate due to its fragmentation. It is the reason for the absence of sorbitol ion in the mass spectrum. The most probable process of sorbitol fragmentation is the  $\alpha$ -decay followed by the loss of the olefin molecules as a result of the rearrangement processes. The most intense peaks in the mass spectrum correspond to the  $\text{CH}_3^+$ ,  $\text{H}_2\text{O}^+$ ,  $\text{C}_2\text{H}_5^+$ ,  $\text{C}_2\text{H}_5\text{O}^+$  and  $\text{C}_4\text{H}_9\text{O}^+$  fragment ions with  $m/z = 15, 18, 29, 61, 73$ , respectively. Alcohols effectively absorb the water molecules, this fact can give an explanation for the intense peak of  $\text{H}_2\text{O}^+$  in the mass-spectrum. It has been proven to be true during the experiment when with rising sorbitol temperature the intensity of  $\text{H}_2\text{O}^+$  decreased. The water molecules can also be formed as a result of elimination of ethylene. The energy dependence of the dissociative ionization cross sections of the dominant fragment ions of sorbitol were also measured as well as their appearance energies were identified.

The total ionization cross section for the sorbitol molecule within the energy range from the threshold up to 28 eV was measured using the HES (Fig. 2). The first ionization potential (IP) was determined to be  $10.5 \pm 0.03$  eV, this value coincides well with that of the  $\text{CH}_3$  molecule obtained from the mass spectrometric studies. Weak features in a form of break (increase or decrease of slope) in the measured curve due to direct ionization or formation of fragments by dissociation can be observed. The energies of these features were determined by approximating the measured curve by a series of linear segments whose points of intersection reflect the onset and thus the appearance energies ( $\text{AE}_n$ ,  $n=1-6$ ) of new ionization processes. The following energies were obtained: 11.22, 12.24, 14.40, 17.78, 22.02 and 26.64 eV. The features at the energies of 11.22 eV and 12.24 eV were identified to correspond to the appearance energies of  $\text{C}_4\text{H}_9\text{O}^+$  and  $\text{C}_2\text{H}_5\text{O}^+$ .

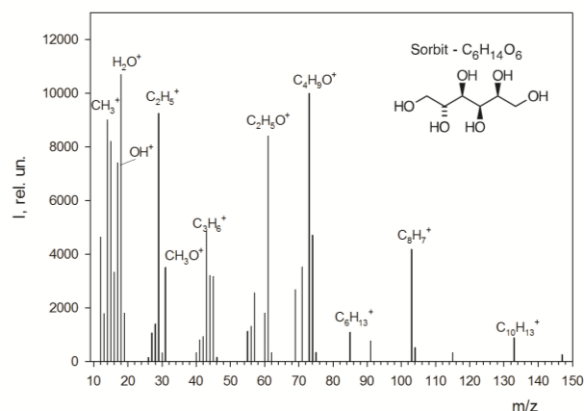


Fig. 1. Sorbitol molecule mass spectrum.

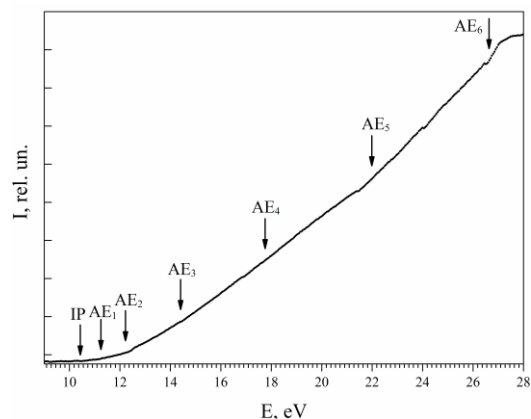


Fig. 2. Total ionization cross section of the sorbitol molecule.

### 4. References

- [1] Yan W and J Suppes G 2008 *J. Chem. Eng. Data.* **53** 2033.
- [2] Zavilopulo A N, Mykyta M I, Mylymko A N and Shpenik O B 2013 *Technical Physics. Volume* **58**(№. 9) 1251.

[3] Zavilopulo A N, Shpenik O B, Markush P P, Mykyta M I 2014 *Technical Physics Letter. Volume 40*(№. 1) 13.

## IONIZATION OF CYTOSINE MOLECULE BY ELECTRON IMPACT

Anatoly Zavilopulo, Mykhailo Mykyta, Olha Pylypchynets, Pavlo Markush

*Institute of Electron Physics, National Academy of Sciences of Ukraine, 88017, Uzhgorod, Ukraine*

E-mail: gzavil@gmail.com

The technique and the results of study of the yield of positive ions at the mass-spectrometric studies of ionization of cytosine molecule by electron impact. Mass spectra of the cytosine molecule at the electron energies of 20, 50, and 70 eV are obtained. Energies of appearance of the fragment ions are obtained from the ionization efficiency curves. The dynamics of formation of the most intense fragment ions is studied in the temperature range 300–480 K. The energy dependences of the ion formation efficiency are analyzed, their appearance energies are determined. The total ionization cross-section for the cytosine molecule is obtained in the electron energy range 5–90 eV.

### 1. Introduction

Exceptional biological significance of nitrogenous bases such as cytosine, adenine, thymine, guanine and uracil (derivatives of pyridine) gave a strong impetus to the studies of inelastic processes of interaction of these molecules with electrons. A special role in these studies is devoted to processes of ionization (total and dissociative) which result in destructive changes of biostructures on the molecular level. Note that at the ionizing electron energies exceeding the molecule ionization energy there is a great probability of formation of ions in electronically excited states. The dissipation of the energy of such states can be achieved in two ways – radiative, when the electron configuration is changed, and nonradiative, due to the potential surface intersection, i.e. the excited ion can transit into the ground state with an excessive vibrational energy, and at the potential surface intersection the ion transition to the ground state is not the only possibility. It seems important to perform a detailed study of the processes of cytosine fragmentation by electron impact which is the aim of this work.

### 2. Experiment

The experiment was carried out using a monopole mass spectrometer, the method of crossing electron and molecular beams being employed [1]. The molecular beam was formed by evaporating the investigated substance using an effusive multichannel source of neutral particles. The concentration of molecules in the region of interaction with the electron beam was not lower than  $10^{11}$ – $10^{12}$  cm<sup>-3</sup> at the residual gas pressure of  $10^{-6}$  Torr in the vacuum chamber. In order to avoid condensation of the substance under investigation on the vacuum chamber walls and the mass spectrometer electrodes, the mass analyzer chamber was heated to the temperature 340–420 K. Molecules were ionized in an ion source with electron bombardment. This source enables the electron beams of controlled energy to be obtained in the electron current stabilization mode at the current values 0.03–0.3 mA and with the energy spread not worse than  $\Delta E=250$  meV. The ions extracted from the source were focused into a beam, moved to the analyzer (mass filter) electrode area, separated according to their mass and detected by a secondary electron multiplier or an ion collector in the form of a Faraday cup. Our experimental setup makes it possible to measure, besides the mass spectra, the energy dependence of dissociative ionization cross sections in the energy range from the threshold to 90 eV. The mass scale was calibrated using the mass lines of N<sub>2</sub>, Ar and Kr.

### 3. Results

The cytosine molecule mass spectrum was measured at the ionizing electron energy of 70 eV and the temperature of 440 K (Fig. 1). As one can see, the mass spectrum has a large number of intense molecular

ion peaks which arise from the fragmentation of the initial molecule. The most intense peaks in the mass spectrum correspond to the  $\text{C}_4\text{H}_5\text{N}_3\text{O}^+$  parent ion with  $m/z=111$  and the fragment ions with  $m/z = 18, 28, 41, 69, 83$ . It might be supposed [2] that the fragmentation process begins with the loss of HNC $\text{O}$  neutral fragment ( $m/z = 43$ ) which results in the formation of  $\text{C}_3\text{H}_4\text{N}_2^+$  fragment ion ( $m/z = 68$ ). The formation of the  $\text{C}_3\text{H}_5\text{N}_2^+$  molecular ion at  $m/z = 69$  is due to the loss of NCO radical ( $m/z = 42$ ). The  $\text{C}_2\text{H}_3\text{N}^+$  ( $m/z = 41$ ) and  $\text{C}_2\text{H}_2\text{N}^+$  ( $m/z = 40$ ) fragment ions are formed from ions with larger  $m/z$  through the loss of CN fragment. The fragmentation of the parent ion with the loss of the  $\text{C}_3\text{H}_5\text{N}_2$  neutral fragment ( $m/z = 69$ ) leads to the formation of  $\text{NCO}^+$  ( $m/z = 42$ ).

The appearance of the intense line at  $m/z = 28$  in the mass spectrum can be related to the decay of the autoionizing states in cytosine causing the formation of  $\text{CO}^+$  ion. The appearance of low-intensity lines around the intense ones in the direction of increasing  $m/z$  can be explained by the presence of  $^{13}\text{C}$  and  $^{15}\text{N}$  isotopes in the initial molecule (see Fig. 1), whereas those toward decreasing  $m/z$  are caused by the detachment of hydrogen atoms from the ions.

Note the presence of an intense line in the mass spectrum at  $m/z = 28$ , the appearance of which is probably related to the decay of autoionizing states of the cytosine molecule with the formation of  $\text{CO}^+$  ions. Low-intensity peaks observed in the mass spectrum in Fig. 1 as satellites of the intense peaks toward increasing  $m/z$  can be explained by the presence of  $^{13}\text{C}$  and  $^{15}\text{N}$  isotopes in the initial molecule. Other satellite peaks in the vicinity of the main peaks at  $m/z = 28, 41, 69, 83, 111$  observed in the mass spectrum toward decreasing  $m/z$  can be explained by the detachment of a hydrogen atom from the ions in the course of the fragmentation.

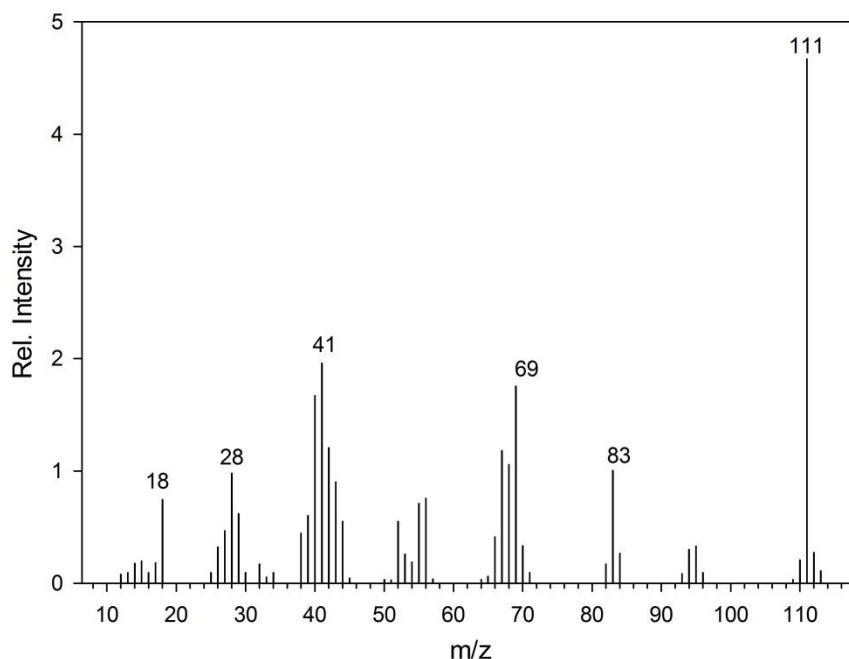


Fig. 1. Cytosine molecule mass spectrum  $T=440\text{ K}$ ,  $U_e=70\text{ eV}$ .

Fig. 2 **a** shows the energy dependence of the total ionization cross section of the cytosine molecule. It is obvious that the largest contribution to the total ionization cross section is given by the  $\text{C}_4\text{H}_5\text{N}_3\text{O}^+$  molecular ion ( $m/z = 111$ ). Consequently, it indicates the stability of the cytosine molecule during its interaction with electrons. This is not common for the majority of complex organic molecules, such as alkane groups, as in their mass spectra the molecular ion peak either has low intensity or is absent. The energy dependence of the total ionization cross section and the dissociative ionization cross section of the  $\text{C}_3\text{H}_5\text{N}_2^+$  fragment ion ( $m/z = 69$ ) show a similarity, but their threshold energies are different. The ionization potential of the cytosine molecule was determined the method [3] of the curve energy

dependence of the total cross section (Fig. 2a) to be  $E_i = 8,93$  eV which coincides well with  $E_i = (9,00 \pm 0,1)$  eV obtained in [4]. We determined the appearance potential for the  $C_3H_5N_2^+$  fragment ion as  $E_{AP} = 10,3 \pm 0,2$  eV, no corresponding data being presented in [4].

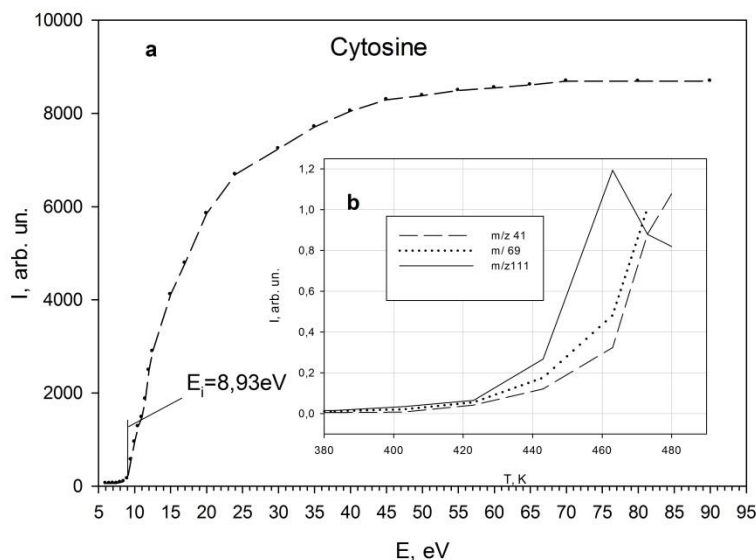


Fig. 2. Energy dependence of the total ionization cross section of the cytosine molecule (a), temperature dependence of formation of the  $C_4H_5N_3O^+$ ,  $H_2O^+$ ,  $C_3H_5N_2^+$  ions (b).

The temperature dependences of formation of the  $C_4H_5N_3O^+$ ,  $H_2O^+$ ,  $C_3H_5N_2^+$  ions were also measured (Fig. 2 b). It is worth noticing that all curves have a smooth rise in the temperature range of 340–420 K and then a sharp rise in the range of 420–470 K. At the temperature  $T=460$  K the  $C_4H_5N_3O^+$  ion has a maximum followed by a decrease of intensity. With regard to the  $H_2O^+$ ,  $C_3H_5N_2^+$  fragment ions, their intensity continues to increase with the further increase of temperature. It can be explained by thermal degradation of the cytosine molecule as the intensities of fragment ion peaks increase while that of the molecular ion decreases. Thus, the current study confirms the assumption [2] of the cytosine stability during its interaction with electrons. With regard to the temperature dependences of the ion formation, additional experiments in a wider temperature range should be carried out.

We studied the dynamics of formation of the most intense fragment ions versus the molecule source temperature. The measured temperature dependences of formation of  $C_2H_3N^+$  ( $m/z = 41$ ),  $C_3H_5N_2^+$  ( $m/z = 69$ ), and  $C_4H_5N_3O^+$  ( $m/z = 111$ ) ions are shown in Fig. 2 b. As can be seen from the figure, a characteristic feature of these dependences is a similar gradual increase in the temperature range 380–420 K followed by a sharp increase in the range 420–460 K. For the  $C_4H_5N_3O^+$  molecular ion a saturation is observed at the temperature  $T=460$  K followed by an intensity decrease. With regard to the  $C_2H_3N^+$  and  $C_3H_5N_2^+$  fragment ions, their intensity continues to increase with temperature. One can assume that in the temperature range 460–480 K the process begins with the temperature destruction of the  $C_4H_5N_3O$  cytosine molecule when the molecular peak intensity decreases and the fragment ion peak intensity continues to grow.

Thus, the studies performed confirm the assumption made in [2] on the stability of cytosine toward destruction under electron impact. Regarding the temperature dependences of the ion formation, additional experiments should be carried out in a broader temperature range.

#### 4. References

- [1] A. N. Zavilopulo, M. I. Mykyta, A. N. Mylymko, and O. B. Shpenik 2013, *Technical Physics Vol. 58* (No. 9) 1251.
- [2] M.I. Shafranyosh, I.Yu. Khmara, M.I. Sukhoviya, M.S. Golovnja, I.I. Shafranyosh 2013, *Uzhhorod University Scientific Herald. Series Physics*. Issue **33** 137.
- [3] M. Stano, S. Matejcik, J. D. Skalny, et al., 2003 *J. Phys. B* **36** 261.



[4] NIST *Standard Reference Database*, Ed. by W. G. Mallard and P. J. Lindstrom 2000, (No. 69).

# POSITIVE AND NEGATIVE ION FORMATION IN THE GLYCEROL VAPOUR BY ELECTRON IMPACT

Pavlo Markush

*Institute of Electron Physics, Ukrainian National Academy of Sciences,  
21 Universitetska str. Uzhgorod 88017, Ukraine*

E-mail: 1988.markus@gmail.com

In this work, the positive and negative ion formation of the gas-phase glycerol by electron impact has been studied. The experiment was performed using a hypocycloidal electron spectrometer with a gas-filled cell. The negative ion formation of glycerol has been investigated in the energy range from 0 to 15 eV. It has been found that both fragments of water and the OH, CH groups in the bound state in glycerol could form negative ions in the energy range of 6-8 eV due to electron attachment to them. The total ionization cross section for the glycerol molecule within the energy range from the threshold up to 35 eV has been measured. The first ionization potential has determined to be 10.1 eV.

## 1. Introduction

Glycerol (sugar alcohol) widely present in nature as an intermediate in many biological pathways, is used in pharmaceutical formulations, and furthermore is applied as a model system to understand sugar chemistry [1]. Along with methanol, ethanol, methyl and ethyl esters of fatty acids as well as terpenoids glycerol is treated as a potential green fuel to replace the traditional fossil fuel. In particular, the possibility of using glycerol as a biofuel makes it important to extend our knowledge on its physical properties. There are no theoretical or experimental data, as far as we know, on the negative ions of glycerol. In this work, we report for the first time on the anion formation of glycerol in the gas phase by electron impact.

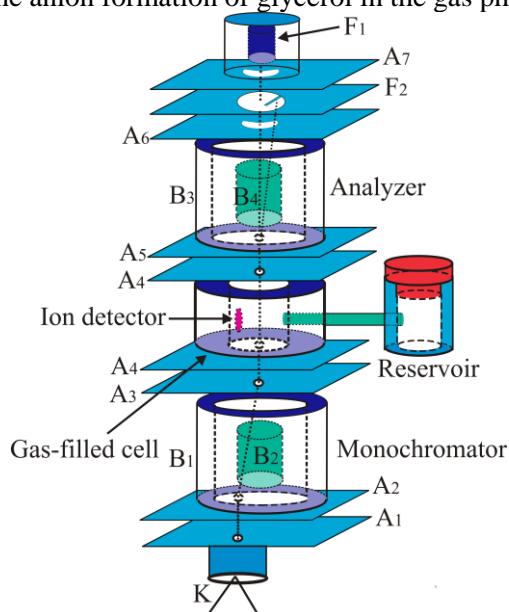


Fig. 1. The layout of a hypocycloidal electron spectrometer.

## 2. Experiment

The experiment was carried out using a hypocycloidal electron spectrometer (HES) with a gas-filled cell (collision region) [1]. Liquid glycerol placed in the reservoir was heated resistively to 30 °C to obtain its gas phase. The temperature of the spectrometer was maintained 50 °C higher than that of the reservoir to avoid condensation of glycerol on the HES elements. The residual gas pressure in the vacuum chamber under operating conditions did not exceed  $2 \cdot 10^{-6}$  Torr. The complete collection of electrons was ensured

by an electron collector in a form of a deep Faraday cylinder (F1). The energy spread (full width at half-maximum of the differentiated current-voltage characteristic) of electrons in the beam did not exceed 0.3 eV for the negative ions and was 0.1 eV in case of the positive ions. The different electron energy spread is explained by the magnitude of the current needed to obtain the necessary positive and negative ion signals. Ions formed in the collision region as a result of interaction with electrons were extracted to the ion detector, to which the positive and negative potentials of  $\sim 6$  V were applied. The current to the ion detector was measured by means of a digital picoammeter. The zero point of the energy scale was determined from the current-voltage characteristics.

### 3. Results and discussion

#### *Positive ion formation*

The total ionization cross section for the glycerol molecule within the energy range from the threshold up to 35 eV has been measured (Fig. 2) The first ionization potential (IP) has been determined to be 10.1 eV, this value coincided well with that for the  $\text{C}_2\text{H}_4\text{O}^+$  (IP=10.2 eV) molecule obtained from the mass spectrometric studies of glycerol in [3]. Weak features in a form of break (increase or decrease of slope) in the measured curve due to direct ionization or formation of fragments by dissociation can be observed. The energies of these features were determined by approximating the measured curve by a series of linear segments whose points of intersection reflect the onset and, thus, the appearance energies ( $\text{AE}_n$ ,  $n=1-6$ ) of new ionization processes. The following energies were obtained: 11.06, 12.86, 14.2, 18.08, 24.97 and 26.06 eV.

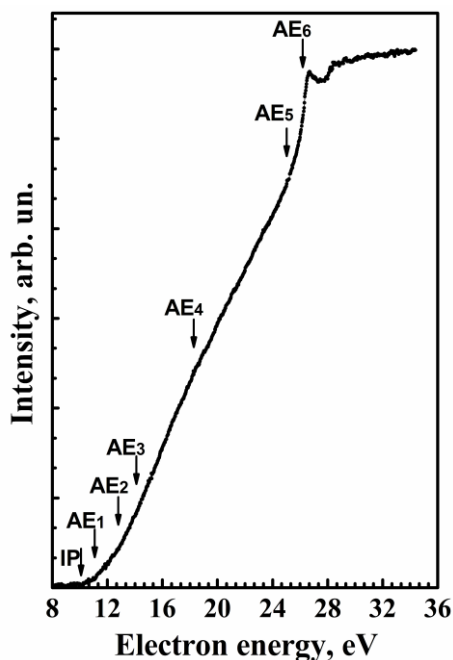


Fig. 2. Total ionization cross section of the glycerol molecule.

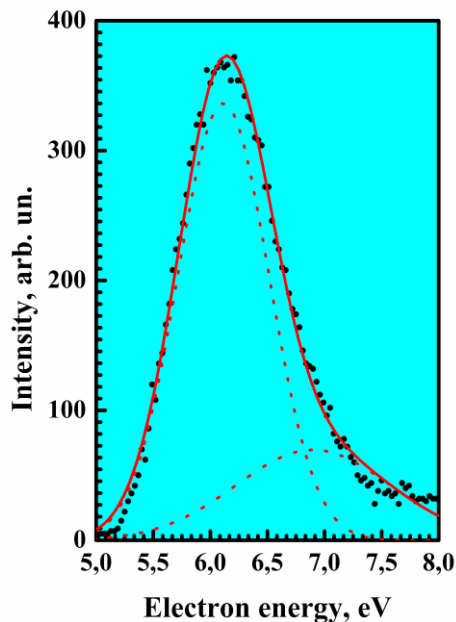


Fig. 2. Energy dependence of the anion formation of glycerol in gas phase. The circles denote the measured signal, whereas the dotted red lines show the two Gaussians that were fitted to the experimental curve. The solid red line is the sum of the Gaussians.

#### *Negative ion formation*

The anion formation in glycerol has been investigated in the energy range from 0 to 15 eV. However, no signal from negative ions was detected, except for that in the energy range between 5 and 8 eV where a broad feature could be observed (Fig. 3). The relatively large energetic width of the feature suggests that it results from the formation of at least two negative ions with the appearance energies close to each another. Detailed mathematical analysis of the experimental curve allowed us to determine their energies being 6.1 and 6.9 eV, respectively. Our result is supported by the work [4], in which a negative ion resonance in glycerol was found at the incident energy of 8 eV studying the inelastic scattering of low energy electrons from liquid glycerol. Formation of the resonance was attributed to the excitation of the OH and CH groups in glycerol as a result of electron attachment to them. In [5], the dehydration mechanisms (a loss of water) were observed during glycerol evaporation. Taking into consideration that the water molecules are present in the glycerol vapor, formation of their negative ions cannot be excluded. The authors [6] studying the dissociative electron attachment to the water molecule reported the negative ion formation of the  $\text{H}^-$ ,  $\text{O}^-$  and  $\text{OH}^-$  fragments at 6.5 eV. In addition,  $\text{H}^-$  has the largest intensity among them. In our case, it is difficult to identify unambiguously the origin of the observed feature as both water fragments and the OH, CH groups in bound state in glycerol could cause it.

This work has been supported by the Collegium Talentum grant.

#### 4. References

- [1] Bell F, Ruan Q, Golan A, Horn P, Ahmed M, Leon S and Head-Gordon M 2013 *J. Am. Chem. Soc.* **135** 14229.
- [2] Romanyuk N I, Shpenik O B, Mandy I A, Papp F F, Chernyshova I V 1993 *Zh. Tech. Phys.* **38** 138.
- [3] Franziska B, Qiao N R, Amir G et al. 2013 *J. Am. Chem. Soc.* **135** 14229.
- [4] Krebs T, Andresson G, Morgner H 2007 *Chem. Phys.* **340** 181.
- [5] Nimlos M, Blanksby S, Qian X, Himmel M, and Johnson D 2006 *J. Phys. Chem. A.* **110** 6145.
- [6] Itikawaa Y, Mason N 2005 *J. Phys. Chem. R ef. Data.* **34** №1.

# POSITIVE AND NEGATIVE ION FORMATION IN URACIL BY LOW-ENERGY ELECTRONS

Irina V. Chernyshova, Jeno E. Kontros, Pavel P. Markush, Otto B. Shpenik

*Institute of Electron Physics, Ukrainian National Academy of Sciences,*

*21 Universitetska str., 88017 Uzhgorod, Ukraine*

E-mail: irinav.chernyshova@gmail.com

Total cross section for the electron attachment (EA) to uracil (U) has been studied in the electron energy range from 0 to 9 eV using a hypocycloidal electron spectrometer. The dominant negative ion formed via the EA reactions to U is  $(U-H)^-$ . In the energy range between about 3 and 9 eV a total contribution of the  $(C_3H_3N_2O)^-$ ,  $(C_3H_2NO)^-$ ,  $(C_2H_3N)^-$ ,  $(OCN)^-$ ,  $(CN)^-$  and  $(O)^-$  fragment anions is observed, however, with significantly lower cross section values. The total ionization cross section for the U molecule within the energy range from the threshold up to 26 eV has been also measured. The ionization potential for the uracil molecule was determined to be  $E_i = 9.47 \pm 0.05$  eV. The most prominent features of the cross section are observed at 10.88, 16.68, 20.35 eV.

## 1. Introduction

Ionizing radiation ( $\alpha$ ,  $\beta$ , X and  $\gamma$ -rays) may induce genotoxic damage in cell such as single- and double-strand breaks (SSB and DSB). The primary radiation is responsible for about one third of the mutagenic damages and about two thirds of the damages can be linked to secondary species such as electrons and radicals formed in the interaction of the primary radiation with the irradiated medium [1]. The most abundant secondary species are electrons, which are produced with the energies up to 20 eV. Sanche and co-workers [2] demonstrated that low energy ( $E < 20$  eV) electrons may induce SSB and DBS in DNA.

The uracil molecule ( $C_4H_4N_2O_2$ ) is one of the four nucleic acid bases involved in the DNA molecule composition, which plays an essential role in living activity of live organisms, therefore, the comprehensive studies of the properties of this molecule are of great importance.

Here we report on the results of our studies on the total cross sections for the production of both positive and negative ions of the uracil molecule by slow ( $E < 30$  eV) electrons.

## 2. Experiment and discussion

The ionization cross section and the electron attachment cross section for uracil were studied using a hypocycloidal electron spectrometer (HES) [3] with a gas-filled cell (Fig. 1), which we suc-

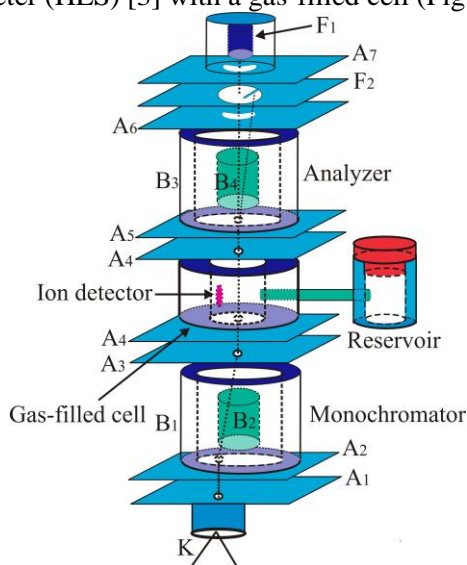


Fig. 1. Schematic view of the experimental setup.

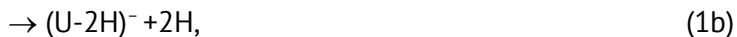
cessfully used previously to investigate thymine [4]. This instrument consists of two identical successive hypocycloidal electron monochromators (HEMs) [5]: one of them operates like a monochromator, while the other is a scattered-electron analyzer. They are separated by a gas-filled cell, which serves as a collision chamber. We chose the HEM to form an electron beam because it provides beams of rather high density and small electron-energy spread and makes it possible to operate at very low (close to zero) energies. The complete collection of electrons was ensured by an electron collector in a form of a deep Faraday cylinder (F1). The best HEM energy resolution in these measurements was  $\Delta E_{1/2} = 80$  meV (full width at half maximum of the electron-energy distribution) at an electron current of 10–20 nA.

The target in the gas phase was formed in a reservoir. It is a hollow stainless-steel cylinder heated resistively to desired temperature, at which there are no structural changes in the uracil molecule ( $T_m = 320$ – $325^\circ\text{C}$ ). The heating temperature was controlled by a calibrated chromel-alumel thermocouple fixed at the reservoir bottom. The uracil powder (99% purity, Sigma-Aldrich product) placed into a quartz ampoule was heated up to  $\sim 100^\circ\text{C}$  in the reservoir, filling, thus, the gas cell (at  $P \approx 10^{-3}$  Torr). The ions produced were extracted to the collector (ion detector) mounted perpendicularly to the ion beam direction. The temperature of the spectrometer was maintained  $30^\circ\text{C}$  higher than that of the reservoir to avoid condensation of uracil on the HES elements. A low negative potential was applied to the collector when detecting the positive ions, while for the negative-ion detection its polarity was changed to the positive one. The current to the ion detector was measured by means of a digital picoammeter. The zero point of the energy scale was determined from the current-voltage characteristics.

### 3. Results and discussion

#### *Negative ion formation*

Figure 2 shows the total dissociative electron attachment cross section for the uracil molecule as a function of electron energy from 0 to 9 eV. The absolute value of the cross section was obtained by normalizing it to the data [6] at electron energy 1 eV. An intense structure with maximum at 1.0 eV was observed in the 0–3 eV energy region. As the mass-spectrometric studies [6] have shown, this structure was due to the  $(\text{U-H})^-$  negative ion formation via the dissociative electron attachment to the initial molecule (see process (1a)). Vibrational structures (indicated by arrows) can be observed in the measured curve similarly to the case of thymine [4]. Above 3 eV the shape of the cross section is determined by the total contribution of the  $(\text{U-2H})^-$ ,  $(\text{C}_3\text{H}_3\text{N}_2\text{O})^-$ ,  $(\text{C}_3\text{H}_2\text{NO})^-$ ,  $(\text{C}_2\text{H}_3\text{N})^-$ ,  $(\text{OCN})^-$ ,  $(\text{CN})^-$  and  $(\text{O})^-$  fragment anions formed in following processes [6]:



The dissociative EA cross section for  $(\text{C}_3\text{H}_2\text{NO})^-$  and  $(\text{OCN})^-$  fragment anions are larger in energy range from 3 to 9 eV.

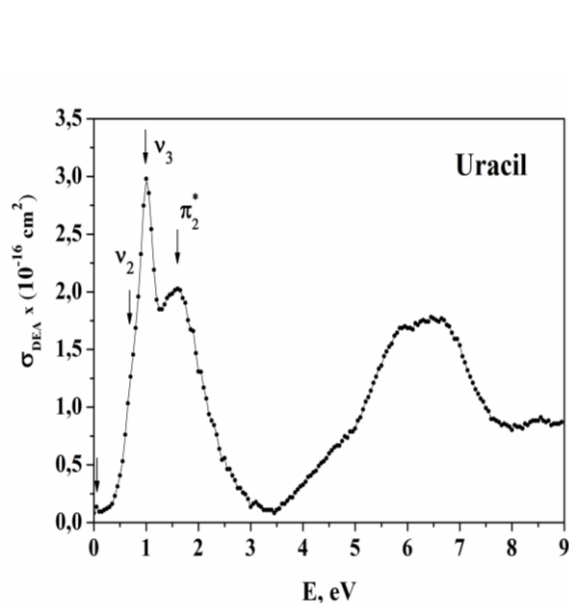


Fig. 2. Total dissociative electron attachment cross section for a gas-phase uracil as a function of electron energy.

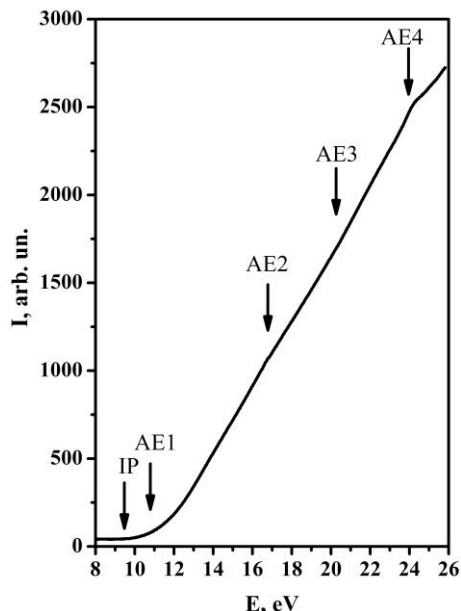


Fig. 3. Total ionization cross section for uracil as a function of electron energy.

### Positive ion formation

The total ionization cross section for the U molecule within the energy range from the threshold up to 26 eV was also measured. The ionization potential for the uracil molecule was determined to be  $E_i = 9.47 \pm 0.05$  eV. The thorough measurements allowed the weak features in the ionization curve to be observed being related to the formation of the positive ionic fragments of the initial molecule. The most prominent features of the cross section are observed at 10.88, 16.68, 20.35 and 23.54 eV. The first one is related to the formation of the  $\text{C}_3\text{H}_3\text{NO}^+$  ionic fragment of the initial molecule [7]. The two last features could be assigned to the involvement of the double U molecule ionization predicted in [8].

## 4. References

- [1] Michael B D and O'Neill P A 2000 *Science* **287** 1603.
- [2] Cobut V, Fongillo Y, Patau J P et al. 1998 *Radial. Phys. Chem.* **51** 229.
- [3] Kontros J E, Szoter L, Chernyshova I V, Shpenik O B 2002 *J. Phys. B.* **35** 2195.
- [4] Chernyshova I V, Kontros J E, Shpenik O B et al. 2011 *Materials Science (Medziagotyra)* **17** №3 322.
- [5] Romanyuk N I, Shpenik O B, Mandi I A et al. 1993 *Zh. Tekh. Fiz.* **63** 138.
- [6] Denifl S, Ptasinska S, Hanel G et al. 2004 *J. Chem. Phys.* **120** 6557.
- [7] Trofimov A B, Schirmer J, Kobychiev V B et al. 2006 *J. Phys. B* **39** 305.
- [8] Champeaux J-P, Carcabal P, Sence M et al. 2011 *J. Phys. B* **44** 045205 (6pp).

# MODIFICATION OF THIN FILMS INDUCED BY SLOW HEAVY IONS ANALYZED WITH PIXE AND SRIM

Małgorzata Antoszewska\*, Romuald Brzozowski, Marek Moneta

Uniwersytet Łódzki, Wydział Fizyki i Informatyki Stosowanej,  
Pomorska 149, PL 90-236 Łódź, Poland  
E-mail: \*m\_ateno@interia.pl

Particle induced characteristic X-rays (PIXE) emitted during impact of ions on a solid surface provide not only information on fundamentals of atomic excitation and further recombination processes, but can also give practical information on elemental composition and dynamics of restructuring of the subsurface region measured in time of irradiation. In this work PIXE emitted during interaction of slow heavy ions with specially prepared thin films were used. Kinematics was simulated numerically with SRIM in grazing incident-exit angle geometry and in time sequence in order to determine dynamics of formation of subsurface region damaged through implantation, sputtering and interface mixing. It was shown that structure and composition of films and surfaces are not stable against HI irradiation due to preferential sputtering and implantation of ions and recoils and that dynamics of such the modification can *in-situ* be monitored with PIXE and analysed with SRIM.

## 1. Instability of thin films induced by Ar with PIXE and SRIM

In order to determine stability of the films against HI sputtering and recoil implantation, we used time sequence in measuring X-ray signals coming from the films or implanted elements and related them to the signal from Si base. Detailed analysis of PIXE induced by Ar impact onto Fe(10nm)/Si film shown in Fig.(1) is presented in ref.[1]. The X-ray intensity from Ar increases monotonically and shortly becomes comparable with the decreasing signal from Si. The Ar atoms which, in this geometry, are mainly RBS-scattered (50%), tend to be uniformly distributed in the film with a slight density increase (up to 0.06%) in the region of mixed Fe/Si interface [1], thus intensifying radiation through molecular effect in symmetric collisions. The declining radiation from Si substrate can be understood as an effect of absorption of the radiation by additional Ar component of the film. The decrease of the signal from Fe can be explained by intensive surface sputtering which, at this geometry is  $Y \approx 30\text{Fe}/\text{Ar}$  [1], thus thinning the film at the speed of 1A of Fe per  $10^{12}\text{Ar}/\text{cm}^2$ , as it is illustrated in Fig.(1).

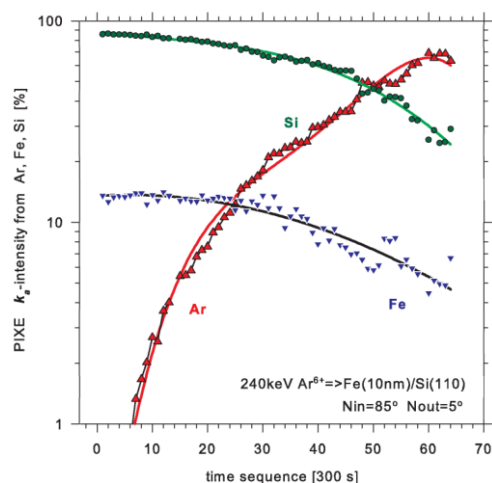


Fig. 1. PIXE from Fe, Si and Ar tri-layer [1].

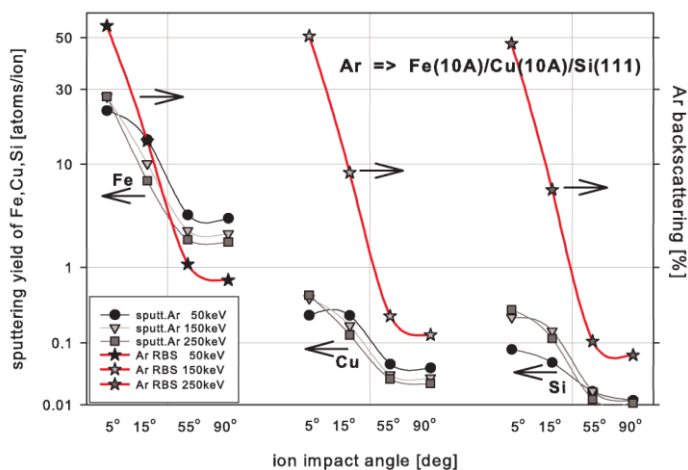


Fig. 2. sputtering of Fe(10A)/Cu(10A)/Si(111) films [2].



In order to get some insight into the ion scattering process, the present experimental arrangement with 50-250keV Ar ion beam impact on Fe/Cu/Si tri-layer at 5° angle of incidence (and other appropriate initial parameters) were simulated with SRIM [1] and presented in Fig.(2). They reveal that emission of atomic species from the irradiated surface is strongly energy and incident angle dependent. Also reflection of incident ions from the surface shows the similar angular dependence. In the grazing incidence geometry  $\varphi_{in} < 5^\circ$ , an Ar ion can sputter about 30 Fe atoms and about 50% incident Ar ions fluence is scattered back from the surface, whereas the remaining part is implanted.. The Cu film and Si substrate are expected to be sputtered at a negligible yield of 0.45 Cu/Ar and 0.35 Si/Ar, respectively, thus being completely screened by Fe film. In consequence of HI irradiation we observe, for instance: extensive vacancies creation in Fig.(3) and depth distributions of recoils Fig.(4).

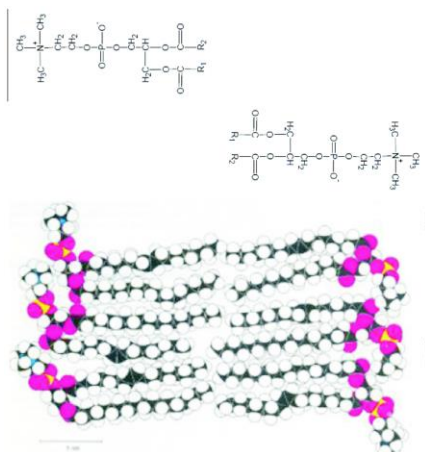


Fig. 3. Cross section of the cell wall.

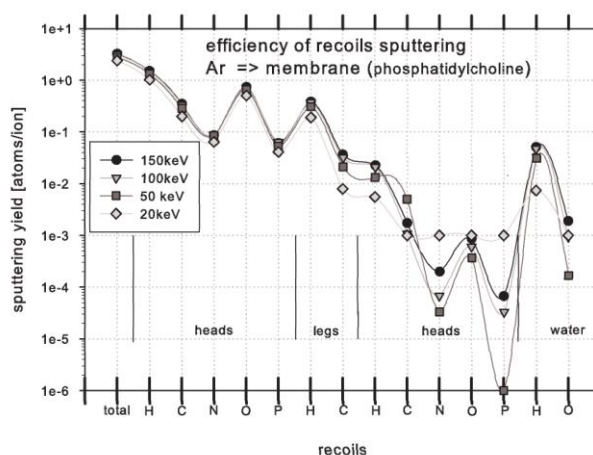


Fig. 4. Sputtering efficiency of recoils.

## 2. Stability of cellular membrane against HI irradiation with SRIM

Cellular membranes, composed mainly of light elements, like H, C, N or O, are typically 7 - 10 nm thick with two regular layers of lipid molecules containing various types of protein molecules.

For the present simulations of ion beam impact on cellular membrane we accepted a model in which the membrane, illustrated in Fig.(3), is composed of a double layer of phosphatidylcholine separating the cellular interior filled with water from the exterior of the cell, set as a diluted gas phase. Heads of the phospholipids are represented by structures:  $H_{18}C_{10}NO_8P_1$ . Fatty tails of the molecules, composed of hydrogens and carbons in the proportion  $C_{32}H_{64}$ , which belong to palmitic and oleic acids, were arranged in an internal matrix of 6nm thick placed between hydrophobic heads, each 1.5 nm thick. Ar ions of the energy 50-250keV were directed either at grazing incidence or perpendicularly to the membrane surface and the basic scattering characteristics were accumulated.

Sputtering efficiency of recoils from selected regions of cell membrane under impact of Ar ions of different energies at normal incidence is shown in Fig.(4). The regions of *heads*, *legs* and water forming cell interior were separated. Sputtering of hydrogen is prevailing, which means that H atoms are subjected to hard collisions, which can lead to ionization, scattering and creation vacancies. It can be also seen that O from external *heads* exposed to ion beam, is an order of magnitude more effectively sputtered than N and P belonging to the same structure, and that this effect is approximately independent of ion energy. Atomic species from internal *heads* are sputtered and excited  $10^3$  times less effectively than these from external *heads*.

### 3. References

- [1] M. Antoszewska, R. Brzozowski, J. Balcerski, K. Dolecki, E. Frątczak, B. Pawłowski, M. Moneta, Nuclear Instr. Meth. Phys. Res. B310 (2013) 27-31
- [2] J.F. Ziegler, J.P. Biersack and M.D. Ziegler, *The Stopping and Range of Ions in Solids*, (2008)  
<http://www.SRIM.org>

# ELECTRON-IMPACT IONIZATION CROSS SECTIONS CALCULATIONS FOR PURINE AND PYRIMIDINE MOLECULES

Bożena Żywicka<sup>1</sup>, Paweł Możejko<sup>1</sup>

<sup>1</sup>Atomic Physics Division, Department of Atomic, Molecular and Optical Physics, Faculty of Applied Physics and Mathematics, Gdańsk University of Technology, ul. Gabriela Narutowicza 11/12, 80-233 Gdańsk, Poland

E-mail: boshena@mif.pg.gda.pl, paw@mif.pg.gda.pl

Cross sections for electron-impact ionization of purine and pyrimidine molecules have been calculated using binary-encounter-Bethe method for electron energies ranging from the ionization threshold up to 5 keV. Ionization cross section for purine molecules is 1.4 times higher than for pyrimidine molecules. Acceptable agreement between experimental and theoretical ionization data for pyrimidine molecule has been found.

## 1. Introduction

The low and intermediate-energy electrons interactions with biomolecules have been extensively studied during last fifteen years. They play important role in the damage induced to the living cells by ionizing radiation [1]. In the present work we report ionization cross section calculations for two important compounds i.e. purine (C<sub>5</sub>H<sub>4</sub>N<sub>4</sub>) and pyrimidine (C<sub>4</sub>H<sub>4</sub>N<sub>2</sub>) molecules. Pyrimidine molecule is a base compound of pyrimidine DNA and RNA bases: cytosine, thymine and uracil. Purine is one of the most occurring nitrogen-containing heterocyclic molecules in the nature. It is a base compound of two DNA bases i.e. guanine and adenine. Calculations have been performed using binary-encounter-Bethe method. This method has been employed successfully in electron-molecule and biomolecule ionization cross sections calculations in our previous studies e.g. [2-5].

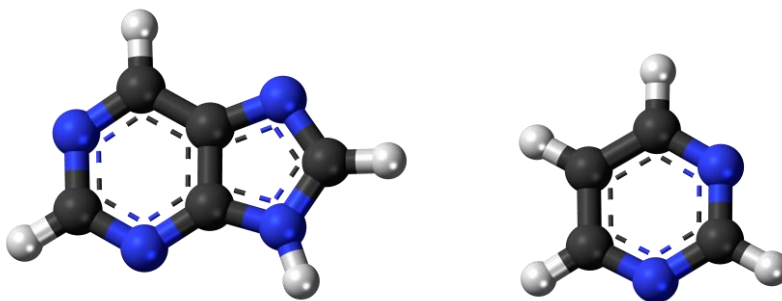


Fig. 1. Geometry of purine and pyrimidine molecules.

## 2. Theoretical method

According to the BEB model [6,7] the electron-impact ionization cross section per molecular orbital is given by

$$\sigma^{BEB} = \frac{S}{t+u+1} \left[ \frac{\ln t}{2} \left( 1 - \frac{1}{t^2} \right) + 1 - \frac{1}{t} - \frac{\ln t}{t+1} \right], \quad (1)$$

where  $u = U/B$ ,  $t = T/B$ ,  $S = 4\pi a_0^2 N R^2 / B^2$ ,  $a_0 = 0.5292 \text{ \AA}$ ,  $R = 13.61 \text{ eV}$ , and  $T$  is the energy of impinging electrons. Finally, the total cross section,  $\sigma^{ion}$ , for electron-impact ionization can be obtained as:

$$\sigma_{Ion} = \sum_{i=1}^{n_{MO}} \sigma_i^{BEB},$$

(2)

where  $n_{MO}$  is the number of the given molecular orbital. The electron binding energy  $B$ , kinetic energy of the orbital,  $U$ , and orbital occupation number,  $N$ , have been calculated for the ground states of the geometrically optimized molecules with the Hartree-Fock method using the GAUSSIAN code [8], and Gaussian 6-311G basis set. Obtained in this way, ionization energies are not precise enough and usually are higher more than 1 eV from experimental ones. Therefore we performed also outer valence Green function (OVGF) calculations of ionization potentials [9-12] using the GAUSSIAN code [8]. Obtained in that way the first ionization potentials are equal to 9.068 eV for purine and 9.151 eV for pyrimidine molecules.

### 3. Results

Calculated ionization cross sections for purine and pyrimidine molecules are shown in figure 2.

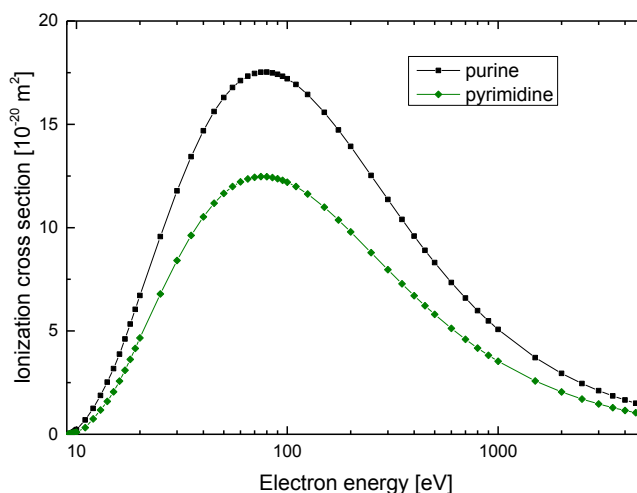


Fig. 2. Ionization cross section for purine and pyrimidine molecules calculated with the BEB method.

In the whole studied energy range ionization cross section for purine is significantly higher than those for pyrimidine. For purine molecules ionization cross section maximum of  $17.53 \times 10^{-20} \text{ m}^2$  is located at 80 eV while the ionization cross section maximum of  $12.47 \times 10^{-20} \text{ m}^2$  for pyrimidine is peaked at 75 eV.

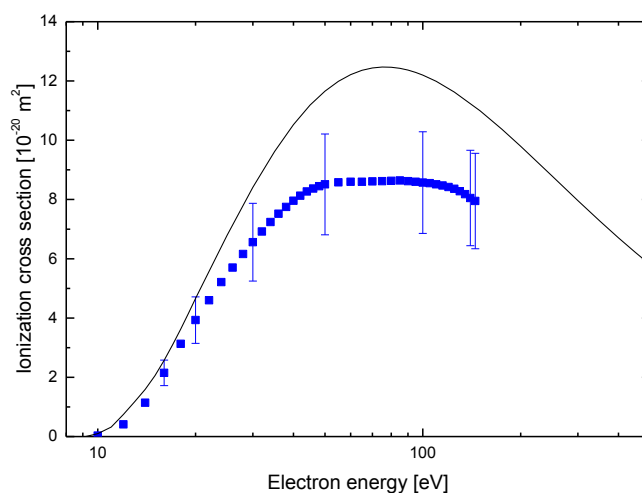


Fig. 3. Comparison between calculated (-) and measured (■) [13] ionization cross sections for pyrimidine molecules.

In Fig. 3 the electron-impact ionization cross section calculated for pyrimidine is compared with recent experimental data obtained for that molecule [13]. The ionization threshold energy dependence of theoretical and experimental curves are very similar. For collision energies higher than 50 eV computed cross sections values are significantly higher than experimental data. On the other side, these discrepancies are still within combined declared experimental uncertainties (~20%) and standard binary-encounter-Bethe method accuracy (~15%).

**Acknowledgments:** This work has been partially sponsored by the Polish Ministry of Science and Higher Education (MNiSzW). Numerical calculations have been performed at the Academic Computer Center (TASK) in Gdańsk.

#### 4. References

- [1] Sanche L 2005 *Eur. Phys. J. D* **35** 367.
- [2] Możejko P and Sanche 2003 *Radiat. Environ. Biophys.* **42** 201.
- [3] Możejko P and Sanche 2003 *Radiat. Phys. Chem.* **73** 77.
- [4] Żywicka B and Możejko P 2012 *Eur. Phys. J. D* **66** 54.
- [5] Żywicka B and Możejko P 2013 *Eur. Phys. J. Spec. Topics* **222** 2285.
- [6] Kim Y-K and Rudd M E 1994 *Phys. Rev. A* **50** 3954.
- [7] Hwang W, Kim Y-K and Rudd M E 1996 *J. Chem. Phys.* **104** 2956.
- [8] Firsich M J et al 2003 *GAUSSIAN 03 Revision B.05* (Pittsburgh: Gaussian).
- [9] Cederbaum L S 1975 *J. Phys. B* **8** 290.
- [10] von Niessen W, Schirmer J and Cederbaum L S 1984 *Comp. Phys. Rep.* **1** 57.
- [11] Ortiz J V 1988 *J. Chem. Phys.* **89** 6348.
- [12] Zakrzewski V G and von Niessen W 1994 *J. Comp. Chem.* **14** 13.
- [13] Linert I, Dampc M, Mielewska B and Zubek M 2012 *Eur. Phys. J. D* **66** 20.

# MEASUREMENTS OF ABSOLUTE TOTAL CROSS SECTIONS FOR LOW- AND INTERMEDIATE-ENERGY ELECTRON SCATTERING FROM ANALOGUES OF BIOMOLECULES

Paweł Możejko<sup>1</sup>, Czesław Szmytkowski<sup>1</sup>

<sup>1</sup>Atomic Physics Division, Department of Atomic, Molecular and Optical Physics, Faculty of Applied Physics and Mathematics, Gdańsk University of Technology, ul. Gabriela Narutowicza 11/12, 80-233 Gdańsk, Poland

E-mail: paw@mif.pg.gda.pl, czysz@mif.pg.gda.pl

Absolute total cross sections measured over last decade for electron scattering from analogues of important biomolecules will be reviewed. We will discuss accuracy of different experimental methods employed in total cross section measurements. As an example in this short contribution we have described linear transmission method employed in our experiments. We have presented also comparison of total cross sections measured for tetrahydrofuran, furan and isoxazole molecules.

## 1. Introduction

Electron scattering on atoms and molecules is an important tool in investigation of electron interactions with matter. The complete knowledge of electron interaction with matter is necessary in many fields of scientific research like atomic and molecular physics, low temperature plasma physics, astrophysics and astrobiology. Moreover, low energy electrons can induce serious damage to the living cell via direct and resonant interaction [1]. Thus it is essential to study interaction of low energy electrons with building blocks of biologically important tissues and with their simple molecular analogues in different phases. The efficiency of scattering phenomena can be described in terms of cross sections. Cross section for electron collision with atoms or molecules is time-dependent probability for occurrence of particular process during collisional phenomena. Total cross section (TCS) is the sum of cross sections for all particular processes. Thus it contains quantitative and qualitative information of all possible processes which occurs in collision phenomena.

In the last decade significant number of experimental and theoretical works devoted to electron interaction with complex and simple analogues of biomolecular compounds have been published. In our contribution we will review data of systematical measurements of the total cross section (TCS) for electron collisions with polyatomic molecules of biological interest.

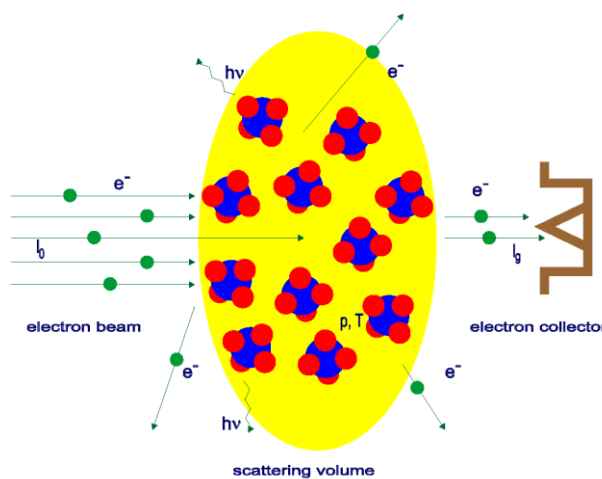


Fig. 1. Schematic diagram of the transmission method.

## 2. Experimental method

The transmission method is one of the most popular experimental techniques used in total cross section measurements. The method (see fig. 1) is based on measurements of the attenuation of the intensity of the projectile-particle beam transmitted through the volume filled with the target particles. In the ideal transmission experiment - i.e. when (i) the projectile beam is monoenergetic, parallel and very narrow, (ii) the concentration of target molecules,  $n$ , is low enough for interactions with projectiles to be single only, and (iii) only those projectiles are registered which have not interacted with target molecules, while (iv) the solid angle subtended by the detector is very near zero - the TCS,  $Q(E)$ , is related to attenuation of the electron beam as follows:

$$Q(E) = \left( \int_a^b n(x) dx \right)^{-1} \ln \frac{I_0(E)}{I_g(E)}, \quad (1)$$

where  $I_g(E)$  and  $I_0(E)$  are intensities of detected transmitted electron currents of energy  $E$  in the presence or absence of the target in the scattering volume, respectively;  $n(x)$  is the target density at point  $x$  of the electron pathway, while integration is performed over the entire path of the electron beam where  $n(x) \neq 0$ . Accuracy of TCS measured with transmission technique depends on electron beam resolution, electron energy, uncertainties in target pressure and temperature measurements, and etc. In experiments carried out in our laboratory systematic uncertainties are less than 10% for low collisions energies and lower than 5% for intermediate energies [2].

## 3. Results

For example in figure 2 total cross sections for electron scattering from the simplest molecular analogue of deoxyribose i.e. tetrahydrofuran, measured in different laboratories [3-6], are shown. Generally good agreement between our data [4] and measurements of Fuss et al. [5] and Baek et al. [6] can be observed. Total cross section obtained by Zecca et al. [3] differ distinctly from other data with respect to the magnitude.

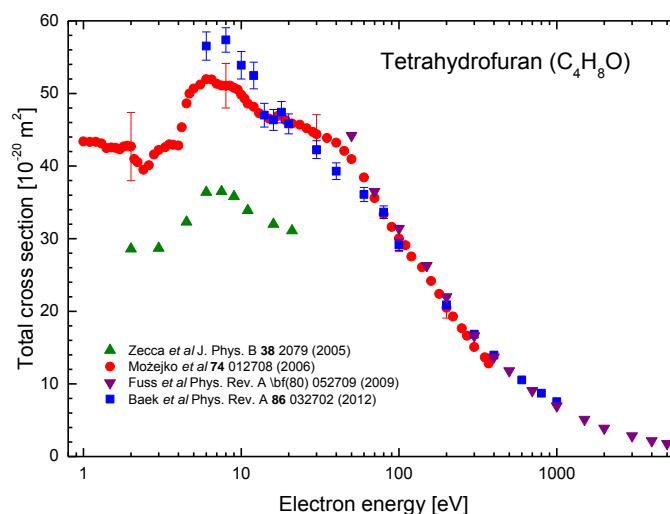


Fig. 2. Total cross section for electron scattering from tetrahydrofuran measured in different laboratories: (▲) [3], (●) [4], (▼) [5], (■) [6].

In figure 3 comparison between total cross sections measured for furan [7] and isoxazole [8] molecules is shown. At low impact energies, below 6 eV, compared total cross sections differ distinctly in the

magnitude. That difference increases toward lower energies: the low-energy total cross section for isoxazole steadily increases with the energy decrease while the total cross section for furan shows rather opposite behaviour. On the other hand, below 6 eV, there is also some similarity between compared curves: two resonant structures visible in the total cross section curve for isoxazole at 1.2 eV and 2.7 eV have their equivalents located at 1.8 eV and 3.1 eV, respectively, in the total cross section for furan, and can be associated with the formation of shape resonances. Above 10 eV the total cross section curves for isoxazole and furan looks similar in the shape and also in magnitude; that is especially evident above 30 eV.

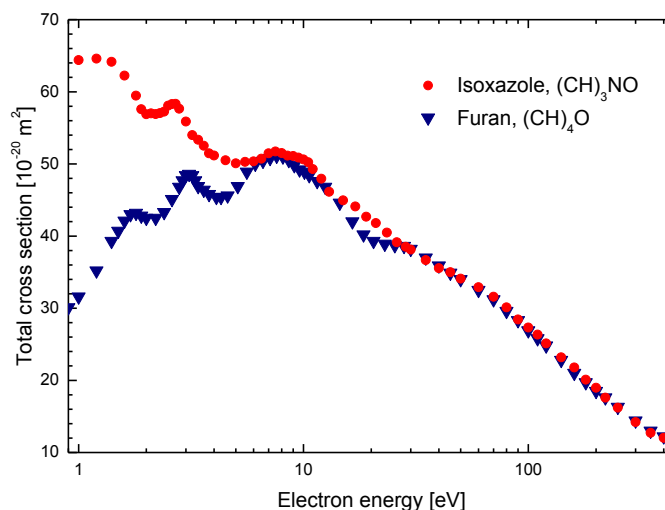


Fig. 3. Comparison between absolute total cross sections measured for furan (▼) [7] and isoxazole (●) [8] molecules.

Detailed discussion and review of recent experimental results will be presented during Conference.

**Acknowledgments:** This work has been partially sponsored by the Polish Ministry of Science and Higher Education (MNiSzW).

#### 4. References

- [1] Sanche L 2005 *Eur. Phys. J. D* **35** 367.
- [2] Szmytkowski Cz and Możejko P 2001 *Vacuum* **63** 549.
- [3] Zecca A, Perazzolli Ch and Brunger M J 2005 *J. Phys. B* **38** 2079.
- [4] Możejko P, Ptasińska-Denga E, Domaracka A and Szmytkowski Cz 2006 *Phys. Rev. A* **74** 012708.
- [5] Fuss M, Muñoz A, Oller J C, Blanco F, Almeida D, Limão-Vieira P, Do T P D, Brunger M J and García G 2009 *Phys. Rev. A* **80** 052709.
- [6] Baek W Y, Bug M, Rabus H, Gargioni E and Grosswendt B 2012 *Phys. Rev. A* **86** 032702.
- [7] Szmytkowski Cz, Możejko P, Ptasińska-Denga E and Sabisz A 2010 *Phys. Rev. A* **82** 032701.
- [8] Możejko P, Ptasińska-Denga E and Szmytkowski Cz 2012 *Eur. Phys. J. D* **66** 44.



# SYNCHROTRON RADIATION INDUCED DEFECT FORMATION KINETICS IN RARE-GAS SOLIDS

Alexander N. Ogurtsov, Natalia Masalitina, Olga N. Bliznjuk

*National Technical University, Frunse Street 21, Kharkov, 61002, Ukraine*

E-mail: anogurtsov@ukr.net

Kinetic model for the process of point defect formation induced by electronic excitation relaxation in condensed systems is proposed. The analysis of dose curves of rare-gas solids luminescence bands was made. The determined characteristic kinetic constants are found to be in good agreement with known hierarchy of electronic excitation relaxation processes.

## 1. Kinetic model

Material modification by electronic excitation is an important prerequisite for many novel technological applications in material and surface engineering, photochemistry, micro- and nanoelectronics. The basis for the electronically induced lattice modification is a localization of the excitation energy mainly during exciton self-trapping followed by the energy transfer to the material surroundings. Rare-gas solids (RGS) are widely used as the model systems in fundamental investigations and as the working media of particle detectors and positron moderators. The electronic excitations in RGS have been under investigation since seventies and now the overall picture of creation and trapping of electronic excitations is basically complete [1]. Using synchrotron radiation at HASYLAB (DESY, Hamburg, Germany) the spectroscopic properties of radiation-induced processes in RGS were well studied recently [2]. But the methods of chemical kinetics of solids were not applied up to now to analysis of the processes of RGS modification by irradiation. In the present study we apply these methods for numerical simulation of defect processes in irradiated crystals and harness the rich luminescence spectra of RGS for real-time monitoring of their crystal structure.

Initial increase of the intensity of the 'defect' luminescence during irradiation reflects the accumulation of Frenkel pairs in the lattice as a result of exciton creation and self-trapping. The process of defect formation we will consider as a combination of three separate processes:



Process (1) is a trapping of mobile excitation,  $E$ , with a rate constant  $k_1$  on trapping center,  $T$ , and formation of an excited metastable trapped center,  $MTE$ , which may be considered as metastable short-lived lattice defect. Depending on the system studied such a  $MTE$ -center may be a self-trapped exciton (STE), self-trapped hole (STH), or trapped electron. In the case of perfect lattice the self-trapping of mobile excitations can occur at every atomic position within the lattice. Radiative decay of the short-lived  $MTE$ -center either returns the lattice with a rate constant  $k_{-1}$  into the initial state without permanent defect (process (2)), or forms the permanent point defect,  $D$ , in the process (3) with a rate constant  $k_2$ . It is assumed that low level of irradiation under steady state conditions creates a constant low concentration of mobile excitations,  $N_0$ , which is much less then concentration of the trapping centers,  $n_T \gg N_0$ , and at the beginning of irradiation  $n_T$  can be taken as constant. Consequently, introducing the constant  $B_1 = k_{-1}/k_1$ , and, taking into account the fact, that irradiation produced electronic excitations may be either free, or trapped,  $N_0 = n_E + n_{MTE}$ , one can express  $dn_D/dt = B_2$ , where  $B_2 = k_2 N_0 n_T (B_1 + n_T)^{-1}$  is the constant. Thus, at the beginning of irradiation (concentration of defects  $n_D$  is small), defect concentration should grow linear with time,  $n_D = B_2 t$ , but at  $t \rightarrow \infty$  the process kinetic curve saturates and the time dependence of intensity of defect-related luminescence,  $I(t)$ , under steady-state irradiation conditions may be expressed in form

$$I(t) = I(0) + K \cdot t \cdot (L + t)^{-1}, \quad (4)$$

where  $I(0)$  is the initial intensity of 'defect' luminescence due to  $n_D \neq 0$  at  $t=0$ ;  $K=k_2N_0$  is the saturation value of  $I(t) - I(0)$  at  $t \rightarrow \infty$ ;  $L = (k_{-1} + k_2)/(k_1B_2)$  is a characteristic constant of a sample [3].

## 2. Results and discussion

Because of strong interaction with phonons the excitons and holes in RGS are self-trapped, and a wide range of trapping channels are realized: atomic-like self-trapped excitons (A-STE), molecular-like self-trapped excitons (M-STE), self-trapped holes (STH) and electrons trapped at electron traps. All these trapping processes stimulate point defect formation in RGS. Free and trapped excitations coexist in RGS, which results in the presence of a wide range of luminescence bands with well-studied internal structure in their emission spectra [1]. In the row Xe, Kr, Ar, Ne the atomic polarizability decreases as well as the crystal electron affinity; the latter becomes negative in the case of solid Ar and Ne. As a consequence, the main channel of exciton self-trapping in Xe and Kr is the formation of molecular-type self-trapped exciton, M-STE, which is equivalent to a molecular eximer  $R_2^*$  imbedded into the host lattice ( $R$ =rare gas atom). In luminescence the M-STE formation results in eximer-like  $M$ -band. In the opposite case of solid Ne the negative electron affinity results in strong repulsion of the Rydberg orbital of the lowest  $2p^53s$  excitation with the closed shell of the nearest neighbour atoms, which are pushed outwards. Such local lattice rearrangement leads to formation of atomic-like self-trapped exciton, A-STE, which is equivalent to an excited atom  $R^*$  into the cavity (or 'bubble'). Radiative decay of A-STE results in an  $A$ -band in luminescence. In the intermediate case of solid Ar both M-STE and A-STE coexist, therefore the luminescence spectrum of solid Ar contains both  $A$  and  $M$  bands. Additionally in luminescence spectra of RGS there are bands  $W$ , which correspond to radiative decay of vibrationally 'hot' eximers  $R_2^*$ , and bands  $H$ , which corresponds to radiative decay of excited self-trapped holes  $(R_2^+)^*$ . From the analytical point of view it is important, that most of luminescence bands contain subbands, which are definitely related to correspondent trapped excitations at the lattice imperfections. The analysis of evolution of these 'defect' subbands under irradiation allows to distinguish various contributions from different relaxation channels into process of point defect formation. The luminescent experiments were carried out at the SUPERLUMI-station at HASYLAB. The selective photon excitation was performed by near-normal incidence 2 m primary monochromator with photon flux about  $10^{12}$  photons/s at spectral resolution  $\Delta\lambda = 0.2$  nm. The VUV-luminescence analysis was performed both with low-resolution,  $\Delta\lambda = 2$  nm, Pouey high-flux monochromator equipped with a multisphere plate detector and with high-resolution,  $\Delta\lambda = 0.1$  nm, secondary 1 m near-normal incidence monochromator equipped with a position-sensitive detector. The numerical fitting by Eq. (4) of dose curves of 'defect' subbands  $M_1$  of solid Xe and  $A_1$  of solid Ne for the samples with very similar crystal properties under irradiation by photons with energies below  $E_g$  at  $T=5$  K gives values of characteristic constants  $K_{Xe} = 1600$  cps,  $K_{Ne} = 600$  cps,  $L_{Xe} = 2.4 \cdot 10^3$  s,  $L_{Ne} = 1.4 \cdot 10^4$  s, which is in line with general increase of defect formation efficiency in the sequence Ne, Ar, Kr, Xe. Another experiment was carried out with sample of solid Ar irradiated by photons with energies above  $E_g^{Ar} = 14.15$  eV. In this case in addition to excitons the electron-hole pairs are also excited. The hole self-trapping with subsequent excitation by excitons results in  $H$ -band emission, which is also rather sensitive to crystal structure imperfections [4]. The numerical fitting of dose curves for bands  $M_1$  and  $H$  from the same sample gives values of characteristic constants  $L_M = 50$  s and  $L_H = 100$  s, which indicates the higher stability of ionic excited eximer center  $(R_2^+)^*$  relatively to neutral excimer center  $R_2^*$ , and confirms the assumption about population of ionic center both during exciton self-trapping, and during electron-hole recombination processes.

To conclude, the proposed analytical kinetic model may be applied for condensed systems with pronounced effects of trapping of electronic excitations followed by point defect formation. The application of the model to luminescent analysis of point defect accumulation kinetics in RGS under photon irradiation allows real-time monitoring of crystal structure and obtaining the characteristic kinetic constants of the samples. This approach provides a way of qualitative and quantitative analysis and certification of Rare-Gas Solids, which is indispensable at any attempt of comparison of data from experiments with different samples.

### 3. References

- [1] Ogurtsov A N 2009 *Cryocrystals Modification by Electronic Excitations* (Monograph), NTU "KhPI", 368 p.
- [2] Ogurtsov A N 2004 In: E.C. Faulques et al., *Spectroscopy of Emerging Materials*, Kluwer, 45.
- [3] Ogurtsov A N, Masalitina N Yu, Bliznjuk O N 2007 *Low Temp. Phys.* **33** 591.
- [4] Ogurtsov A N, Bliznjuk O N, Masalitina N Yu 2013 *Int. Techn. & Energy Saving* **4** 24.

# IONIZATION OF ADENINE AND THYMINE MOLECULES BY ELECTRON IMPACT

Anna Ostroverkh<sup>2</sup>, Anatoly Zaviolopulo<sup>1</sup>, Otto Shpenik<sup>1</sup>, Mykhailo Mykyta<sup>1</sup>

<sup>1</sup>*Institute of electron physics NAS of Ukraine, 88017, Uzhgorod, Ukraine*

<sup>2</sup>*Institute of physics NAS of Ukraine, 03028, Kiev, Ukraine*

E-mail: gzavil@gmail.com

The method and results of the study of positive ions yield in the mass-spectrometric investigations by electron impact ionization of molecules of adenine and thymine are described. Mass spectrum obtained by electron impact ionization at the electron energy 20, 50 and 70 eV. The ionization energy of the molecule and the appearance potential of some fragment ions were obtained. The mass spectra and fragmentation schemes of adenine and thymine molecules by electron impact were analyzed.

## 1. Introduction

Investigation of the structure and properties of nucleic acids was a hot topic since their discovery. Extensive knowledge and understanding of genetic material and its physicochemical properties is one of the natural goals of science [1, 2].

In order to better understand these mechanisms, the various DNA components are initially studied in the gas phase, particularly isolated nucleobases and progressively upgrading towards the study of oligonucleotides. From an experimental point of view, free electron interactions with gas-phase adenine and thymine [3-6] have been studied particularly intensively. Fragmentation channels have been characterised as a function of the incident electron energy. Complementary experimental work in the literature includes mass-spectrometry of electron impact, [7, 8] shape resonance and radiation damage [9, 10] time-of-flight analysis by Rydberg electron transfer [11, 12], electron transmission spectroscopy [13, 14] measurements, and negative ion photoelectron spectroscopy [15].

The mass spectrometry is the one of the leading methods in these studies. It allows to get the structure of these molecules, and to determine their fundamental characteristics: the ionization potential and electron affinity. Genetic **material in living things is stored** in the nucleus of the cells which contain the **nucleic acids DNA** and RNA. Deoxyribonucleic acid (DNA) has three main components: 1 - purine (adenine, guanine) and pyrimidine (thymine, cytosine) bases, 2 - deoxyribose sugars and 3 - phosphate group.

Hydrogen bondings between purine and pyrimidine basics constitute a specific sequence, which is the key to genetic information and heredity. One of the essential components of genetic material is adenine. Indeed, adenine is central to life functions in most, if not all, organisms. [1, 2] Another aspect of such molecule research that traces of nucleobases and life-base molecules have been found in meteorites [16, 17] cometary grains [18, 19] interstellar regions [20] and it is still unclear how these molecules could be formed in interstellar conditions [21]. For example, water and carbon dioxide, formaldehyde, nitrogen, hydrogen cyanide, hydrogen sulphide and methane were detected in the comets composition. This leads to intensive searches of interstellar molecules potentially interesting for astrobiology as well as speculations on the possible mechanisms involved in the formation of these molecules.

Adenin molecule can be **formed** under certain conditions by HCN **pentamerization** in gas, liquid, and condensed phases [22]. There is a lot of speculation about the presence of HC polymers on Jupiter and Saturn. Well aware of the existence of a significant number of molecules HC and HNC in interstellar space [23]. Ionization of DNA bases initiate damage and mutations: 2 electrons and a hole, which is included in the ionization process in the DNA migrates through the DNA by proton transfer and dissociation. It is well known that high energy radiation is harmful to living organisms. For molecular systems it may be dissociation or ionization channels depending on the energy and intensity of the radiation.

This paper presents experimental results of a study of the mass spectra of adenine and thymine molecules by electron impact. Therefore, we investigate the mass spectra of the molecule at different temperatures.

## 2. Experimental details

The experimental setup, used for the studies of partial cross sections of dissociative ionization of molecules by electron impact, was described in detail in our earlier paper [24]. The monopole mass spectrometer (MS), type MX-7304A was used as an analytical device, which belongs to a class of dynamical mass analyzers.

The main feature of the ion source is the electrons penetrate in a bounded region by an anode grid (ionization region), and some of them will interact with the gas and will ionize it. Other electrons reach the opposite side of the anode and those that are not impact with a grid fall in the braking field will back to the ionization region. This increases the effective length of the path of the electrons in the ionization region. Ions are extended by an electric field created of a potential difference between the anode and the extending electrode. Ion beam formed by focusing electrode and insert (inject) to the mass-analyzer.

Monopole mass - analyzer, unlike the quadrupole due to the presence of additional border separates ions not only orthogonal, but also in the direction of insertion into the analyzer. Thus, the ion beam must be parallel, and monochromatic in the direction entrance diaphragm of the analyzer. SIMION. For the optimization of the ionization efficiency and optimal modes of the ion source and ion - optical system, we analyzed its work by SIMION program. By ion source simulation were determined some disadvantages. Thus, the cathode and reflector fields change the ion symmetry in the ionization area to make ions lost or obstruct. Was calculated another location of cathodes to correct this effect. The cathodes assembly arranged in a plane perpendicular to the axis of the ionizer, on the edge portion of the base of the cylindrical anode. However, they do not remove the ions through the anode and electrons are not deflected from the axis, as the oscillation of the electrons occurs above the cathodes place. Experimental test of the upgraded cathode assembly showed that the useful signal at the collector ions increased by 9 times.

The modernized MS ion source [24-26] with electron bombardment operates in stabilizing the electron current and allows to change energy of electron beam in the range 5-90 eV with current 0.003-0,3 mA and energy spread not more than 250 meV (full width at half maximum of the distribution). Ions are recorded by the measuring system make the digital and analog indication of the mass number of fragments and the intensity of the desired signal in the Manual mode as cyclic and program scan. Large value of the ion current is registered by Farady Cup, in this case the characteristics discrimination of masses is decreases by comparing with the secondary electron multiplier (SEM). For the detection of weak signals counting mode is used, and the useful signal is detected form SEM. All parameters of the mass spectrometer is controlled via computer. That's allows you to measure the mass spectra of molecule and cross sections of the ionization of atoms and molecules by electron impact in the energy range from the threshold up to 100 eV. The mass scale was calibrated using Ar and Xe beams, the energy scale was calibrated from the initial part of the Kr atom ionization cross-section what enabled the electron energy scale to be determined with the accuracy better than 0.25 eV.

A beam of the thymine and adenine molecules is formed by a multichannel source of effusion type providing the molecule concentration in the area of interaction with the electron beam within  $10^{10}$ – $10^{11}$  cm<sup>-3</sup>. The temperature range was from 20 to 400<sup>0</sup>C. We investigate the temperature effects of the different fragments of the mass spectra. By mass spectrometry was studied purine nucleic bases - adenine and thymine. The electron impact ionization of guanine was studied in previous work [7].

Adenine C<sub>5</sub>H<sub>5</sub>N<sub>5</sub> (m / z = 135) is a purine derivative compound (6 - aminopurine). As a guanine, adenine has an even high temperature, but soluble in water. In aqueous solutions will crystallized with three molecules of hydrated water. Figure 1 shows the mass spectra of adenine molecule which is measured at different temperatures and energy of electrons. As with the guanine molecule, the most intense peak in the mass spectrum of adenine is the molecular peak, that forms the all other fragments. The main dissociation channel of adenine molecule is successive emission of neutral HCN [27-31]. And first step of fragmentation gives a fragment C<sub>4</sub>H<sub>4</sub>N<sub>4</sub><sup>+</sup>.

Fragmentation scheme of adenine molecule by electron impact is shown on Figure 2. The resulting molecular ions ( $m/z = 108$ – $110$ ), by dissociative ionization of molecules  $C_5H_5N_5$  ( $m/z = 135$ ), sequentially loses  $CH_2N_2$  or HCN molecule then loses a hydrogen atom (H) or again molecule HCN.

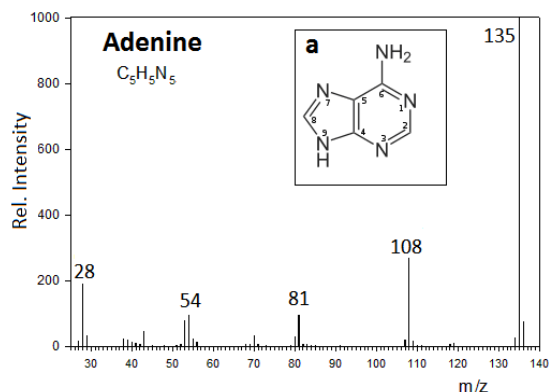


Fig. 1. Mass spectra of adenine molecule  $E_i = 70$  eV,  $T = 469$  K, the inset a: Representation structure of adenine nucleobase

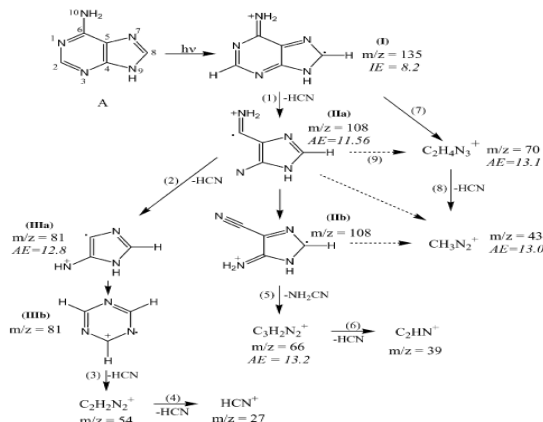


Fig. 2. Fragmentation scheme of adenine molecule a: under electron impact

The mass peaks with  $m/z = 118$ – $119$  probably corresponds to the loss of fragments of the aminogroup on the charge localization on N-1. The feature of adenine fragmentation is main peaks with  $m/z = 108$ ,  $81$  and  $54$  due to the loss of three molecules of HCN.

Thymine  $C_5H_6N_2O_2$  (5 - methyluracil) - one of three pyrimidine derivatives, it is present in all organisms and, with the deoxyribose includes in nucleoside thymidine. DNA base includes deoxyribonucleotides thymine and in the RNA base in its place has uracil ribonucleotide. Complementary to adenine, thymine is forming two hydrogen bonds. Molecular weight of thymine is the highest among the pyrimidine bases 126 amu for the parent molecule  $C_5H_6N_2O_2$ . Mass spectra of thymine molecule was measured at different energies of electrons 25, 30, 70 and 90 eV. The mass spectra obtained at different ionization energies are almost identical except for some features in the relative intensities of the peaks. Thus, at an energy of 25 eV is maximum intense for molecular ion peak, whereas at 90 eV is fragmented peak  $m/z = 55$  with more intense. Also at an energy of 25 eV is observed smaller amounts of fragment peaks, that indicate less fragmentation of the molecule at lower energies. Figure 3 shows a mass spectrum of thymine molecule with  $E_i = 70$  eV,  $T = 413$  K, while the inset shows the block diagram. Thymine fragmentation under electron impact (Fig. 4) is similar to the fragmentation of the uracil molecule [8-10]. Based on the comparison of the intensities of the ion peaks in the mass spectra of the thymine molecule, we can conclude that the main dissociative channel is the fragmentation of the thymine is the loss of the ring breaking neutral fragment HNCN (isocyanic acid). This forms a charged fragment form  $m/z = 83$ .

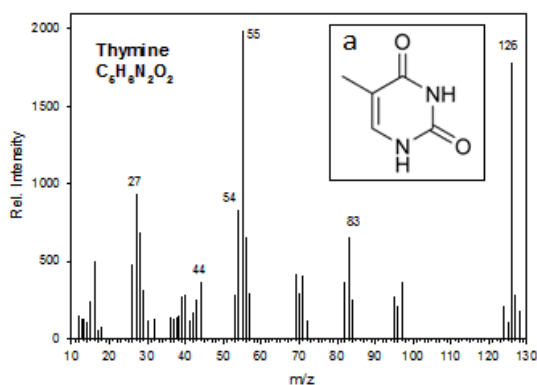


Fig. 3. Mass spectra of thymine molecule  
 $E_i = 70$  eV,  $T = 413$  K, *the inset a*:  
 Representation structure of thymine nucleobase

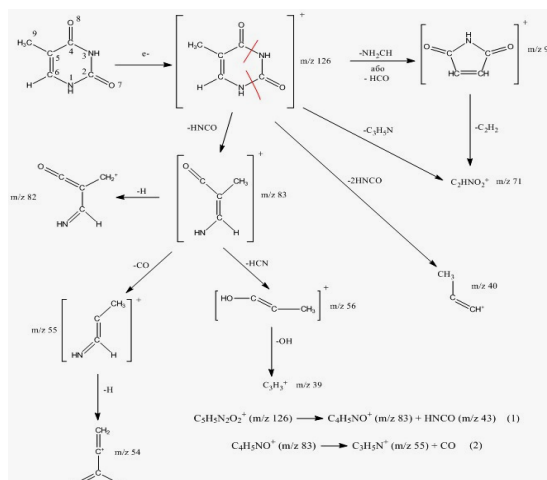


Fig. 4. Fragmentation scheme of thymine molecules under electron impact

This process occurs in the retro Diels - Alder which includes the braking of the two bonds N3 - C4 and C2 - N1 in the molecular ion. The loss of two units of HNC O is another channel of thymine fragmentation, which leads to the appearance of the ion with  $m/z = 40$  in mass spectra. This process occurs due to bond braking in C4 - C5 and N1 - C6 . Further fragmentation occurs through the process of sequential loss of CO molecule and H ion from fragment with  $m/z = 83$  with next ion formation  $[C_3H_5N]^+ (m/z = 55)$  and  $[C_3H_4N]^+ (m/z = 54)$ , the first of which is the most intense peak in the mass spectra.

Thus, the fragment ion  $[C_2HNO_2]^+$  ( $m/z = 71$ ) can be formed by two equally possible ways: first – elimination of neutral  $C_3H_5N$  fragment from the molecular ion, the second – breaking of neutral particles  $NH_2CH$  or  $HCO$  with forming an ion  $[C_4H_3NO_2]^+$  ( $m/z = 97$ ), without  $C_2H_2$ .

### 3. References

1. Townsend J S and Tiyard H T 1912 Proc. of the Royal Society of London. Series A **87** 357.
2. D. Almeida, R. Antunes et al, Phys. Chem. Chem. Phys., 2011, 13, 15657–15665.
3. R. Abouaf, J. Pommier and H. Dunet, Int. J. Mass Spectrom., 2003, 226, 397–403.
4. S. Denifl, S. Ptasinska, M. Probst, J. Hrusak, P. Scheier and T. D. Mark, J. Phys. Chem. A, 2004, 108, 6562–6569.
5. S. Denifl, S. Ptasinska, G. Hanel, B. Gstir, P. Scheier, M. Probst, B. Farizon, M. Farizon, S. Matejcik, E. Illenberger and T. D. Mark, Phys. Scr., 2004, T110, 252–255.
6. Stoken, H. S. Organic and Biological Chemistry; Brooks/Cole Pub Co.: Belmont, 2008
7. Zavilopulo A. N., Shpenik O. B., Agafonova A. S. Phys. B.: Mol. Opt. Phys., 2009, V.42, P.1-6.
8. Monika Dargiewicz, Malgorzata Biczysko, Roberto Improta and Vincenzo Barone Phys. Chem. Chem. Phys., 2012, 14, 8981–8989
9. Stefano Tonzani, Chris H. Greene, J. Chem. Phys. 124, 054312 2006
10. Amar Dora, Lilianna Bryjko, Tanja van Mourik, and Jonathan Tennyson J. Chem. Phys. 136, 024324 (2012)
11. C. Desfrancois, V. Periquet, Y. Bouteiller and J. P. Schermann, J. Phys. Chem. A, 1998, 102, 1274–1278
12. C. Desfrancois, H. Abdoul Carime and J. P. Schermann, J. Chem. Phys., 1996, 104, 7792–7794.
13. Aflatooni, G. A. Gallup and P. D. Burrow, J. Phys. Chem. A, 1998, 102, 6205–6207.
14. A. M. Scheer, K. Aflatooni, G. A. Gallup and P. D. Burrow, Phys. Rev. Lett., 2004, 92, 068102.
15. J. H. Hendricks, S. A. Lyapustina, H. L. deClercq, J. T. Snodgrass and K. H. Bowen, J. Chem. Phys., 1996, 104, 7788–7791.
16. C. El Amri, M.-H. Baron, and M.-C. Maurel, J. Raman Spectrosc. 35, 170, 2004.
17. M. A. Sephton and I. Gilmour, Mass Spectrom. Rev. 20, 111, 2001.
18. J. Kissel, R. Z. Sagdeev, J. L. Bertaux, et al, Nature (London) 321, 280 1986.
19. Miller SL, Urey HC (1959) Science 130: 245.
20. C. Floss, F. J. Stadermann, J. Bradley, Z. R. Dai, S. Bajt, and G. Graham, Science 303, 1355, 2004.
21. Z. Peeters, O. Botta, S. B. Charnley, R. Ruiterkamp, and P. Ehrenfreund, Astrophys. J. Lett. 593, L129, 2003.
22. Townsend J S and Tiyard H T 1912 Proc. of the Royal Society of London. Series A, 87, 357.
23. Ishii K, Tajima A, Taketsugu T, Yamashita K (2006) Astrophys J 636: 927.
24. A. C. Агафонова, В. А. Сурков. Наук. вісник Ужгор. Університету. Ужгород, 2007, С.63-70.
25. A. V. Kukhta, I. N. Kukhta, A. N. Zavilopulo, A. S. Agafonova, O. B. Shpenik Eur. J. Mass Spectrom. – 2009. – V.15. – P.563-570.
26. А.Н. Завилопуло, Е.А. Миронец, А.С. Агафонова ПТЭ **1**, 73-79 (2012).
27. I. W. M. Smith, D. Talbi, and E. Herbst, Astron. Astrophys. 369, 611 2001
28. Richard Brédy, Jérôme Bernard, Li Chen, Guillaume Montagne, Bin Li, and Serge Martin IJ. Chem. Phys. 130, 114305 2009
29. S. Martin, R. Brédy, A. R. Allouche, J. Bernard, A. Salmoun, B. Li, and L. Chen, Phys. Rev. A 77, 062513 2008
30. D. Roy, K. Najafian, and P. von Rague Schleyer, Proc. Natl. Acad. Sci. U.S.A. 104, 17272 2007
31. L. Chen, R. Brédy, J. Bernard, G. Montagne, A. R. Allouche, and S. Martin J. Chem. Phys. 135, 114309 (2011)



# TOWARDS COMPLEX RESONANCE ENERGIES FROM REAL CALCULATION

Ivana Paidarová<sup>1</sup>, Philippe Durand<sup>2</sup>, Jiří Horáček<sup>3</sup>, Roman Čurík<sup>1</sup>

<sup>1</sup>*J. Heyrovský Institute of Physical Chemistry, AS CR, v.v.i., Prague, Czech Republic*

<sup>2</sup>*LCPQ, IRSAMC, Université de Toulouse et CNRS, Toulouse, France*

<sup>3</sup>*Faculty of Mathematics and Physics, Charles University, Prague, Czech Republic*

E-mail: ivana.paidarova@jh-inst.cas.cz

The two complementary approaches demonstrate how the resonance energies and widths can be computed with a good accuracy by using standard quantum chemistry codes: i) The analytic continuation in coupling constant method of Kukulín and Krasnopol'sky [J. Phys. A 1977 **10**, L33] was recently applied to resonances of amino acid molecules [Papp et al. Chem. Phys. 2013 **418**, 067301], and to the B<sub>2g</sub> shape resonance of ethylene [Horáček et al. J. Phys. Chem.A 2014 *submitted*]. ii) The second approach based on a non-unitary transformation of the Hamiltonian and on the analytical properties of the Fourier-Laplace transformation is presented and applied to the two models and to the anion H<sub>2</sub><sup>-</sup> by Durand and Paidarová [J. Phys. B 2013 **46** 07500].

## 1. The method of analytical continuation in the coupling constant

The method of analytical continuation in coupling constant (ACCC) is described in detail in the monograph [1]. The complex resonance energy is obtained from Padé approximation of the inverse function of  $k(\lambda) = \sqrt{\Delta E(\lambda)}$ , where  $\lambda$  is the parameter of an attractive perturbation  $V(\lambda)$ , that may be an additional nuclear charge or a coordinate-dependent potential, and  $\Delta E(\lambda) = E^{\text{neutral}}(\lambda) - E^{\text{anion}}(\lambda)$  describes the energy difference between the neutral molecule and its negative anion. Recent applications of the ACCC method to real molecular resonances, the <sup>2</sup>Π<sub>g</sub> state of N<sub>2</sub><sup>-</sup> [2] and to resonances of amino acid molecules [3], proved that the method can yield accurate resonance energies and widths based on data obtained by using standard quantum chemistry codes.

In the last application [4] the performance of the ACCC method was further improved and applied to the B<sub>2g</sub> shape resonance of ethylene. The procedure is done in two steps. In the first step the energies of a neutral molecule and of a negative ion are calculated using the highly correlated ab initio method (CCSD-T) with augmented correlation-consistent basis set of quadruple-zeta quality (aug-cc-pVQZ). In both calculations the Hamiltonian is altered by additional Coulomb field created by extra charges  $\lambda$  positioned on all the nuclear centres that stabilizes the resonance state. The inter-nuclear distance R<sub>C-C</sub> was varied with other geometry parameters kept fixed at the equilibrium values (R<sub>C-C</sub>=0.134 nm, R<sub>H-C</sub>=0.109 nm, and the C-C-H angle of 121°). The parameter  $\lambda$  was varied from 0.001 a.u. to 0.1 a.u. with the step of 0.001 a.u. Depending on the R<sub>C-C</sub> distance this resulted in 40 to 90 points describing the curves  $E^{\text{neutral}}(\lambda)$  and  $E^{\text{anion}}(\lambda)$ . In the second step the function arising from energy difference  $\Delta E(\lambda)$  was analytically continued by the use of statistical Padé approximation that enabled to determine not only the resonance energy (often seen in literature as extrapolation  $\lambda \rightarrow 0$ ) but also the resonance width. The computed resonance energy and width at equilibrium geometry agree very well with previous scattering calculations with complex Kohn method [5] as shown in the Fig. 1.

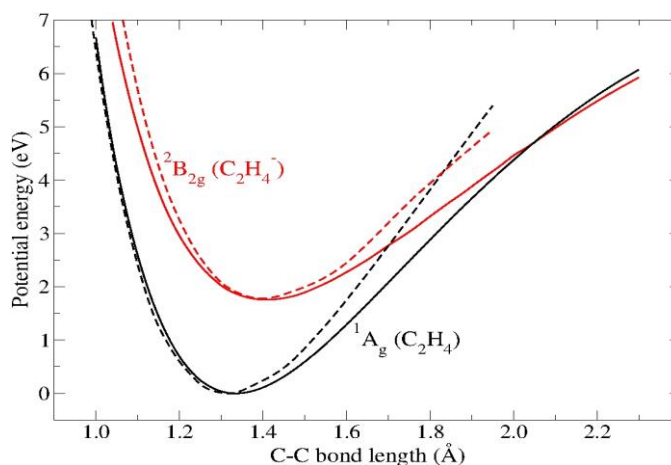


Fig. 1. Potential energy curves for the ground state  $^1A_g$  of the neutral  $C_2H_4$  molecule (full black line) as a function of C-C bond length distance. Resonant energy curve of the temporary negative ion  $^2B_{2g}$  obtained by the present approach is shown with full red line. The results of the complex Kohn calculations of Trevisan et al. [5] are displayed with corresponding dashed lines.

## 2. Non-unitary transformation of the Hamiltonian and analytical continuation in energies

The second approach is based on a unified formulation of the quantum theory of unstable states and of their dynamics [6]. The method has a simple and rigorous mathematical framework and is based on non-hermitian changes of representation of the dynamics and on the analytical properties of the Fourier-Laplace transformation [7]. A hybrid computational scheme borrows from both the stabilization method and non-hermitian approaches using complex absorbing potentials. In order to stabilize the resonance we consider the Hamiltonian  $H(\lambda) = H + \lambda V$  where  $\lambda$  is a scaling real parameter and  $V$  is an hermitian operator. In Ref. [7] we have shown, how the time dependent transformation  $S = \exp(-\lambda V t/\hbar)$  led to the non-hermitian Hamiltonian  $H(-i\lambda) = H - i\lambda V$ . The real eigenenergies  $E(\lambda)$  of  $H(\lambda)$  provided by standard codes of quantum chemistry (or by model calculations) are converted into complex energies by the transformation  $\lambda \rightarrow -i\lambda$ . From them the resonances are obtained by use of some stabilization criteria. The approach has two advantages: it closely relates the energy of the resonances to their dynamics and it keeps the survival amplitudes of the resonances. Similarly as in the ACCC method, the resonances are extracted from real calculations. The computational scheme and applications are published in Ref. [7]. The solution of two models i) discrete Fano model and ii) simple model of shape resonance enables to deepen the understanding of the approach and to contribute to further development of the theory. The successful application to the anion  $H_2^-$  proved that the method can be applied to real systems.

## 3. References

- [1] Kukulin V I, Krasnopol'sky V M and Horáček J 1989 Theory of Resonances: Principles and Applications (Praha: Academia).
- [2] Horáček J, Mach P, Urban J 2010 Phys. Rev. A **82**, 03271.
- [3] Papp P, Matejčík Š, Mach P, Urban J, Paidarová I, Horáček J, 2013 Chem. Phys. **418**, 067301 .
- [4] Horáček J, Paidarová I and Čurík R 2014 *submitted to* J. Phys. Chem. A.
- [5] Trevisan C S, Orel A E, Rescigno T N, Phys. Rev. A 2003 **68**, 06270
- [6] Paidarová I and Durand P 2010: Unstable states: from quantum mechanics to statistical physics Advances in Quantum Chemistry: Unstable States in the Continuous Spectra, Part I: Analysis, Concepts, Methods, and Results (ed C A Nicolaides and E Brändas) vol **60** (San Diego, Elsevier) p 1

[7] Durand P and Paidarová I 2013 J. Phys. B: At. Mol. Opt. Phys. 46 075001.

# URACIL CLUSTER FORMATION UNDER THE CONDITIONS OF DISCHARGE ABOVE THE SURFACE OF WATER SOLUTION

Ivan Shafranyosh, Yuri Svyda, Miroslav Shafranyosh, Serhiy Gala,

Maria Sukhoviya

*Uzhgorod National University*  
E-mail: ivanshafr@gmail.com

Spectral study of electric discharge above the surface of the water solution of the base RNA uracil molecules in the wavelength from 200 to 600 nm are fulfilled. The physical nature of characteristics which were detected at the spectrum of radiation discharge is associated with the cluster formation of uracil molecules.

## 1. Experimental technique

Interest in research of clusters caused by their unique properties that open new possibilities in nanoelectronics, new materials, environmental control, etc. On the other hand, the systematic research of clusters such as atomic and molecular, especially biomolecular, are few due to the complexity of the experiment and methods of identification of clusters. At present time the identification of the cluster is formed mainly by absorption spectra that is not sufficiently informative. Therefore, the experimental studies of clusters during various excitation processes that allow one to receive important information about their physical properties are currently valid.

This work is dedicated to the experimental study of cluster formation of uracil molecules in binary mixtures with water vapor when it is excited by electrical discharge. The essence of the method consists in spectroscopy experiment study of electrical discharge above the surface solution of uracil. Experimental setup consists of a system of preparation and the overlap of a water solution of uracil, a high voltage generator for powering of discharge, emission registration system. A prototype of our setup is described in work [1]. The conditions of the experiment were as follows: discharge current:  $I_p = 20$  mA, the voltage at the discharged interval of 1.0 – 2.0 kV, the distance between the electrode and the surface of the water was 5 – 7 mm. The concentration of the solution was 0.5 % of uracil.

## 2. Results

In the course of the research we have obtained spectra of glow discharge over the surface of a water solution of uracil in wavelengths from 200 to 600 nm. In the analysis of these spectra were found two spectral bands in the spectral region 430 – 475 nm and 510 – 560 nm. The availability of these bands in the spectrum can be explained as follows. Molecules of uracil in water solution form clusters. The shape of the cluster is defined, first of all, by the formation of links between the molecules of uracil, when the total energy of the formed cluster will be less than total energy of the source molecules. Logically one can assume that this may be a form similar to sandwich form, where the molecules of uracil, which are planar, packed in layers. There are hydrogen links between the layers which provide the relative strength of this new formed object (cluster). Cluster formation is accompanied by a redistribution of charge density, changes in spatial parameters in molecule (link, length, angles). As a consequence, we can see the shifting of electronic and vibrational levels in each molecule of uracil, which is part of the cluster and, accordingly, the shifting of spectral bands of luminescence of uracil molecules.

## 3. References

[1] Pereganec V V, Minda I Y, Grinush V V, Shafranyosh I I 2009 *NANOBIOFIZIKA: fundamental and applied aspects, Kharkov, Ukraine* 95.

# ON THE INFLUENCE OF LOW- AND HIGH-ENERGY IONIZING RADIATION ON THE AMINO ACID MOLECULE STRUCTURE: PROLINE

Alexander V. Snegursky<sup>1</sup>, Vasyl S. Vukstich<sup>1</sup>, Liudmila G. Romanova<sup>1</sup>,  
Jelena Tamuliene<sup>2</sup>, Ivan G. Megela<sup>1</sup>, Alexander V. Papp<sup>1</sup>, Laura Baliulyte<sup>2</sup>

<sup>1</sup> *Institute of Electron Physics, Ukr. Nat. Acad. Sci., 21 Universitetska str.,  
88017 Uzhgorod, Ukraine*

<sup>2</sup> *Vilnius University, Institute of Theoretical Physics and Astronomy, 12 A. Goštauto str.,  
01108, Vilnius, Lithuania*

e-mail: snegursky.alex@gmail.com

New data on the electron-impact fragmentation of the amino acid proline molecule are presented being related to the formation of the ionized products due to the influence of both low- and high-energy ionizing radiation on the above molecule. An extensive DFT-theory based theoretical approach enabled the main pathways of the proline molecules fragmentation to be elucidated. The effects caused by the persistent changes resulted from the high-energy microtron-induced ionizing radiation have been found. A series of fragments produced have been identified. For some of them the absolute appearance energies have been both measured experimentally and calculated theoretically. The data of experimental studies and theoretical calculations are compared and analyzed.

## 1. Introduction

Previously, we used mass-spectrometric technique combined with theoretical analysis to study ion fragment production under the influence of high- (~10 MeV) and low- (~70 eV) energy electrons on the tryptophan molecule [1, 2]. These investigations have exhibited persistent changes in the amino acid molecule structure due to irradiation leading to the appearance of fragments either with the same mass but different chemical composition and/or those with the same mass and chemical composition but produced via different dissociation pathways.

This work is a continuation of our studies on ionizing radiation interaction with the molecules of biological relevance. It deals with the proline (C<sub>5</sub>H<sub>9</sub>NO<sub>2</sub>) molecule being the non-essential  $\alpha$ -aminoacid synthesized by the human body. It is unique among the 20 protein-forming amino acids, because its amine nitrogen is bound to two alkyl groups, i.e. it is a secondary. The experimental technique used in this work was described in detail elsewhere (see, e.g. [3]).

The experimental apparatus is based on the magnetic mass spectrometer capable of operating within the 1–600 a.m.u. mass range. High sensitivity ( $\sim 10^{-16}$  A) and resolution ( $\pm 0.25$  a.m.u.) of the mass analyzer enabled the fragments of the target molecule to be reliably separated and detected even at low levels of ion currents reaching the ion detector. The primary molecular beam was formed by means of an effusion source with a resistive oven providing target molecule concentrations not less than  $10^{10}$  molecule/cm<sup>3</sup>. The operating temperature of the molecular beam source was varied up to 150°C and controlled by a thermocouple enabling the temperature dependences of the fragments yield to be determined. The temperature and pressure conditions of the molecular beam formation excluded the possibility of molecular cluster formation. A specially designed three-electrode electron gun provided an electron current of 30–50  $\mu$ A over a wide energy range. This source enabled the energy dependences of the ionization and dissociative ionization cross sections to be measured in the incident electron energy range from the threshold up to 150 eV without the need of using a magnetic field (contrary to the conventional source). The ions, produced in the ion source and extracted by the electric field, entered the magnetic ion separator and were detected by means of an electrometer. The data acquisition and processing system was controlled by a PC. Special measures were taken to stabilize the mass analyzer transmission thus making the mass of the fragment under study to be reliably fixed. An electron energy

scale was calibrated with respect to known ionization thresholds for argon atom and nitrogen molecule (see below) with the accuracy of  $\pm 0.1$  eV.

## 2. Results and discussion

Both non-irradiated and irradiated proline molecule mass spectra were measured at the 70 eV electron energy, the appearance energies for the positive fragment ions were determined within the 5–30 eV energy range with the  $\pm 0.1$  eV accuracy. To identify the influence of high-energy ionizing radiation, the 11.5 MeV energy electron beam generated by an M-30 electron accelerator (microtron) was applied to irradiate the proline powder at the doses varied from 5 to 20 kGy.

A theoretical method used allowed the possible processes occurring at electron impact to be predicted. The results of theoretical calculations using the DFT approach [4] were compared with the experimental data in order to check the theoretical predictions, identify the possible fragmentation pathways and discover possible irreversible structural changes in the proline molecule under the influence of high-energy ionizing radiation. Thus, fragmentation of three conformers having different geometrical structure but approximately equal total energy was studied.

We have found the effects caused by the persistent changes due to irradiation taking into account our studies on the fragmentation of irradiated and non-irradiated tryptophan molecule. Figure 1 shows the views of both non-irradiated and irradiated proline molecule mass-spectra. One may note that the mass spectra are rather similar, however, for several fragments the intensities of the relevant peaks significantly differ in their values. The most clearly such regularity is revealed for the fragments with the  $m/z=28$ , 41 and 43 a.m.u. masses. The theoretical results prove that the energies of formation of the same fragments from different proline conformers differ as well (see Table 1).

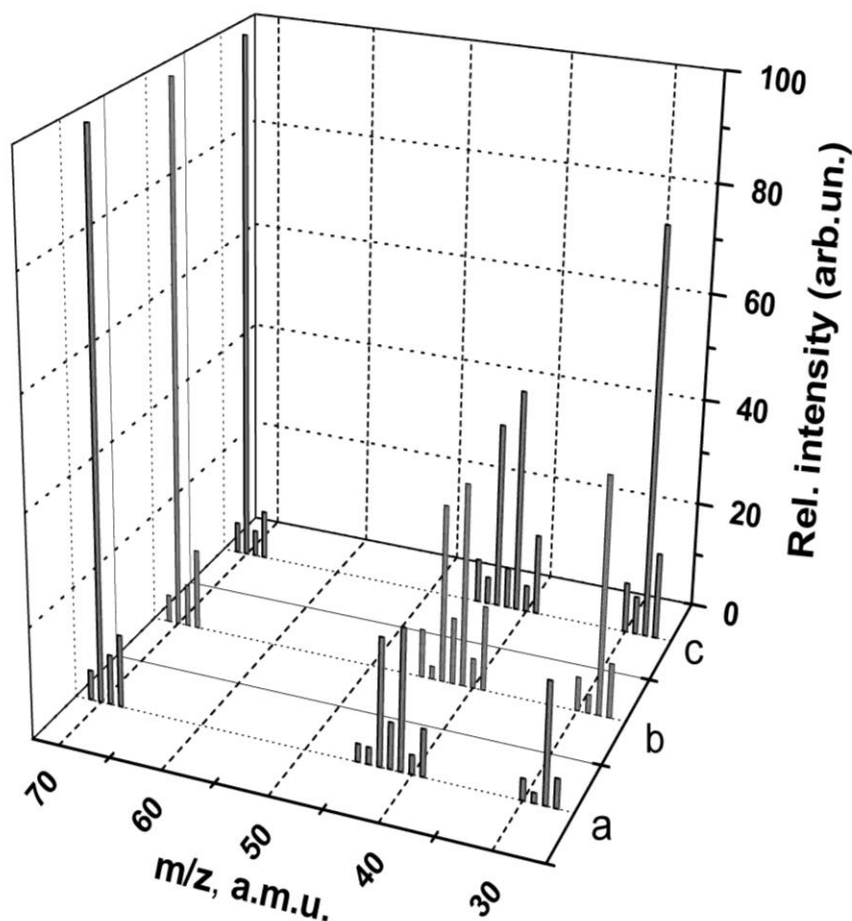
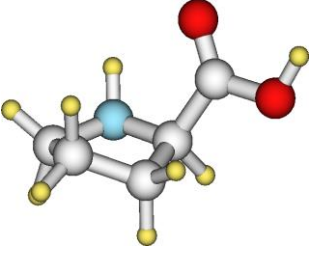
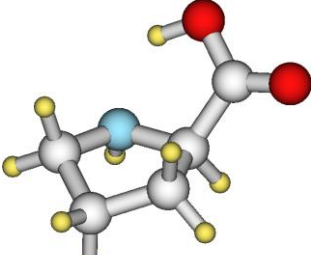
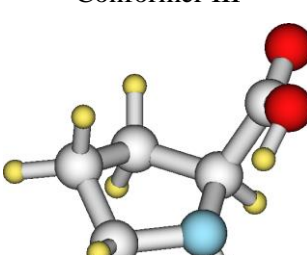


Figure 1. Comparison of the mass-spectra of non-irradiated (a) and irradiated

(b – 5 kGy dose, c – 20 kGy dose) proline molecule.

Table 1. Appearance energies for the fragments produced from different proline molecule conformers.

Fragment mass, a.m.u.	Appearance energy, eV		
	Conformer I 	Conformer II 	Conformer III 
70 (C <sub>4</sub> H <sub>6</sub> N)	8.68	8.65	8.67
68 (C <sub>4</sub> H <sub>4</sub> N)	11.63	11.94	11.96
43 (C <sub>2</sub> H <sub>5</sub> N)	10.18	10.51	10.49
43 (C <sub>3</sub> H <sub>7</sub> )	10.15	8.28	8.30
41(C <sub>2</sub> H <sub>3</sub> N)	10.13	9.86	9.45
28 (CH <sub>2</sub> N)	10.40	9.49	9.51
28 (C <sub>2</sub> H <sub>4</sub> )	11.99	8.28	11.52

According to the results of our studies, the fragment with the mass  $m/z=28$  a.m.u. could be CH<sub>2</sub>N<sup>+</sup> or C<sub>2</sub>H<sub>4</sub><sup>+</sup>, while fragment with the  $m/z =43$  a.m.u. mass could be C<sub>2</sub>H<sub>5</sub>N<sup>+</sup> or C<sub>3</sub>H<sub>7</sub><sup>+</sup>. Referring to the appearance energies calculated we may predict that one of the reasons of the increasing peak intensities in the proline molecule mass spectra under irradiation could be related to the appearance of other fragments with the same mass but different chemical compositions.

A tentative assignment of these fragments and the possible fragmentation channels would be discussed at the Conference.

### 3. REFERENCES

- [1] Tamuliene J, Vukstich V S, Romanova L G, Papp A V, Snegurskaya T A, Snegursky A V and Baliulyte L 2014 *5<sup>th</sup> Int. Conf. Radiat. Interact. Mater. Abstr. Contr. Pap. Kaunas*.
- [2] Vukstich V S, Romanova L G, Megela I G and Snegursky A V 2014 *Tech. Phys. Let.* **40** 263.
- [1] [3] Vukstich V S, Imre A I and Snegursky A V 2011 *Instr. Exper. Tech.* **54** 66.
- [2] [4] Becke A D 1993 *J. Chem. Phys.* **98** 5648.

# PHOTOIONIZATION DYNAMICS OF THE RYDBERG STATES OF C<sup>2+</sup> ION

Viorica Stancalie

<sup>1</sup>*National Institute for Laser, Plasma and Radiation Physics, Department of Lasers, Atomistilor 409,  
P.O.Box MG-36 Magurele-Ilfov, 077125 Romania  
E-mail: viorica.stancalie@inflpr.ro*

The goal of this work is to examine in detail the ionization dynamics of Rydberg states belonging to Be-like C ions. To this aim we used the two-state model for dressed atomic states. In order to get photoionization spectra starting at proper transition frequency, both the C<sup>2+</sup> ground state and the C<sup>3+</sup> target state energies have been carefully calculated. We report results from a detailed and systematic study of photoionization in laser field and the frequency-dependent polarizability,  $\alpha_d(\omega)$  of Rydberg states in C<sup>2+</sup> ion. To calculate the polarizability we used the finite-field method for a variety of values of field strength. Results obtained from the use of sum-over-state method are also presented for data assessment purpose.

## 1. Introduction

The excitation to Rydberg states opens up several additional decay channels due to finite radiative lifetime of the Rydberg state, off-resonant coupling to autoionizing states and direct photoionization of the Rydberg electron [1,2]. Atoms with two valence electrons offer a promising approach for demonstrating the response of Rydberg atoms to external perturbation, as the remaining valence electron of a singly excited Rydberg state provides an additional degree of freedom to probe and manipulate the atom [3]. Theoretical proposals based on the particular level structure of low-lying states in two-electron systems have described new scheme for quantum simulations [4,5] and quantum information processing [6].

The Be-like ions including C have been subject of many detailed experimental and theoretical works [7,8 and references]. These studies have shown that, except for the resonances converging to the C<sup>3+</sup> 2p threshold, all the resonance series are perturbed by overlapping series converging to other thresholds. The goal of present work is to examine in detail the ionization dynamics of Rydberg states belonging to Be-like C ions. In order to get photoionization spectra starting at proper transition frequency, both the C<sup>2+</sup> ground state and the C<sup>3+</sup> target state energies have been carefully calculated. To achieve this, we employ the *R*-matrix approach incorporating an extensive description of the C<sup>3+</sup> structure. In a previous paper [9] we have characterized the doubly excited autoionizing states in C<sup>2+</sup> ion with respect to the effect that quantum interference term, between radiative and dielectronic recombination, has on the energy dependence profile of photo-recombination cross section. The numerical evaluation has been performed across all the autoionizing Rydberg series of resonances  $1s^2 2pns(^1P^0)$  converging to Li-like ion 2p threshold. In another study, we have illustrated that the  $1s^2 2sns$  and  $1s^2 2pns$  Rydberg states embedded by a laser field are completely degenerated [10]. Results have been analyzed with the two-state model where, an initial bound state and an autoionizing state of a complex ion resonantly coupled by a radiation field, can both be characterized in a Floquet approach by complex quasi-energies. For certain values of the field's intensity and frequency, the two quasi-energies become equal, giving rise to laser-induced degenerate states (LIDS).

In the present work we make use of our previously reported studies and provide new theoretical calculation in order to accurately characterize these Rydberg states and their photoionization properties. Section 2 gives model of calculation and selected results. We report results from a detailed and systematic study of photoionization in laser field and the frequency-dependent polarizability,  $\alpha_d(\omega)$  of Rydberg states in C<sup>2+</sup> ion. To calculate the polarizability we used the finite-field method for a variety of values of field strength ( $F$ ). The direct solution of the Schrodinger equation for working ions in the presence of an electric field and the subsequent determination of the polarizability has been done using results from the earlier *R*-matrix Floquet calculation. Results obtained from the use of sum-over-state method are also



presented for data assessment purpose. The method requires accurate evaluation of energies and wavefunction of the system. Section 3 gives our concluding remarks and further directions of research.

## 2. Model of calculation and results

Considering photoionization of the  $1S^e$  ground state of Be-like carbon ion, in an energy range that extends to final states close to the  $C^{3+}(2p)$  ionization threshold, in a standard  $LS$  coupling approximation, an electric dipole photon excites only  $1P^0$  final states. Focusing just on the ionization channels attached to the  $2p$  ionic state, two relevant channels are specifically excited, namely  $2pns(1P^0)$  and  $2pnd(1P^0)$ . In general one associates double-resonant processes with processes induced by two lasers. In our study the ‘two beams’ are the laser beam and the electron beam. Thus, instead of using a probe laser to reach a high-lying state in the continuum, this state can be reached by choosing the energy of the incident electrons to be at resonance with the resonant state of the composite  $(N+1)$  electron - atom system. Starting with the  $1s^2 2s$  ( $2S$ ) and  $1s^2 2p$  ( $2P^0$ ) target states of the remaining Li-like target ion, the  $1s^2 2s^2(1S)$  and  $1s^2 2p^2(1S)$  states of Be-like ion, have been obtained with a configuration interaction expansion using the  $R$ -matrix method. The resulting  $1s^2 2s^2(1S^e)$  and  $1s^2 2p^2(1S^e)$  ground states energy in  $C^{2+}$  ion are at  $-1.755855$  atomic units (au) and  $-0.90275$  au, respectively. The  $1s^2 2sns(1S^e)$ , and  $1s^2 2pns(1P^0)$ ,  $1s^2 2pnd(1P^0)$  excited Rydberg states were identified based on their effective quantum numbers. We reproduce in Fig.1, from Ref. 9, the Edlén plot for the  $1s^2 2pns(1P^0)$  and  $1s^2 2pnd(1P^0)$  Rydberg resonance series in  $C^{3+}$  showing the quantum defects of each resonance against the resonance energies relative to the  $2P^0$  threshold energy.

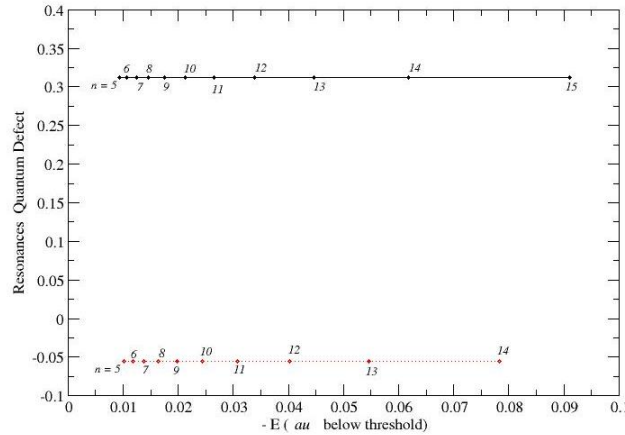


Fig. 1.  $R$ -Matrix Edlén plot for  $1s^2 2pns(1P^0)$  (solid) and  $1s^2 2pnd(1P^0)$  (dotted) Rydberg series of resonances in  $C^{3+}$ , as function of the resonance position (in atomic units, au) below the  $2P^0$  threshold. The  $n$  values are the principle quantum numbers for the associated data point.

For optical frequencies the photoionisation of  $1s^2 2sns(1S^e)$  states takes place far above threshold and the corresponding cross sections are small. An initial calculation has been done to output the lifetime due to spontaneous decay for unperturbed  $1s^2 2sns(1S^e)$  Rydberg states. We used the multi-configuration Dirac-Fock (MCDF) method with configuration interaction option implemented in the General-purpose Relativistic Atomic Structure Package (GRASP) [11]. The configuration interaction approach is useful as it provides a straightforward way to evaluate the atomic polarizability [12].

The lifetime of  $1s^2 2pns(1P^0)$  Rydberg states have been extracted from earlier LIDS calculation. Denoting by  $\Gamma^{r,n}$  radiative width in the channel  $n$ , with  $\omega_n$  the LIDS frequency and  $I$  the laser intensity, we have:

$$\Gamma^{r,n} = I/\omega_n \quad (1)$$

Table 1 gives our results for radiative rates of the  $1s^2 2pns$  ( $^1P^0$ ) Rydberg states in  $C^{2+}$  ion.

Tab. 1. Radiative rates  $\Gamma^{r,n}$  (in  $\text{sec}^{-1}$ ) calculated for the  $1s^2 2pns$  ( $^1P^0$ ) Rydberg states in  $C^{2+}$  ion.

$2pns$ ( $^1P^0$ )	$n=5$	$n=6$	$n=7$	$n=8$	$n=9$	$n=10$	$n=11$	$n=12$
$\Gamma^{r,n}$	$3.34 \times 10^{11}$	$1.20 \times 10^{11}$	$5.64 \times 10^{10}$	$2.51 \times 10^{10}$	$1.57 \times 10^{10}$	$1.26 \times 10^{10}$	$2.51 \times 10^{10}$	$4.40 \times 10^{10}$

The interaction between highly excited (Rydberg) atoms with an external field has been studied for two cases. First, we have considered the case of slowly varying electric field (when the characteristic field frequency tends to zero) and the dynamic polarizability reduces to the static one. In the second case, the other limiting case (high frequency regime) the problem usually reduces to a discussion of the motion of a free electron.

An initial calculation has been performed to output the contribution of these Rydberg states to the static static polarizability. The perturbation theory leads to a sum-over-states formula for the static –dipole polarizability which is usually expressed, in his compact form, in terms of oscillator strengths:

$$\alpha_0 = \sum_n \frac{f_{gn}}{(\Delta E_{ng})^2} \quad (2)$$

Here,  $f_{gn}$  is the absorption oscillator strengths for a dipole transition from level  $g$  to level  $n$  and  $\Delta E_{gn} = E_n - E_g$ . The sum-over-states approach can be used with oscillator strengths (or electric-dipole matrix elements) obtained from atomic structure calculations. The accuracy of its calculation depends on how precise the energies and wavefunctions of the ground state are evaluated. We have used the GRASP code with the configuration interaction option. Additional relativistic corrections arising from the Breit interaction and quantum electrodynamics (QED) are also included. To calculate the static polarizability of the excited  $1s^2 2s5s$  Rydberg state, we used a set of 15 bound orbitals which is optimized over all the levels included. The resulting relativistic orbitals produced 162  $J\pi$  levels,  $J=0-5$ , even and odd parity. Selected results are shown in Table 2 for the  $1s^2 2s5s_{1/2}$  ( $^1S^e$ ) Rydberg state.

Tab. 2. The contributions(selection, in atomic units) to the scalar polarizability,  $\alpha_0(5s)$ , of the  $C^{2+}$  ion in the  $1s^2 2s5s$  ( $^1S^e$ ) state. The corresponding energy differences  $\Delta E_{gn} = E_n - E_{5s}$  are given in atomic units(au).  $a^b$  reads  $a \times 10^b$ .

Contribution	$\Delta E(\text{au})$	$f_{5s,n}$	$\alpha_0(5s)$
$2s5s_{1/2} \rightarrow 5p_{1/2}$	$4.5524^{-03}$	$3.5752^{-06}$	$0.7853^{-03}$
$\rightarrow 5p_{3/2}$	$8.8621^{-03}$	$9.8315^{-01}$	$110.94^{00}$
$\rightarrow 6p_{1/2}$	$6,2496^{-02}$	$5.9520^{-06}$	$0.9524^{-04}$
$\rightarrow 7p_{3/2}$	$6,4870^{-02}$	$9.9059^{-02}$	$1.5270^{00}$
$\rightarrow 8p_{1/2}$	$9,6860^{-02}$	$1.7075^{-06}$	$0.1763^{-04}$
$\rightarrow 8p_{3/2}$	$9,8218^{-02}$	$4.7571^{-03}$	$0.4843^{-01}$
$\rightarrow 9p_{1/2}$	$1,1916^{-01}$	$7.8027^{-06}$	$6.5481^{-05}$

$\rightarrow 9p_{3/2}$	$1.1988^{-01}$	$1.7396^{-02}$	$1.4511^{-01}$
------------------------	----------------	----------------	----------------

The dynamic polarisability,  $\alpha_d(\omega)$ , has been obtained as a measure of the energy shift of the ion given by the following equation:

$$\Delta E = -\frac{1}{2} \alpha_d(\omega) F^2 \quad (3)$$

where  $\alpha_d(\omega)$  is the polarizability of the quantum state at frequency  $\omega$ , and  $F$  is a measure of the strength of the ac electromagnetic field. The value of the dynamic polarizability in the  $\omega \rightarrow 0$  limit is the static dipole polarizability. We used the earlier R-matrix Floquet calculation to output the energy shift and the frequency dependent polarizability of studied Rydberg states.

### 3. Conclusions

In the present work we have studied the ionization dynamics of Rydberg states belonging to  $C^{2+}$  ion. For assessment purposes, two different direct methods have been used to output static polarisability. The dynamic dynamic polarizability of an atom gives a measure of the energy shift of the atom or ion in an electromagnetic field. We used results from earlier Floquet calculation to output the dynamic polarisabilities of studied Rydberg states. Recent studies propose using Rydberg dressing to explore many-body physics ultracold chemical reactions. As the spontaneous emission provide an intrinsic heating mechanism we intend to extend our work allowing the study o thermalization phenomena with full tunability of system parameters.

### 4. References

- [1] Gallagher T F, 1994 *Rydberg Atoms* (Cambridge university Press, Cambridge, England).
- [2] Zimmerman M L et al. 1979 *Phys.Rev. A* **20**, 2251(1979).
- [3] Millen J, Lothead G, and Jones M P A 2010 *Phys. Rev. Lett.* **105**, 213004 (2010).
- [4] Gorshkov A V, Hermele M, Gurarie V, Xu C, Julienne P S, Ye J, Zoller P, Demler E , Lukin M D , Rey A M 2010 *Nature Physics* **6** 289.
- [5] Hermele M , Gurarie V and Rey A M 2009 *Phys Rev Lett* **103** 135301.
- [6] Daley A J, Boyd M M, Ye J, Zoller P 2008 *Phys Rev Lett* **101** 170504.
- [7] Kim D S and Kwon H D 2012 *J. Phys. B: At. Mol. Opt. Phys.* **45** 185201
- [8] Kim D S and Manson S T 2010 *J. Phys. B: At. Mol. Opt. Phys.* **43** 155205
- [9] Stancalie V 2013, *Eur. Phys. J. D* **66** 223.
- [10] Stancalie V 2005 *Physics of Plasmas* **12**, 043301.
- [11] Dyal K G, Grant I P, Johnson C T, Parpia F A, Plummer E P 1989 *Comput Phys Commun.* **55** 425 .
- [12] Mitroy J, Safronova M S and Clark Ch W 2010 *J. Phys. B: At. Mol. Opt. Phys.* **43** 202001.

# EFFECT OF SMALL ADMIXTURE OF H<sub>2</sub>O ON THE ELECTRON DRIFT VELOCITY IN ARGON: EXPERIMENTAL MEASUREMENTS AND CALCULATIONS

Michal Stano<sup>1</sup>, Detlef Loffhagen<sup>2</sup>, Zoltán Donkó<sup>3</sup>, Nuno Pinhão<sup>4</sup>,  
Marek Kučera<sup>1</sup>, Štefan Matejčík<sup>1</sup>

<sup>1</sup>*Department of Experimental Physics, Comenius University, Mlynská dolina F2, 842 48 Bratislava*

<sup>2</sup>*Leibniz Institute for Plasma Science and Technology, Felix-Hausdorff-Str. 2, 17489 Greifswald, Germany*

<sup>3</sup>*Institute of Solid State Physics and Optics, Wigner Research Centre for Physics, Hungarian Academy of Sciences, 1121 Budapest, Konkoly Thege M. Str. 29-33, Hungary*

<sup>4</sup>*Institute of Plasmas and Nuclear Fusion, IST, University of Lisbon, Estrada Nacional 10, 2686-953 Sacavém, Portugal*

E-mail: stano@fmph.uniba.sk

The electron drift velocity in argon with admixtures of 50 to 10000 ppm of H<sub>2</sub>O was measured for reduced electric fields ranging from 0.05 to 2.5 Td. The results are compared with those obtained by Monte Carlo simulation and from the solution of the electron Boltzmann equation using a multiterm method based on Legendre polynomial expansion of the angular dependence of the velocity distribution function and the  $S_n$  method applied to a density gradient expansion representation of the distribution function. The calculations were performed using two sets of cross section data for H<sub>2</sub>O. In addition, the electron drift velocity was calculated using the same cross section data for pure H<sub>2</sub>O vapour and the results are compared with data from literature.

## 1. Introduction

Small admixtures of molecular gases are known to have a strong effect on electron transport parameters in argon. Electrical discharges in argon have a broad field of application in research and industry and properties of these discharges can be strongly influenced by small amounts of molecular admixtures [1]. The effect of the molecular admixture is due to inelastic electron collisions with the molecular admixture. In pure argon, all collisions of low energy electrons below 11.5 eV are inevitably elastic. When a molecular admixture is added, rotational and vibrational excitations become available and contribute strongly to the electron energy loss per collision. As a result, the electron energy distribution function is influenced and the electron transport parameters can change notably.

The electron drift velocity  $W$  is one of the transport parameters that can be measured with high accuracy. It has been observed that the addition of molecular admixtures in argon results in an increased  $W$  in a finite range of reduced electric field,  $E/n$ . If the increase of  $W$  is significant, it results in a local maximum of  $W$  as a function of  $E/n$ . The maximum is followed by a decrease of  $W$  with  $E/n$ , known as negative differential conductivity (NDC). It has been recognized that the occurrence of NDC depends mostly on the momentum transfer cross section and the cross sections of inelastic processes in a given gas mixture. Conditions for NDC are very favorable in argon with molecular admixtures, where inelastic collisions of electrons with a molecular admixture are present at electron energies where the momentum transfer cross section for argon rapidly increases due to the Ramsauer-Townsend effect [2].

The high sensitivity of  $W$  on molecular admixtures offers an opportunity to verify and improve cross section sets for the molecular admixture, in particular cross sections for rotational and vibrational excitation by electron impact. In the present contribution, experimental and theoretical studies of the electron drift velocity in argon with small amounts of water vapour are reported for low reduced electric field values between 0.05 and 2.5 Td with 1 Td =  $10^{-21}$  V m<sup>2</sup> and admixtures of up to 10000 ppm H<sub>2</sub>O. After a description of the main aspects of the electron drift velocity measurement and of the two different numerical techniques used, results of the drift velocities calculated using two cross section data sets are

discussed and compared with present experimental data and with earlier results available from the literature.

## 2. Experimental setup

The measurements have been performed using a single shutter drift tube at ambient pressure and room temperature. The drift tube is shown schematically in Figure 1. A detailed description of the instrument is given in [3]. Free electrons generated by a corona-like discharge are periodically released into the drift tube in short pulses (0.5 or 1  $\mu$ s) using an electronic shutter. The electron current is measured at the end of the drift tube using a shielded collector and amplified and recorded by a digital oscilloscope. The drift velocity is determined from the drift time of electrons between the shutter and the collector. The discharge is fed by argon with an admixture of few percent nitrogen. The role of the nitrogen is to improve the stability of the discharge. The drift tube is fed by argon with an admixture of H<sub>2</sub>O. The gas mixture is prepared by mixing pure argon with “wet” argon. All flows are controlled using MKS<sup>TM</sup> mass flow controllers and the concentration of H<sub>2</sub>O admixture is monitored using a Cermet II hygrometer from Michell Instruments.

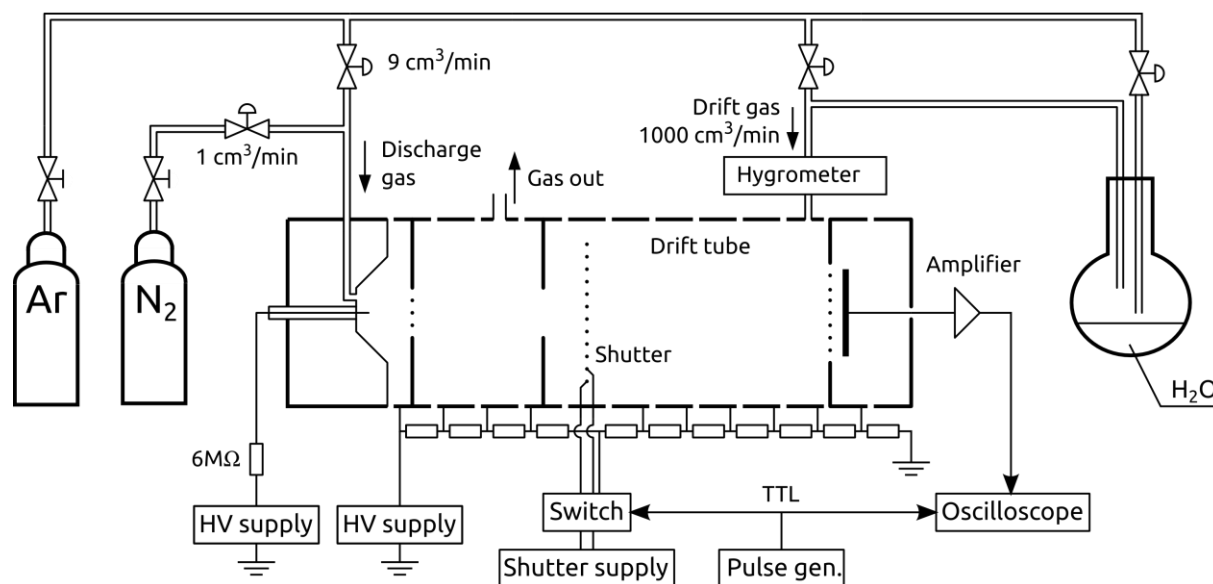


Fig. 1. Schematics of the experimental setup.

## 3. Simulation of electron swarm

Calculations of the electron drift velocity have been performed using three different methods: Monte Carlo simulation (referred to as I), a multiterm method for solving the time- and space-independent Boltzmann equation for the electron velocity distribution function (evdf) for given  $E/n$  (referred to as II) and a discrete ordinates method to solve the Boltzmann equation for density gradients expansion representation of the evdf (referred as III). Details of the numerical methods can be found in [3] and references therein.

All calculations used the electron-argon cross sections recommended by [4], while two sets of cross sections on electron-water vapour collisions were used for the calculations. The first one is recommended by Yousfi and Benabdessadok [5] (referred to as Y-B set), while the second one (referred to as L-B set) uses the more recent elastic momentum transfer cross section for H<sub>2</sub>O from [6] and neglects the first four rotational excitation cross sections of [5] resulting from Born approximation calculations.

#### 4. Results

In Figure 2, measured and calculated values of the electron drift velocity are shown as a function of  $E/n$ . The Y-B set of cross sections was used for calculations by the numerical approaches for H<sub>2</sub>O concentrations up to 2500 ppm, neglecting super-elastic collisions. All the methods give almost identical results indicating the high accuracy of each technique. In addition, Method II was used for calculations up to 10000 ppm H<sub>2</sub>O using the same set of cross sections, and also for calculations using the L-B set of cross sections in the whole range of H<sub>2</sub>O concentrations studied. Furthermore, Method III was used up to 5000 ppm and to study the influence of super-elastic collisions with the rotational levels. Moreover, the present experimental results and earlier results by Hurst et al. [7] are also shown.

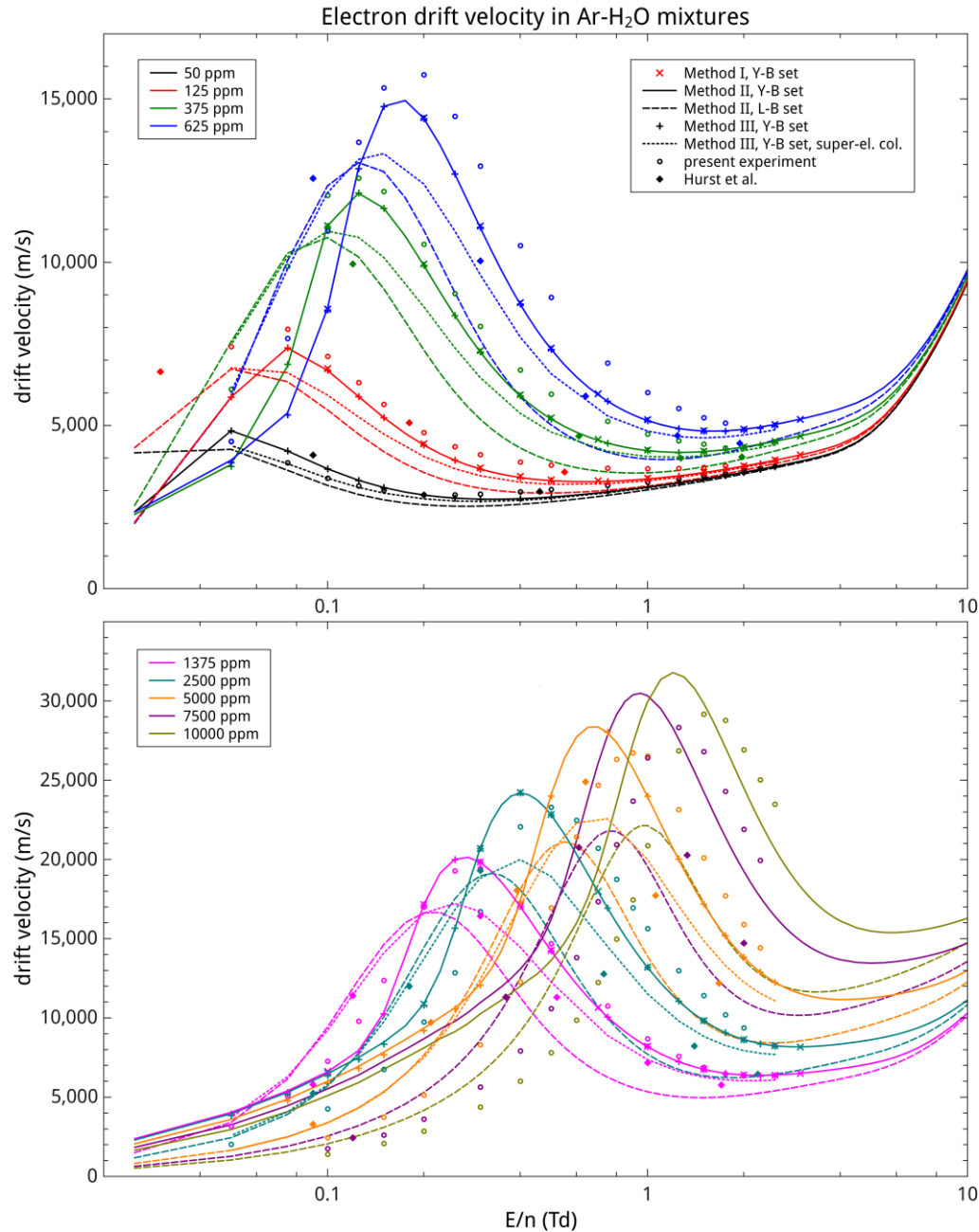


Fig. 2. Present experimental and calculated results of  $W$ . The sets of cross sections are indicated in the legend.

Both the experimental and calculated results show the same trends and exhibit a distinguished maximum of  $W$  at low  $E/n$ . Calculations performed using the two different cross section data sets differ significantly from each other and demonstrate the high sensitivity on the choice of the cross section data. In particular, the momentum transfer cross section of elastic collisions and the rotational excitation cross sections of  $\text{H}_2\text{O}$  have a remarkable impact on the drift velocity in the  $E/n$  range considered in the present studies. Super-elastic collisions with the rotational levels lead to a significant change on the results from the Y-B set and to a much better agreement with the experimental results from Hurst et al. [7]. The comparison of the calculated results with the present experimental ones shows that reasonable agreement is obtained only with Y-B set of cross sections. The agreement is generally better for low  $\text{H}_2\text{O}$  concentrations.

In addition to the study in Ar- $\text{H}_2\text{O}$  mixture, the electron drift velocity was also calculated for pure water vapour using both sets of cross sections. The results are shown in Fig. 3 together with experimental data measured by Lowke and Rees [8].

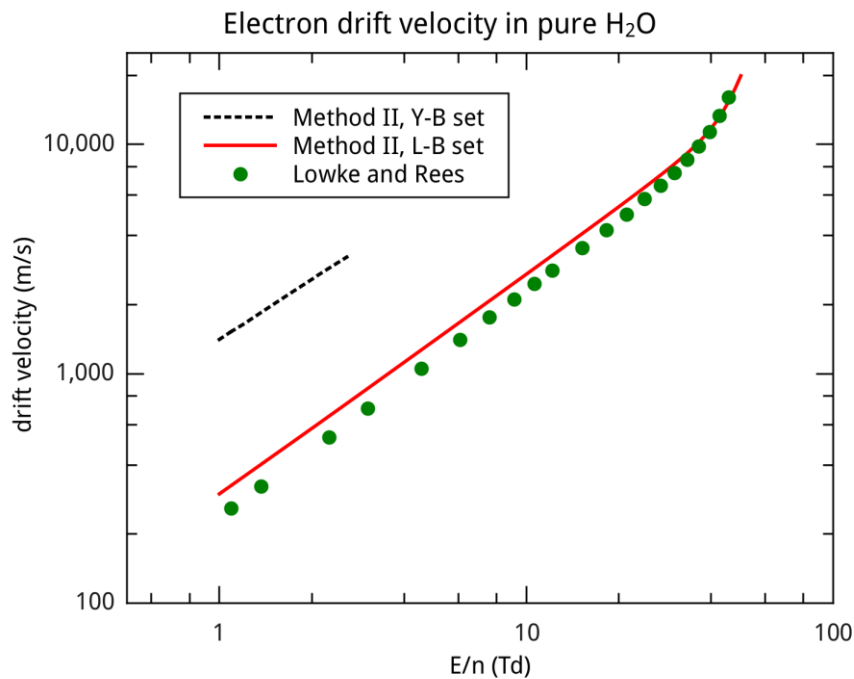


Fig. 3. Comparison of electron drift velocity in pure water vapour calculated using the same cross section data sets as in the Figure 2 and earlier experimental results by Lowke and Rees [8].

In contrast to the previous situation in Ar- $\text{H}_2\text{O}$  mixtures, good agreement of calculated results with the measured data is obtained when the L-B set of cross sections is used. The results of calculations based on the Y-B cross sections exceed the measured data by about a factor of five in this case.

It can be seen that although each set of cross sections leads to satisfactory results in one or the other situation, none of the cross section sets is satisfactory for the electron drift velocity in both argon-water mixtures and in pure  $\text{H}_2\text{O}$  vapour. Due to the high importance of electron-water collisions and simulations involving these collisions, further measurements and calculations are necessary to find reliable cross section data for a broad range of conditions.

## Acknowledgement

The work was supported by German Research Foundation within the Collaborative Research Centre Transregio 24, by the Hungarian Fund for Scientific Research (Grant OTKA - K105476), by the Slovak Research and Development Agency under Contract No. APVV-0733-11 and VEGA grant agency project Nr. 1/0514/12.

## References

- [1] Y. Z. Ionikh, N. A. Dyatko, A. V. Meshchanov, A. P. Napartovich, F. B. Petrov, *Plasma Sources Sci. Technol.* **21** (2012) 055008.
- [2] Z. L. Petrovic, R. W. Crompton, G. N. Haddad, *Aust. J. Phys.* **37** (1984) 23.
- [3] M. Stano, N. Pinhao, D. Loffhagen, M. Kucera, Z. Donko, S. Matejcik, *Eur. Phys. J. D* **65** (2011) 489.
- [4] M. Hayashi, in *Plasma Material Science Handbook* (Japan Society for the Promotion of Science, Ohmsha, Ltd. Tokyo), pp. 748
- [5] M. Yousfi, M. D. Benabdessadok, *J. Appl. Phys.* **80** (1996) 6619.
- [6] M. Elford, S. Buckman, M. Brunger, *6.3 Elastic momentum transfer cross sections*, Y. Itikawa (ed.), SpringerMaterials – The Landolt-Börnstein Database (<http://www.springermaterials.com>)
- [7] G. S. Hurst, L. B. O’Kelly, T. E. Bortner, *Phys. Rev.* **123** (1961) 1715.
- [8] J. J. Lowke and J. A. Rees, *Aust. J. Phys.* **16** (1963) 447.



# COLLISIONAL FORMATION OF H<sup>-</sup> ANIONS AND PROTONS FROM HYDROGEN-CONTAINING MOLECULAR SPECIES VIA A BINARY-ENCOUNTER PROCESS

Z. Juhász<sup>2</sup>, E. Lattouf<sup>1</sup>, J.-Y. Chesnel<sup>1</sup>, S. T. S. Kovács<sup>2,3</sup>, E. Bene<sup>2</sup>, P. Herczku<sup>2,3</sup>,  
B. A. Huber<sup>1</sup>, A. Méry<sup>1</sup>, J.-C. Pouilly<sup>1</sup>, J. Rangama<sup>1</sup> and B. Sulik<sup>2,\*</sup>

*1 Centre de Recherche sur les Ions, les Matériaux et la Photonique (CIMAP), Unité mixte CEA-CNRS-Ensicaen-Université de Caen Basse-Normandie, UMR 6252, 6 Boulevard Maréchal Juin, F-14050 Caen cedex 04, France*

*2 Institute for Nuclear Research, Hungarian Academy of Sciences (MTA Atomki), H-4001 Debrecen, P.O. Box 51, Hungary*

*3 University of Debrecen, Ph.D. School of Physics, H-4032 Debrecen, Egyetem tér 1, Hungary*  
E-mail: sulik@atomki.mta.hu

Molecular fragmentation leading to the formation of negatively and positively charged hydrogen ions in 7-keV OH<sup>+</sup> + Ar collisions and other collision systems is investigated experimentally. The double-differential fragment-ion spectra show that the emission of H cores is driven by their scattering on the atomic target. However, in addition to this binary-encounter process, dissociative electronic excitation of the molecular projectile has to be invoked to explain the observed fragmentation patterns. Surprisingly, the negative and positive hydrogen ions are emitted with very similar angular dependencies. The H<sup>-</sup> to H<sup>+</sup> ratio was larger than 1%. Emission of the highly reactive H<sup>-</sup> ions with such yields may be important in astrophysics and biology.

## 1. Introduction

In this work we report observation of H<sup>-</sup> and H<sup>+</sup> formation in collisions of 7-keV OH<sup>+</sup> projectiles with Ar atoms. Similar collision systems have also been measured. Hydrogen anions can be formed in collisions between cations and neutral atoms or molecules. Several studies have shown the formation of H<sup>-</sup> ions in soft collisions involving negligible momentum transfer between the collision [1-6]. However, in a recent study [7], we observed that H<sup>-</sup> ions can also be created in hard collisions involving energetic encounters between atomic cores. In OH<sup>+</sup> + Ar collisions, the observed H<sup>-</sup> ions were formed by a combined process, in which the incoming proton was scattered by the Ar target to large angles and then captured two electrons when leaving the collision complex. In the whole investigated angular range (30°-150°), the kinematics of the H<sup>-</sup> fragment could be well described by a simple two-body scattering calculation for the binary collision of the H atom on the Ar target. In the present work we extend our experiments to much smaller angular ranges, down to the limit, where two-body collisions cannot provide sufficient energy transfer for breaking the molecular bond. Another extension of the earlier studies is that we measured both the H<sup>-</sup> and H<sup>+</sup> productions directly.

## 2. Experiment

The experiments were conducted at the ECR ion source of the ARIBE facility, at GANIL in Caen, France. Electrons and negative ions produced in the collision were detected at angles ranging from 3° to 150° with respect to the beam direction. The same experimental method has been described in a previous work [7]. It consists in a crossed-beam type experiment in the gas phase. The ion beam was delivered by an ECR ion source. In the collision chamber, it interacted with an effusive gas jet before ending up in a Faraday cup. The latter was used for continuous measurement of the ion beam current in order to normalize the cross sections. The fragments emerging from the investigated collisions were selected according to their kinetic energy per charge unit by means of a 45° parallel plate electrostatic analyzer, with an energy resolution of 5%. This spectrometer was fixed on a rotatable ring allowing the selection of

the angle of detection with respect to the ion beam direction, with an angular acceptance of  $2^\circ$ . The particles transmitted by the spectrometer were post-accelerated to  $\sim 1$  keV and detected by a channel electron multiplier (channeltron). In the present experiments both atomic and molecular projectile ions have been impacted on atoms and small molecules (eg., Ar, H<sub>2</sub>O). Moreover, both the positive, and the negative charged particles have been analysed by changing the polarity of the analyser voltage.

### 3. Results

The most remarkable feature of the spectra of the negative particles was the appearance of well-defined peaks [7]. These structures could not be attributed to electron emission. A kinematic analysis has shown that the peaks were due to the emission of H<sup>-</sup> ions from the OH<sup>+</sup> projectile ion and the molecular targets. From the peak areas, we determined the cross sections for the H<sup>-</sup> production, and compared them with classical two-body potential-scattering calculations. A notable feature of H<sup>-</sup> emission is that its cross section is proportional to the calculated elastic scattering cross sections (H + Ar for the emission from the projectile, and the sum of H + C and H + O cross sections for the emission from the acetone target). We also measured the spectra of the positive ions in the same energy regions. As it was expected, the same peaks appeared in the cation (proton) and anion spectra. Comparison of the line energies and the measured cross sections with model calculations and other experiments are shown in Figs 1 and 2 for the OH<sup>+</sup> + Ar collision system.

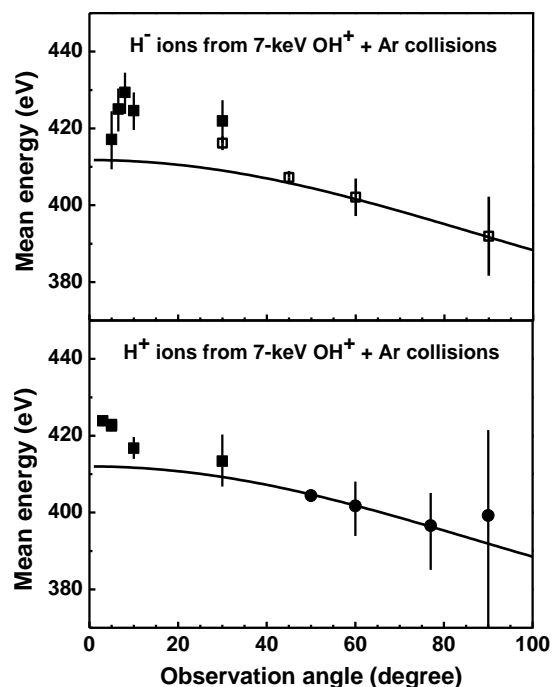


**Fig. 1.** Average kinetic energy of H<sup>-</sup> (top) and H<sup>+</sup> (bottom) ions resulting from binary encounter collisions between the H atom of the projectile and the Ar target atom. Filled squares: present results. Open circles: earlier results from [7]. Solid line: predicted final energy of the H ions assuming a pure two-body elastic scattering of a 412-eV H atom on Ar [7].

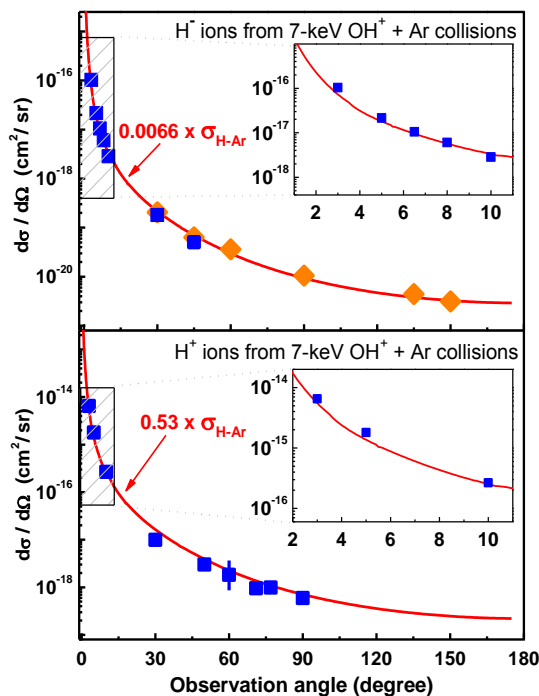


**Fig. 2.** Single differential cross sections (SDCS) for H<sup>-</sup> (top) and H<sup>+</sup> (bottom) emission as a function of the observation angle (blue squares). Only relative error bars (due to statistical uncertainties and due to the sin(θ) correction) are shown. Orange diamonds: earlier results from [7] with the present normalization procedure. Red curves: calculated cross section for two-body elastic scattering of 412-eV H on Ar, multiplied by factors representing the fraction of the different charge state components.

Our most important findings can be summarized as follows. Negative and positive hydrogen ions are emitted in  $\text{OH}^+ + \text{Ar}$  collisions with nearly the same angular dependence from very small to large scattering angles. For both  $\text{H}^+$  and  $\text{H}^-$  fragments, the measured emission cross sections are proportional to the calculated single differential cross section for elastic scattering of an incident H atom on an Ar atom. This feature is not only true for large emission angles ( $> 10^\circ$ ) due to violent binary collisions involving non-negligible momentum transfer at small impact parameter ( $< 1$  a.u.), but also for small angles ( $< 10^\circ$ ) resulting from soft collisions at large impact parameters ( $> 1$  a.u.). The comparison of the experimental data with the results of a three-body scattering simulation leads to a similar finding. Consistently, the ratio of  $\text{H}^-$  to  $\text{H}^+$  cross sections has been found to be constant in the whole investigated angular range. The fractions of negative and positive H ions among all the emitted H fragments do not depend on the emission angle, and thus, barely depends on the momentum transferred to the proton during the collision.

Accordingly the production of negative hydrogen ions can be explained in terms of a two step process: (i) A large momentum transfer collision liberates a proton. (ii) The receding proton grabs two electrons in a double capture process with a practically observation-angle-independent probability. We also found a surprising agreement between the two-body model calculations and some earlier experimental data [2] for  $\text{H}^{2+} + \text{Ar}$  collisions at the same velocity. The process seems to be a generally relevant one since it may take place in any collisions of H-containing molecules at few-keV energies.

This work was supported by the Transnational Access Program ITS-LEIF, the European Project HPRI-CT-2005-026015, the Hungarian National Science Foundation OTKA (K73703 and K109440), the French-Hungarian Cooperation Program PHC Balaton (27860ZL, T  T\_11-2-2012-0028, T  T F-30/06), the French-Hungarian CNRS-MTA Cooperation number 26118 (ANION project) and the T  MOP-4.2.2/B-10/1-2010-0024 projet, co-financed by the EU and the European Social Fund.

## 4. References

- [<sup>1</sup>] A.R.P. Rau, *J. Astrophys. Astron.* **17**, 113 (1996)
- [<sup>2</sup>] A. Dreuw and L. S. Cederbaum, *Chem. Rev.* **102**, 181 (2002)
- [<sup>3</sup>] T. Andersen, *Phys. Reports* **394**, 157-313 (2004).
- [<sup>4</sup>] S. C. Glover, D. W. Savin, A.-K. Jappsen, *Astrophys. J.* **640**, 553 (2006)
- [<sup>5</sup>] T. Ross *et al.*, *Astrophys. J.* **684**, 358-363 (2008).
- [<sup>6</sup>] O. Martinez Jr., Z. B. Yang, N. J. Demarais, T. P. Snow, V. M. Bierbaum, *Astrophys. J.* **720**, 173-177 (2010) and references therein.
- [7] Z. Juh  sz, B. Sulik, J. Rangama, E. Bene, B. Sorgunlu-Frankland, F. Fr  mont, and J.-Y. Chesnel, *Phys. Rev. A* **87**, 032718 (2013).

# CLASSICAL AND QUASI-CLASSICAL MONTE CARLO CODE FOR THE ANALYSIS OF ION-ATOM COLLISIONS

Roland Lohner<sup>1</sup>, and Károly Tőkési<sup>1</sup>

<sup>1</sup>*Institute for Nuclear Research, Hungarian Academy of Sciences, Debrecen, Hungary, EU*

E-mail: lohner.roland@gmail.com, tokesi@atomki.mta.hu

A renaissance in classical methods, particularly methods based on trajectory calculation started over the 60's in atomic physics. In order to revise these classical calculations and investigate ion-atom collisions we developed a Monte-Carlo simulator program. The program written in C++ is flexible so that it can be easily modified in order to use an arbitrary quasi-classical atomic model or an arbitrary number of particles. The software has a high-level abstraction in the domain of atomic physics, the computer model represents atoms, nuclei, electrons, orbitals. To highlight the efficiency of the code we present cross-sections of different collision processes involving charge transfer. Our calculations fit in well with preliminary computational and experimental results.

## 1. History of the Field

A renaissance in classical methods, particularly methods based on trajectory calculation started over the 60's in atomic physics. The investigation of ion-atom collisions has been strongly motivated by a paper of Abrines and Percival [1] in year 1966. They published results on collision of classically represented hydrogen atom and proton. This was followed by a large amount of papers investigating classical description of atomic collisions and researching into quasi-classical models of multi-electron systems up to atomic number  $z=94$  in the next decades. A very prominent quasi-classical atomic model was introduced and applied by Kirschbaum and Wilets [2] in 1980. This model introduced new types of interactions between the particles in order to represent quantum-mechanical effects like the Heisenberg uncertainty principle and the Pauli Exclusion Principle in the classical description. These impulse-dependent interactions stabilize multi-electron systems.

## 2. The Monte-Carlo simulator program

In order to carry out quasi-classical calculations of ion-atom collisions we developed a Monte-Carlo simulator program which can host classical and quasi-classical atomic models. The program written in C++ implements a flexible framework so that it can be easily modified in order to use an arbitrary quasi-classical atomic model or an arbitrary number of particles. The atomic models hosted by the framework are based on classical trajectory calculation of the nucleus and electrons. The hosted model may contain an arbitrary number of two-body interactions defined by the framework user.

The software has a high-level abstraction in the domain of atomic physics; the computer model represents atoms, nuclei, electrons, orbitals. Physical properties like binding energies, momenta, or angular momenta can be queried referred to the whole atom or to individual electrons. Introduction of a specific atomic model is as easy as defining two class methods which are responsible for (1) setting up the initial conditions of the particles inside an atom and (2) declaring the interactions between intra-atom particles. We worked out two specific atomic models; the classical Abrines-Percival model and the quasi-classical Kirschbaum-Wilets model.

Figure 1. shows the software component diagram. The applied program libraries, Boost, Odeint and the standard C++ library, are denoted in the bottom. Boost is a program library developed for the C++ language and supports common data types and programing tasks. Odeint is a modern, highly flexible C++ library for numerically solving ordinary differential equations at top performance. The Multibody

Dynamics Module implements a general purpose many body (n-body) simulator which numerically integrates the equations of motion of a mechanical system consisting of arbitrary bodies and interactions. The features of various numerical integration methods and error control are provided by Odeint.

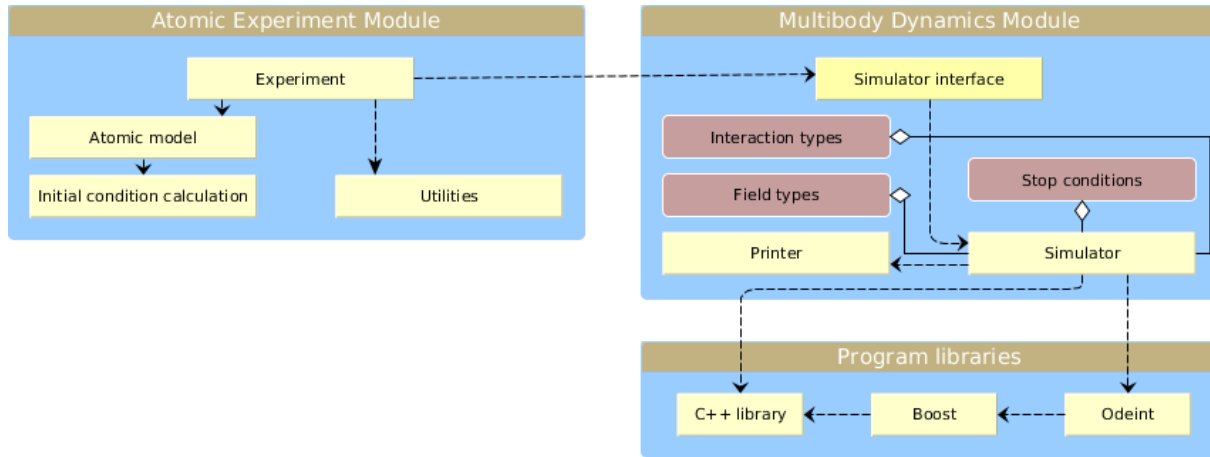


Fig. 1. Software component diagram

### 3. Classical calculations

With the help of the new simulator program we investigated atomic collisions and calculated cross-sections of different collision processes involving charge transfer. First we analyzed the collision of proton projectile and hydrogen atom in the energy range of 20-600 keV using the atomic model worked out by Abrines and Percival [1]. We reconstructed and revised preliminary calculations of Cohen [3] in order to (1) prove the proper functioning of the Monte-Carlo simulator program developed and to (2) carry out these calculations using much higher multitude of trajectories, resulting in lower statistical errors.

The nucleus and electron of the hydrogen atom and the proton projectile form a three-body system. The Abrines-Percival model is a purely classical approach, thus it only considers Coulomb-interactions between the particles. The electron is revolving around the nucleus on an ellipse-shaped Kepler orbit. Initial conditions of the motion are set using random numbers, so the orbital eccentricity, the phase of revolution and the direction of the Kepler plane are chosen randomly using appropriate distributions. Consequently, the spherical hydrogen orbital is represented by a population of planar Kepler orbits oriented in random directions.

During the calculations three types of main collision processes might take place: a) direct process b) ionization and c) electron capture. We calculated the total cross-sections of the ionization process and the electron capture process determining 1.000.000 trajectories in case of each collision energy.

In comparison with preliminary computational and experimental measurements our results appeared to be quite accurate. Figure 2. shows cross-section of the ionization process. Our results marked with red circles are quite close to preliminary calculations of Cohen [3] marked with blue circles and to experimental results of Shah [4]. Looking at the diagram more carefully we can decide that our results are closer to experimental measurements than results of Cohen regarding every collision energy. The calculated cross-section of the electron capture process is also in quite good agreement with preliminary results.

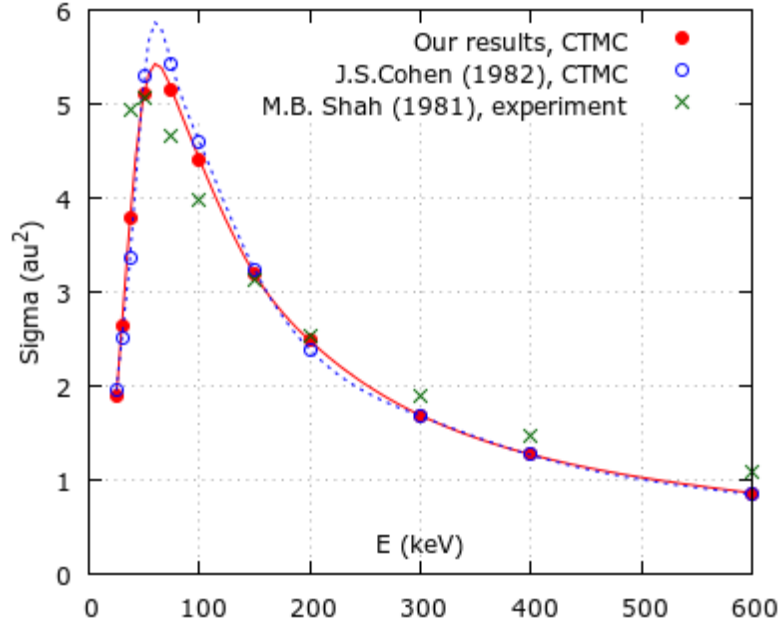


Fig. 2. Cross-section of the ionization process  $p^+ + H \rightarrow p^+ + p^+ + e^-$

#### 4. Quasi-classical calculations

The purely classical Abrines-Percival model described in the previous chapter cannot handle multi-electron systems. Even helium atom behaves unstably and goes into auto-ionization within the confines of the model. In order to stabilize multi-electron atoms we implemented and applied the Kirschbaum-Wilets atomic model [2]. This quasi-classical atomic model introduces new types of interactions between the particles in order to represent quantum-mechanical effects. The so-called Heisenberg potential represents the Heisenberg uncertainty principle in the classical description and can be written in the form:

$$V_H(r_i, p_i) = \frac{(\xi_H \hbar)^2}{4\alpha r_i^2} \exp \left( \alpha \left[ 1 - \left( \frac{r_i p_i}{\xi_H \hbar} \right)^4 \right] \right) \quad (1)$$

where  $r_i$  and  $p_i$  are the relative position and momentum of electron (i) referenced to the nucleus. The value of  $\xi_H$  is determined by requiring  $r_0 p_0 = \xi_H$  for the ground state.  $\alpha$  is called the hardness parameter. Deployment of this impulse-dependent interaction stabilizes helium atom and other multi-electron systems. Figure 3. shows the two orbits of a stable helium atom represented in the Kirschbaum-Wilets model. The radial oscillation is a consequence of the Heisenberg potential applied.

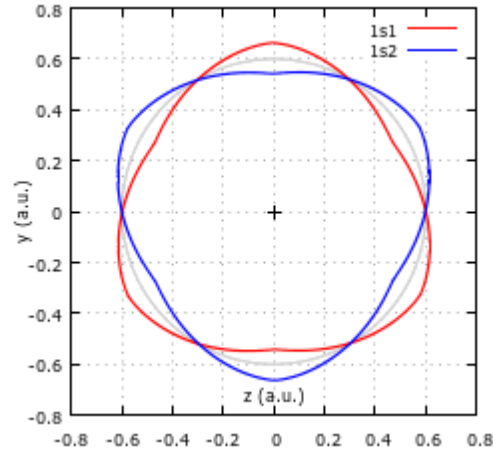
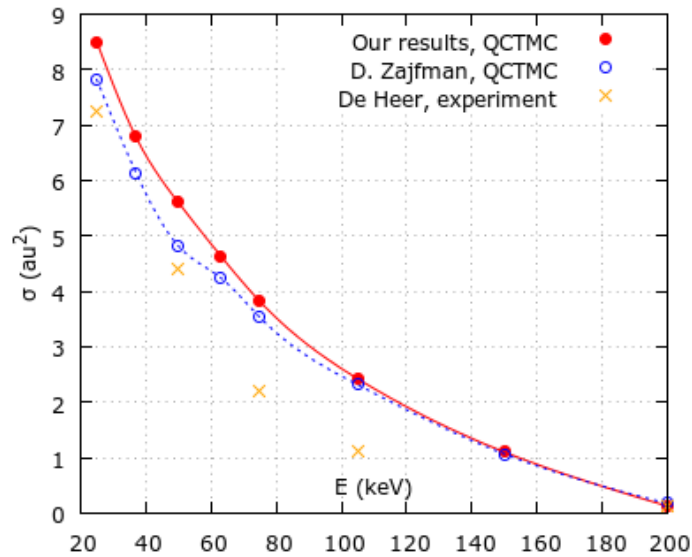


Fig. 3. Orbits of a helium atom represented in the Kirschbaum-Wilets model

Last, we simulated the collision of proton and helium atom using the Kirschbaum-Wilets model and determined the cross-sections of the single ionization process and the single electron capture process. Our calculations fit in well with preliminary computational and experimental results. Figure 4. shows the total cross-section of the single electron capture process. Our results marked with red circles are close to preliminary calculations of Zajfman [5] marked with blue circles and estimate moderately experimental



results of De Heer [5].

Fig. 4. Cross-section of the single electron capture process  $p^+ + \text{He} \rightarrow \text{H} + \text{He}^+$

## 5. References

- [1] R. Abrines and I. C. Percival 1966 *Proc. Phys. Soc. London* **88** 861.
- [2] C. L. Kirschbaum and L. Wilets 1980 *Phys. Rev. A* **21** 21.
- [3] James S. Cohen 1982 *Phys. Rev. A* **26** 3008.
- [4] M. B. Shah and H. B. Gilbody 1981 *J. Phys. B* **14** 2361.
- [5] D. Zajfman and D. Maor 1986 *Phys. Rev. Lett.* **56** 320.

# ELASTIC AND INELASTIC GUIDING OF ELECTRONS THROUGH MICROMETER-SIZED FUNNEL-SHAPED GLASS CAPILLARIES

S. J. Wickramarachchi<sup>1</sup>, T. Ikeda<sup>2</sup>, D. Keerthisinghe<sup>1</sup>, B. S. Dassanayake<sup>3</sup>  
and J. A. Tanis<sup>1</sup>

<sup>1</sup>*Department of Physics, Western Michigan University, Kalamazoo, MI 49008, USA*

<sup>2</sup>*RIKEN Nishina Center for Accelerator Based Science, 2-1 Hirosawa Wako, Saitama 351-0188, Japan.*

<sup>3</sup>*Department of Physics, Faculty of Science, University of Peradeniya, Sri Lanka*

E-mail: samanthi.j.wickramarachchi@wmich.edu

An experimental study of electron transmission for 500 and 1000 eV incident energies through a micrometer sized funnel-shaped (tapered) glass capillary with inlet diameter 800  $\mu\text{m}$ , outlet diameter 100  $\mu\text{m}$  and a length of 35 mm has been made. Both elastic and inelastic transmissions leading to separate peaks are present in the beam profile. Elastic guiding dominates the transmission for 500 eV while inelastic guiding is dominant for 1000 eV.

Beam transmission through single glass capillaries (straight, conical and funnel-shaped) has been studied from the point of view of fundamental characteristics and has also been used to study the applications of micro-beams, which are useful in various biological and technical applications [1]. In the present work, the energy and angular dynamics of electron transmission through a funnel-shaped (tapered) borosilicate glass capillary have been studied for 500 and 1000 eV incident energies. These measurements were done at Western Michigan University using a sample obtained from the RIKEN laboratory in Japan.

The transmission of electrons through the funnel-shaped glass capillary was obtained for a range of tilt angles of the capillary axis with respect to the incident beam direction. The tilt angle is referred to as  $\psi$  and the observation angle as  $\theta$ . The capillary had inlet/outlet diameters of 800  $\mu\text{m}$ /100  $\mu\text{m}$  and a length of 35 mm. The beam was transmitted for experimental tilt angles as large as  $\sim 6.0^\circ$  at 500 eV and  $\sim 8.0^\circ$  at 1000 eV. The experimental method and a schematic of the experimental set up can be found in Ref. [2].

In Figure 1(a) contour plots for 500 eV are shown for three different tilt angles for which the highest intensity of the transmission occurs at about 512 eV and the width of the energy distribution (along the y axis) is about 15 eV. These values are the centroid energy of the incident beam (without the sample in place) and approximate energy resolution of the spectrometer, respectively. The same behavior was observed up to  $\psi = -5.5^\circ$ . Accordingly, the studied spectra for 500 eV show a dominance of elastically transmitted electrons for tilt angles up to  $-5.5^\circ$ . Figure 1(b) shows data for 1000 eV with the transmitted electrons having energies generally smaller than the incident beam energy (1024 eV) and widths significantly broader than the spectrometer energy resolution of about 30 eV. The centroid energies and widths of the transmitted beam represent significant energy losses. These energy losses were observed even for a small tilting of the capillary axis as seen in the figure for  $\psi = -3.0^\circ$  and  $-0.6^\circ$  (center and right-hand panels), indicating that electrons undergo inelastic scattering with the inner surface of the capillary for 1000 eV. Elastic transmission at 1000 eV was observed within the range of the aspect ratio ( $-0.8^\circ \leq \psi \leq -0.4^\circ$ ) as seen for  $\psi = -0.6^\circ$ , where electrons do not interact with the inner capillary walls.

The differences in the transmission mechanism for the two energies can be explained by the potentials resulting from the charge patch(es) that are formed when the incident beam strikes the inner wall of the capillary. For 500 eV this potential is sufficient to cause the electrons to be deflected without hitting the wall, while this is apparently not the case for 1000 eV. These results suggest that the corresponding potential for 1000 eV is insufficient to bend the electron trajectories, in which case



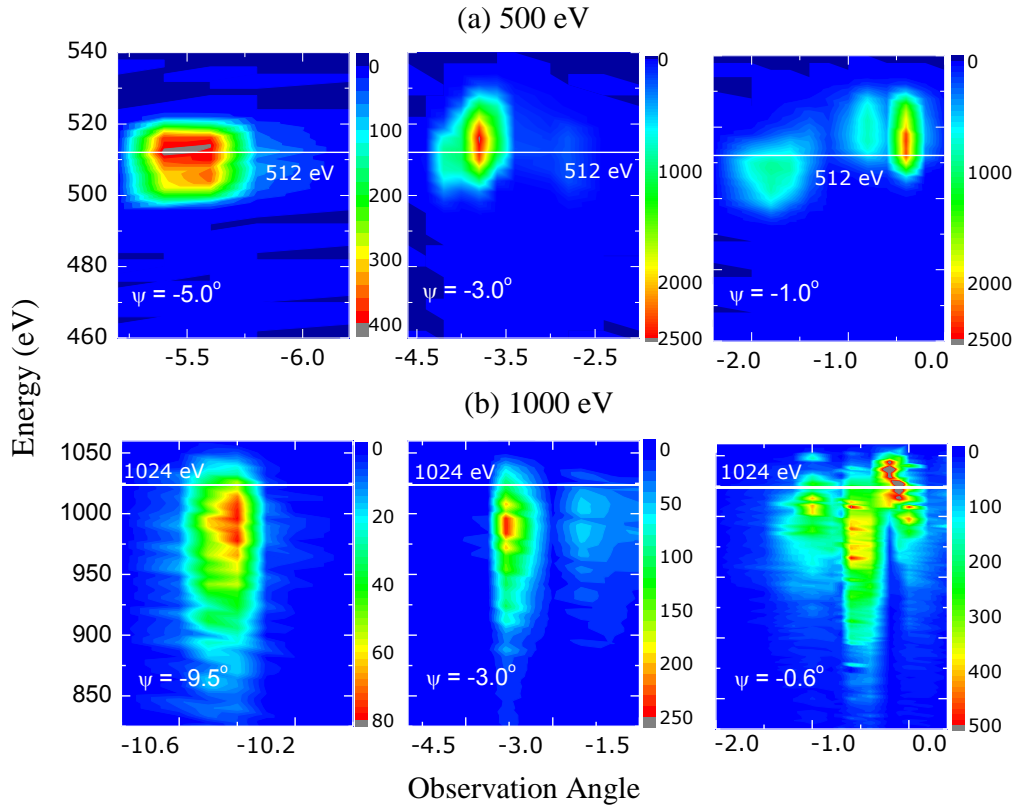


Fig. 1. Contour plots at (a)  $\psi = -5.0^\circ$ ,  $-3.0^\circ$  and  $-1.0^\circ$  for 500 eV and (b)  $\psi = -9.5^\circ$ ,  $-3.0^\circ$  and  $-0.6^\circ$  for 1000 eV showing the intensities vs. the electron energy and the observation angle at each tilt angle. The colors from blue (minimum) to red (maximum) show the number of electron counts. The horizontal white solid lines show the incident beam energy (512 eV and 1024 eV).

most of the transmitted electrons undergo close collisions with the wall and lose some of their incident energy. However, compared to HCIs electron bombardment is insufficient to form strong charge patches on insulator surfaces [3] due to the secondary electron emission that occurs upon electron impact. Further measurements are planned to understand the fundamental properties of electron transmission when traveling through insulating glass capillaries.

